Geology and Mineralisation of the Endeavour 41 Gold Deposit, Cowal District, NSW, Australia

by
Wojciech Zukowski
M.Sc.

Submitted in fulfilment of the requirements for the degree of
Doctor of Philosophy
November, 2010

UNIVERSITY
OF TASMANIA

CODES, ARC Centre of Excellence in Ore Deposits at the University of Tasmania

Statement

This thesis contains no material which has been accepted for the award of any other degree or diploma in any tertiary institution and, to the best of my knowledge and belief, contains no copy or paraphrase material previously published or written by another person, except where due reference is made in the text of the thesis.

Date:

Signature:

Authority of access

This thesis is not to be made available for loan or copying for one year following the date this statement was signed. Following that time the thesis may be made available for loan and limited copying in accordance with the *Copyright Act 1968*.

Date:

Signature:

Abstract

Epithermal and porphyry styles of alteration and mineralisation occur at the Endeavour 41 (E41) gold deposit in the Cowal Igneous Complex, New South Wales, Australia. E41 is one of three economically significant gold centres (E46, E42 and E41) in the Cowal district. These deposits formed within the Ordovician Macquarie island arc by subduction-related processes, and are hosted by a subaqueous volcano-sedimentary succession of interbedded sedimentary and resedimented volcaniclastic facies, trachyandesite and porphyritic andesites. The volcanic facies architecture at E41 is consistent with a distal submarine volcanic setting.

The host succession at E41 has been intruded by numerous sills, dykes and stocks, which define the E41 intrusive complex. The magmas evolved from mafic to more felsic and then back to mafic compositions with time. There is evidence of both mafic and silicic magmatism of high-K to shoshonitic affinity at the time of gold mineralisation, consistent with an alkalic association for gold mineralisation.

The pre-mineralisation Muddy Lake diorite intruded the Cowal district at 461 ± 5.2 Ma. The stratigraphy was then tilted prior to the emplacement of numerous dykes and mineralised veins. A mafic monzonite intrusion emplacement after tilting at 458.5 ± 5.2 Ma provides the upper age constraint on deformation. Magmatic activity culminated in the emplacement of a series of post-mineralisation dioritic dykes around 450 to 447 Ma. Geochronological results have identified two mineralising events in the Cowal district: (a) calc-alkalic Cu-Au porphyry deposits formed in the southeastern part of the district at around 463 Ma, based on Re-Os dating of molybdenite from E43, and (b) epithermal deposits formed in the central western part of the district around 455 Ma (E41, E42 and E46).

The earliest fluids that caused hydrothermal alteration at E41 were magmatic-hydrothermal in origin. They produced potassic alteration (magnetite ± biotite) in clastic units and high temperature propylitic alteration (actinolite – magnetite) in diorite. Rare magnetite- and andradite-bearing veins formed during this early phase of magmatic-hydrothermal activity. These early fluids were relatively oxidised (hematite- and andradite-stable), hot ~ >400º C (biotite- and actinolite-stable) and had near-neutral to alkaline pH (feldspar-calcite stable).

The early high-temperature alteration assemblages and veins have been overprinted by gold-mineralised domains associated with lower-temperature alteration facies. Gold mineralisation at E41 formed during two veining events: (1) quartz – pyrite ± calcite ± adularia veins (stage 3); and (2) carbonate-base metal sulphide

veins that contains calcite, ankerite, quartz, pyrite, sphalerite, galena, chalcopyrite, Ag-tellurides, arsenopyrite, hematite, apatite, illite ± muscovite and chlorite (stage 4). Gold occurs principally in the crystal lattice of arsenian pyrite. Stage 4 mineralisation produced Au-Ag-tellurides and Au inclusions in pyrite, sphalerite and chalcopyrite. Hydrothermal alteration halos associated with stage 3 veins evolved from high temperature epidote and K-feldspar – epidote to illite – muscovite – K-feldspar alteration. Stage 4 mineralisation is spatially and temporally associated with illite – muscovite – carbonate alteration assemblages. Late stage gypsum-, calcite-, epidote-, prehnite-, hematite-, and ankerite-bearing veins are unmineralised.

Fluid inclusions from actinolite-bearing stage 1 and garnet-bearing stage 2 veins have low (~250ºC) homogenisation temperatures, suggesting either that these fluid inclusions have re-equilibrated, or that significant pressure corrections are required for these temperature estimates. The salinities of stages 1 and 2 were around 11.0 and 7.0 wt. % NaCl, respectively. Main-stage quartz – pyrite veins (stage 3) trapped vapour- and liquid-rich, moderate salinity (~9.0 wt. % NaCl) fluid inclusions under boiling conditions at temperatures around 310ºC. Stage 3 veins are estimated to have formed approximately 1 km below the paleosurface at hydrostatic pressure (~90 bars). No fluid inclusions were found in stage 4 veins, but the presence of illite indicates formation temperatures below ~280ºC.

Sulfur isotope analyses have provided evidence for a magmatic sulfur component prior to and during gold mineralisation. The $\delta^{34}S_{sulfide}$ values for early vein stages range between -4.9 to -0.5 per mil. The stage 3 has $\delta^{34}S_{sulfide}$ values ranging from -5.2 to +0.8 per mil with the most ^{34}S-enriched sulfides values deposited away from the mineralised centre. Stage 4 sulfides have isotopic compositions from +2.5 to -7.5 per mil. The negative isotopic values are consistent with sulfate-predominant magmatic-hydrothermal fluids. Sulfur isotopic zonation patterns defined by stage 3 and 4 sulfides at E41 broadly correlate with high-grade domains.

Stage 3A-c calcite has $\delta^{13}C_{calcite}$ and $\delta^{18}O_{calcite}$ values that range from -5.2 to -4.6 and from +11.6 to +12.1 per mil, respectively. Calculated fluids for these mineral values at 300ºC ($\delta^{13}C_{fluid}$ = -3 per mil; $\delta^{18}O_{fluid}$ = +6 per mil) are consistent with a magmatic-hydrothermal source of carbon and oxygen during stage 3A-c. A component of meteoric waters is inferred for stage 4, because $\delta^{13}C_{carbonate}$ and $\delta^{18}O_{carbonate}$ values range from -6.9 to -0.5 and from +10.9 to +30.1 per mil respectively, corresponding to $\delta^{13}C_{fluid}$ and $\delta^{18}O_{fluid}$ values of -5 and -2 per mil at 200-250ºC. The involvement of external waters during stage 4 is also supported by the $\delta D_{illite\text{-}muscovite}$ and $\delta^{18}O_{illite\text{-}muscovite}$ compositions that range from -67.7 to -54.4 and +5.0 to +9.5 per mil, respectively. These values correlate to $\delta^{18}O_{H_2O}$ and δD_{H_2O} values of +2.9 and -85.4 per mil at 250ºC,

and are consistent with meteoric fluids that have partially equilibrated with volcanic rocks.

Gold is inferred to have been transported as a bisulfide complex in stage 3 and 4 in weakly acidic to alkaline aqueous fluids. Gold precipitated due to a combination of boiling and wall rock sulfidation. Some evidence for fluid mixing is provided by C-O and D-O isotopic data from stage 4, and this process may also have been important for ore formation.

E41 records the transition from deep, porphyry-style to shallow-level epithermal style magmatic-hydrothermal activity, and potentially implies unroofing of the system synchronous with mineralisation. High-temperature propylitic actinolite and epidote, and potassic assemblages (biotite, orthoclase, magnetite) indicate that E41 is located proximal to an alkalic centre of magmatic – hydrothermal activity. This is the first documented occurrence of low-sulfidation alkalic-style epithermal mineralisation in the Macquarie Arc. Continued exploration around E41 may lead to the discovery of an alkalic porphyry Cu-Au deposit.

Acknowledgements

This PhD dissertation was completed as part of an MDRU-CODES Alkalic Project investigating shallow and deep-level alkalic mineral deposits. Full sponsorship for the project was provided by Barrick Gold Corp., Newmont Mining, Teck, and AngloGold Ashanti, with logistical and field support provided by Barrick Gold of Australia Ltd. Additional funding was provided by Society of Economic Geologists which is gratefully acknowledged.

I would like to thank my principal supervisor Professor David Cooke for including me in the alkalic project and giving me the opportunity to travel the world and work with excellent geologists. Thanks for your constant encouragement, guidance, advice and your patience while correcting chapters written in English-ish. I am especially grateful for keeping me motivated over the last few months when the brain was particularly resistant.

I would also like to thank my two additional co-supervisors Tony Crawford and Bruce Gemmell who provided advice and technical support during my time at CODES. Cari Deyell is thanked for her time and teaching at the early stage of this project. Anthony Harris, Sebastien Meffre, Zhaoshan Chang and Julie Hunt also provided stimulating and insightful discussions and feedback. The field advice, support and reviews of Kirstie Simpson, Thomas Bissig and Dick Tosdal are greatly appreciated as well. Lots of serdecznych dziekuję to Amber Henry for a great time at Cowal and numerous chats not only about Cowal geology.

A big thank-you goes to all the geologists and field assistants at Cowal. In particular, Paul McInnes is thanked for his support, guidance, teaching and fantastic hospitality over my field seasons at Cowal. Phil Greenhill, Steve Casey, Lyndall Freer, Paul Balind, Andrew Bywater, Reuben Morrison, Adrian Ferguson, Damien Hart, Trent Strickland and Stuart Mathews are all gratefully acknowledged.

I am grateful to the CODES/SES support staff, which provided top quality service in processing samples and thesis preparation. Simon Stephens is thanked for polished slab and thin section preparation. June Pongratz is thanked for her art-eye opinion and assistance with graphic software and printing. To Dianne Steffans, Helen Scott and Christine Higgins, thank you for dealing with all the travel and finance documents.

To all my fellow PhD students, too many to list here, but you've all provided inspirational insights into my project, much needed mental escapes, and plenty of unforgettable moments. Thanks to you all for sharing this unique experience of happiness and frustration that comes with the PhD.

Jacq, thanks a lot for the last two weeks with all your help while putting this thesis together. A massive vodka and polskie ogorki session is inevitable now!

And finally to my family and friends in Poland: Tato i Mamo, bardzo Wam dziekuje za wsparcie przez te wszytskie lata edukacji. Obiecuje, ze na tym koniec! Aska, dzieki za telefony, musze przyznac, ze niejednokrotnie motywowaly mnie one do pracy. Agnieszko, Marku, Agnieszko i Piotrku ogromnie Wam jestem wdzieczny za widomosci, listy, rozmowy i czeste: 'Wojtku, do domu marsz' – bez watpienia ukonczenie tej pracy w duzej mierze zawidzieczam wlasnie Wam moi przyjaciele.

Table of Contents

List of Figures

Chapter 1. Introduction

Chapter 2. Regional- and District-scale geology

Chapter 3. Geology of the E41 deposit

Chapter 4. Igneous Geochemistry

Chapter 5. Veins and Altered Rocks

Chapter 6. Mineral and Hydrothermal Geochemistry

Chapter 7. Genetic Model

List of Tables

List of Appendices

Appendices are provided electronically on accompanying CD.

CHAPTER 1
Introduction

1.1 Preamble

Alkalic-type porphyry and epithermal ore deposits are an intriguing group, because they can be more gold-enriched than their calc-alkaline counterparts (Sillitoe, 2002). While epithermal and porphyry deposits related to calc-alkaline magmatism have been well-defined and well-documented (e.g., Beane and Titley, 1981; Titley and Beane, 1981; Sillitoe et al., 1989; White and Hedenquist, 1990; Cooke and Simmons, 2000; Sillitoe, 2000; Richards, 2003; Seedorff et al., 2005; Simmons et al., 2005), the deposits that are associated with alkalic magmatism remain comparatively under-studied. Only a few alkalic porphyry and epithermal systems have been subjected to detailed investigation, including New South Wales (NSW) and British Columbia's Au-Cu porphyries (e.g., Lang et al., 1995a; Cooke et al., 2007; Lickfold et al., 2003, 2007; Wilson, 2003; Wilson et al., 2003; 2005; 2007a and b), and epithermal deposits of the SW Pacific such as Emperor, Fiji (e.g., Ahmad et al., 1987; Begg, 1996; Pals et al., 2003), Lihir (e.g., Carman, 2003), and Porgera, Papua New Guinea (e.g., Richards, 1992; Richards and Kerrich, 1993; Ronacher et al., 2004), and also Cripple Creek in the United States (e.g., Jensen and Barton, 2000; Jensen, 2003) The current understanding of alkalic mineralised systems is largely based on features described from the aforementioned deposits.

Although models for the 'classic' porphyry and epithermal environments are well-established (e.g., Hedenquist and Richards, 1998; Sillitoe, 2000; Tosdal and Richards, 2001; Sillitoe and Hedenquist, 2003; Seedorff et al., 2005), there are mineralised domains of hydrothermal alteration that can occur in transitional regions between classic shallow-crustal epithermal and deeper-level porphyry environments (e.g., Corbett and Leach, 1998; Fig. 1.1) that are more poorly understood and can be difficult to categorise. A temporal link to magmatism is not always easy to recognise in these transitional epithermal settings, making it difficult to demonstrate an affiliation with calc-alkalic or alkalic magmatism. Certain mineral assemblages and their paragenetic sequencing, however, may provide a useful indicator of physiochemical condition(s) that prevailed during hydrothermal alteration and mineralisation. This information can also be used to infer the nature of associated magmatism and a spatial relationship to the magmatic centre. Alkalic epithermal systems can contain distinctive mineral assemblages (e.g., roscoelite – Porgera, Emperor; anhydrite – Lihir) and, atypical

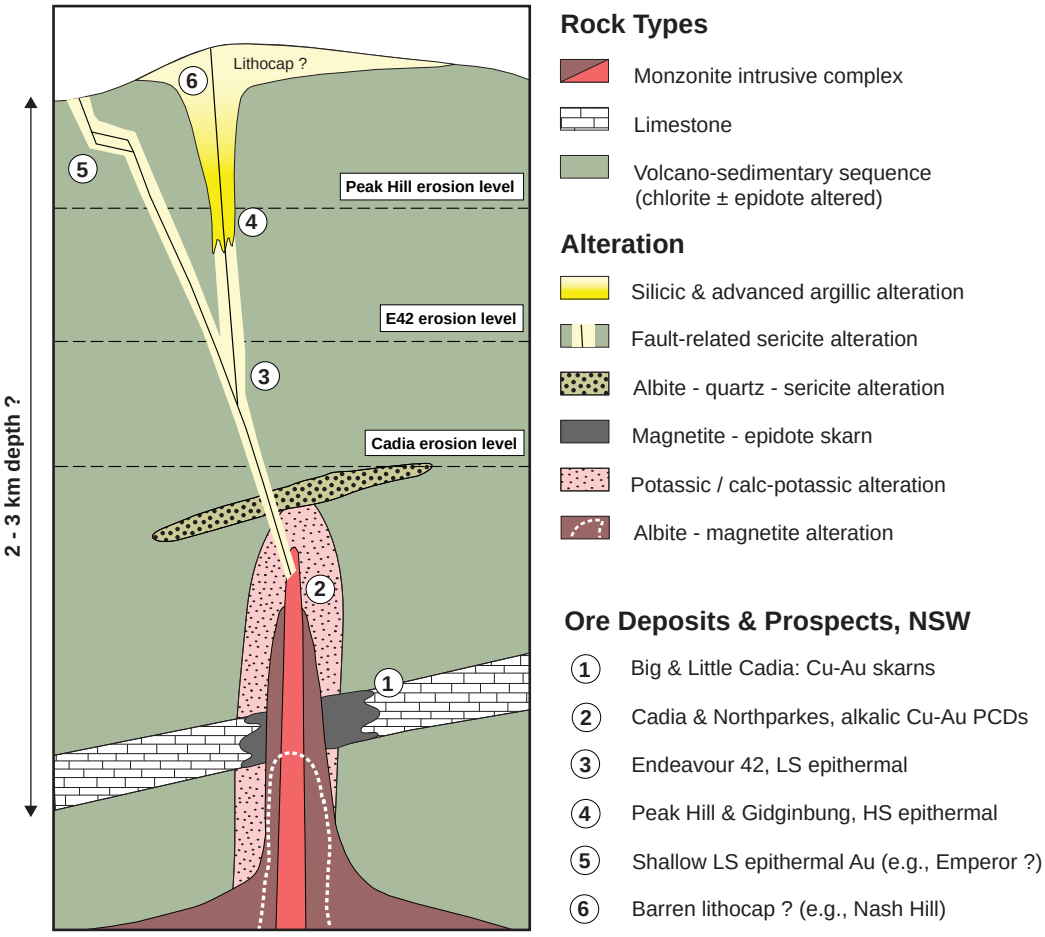

Figure 1.1 Schematic model of alkalic porphyry gold-copper deposits and related epithermal systems in NSW, associated with monzonite intrusive complexes (adopted and modified from Cooke et al., 2007). The figure shows a transition between porphyry and epithermal environment.

for epithermal environments, direct spatial relationships with a porphyry system. In fact, many alkalic epithermal deposits have high-temperature (i.e., porphyry-style) alteration assemblages overprinted by lower temperature epithermal features (e.g., Porgera: Fleming et al., 1986; Richards, 1992; Richards and Kerrich, 1993, Lihir: Moyle et al., 1990; Muller, 2002; Carman, 2003, Emperor: Anderson and Eaton, 1990; Kwak, 1990; Begg, 1996; 1997; Golden Sunlight: Spry et al., 1996).

The genesis of gold mineralisation in Ordovician rocks of the Cowal district, NSW, Australia, has been interpreted previously in several ways. The gold deposits have been described (Bastrakov, 1996, 2000; Cooke et al.,2007) as deep-level epithermal systems related to calc-alkaline intrusions that conform to the low-sulfidation quartz-pyrite and carbonate-base metal gold style of Corbett and Leach (1998). An inferred deeper crustal setting for mineralisation led Barrick Gold of Australia Ltd. geologists to classify the Cowal gold centres as orogenic (‘mesothermal’). This latter model has been favoured by many geologists involved in exploration or mining of the district (e.g., McInnes, 1998; Bywater et al., 2004).

The gold mineralisation at Cowal has many hydrothermal features that are atypical for calc-alkalic epithermal deposits, and are more comparable to the NSW alkalic copper-gold porphyries at Cadia (Wilson et al., 2005; Cooke et al., 2007) and Northparkes (Lickfold et al., 2003). 'Red rock' alteration (finely disseminated hematite alteration of K-feldspar), telluride occurrences, the local presence of gypsum and negative sulfur isotopic compositions of sulfides from the E42 deposit are just a few features that are consistent with the NSW alkalic porphyry deposits and alkalic epithermal systems. This research aims to test whether the Cowal mineralised centres recorded magmatic-hydrothermal evolution related to alkalic magmatism.

This PhD study of the Endeavour 41 (E41) gold deposit in the Cowal district of NSW formed part of an industry-sponsored collaborative research project entitled 'Shallow and deep-level alkalic mineral deposits: an integrated exploration model'. The 'Alkalic Project' was undertaken by researchers at CODES, the Australian Research Council's Centre of Excellence in Ore Deposits at the University of Tasmania, and at the Mineral Deposit Research Unit (MDRU) at the University of British Columbia, Canada. The study was undertaken through two modules – porphyry and epithermal – and had several PhD and MSc students investigating alkalic porphyry and epithermal deposits around the world (Fig. 1.2). The alkalic project aimed to advance understanding of the characteristics of individual alkalic systems and integrate that information into a coherent model for the porphyry and epithermal environments.

1.2 Location and environment

The Cowal district is located in central NSW, approximately 480 km west of Sydney. Access to the Cowal district is by sealed and unsealed roads. The district is situated on

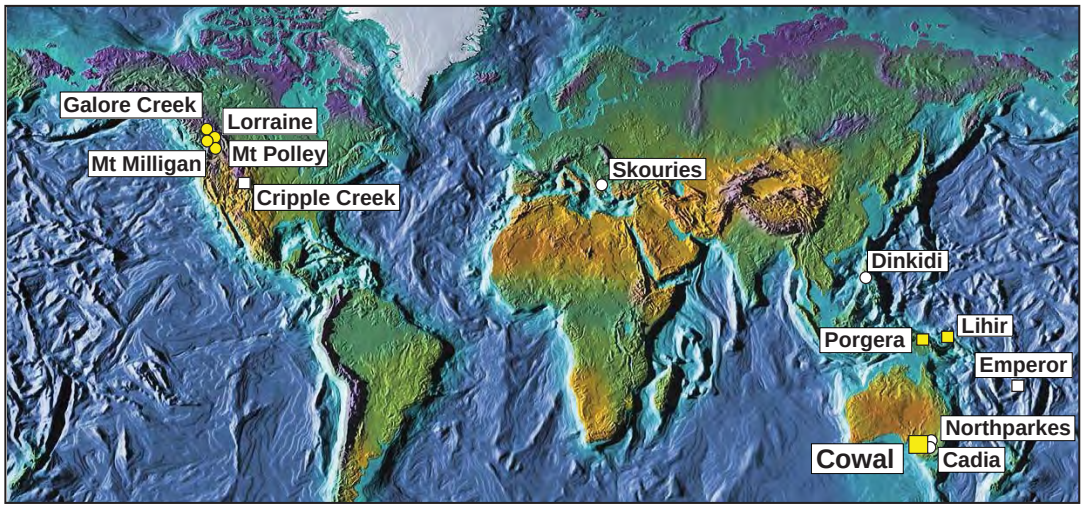

Figure 1.2 Location of alkalic porphyry deposits (yellow dots - alkalic project study sites, white dots - important alkalic deposits not subjected to detailed investigation by the alkalic project) and alkalic epithermal deposits (yellow squares - alkalic study sites, white squares - reviewed deposits) that were studied as part of the alkalic project.

the western shore of Lake Cowal, a shallow ephemeral lake located 43 km northwest of the town of West Wyalong, and approximately 60 km south west of Forbes, within the Bland Shire of New South Wales (Fig. 1.3). Lake Cowal is approximately 14 km long and 8 km wide with an average depth of around 2 m. Historically, Lake Cowal has been dry for periods of up to 20 years and last contained water in June, 2006. Lake Cowal is located on the boundaries of the south-eastern semi-arid region and the south-eastern temperate region of Australia. Average temperature interval ranges are from 15.5 – 30ºC in January to 6 – 13.5ºC in July (http://www.weatherzone.com.au). The area is strongly influenced by winds from the southwest. Rainfall is evenly distributed throughout the year with an average annual precipitation of 476 mm. Most of the land surrounding the Cowal district is cultivated for cereal crops. The native vegetation has been modified by land clearing, fire and live stock grazing. Swamp-canegrass species dominate the landscape around Lake Cowal. *Eucalyptus, lignum* trees is the predominant native species. They are limited to scattered bushes and deprived isolated woodlands that are a remnant of natural forests in the area.

Three economically significant gold centres have been discovered in the Cowal district. From north to south, they are: Endeavour 46 (E46), Endeavour 42 (E42) and

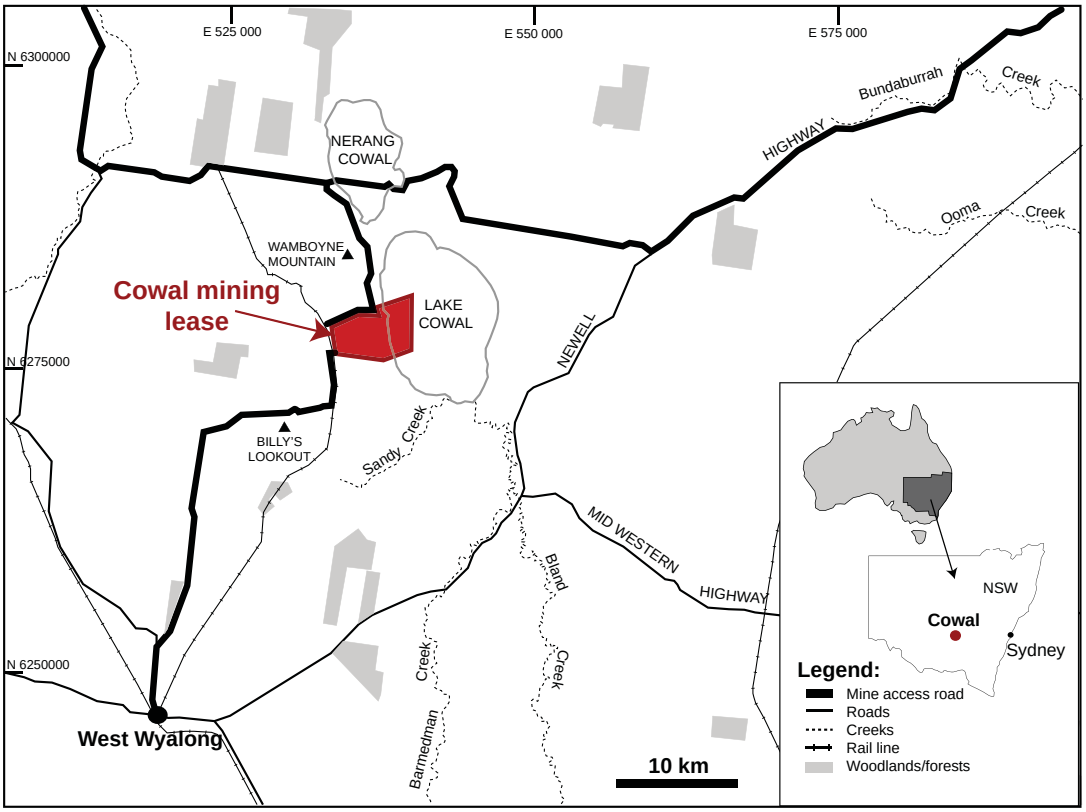

Figure 1.3 Location of the Cowal district, central New South Wales, Australia (modified from Cowal Gold Mine environmental assessment report, sourced from Barrick Gold Corporation Home Page: http://www.barrick.com/GlobalOperations/AustraliaPacific/Cowal/default.aspx).

E41. Endeavour 40 (E40) is an exploration prospect that is located further south of E41. The Cowal gold mine exploits the E42 deposit. It is the only mine in the district, and commenced operation in June 2006. At the time of writing, the E42 deposit has an estimated resource of 82.8 Mt @ 0.99 g/t gold (2.88 M oz; Barrick Year End Report, 2007). Ore reserves for E46 and E41 have not been published by Barrick Gold of Australia Ltd.

1.3 Exploration history

The Cowal district is almost entirely covered by lacustrine sediments. Only limited exploration activities were undertaken prior to 1980, when Geopeko Ltd., the exploration arm of Peko Wallsend Ltd., selected the area for a porphyry copper-gold exploration program. Geopeko Ltd. had discovered porphyry-style Cu-Au mineralisation to the north of the Cowal in the Goonumbla district in 1971 (Jones, 1985). The similar aeromagnetic signature of the Cowal and Goonumbla district, led Geopeko Ltd. to extend their exploration program further south. The exploration program designed for the Lake Cowal area relied almost entirely on aeromagnetic and gravity methods and reconnaissance drilling to develop a geological, structural and geochemical understanding of the area. The program identified a copper bedrock anomaly approximately 4 km x 2 km in size (Endeavour 39 – E39), which became the focus of exploration activity for a number of years (McInnes et al., 1998). E39[1] was eventually identify as a poorly mineralised porphyry Cu-Au system. Subsequently, Geopeko Ltd. targeted satellite plugs and intrusive around the margins of the parent E39 stock. A zone of geochemical anomalies were identified to the north of E39, however further exploration was prevented by the flooding of Lake Cowal and exploration was postponed until the lake partially dried up in 1988. Once exploration activities resumed, rotary air-blast (RAB) and aircore drilling delineated zones of anomalous gold mineralisation within a northerly trending zone. At this time, flooding of the lake required innovative exploration involving use of a hovercraft, drill rigs on raised platforms, and 4WD vehicles modified for exploration within the lake (McInnes et al., 1998).

In 1988, North Ltd. was created through a merger between Geopeko Ltd. and North Broken Hill Ltd. From 1993 to 1995, North Ltd. completed a preliminary feasibility study, a resource delineation drilling program, and finally a detailed feasibility study of the E42 deposit (McInnes et al., 1998; Henry, 2008). North Ltd.'s development proposition for E42 was not approved until 1999, by which time the

[1] The 'E' label indicates that Geopeko Ltd. discovered this prospect. Any new prospect they had drilled with a diamond hole in NSW was named 'Endeavour'.

company had been taken over by Rio Tinto. The Lake Cowal property was sold to Homestake Mining in 2001 and as part of its merger with Homestake Mining that year, Barrick Gold of Australia Ltd. acquired the Cowal gold project (Henry, 2008). An intensive resource drilling and feasibility study was undertaken by Barrick Gold of Australia Ltd., from 2001-2005, including extensive drilling of the E46, E41 and E40 prospects. Production from the Cowal gold mine started in July, 2006, exploiting the largest gold resource, E42. At the time of writing, Cowal is the newest gold mine in New South Wales.

1.4 Previous work at Cowal district

To resolve some of the conflicts between genetic models proposed for Cowal gold, the Cowal district has been the subject of several research projects. Of the four mineralised centres that occur in the district, E42 has been studied most frequently. Love (1992) was the first to describe the host rocks to the E42 deposit and assigned the name of the 'Lake Cowal Volcanic Complex' (LCVC). Miles (1993) completed an honours project studying the paleo-volcanology of the host rocks. The geology and mineralisation of the deposit was then described in detail by North Ltd.'s geologists in a number of unpublished company reports that were summarised by McInnes et al. (1998). The geology, structural architecture and alteration at E42 were documented by Miles and Brooker (1998). Bastrakov (2000) undertook a PhD research project focused on ore-forming processes at E42. Barrick Gold of Australia Ltd. then produced numerous internal reports that helped to better constrain the deposits geology, mineralisation and alteration (e.g., Ashley, 2003a and b; 2004; 2005; McInnes, 2003). Major syntheses by Smolonogov (2003) and Cannell (2003) provided new insights into the volcanic facies architecture of the Cowal district. A regional geochemical study of intrusive and volcanic suites from the Cowal district and other parts of the Macquarie Arc was published by Crawford et al. (2007a and b). Anderson (2003) characterised dyke suites that occur at E42 deposit and the geology of E42 was summarised by Bywater et al., (2004). Ingpen (1995), Dykmans (2004a) and Munroe et al. (2005) reviewed the district- and regional-scale structural features. Borthwick (2004) investigated the vein paragenesis and gold associations, and Strickland (2005) documented the geology of a magmatic-hydrothermal breccia complex at E42. The most recent study of E42 was the MSc thesis of Henry (2008), who documented the structural evolution of the system based on open pit mapping and core logging. Henry (2008) also investigated sericite geochemistry associated with mineralisation and structural links between the Cowal block and other Ordovician deposits of the Lachlan Fold Belt.

Neither E46 nor E41 have been investigated in detail previously. Simpson and Cooke (2006) and Simpson (2008) conducted the first study on the volcanic and sedimentary facies architecture of E46. Bastrakov (2000) provided some geological and geochemical data for E41 as a comparator to E42. Some of the results from the current PhD study of E41 have been presented at several conferences (Zukowski et al., 2007a and b; Zukowski and Cooke, 2009). These are the only public domain literature currently available for E41.

1.5 Characteristics of alkalic porphyry and epithermal deposits

Alkalic igneous rocks are those in which the total Na_2O+K_2O content is high enough (at any given silica content) to plot in or above the basanite, trachybasalt, shoshonite, latite, and trachyte fields in the IUGS classification scheme for volcanic rocks (Le Maitre et al., 1989; Fig. 1.4). Alkalic rocks may have normative quartz or feldspathoids, and may have olivine. They can therefore be silica-oversaturated, -undersaturated or -saturated (Jensen, 2003). In mineralised centres, alkalic rocks range broadly from ultramafic to felsic, from silica-saturated to silica-undersaturated and from potassic to sodic, although the last division may be problematic as mineral deposits associated with alkalic intrusions tend to be intensely affected by potassic and sodic metasomatism (e.g., Jensen and Barton, 2000; Cooke et al., 2007). Key characteristics of alkalic rocks associated with gold deposits are their hydrous and oxidised nature, as well as their ability to produce hydrothermal systems with ideal chemistries for transporting gold (Richards, 1995).

Several key geological parameters for alkalic systems have been identified. Rifted arc terranes, back-arc sites, extensional and post-subduction settings are especially favourable for alkalic igneous domains and associated mineralised centres

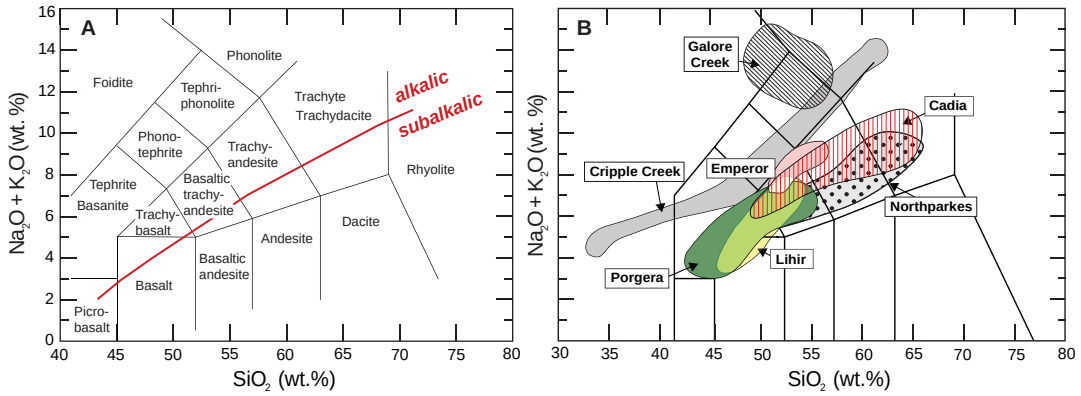

Figure 1.4 A. Total alkali-silica (TAS) diagram of Le Maitre (1989), showing rock fields defined on the basis of $Na_2O + K_2O$ vs SiO_2. **B.** Geochemical compositions for selected alkalic porphyry and epithermal deposits (modified and compiled from Muller, 2001; Jensen, 2003; Wilson, 2003).

(e.g., Richards, 1995; Sillitoe, 2002). There are numerous examples of alkalic deposits that occur in clusters or in terranes with repetitive episodes of alkalic magmatism (Jensen and Barton, 2000; Cooke et al., 2007). In addition, some giant porphyry deposits that are related to calc-alkaline magmas have subordinate alkaline affinities (e.g., Grasberg and Bingham Canyon: Maughan et al., 2002; Appendix A.1).

Alkalic gold-(copper) porphyry deposits include some of the world's highest-grade porphyry gold resources (Appendix A.2) and some of the largest gold accumulations in epithermal environments (Appendix A.3). Deposits of alkalic magma affinity record distinctive hydrothermal alteration assemblages and associated styles of mineralisation as well as specific metal zonation and geochemical patterns. Figure 1.5A and 1.5C show typical alteration zonation patterns from two silica-saturated and silica-undersaturated alkalic porphyry deposits, respectively. At Ridgeway (Fig. 1.5A; Appendix A.2), one of the six mineralised centres in the Cadia district, the core of the deposit is characterised by potassic and calc-potassic assemblages. These assemblages are enclosed by a propylitic halo that changes from hematite-present to hematite-absent outward from the deposit centre (Wilson, 2003; Wilson et al., 2005). Mt. Polley is a silica-undersaturated alkalic Cu-Au system hosted by a magmatic-hydrothermal breccia complex (Appendix A.2). It has some common hydrothermal features with Ridgeway. Mineralisation is associated with hematite-dusted K-feldspar – magnetite ± biotite (potassic assemblage) and garnet-bearing assemblages (calc-potassic) that pass upwards to biotite – chlorite and downwards to actinolite – epidote (Lang et al., 1995b; Jackson, 2008; Fig. 4.2C; Appendix A.2). Calc-potassic alteration zones have been also reported from other alkalic deposits (Appendix A.2) including: Galore Creek (Lang et al., 1995b; Byrne, 2008, Micko, 2008), Lorraine (Nixon and Peatfield, 2003) and Mt. Milligan (Jago, 2008). Thus the calc-potassic assemblage is a distinguishing feature of alkalic porphyry deposits. It is lacking in calc-alkalic porphyries (Fig. 1.5B). Pervasive hematite alteration is another distinctive feature associated with the core of mineralisation in several deposits. Other distinguishing characteristics include carbonate veins throughout the paragenesis, fault-related phyllic alteration and a general lack of pervasive phyllic domains (common in calc-alkalic porphyries; Fig. 1.5B), and a lack of argillic alteration (possibly excluding Dinkidi: Wolfe, 2001). Such features characterise hydrothermal activity associated with alkalic porphyry systems (Lang et al., 1995b; Cooke et al., 2004; Cooke et al., 2007). Phyllic alteration can be widespread (e.g., Red Chris; Baker and Thompson, 1998; Fig. 1.5D) or restricted to the core of the deposit (e.g., E48; Wolfe, 1994; Wolfe et al., 1996); controls on phyllic alteration remain poorly understood.

Alkalic epithermal deposits are characterised by Au-rich, base metal-poor veins with high Au/Ag ratios and Au commonly present in Au-Ag tellurides (Bonham and

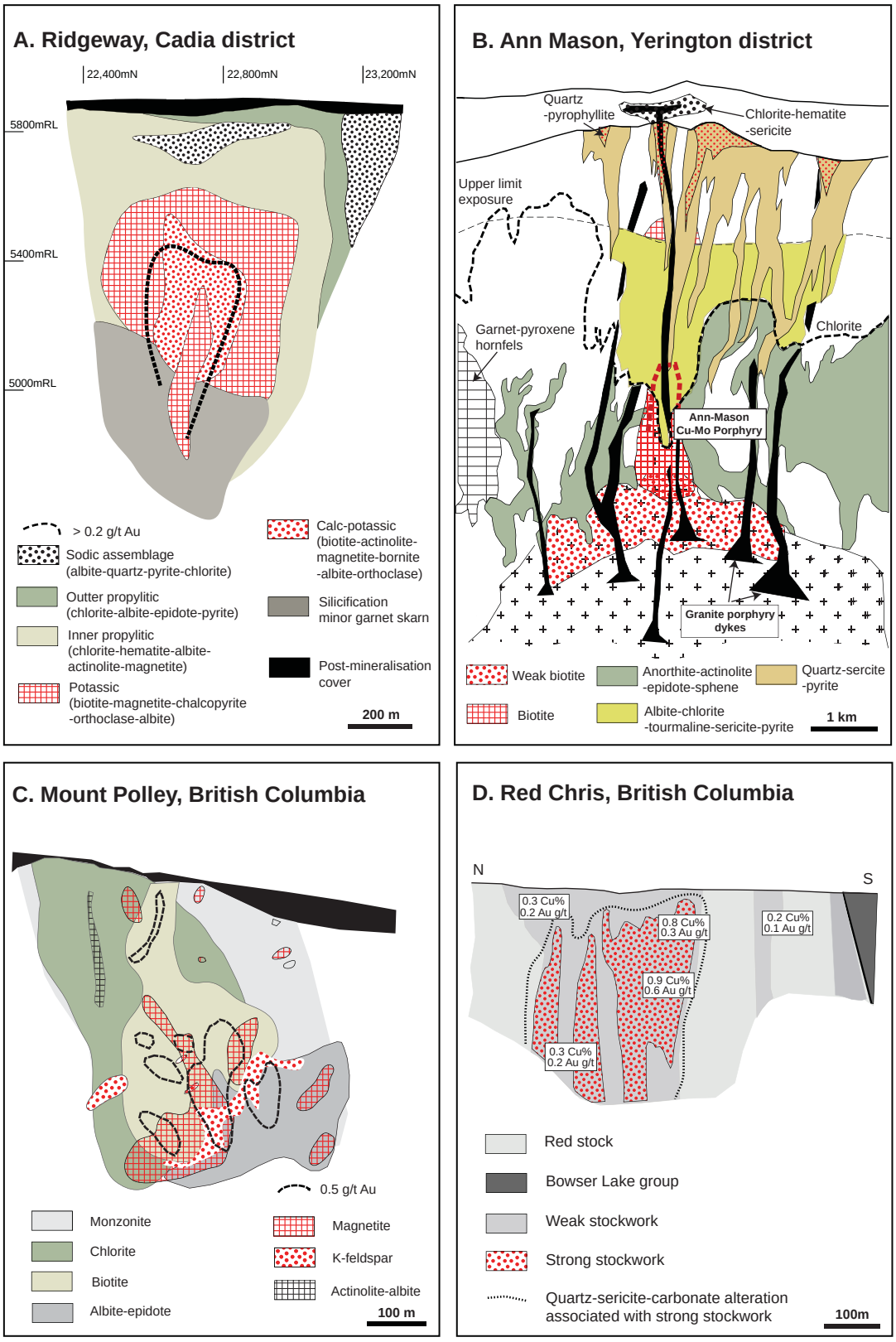

Figure 1.5 Cross sections with distribution of alteration facies in selected alkalic and calc-alkalic porphyry systems. **A.** Ridgeway silica-saturated alkalic gold-copper deposit, Cadia district, NSW, Australia (modified from Wilson, 2003). **B.** Ann Mason calc-alkalic porphyry deposit, Yerington district, U.S.A. (modified from Dilles et al., 2000). **C.** Mount Polley (NE zone), silica-undersaturated alkalic copper-gold porphyry deposit, British Columbia, Canada (modified from Jackson, 2008). **D.** Red Chris copper-gold deposit, hosted by an intrusion with composition intermediate between the alkalic and subalkalic, porphyry-related intrusive suites in the Canadian Cordillera. British Columbia, Canada (modified from Baker and Thompson, 1998).

Giles, 1983; Richards, 1995; Jensen and Barton, 2000). The alkalic epithermal systems have mineralogical and geochemical features similar to the low-sulfidation class of calc-alkalic epithermal deposits. Low sulfidation, in a purely mineralogical sense, implies presence of quartz ± calcite ± adularia ± illite that reflect the pH of hydrothermal solutions (e.g., Simmons et al., 2005), and arsenopyrite and/or pyrrhotite, reflecting a low sulfur fugacity (or sulfidation state; Einaudi et al., 2003). Figures 1.6 A-D show examples of four low-sulfidation epithermal systems associated with alkalic (Figs. 1.6A and B) and calc-alkalic magmatism (Figs. 1.6C and D). At Ladolam, Lihir Island, early biotite – K-feldspar (orthoclase) alteration predated the epithermal mineralisation (Carman, 1994; Muller et al., 2002). Early biotite alteration has also been recognised as a precursor to alkalic epithermal mineralisation at Cripple Creek (Thompson et al., 1985; Jensen, 2003) and Porgera (Ronacher et al., 2004; Cooke et al., 2006). These early high-temperature mineral assemblages have been overprinted by low-temperature alteration minerals (i.e., illite – carbonate – adularia) that are associated with high gold concentrations. In contrast, in calc-alkalic epithermal systems low-temperature gold-bearing assemblages commonly overprint low- to medium- temperature propylitic alteration (sericite-, chlorite-, to epidote-bearing;) that formed distal to the calc-alkalic magmatic centres (e.g., Gosowong, Kelian; Figs. 1.6C and D; Appendix A.4).

Gold mineralisation in alkalic epithermal environments is typically associated with roscoelite in mafic rocks (e.g., Porgera, Richards and Kerrich, 1993; Emperor: Ahmad at al., 1987; Kwak, 1990) or fluorite in felsic rocks (e.g., Central City: Rice et al., 1985). Abundant tellurides (e.g., Emperor, Cripple Creek, Porgera, Gies: Zhang and Spry, 1994; Jensen and Barton, 2000), anhydrite (e.g., Lihir: Carman, 1994), and ubiquitous K-feldspar and carbonate alteration throughout the paragenesis (e.g., Richards, 1995; Jensen and Barton, 2000) are also characteristic of alkalic epithermal veins and breccias.

The sulfur isotopic composition of sulfides from alkalic porphyry and epithermal deposits (e.g., Dipidio, Philippines: Wolfe, 2001; Mt Polley BC: Deyell and Tosdal, 2005; Deyell, 2005; Northparkes and Cadia, NSW: Heithersay and Walshe, 1995; Radclyffe, 1995; Lickfold, 2002; Wilson, 2003; Wilson et al., 2007a; Lihir: Carman, 1994; Gemmell et al., 2004; Porgera: Richards and Kerrich, 1993; Emperor: Ahmad et al., 1987) are typically negative, a feature characteristic of sulfides deposited from oxidized (sulfate-predominant) magmatic fluids (Rye et al., 1993; Wilson et al., 2007a). These oxidised fluids discriminate alkalic epithermal deposits from their reduced calc-alkalic counterparts, which have sulfide minerals with homogeneous, positive sulfur isotopic compositions (e.g., Kerikil: Wurst, 2004; Kelian: Davies et al., 2008; Appendix A.4).

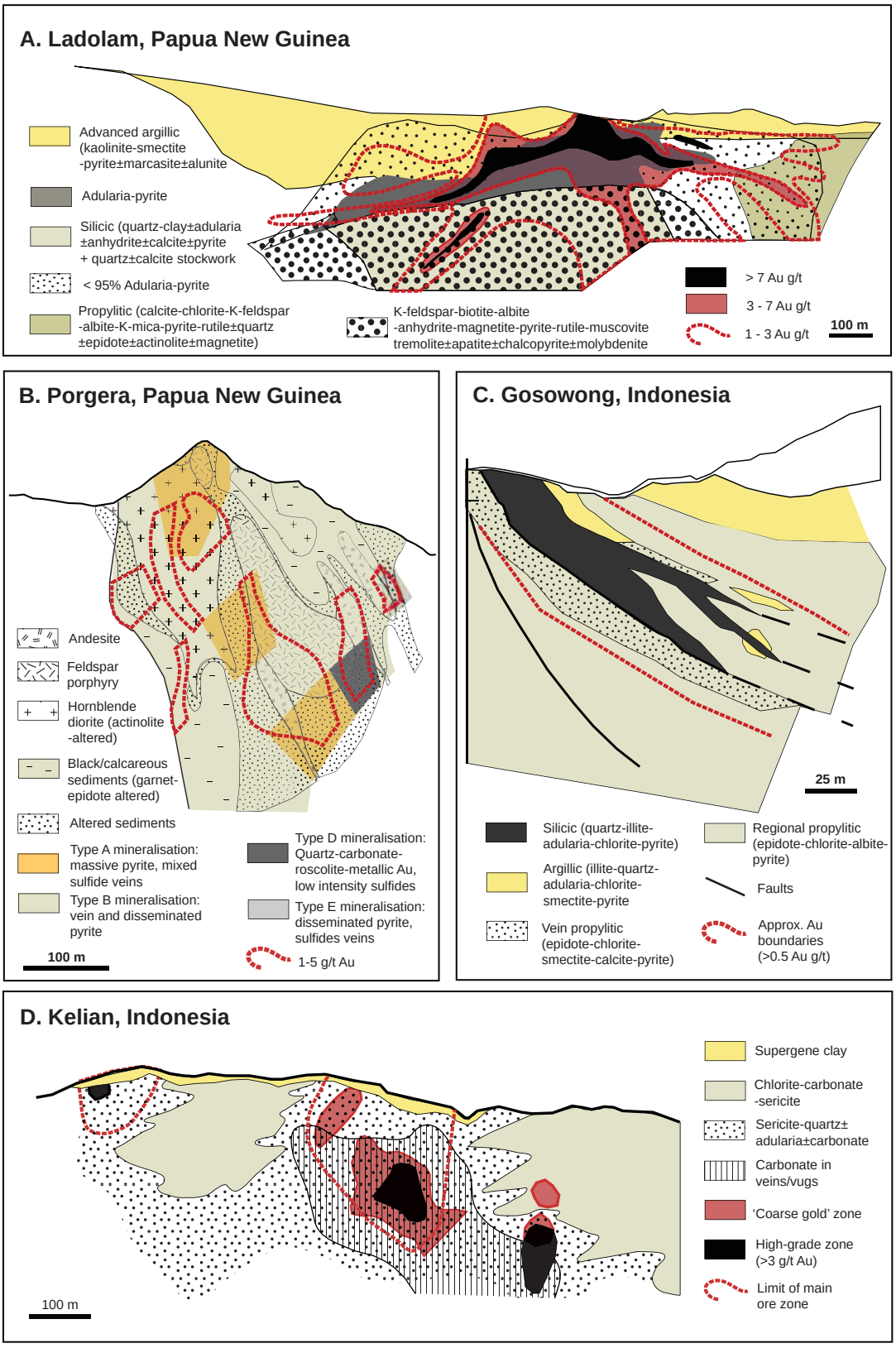

Figure 1.6 Cross sections with distribution of alteration facies in selected alkalic and calc-alkalic epithermal systems. **A.** Ladolam, alkalic epithermal deposit, Lihir Island, Papua New Guinea (modified from Carman, 2003). **B.** Porgera, alkalic epithermal system, Highlands, Papua New Guinea (modified from Fleming et al., 1986). **C.** Gosowong, calc-alkalic epithermal system, Halmahera, Indonesia (modified from Gemmell, 2007). **D.** Kelian, calc-alkalic epithermal system, Kalimantan district, Indonesia (modified from van Leeuwen et al., 1990).

1.6 Thesis aims and objectives

The principal aim of this PhD study is to determine the genesis of gold mineralisation at E41. This will be achieved by:

- Documenting and interpreting the geology of E41 through analysis of the local stratigraphy, and to correlate it with the already known stratigraphic succession of the E46, E42 and E40 mineralised centres. This will enable characterisation of the paleoenvironment of the host rocks and help to constrain volcanic facies architecture.

- Constraining the intrusive history of E41 and to investigate relationships between magmatic events and gold mineralisation.

- Documenting the detailed paragenetic sequence of veining and alteration, and characterising the different styles of gold mineralisation and their relationships with specific mineral assemblages, in order to help unravel the complexity of the hydrothermal system.

- Investigating the stable and radiogenic isotopes to constrain the fluid chemistry and to identify likely fluid sources.

- Analysing and mapping the trace element chemistry of sulfides to determine the host for gold and other trace elements.

- Studying fluid inclusions associated with the various alteration assemblages to determine the P-T-X conditions that prevailed during mineralisation.

- Evaluating whether gold mineralisation at Cowal is related to alkaline magmatism, and assessing whether there is potential for Northparkes or Cadia-style alkalic porphyry copper-gold mineralised centres in the Cowal district.

- Comparing the E41 genetic model to established models for porphyry and epithermal systems and to comment on exploration implication both in the Cowal district and in porphyry and epithermal provinces world-wide.

1.7 Methodology and analytical work completed during this study

Most of the data presented in this thesis were collected by the author over four field seasons (September, 2005; May-June, 2006; September, 2006; November-December, 2007). The geological observations are entirely based on detailed graphic logging of 7,173 m of diamond drill core from 37 drill holes throughout the E41 deposit, using the techniques of McPhie et al. (1993) and the modified Anaconda method (Einaudi, 1997). Three cross sections were constrained from the results of graphic logging. Drill holes from two perpendicular sections (86800E and 34900N) were studied from the eastern part of the deposit (east pod). A continuation of the 34900N section was analysed through the western part of the deposit (west pod). Additionally, an orthogonal N-S section was completed through west pod (68200E).

Polished slabs were prepared from representative samples to facilitate descriptions of igneous and volcanic textural features, and to help determine the relative timing and characteristics of hydrothermal features. Detailed examination of polished slabs was absolutely essential for these purposes prior to petrographic examination. Approximately 200 polished thin sections were studied petrographically as part of this research. Additional polished thin sections (n=29) and petrographic descriptions were also provided by Barrick Gold of Australia Ltd.

Laboratory-based methods were used to supplement mineral identification made during core logging and thin section petrography. Scanning electron microprobe (SEM) analyses, electron microprobe (EMP), energy dispersive spectrometry (EDS) and back scattered electron (BSE) imaging were carried out at the Central Science Laboratory (CSL), University of Tasmania under the supervision of Dr. Karsten Goemann. In many cases, EDS analyses coupled with SEM and BSE imaging were used to identify the composition and textural relationships of finely-crystallised alteration minerals that could not be determined during petrographic examination. Certain mineral groups, including carbonate, garnet, chlorite and epidote, were analysed for their chemical compositions. X-ray diffraction (XRD) analyses were used to assist with alteration mineral identification. XRD analyses were conducted by the author at the Mineral Research Unit (MDRU), University of British Columbia, Vancouver. A portable infrared mineral analyser (PIMA) was used in the field in order to assist with mica and clay mineral identification. Staining of sawn slabs with cobaltinitrite was used for K-feldspar identification. This work was conducted at CODES. Whole rock geochemical analyses of major, trace and REE (XRF and ICP-MS) compositions were conducted at CODES by Mr. Phil Robinson and in Brisbane by Barrick Gold of Australia Ltd. Stable isotope analyses, including S-isotopic analysis of sulfides and sulfates and C-O isotopic analyses of carbonates were performed by Ms. Christine Cook

and Mr. Keith Harris at the CSL, University of Tasmania. Oxygen-deuterium isotopes of sericite were analysed at Ministry of Agriculture and Forestry, GNS Science, Rafter Stable Isotopes Laboratory in Wellington by Dr. Kevin Faure. Dr. Sebastien Meffre and Sarah Gilbert performed Pb radiogenic isotope analyses of galena samples, the sulfide chemistries and mapping. Fluid inclusion studies involved petrographic examinations, cathodo-luminescence (CL) imaging of quartz crystals, microthermometry analyses of individual inclusions, were carried out at CODES.

1.8 Thesis organisation

Following this introduction, there are six chapters that describe and interpret the E41 gold deposit:

- **Chapter 2** discusses the regional geology and tectonic setting and reviews other significant occurrences of Ordovician porphyry and epithermal deposits in the Macquarie Arc. It briefly reviews the geology of the E46, E42 and E40 mineralised centres.

- **Chapter 3** presents a detailed description of the E41 deposit, including the volcano-sedimentary succession and the intrusive history. This is followed by an interpretation of the facies architecture and a brief discussion of the Ordovician paleoenvironment of the district. E41 geochronological constraints integrated into district framework conclude the chapter.

- **Chapter 4** presents and discusses whole rock geochemical data, including classification of the igneous rocks as alkalic or calc-alkalic. The Cowal volcanic and intrusive rocks are compared with well-documented geochemical data from the Northparkes and Cadia volcano-intrusive centres, and the Cowal intrusive complex is interpreted in the context of the tectonic and magmatic evolution of the Macquarie Arc.

- **Chapter 5** documents veins and altered rocks from E41, including the varying styles of precious and base-metal occurrences. A detailed paragenetic sequence for mineralisation and alteration is provided, together with interpretation of alteration zonation patterns.

- **Chapter 6** determines the physicochemical environment of ore deposition and

hydrothermal alteration based on fluid inclusion, stable and radiogenic isotopic data.

- **Chapter 7** concludes this thesis by proposing a genetic model for the formation of E41.

CHAPTER 2
Regional- and District-scale geology

2.1 Introduction

This chapter reviews the key geological features, from continental to regional scales, that allow the tectonic setting of the Cowal gold deposits to be interpreted. This includes a review of the metallogeny of the Ordovician Macquarie Arc, and a description of the Cowal Igneous Complex.

The Cowal district is located in the Lachlan Orogen (Fig. 2.1 and Fig. 2.2) of south-eastern Australia. The orogen forms part of the larger tectonic block, the Tasman Fold Belt System (Fig. 2.1). Multiple cycles of compression, extension and episodic magmatism have produced a collage of orogenic belts in the Tasman Fold Belt System that ultimately resulted in the growth of the eastern Australian continental margin (Glen, 2005; Gray et al., 2004). Each orogenic belt within the Tasman Fold Belt System has been divided into several subprovinces that have been further partitioned into structural zones and blocks. This chapter focuses on the Lachlan Orogen, which forms the south-eastern subprovince of the Tasman Fold Belt System (Fig. 2.1).

Rocks of the Lachlan Orogen record a history that spans from Late Proterozoic to the Late Mesozoic (Glen, 2005; Gray et. al., 2006). Within the Lachlan Orogen, Early Ordovician to Early Silurian volcano-intrusive complexes formed in an intra-oceanic island arc setting that Glen et al. (1998) termed the Macquarie Arc. The Cowal Igneous Complex was produced by Ordovician magmatic and sedimentary activity within the Macquarie Arc. Similar intrusive units elsewhere in the Macquarie Arc host the world class alkalic Au-Cu porphyry deposit of Cadia and Northparkes (Crawford et al., 2007b).

2.2 The Tasmanides

The Tasman Fold Belt System, or Tasmanides, occupies the eastern part of the Australian continent, forming a complex, north-striking orogenic belt over 4000 km long and up to 1500 km wide. The western margin of the Tasman Fold Belt System is defined by the Tasman Line, the major tectonic feature between the Australian Craton to the west and the Neoproterozoic and younger rocks to the east (Walshe et al., 1995; Glen, 2005). Similarly to the north-trending Tasman Line, the Tasman Fold Belt System is characterised by north-trending fault systems (Fig. 2.1). Subtle west-northwest structural trends appear to be inherited Proterozoic basement structures that

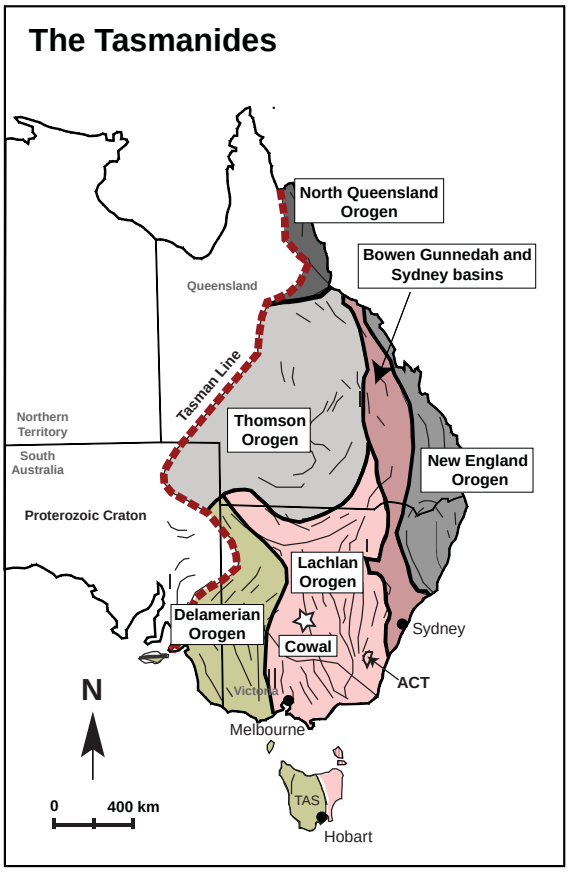

Figure 2.1 The orogenic architecture of the Tasmanides modified from Walshe et al. (1995) and Glen (2005). Structural lines have been adopted from Gray and Foster (2004). Major components of the Tasmanides include the Delamerian, Lachlan, New England, Thomson and North Queensland orogens, and the Bowen – Gunnedah and Sydney basins.

exerted important controls on the distribution of the major mineral provinces in the Tasman Fold Belt System (Walshe et al., 1995).

The Tasman Fold Belt System comprises several orogenic belts that record break-up of a Mesoproterozoic supercontinent, the creation of a Late Neoproterozoic passive margin, and the formation of a series of convergent margin orogenic belts along the Pacific margin of Gondwana. Convergence commenced in the Middle Cambrian (Glen, 2005). The Tasman Fold Belt System, as described by Glen (2005), is subdivided into five main orogenic belts and a foreland basin (Fig. 2.1). The orogenic belts, which generally young from west to east include: the Delamerian, Lachlan, Thbmpson, and North Queensland Orogens (Fig. 2.1). The Bowen – Gunnedah – Sydney Basin system separates both the Lachlan and Thomson orogens from the New England Orogen. This subdivision of the Tasman Fold Belt System was primarily based on age of the rock units that were recognised in each orogenic belt. Glen (2005) suggested that the development of Tasman Fold Belt System is more complicated than this simple subdivision implies, because older rocks have commonly been identified in younger provinces. To integrate time- and space-features of the Tasman Fold Belt System, Glen (2005) proposed a model of evolutionary history using tectonic cycles. In Glen's (2005) model, each cycle includes sedimentation and igneous activity followed by a

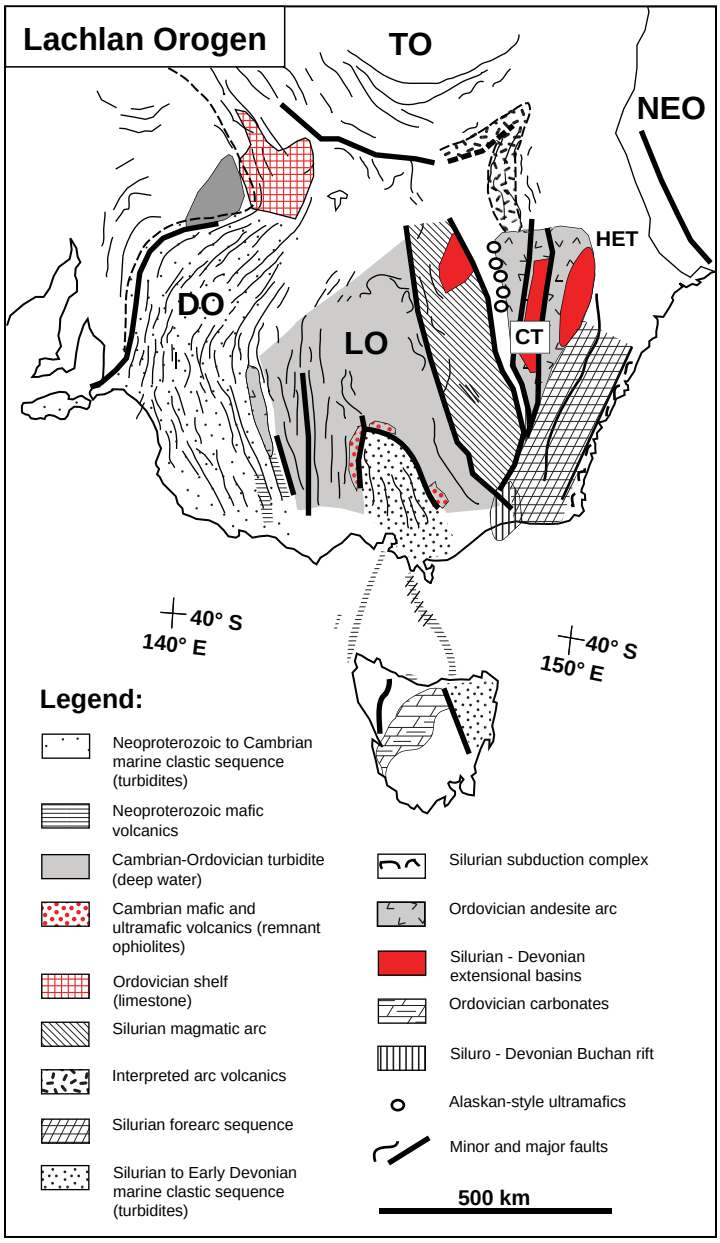

Figure 2.2 Major elements of the Lachlan Orogen (modified from Gray and Foster, 2004). Abbreviations: DO=Delamarian Orogen, LO=Lachlan Orogen, TO=Thomson Orogen, NEO=New England Orogen, CT=Cowra trough, HET=Hill End Trough.

deformation phase that appears to reflect the accretion of a terrane, such as an arc or subduction complex, to Gondwana (Glen, 2005; 2006). Glen (2005) distinguished three major tectonic episodes: the Delamerian cycle (830 – 490 Ma), the Lachlan supercycle (490 – 320 Ma), and the Hunter-Bowen supercycle (320 – 230 Ma). The Lachlan supercycle has been subdivided into the Benambran (~443 – 430 Ma), Tabberabberan (~380 Ma), and Kanimblan cycles (~340 Ma; Glen, 2005). The Lachlan supercycle is described briefly below, since it had the greatest influence on the formation of the Lachlan Orogen.

2.2.1 Benambran cycle

The Benambran cycle commenced with molasse sedimentation on the older Delamerian Orogen. It was then controlled by rollback of the southern part of the proto-Pacific plate (Glen, 2005). A new plate boundary formed about 1000 km east of the Delamerian margin, and led to the formation of the intraoceanic mafic to intermediate Macquarie Arc (Glen, 2005). Two distinctive collisional phases characterise the Benambran Orogeny (Glen et al., 2007a). The first phase at around 443 Ma resulted in folds, thrusts, cleavage formation and some strike-slip faults deforming Ordovician turbidites and black shale. Deformation was synchronous with alkalic porphyry mineralisation at Northparkes (Lickfold et al., 2007) and Cadia (Wilson et al., 2007a). These deformations are attributed to east-west shortening (Glen, 2005; Glen et al., 2007a). At this stage, volcanism in the Macquarie Arc had ceased and arc rocks were thrusted over and accreted onto back-arc turbidites (Glen, 2005). The second collisional phase (433-430 Ma) of the Benambran Orogeny was manifested by thrust in the Central Lachlan and translation of the Macquarie Arc to the southwest (Glen, 2005; Glen et al., 2007a). This was synchronous with uplift and thrusting of turbidites as well as a portion of the arc itself (Glen, 2005). The second collisional event resulted in the emplacement of S-type granites (Glen et al., 2007a).

2.2.2 Tabberabberan cycle

A large part of Gondwanaland is inferred to have been under extension during the Tabberabberan cycle (430 – 380 Ma: Glen, 2005; Glen, 2006). During the Tabberabberan cycle, the Lachlan Orogen experienced widespread rifting, resulting in formation of several major basins and granite emplacement (Glen, 2005). Granites are divided into I-type granites in the east and mixed I- and S-type granites in the west (Chappell and White, 1984; Glen, 2005). The culmination Tabberabberan phase of deformation resulted from the collision of an intra-oceanic arc that was generated during the previous convergent phase. The arc was accreted to the continental margin in the Northern New England Orogen (Glen, 2005). The Eastern Lachlan Orogen was subjected to northeast-directed shortening at 380 Ma (Miller et al., 2001). Inversion of basins in the Lachlan Orogen during the Middle Devonian typified the Tabberabberan deformation event (Willman et al., 2002).

2.2.3 Kanimblan cycle

The Kanimblan cycle commenced with rifting in the Early to Middle Devonian. Granites intruded and volcanics were erupted into small, narrow rifts (Glen, 2006). The Kanimblan deformation phase began at approximately 340 Ma, and marked the

last major deformation to affect the Lachlan Orogen. Shortening was predominantly east-directed, and minor strike-slip faults were developed locally (Glen, 2005). In the eastern Lachlan Orogen, north-striking faults were reactivated during basin inversion and produced folds and axial planar cleavages (Glen, 2005).

2.3 Lachlan Orogen

The Lachlan Orogen extends from southern Queensland to Tasmania, and underlies most of New South Wales and Victoria (Fig. 2.2). Compared to neighbouring orogens, the Lachlan Orogen has a particularly complex evolutionary history (Gray and Foster, 2004). The Lachlan Orogen formed as a result of episodic accretion of deformed oceanic sequences, volcanic arcs and arc-related rocks, and microcontinents to the Gondwana margin during the Lachlan tectonic supercycle (Gray and Foster, 2004; Glen, 2005). Figure 2.2 shows the principal components of the Lachlan Orogen, which is dominated by turbidites that were deposited in a back-arc environment. The turbidites have undergone low-grade metamorphism with local high-temperature low-pressure metamorphic complexes also present (Barron, 1999). Arc-related igneous complexes characterise the eastern portion of the Lachlan Orogen (Fig. 2.2).

A Neoproterozoic to Cambrian marine clastic sequence of turbidites characterises the western Lachlan Orogen (Gray and Foster, 2004). The marine sedimentary rocks are associated locally with mafic and rare ultramafic volcanic rocks interpreted to be related to an Early to Middle Cambrian oceanic island arc (Crawford and Keays, 1987). Overlying the Cambrian sequence are extensive Ordovician and Early Silurian turbidites. The turbidites comprise sandstones and shales, with minor mafic volcanic and carbonate rocks and cherts (Powell, 1984; Wyborn, 1992; Gray and Foster, 2004). Locally, feldspathic arenites, intercalated with quartzose sedimentary rock units, might have been derived from the Macquarie Arc (Glen and Walshe, 1999). Craton-sourced quartzose sediments occur in both back-arc (Wagga Marginal Basin) and fore-arc (Monaro Fore-Arc Basin) regions relative to the Late Ordovician Macquarie Arc. Glen et al. (1998) suggested that the current ‘fore-arc’ sediments may have been structurally relocated from an original back-arc setting. This turbiditic package together with associated accreted rocks, was repeatedly thickened by folding and thrusting, dismembered by strike-slip faulting, thinned by extension-related faulting, intruded by plutons and finally amalgamated during accretion.

2.4 Macquarie Arc

In its eastern part, the Lachlan Orogen contains mafic to intermediate volcanic and volcaniclastic rocks of Ordovician to Early Silurian age (Fig. 2.2). This rock association constitutes the Macquarie Arc (Glen, 1998), which now crops out as a series of north-trending, fault-limited belts.

The Macquarie Arc is composed of subaqueous volcanic and volcaniclastic rocks and associated shallow-level intrusions of calc-alkalic, high-K calc-alkalic and shoshonitic magmatic affinities (e.g. Crawford et al., 2007a; Cooke et al., 2007). Magmatic activity in the Macquarie Arc commenced in the Early Ordovician, at the convergent margin between the Australian and proto-Pacific plates (Glen et al., 1998; Glen, 2005; Glen et al., 2007b; Meffre et al., 2007). The volcanic arc had an intra-oceanic setting from Early Ordovician to Early Silurian times (Crawford et al., 2007a; Glen et al., 2007b). The arc evolved through episodic magmatic pulses for a 50 m.y. period until magmatism ceased in the Early Silurian (Glen et al., 2007c). Formation of the Macquarie Arc has been attributed to magmatism associated with a west-dipping subducting slab that underwent slab rollback. This resulted in the eastward migration of magmatism and is reflected in a general eastward younging of the arc (Percival and Glen, 2007).

The Macquarie Arc consists of several igneous complexes that were dismembered and deformed during Early Silurian accretion to the Gondwana margin. Their geometries were strongly affected by the interplay of two regional-scale strike-slip fault systems: the Tullamore and Gilmore Fault zones (Glen, 2005). The Macquarie Arc now comprises four elongate belts (Fig. 2.3). These are, from west to east: the Junee-Narromine Volcanic Belt (JNVB); the Molong Belt (MVB); the Rockley-Gulgong Volcanic Belt (RGVB); and, in the south, the Kiandra Volcanic Belt (KVB). The current architecture of the volcanics and associated intrusive complexes is attributed to splitting of a single arc by pure extension or sinistral strike-slip fault movement (Glen et al., 1998).

2.4.1 Junee-Narromine belt

The northerly-striking, more than 200 km long, Junee-Narromine Volcanic Belt (Fig. 2.3) is the western-most belt in the Macquarie Arc. Exposure is poor, as most of the rock units lie beneath younger Paleozoic to Holocene cover. The current understanding of this belt is based largely on drilling, aeromagnetic and gravity data, randomly scattered outcrops and mine exposures (Glen et al., 2007d). The southern part of the north-northwest-trending belt hosts the Cowal gold district. Cowal is located to the west of the north-striking Tullamore Fault (Fig. 2.3). The central portion of the belt is

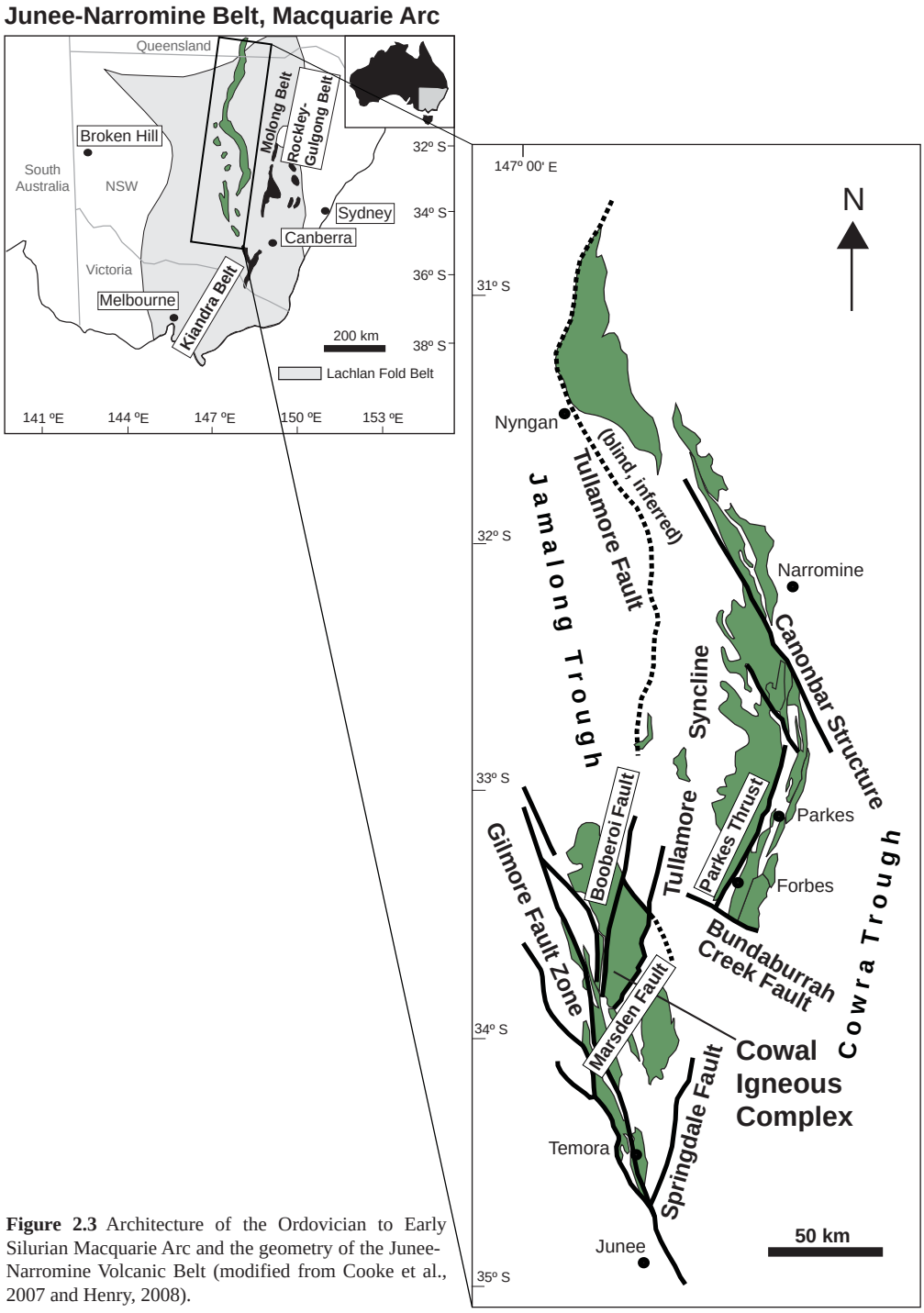

Figure 2.3 Architecture of the Ordovician to Early Silurian Macquarie Arc and the geometry of the Junee-Narromine Volcanic Belt (modified from Cooke et al., 2007 and Henry, 2008).

curved and has been fragmented by the Parkes and Bundaburrah Creek faults, and by the Cabonbar Structure. The central part of the JNVB hosts the Northparkes porphyry Cu-Au deposits.

Volcanic facies architecture analysis and the geochemical affinities of the igneous rocks suggest that the JNVB formed the volcanic centre of the Macquarie Arc (Crawford et al., 2007a; Glen et al., 2007b; Percival and Glen, 2007). The JNVB

consists of several compositionally distinctive igneous complexes, each of which comprises volcanic and volcaniclastic successions that were intruded by various porphyries (Glen et al., 2007d). Mafic to intermediate volcaniclastic rocks, shales, limestones, and various dioritic to monzonitic intrusions are characteristic of the JNVB. The JNVB experienced two major periods of volcanic activity (Early Ordovician and Late Ordovician to earliest Silurian) and the volcanic hiatus was marked by deposition of early Late Ordovician limestones (Glen et al., 1998). In the Northparkes district, the Late Ordovician shoshonitic Wombin Volcanics are associated with high-level monzodioritic intrusions which host Cu-Au porphyry mineralisation.

2.4.2 Molong and Rockley-Gulgong belts

The Molong Belt is the best researched region of the Macquarie Arc, because it is well exposed compared to the JNVB. Both the central Molong and eastern Rockley-Gulgong belts (Fig. 2.3) consists of basal Ordovician to Lower Silurian submarine, deep-water volcaniclastic rocks that vary from basaltic to andesitic and latitic (Crawford et al., 2007a). Most rocks in the Molong belt are mafic (Glen et al., 2002). Local quartz-bearing phases include dacite, quartz diorite, rhyolite and quartz-bearing monzonites (Gray and Foster, 2004). The early Late Ordovician limestone packages that marked the volcanic hiatus in the JNVB also occur in the Molong and Rockley-Gulgong belts (Percival and Glen, 2007). In the Molong belt, the Late Ordovician – Early Silurian shoshonitic Forest Reefs Volcanics host monzonites, which contain Cu-Au mineralisation in the Cadia district. (Walshe et al., 1995; Cooke et al., 2007).

2.4.3 Magmatism

Four major magmatic pulses contributed to the formation of the Macquarie Arc (Crawford et al., 2007a). Each magmatic pulse produced igneous rocks with distinctive chemical compositions that reflect the progressive evolution of the Macquarie Arc. Phase 1 of magmatic activity (490 – 475 Ma) produced the Nelungaloo and Cowal Volcanics, and the Mitchell Formation sedimentary rocks (Crawford et al., 2007a; Glen et al., 2007c). In the Northparkes district, the Nelungaloo Volcanics comprise volcaniclastic and primary volcanic rocks that have been intruded by early Ordovician monzonites (Crawford, 1999; Glen et al., 2007b). The Mitchell Formation forms the basement to the Molong Belt and consists of volcaniclastic conglomerate, sandstone and siltstone with minor lavas (Glen et al., 2007b). Compositionally, the early Ordovician phase of Macquarie arc magmatism was dominated by high-K calc-alkaline to shoshonitic basalts, basaltic andesites and andesites. More felsic lavas (SiO_2 > 63%) are absent, in contrast to younger Macquarie Arc suites (Glen et al., 2007b).

The εNd isotopic values of Phase 1 rocks indicate an absence of any old continental crust component in the petrogenesis of the Phase 1 volcanics, supporting the intra-oceanic arc interpretation (Glen et al., 2007b). An approximate 9 m.y. period separated Phase 1 and 2 magmatism, possibly corresponding to opening of the Wagga back-arc basin (Crawford et al., 2007a).

The second phase of Macquarie Arc magmatism (467 – 455 Ma) was a major volcano-plutonic pulse. Phase 2 magmatism produced some of the Cowal intrusions (E35, E39, E43 and around Marsden prospect), the Narromine Intrusive Complex, Cargo Volcanics, Byng and Blayney Volcanics and Fairbridge Volcanics (Crawford, 1999; Crawford et al., 2007a). This phase is characterised by three compositionally distinctive rock suites: (i) medium-K calc-alkaline lavas; (ii) medium- to high-K dioritic to monzonitic intrusions; and (iii) medium-K to dominantly high-K calc-alkaline rocks with a clear trend to shoshonitic compositions late in the Phase 2 (Crawford et al., 2007a).

Phase 3 (452 – 445 Ma) was a short, sharp tectono-magmatic event that resulted in regional uplift, and produced limestones, and the distinctive, relatively widespread but small volume, Copper Hill-type high-level quartz-phyric intrusions. The Copper Hill-type intrusions were emplaced during an extensive volcanic hiatus marked by development of shallow-marine limestones and overlying deeper water fine-grained clastic rocks in the Junee-Narromine and western Molong Belt (Crawford et al., 2007a). The Copper-Hill type magmatism generated porphyritic dacites, holocrystalline diorites and granodiorites typified by medium-K calc-alkaline compositions (Crawford et al., 2007a).

Late Ordovician – Early Silurian magmatism (445 – 438 Ma) was dominated by relatively evolved (compared to Phase 2 lavas) shoshonitic lavas and monzonitic porphyries (Perkins et al., 1995; Lickfold et al., 2003; Crawford et al., 2007a). These Phase 4 shoshonitic rocks host significant Cu-Au porphyry mineralisation at Cadia and Northparkes (e.g. Blevin, 2002; Holliday et al., 2002; Cooke et al., 2007; Lickfold et al., 2007).

Glen et al. (2007c) interpreted phase 1, 2 and 3 magmatism to be pre-accretionary in nature. At this time, the arc was located on the Gondwana Plate, above a west-dipping subduction zone, and was separated from the Gondwana margin by the Wagga Basin (Glen et al., 2007c). In contrast, the Late Ordovician – Early Silurian shoshonitic porphyries (Phase 4 magmatism) are syn-accretionary, and were emplaced into tilted and strongly deformed volcanic and volcaniclastic packages during a relaxation event in the multiphase Early Silurian Benambran cycle (Glen, 2005; Glen et al., 2007c). It appears that the northwest-trending Lachlan Traverse Zone (cross-arc structure) was

a favorable loci for Phase 4 shoshonitic porphyries in both the Northparkes and Cadia districts (e.g. Glen and Walshe, 1999; Lickfold et al., 2003; Wilson et al., 2003; Cooke et al., 2007; Glen et al., 2007c).

2.4.4 Metallogeny of the Macquarie Arc

Figure 2.4 shows the location of major gold and copper deposits in the Macquarie Arc. Apart from the Cowal gold deposits, porphyry-style mineralisation is associated with calc-alkalic and shoshonitic magmatism, and also high-sulfidation Au(Cu) and skarn deposits are present. Economically, the most significant deposits are the alkalic (shoshonitic) Au-Cu porphyry systems at Cadia and Northparkes districts (Walshe et al., 1995; Cooke et al., 2007).

Three significant calc-alkalic porphyry deposits have been discovered in the Macquarie Arc: Copper Hill, Cargo and Marsden (Fig. 2.4). The Copper Hill deposit (133 Mt @ 0.32% Cu, 0.28 g/t Au; Harris et al., 2008) is related to a composite intrusive complex of tonalite, quartz diorite and dacite (Girvan, 1992; Cooke et al., 2007). The Cargo calc-alkalic Au-Cu porphyry prospect also occurs in the Molong Belt. Cargo consists of a central breccia complex that has been cut by late-stage veins that carry the bulk of gold mineralisation (3.7 Mt @ 1.24 g/t Au; Harris et al., 2008). As yet, no significant resources have been delineated at Cargo (Cooke et al., 2007). The Marsden porphyry centre occurs on the eastern side of the Cowal Volcanic Complex, and is the

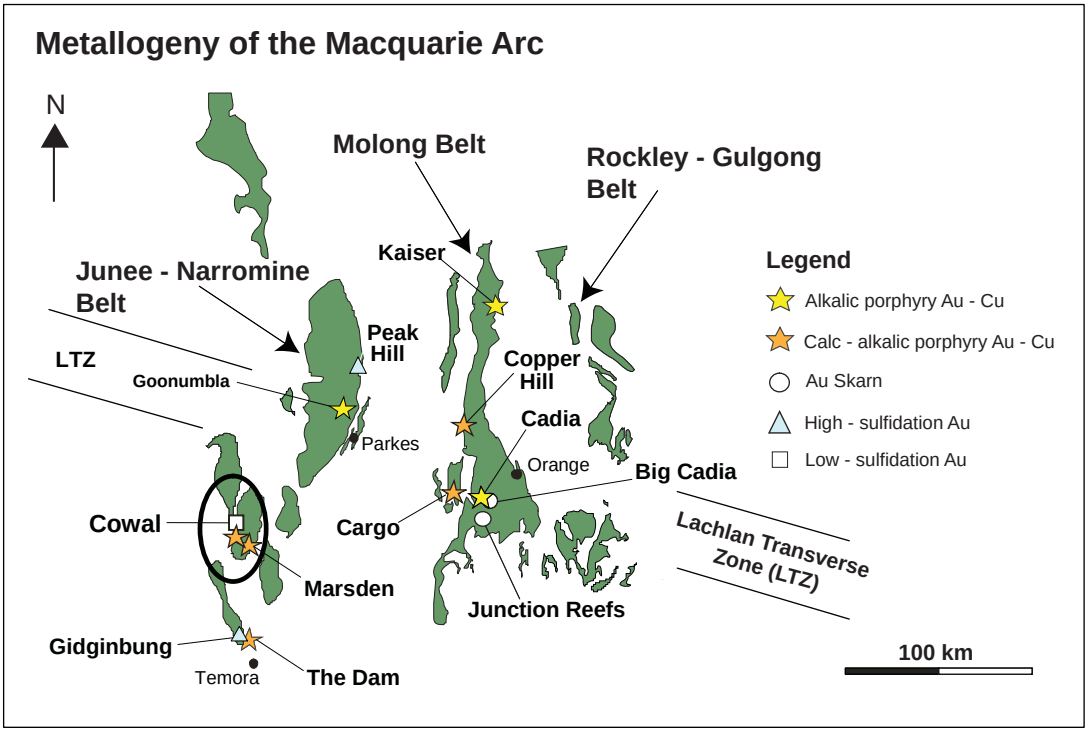

Figure 2.4 Selected porphyry, epithermal and skarn deposits related to Ordovician and Early Silurian magmatism in the Macquarie Arc (modified from Holliday et al., 2002).

largest mineralised system associated with calc-alkalic intrusions in the Macquarie arc (76.7 Mt @ 0.5 % Cu, 0.3 g/t Au; Harris et al., 2008). Other sub-economic calc-alkalic porphyry deposits occur at Mandamah, The Dam and Culingerai in the Rain Hill district (Smith et al., 2004; Cooke et al., 2007). In the Cowal district, subeconomic calc-alkalic porphyry prospects occur at Endeavour 39 (E39) and Endeavour 43 (E43; Fig. 2.5) and are described in more detail below in section 2.5.5.

Skarns occur at several localities in the Macquarie Arc (Fig. 2.4). Examples include the Big Cadia and Little Cadia magnetite-copper-gold skarns in the Cadia district, the Endeavour 6, Endeavour 7 and Endeavour 44 Au-Pb-Zn skarns in the Northparkes district and the Au-skarn at Junction Reefs (Jones, 1985; Gray et al., 1995; Cooke et al., 2007).

Ordovician high-sulfidation epithermal Au deposits have been discovered at Peak Hill, Temora and Dobroyde (Masterman et al., 2002; Cooke et al., 2007). In the Cowal district, the E35 prospect (Fig. 2.5) has alteration features consistent with a high-sulfidation style of mineralisation (P. McInnes pers. comm., 2007). The gold deposits are associated with zones of advanced argillic alteration, typified by pyrophyllite, alunite and muscovite. Vuggy quartz is uncommon and pyrophyllite is abundant, implying that the upper parts of these high-sulfidation systems have been eroded (Masterman et al., 2002). A deeper level of erosion is consistent with exposure of mineralised porphyry centres elsewhere in the Macquarie Arc (Cooke et al., 2007).

2.5 District-scale geology

2.5.1 Cowal Igneous Complex

The Cowal Igneous Complex (CIC), as termed by Crawford et al. (2007b), is located in the southern portion of the Junee-Narromine Volcanic Belt (Fig. 2.3 and Fig. 2.4), situated between Gilmore Fault Zone to the west and the Parkes Thrust to the east (Miles and Brooker, 1998).

The CIC has an oval shape in plan (Fig. 2.5) and is approximately 40 km long and 15 km wide. Although outcrop in this region is extremely limited, the volcanic complex is obvious on regional-scale aeromagnetic images, forming a distinctive magnetic high (Fig 2.5). The CIC consists of primary, reworked and resedimented volcanic, volcaniclastic and sedimentary rocks and multi-phase intrusions (Crawford et al., 2007b). The central and northern portions of the CIC are dominated by volcano-sedimentary successions that have been intruded by gabbro, diorite to syenite intrusive suites (McInnes et al., 1998; Miles and Brooker, 1998), whereas the southern part consists of large, multi-phase calc-alkalic intrusions (McInnes et al., 1998).

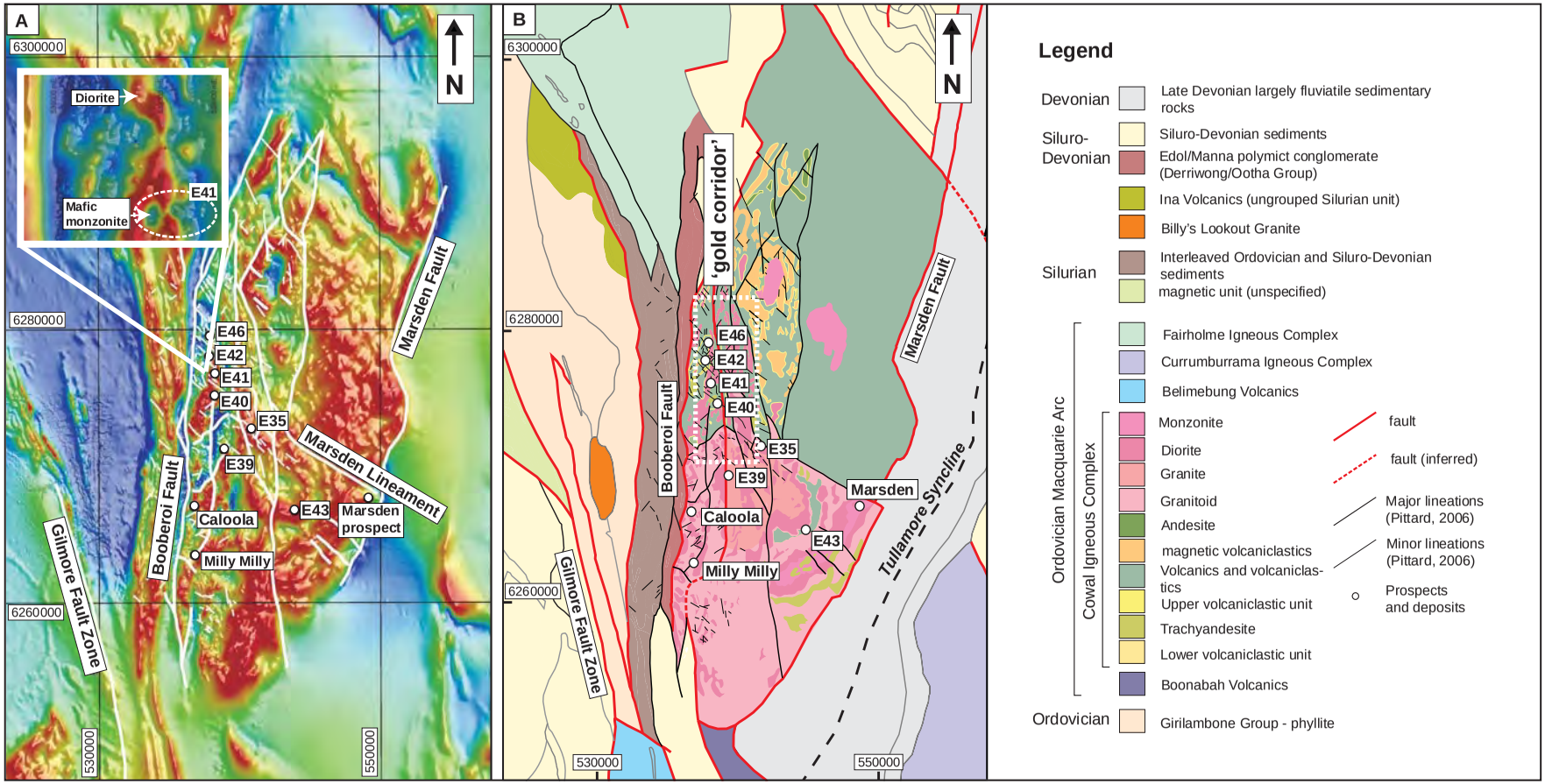

Figure 2.5 A. Aeromagnetic image of the CIC and surrounding rock units, highlighting the location of gold deposits and prospects. **B.** Geology of the CIC (adapted from Henry, 2008).

2.5.2 Cowal Volcanic Complex

The Cowal Volcanic Complex dominates the central and northern parts of the CIC and are subordinate in the southern portion of the district (Fig. 2.5). The volcanic rocks include lavas, monomictic and polymictic volcanic and volcaniclastic breccias and conglomerates (Miles, 1993; Miles and Brooker, 1998; Bastrakov, 2000; Cannell, 2003; Simpson and Cooke, 2006; Crawford et al., 2007b). Laminated mudstone facies also constitute part of the Cowal volcano-sedimentary succession (e.g. Miles and Brooker, 1998).

Volcanic and intrusive associations of the Cowal district are reviewed briefly below, based primarily on previous studies of the E42 deposit, and E46 and E40 prospects. They are described in geographical order from north to south (Fig. 2.5). A detailed description of the E41 host stratigraphy is presented in Chapter 3.

2.5.2.1 Facies architecture of E46

The E46 prospect is located approximately 2 km north of E41 (Fig. 2.5). Simpson and Cooke (2006) recognised 15 principal volcanic and sedimentary facies in the Cowal volcanics at E46 and classified them into three major groups: (1) coherent facies; (2) monomictic breccia facies; and (3) polymictic breccia, sandstone and mudstone facies.

Coherent facies at E46 include dykes, sills and lavas. They are largely represented by variably plagioclase-phyric coherent facies. Volumetrically subordinate aphyric and amygdaloidal plagioclase + K-feldspar-phyric facies are also present. The monomictic breccia facies are massive, matrix-supported and dominated by clasts of either feldspar-phyric or aphyric rocks. The breccias are locally associated with lava and are interpreted as hyaloclastite and/or peperite. Polymictic breccia facies include; (a) variably crystal ± fiamme ± lithic-rich breccia, (b) aphyric and feldspar-phyric wispy fiamme (pumice) breccia, and (c) minor polymictic amygdaloidal-clast-bearing breccia. Sandstone and mudstone facies are typically interbedded with each other and/or polymictic breccia facies. Sandstone facies are commonly crystal-rich and mudstone facies typically have a distinctive red colour.

The environment of deposition at E46 has been interpreted as a subaqueous basin or depocentre, proximal to an Early Ordovician volcano (Simpson and Cooke, 2006; Simpson, 2008).

2.5.2.2 Facies architecture of E42

The E42 deposit is located less than 1 km north of E41 (Fig. 2.5). The volcano-sedimentary host stratigraphy of E42 is divided into upper and lower sequences of

polymictic breccia, sandstone and mudstone facies separated by a trachyandesitic lava and capped by an andesitic cryptodome (Miles, 1993; Miles and Brooker, 1998; Cannell, 2003; Smolonogov, 2003; Strickland, 2005). The lower sequence is characterised by polymictic breccia and sandstone facies interbedded with laminated, red mudstone. Above this is a trachyandesite lava with associated hyaloclastite and peperite breccia facies. The major features of the upper polymictic breccia and sandstone sequence are feldspar-phyric clasts, wispy chlorite-altered fiamme (vitric) clasts and crystal-rich sandstone (Cannell, 2003). The stratigraphy is capped by a weakly porphyritic andesite with associated hyaloclastite breccia interpreted as a partially emergent cryptodome (Cannell, 2003).

The E42 volcano-sedimentary succession was interpreted to have formed in a relatively deep water environment (Miles and Brooker, 1998) with episodic injections of magma into either consolidated or wet sediments, as indicated by the presence or lack of peperite. The upper polymictic facies with a pyroclastic component are interpreted as mass flow units and imply a proximal volcanic setting.

2.5.2.3 Facies architecture of E40

The E40 prospect is located less than 1 km southeast of E41 (Fig. 2.5). Based on cursory drill core examination as part of this study, the host sequence at E40 is dominated by distinctive dark red (locally dark grey) massive to laminated mudstone. Sandstone facies are rare and polymictic breccia facies are absent. Relatively little data from this prospect has been collected by Barrick Gold of Australia Ltd., as the drilling program consists of only a few diamond drill holes. The abundance of mudstone and lack of coherent facies implies a distal volcanic setting, in contrast to the settings of E42 and E46.

2.5.3 Intrusive rocks

The Cowal Volcanics have been intruded by many sills, dykes and stocks. The northern portion of the CIC has been intruded by high-level K-feldspar + quartz-phyric monzogranites with distinctive, locally aplitic textures (Crawford et al., 2007b). The western side of the central part of the district has been intruded by a large north-trending diorite sill that has localised gold mineralisation at E46, E42 and E41. The diorite sill and the Cowal Volcanics have been cut by many dykes (Miles and Brooker, 1998), including variably plagioclase-phyric dykes (E42 and E46: Strickland, 2005; Simpson and Cooke, 2006), mafic, megacrystic- and pyroxene-phyric dykes and amygdaloidal dykes (E42: Strickland, 2005). These are described in detail in Chapter

3. Granodiorite, diorite and monzonite intrusions dominate the southern part of the CIC (Fig. 2.5). These are described in section 2.5.7.

2.5.4 Derriwong Group

The CIC rocks are surrounded by and unconformably overlain by Siluro-Devonian sedimentary and volcanic rocks of the Derriwong Group (Ootha beds and Manna Conglomerate). These marine sediments crop out to the north, south and west of the Cowal district, in a series of hills that include the Booberoi Hills, and the Wamboyne and Manna mountains (Miles, 1993). The conglomerate is a poorly sorted, massive, matrix-supported unit, containing quartz pebbles and less abundant metasedimentary clasts that range from 0.5 mm to over 1 m in diameter (Miles and Brooker, 1998). The rocks of the Booberoi Hills and Wamboyne Mountains are highly deformed and define a structure known as the Booberoi Fault (Ingpen, 1995). This structure forms a prominent series of hills in otherwise flat topography. This north-trending structure is apparent on regional aeromagnetic images (Fig. 2.5) on the western side of the CIC and is interpreted to be a splay off the Gilmore Fault zone (McInnes et al., 1998).

2.5.5 Recent sediments

The CIC is covered by recent lake sediments (transported soils), up to 30 m thick, which are dominated by clays with variable sand and gravel contents. Quaternary to Tertiary lacustrine sedimentary rocks overlie a Tertiary laterite profile, comprising a mottled zone and underlying saprolite zone that averages 10 to 20 m in thickness, lying beneath the transported sequence. Saprolite is applied to all completely weathered rocks. Saprock that underlies saprolite, in the general weathering profile, is defined by rocks with residual rock textures (Dykmans, 2004b). Figure 2.6 shows the laterite profile in the walls of the E42 open pit.

2.5.6 District-scale structure

Aeromagnetic geophysical surveys have been useful for understanding the structural architecture of the CIC. A series of north-, northwest to northeast-trending principal structures are obvious on the aeromagnetic image of the CIC (Fig. 2.5A). These lineaments separate what are interpreted to be fault-bounded blocks that behaved as individual bodies during deformation cycles and were rotated heterogeneously with respect to each other (Henry, 2008). Due to morphological features that are distinctive on aeromagnetic images (Figs. 2.5A and B), the CIC itself is interpreted to be much less deformed than other Ordovician volcanic rocks to the west and south of the district (Glen and Fleming, 2000; Glen at al., 2002).

Figure 2.6 E42 open pit photograph showing the laterite profile (looking west).

Several major faults have been recognised in the CIC. The district is bounded to the east by the Marsden Fault (Fig. 2.5A and B) which is a north-northeast trending, west-dipping thrust that juxtaposes Ordovician rocks over Devonian sandstones (Glen et al., 2007b). To the west, the CIC is bounded by the Booberoi Fault (Fig. 2.5A). The steeply west-dipping Booberoi Fault is a major shear zone that has deformed the basal conglomerate of the Siluro-Devonian Ootha Group. The fault changes orientation from north-trending near E42 to northwest-trending near Temora (Ingpen, 1995). Multiple deformation events are recorded within this fault (Ingpen, 1995).

The west-northwest-trending Marsden Lineament divides the Cowal district into two separate blocks: (1) a northern block dominated by volcanic and sedimentary rocks, and (2) a southern block dominated by intrusive rocks (Fig. 2.5B). The southern igneous complex appears to have been uplifted relative to the units located to the north of the Marsden Lineament (P. McInnes per. comm., 2006), potentially providing an insight into the root zone of the northern and central parts of the CIC.

There are lineaments in the CIC magnetic image that have similar orientations to both the north-trending Tullamore and northwest-trending Gilmore faults of the Junee-Narromine Belt (Fig. 2.3). These north- and northwest-trending structures appear to reflect deep-seated crustal weaknesses in the Macquarie Arc that may have developed possibly in response to reactivation of Proterozoic basement structures (Scheibner, 1973; Glen and Walshe, 1999). The west- and northwest-trending structures within the Cowal district are consistent with the trend of a major regional lineament, the Lachlan Traverse Zone (LTZ; Fig. 2.4). The LTZ is interpreted to be the major cross-arc structural trend in the Macquarie Arc (Glen et al., 1998; Glen and Walshe, 1999).

Alkalic (shoshonitic) mineralising intrusions at Northparkes and Cadia are spatially related to the LTZ structural trend (Heithersay et al., 1990; Holliday et al., 2002; Lickfold et al., 2003; Wilson et al., 2003). Although the Cowal district is located more than 100 km south of the LTZ, similar NNW structural trends have been documented by Henry (2008) at E42, where many faults, dykes, and sheeted gold-bearing veins are related to northwest-trending structures.

2.5.7 Mineral deposits of the Cowal district

A number of significant mineral deposits occur in the CIC. The southern part of the district is where several calc-alkalic porphyry copper prospects occur. These are: Marsden, E39 and E43 (Cooke et al., 2007; Bissig, 2007). The Marsden prospect is located on the south-eastern edge (Fig. 2.5) of the CIC, 15 km SE of E42. It is characterised by intrusive rocks that range from mafic gabbros to high-level granophyric felsic intrusive rocks (Crawford et al., 2007b). E39 is a large, low grade (0.25% Cu) porphyry Cu prospect, hosted by granodiorite. Although biotite – K-feldspar, magnetite and sericite alteration as well as quartz – chalcopyrite veins have been identified, no economic grades have been found at E39.

The E43 prospect is located to the southeast of E39 (Fig. 2.5). Bissig (2007) recognised ten intrusive units at E43 that range from early diorite, granodiorite and monzonite porphyries and minor aplites to syn-mineralisation pyroxene-phyric and dacite porphyries. There is also a syn-mineralisation magmatic – hydrothermal breccia at E43 (Zukowski, 2009). Late- to post-mineralisation intrusive units at E43 include a vesicular dyke and equigranular monzonite. Mineralisation at E43 is characterised by quartz – chalcopyrite ± magnetite ± K-feldspar veins hosted by coherent andesites and volcaniclastic rocks that have been intruded by dacites, granodiorites, monzodiorites and monzonites (Bissig et al., 2008). Re-Os dating of molybdenite from E43 returned an age of 463.5 ± 2.1 Ma for the Cu-Au porphyry-style of mineralisation at CIC (Bissig et al., 2008; Chapter 3).

E35 prospect is situated northeast of E39. It consists of granodiorite and subordinate monzonite suites (Crawford et al., 2007b). A zone of high-sulfidation style advanced argillic alteration at E35 was reported by Bastrakov (2000). The prospect is characterised by kaolinite and alunite alteration (Bissig et al., 2008) and scattered Au, Cu, Pb, and Zn mineralisation (P. McInnes per. comm., 2009). Ar^{40}-Ar^{39} age of 465.6 ± 4.7 Ma (Bastrakov, 2000) for hydrothermal sericite from the E35 prospect indicates a potential temporal relationship to porphyry mineralisation at E43.

The central part of the CIC contains four gold deposits. From north to south, these are the E46, E42, E41 and E40 systems (Fig. 2.5). They occur adjacent to and

within the north-trending diorite body. This north-trending zone of gold mineralisation has been named the ‘gold corridor’ by mine workers. It is approximately 6 km long and 2 km wide (Fig. 2.5). The mineralisation and associated alteration features are described in Chapter 5.

The ‘gold corridor’ appears to extend to the south of E40, based on the discovery of weak gold and copper mineralisation at the Caloola, Phoenix, and Milly Milly prospects (McInnes et al., 1998; Fig. 2.5). Aeromagnetic data suggest that the Muddy Lake diorite extends southwards to these prospects, where it may have intruded a large granodiorite intrusive complex. The southern gold prospects are subeconomic, and are spatially associated with a porphyry-copper style system at E39 that appears to have been overprinted by weak structurally controlled gold mineralisation (P. McInnes per. comm., 2009). The best Au and Cu mineralisation occurs at shallow depths. For example, the highest grade hole at Phoenix returned 8m (40 – 48 m) averaging 1.61g/t Au and 0.59% Cu and may relate at least in part to supergene enrichment of weak hypogene mineralisation (P. McInnes per. comm., 2009).

2.6 Summary

The Cowal Igneous Complex (CIC) formed in an Early Ordovician submarine oceanic island arc. It was accreted to the Australian continent in the Late-Ordovician to Early Silurian. Four major pulses of volcanism and magmatism contributed to the overall formation of the Macquarie Arc; of these, Phase 1 and 2 magmatic activity had the greatest influence on the CIC, producing volcanic and most of the intrusive rock units. Episodic calc-alkaline and shoshonitic magmatic pulses have produced porphyry- and epithermal mineralisation in the CIC.

CHAPTER 3
Geology of the E41 deposit

3.1 Introduction

This chapter documents the geological environment of the E41 gold deposit. The Ordovician volcanic and sedimentary facies architecture and intrusive history are interpreted from cross sectional relationships. The host succession is compared to the stratigraphy of E42 and E46 to provide context for and to aid in the interpretation of the depositional environment of the host succession. In addition, new geochronological data for intrusive rocks from the E41 deposit are integrated with previous geochronology of the Cowal Igneous Complex.

No detailed geological descriptions have been completed for the E41 deposit prior to this study. There are several unpublished company reports, including: McInnes (1997), Ashley (2004; 2005), Dykmans (2004a), and Munroe et al. (2005) that described geology and some structural features of the E41 deposit. Crawford et al. (2007b) showed that the E41 intrusive complex comprises mafic and ultramafic rocks. The current study is the first detailed investigation of the volcano-sedimentary facies architecture and intrusive history. Preliminary results were provided in Zukowski et al. (2007 a and b).

Figure 3.1 is a plan view of the interpreted district geology, highlighting the location of E41 in relation to E42. It shows the locations of three cross sections that have been studied in detail at E41. Figure 3.2 presents interpreted deposit geology, showing the geometry, spatial relationships and distribution of clastic and intrusive rocks.

3.2 Pre-mineralisation volcano – sedimentary stratigraphy

3.2.1 Mudstone facies

The mudstone facies is volumetrically the most abundant sedimentary unit at E41. It has been intersected only in the E41 east pod. Mudstone thickness increases towards the south, reaching a thickness of 230 m (section 86800E; Fig. 3.2). The mudstone packages are mostly thinly laminated to thickly bedded, with laminae ranging from 3 mm to 1 cm thick (Figs. 3.3A and B). Massive beds are also present locally. Mudstone facies range from maroon red (Fig. 3.3A) to red-green to pale and dark grey, with red mudstone being the most common. The colour of the mudstone facies is related to the composition of individual laminae. Grey beds are dominated by plagioclase,

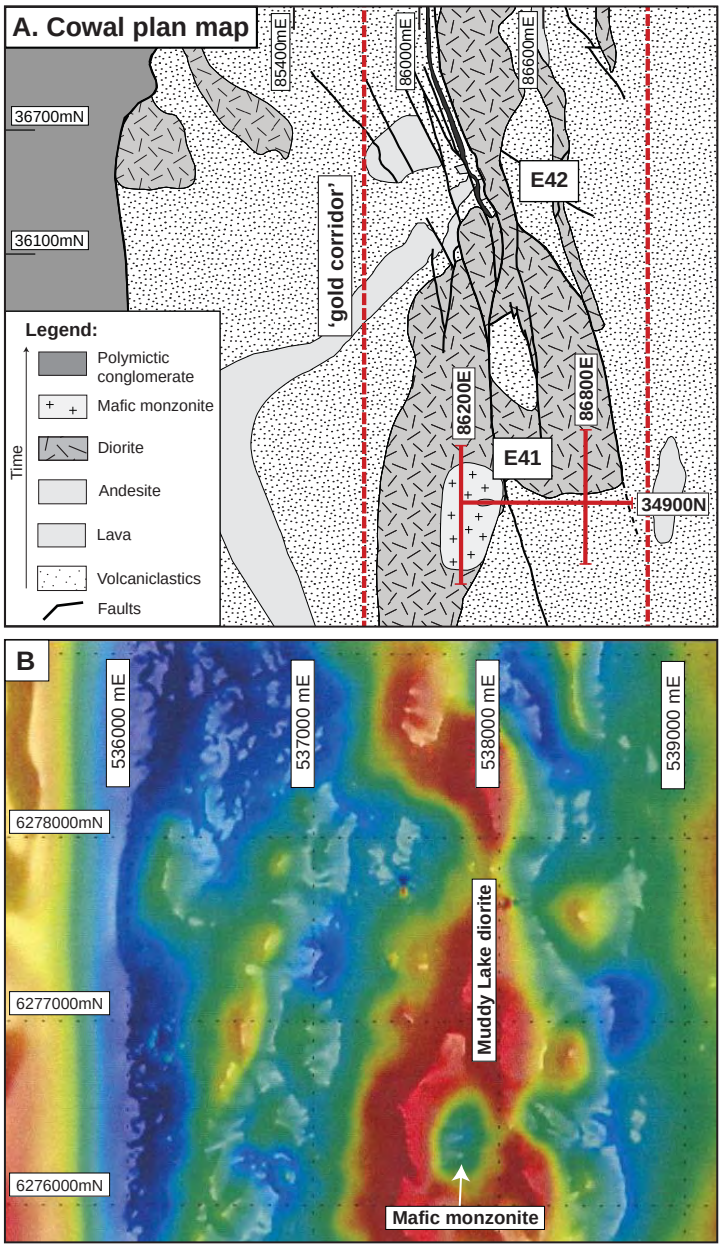

Figure 3.1 A. Location of the E41 and E42 deposit and basement geology of the Cowal district. Both E41 and E42 are spatially associated with the north-trending diorite intrusion (Muddy Lake diorite). Cross sections that were studied as part of this research thesis are indicated. The geological plan is based on modified unpublished mapping by Barrick Gold of Australia Ltd. **B.** Aeromagnetic image of 'gold corridor'. Red anomaly indicates elongated Muddy Lake diorite intrusion. Circular magnetic low at E41 marks the mafic monzonite intrusion. Note that the basement geology is based in drilling and geophysical data. The entire district, outside of E42 open pit is covered by Quaternary to Tertiary cover and recent lake sediments (transported soils), up to 30 m thick, which are not shown on this figure.

carbonate and chlorite whereas red beds consist of hematite, plagioclase, carbonate and chlorite. Many of the mudstone beds are dislocated by microfractures. Some beds are convoluted, potentially indicating the effect of folding or soft sediment deformation. Locally, mudstone is interbedded and/or gradational with well-sorted feldspathic sandstone. The interbeds of mudstone and sandstone are particularly common in places where lenses of polymictic volcanic breccias occur.

Massive to laminated mudstone facies have been documented from the lower portion of the E42 deposit, and also from the Eastern volcaniclastic sequence (McInnes et al., 1998; Miles and Brooker, 1998; Cannell, 2003; Strickland, 2005). Mudstones have been noted from E46 (Simpson and Cooke, 2006; Simpson 2008), and they

Geology of Endeavour 41, Cowal district

Legend

Geology

Inferred time of emplacement

- Mudstone
- Polymictic volcaniclastic breccia
- Polymictic volcaniclastic sandstone
- Muddy Lake diorite
- Plagioclase-phyric dyke
- Mafic dyke
- Mafic monzonite
- Hybrid zone
- Quartz-monzonitic, aplite and syenitic dykelets
- Pyroxne-phyric dykes
- Plagioclase-phyric dyke ('diorite' dyke)
- Amygdaloidal dyke
- Post-mineralisation hydrothermal breccia
- Transported
- regolith
- faults
- inferred faults
- shear zone
- diamond drill hole

Magmatic-hydrothermal textures:

- miarolitic cavities

Mineralisation:

- > 0.4 ppm Au
- Supergene enrichment

A. E41 plan map - level 1050

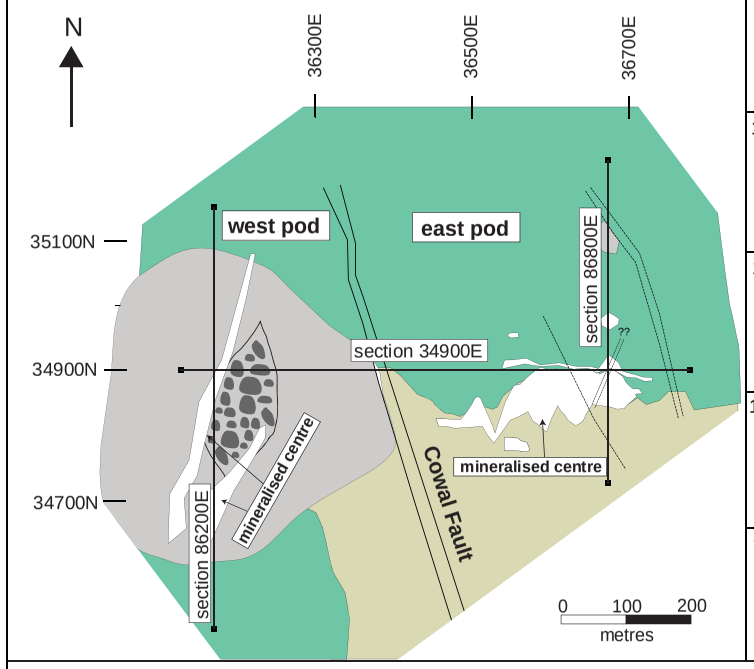

B. Section 34900N, west and east pod

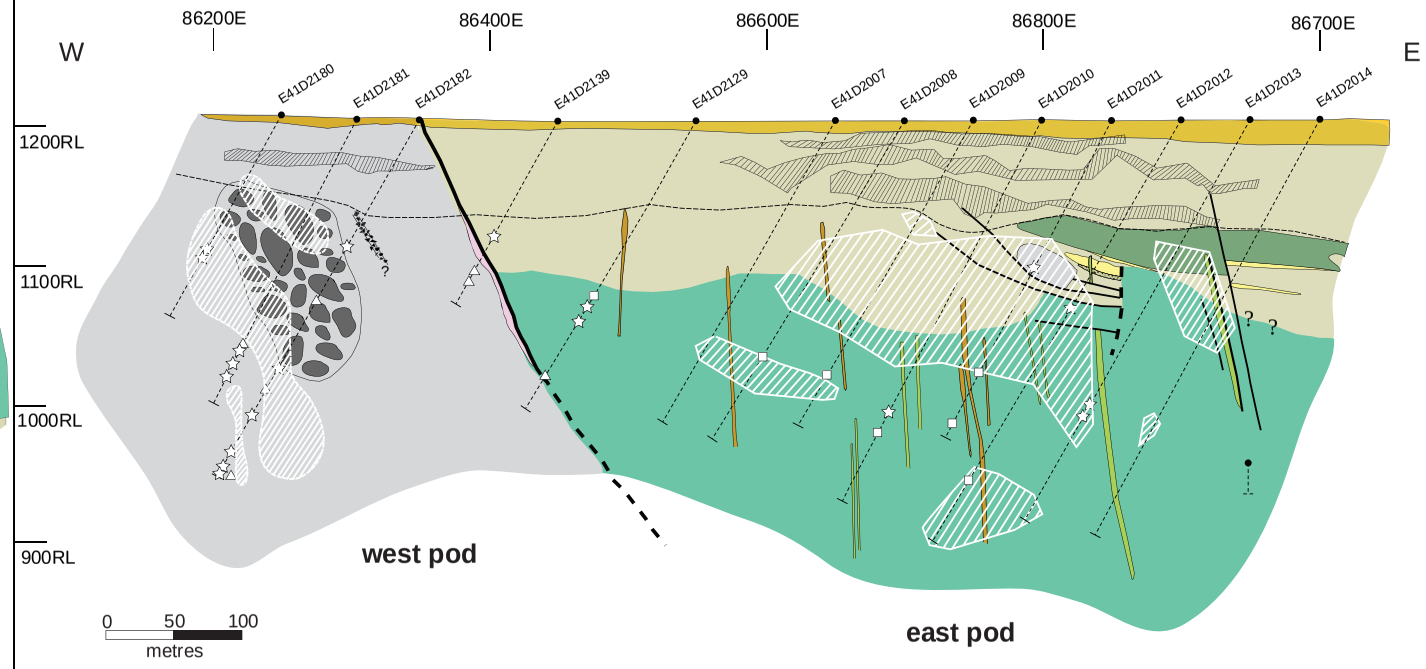

C. Section 86200E, west pod

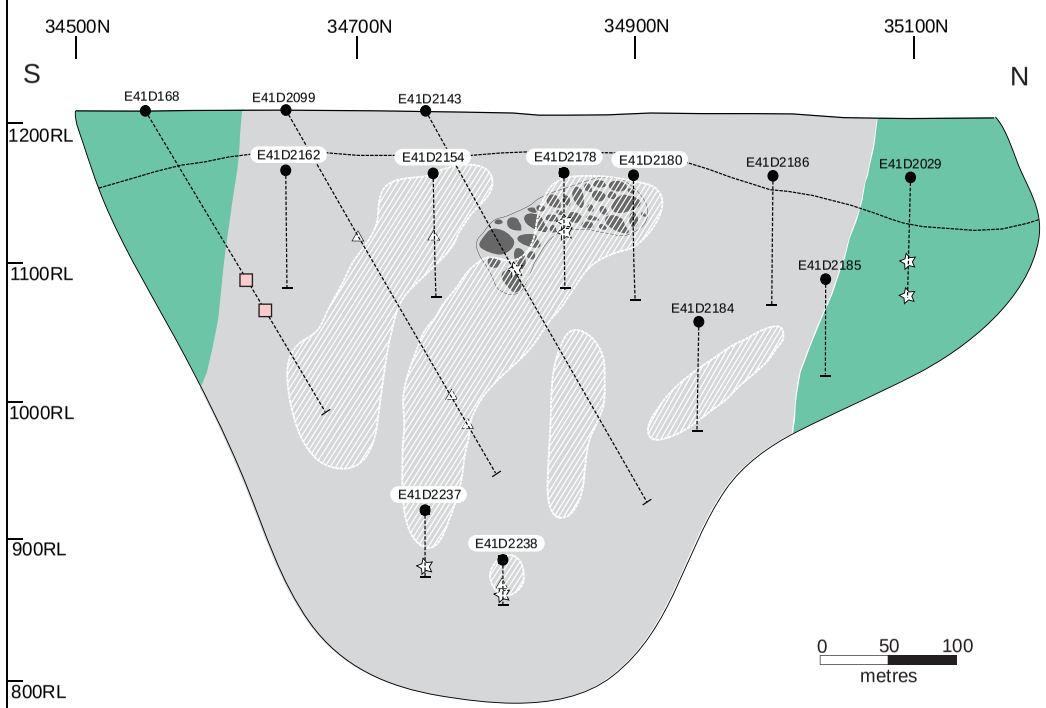

D. Section 86800E, east pod

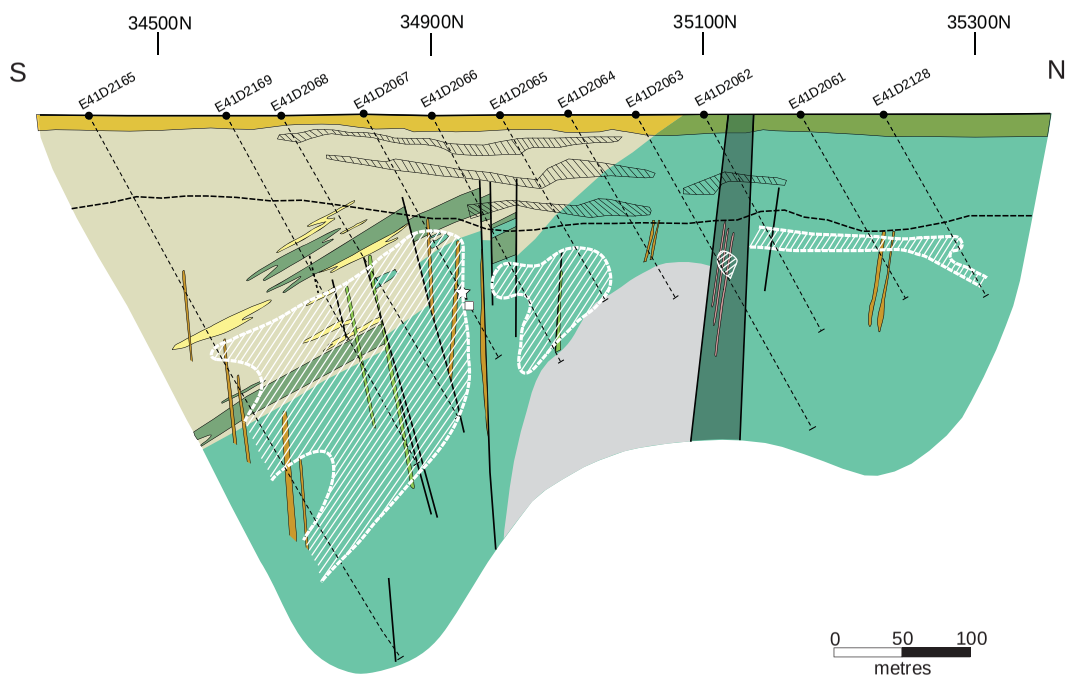

Figure 3.2 Geological cross section through E41 deposit, Cowal district. **A.** Simplified plan map (level 1050) showing west and east pod separated by the Cowal fault. Locations of the studied cross sections are shown. **B.** East-west cross section intersecting east and west pod. **C.** North-south cross section through the west part of the prospect (west pod). **D.** North-south cross section intersecting east pod only.

dominate the host stratigraphy at E40 (McInnes, 1997). The E41 mudstone facies is therefore interpreted to have been deposited contemporaneously with the lower portions of the E42 and E46 volcanic successions, in a subaqueous, relatively deep and quiescent water pelagic environment (Miles and Brooker, 1998; Simpson, 2008) through suspension settling onto a possibly near-horizontal surface.

3.2.2 Polymictic volcaniclastic breccia

Polymictic volcaniclastic breccia facies form ≤ 5 to 10 m thick lenses in the eastern part of the east pod of E41 (section 34900N; Fig. 3.2B). The facies has also been intersected on section 86800E (Fig. 3.2D). The breccias are typically massive to normally graded with medium to thick planar beds. The facies is moderately to well-sorted, and is typically matrix-supported. Contacts with mudstone and sandstone beds are gradational and/or sharp. Angular to subrounded mudstone clasts (Figs. 3.4A and B), black-grey lithic clasts and uncommon rounded fragments of coherent felsic holocrystalline rock (Fig. 3.5B) are the most common clast types. The polymictic breccias contain abundant broken plagioclase (Fig. 3.5A) and rare K-feldspar crystals locally. Clasts size range from 2 to 60 mm. Rare, conspicuous, wispy fiamme fragments (≤10 mm) are also present (Fig. 3.5A). Many of the clasts have been typically affected by hydrothermal alteration, which has in some cases modified their shapes and obscured their primary character. The matrix typically comprises 30 to 90% of breccia beds and is composed of mud- to sand-sized particles. It is typically massive (Fig. 3.4A) but can be thinly laminated locally (Fig. 3.4B). The matrix is strongly altered.

The spatial association of the breccia facies with the volumetrically more abundant mudstone and sandstone facies, combined with the polymictic variety of clasts, is consistent with the breccias being reworked mass flow deposits that settled

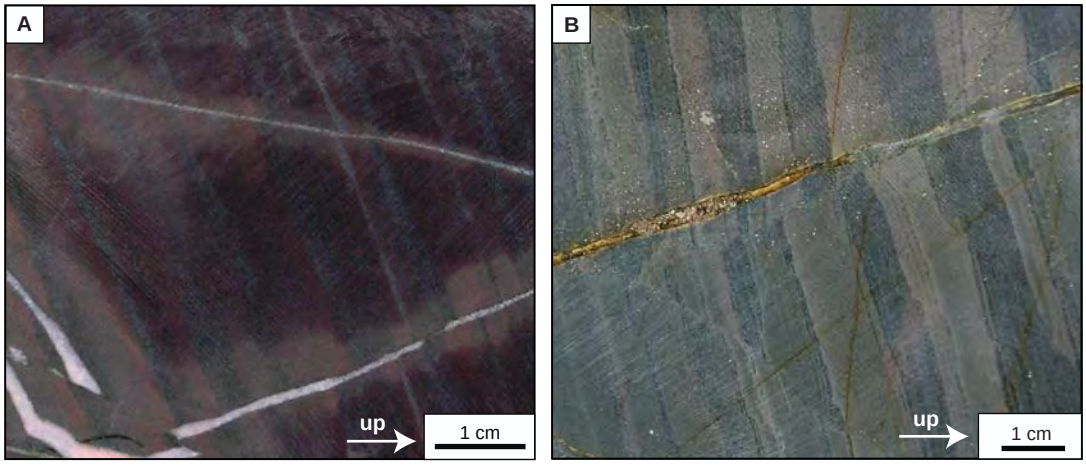

Figure 3.3 A. Red-coloured hematitic, weakly laminated mudstone with bleached halos (carbonate alteration) around calcite veinlets and quartz-pyrite-calcite veinlet (E41D2068, 83.4m). **B.** Grey, laminated mudstone cut by quartz-pyrite-carbonate vein (E41D2068, 71.4m).

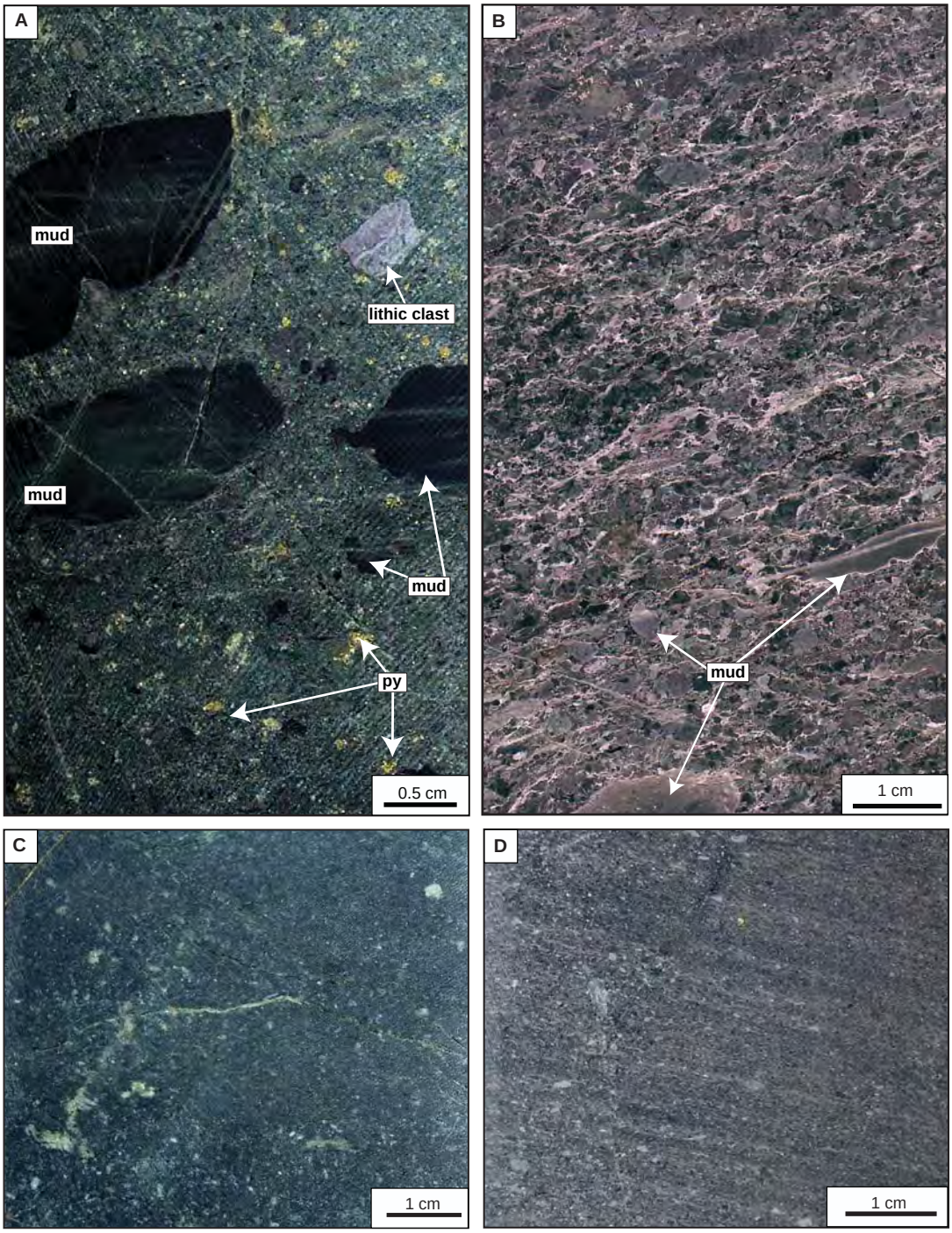

Figure 3.4 Pre-mineralisation volcaniclastic facies. **A.** Polymictic volcaniclastic breccia with mudstone clasts, broken crystals and lithic clasts. Chlorite - pyrite - sericite altered matrix is dominated by fine-grained particles of mudstone and plagioclase crystals (E41D2068, 116.8m). **B.** Monomictic to polymictic, weakly laminated mudstone clast-dominated volcaniclastic breccia facies. Bleached and rimmed mudstone clasts are sericite-altered. Matrix is has been strongly altered to carbonate ± sericite (E41D2014, 113.4m.). **C.** Massive crystal-rich sandstone facies. Sample is altered to magnetite - calcite - epidote - chlorite (E41D2067, 82.5m). **D.** Laminated, mudstone clast-dominated sandstone facies. Sample has been altered to sericite-chlorite and carbonate (E41D2014, 120.1 m). Abbreviations: mud=mudstone clast, py=pyrite.

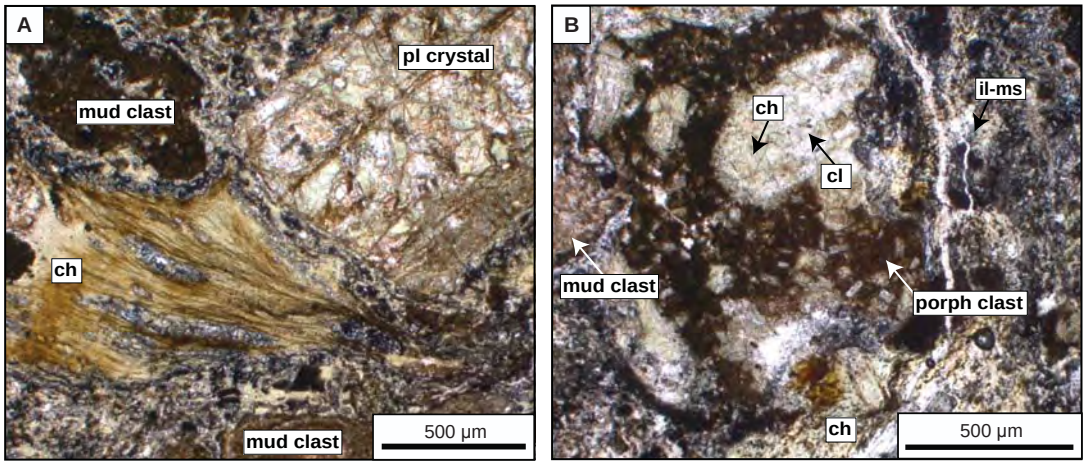

Figure 3.5 E41 volcano-sedimentary facies. **A.** Photomicrograph (xpl) of polymictic volcaniclastic breccia facies showing chloritised wispy fragments (fiamme?). Broken plagioclase crystal and the brown clast of mudstone have been altered to carbonates and Fe-oxides. Matrix is mostly feldspathic and has been intensely altered to sericite - carbonate - chlorite (E41D2013, 99.2m). **B.** Photomicrograph (ppl) of polymictic volcaniclastic breccia facies. The plagioclase-phyric rounded clast has been altered to hematite - chlorite - calcite. Matrix composed of plagioclase crystals and mudstone clasts has been strongly altered to carbonates, illite and muscovite (E41D2013, 99.2m). Abbreviations: chl=chlorite, cl=calcite, il-ms=illite-muscovite, mud=mudstone clasts, pl=plagioclase crystals, porph clasts=clasts of porphyritic coherent facies.

in a distal apron to subaqueous volcanic activity (Allen, 2004; Allen et al., 2007). A similar polymictic breccia facies has been encountered in parts of the E42 and E46 stratigraphy. An important distinction is that the E42 and E46 polymictic breccias include a component of reworked andesite hyaloclastite that indicates a medial to proximal volcanic setting (Cannell, 2003; Simpson and Cooke, 2006; Simpson, 2008).

3.2.3 Sandstone facies (monomictic to polymictic)

Sandstone constitutes a minor portion of the clastic facies at E41. The sandstones are massive (Fig. 3.4C), rarely laminated (Fig. 3.4D), fine- to coarse-grained, well-sorted and normally-graded. The sandstones are typically composed of < 2 mm angular crystals and well-sorted lithic fragments. Subrounded, pale-pink mudstone clasts are present locally. Typically, sandstone occurs as 10 cm interbeds within the mudstone facies or the polymictic volcaniclastic breccia facies. There are rare sandstone beds up to 50 cm thick.

The sandstone facies occurs on the eastern side of the E41 east pod, where it is intercalated with lenses of polymictic volcaniclastic breccia in intervals up to 6 m thick (section 34900N; Fig. 3.2B). It has also been recognised in a similar facies association over 7 m on section 86800E (Fig. 3.2D). The sandstone facies appears to pinch out to the south (Fig. 3.2D). Because of the intimate association and most likely contemporaneous formation with polymictic volcaniclastic breccia facies, the sandstone facies is interpreted to have been deposited in the same distal volcanic environment as the volcaniclastic breccia facies.

3.3 Intrusive history

At E41, the Early Ordovician volcano-sedimentary succession has been intruded by many dykes, sills and stocks. Fifteen intrusive units have been identified on the basis of their textural and mineralogical characteristics. Phenocryst compositions, sizes, morphologies and abundances, as well as groundmass features, were used to distinguish the different coherent units (Table 3.1). Igneous rocks have been named according to the IUGS classification scheme (La Maitre, 1989). A detailed study of the intrusive relationships, in conjunction with the grade distributions, has been undertaken to determine which of the intrusive phases were related to ore formation (Fig. 3.6). In order to unravel the intrusive history, some of the criteria for porphyry systems proposed by Sillitoe (2000) were used to define timing of intrusive units. These criteria include: (1) abrupt termination of early veins in older intrusive contacts; (2) xenoliths of refractory quartz veins derived from older intrusions that now occur in younger intrusions close to their intrusive contacts; (3) abrupt decrease in gold and copper grade from the older to younger intrusion, and (4) better textural preservation and lower vein densities in the young phase relative to the old one. Because of the relatively shallow drilling at E41 (to a maximum depth of ~400 m), cross-cutting relationships between some of the intrusive units were rarely observed or ambiguous, which made it difficult to constrain timing with respect to mineralisation and to the other intrusive units within the system. Consequently timing relationships between some of the coherent rock units, especially between dykes, remain undetermined. It was also difficult to establish dyke orientations as many contacts have been obscured by pervasive hydrothermal alteration and/or have been faulted. Thus, the intrusive history of E41 has been primarily based on the paragenetic sequence for vein stages and associated alteration facies presented in Chapter 5. The intrusive rocks have been divided into pre-, syn-, late-, and post-mineralisation (Table 3.2). There are dykes at E41, however, that have intruded in between two mineralising events at E41, consistent with an inter-mineralisation timing. These dykes have close temporal relationships with Au-mineralisation and are tentatively assigned a syn-mineralisation timing in the absence of more definitive cross-cutting relationships.

Each magmatic stage at E41 is characterised as follow:

- Pre-mineralisation intrusive units are predominantly mafic to intermediate rocks, typically clinopyroxene- and plagioclase-bearing, with subordinate hornblende, accessory biotite, apatite, titanite and magnetite. This group includes: diorite (Muddy Lake diorite), plagioclase-phyric dykes, a trachyte dyke, mafic dykes, a blocky plagioclase-phyric unit and more evolved intrusive

TABLE 3.1 Petrographic characteristics of the intrusive facies of the E41 deposit.

Relative age	Field term (coherent facies)		IUGS Classification	Texture	Phenocryst assemblage mineral /vol.% /size mm	Groundmass	Geometry/ thickness/ distribution
Pre-mineralisation intrusive rocks	Muddy Lake diorite		diorite	holocrystalline, equigranular to weakly porphyritic	pl/ 15 – 40/ 0.5 – 2; di/ 20 – 35 /0.5 – 3; hb(?)/ ~7 – 10/ 2 – 4;	Medium- to fine-grained mass of pl, with rare interstitial quartz; euhedral to anhedral accessory crystals of ap/ 250 – 500 µm, bt/ ~100 µm (altered to chlorite clots); bt/ ≤100 µm enclosed poikilitically in cpx	sill/ at least 200 m
	feldspar phyric - facies	feldspar-phyric dyke	diorite	porphyritic (crowded to sparse)	pl/ 5 – 15/ 1 – 5;	Fine-grained mass of pl and unidentified altered mafic minerals, $FeTiO_x$	dyke/ 20 cm – 5 m/ typically associated with faults
		blocky plagioclase-phyric dyke (‘Robin’s lode’)	diorite	porphyritic	pl/ 5 – 20/ 2 – 7; ap/ 5 – 7/ up 1	Fine-grained, typically red-brown groundmass of pl (50 – 100 µm) and minor mafics; lx	sill or dyke/
		trachyte dyke	diorite	aphyric to porphyritic	phenocrysts (?) replaced by Kf – py – ep – cl – tt – ap/ 15/ ~3 – 10 (?)/ or apparent phenocrysts (?)	Fine-grained mass of pl, rest of the primary mineralogy of groundmass due to extremely strong alteration is undetermined	dyke/ 4 m/ centre of the hydrothermal system in the east pod
		crowded plagioclase-phyric dyke	diorite	equigranular	pl/ 40 – 50/; hb/ 20	Coarse-grained plagioclase crystals in between phenocrysts	dyke/ 2 m/ east fringe of the west pod
	mafic dykes		diorite	aphanitic to weakly porphyritic	pl/ 5/ <1 – 2; cpx/ 5/ ~1	Very fine-grained feldspathic (~100 µm microcrystals) groundmass, ferromagnesian minerals (cpx, hb) altered, accessory minerals include $FeTiO_x$ and mt	dyke, typically associated with fault zone/ 1 – 2 m
	monzodiorite dyke		quartz monzodiorite to monzodiorite	equigranular	pl/ 30 – 40; Kf/ 15 – 30/ 2 – 3; hb/ 25/1 – 3 and cpx/ <5/ ≤1	Fine-grained feldspathic mass with qt/ ~5 – 7/ ~200 µm; ap/ ~100 µm	dyke/ 8 m/ east fringe of the east pod/
	mafic monzonite		monzonite to monzodiorite	equigranular	pl/ 25 – 40/ 0.5 – 3; Kf/ 20 – 35/ 0.5 – 2; cpx and/or hb/ 7 – 15/ 0.2 – 2;	Blocky euhedral to anhedral tabular interstitial pl and Kf crystals, fine grained qt/ 0.2 – 1, ap/ 0.1 – 0.4; sh/up to 0.3; and rare bt(?)	vertical intrusion (west pod)/ ~500 wide by 1100 m; geometry undetermined in the east pod
	hybrid zone	enclaves of mafic micromonzodiorite	monzonite to monzodiorite	aphanitic to equigranular	no phenocrysts	Fine grained mass of pl – Kf – qt and altered ferromagnesian mineral, accessory $FeTiO_x$ and ap	hybrid zone extends over 200 m from N-S, thickness (max. 100 m) increases towards east
		enclaves of mafic monzodiorite with megacrystals	monzonite to monzodiorite	porphyritic	pl/ 5 – 15/ 10 – 15; hb/ 3 – 5/ 1 – 5;	Fine grained pl – Kf – ch – qt mass either holocrystalline or microcrystalline	
Syn-mineralisation intrusive rocks	aplite dykelets		syenite – quartz syenite	fine grained equigranular to weakly porphyritic	no phenocrysts/ in porphyritic phases - Kf/ 5/ 0.5	Fine-grained (≤ 0.1) mosaic intergrowth of Kf – pl – qt and ch (after mafics) forming coherent mass	dykelets/ 5 mm – 10 cm
	quartz-monzonite dykelets		monzonite to quartz monzonite	equigranular	pl/ 35 – 45/ 1 – 2; or/ 15 – 25/ 1 – 2/ former mafic minerals (hb?) altered/ 7/ ≤1 – 2;	Fine-grained pl and minor ferromagnesian minerals, interstitial qt and mt, accessory ap, tt	dyke/ 5 cm – 1 m

TABLE 3.1 (Cont.)

	pyroxene-phyric dykes and sills		porphyritic (crowded and sparse)	cpx/ <15 – 40/ 1 – 5;	Fine-grained, aphanitic rich in pl and Kf, ferromagnesian minerals and accessory mt, ap and $FeTiO_x$	dykes and sills (?)/ 0.1 – 5 m
Late-mineralisation intrusive rocks	syenite	quartz syenite	equigranular	pl/ 10/ 0.5; Kf/ >50/ 0.3 – 2; qt/ 10 – 15/ 0.5 – 1	Euhedral hb/ 7/ ≤0.5, sh/ 3/ 0.3	dyke/ 20 cm/ close to the mineralised zone in east pod
	hornblende-phyric quartz-rich dyke	monzogranite	porphyritic	hb/ 20/ 2 – 3; pl/ 15/ ≤1 – 2;	Fine grained qt, or, pl (100 – 200 μm) mosaic groundmass with $FeTiO_x$	dyke/ 27 m
Post-mineralisation intrusive rocks	Amygdaloidal dyke	diorite	porphyritic	cpx and hb(?)/ ~10/ up 1; amygdales filled with cl and ht/ 10/ 2 – 5;	Fine grained feldspathic groundmass (≤100μm), ferromagnesian minerals altered, $FeTiO_x$ dispersed	dyke / 1 – 3 m/ occurs in northern part of the east pod; intruded into shear zone
	plagioclase-phyric (‘diorite’ dyke) dyke	diorite	porphyritic	pl/ 30 – 50/ 2 – 4; hb/ 10 – 15/ 1 – 4	Fine grained feldspathic groundmass, pl has reddish colour, interstitial qt and altered specs of hb and cpx, accessory mt, $FeTiO_x$ and ap	dykes intruded into fault zone/ 4 m/ occurs between east and west pod
	Hornblende-phyric (lamprophyre) dyke	diorite	porphyritic	hb/ 20 – 30/ 2 – 5;	Distinctive blocky pl crystals within groundmass, fine grained mass of pl and cpx	dyke/ 5 m/ occurs between east and west pod

Abbreviations: ap=apatite, bt=biotite, ch=chlorite, cl=calcite, cpx=clinopyroxene, di=diopside, ep=epidote, hb=hornblende, ht=hematite, Kf=K-feldspar, lx=leucoxene, mt=magnetite, pl=plagioclase, py=pyrite, qt=quartz, sh=sphene, tt=titanite.

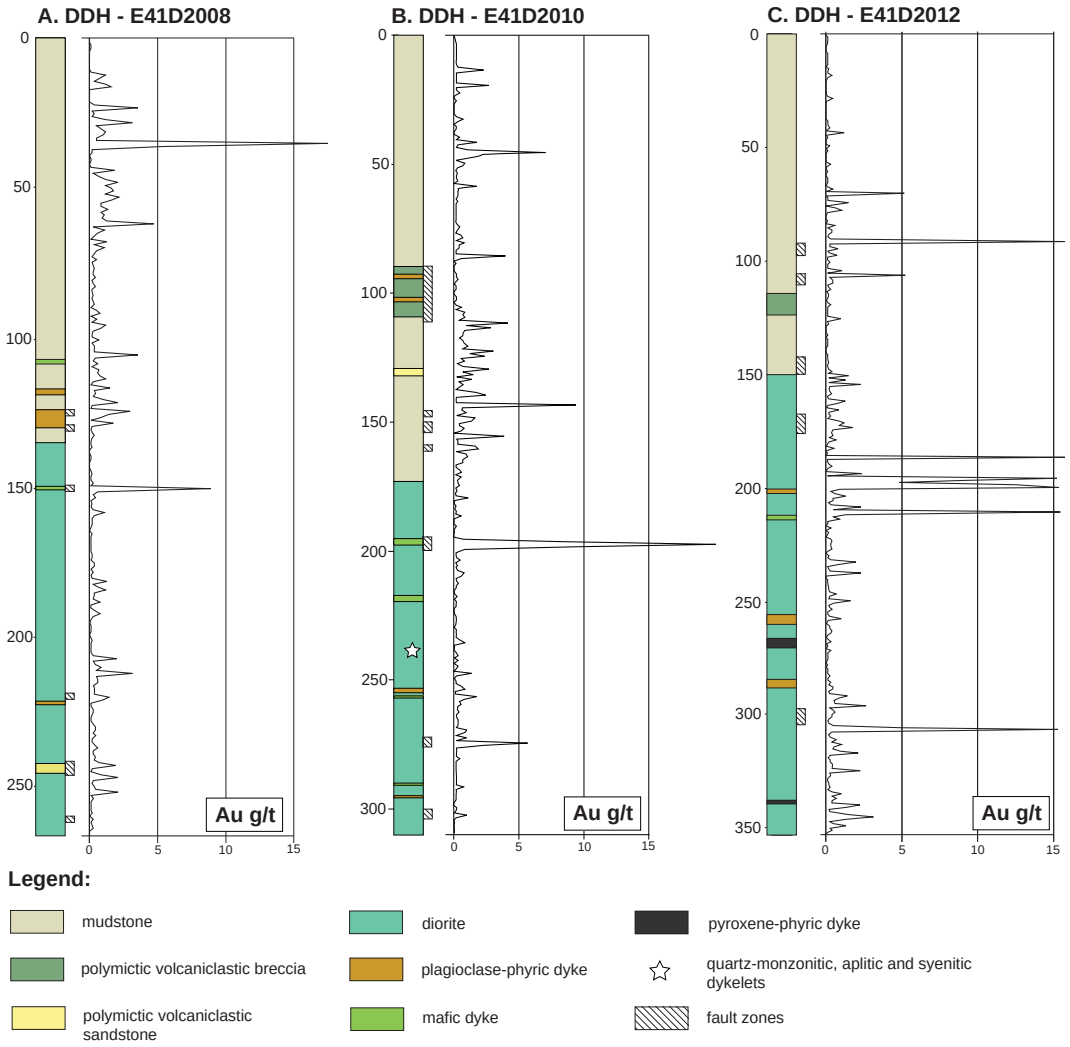

Figure 3.6 Simplified representative geological logs from E41 deposit (east pod) showing spatial relationships between mineralisation and stractural features and lithology. **A.** Highly mineralised zones occur in regolith (above 100m) and are spatially associated with fault zones and dyke margins. **B.** Mineralised zone occurs above the contact of diorite with mudstone. Minor domains associated with faults zones and dyke contacts. **C.** Mineralisation related to faults and dykes.

suites: a monzodiorite dyke and mafic monzonite;

- The syn-mineralisation magmatism is characterised by distinctive intrusive phases: quartz + K-feldspar + hornblende-bearing quartz-monzonite and aplite dykelets; and pyroxene-bearing dykes;
- Late-mineralisation intrusions include: a syenite dykelet and a hornblende-phyric quartz-rich dyke;
- Post-mineralisation intrusive units are exclusively mafic in character. They are plagioclase + hornblende-bearing and comprise a hornblende-phyric dyke, plagioclase-phyric ‘diorite’ dyke and an amygdaloidal dyke.

The intrusive units are described below in their interpreted sequence of emplacement.

TABLE 3.2 Alteration and mineralisation features of intrusive rock units that have helped define relative timing relationships. Detailed descriptions of hydrothermal alteration and mineralisation features are provided in Chapter 5.

Timing	Rock unit		Alteration facies	Mineralisation features
Pre-mineralisation intrusive rocks	Muddy Lake diorite		***Pre-early stage alteration facies:*** actinolite – magnetite; K-feldspar – albite; ***Main stage alteration facies:*** epidote; K-feldspar – epidote; illite – muscovite –chlorite – carbonate; K-feldspar; ankerite – arsenopyrite; ***Post-mineralisation alteration facies:*** illite – muscovite – carbonate – chlorite	***Early stage veins:*** 1B; ***Main-stage veins:*** 3A-a, 3A-b, 3A-c, 3B, 4A, 4B, 4C; ***Late stage veins:*** 5, 6, 7
	feldspar phyric-dykes	feldspar-phyric dyke	***Main stage alteration facies:*** epidote facies; K-feldspar – epidote; illite – muscovite – chlorite – carbonate; ***Post-mineralisation alteration facies:*** illite – muscovite – carbonate – chlorite	***Main-stage veins:*** 3A-a, rare 3A-b, 3A-c, 3B, 4A, 4C; ***Late stage veins:*** 6, 7
		blocky plagioclase phyric dyke (or sill: 'Robin's lode')	***Main stage alteration facies:*** epidote; illite – muscovite – chlorite – carbonate; ***Post-mineralisation alteration facies:*** illite – muscovite – carbonate – chlorite	***Main-stage veins:*** 3A-c; ***Late stage veins:*** 6
		trachyte dyke	***Main stage alteration facies:*** epidote; K-feldspar – epidote; illite – muscovite – chlorite – carbonate	***Main-stage veins:*** 3A-c, 3B
		crowded plagioclase phyric dyke	***Pre-early stage alteration facies:*** actinolite – magnetite; ***Main stage alteration facies:*** K-feldspar – epidote; weak illite – muscovite – chlorite – carbonate	***Main-stage veins:*** some pyrite stringers; 3A-c; ***Late stage veins:*** 6
	mafic dyke		***Main stage alteration facies:*** epidote; K-feldspar – epidote; illite – muscovite – chlorite – carbonate; K-feldspar; ankerite – arsenopyrite; ***Post-mineralisation alteration facies:*** illite – muscovite – carbonate – chlorite	***Main-stage veins:*** 3A-a, rare 3A-b, 3A-c, 3B, 4A, 4B, 4C; ***Late stage veins:*** 6, 7
	Monzodiorite dyke		***Pre-early stage alteration facies:*** actinolite – magnetite; ***Main stage alteration facies:*** illite – muscovite – chlorite – carbonate	***Main-stage veins:*** 3A-c; ***Late stage veins:*** 6
	mafic monzonite		***Pre-early stage alteration facies:*** albite – chlorite; illite – muscovite – ankerite; ***Main stage alteration facies:*** rare epidote ± K-feldspar – epidote; illite – muscovite – calcite – ankerite; arsenopyrite; ***Post-mineralisation alteration facies:*** illite – muscovite – ankerite, and illite – muscovite – carbonate – clays	***Early stage veins:*** 1, 2 ***Main-stage veins:*** 3A-a/b, 3A-c, 4A, 4B, 4C; ***Late stage veins:*** 5, 6, 7
	hybrid zone		***Main stage alteration facies:*** rare epidote; albite – chlorite and illite – muscovite – ankerite	***Early stage veins:*** 1; ***Main-stage veins:*** rare 3A-c
Syn-mineralisation intrusive rocks (no early stage veins)	aplite dykelets		Cuts actinolite – magnetite alteration and locally epidote; ***Main stage alteration facies:*** weak to intensive illite – muscovite – carbonate ± chlorite	***Main-stage veins:*** some of the aplites host 3A-c veinlets (≤ 1mm) or post-date 3A-c; locally aplites intruded into 3A-c veins; pyritic clots in aplitic dykes in west pod are highly-mineralised; spatial relationship to stage 4 remains undetermined
	quartz-monzonite dykelets		Cuts actinolite – magnetite alteration; ***Main stage alteration facies:*** weak epidote, illite – muscovite – carbonate ± chlorite; some hematite-dusted K-feldspar; strong hematite reddening up to a few metres around these dykelets	***Main-stage veins:*** rare 3A-c veinlets, disseminated pyrite throughout; ***Late stage veins:*** 6
	pyroxene-phyric dykes		Cuts actinolite – magnetite alteration, post-date the first main-stage alteration: epidote and K-feldspar – epidote; ***Main stage alteration facies:*** dominantly carbonate – illite – muscovite – chlorite	Post-dates some mineralised vein stages, e.g. stage 3A-a, 3A-b; ***Main-stage veins:*** some 3A-c and 4A; some gold mineralisation is associated with disseminated pyrite; ***Late stage veins:*** 5

TABLE 3.2 (Cont.)

Late-mineralisation intrusive rocks	syenite dyke	Cuts actinolite – magnetite alteration; ***Main stage alteration facies:*** weak illite – muscovite – chlorite and pervasive K-feldspar alteration	No mineralised veins, minor disseminated pyrite throughout; ***Late stage veins:*** 6
	hornblende-phyric quartz rich dyke	Cuts actinolite – magnetite facies and epidote facies; ***Main stage(?)*** *alteration facies* weakly altered by pervasive illite – muscovite – carbonate – chlorite facies; rare epidote replacements	Weakly mineralised pyrite stringers; no spatial and temporal relationship to stage 4 stage veins determined
Post-mineralisation intrusive rocks	amygdaloidal	Cuts older alteration facies; ***Post-mineralisation alteration facies:*** carbonate – hematite; illite – muscovite – carbonate – chlorite – clays	No mineralised veins; ***Late stage veins:*** 6
	plagioclase-phyric ('diorite' dyke)	Cuts older alteration facies; ***Post-mineralisation alteration facies:*** some albite and epidote alteration, weak illite – muscovite – carbonate – chlorite – clays and carbonate – hematite facies	No mineralised veins; ***Late stage veins:*** 6, 7
	hornblende-phyric (lamprophyre) dyke	Cuts older alteration facies; ***Post-mineralisation alteration facies:*** some epidote alteration and illite – muscovite – carbonate – chlorite	No mineralised veins; ***Late stage veins:*** 6

3.3.1 Pre – mineralisation intrusions

3.3.1.1 Diorite

In E41, the earliest and volumetrically most significant intrusive unit is the Muddy Lake diorite (Miles and Brooker, 1998). This diorite intruded discordantly into the consolidated volcano-sedimentary succession (Cannell, 2003). Based on its geometric relationships with the volcano-sedimentary units at E42 (Miles and Brooker, 1998) and at E41, the diorite body is interpreted to be a sill. It has a minimum thickness of 230 m at E42 (Smolonogov, 2003) and about 200 m (minimum) at E41 (Fig. 3.2B). The diorite sill appears to follow the north-trending structures that characterise the Cowal district (Chapter 2). The diorite and host volcano-sedimentary stratigraphy is interpreted to have been tilted after emplacement (McInnes et al., 1998; Cannell, 2003; Henry, 2008).

The diorite sill is spatially associated with mineralisation in the E41 east pod, and also at E42 (McInnes et al., 1998; Miles and Brooker, 1998; Bastrakov, 2000; Bywater et al., 2004) and E46 (Simpson and Cooke, 2006). The north-trending diorite body is about 1000 m wide at E41. It has a strike length of at least 10 km (Fig. 2.5). In the E41 east pod, a series of south- and southeast-dipping fractures and faults have dismembered the contact between clastic units and the diorite (Figs. 3.2B and D).

The diorite is heterogeneous, ranging from plagioclase-dominated diorite to more clinopyroxene-rich gabbroic phases. Within the diorite, subtle textural variations exist, including massive, coarse-grained holocrystalline phases and equigranular to weakly porphyritic phases. Two mineralogically distinctive diorite phases have been

identified; one dominated by plagioclase (~30%), and one by diopside (~35%; Fig. 3.7A). Contacts between different diorite phases are diffuse and typically gradational. The diorite contains euhedral to subhedral diopside phenocrysts (Fig. 3.7B) and plagioclase crystals that have been typically obscured by hydrothermal alteration. Plagioclase ranges from pink and cream to dull green, with the latter resulting from ubiquitous albitisation. Hornblende locally comprises about up to 10% of the unit. Primary biotite occurs in deeper parts of the intrusion, and in less altered diorite, defining poikilitic textures within diopside crystals (Fig. 3.7B). Locally, interstitial quartz and rare K-feldspar occur in the plagioclase-dominated groundmass. Euhedral apatite occurs interstitially as an accessory phase, and is commonly associated with diopside (Fig. 3.7E). Titanite and magnetite are disseminated throughout. The diorite has been intensely altered (Chapter 5) by all of the hydrothermal events at Cowal, and therefore has a pre-mineralisation timing (Table 3.2). The diorite sill at E41 has been intruded by numerous dykes and a mafic monzonite intrusion (Fig. 3.2).

The compositional and textural variations within the Muddy Lake diorite have been attributed to the existence of several discrete intrusive phases (Miles and Brooker, 1998). The feldspar-rich diorite exposed in the deeper levels of E42 has been described as monzodiorite by Ashley (2003a and b) and Smolonogov (2003). Similar feldspar-rich diorite has been encountered at depth at E41, but the K-feldspar in this unit is interpreted as a hydrothermal alteration halo to a later mafic monzonite intrusion rather than a separate intrusive unit or a separate phase. This alteration halo is described in details in Chapter 5.

3.3.1.2 Plagioclase-phyric dykes

Pre-mineralisation plagioclase-phyric dykes (Figs. 3.8A and E) are most common in the E41 east pod. They contain 5 to 25% euhedral, elongated, typically hydrothermally altered, plagioclase phenocrysts set in a typically fine-grained crystalline to aphanitic groundmass. The groundmass is dark-green to brown-red, and is dominated by feldspars and ferromagnesian minerals. Fe-Ti oxides are disseminated throughout the groundmass. Locally, on the fringes of the deposit, the plagioclase-phyric dykes have well-preserved primary textures, although feldspar phenocrysts are red-coloured due to secondary hematite dusting. More commonly, hydrothermal alteration has completely obscured primary textures and mineralogies.

The plagioclase-phyric dykes are predominantly 0.5 to 3 m in thickness. Many of these dykes have sheared margins, suggesting that they intruded active fault zones, and/or pre-date at least some deformation. They have cut the diorite, and locally been intersected at shallower levels cross-cutting volcano-sedimentary intervals.

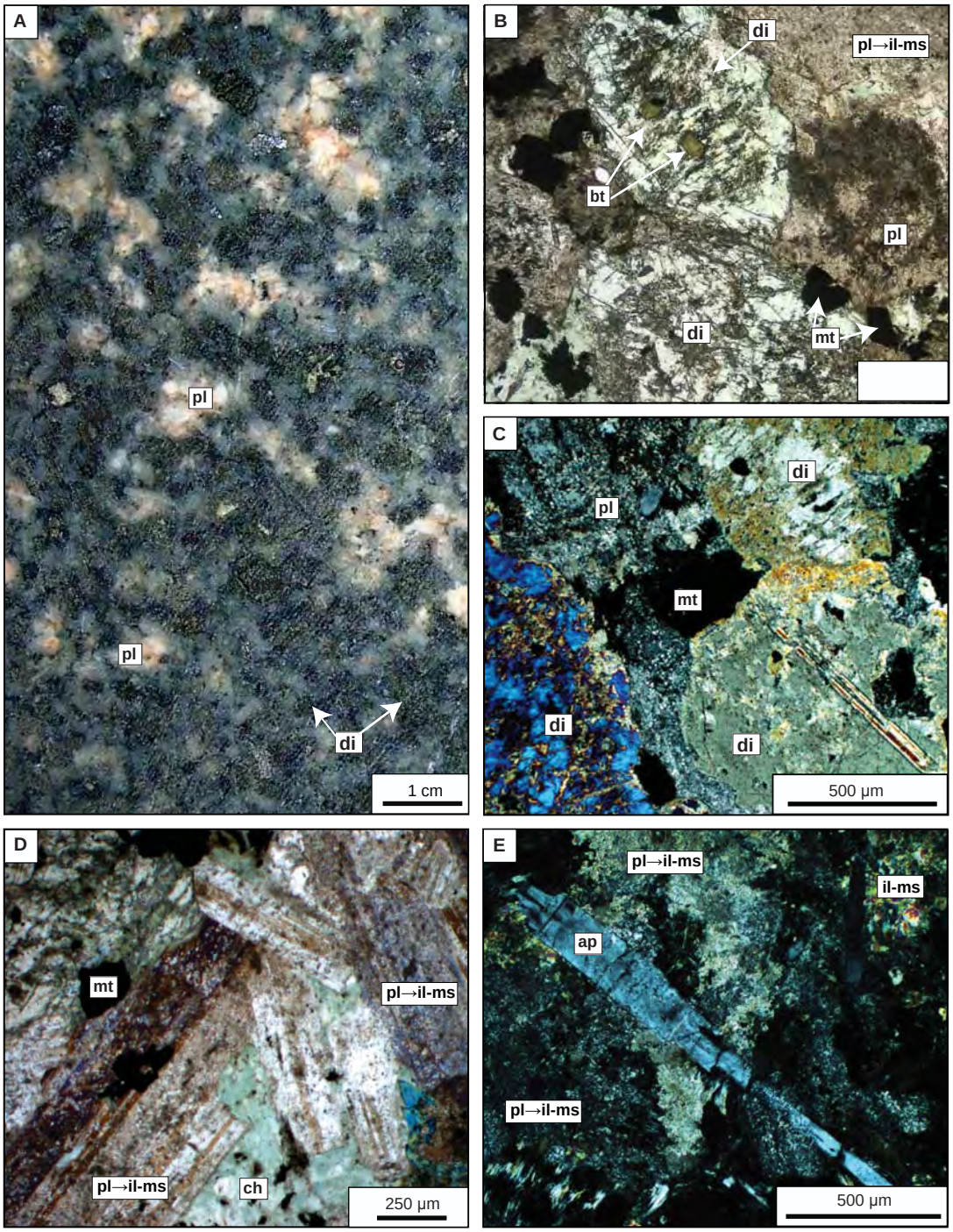

Figure 3.7 Muddy Lake diorite at E41. **A.** Sample of holocrystalline, equigranular diorite. Diopside and hornblende have been pseudomorphed by actinolite and magnetite ± chlorite. Locally pyrite has partially replaced mafic minerals. Cream and pink-coloured plagioclase crystals have been altered to albite and K-feldspar (E41D2010, 204.1m). **B.** Photomicrograph (ppl) showing diopside crystals with igneous biotite that has been poikiliticly enclosed within pyroxene (E41D2068, 219.4m). **C.** Photomicrograph (xpl) showing accessory magnetite in between diopside crystals. Euhedral diopside crystals have been weakly altered to chlorite and carbonates. Plagioclases have been dusted by illite-muscovite (E41D2068, 219.4m). **D.** Photomicrograph (xpl) of diorite with well-preserved plagioclase twinning whereas mafic minerals have been completely altered to chlorite (E41D2068, 219.4m). **E.** Photomicrograph (xpl) of euhedral apatite enclosed interstitially between plagioclase crystals. Pervasive illite-muscovite alteration facies has completely replaced plagioclase (E41D2068, 219.4m). Abbreviations: ap=apatite, bt=biotite, cb=carbonates, di=diopside, hb=hornblende, ch=chlorite, mt=magnetite, il-ms=illite-muscovite, pl=plagioclase, pl→il-ms=plagioclase altered to illite-muscovite.

Plagioclase-phyric dyke suites occur throughout the district (Miles and Brooker, 1998; Bastrakov, 2000; Anderson, 2003; Smolonogov, 2003). The primary mineralogies of the dykes suggest original andesitic to latitic compositions (Ashley, 2003b).

3.3.1.3 Blocky plagioclase-phyric coherent unit ('Robin's lode')

This coherent unit has been intersected in two drill holes at E41 (E41D2012 and E41D2014) on the eastern margin of east pod at approximately similar elevations (~260 m RL), possibly indicating a sill-like geometry. It has distinctive blocky plagioclase phenocrysts (Fig. 3.8C) and large (up to 1 mm) apatite crystals (Fig. 3.8D). White plagioclase phenocrysts are well-preserved, euhedral, randomly dispersed and locally form multi-crystal clots. Phenocryst abundances range between 5 and 20%. Titanomagnetite crystals are common. The crystalline groundmass is commonly dark red or brown and rich in plagioclase. The red colour is interpreted to be the result of secondary hematite dusting.

A similar blocky plagioclase-phyric unit has been described at E42, where it occurs as randomly distributed domains (10 cm – 5 m diameter) within the diorite sill (McInnes, 2003). This unit has been interpreted previously as a more fractionated part of the diorite, potentially related to mineralisation (S. Halley, pers. comm., 2006). This interpretation is not consistent with observations made at E41, where 'Robin's lode' hosts alteration facies associated with mineralised veins, indicating a pre-mineralisation timing (Table 3.2).

'Robin's lode' contains abundant apatite microphenocrysts (up to 7 – 10 %) throughout. This feature is characteristic of some rocks of shoshonitic affinity (e.g., Crawford et al., 1992). Ubiquitous stout prisms of apatite (microphenocrysts) have also been documented from the shoshonitic middle Ordovician Goonumbla Volcanics, ~ 100 km north of the Cowal district (Crawford, 1999; Crawford et al., 2007a).

3.3.1.4 Crowded plagioclase-phyric dyke

A crowded plagioclase-phyric dyke (Figs. 3.9A and B) was intersected along the Cowal fault between the E41 east and west pods (E41D2139: 108.6 – 110.5 interval). It is unclear whether the Cowal fault cuts, or has been intruded by it. The dyke is coarse-grained and holocrystalline, consisting of crowded euhedral plagioclase and smaller subhedral to anhedral hornblende crystals. The relatively coarse–grained chlorite-altered groundmass is mostly composed of fine-grained feldspars. Broader intersects of this unit were encountered in the northern part of E41, possibly indicating the presence of a larger source intrusion at depth (P. McInnes, pers. comm., 2007).

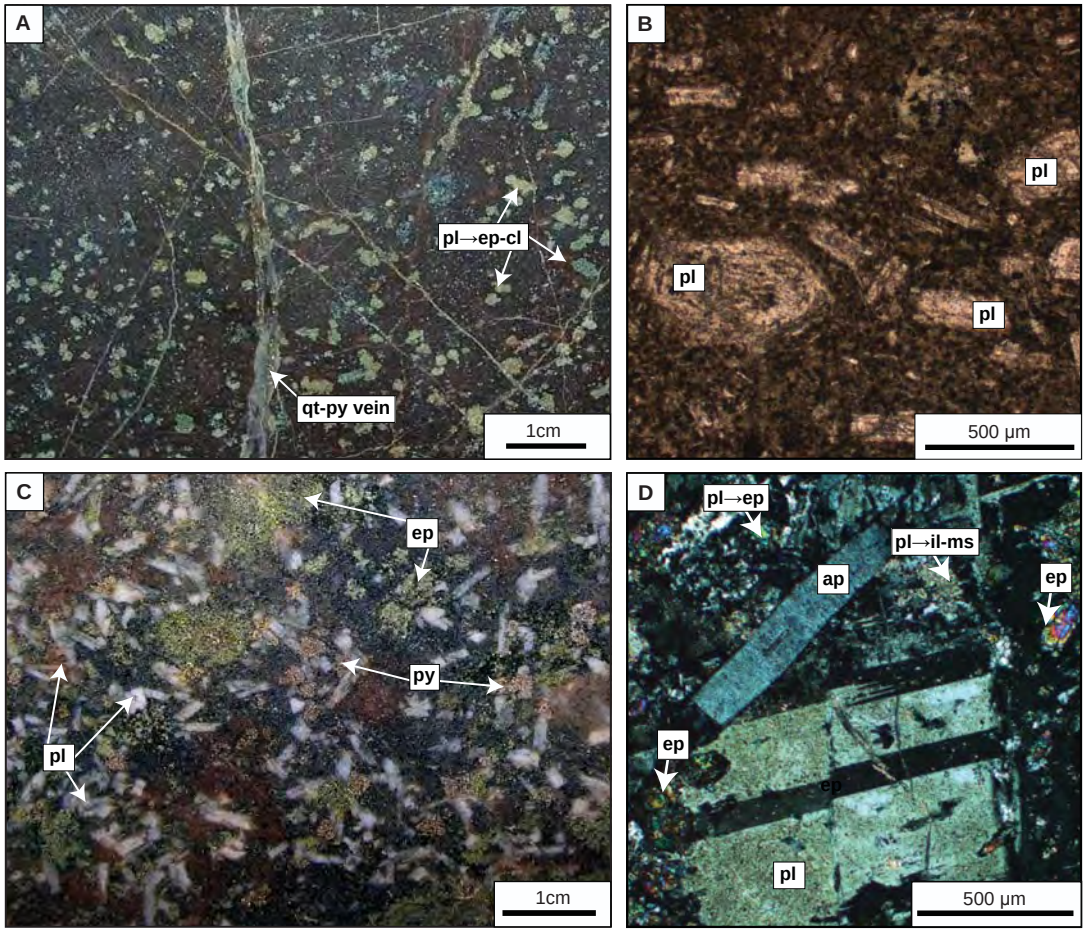

Figure 3.8 Pre-mineralisation feldspar-phyric dyke suites. **A.** Plagioclase-phyric dyke with plagioclase phenocrysts that have been entirely pseudomorphed by epidote and calcite. A quartz-pyrite vein and pyrite stringers have cut the sample. The red coloration of the groundmass relates to hematite dusting of plagioclase (E41D2067, 153.3m). **B.** Photomicrograph (ppl) of plagioclase phenocrysts in feldspatic strongly illite - muscovite - carbonate - chlorite altered groundmass (E41D2067, 167.5m). **C.** Blocky plagioclase-phyric dyke ('Robins lode') overprinted by epidote and weak carbonate - illite - muscovite alteration. Pyrite clots are disseminated throughout the rock (E41D2014, 304.7m). **D.** Photomicrograph (xpl) of blocky plagioclase-phyric dyke showing euhedral plagioclase crystals weakly altered to carbonate - illite - muscovite. Groundmass composed of plagioclase altered to epidote, carbonates and illite - muscovite. Large euhedral apatite crystals are interpreted to be a primary component of this unit (E41D2014, 304.3m). Abbreviations: ap=apatite, cl=calcite, ep=epidote, hb=hornblende, Kf=K-feldspar, pl=plagioclase, pl→ep=plagioclase altered to epidotepy=pyrite, pl→il-ms=plagioclase altered to illite-muscovite, qt=quartz.

Although there has been speculation that this unit may have been directly related to mineralisation (R. Tosdal, pers. comm., 2006), the alteration facies that it contains indicate a pre-mineralisation timing (Table 3.2).

3.3.1.5 Trachyte dykes

The trachyte at E41 has an apparent porphyritic texture, with feldspar altered phenocrysts up to 15 mm in diameter (Figs. 3.9C and D). There are also scattered ferromagnesian microphenocrysts up to 0.5 mm across. The crystalline groundmass is composed of aligned, fine-grained euhedral, tabular crystals (0.4 mm long), of plagioclase (Fig. 3.9D) and possibly magmatic K-feldspar (strongly altered to sericite) define a classic

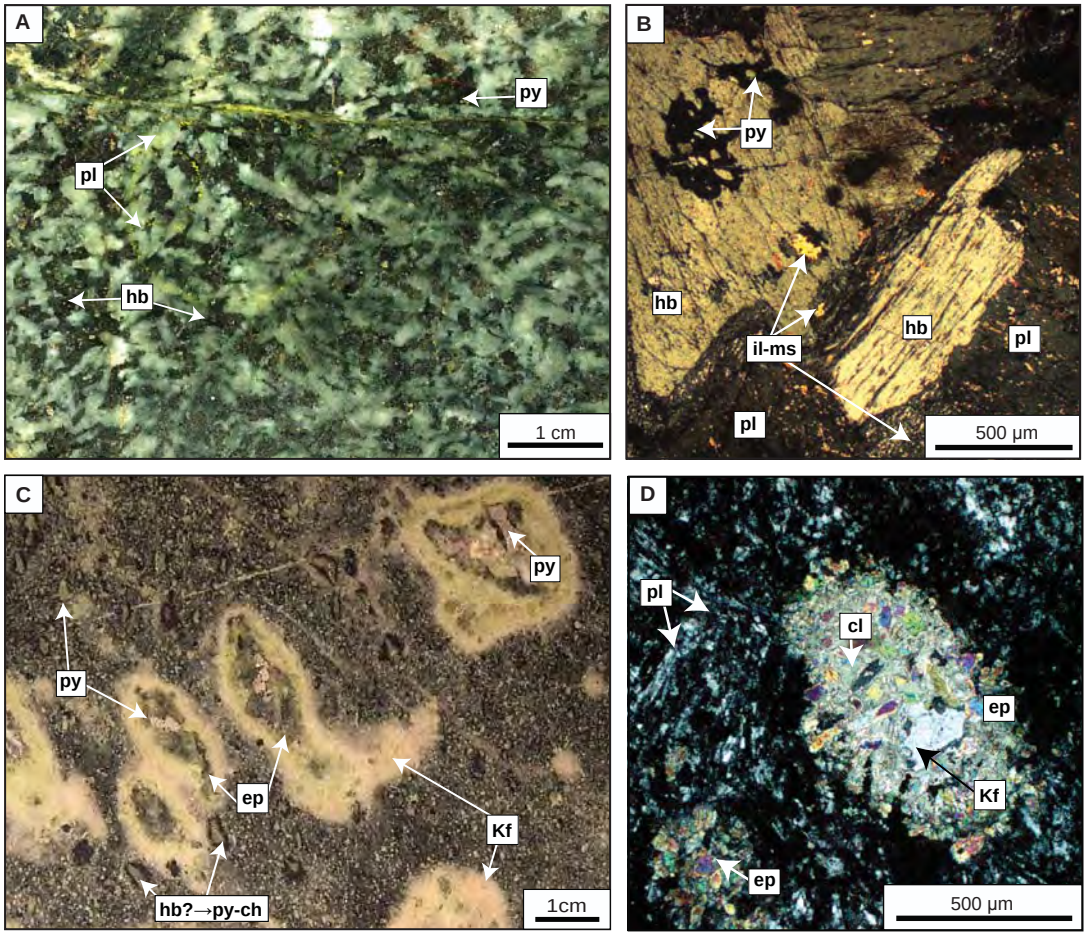

Figure 3.9 Pre-mineralisation feldspar-phyric dykes. **A.** Crowded plagioclase-phyric dyke with abundant hornblende and plagioclase phenocrysts. Secondary pyrite has typically replaced hornblende (E41D2139; 109.5m). **B.** Photomicrograph (xpl) of crowded plagioclase dyke showing relatively well-preserved hornblende crystals. Euhedral plagioclase crystals have been weakly altered to illite - muscovite (E41D2139, 109.5m). **C.** Trachyte dyke that has been selectively pervasively altered to K-feldspar - epidote (E41D2012, 256.1m). **D.** Photomicrograph (xpl) of trachyte dyke showing characteristic 'trachyte' texture of plagioclase crystals that constitute the groundmass of this unit. Vesicules and/or phenocrysts have been completely replaced by epidote - K-feldspar - calcite clots (E41D2012, 256.0m). Abbreviations: cl=calcite, ep=epidote, hb=hornblende, hb?→ py-ch=most likely hornblende phenocrysts altered to pyrite and chlorite, Kf=K-feldspar, pl=plagioclase, py=pyrite.

'trachytic' texture (e.g., Bates and Jackson, 1980) and the name of this coherent facies has been assigned based on this texture. Fine-grained opaque minerals (magnetite) are also present. Trachyte dykes have cut the diorite intrusion and have been affected by alteration assemblages related to main-stage mineralisation (Table 3.2), and have been consequently classified as pre-mineralisation.

3.3.1.6 Mafic dykes

Mafic dykes were only intersected within the east pod at E41. They typically have aphanitic textures (Figs. 3.10A and C), but porphyritic varieties have been observed locally. The aphanitic mafic dykes are strongly altered (Table 3.1), and mostly consist of relict, fine-grained plagioclase and abundant magnetite. The porphyritic dykes contain pyroxene or plagioclase phenocrysts in a crystalline groundmass that consists

of more than 30% blocky tabular plagioclase crystals (Fig. 3.10C). It is likely that primary mafic minerals have also been part of the groundmass but they have been completely replaced by Ca-bearing hydrothermal minerals such as epidote and calcite (Chapter 4).

Individual dykes are typically ≤ 1 m and rarely > 1 m thick. They commonly occur within fault zones. Primary textures and mineralogy have been strongly modified by hydrothermal alteration (Tables 3.1 and 3.2; Chapter 5).

Mafic dykes have also been recognized at E42 (Miles and Brookers, 1998; Bastrakov, 2000; Smolonogov, 2003; Strickland, 2005). Based on petrographic investigations of the E42 mafic dykes, Ashley (2003a) described the dykes as intermediate to mafic in composition.

3.3.1.7 Monzodiorite dyke

A monzodiorite dyke was intersected at one locality along the east edge of the east pod (DDH-E41D2014). This unit is equigranular (Fig. 3.10B). It has textures similar to the Muddy Lake diorite, but is distinguished by the presence of abundant fine- to medium-grained, mostly euhedral K-feldspar crystals and interstitial subhedral to anhedral quartz. K-feldspar crystals comprise up 20% and form a crystalline groundmass that has engulfed coarser crystals of hornblende and subordinate clinopyroxene. The margins of the dyke are finer-grained than its interior. The presence of mineralised veins in this unit is consistent with a pre-mineralisation timing (Table 3.2).

3.3.1.8 Mafic monzonite

Equigranular, medium-grained mafic monzonite has previously been described as a monzonite/monzodiorite intrusion (McInnes, 1997) and as monzogranite (Ashley, 2004; 2005). It is the main host rock to mineralisation in the E41 west pod. It has also been encountered under the east pod (~100 m below surface; 86800E section), and it possibly extends further to the north (Fig. 3.2D). The mafic monzonite intrusion appears to be a vertical body (Fig. 3.2C; McInnes, 1997). It is 300 m wide, has a 500 m strike length and remains open at depth. The mafic monzonite body is obvious on aeromagnetic images of the Cowal district, defining an elliptical magnetic low within the magnetic high defined by the diorite sill (Fig. 2.5). The mafic monzonite intrusion is elongated and parallel to the district north-trending structural fabric (Fig. 3.1).

The mafic monzonite contains abundant, euhedral to subhedral, blocky and tabular plagioclase and euhedral K-feldspar laths (Fig. 3.11A). In thin section, plagioclase and K-feldspar are characterised by a turbid appearance, caused by the presence of hematite inclusions (Figs. 3.11B and C). K-feldspar crystals appear to have

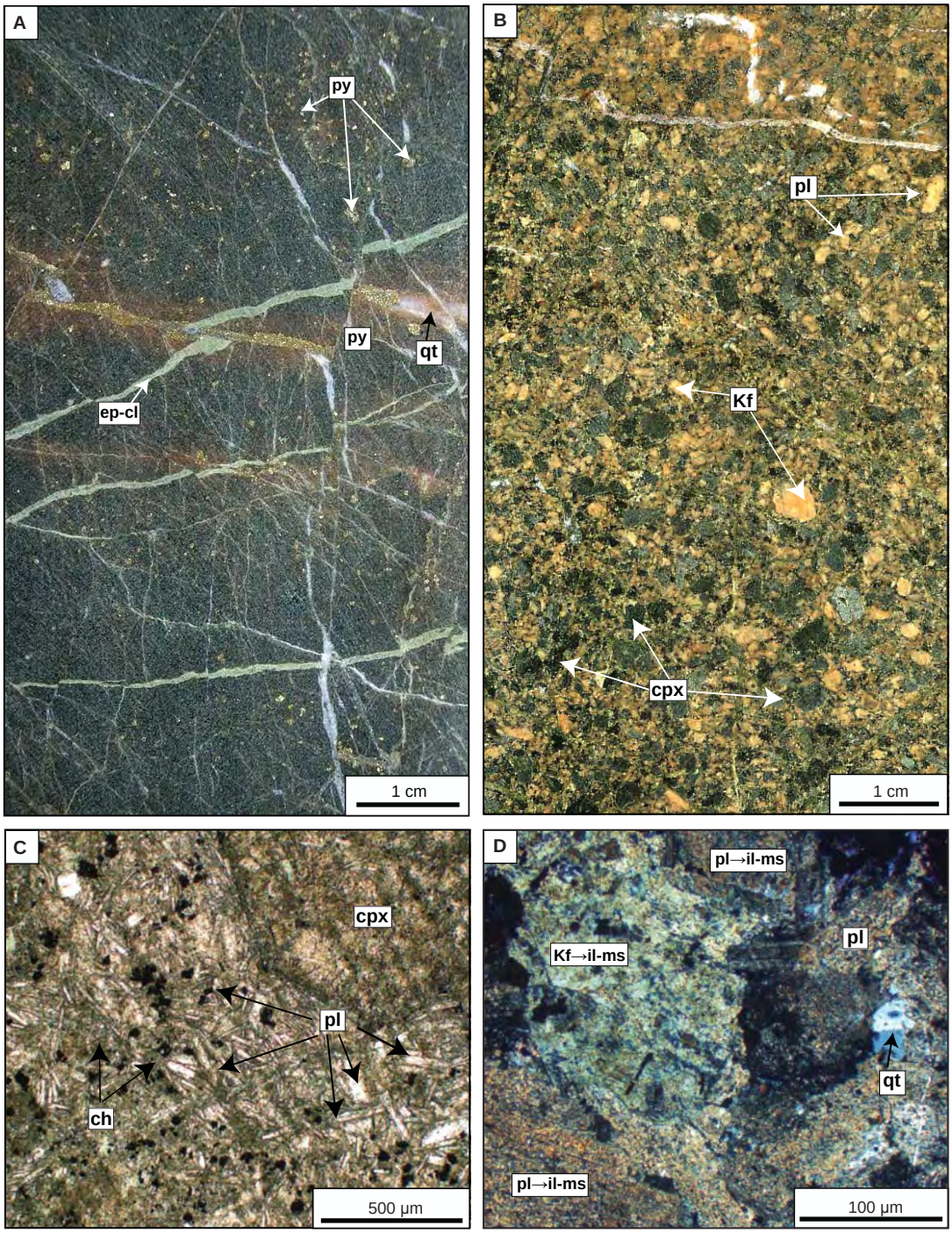

Figure 3.10 Pre-mineralisation dykes. **A.** Weakly porphyritic mafic dyke. Sample overprinted by pyrite - illite - muscovite - chlorite - carbonate alteration and cut by quartz-pyrite vein and late epidote - carbonate veinlets (E41D2063, 148.9m). **B.** Equigranular monzodiorite dyke showing abundant K-feldspar phenocrysts and clinopyroxene and hornblende that have been altered to actinolite. Pyrite is disseminated throughout the rock (E41D2014, 209.2m). **C.** Photomicrograph (ppl) of mafic dyke showing interlocked euhedral, tabular plagioclase crystals that are partially altered to carbonate, illite - muscovite and chlorite. The chlorite that occurs between plagioclase crystals has most likely replaced ferromagnesian minerals. Rare euhedral clinopyroxene crystals are supported in a plagioclase rich groundmass. Magnetite is disseminated throughout the sample (E41D2063, 126.6m). **D.** Photomicrograph (xpl) of monzodiorite dyke showing euhedral plagioclase and anhedral K-feldspar crystals that have been intensely altered to illite - muscovite (E41D2014, 209.2m). Abbreviations: cl=calcite, ep=epidote, il-ms=illite-muscovite, Kf=K-feldspar, Kf→il-ms=K-feldspar altered to illite-muscovite, pl=plagioclase, pl→il-ms=plagioclase altered to illite-muscovite, py=pyrite, cpx=pyroxene, qt=quartz.

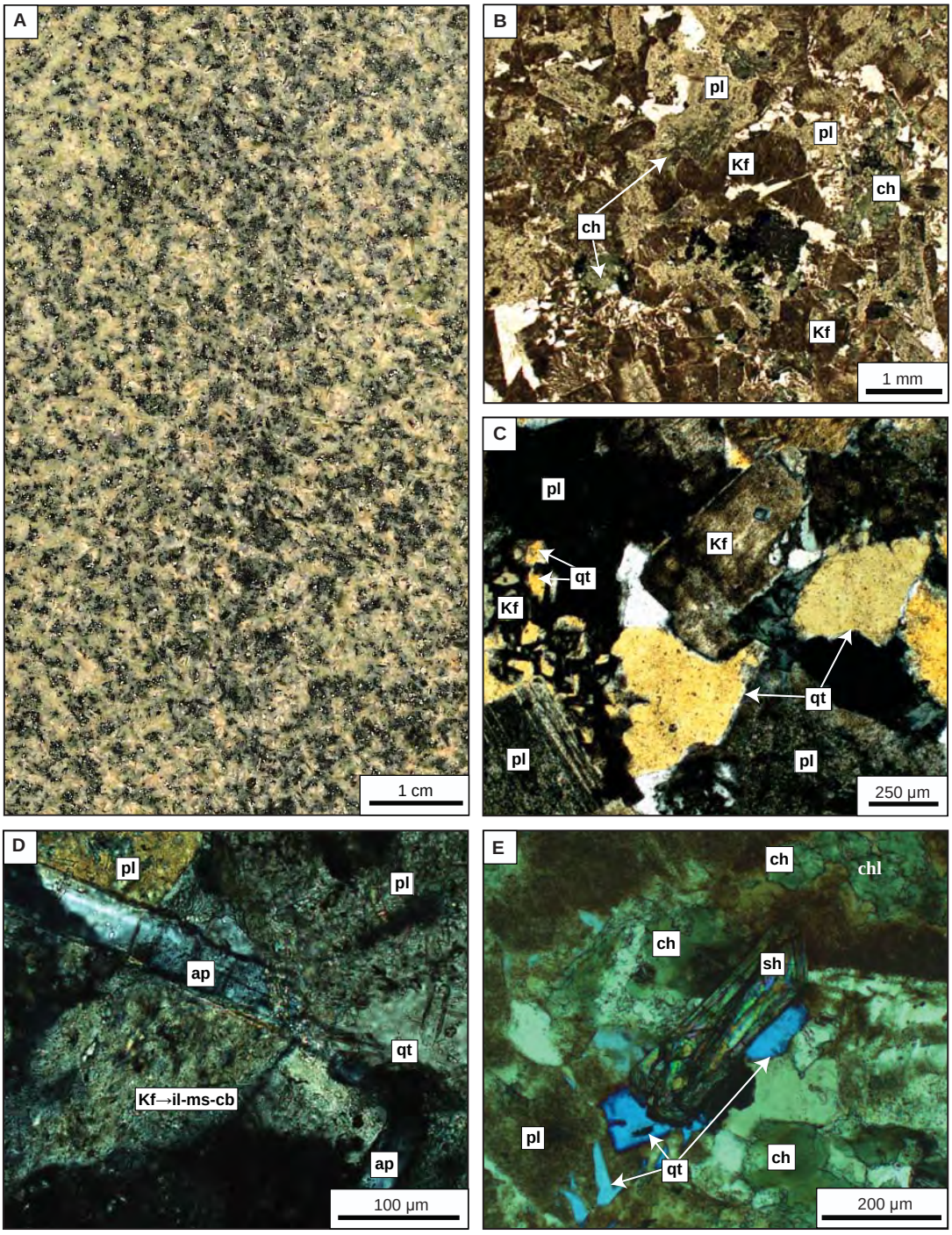

Figure 3.11 Pre-mineralisation mafic monzonite intrusion. **A.** Equigranular mafic monzonite showing abundant plagioclase, K-feldspar and altered ferromagnesian minerals. Pyrite is disseminated throughout the rock, occurring in mafics sites (E41D2180, 148.8m). **B.** Photomicrograph (ppl) showing equigranular texture of mafic monzonite. Plagioclase has been weakly altered to muscovite - illite and carbonate. Former hornblende has been partially to entirely replaced by chlorite. Chlorite is locally associated with secondary titanite (E41D2182, 243.4m). **C.** Photomicrograph (xpl) showing euhedral plagioclase crystals in mafic monzonite. These have myrmekitic intergrows of quartz and K-feldspar, and quartz also occurs between plagioclase crystals (E41D2182, 243.4m). **D.** Photomicrograph (xpl) showing elongated euhedral apatite enclosed between plagioclase crystals. Plagioclase crystals have been weakly altered to muscovite - illite ± carbonate, giving them a turbid character (E41D2182, 243.4m). **E.** Photomicrograph (xpl) showing sphene hosted in holocrystalline mafic monzonite. Plagioclase crystals are intensely hematite dusted, causing brown colouration in thin section. Quartz is interstitial to plagioclase (E41D2182, 243.4m). Abbreviations: ap=apatite, ch=chlorite, Kf=K-feldspar, Kf→il-ms-cb=K-feldspar altered to illite-muscovite-carbonate, pl=plagioclase, qt=quartz, sh=sphene

been particularly susceptible to hematite alteration. Altered ferromagnesian minerals comprise ~7 to 15% of the unit. Anhedral quartz constitutes up to 10% of the rock and locally have myrmekitic intergrowths with K-feldspar (Fig. 3.11C). Elongated euhedral apatite and sphene occur as accessory phases throughout the intrusion (Figs. 3.11D and E).

Quartz occurs in the mafic monzonite as a primary igneous phase, locally as a hydrothermal mineral, and as igneous 'quartz eyes'. These quartz eyes are interpreted to be composite grains that grew in miarolitic cavities (e.g., Harris et al., 2004; Figs. 3.12A and B), which occur throughout the mafic monzonite (distribution indicated on Fig. 3.2). They are more common in the 'hybrid zone' (described below). Miarolitic cavities are also present over a 30 cm intersection along the contact between the mafic monzonite and the diorite (DDH: E14D2129 at 212.2 – 3 m). They are characterised by spherical intergrowths of quartz crystals surrounded by a fine-grained aplitic-dominated groundmass. In thin section, the quartz crystals are generally euhedral, although some have wavy edges. The crystal terminations point towards the centre of the miarolitic pocket. K-feldspar that occurs in the miarolitic cavities is typified by a myrmekitic texture. Miarolitic cavities occur either as 2 to 3 mm diameter 'eye-like' clusters (Fig. 3.12B), or as elongated, discontinuous pockets that locally connect into veinlets (Fig. 3.12A). In such cases, quartz comprises the centre part of the veinlet with K-feldspar forming irregular selvages, commonly diffused into the adjacent wall rock. Rare euhedral pyrite occurs within the miarolitic cavities.

The miarolitic cavities are magmatic-hydrothermal textures that are interpreted here to indicate that the mafic monzonite intrusion was enriched in fluids and hence might have contributed to mineralisation (e.g., Candela and Blevin, 1995). They preserve evidence of volatile exsolution and provide a link between magmatic and hydrothermal activity (e.g., Harris et al., 2004). The miarolitic cavities occur within the mafic monzonite and the timing of their formation is inferred to be synchronous with monzonite intrusion. The miarolitic cavities are cut by some mineralised veins (Chapter 5), indicating a pre- or early- mineralisation timing. Similar magmatic features have been found in a number of porphyry systems, including Northparkes (Lickfold, 2002; Lickfold et al., 2003; Lickfold et al., 2007) and Cadia (Wilson, 2003; Wilson et al., 2003), and they appear to be temporally related to mineralisation in those deposits.

A number of aplite and quartz-monzonitic dykelets cut the mafic monzonite. Based on their similar mineralogies, the mafic monzonite is inferred to be a parental intrusion to these syn-mineralisation dykelets (described below) that have penetrated throughout the deposit.

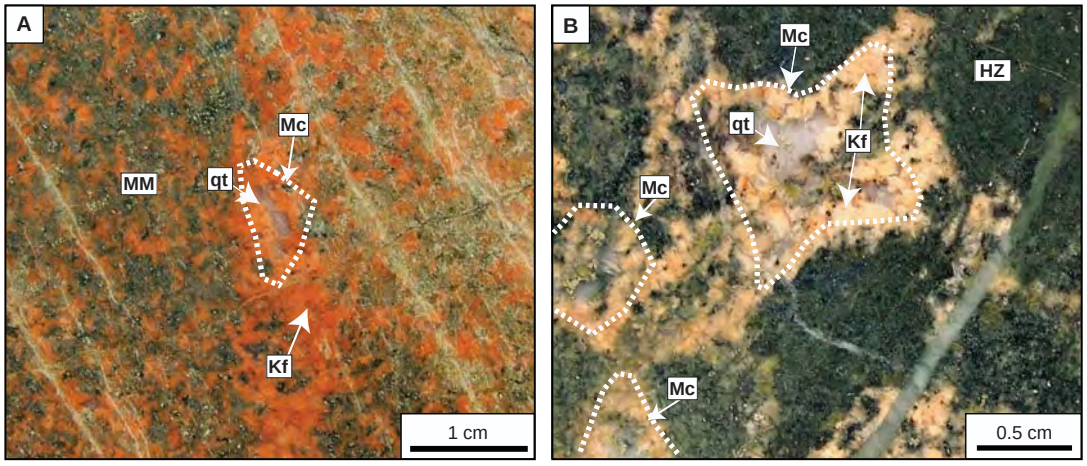

Figure 3.12 Miarolitic cavities. **A.** Miarolitic cavity hosted in mafic monzonite (E41D2143, 82.8m). **B.** Miarolitic cavities hosted between monzodioritic enclaves in the hybrid zone (E41D2129, 213.9m). Abbreviations: HZ=hybrid zone rock, Kf=K-feldspar, Mc=miarolitic cavity, MM=mafic monzonite, qt=quartz.

3.3.1.9 Hybrid monzodiorite – mafic monzonite zone

A hybrid zone has been identified in the E41 west pod mafic monzonite. This zone is characterised by an igneous-cemented breccia defined by black, texturally distinct, fine-grained blebs of monzodiorite intermingled with mafic monzonite (Figs. 3.13A and B). The hybrid zone occupies the centre of the mafic monzonite and extends for >100 m vertically. In plan view, the hybrid zone extends up 50 m horizontally and widens towards the south (Fig. 3.2A).

From their textural features and inferred primary mineralogy, the black blebs are interpreted to vary from monzodiorite to quartz-monzodiorite in composition. The blebs range in diameter from 2 to 10 cm (most common) up to a few metres. They commonly have irregular to sub rounded shapes, with wavy margins. Some are angular. They are strongly altered (Table 3.2), but primary plagioclase, quartz and K-feldspar crystals are recognisable (Fig. 3.13C). Interstitial anhedral quartz crystals are interlocked with fine-grained plagioclase. Some monzodiorite blebs contain euhedral megacrysts of plagioclase (10 – 15 %) which are up to 15 mm long and 5 mm wide, with lath-like habits (Fig. 3.13A). They are white to pale green and randomly dispersed. The megacrystic monzodiorite blebs contain more K-feldspar than their finer-grained counterparts. The equigranular mafic monzonite that occurs between the monzodiorite blebs locally contains abundant euhedral K-feldspar crystals. In some cases the K-feldspar is intergrown with quartz, resulting in local monzogranite domains between the monzodiorite blebs (Fig. 13B). Parts of the monzogranite have myrmekitic textures (Fig. 3.13D). Miarolitic cavities are common in the hybrid zone and their distribution is shown on Figure. 3.2.

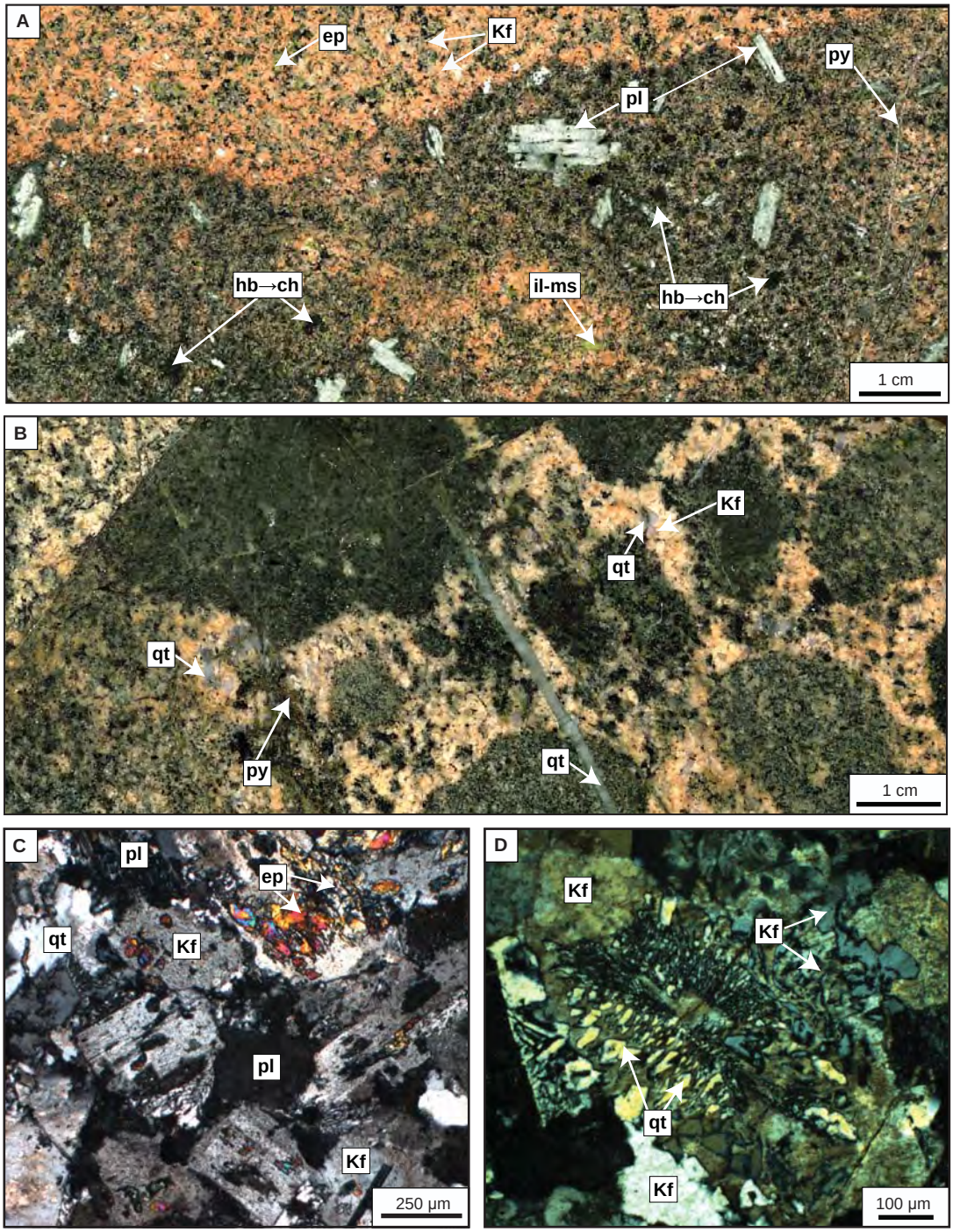

Figure 3.13 Rocks of the hybrid zone in the mafic monzonite. **A.** Sample from the hybrid zone, showing monzodioritic blebs (enclaves) with plagioclase megacrysts hosted in equigranular mafic monzonite. Plagioclase megacrysts are partially pseudomorphed by albite. Hornblende phonocrysts have been selectively pervasively altered to chlorite. Locally illite - muscovite and/or epidote have replaced plagioclase crystals (E41D2143, 117.4m). **B.** Sample from the hybrid zone showing fine-grained aphanitic black monzodioritic blebs hosted in mafic monzonite. In this sample miarolitic cavities occur in between the black blebs (E41D2129, 213.9m). **C.** Photomicrograph (xpl) of monzodiorite bleb. The image shows abundant K-feldspar, plagioclase and subordinate mafic minerals (hornblende). Epidote has replaced plagioclase crystals (E41D2129, 213.9m). **D.** Photomicrograph (xpl) showing myrmekitic texture that characterises spaces between the black monzodioritic blebs (E41D2129, 213.9m). Abbreviations: ch=chlorite, ep=epidote, hb=hornblende, Kf=K-feldspar, il-ms=illite-muscovite, py=pyrite, qt=quartz.

The monzodiorite blebs in the hybrid zone are interpreted to be enclaves of a more mafic intrusion that mingled with the mafic monzonite. The lack of chilled margins around the monzodiorite blebs and the crystalline nature of the igneous 'cement' support this interpretation.

3.3.2 Syn-mineralisation rock units

3.3.2.1 Aplite dykelets

Aplite dykelets at E41 are typically 5 to 50 mm wide, fine-grained, aphanitic and have a distinctive pale pink to red colour (Figs. 3.14A and B). Their spatial distribution is shown on Figure 3.2. Petrographically, the aplitic dykelets have a sugary texture and are composed of K-feldspar and quartz with minor plagioclase (Fig. 3.14C). K-feldspar is typically dusted by hematite. Cross-cutting relationships between this unit and most of the other coherent facies are poorly understood. The exceptions are the Muddy Lake diorite and the mafic monzonite, both of which the aplites cross-cut (Figs. 3.14A and B). In the west pod, some of the aplite dykelets are highly-mineralised, containing gold-bearing pyrite clots. They have cut the mafic monzonite and although these dykelets are locally illite – muscovite – chlorite altered, some dykelets have intruded into quartz – pyrite veins (3A-c vein stage; Chapter 5: Fig. 3.14B) indicating their close temporal association with gold (inter-mineralisation). The aplite dykelets are consequently assigned a syn-mineralisation timing.

3.3.2.2 Quartz-monzonite dykelets

Quartz-monzonite dykelets (5 – 50 cm wide) cut the diorite (Figs. 3.15A and 3.16A) and mafic monzonite. The dykelets are fine- to medium-grained equigranular rocks that consist of plagioclase, euhedral to subhedral orthoclase (determined by XRD; Appendix D.2), quartz and relict hornblende. Titanite, apatite and magnetite occur as subordinate phases. Sphene crystals are rounded to anhedral, whereas magnetite is euhedral to subhedral. Apatite occurs as a subordinate interstitial fine-grained phase. Euhedral to anhedral quartz crystals are locally intergrown with K-feldspar. The quartz-monzonite dykelets are typically pink to red as a result of sub-micron hematite dusting of plagioclase and K-feldspar crystals.

The spatial distribution of quartz-monzonite dykelets is shown on Figure 3.2. On the NS-section through the east pod (Fig. 3.2D), the quartz-monzonite dykelet occurs on the southern fringe of the mafic monzonite. Two quartz-monzonitic dykelets were also intersected in between the west and east pods (DDH: E41D2129) and minor occurrences were encountered in the west pod (Fig. 3.2C). Some of the dykelets appear to have sub-vertical geometries. For example, a quartz-monzonite dykelet in the east

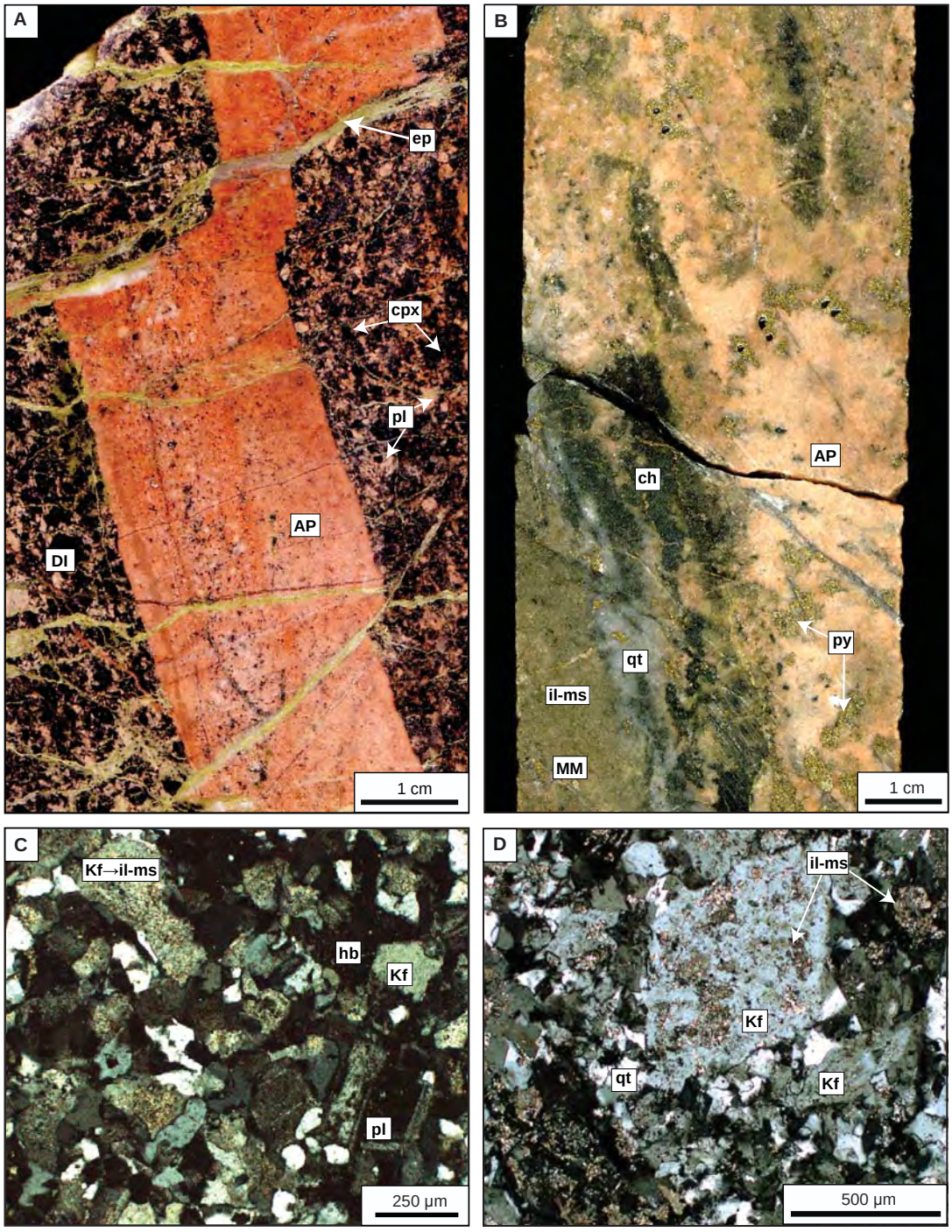

Figure 3.14 Dykelets interpreted to have a syn-mineralisation timing. **A.** Aplitic dykelet cutting diorite intrusion. Minor disseminated pyrite occurs within the dykelet (E41D2011, 121.4m). **B.** Example of an aplitic dykelet intruding a quartz-pyrite-chlorite vein (stage 3-b). Au-bearing pyrite clots (7.53 ppm Au: assay of this sample) are disseminated throughout the aplitic dykelet (E41D2178, 99.1m). **C.** Photomicrograph (xpl) showing mosaic texture of aplitic dykelet with interlocking K-feldspar and quartz. Subordinate hornblende crystals are pseudomorphed to chlorite. Weak muscovite - illite alteration has overprinted the feldspars (E41D2011, 121.7m). **D.** Photomicrograph (xpl) showing weakly porphyritic texture of an aplite dyke. K-feldspar phenocrysts are supported within a groundmass of K-feldspar and quartz. Weak selective pervasive illite-muscovite-carbonate alteration has overprited the feldspars (E41D2178, 99.1m). Abbreviations: AP=aplite, ch=chlorite, cpx=clinopyroxene, DI=diorite, hb=hornblende, Kf=K-feldspar, Kf→il-ms=K-feldspar altered to illite-muscovite, pl=plagioclase, py=pyrite, qt=quartz.

pod (Fig. 3.16A) is oriented sub-parallel to the core axis, which was drilled at an inclination of -70°.

Xenoliths of diorite (1 cm diameter) occur in the quartz-monzonite dykelets (Fig. 3.16A). These dykelets post-date mafic monzonite, actinolite- and epidote-bearing alteration facies and pre-date the carbonate-base metal sulfide mineralisation stage (stage 4; Chapter 5). Locally stage 3A-c veins have cut quartz-monzonite dykelets. The quartz-monzonite is therefore interpreted to have a syn-mineralisation timing (Table 3.2).

3.3.2.3 Pyroxene-phyric dykes

Two discrete phases of pyroxene-phyric dykes have been identified in the east pod: (1) a crowded clinopyroxene-phyric phase with abundant (up to 30 – 40%) euhedral to subhedral clinopyroxene phenocrysts that are 2 to 3 mm in diameter (Fig. 3.15D), and (2) a sparsely clinopyroxene-phyric phase comprising up to 15% euhedral to subhedral phenocrysts between 2 to 5 mm in diameter (Fig. 3.15B). The groundmass of both phases is fine-grained to aphanitic and rich in plagioclase and ferromagnesian minerals that cannot be identified because of intense hydrothermal alteration. The crowded phase has an equigranular texture locally. FeTi oxides occur in the groundmass of both the crystal crowded and sparsely porphyritic phases.

The pyroxene-phyric dykes are typically less than 1 m thick and only locally exceed 2 m. Where preserved, the dyke margins are chilled, but these textures are more commonly obscured by hydrothermal alteration. Both phases of pyroxene-phyric dyke have cut the Muddy Lake diorite. No pyroxene-phyric dykes have been encountered in west pod. At the contact with the diorite, pyroxene-phyric dykes have cut K-feldspar – epidote alteration facies associated with weakly mineralised stage 3A-b veins, which places their timing after the initial gold-forming event at E41 (Fig. 3.16B; Table 3.2 and Chapter 5). Pyroxene-phyric dykes also host gold mineralisation locally in disseminated pyrite, which is interpreted to be related to major gold events at E41. It is not clear whether the disseminated pyrite was produced during stage 3A-c or 4A. The observed cross-cutting and overprinting relationships, however, suggest that pyroxene-phyric dykes post-date porphyry-style hydrothermal activity, and most likely were coeval with epithermal events at E41 (Table 3.2; Chapter 5). Consequently, these dykes are assigned a syn-mineralisation timing.

Pyroxene-phyric dykes have been documented from E42 where they host weak gold mineralisation locally as disseminated pyrite (Anderson, 2003). Pyroxene-phyric juvenile clasts have been recognised in magmatic-hydrothermal breccia that has been intersected by drilling at E42 (Strickland, 2005). The E42 breccia has a northeast-

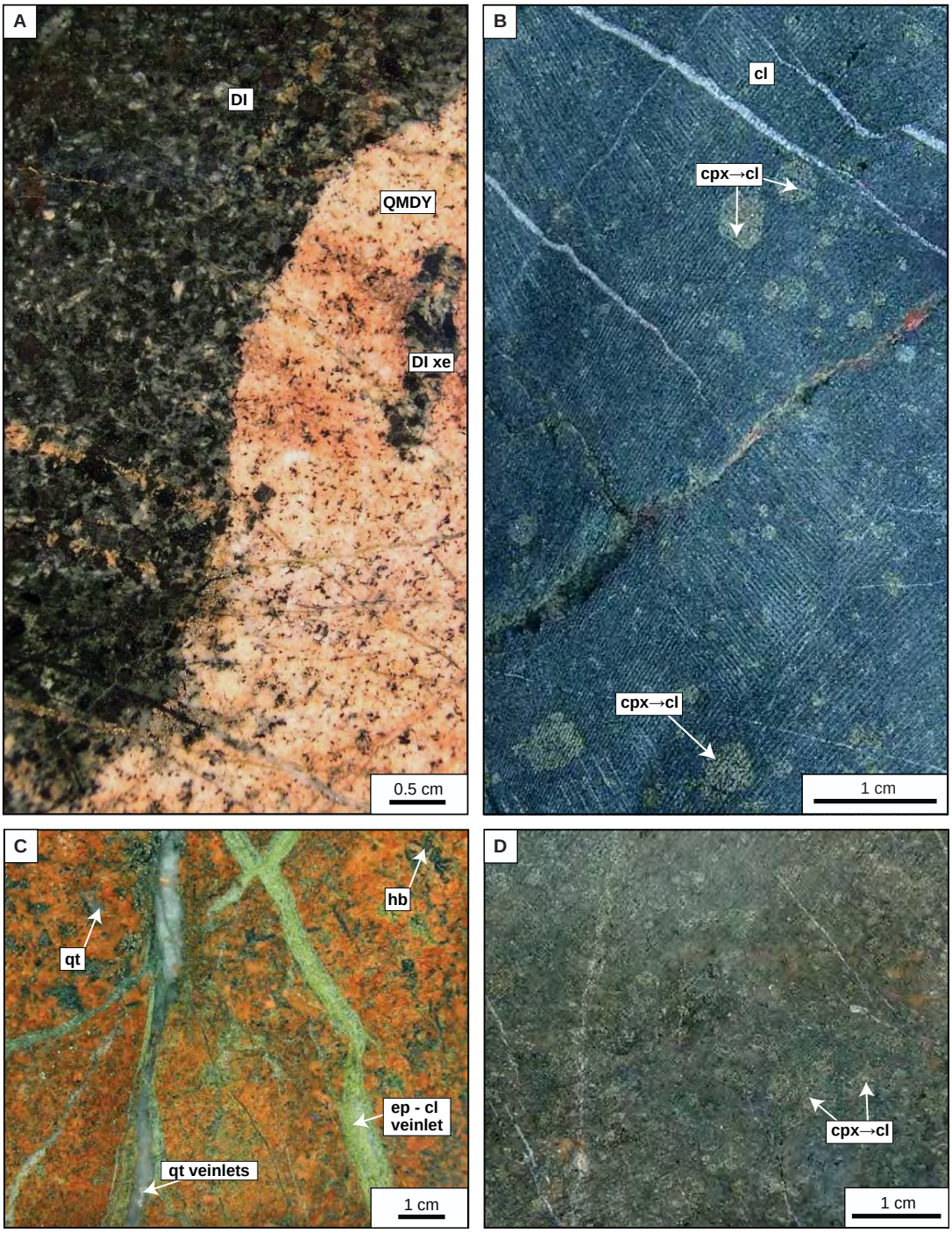

Figure 3.15 Dykes interpreted to have a syn-mineralisation timing. **A.** Intrusive contact between quartz-monzonite dykelet and Muddy Lake diorite. Diorite xenoliths occur in the quartz-monzonite. Ferromagnesian minerals in diorite have been pseudomorphed by actinolite and magnetite and plagioclase crystals have been altered to albite. The pink colour of the quartz-monzonite is related to hematite-dusted feldspars. Thin (~1mm) quartz-pyrite veinlets have cut both rocks. Pyrite is disseminated in the quartz-monzonite but is absent from the diorite (E41D2068, 83.4m). **B.** Pyroxene-phyric dyke with sparsely distributed pyroxene phenocrysts that have undergone weak selectively pervasive calcite alteration. Dark groundmass has been altered to chlorite and carbonates (E41D2067, 159.6m). **C.** Quartz-monzonite dyke from the centre of mineralisation (east pod). Distinctive reddening that characterises this unit has resulted from hematite dusting of feldspars. Most likely this sample has undergone at least two stages of hematite dusting, as epidote - calcite veinlets are commonly associated with hematite halos (which resulted in strong red coloration). Sample is moderately altered to chlorite - epidote - carbonate and illite - muscovite. Quartz - pyrite veins (stage 3A-c) have cross-cut the quartz-monzonite (E41D2067, 147.8m). **D.** Crowded pyroxene-phyric dyke with pyroxene pseudomorphed by calcite. Weak pyrite disseminations occur throughout the rock (E41D2010, 256.7m). Abbreviations: cl=calcite, cpx=clinopyroxene, cpx→cl=clinopyroxene altered to calcite, DI=diorite, Di xe=diorite xenolite, ep=epidote, QMDY=monzonite dyke, qt=quartz.

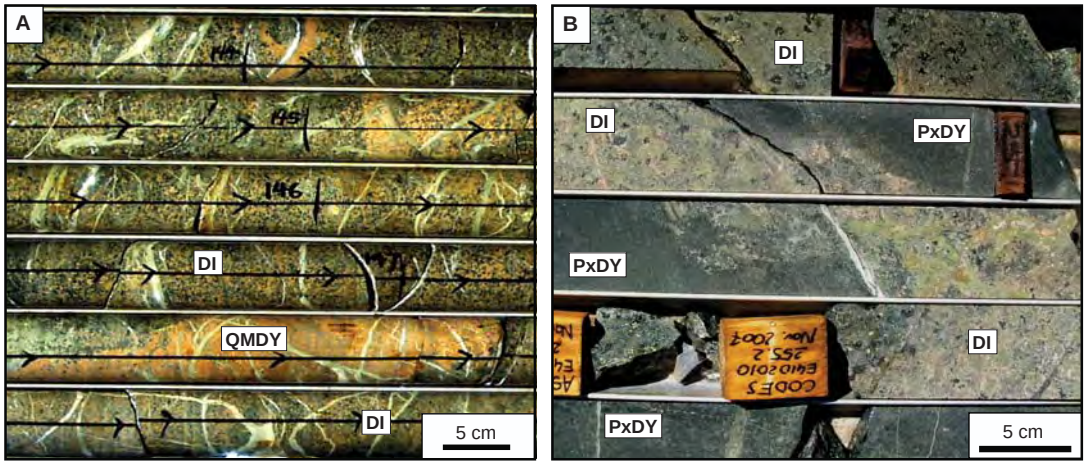

Figure 3.16 Intrusive cross-cutting relationships. **A.** Diorite intruded by quartz-monzonite dykelet. Note strong hematite reddening in diorite around quartz-monzonite. The diorite and quartz-monzonite dykelet have been cut by late epidote - calcite - prehnite veinlets (DDH: E41D2067). **B.** Pyroxene-phyric dyke cutting K-feldspar - epidote altered diorite (DDH: E41D2010). Abbreviations: DI=diorite, QMDY=monzonite dykelet, PxDY=pyroxene-phyric dyke.

trending strike length of greater than 300 m and a maximum width of 140 m. The top of the breccia occurs at around 200 m below the present surface and extends to depths greater than 600 m (Strickland, 2005). The juvenile clasts in the hydrothermal breccia indicate that the pyroxene-phyric unit was the magmatic source of the breccia complex (Sillitoe, 1985; Davies, 2002). The breccia is cut by some mineralised veins, so the dykes are inferred to have an early-mineralisation timing at E42 (Strickland, 2005). Bissig (2007; Bissig et al., 2008) recognised mafic pyroxene porphyry dykes at E43 that texturally and mineralogically resemble those from E42 and E41. Although Bissig (2007) has assigned a syn-mineralisation timing to these dykes and indicated similarities to the pyroxene-phyric dykes observed at E41 and E42 deposits, Zukowski (2009) argued that because Cu-Au mineralisation at E43 occurred prior to Au mineralisation at E41, the pyroxene-bearing porphyries at E43 must have been intruded earlier than those pyroxene-phyric dykes at E41. Nevertheless, based on the observed timing relationships of pyroxene-phyric dykes to mineralisation at E41 and E42, the pyroxene-phyric rocks are inferred to have played an important role during mineralisation at each deposit.

3.3.3 Late-mineralisation rock units

3.3.3.1 Syenite dykelet

A syenite dykelet was intersected in only one drill hole (DDH: E41D2013) in the eastern part of the east pod. It has an equigranular texture and a distinctive brick red colour (Fig. 3.17A). Hematite-dusted euhedral to anhedral K-feldspar crystals are abundant (Fig. 3.17C). Euhedral to subhedral plagioclase is partially intergrown with the K-feldspar. Anhedral quartz is common. Elongate, mostly euhedral crystals of

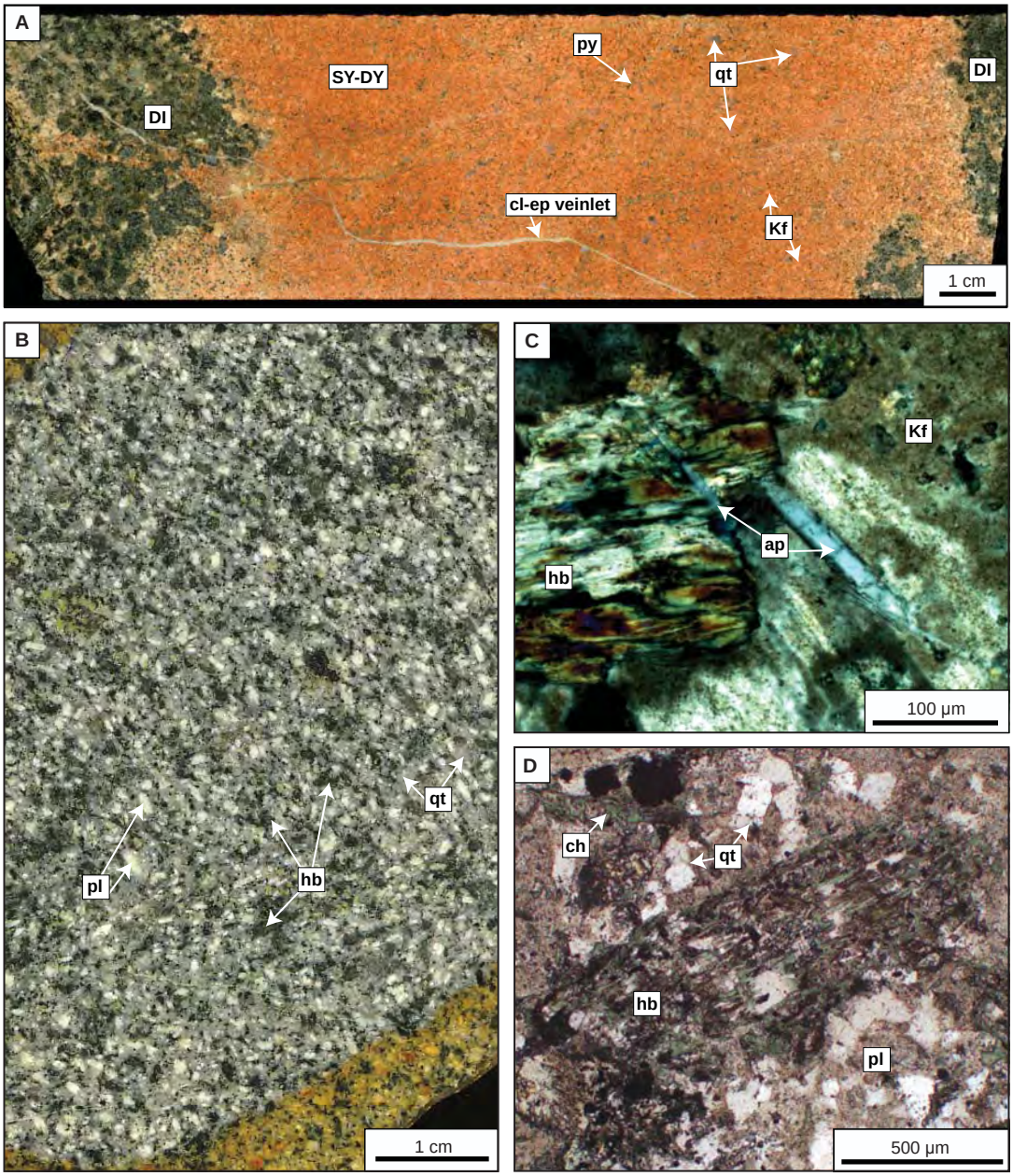

Figure 3.17 Examples of late-mineralisation syenite dykelet and hornblende-phyric quartz-rich dyke. **A.** Hand specimen sample showing syenite dykelet that has intruded the Muddy Lake diorite. Abundant K-feldspar (primary and secondary) crystals have been dusted by hematite. Anhedral, rounded quartz crystals are dispersed throughout the rock. Pyrite occurs as weak disseminations. Some late epidote - calcite veins have cut the syenite dykelet (E41D2013, 237.3m). **B.** Hornblende-phyric quartz-rich dyke with euhedral hornblende phenocrysts. White plagioclase phenocrysts have euhedral to anhedral shapes. Grey-coloured groundmass is composed of quartz and plagioclase crystals (E41D2067, 77.9m). **C.** Photomicrograph (xpl) of syenite dykelet showing hornblende and K-feldspar crystals. Euhedral apatite needle appears to be intergrown with K-feldspar. Brownish turbid occurrence of K-feldspar has resulted from hematite dusting (E41D2013, 237.3m). **D.** Photomicrograph (xpl) of hornblende-phyric quartz-rich dyke showing elongate euhedral hornblende crystal supported within a quartz-plagioclase groundmass. Hornblende has been weakly altered to chlorite. Weak selective pervasive illite - muscovite alteration has affected plagioclase crystals (E41D2067, 77.9m). Abbreviations: ap=apatite, ch=chlorite, cl=calcite, DI=diorite, ep=epidote, hb=hornblende, Kf=K-feldspar, pl=plagioclase, qt=quartz, SY-DY=syenite dykelet.

hornblende are subordinate to K-feldspar and quartz. Apatite occurs as an accessory phase (Fig. 3.17C). FeTi oxides are disseminated throughout the unit.

The syenite dykelet occurs close to the centre of the mineralised domain of the E41 east pod (E41D2013, 237.3 m; Fig. 3.2B). The temporal relationship to mineralisation cannot be resolved easily due to the lack of cross-cutting and overprinting relationships. It is speculated that this dyke may have intruded late with respect to mineralisation, due to the comparatively weak alteration assemblages (Table 3.2).

3.3.3.2 Hornblende-phyric quartz-rich dyke

A hornblende-phyric quartz-rich dyke was intersected in only one drill hole at E41 east pod (DDH: E41D2067: Figs. 3.17B and D). It intruded the upper part of the section, where the rocks are strongly weathered, and therefore its timing relationship is poorly constrained. The dyke contains euhedral hornblende phenocrysts and blocky euhedral to subhedral plagioclase crystals set in a groundmass dominated by fine-grained quartz (Fig. 3.17D). This unit contains weakly mineralised pyrite stringers but overall the texture and primary mineralogy has been particularly well-preserved. This hornblende-phyric quartz-rich dyke is therefore inferred to have a late-mineralisation timing.

3.3.4 Post-mineralisation rock units

3.3.4.1 Plagioclase-phyric diorite dyke

The distinguishing characteristic of this dyke is its crowded plagioclase-phyric texture (Fig. 3.18A). The plagioclase phenocrysts range from 1 to 4 mm. Most of the smaller phenocrysts are euhedral, whereas the larger phenocrysts have rounded shapes. Hornblende phenocrysts are commonly euhedral and elongate (Fig. 3.18D). The groundmass is fine-grained and consists of feldspathic minerals, accessory FeTi oxides, apatite and rare quartz. Subordinate sub-micron hematite disseminations occur throughout the feldspars.

The diorite dyke has intruded the Cowal fault and cut the Muddy Lake diorite and mafic monzonite. Similar plagioclase-phyric dykes have been described from other deposits in the Cowal district (e.g. E42 and E46; Strickland, 2005; Tosdal, 2007; 2008), where they are also spatially related to the northeast-trending Cowal fault, and their timing have been assigned as post-mineralisation.

3.3.4.2 Amygdaloidal dyke

The amygdaloidal dykes vary from aphanitic to porphyritic and are characterised by randomly distributed amygdales filled with calcite and hematite (Figs. 3.18B and E). The amygdales make up around 10% of the rock. The primary mafic phenocrysts are

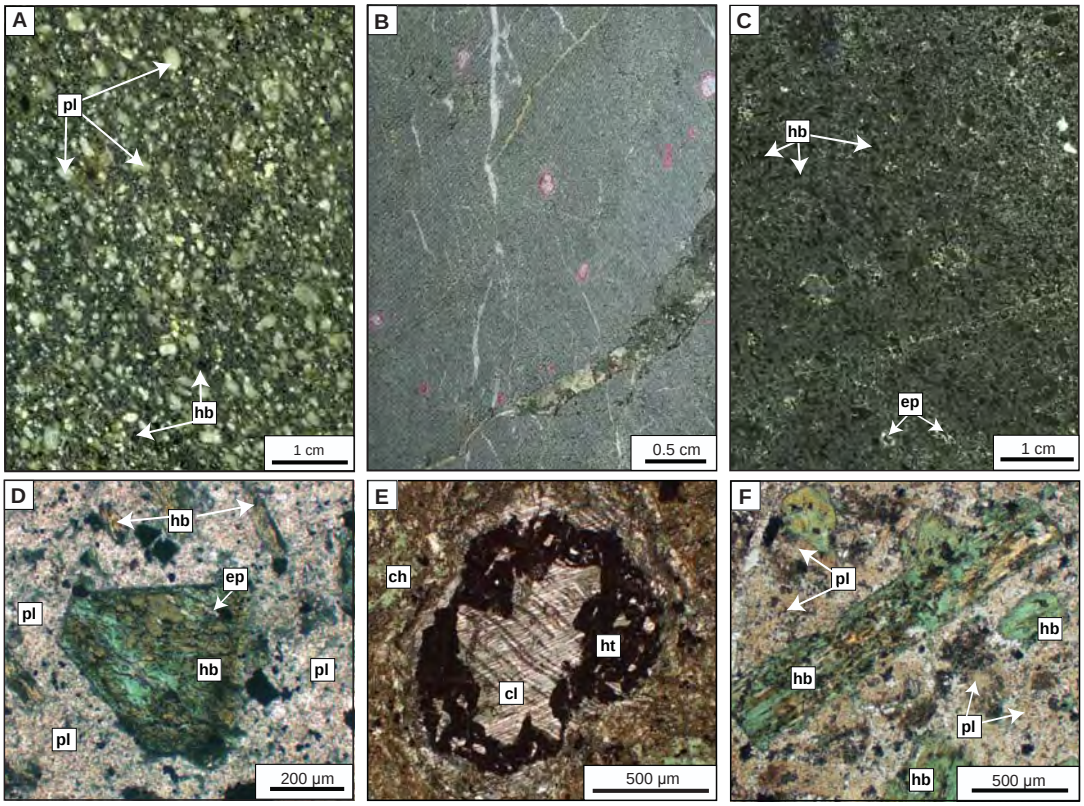

Figure 3.18 Post-mineralisation dykes. **A.** Plagioclase-phyric 'diorite' dyke with characteristic rounded plagioclase crystals (E41D2129, 234.8m). **B.** Amygdaloidal dyke. Randomly distributed amygdales have been filled by calcite and hematite (E41D2063, 117.4m). **C.** Hornblende-phyric dyke ('lamprophyre') with distinctive euhedral hornblende phenocrysts dispersed throughout (E41D2129, 123.9m). **D.** Photomicrograph (ppl) of diorite dyke showing euhedral hornblende phenocrysts in finely-crystallised plagioclase groundmass that have been altered to illite - muscovite and carbonate. Fe-oxides are dispersed throughout the rock (E41D2129, 234.2m). **E.** Photomicrograph (xpl) of amygdaloidal dyke showing calcite-filled vesicule with hematite rims around. Fine-grained groundmass has been altered to chlorite, carbonate, and clays (E41D2063, 117.9m). **F.** Photomicrograph (ppl) of hornblende-phyric dyke showing elongated hornblende phenocryst in plagioclase-dominated groundmass (E41D2000, 262.7m). Abbreviations: ap=apatite, ch=chlorite, cl=calcite, ep=epidote, hb=hornblende, ht=hematite, pl=plagioclase, qt=quartz.

inferred to be amphiboles, based on the elongate shapes of the chlorite pseudomorphs. The groundmass of these dykes is pervasively altered (Table 3.2), such that only relic of plagioclase laths are preserved locally. The thickest intersect of an amygdaloidal dyke is 3 m and this occurs in a post-mineralisation fault zone that has cut the mineralisation and related alteration facies (Table 3.2; Fig. 3.2D). Although the amygdaloidal dyke is strongly illite – muscovite – chlorite – carbonate altered, the alteration post-dates gold mineralisation, as there is no pyrite associated with this particular illite generation. Instead, it is thought to be related to the post-mineralisation faulting at E41.

At E42, an equivalent dyke facies has been described as the 'vesicular' dyke (Miles and Brooker, 1998; Bastrakov, 2000; Strickland, 2005), where it has intruded the Central Fault. Bastrakov (2000) suggested that the 'vesicular' dyke had a late- to post-mineralisation timing. This is consistent with field observations at E41 made during this study.

3.3.4.3 Hornblende-phyric dyke

This coherent facies was intersected in one drill hole (DDH: E41D2129) between the east and west pod at E41. It is characterised by abundant, elongate, euhedral hornblende phenocrysts (Figs. 3.18C and F). The groundmass is black and rich in fine-grained plagioclase, amphibole and clinopyroxene (Fig. 3.18F). This dyke is exceptionally well preserved in terms of primary mineralogy and texture, relative to other dykes in E41. The dyke lacks veins and alteration facies associated with mineralisation (Table 3.2), implying a post-mineralisation timing.

3.4 Structure

This section describes only the orientation of beds, faults and dykes at E41 to indicate the dominant structural trends within the deposit. The data has been collected only from oriented drillholes. Vein orientations are described in Chapter 5. All the data are presented as "strike/dip dip-direction" for planes. Structural measurements are plotted on the lower hemisphere of an equal area (Schmidt) projection.

3.4.1 Bedding

A total of 31 bedding measurements were taken from drill core during this study. The results are listed in Appendix B.2 Bedding measurements display an average orientation of 300/23 SW. These data have been combined with Barrick's unpublished data collected from the entire E41 drilling dataset. Two major clusters, one at approximately 218/28 NW and a secondary cluster 232/48 SE, are obvious on Figure 3.19A. These two populations indicate that the beds may have been folded, with fold-axes plunging gently to the southwest. Dykmans (2004a) also identified a shallowly south-southwest-plunging fold axis (220/17) at E41. It appears that the northwest-dipping limb is more poorly represented by the available bedding data. Although characterised by a gentler dip, the dominant cluster at E41 has an orientation consistent with the orientation of bedding at E42 (200/54 NW; Henry, 2008).

Ingpen (1995) mapped a pair of northwest-plunging syncline and anticline folds to the north of the E42 deposit. Henry (2008) noted that these folds are larger than the E42 open pit, which is why no folds have been observed at E42. She argued that E42 may be situated on the southwestern limb of a similarly oriented anticline to the south of the mapped folds, or dismembered from these folds by faults. Regional folding such as this on a scale larger than the exposure at E42 may account for the

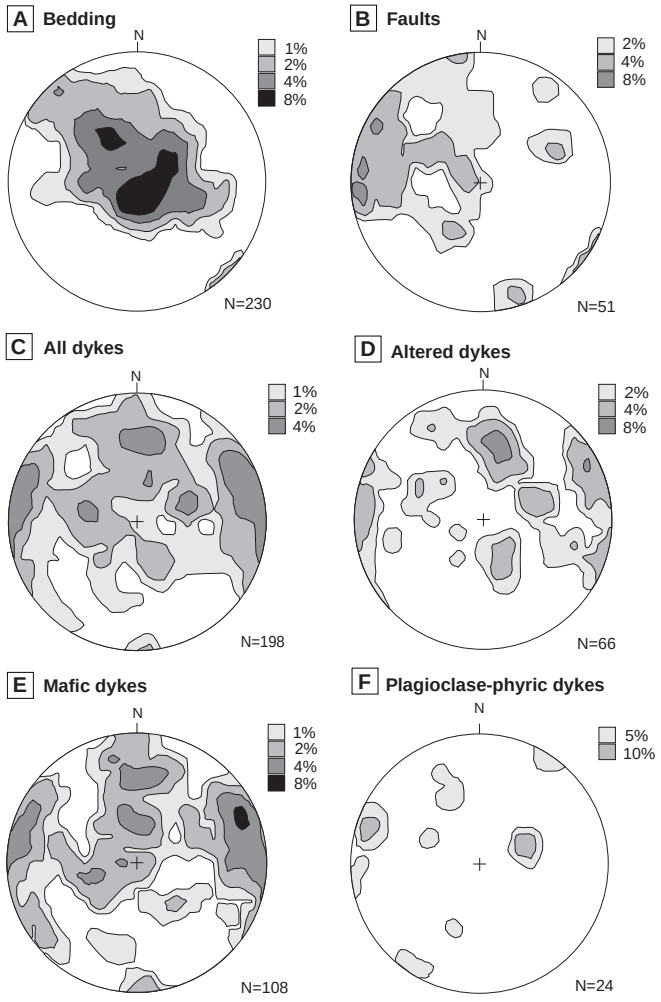

Figure 3.19 Structural features of the E41 deposit. Contoured pole-to-bedding stereoplots. **A.** Bedding measurements collected from drill core. **B.** Dominant north- and northeast-trending faults. **C.** Measurments collected from all dykes recognised in drill core. **D.** Measurements from altered dykes. **E.** Principal orientations from mafic dykes. **F.** Measurements collected from plagioclse-phyric dykes.

current tilted bedding orientation at both E42 and E41. The second, gently southeast-dipping cluster at E41 may be related to deposit-scale folding possibly induced by E41 intrusions rather than regional deformation. Based on current faults geometry at E41, bedding is inferred to have been tilted prior to the dominant faulting event.

3.4.2 Faults

Several faults were observed during logging at E41. These range from <0.5 to >10 m thick. Only a few orientations could be collected from these faults, and the data are scattered (Fig. 3.19B). When fault orientations measured during the current study are combined with unpublished Barrick data, the dominant fault population is characterised by an average orientation of 235/57 SE. Several weak populations are defined by shallow and steep dips, averaging 156/50 NE, 316/58 SW and 51/52 NW (Fig. 3.19B). These faults cut lenses of volcaniclastic units in mudstone as well as strongly dismembered contacts between the diorite and clastic units. Some of these

steep south- and southeast-dipping faults have been intruded by dykes and appear to have exerted an important control on early- and main- stages of mineralisation (Chapter 4).

A sub-vertical northwest-trending shear zone to the north of the mafic monzonite in the E41 east pod (Fig. 3.2D) has offset the northern edge of the mafic monzonite intrusion. It hosts disrupted vein fragments, implying post-mineralisation timing. A post-mineralisation timing of deformation has also been inferred for the north- to northwest-trending, west-dipping fault zone that bounds the eastern edge of the E41 east pod (Figs. 3.1 and 3.2B). This structure has been interpreted to be related to the Tabberabberan orogeny (Munroe et al., 2005). Another major north-northwest-trending structure, the geometry of which conforms to the post-mineralisation northwest-directed structural fabric, is the Cowal fault. This dips moderately to the east-, and northeast at E41 (Figs. 3.2A and B) and is located on the eastern edge of the mafic monzonite (Fig. 3.2A and B). Its exact timing at E41 is uncertain. This fault has been recognised throughout the 'gold corridor', cutting the E41, E42 and E46 systems (Fig. 3.1). It contains fragments of mineralised veins at E42 (Henry, 2008), where it has been interpreted to have recorded pre-, syn- and post-mineralisation episodes of deformation.

3.4.3 Dykes

Dykes have commonly intruded faults at E41. Many dyke contacts with Muddy Lake diorite and clastic units at E41 are hydrothermally altered, mineralised and not amenable to structural analysis from drill core. Some dyke margins were well preserved and these have been measured (Appendix B.2). The results of this study are combined with Barrick data on Figures 3.19C, D, E and F. Although the data are sparse, some possibly indicate sub-horizontal geometries. All dykes plotted on Figure 3.19C display three general orientations. Two dominant steeply dipping populations average 351/63 W and 182/61 E, and the third cluster that has a moderate south-directed dip averages 265/52 S. The third 265/52 S cluster overlaps with the dominant population of altered dykes as shown on Figure 3.19D. The orientation of altered dykes is also consistent with the principal orientation of mineralised vein stages (Chapter 4). It thus appears that some of the mineralised fractures have developed within and along these margins of pre-existing dykes.

Mafic dyke orientations (Fig. 3.19E) are characterised by similar clusters as shown on Figure 3.19C. Twenty four measurements from plagioclase-phyric dykes are scattered, but two weak clusters are apparent (Fig. 3.19F). One cluster is characterised

by moderate dips to the west, whereas the second cluster is defined by steep east-southeast dip directions.

Structural data collected from dykes indicate that they intruded pre-existing east-, north- and northeast-trending shear zones and faults. Many of the dykes have been sheared, indicating that the faults were reactivated after intrusion.

Post-mineralisation dykes are spatially related to north- and northwest-trending faults. An amygdaloidal dyke intruded into a shear zone (Fig. 3.2D), which indicates syn- or post- Tabberabberan timing for this dyke, whereas diorite dykes commonly show a spatial association with the Cowal fault across the Cowal district (E42: Strickland, 2005; E46: P. Balind, pers. comm., 2007).

3.5 Discussion

3.5.1 Volcanic facies associations, architecture and paleoenvironment of the Cowal district

Figure 3.20 shows representative stratigraphic columns from E46, E42 and E41. Figure 3.21 illustrates the inferred depositional environment for the E41 stratigraphy. The Cowal volcano-sedimentary sequences were deposited in subaqueous environments, based on the presence of hyaloclastite, peperite, turbidites (including mudstone and well-sorted sandstone) and other subaqueous sediment gravity flow deposits. A marine origin is also supported by a crinoid fragment found at E46 (Simpson and Cooke, 2006). The dominance of graded and massive, thick beds and the lack of shallow-water sedimentary structures (e.g., cross-bedding) in any of the volcanic and sedimentary clastic facies indicates a below-storm-wave-base environment (Simpson and Cooke, 2006; Simpson, 2008). The depth of storm wave-base typically ranges from 10 – 200 m in modern submarine settings (Johnson and Baldwin, 1996).

Stratigraphic relationships among volcano-sedimentary facies of Cowal deposits are complex, reflecting lateral facies variations, a large volume of laterally discontinuous lavas and associated clastic facies, and a lack of extensive marker horizons. It is therefore difficult to correlate volcanic facies across the district. It has been interpreted, however, that lavas and sills of E46 and E42 might represent the same volcanic event, and that these volcanic facies indicate a proximal setting to the volcanic activity (Simpson and Cooke, 2006). The E46 area was generally dominated by the influx of sediment gravity flows, which deposited a thick succession of syn-eruptive resedimented and post-eruptive reworked volcaniclastic deposits (Simpson and Cooke, 2006; Simpson, 2008). The blocky, curviplanar fragments in polymictic intervals are interpreted as reworked hyaloclastite. Similar facies association at E42, with reworked hyaloclastite and fiamme, may represent the same stratigraphic horizon

A. District stratigraphy

South — North

Endeavour 41

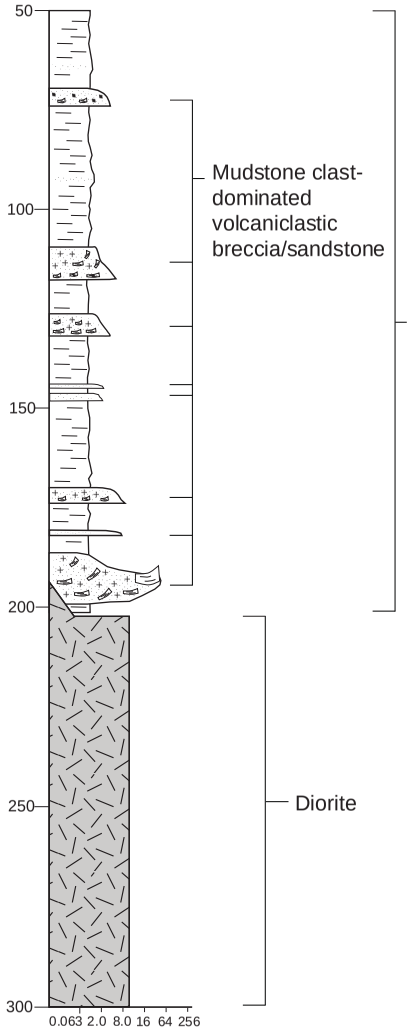

Endeavour 42

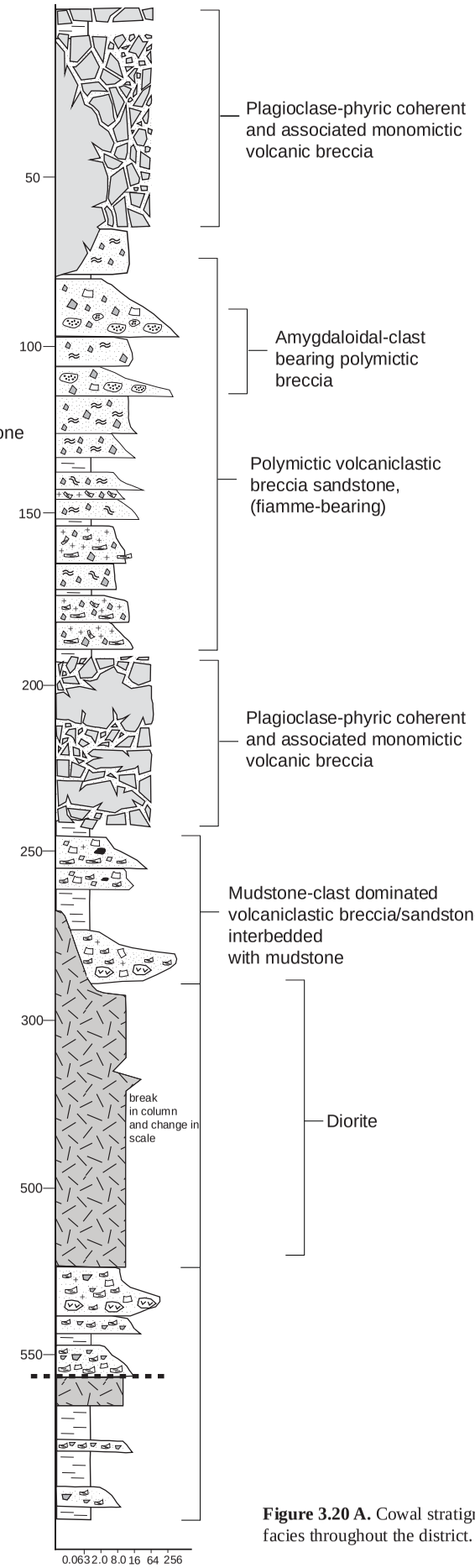

Endeavour 46

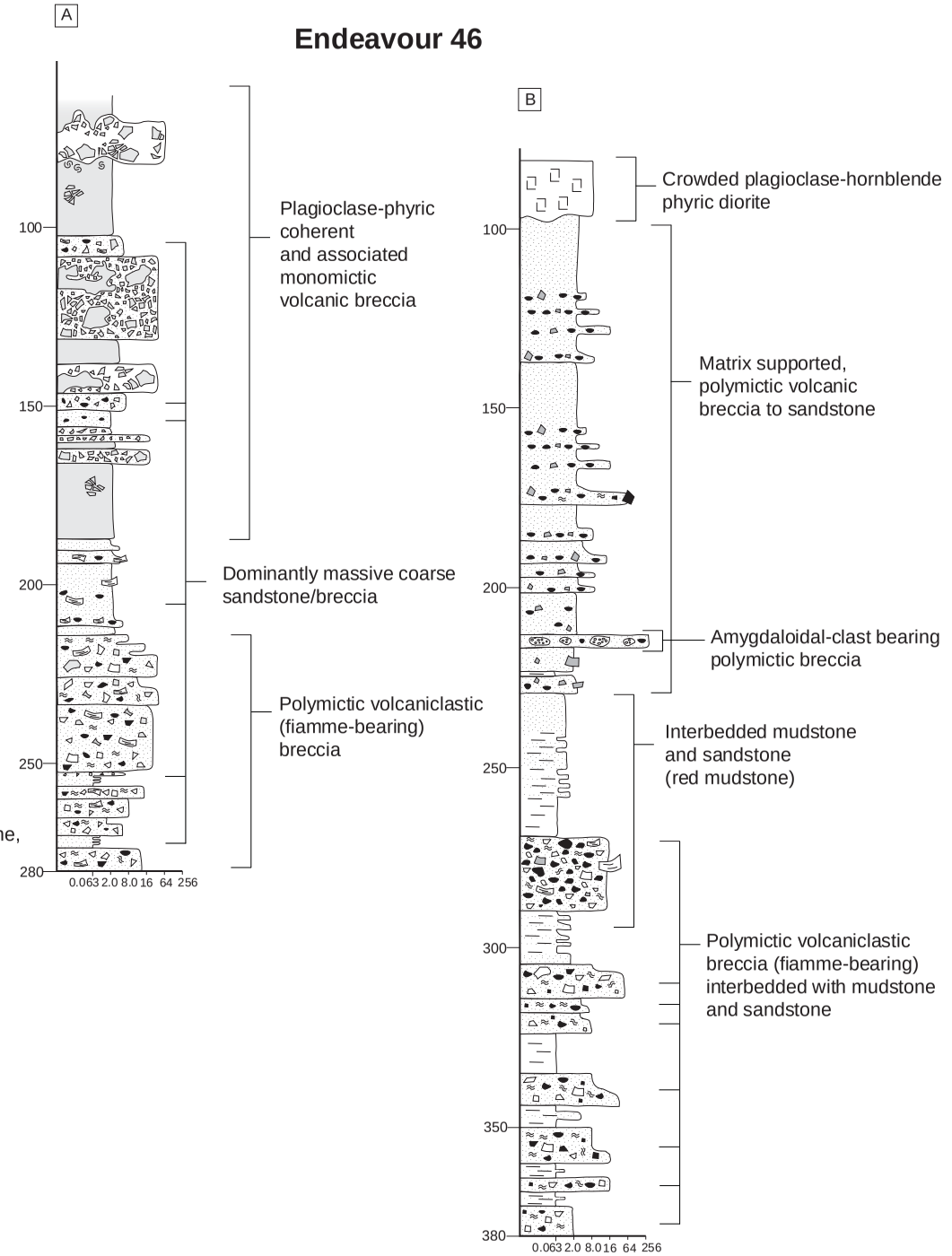

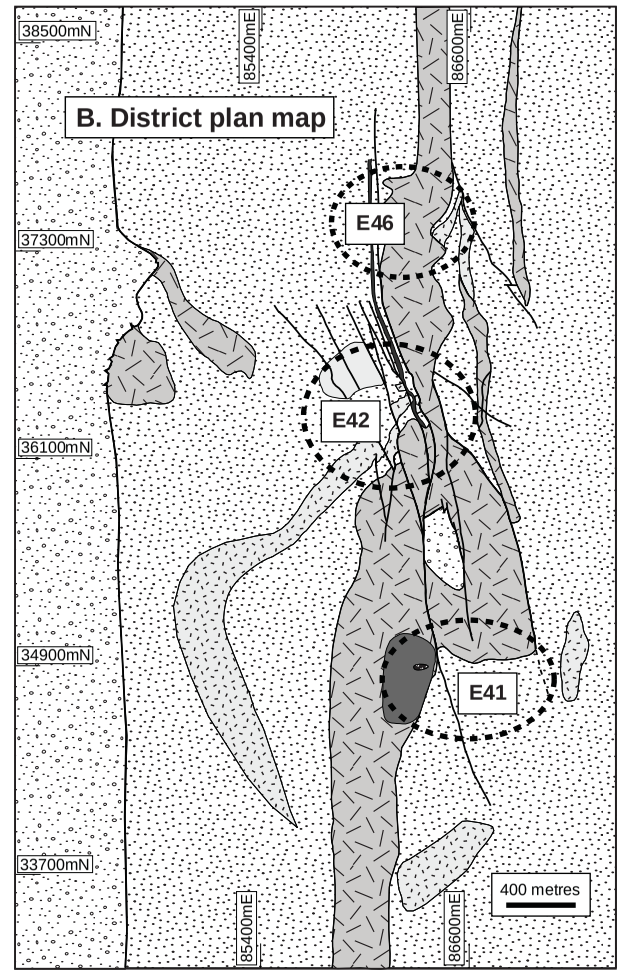

Legend

- Plagioclase-hornblende-phyric diorite
- Plagioclase-phyric andesite/trachyandesite
- Sandstone
- Mudstone
- Monomictic plagioclase-phyric breccia
- Diorite
- Mudstone clasts
- Other lithic fragments
- Feldspar-phyric clasts/ curviplanar clasts
- Crystals and crystals fragments
- Aphyric volcanic clasts
- Amygdaloidal clasts
- Holocrystalline felsic clasts
- Fiamme

Simplified district plan map:

- Volcaniclastic rocks
- Polymictic conglomerate
- Lava
- Andesite
- Mafic monzonite
- Faults

Figure 3.20 A. Cowal stratigraphy from the E46, E42 and E41 mineralised centres (compiled and modified from Cannell, 2003; Simpson and Cooke, 2006; and this study). Stratigraphic columns illustrate principal features of the volcanic facies throughout the district. **B.** Basement geology plan map (modified from Barrick Gold of Australia Ltd.), shows location of mineralised centers and generalised district architecture. The post-Ordovician cover is not shown.

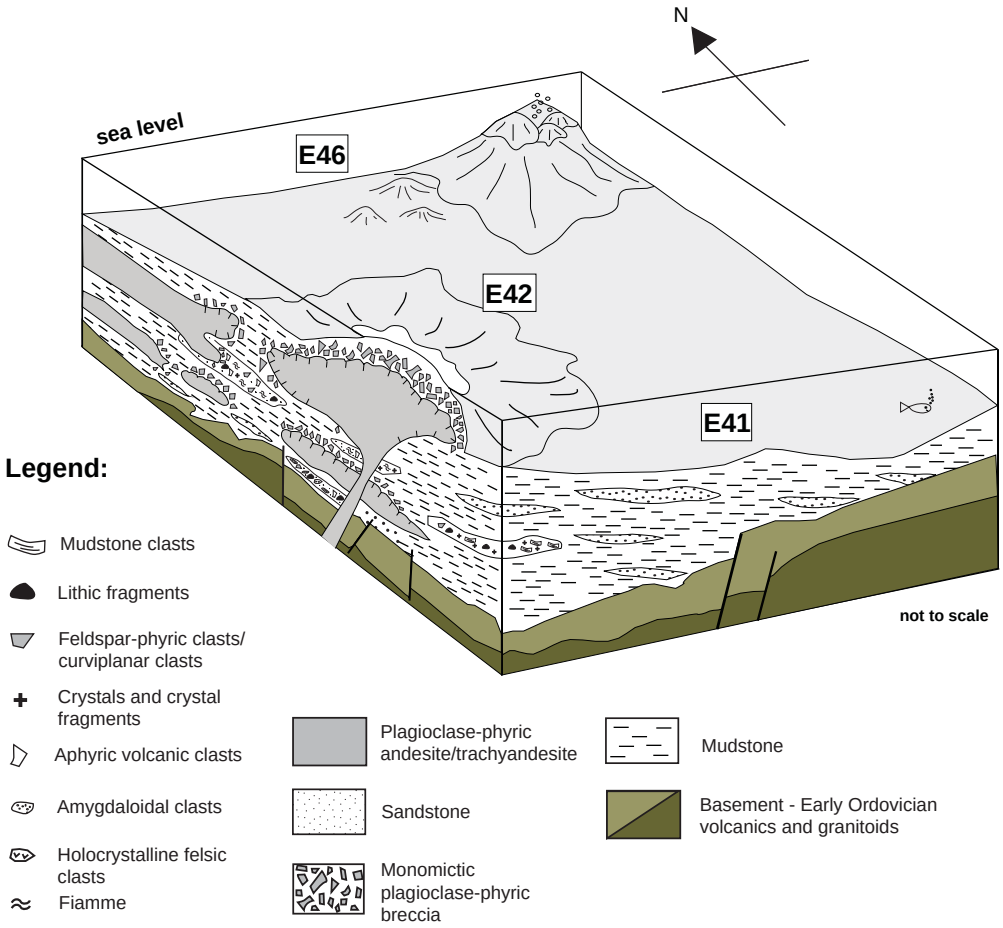

Figure 3.21 Schematic paleogeographic reconstruction and facies architecture of the Cowal subaqueous Early Ordovician volcano-sedimentary succession. E46 and E42 facies were deposited proximal to the volcanic activity whereas E41 formed more distal to the volcanic centre.

with periodic breaks of mudstone sedimentation. Deeper facies of the E42 deposit are mudstone-dominated, and also comprise facies with igneous fragments that may have been derived from erosion of the basement intrusions. E41 and E40 are interpreted to have been more distal to volcanic activity than E42 and E46. The E41 host stratigraphy lacks the plagioclase-phyric coherent units and associated hyaloclastite (either in-situ or reworked) that are common in the northern (E46) and central (E42) part of the Cowal district (e.g. Miles and Brooker, 1998; Cannell, 2003; Simpson and Cooke, 2006). A deep water, quiescent environment with episodic influx of coarser material is therefore inferred for the host succession at E41.

The volcano-sedimentary rocks at Cowal district were deposited in the Early Ordovician, and are correlated with Phase 1 magmatism of the Macquarie Arc (Fig. 3.22). Based on observed stratigraphic relationships, no Phase 4 volcanics were deposited in the Cowal district (Fig. 3.22).

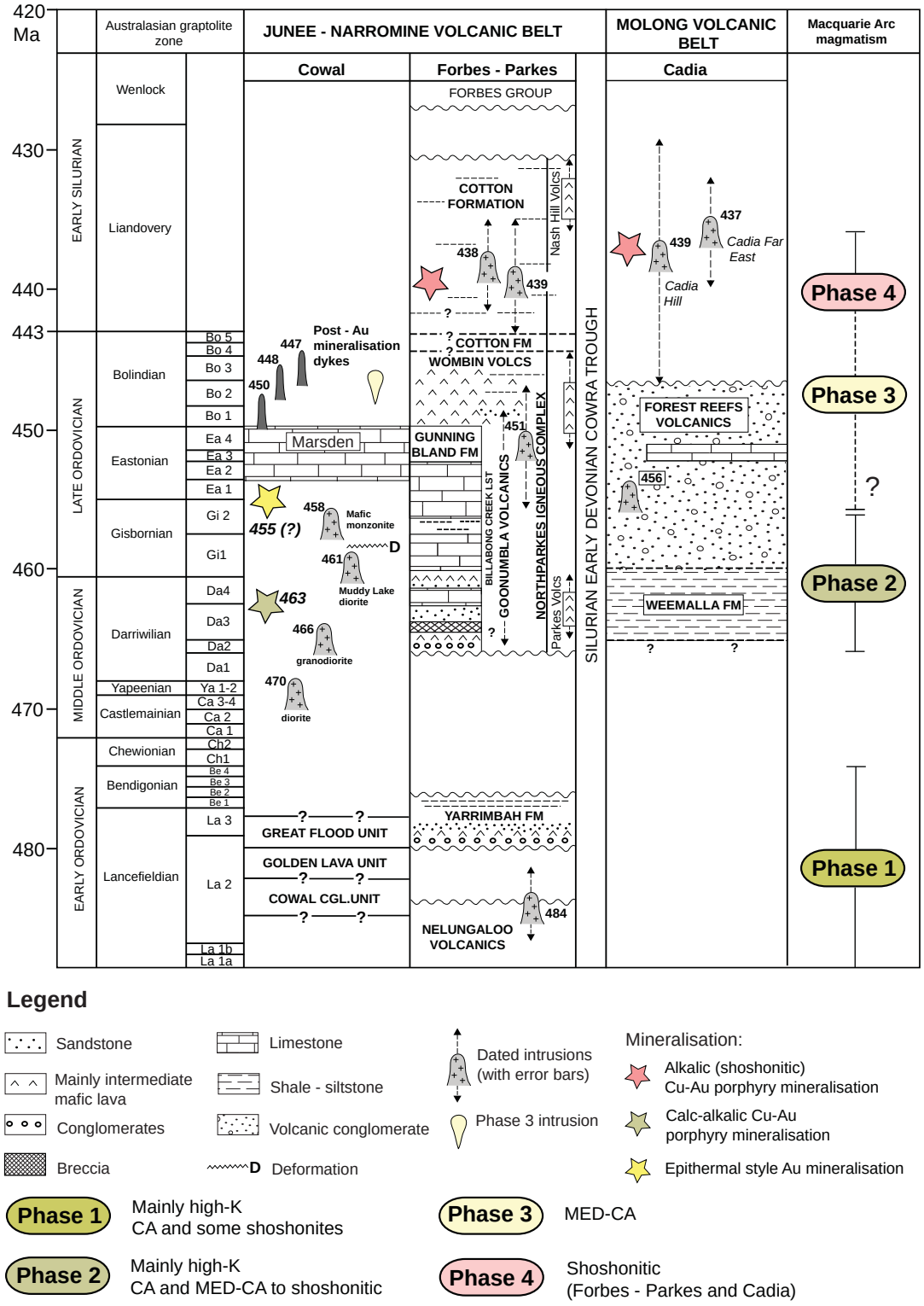

Figure 3.22 Space - time diagram for selected areas of the Junee-Narromine and Molong volcanic belts of the Ordovician Macquarie Arc (compiled from Glen, 1998 and Glen et al., 2007a). Detailed geochronological data for Cowal intrusions are provided in Tables 3.3 and 3.4. Note that Phase 4 magmatism and volcanism is lacking in the Cowal area but the inferred timing of epithermal mineralisation correlates with some early-mineralisation shoshonitic monzonite intrusions at Cadia (~456 Ma; Wilson et al., 2007b). Phase 3 is absent from Northparkes and Cadia districts, it is only marked in the southern part of the CIC.

3.5.2 E41 intrusive sequence and controls on emplacement

Based on recognised compositions of intrusive rocks and their timing relationships at least three discrete pulses of magmatism appear to be recorded at E41. The Muddy Lake diorite and several dyke facies including mafic, variety of plagioclase-phyric and trachyte dykes are considered to be included in the first cycle of magmatism. This early magmatic pulse had a mafic to intermediate character and the rocks produced during that phase experienced all of the hydrothermal events that affected the E41 deposit. The mafic monzonite intrusion, quartz-monzonite and aplite dykelets mark the second major pulse of magmatism that occurred at E41. These monzonitic intrusive units are quartz- and hornblende-bearing and they appear to be temporally related to mineralisation (Table 3.2). Although mafic monzonite has been cut by mineralised veins, the presence of miarolitic cavities in the mafic monzonite provides evidence that the intrusion could have been an important source of volatiles in the early stage of hydrothermal activity. The presence of aplites that have cut altered rocks and are scattered throughout the deposit provide another line of evidence that they could have been sourced from volatile-rich intrusions that underlie the current level of exposed mineralisation at E41. Aplites are common in Cu-Au porphyry systems, they are typically spatially and temporally associated with mineralising intrusions (Sillitoe, 1973). Pyroxene-phyric dykes are inferred to be intruded after the emplacement of quartz-monzonite and aplite dykelets, they post-date quartz – pyrite veins with K-feldspar – epidote alteration halos and pre-date the occurrence of carbonate-base metal sulfide mineralisation stage, indicating their 'inter-mineral' timing of emplacement (Chapter 5; Table 3.2). The occurrence of pyroxene-phyric dykes close in time to monzonitic rocks implies an input of mafic melts into an evolving upper crustal magma chamber at the time of mineralisation. Thus, the second major phase of magmatism at E41 involved mixing and interaction of silicic and mafic melts, which potentially could have contributed to the overall metal-rich volatile budget. The third magmatic pulse at E41 produced a variety of diorite dykes that marked the closure of magmatic activity within the Cowal district. Mineralogical features that characterise these post-mineralisation dykes show that the intrusive sequence of E41 returned to mafic compositions. The magmatic affinity for each intrusive rock is discussed further using whole rock geochemistry data in Chapter 4.

The emplacement of intrusive rocks at E41 was structurally controlled. Pre- and syn- mineralisation north-, northeast and east-trending structures and north- and northwest-trending post-mineralisation structures at E41 seem to have played an important role as loci for intrusive sills, dykes and stocks at E41 and across the district. The Muddy Lake diorite sill and less obviously, the mafic monzonite intrusion, are both elongated along north-trending structural fabrics. North-, northeast- east-, and

northwest-trending structures have also been typically utilised by pre-mineralisation mafic and plagioclase phyric dykes. Some of these structural orientations have controlled mineralised veins as well. If the geometry of the mafic monzonite that sits beneath the east pod is interpreted correctly, it appears that the northeast- and east-trending fractures are localised on the southern edge of the mafic monzonite intrusion. It is interesting to note that quartz-monzonite, aplite and syenite dykelets occur in the vicinity of these fractures (east pod) and it is speculated that although volumetrically minor, these monzonitic and aplitic rocks are indicative of larger monzonitic (?) pipe-like bodies that are probably located at depth, on the fringe or margins of the older mafic monzonite intrusion. Strongly mineralised aplite dykelets also occur in the west pod and are inferred to have been sourced from a larger intrusive body (orebodies?) that cross-cuts the mafic monzonite intrusion at depth. The east- and northeast-trending structures thus appear to have played significant roles in focusing intrusives as well as mineralising fluids at E41. The importance of the northeast-trending structural fabrics is also supported by the magmatic – hydrothermal breccia body at E42, the geometry of which is defined by a northeast-trending strike (Strickland, 2005).

3.5.3 Geochronology

Several conflicting dates are available for the ages of volcanism, intrusive activity and mineralisation in the CIC. Figure 3.23 shows approximate locations of all samples that have been dated. Table 3.3 show compiled geochronological data for the CIC, combined with new results obtained during the alkalic project and as part of this PhD study of E41 (Table 3.4).

Zircon separates that were investigated by Tosdal (2008; Appendix B.3) as part of the alkalic project, show that most of the analysed zircons have complex systematics, indicating a dominance of older xenocrystic zircons in the rocks (Figs. 3.24 and 3.25). The common occurrences of xenocrystic zircons have important implications for the generation of the arc plutonic rocks in an island arc setting. Crawford et al. (2007b) showed that the xenocrystic and inherited zircons in granitoids of the Narromine, Cowal, and Fairholme igneous complexes of the Macquarie Arc were included in the magmas in an upper crustal chamber. Therefore some results presented herein reflect ages of zircons that were most likely incorporated from the basement and/or older wall rocks. In order to visualise the effect of inheritance, Figure 3.25 shows a summary geochronology diagram, in which, apart from the main zircon population, zircons that are characterised by much older ages are also apparent. For example, post-mineralisation diorite dykes contain zircons that are 470 Ma or older and these are interpreted to be inherited from older (basement) rocks. In contrast, there are also

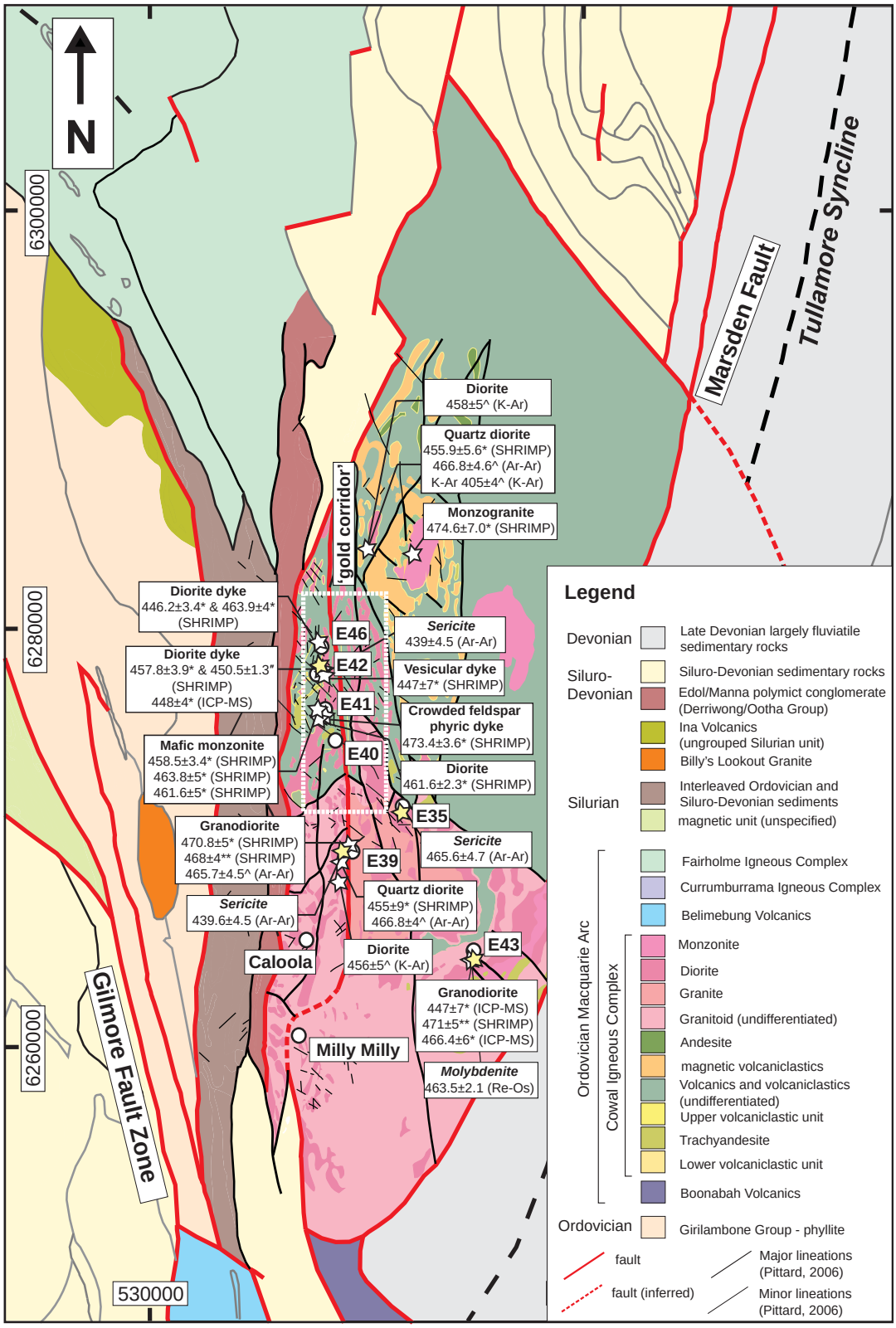

Figure 3.23 Summary geology map (modified from Henry, 2008) of the CIC showing the approximate location of dated samples. Each box lists the analysed rock unit or mineral and methods: *zircon, **titanite, ^hornblende, "monazite. White stars represent dated igneous rock samples, yellow stars indicate dated minerals (written in italic) associated with mineralisation. References for the data are provided in Tables 3.3 and 3.4.

TABLE 3.3 Cowal district geochronology.

Rock unit	Field term	Sample ID	Drill Hole	Depth	Age (Ma)	Method	Mineral	Reference	Inferred Age
Endeavour 46									
plagioclase-phyric diorite porphyry	diorite dyke	E46D3029	D3029	132.2	446.2 ± 4	U/Pb SHRIMP-RG	Zircon	Tosdal (2008)	Post (Au)-mineralisation
quartz-feldspar phyric dacite porphyry	diorite dyke	E46D3029	D3029	208.9	463.9 ± 4	U/Pb SHRIMP-RG	Zircon	Tosdal (2008)	?
Endeavour 42									
hornblende-plagioclase phyric diorite	diorite dyke	E42D1175	D1175	434	457.8 ± 4	U/Pb SHRIMP-RG	Zircon	Tosdal (2008)	Post (Au)-mineralisation
hornblende-plagioclase phyric diorite	diorite dyke	E42D1175	D1175	434	450.5 ± 1.3	U/Pb SHRIMP-RG	Monazite	Tosdal (2008)	Post (Au)-mineralisation
plagioclase-phyric diorite porphyry	diorite dyke	?	?	?	448 ± 4	U-Pb LA-ICPMS	Zircon	Strickland (2005)	Post (Au)-mineralisation
vesicular dyke (basaltic andesite)	vesicular dyke	E4294-0033	?	?	447 ± 7	U/Pb SHRIMP	Zircon	Bastrakov (2000)	Post (Au)-mineralisation
North Cowal									
K-feldspar-quartz phyric monzogranite	monzogranite	LCD12	LCD12	136.4	474.6 ± 7	U/Pb SHRIMP-RG	Zircon	Tosdal (2008)	Pre-syn (Au)? mineralisation
Endeavour 43									
granodiorite	granodiorite	E43_D9	E43_D9	341.5	466. 4 ± 6.2	U-Pb LA-ICPMS	Zircon	this study	Pre Cu-(Au) mineralisation
plagioclase porphyritic diorite	granodiorite	E43H4	H4	159.8	447 ± 11	U-Pb LA-ICPMS	Zircon	Crawford et al. (2007b)	-
plagioclase porphyritic diorite	granodiorite	E43SC	D001	585.25	471 ± 5	U/Pb SHRIMP-RG	Titanite	Tosdal (2008)	-
Endeavour 39									
granodiorite	granodiorite	E39D2	D2	72.05	470.8 ± 5	U/Pb SHRIMP-RG	Zircon	Tosdal (2008)	-
granodiorite	granodiorite	E39D2	D2	72.05	468 ± 4.1	U/Pb SHRIMP-RG	Titanite	Tosdal (2008)	-
granodiorite	granodiorite	E39 93-902	D3	128-138	465.7 ± 4.5 to 439.6 ± 4.5	Ar^{40} - Ar^{39}	Hornblende	Perkins et al. (1995)	-
quartz diorite (E39)		1504/13	1504-AD13	?	455.9 ± 5.6	U-PbSHRIMP	Zircon	Bastrakov (2000)	-
quartz diorite (E39)		1504/13	1504-AD13	?	466.8 ± 4.6	Ar^{40} - Ar^{39}	Hornblende	Bastrakov (2000)	-
Other geochronology data (precise location unknown)									
quartz diorite		1504-GPR24	AD44	?	405 ± 4	K - Ar	Hornblende	Unpub. North Ltd.	-
diorite		1504-GPR24	?	?	458 ± 5	K - Ar	Hornblende	Unpub. North Ltd.	Pre (Au)-mineralisation
Muddy Lake Diorite	diorite	90-176 (in the vicinity of E39)	?	?	456 ± 5	K - Ar	Hornblende	Perkins et al. (1995)	Pre (Au)-mineralisation

Abbreviations: U/Pb SHRIMP/ RG = Uranium lead sensitive high-resolution ion microprobe /– reverse geometry, ICP-MS = Inductively coupled plasma mass spectrometer.

TABLE 3.3 (Cont.)

Mineralisation and alteration Alteration facies/ vein mineralogy/ host rock	Sample ID	Drill Hole	Depth	Age (Ma)	Method	Mineral	Reference	Inferred Age
Endeavour 42								
Quartz – sericite – carbonate alteration	E42 92-211	?	?	439 ± 4.5	Ar^{40}-Ar^{39}	sericite	Perkins et al. (1995)	Syn (Au)-mineralisation
Quartz – sericite – carbonate altered dyke	E42 92-212	?	?	437.6 ± 4.5	Ar^{40}-Ar^{39}	sericite	Perkins et al. (1995)	Syn (Au)-mineralisation
Gold-bearing veins	E42D1178	D1178	257.7	362.7 ± 2.1	Ar^{40}-Ar^{39}	adularia	Henry (2008)	Syn (Au)-mineralisation
Gold-bearing veins	E42RL1155-36	-	155-36	344.5 ± 2.1	Ar^{40}-Ar^{39}	adularia	Henry (2008)	Syn (Au)-mineralisation
Gold-bearing veins	E42RL1155-40	-	155-40	356.3 ± 1.8	Ar^{40}-Ar^{39}	adularia	Henry (2008)	Syn (Au)-mineralisation
Endeavour 43 Volcaniclastic breccia, molybdenite in veins and fractures	E43TB30	DDH-007	348.5	463.5 ± 2.1	Re-Os	molybdenite	Bissig (2008)	Syn (Cu-Au)-mineralisation
Endeavour 35 Quartz altered volcaniclastic rock unit	E35 95-153	?	?	465.6 ± 4.7	Ar^{40}-Ar^{39}	sericite	Bastrakov (2000)	Syn (Cu-Au)-mineralisation
Endeavour 39 Quartz - sericite altered granodiorite	E39 90-172	?	?	439.6 ± 4.5	Ar^{40}-Ar^{39}	sericite	Perkins et al. (1995)	Syn (Cu-Au)-mineralisation

Abbreviations: U/Pb SHRIMP/ RG = Uranium lead sensitive high-resolution ion microprobe /– reverse geometry, ICP-MS = Inductively coupled plasma mass spectrometer.

TABLE 3.4 E41 geochronology.

Rock unit	Sample ID/ DDH	Depth	Age (Ma)	Alternate	Method	Mineral	Reference
Pre-mineralisation intrusives							
Muddy Lake diorite	E41D2614	242-243	461.6 ± 2.3	-	U/Pb SHRIMP-RG	Zircon	Tosdal (2008)
crowded plagioclase-phyric dyke	E41D2131	171.5	473.4 ± 3.6	456±5	U/Pb SHRIMP-RG	Zircon	Tosdal (2008)
mafic monzonite	E41D2180	149.2	458.5 ± 5.2	-	U/Pb SHRIMP-RG	Zircon	Tosdal (2008)
mafic monzonite	E41D2131	283.95	464 ± 5	-	U/Pb SHRIMP-RG	Zircon	Tosdal (2008)
mafic monzonite	E41D2131	300.6	462 ± 5	-	U/Pb SHRIMP-RG	Zircon	Tosdal (2008)
Gold mineralisation							
stage 3B vein	E41D2065	148.9	355.1 ± 1.9	-	Ar^{40} - Ar^{39}	Adularia	this study
stage 3B vein	E41D2065	154.3	349.8 ± 1.9	-	Ar^{40} - Ar^{39}	Adularia	this study
stage 3B vein	E41D2065	148.6	349.8 ± 1.9	-	Ar^{40} - Ar^{39}	Adularia	this study

Abbreviations: U/Pb SHRIMP/ RG = Uranium lead sensitive high-resolution ion microprobe /– reverse geometry.

several zircons that yielded ages younger than 436 Ma (Figs. 3.24 and 3.25). These younger ages were rare and there is no statistical basis for concluding that these rocks are about 440 Ma; thus they are interpreted to reflect Pb loss rather than timing of crystallisation. Geochronological data of the CIC are thus complicated, having been strongly affected by multiple magmatic events that contributed to the growth of the CIC. In order to better understand the timing of magmatism and hydrothermal activity, the integration of absolute ages with well-constrained relative relationships for volcanic and intrusive rocks is presented herein.

The southern part of the CIC contains the E43, E39 and E35 prospects (Fig. 3.23). This appears to have been the focus for the earliest phase of magmatism in the district. Both the E39 and E43 porphyry copper prospects are spatially associated with large, multi-phase granodiorite-plutonic complexes. These porphyry deposits most likely formed at 471 – 465 Ma, based on Re-Os (molybdenite) and $^{206}Pb/^{238}U$ (zircon) ages (Table 3.3; Fig. 3.24). One sample of zircon from the E43 granodiorite returned a much younger age (447 ± 7 Ma; Table 3.3) and may represent a late phase of granodiorite, or alternatively the young age is a product of Pb loss. An additional sample of the intrusive phase that hosts some mineralisation at E43 (Zukowski, 2009) was analysed by the author, returning a $^{206}Pb/^{238}U$ age of 466.4 ± 6.2 Ma (Table 3.3). Re-Os dating of molybdenite from E43 yielded an age of 463.5 ± 2.1 Ma (Bissig et al., 2008). This result indicates that E43 is late Middle Ordovician in age, the oldest known occurrence of porphyry mineralisation in the Macquarie Arc (Fig. 3.22).

There is geochemical evidence (Chapter 4) that the intrusions in the southern part of the district represent a discrete magmatic event, and these intrusive rocks, and spatially and temporally associated porphyry-style mineralisation are genetically

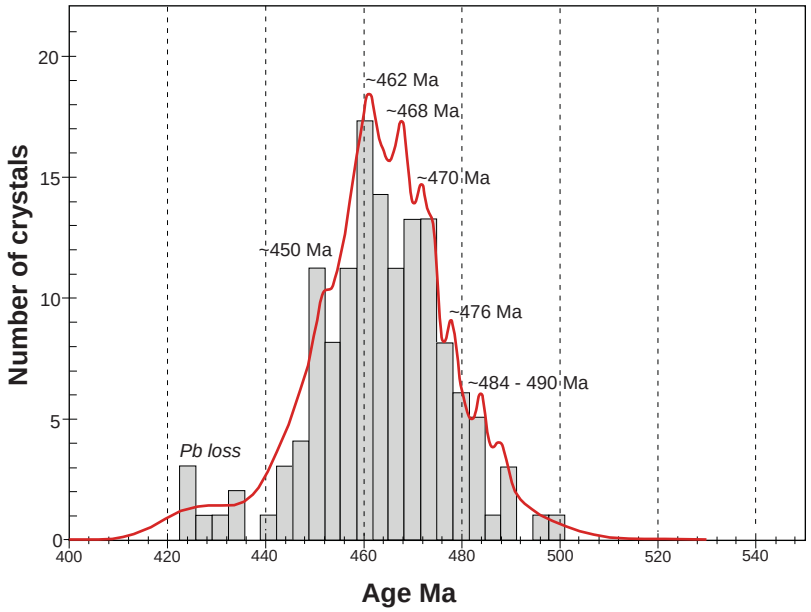

Figure 3.24 Probability density plot of Pb/Pb ages for 138 individual zircons crystals from 10 samples analysed as part of the alkalic project (Tosdal, 2008; Appendix B.3). Histogram shows analyses of both acicular and stubby prismatic crystals as well as analyses from tips and cores of the zircons. Zircon ages of 470 - 462 Ma appear to mark a major magmatic event in the CIC.

unrelated to the younger E41 and E42 gold centers (described below). It appears that the mafic monzonite intrusion at E41 (and E42) marks a second porphyry-like event in the Cowal district that is spatially related to the Cowal epithermal gold centres. A similar relationship of alkalic and calc-alkalic porphyry deposits has been documented from British Columbia, Canada (Wilson et al., 2002).

Several age determinations are available for the Muddy Lake diorite sill that is spatially associated with the E46, E42 and E41 gold deposits. Based on aeromagnetic data and diamond drill holes, the diorite body extends for at least 10 km from the northern part of the district to the south (Fig. 3.23), but its relative timing with respect to the E39 granodiorite pluton and E43 intrusive cluster is uncertain. A $^{206}Pb/^{238}U$ SHRIMP age of 455.9 ± 5.6 Ma and Ar^{40}-Ar^{39} age of 466.8 ± 1.5 Ma were reported by Bastrakov (2000) for 'quartz diorite' from drillhole 1504/13 (EL 1504). Perkins et al. (1995) reported a hornblende K-Ar age of 465.7 ± 4.5 Ma for the diorite. Based on these data, Crawford et al. (2007b) concluded that the diorite intruded between 465 and 456 Ma. The diorite has been overprinted by epithermal-style mineralisation from which associated sericite has been dated at 439 ± 4.5 Ma (Perkins et al., 1995; Table 3.3). This sericite age is considerably younger than the E43 molybdenite age, but is consistent with the age of alkalic mineralisation at Northparkes and Cadia (Lickfold et al., 2003; Wilson, 2003; Wilson et al., 2007b).

In order to resolve the age of gold mineralisation at CIC, and also to help constrain the history of magmatism in the CIC, several samples of late- and post-

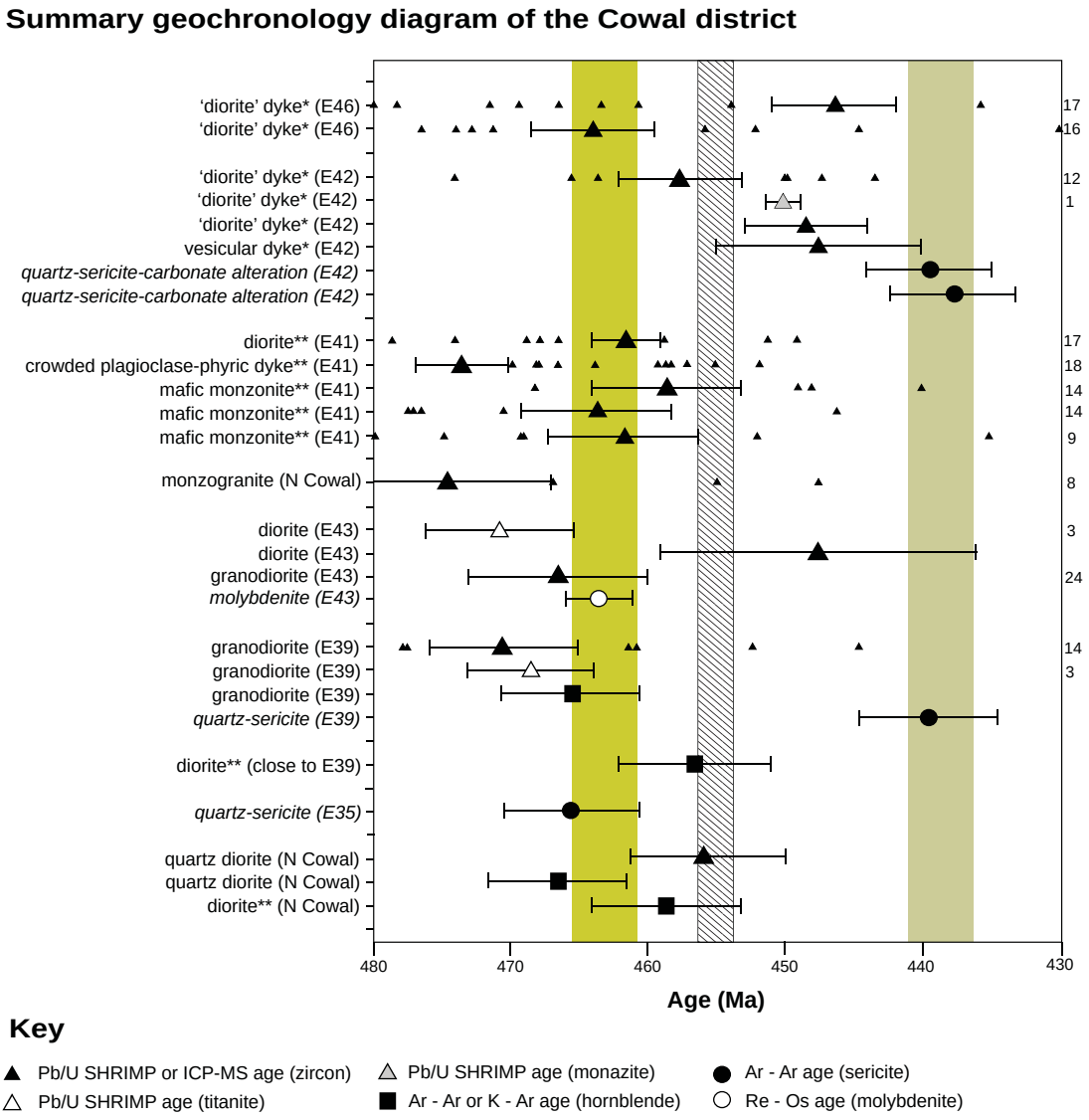

Figure 3.25 Summary geochronological data for samples from the Cowal district (data summarised in Tables 3.3 and 3.4). The brown yellow bar represents the approximate age range of late Middle Ordovician Cu-Au porphyry mineralisation at E43. The pale brown bar represents approximate Early Silurian age of epithermal mineralisation in the Cowal district based on sericite dates from E42 deposit. Cross hatched bar indicates inferred approximate timing of epithermal gold mineralisation at E41 and E42 and E46. Small triangles show zircon outliners plotted for samples analysed as part of the alkalic project. Used key: * inferred post-mineralisation timing of an intrusive unit, ** inferred pre-mineralisation timing of an intrusive unit, minerals in italics represent dated sulfide or alteration minerals associated with mineralisation. The numbers to the right of the diagram indicate number of analysed zircon or titanite grains.

mineralisation dykes suites were subjected to geochronological study (Bastrakov, 2000; Strickland, 2005; Tosdal, 2008).

The plagioclase-phyric 'diorite' dyke that crosscuts the E46 and E42 stratigraphy is interpreted to post-date gold mineralisation because it contains no sulfides or alteration assemblages associated with mineralisation (Strickland, 2005; Simpson and Cooke, 2006; Table 3.2). This dyke yielded $^{206}Pb/^{238}U$ SHRIMP ages of 446.2 ± 4, 463.9 ± 4 Ma (E46) and 457.8 ± 3.9 and 450.5 ± 1.3 Ma (E42; Tosdal, 2008). ICP-MS

analysis of 12 zircons returned an age of 448 ± 4 Ma from the same unit (Strickland, 2005). Thus the five ages available for this particular intrusive unit range from 463.9 ± 4 to 446.2 ± 4 Ma (Fig. 3.22).

A post-mineralisation vesicular dyke (amygdaloidal dyke; this study) cuts gold-bearing veins at E42 (Henry, 2008) and at E41 (Table 3.2). This unit was dated by Bastrakov (2000) and returned an age of 447 ± 7 Ma.

The data from the post-mineralisation dykes have not proven to be reproducible and it is difficult to interpret these ambiguous results. The 450.5 ± 1.3 and 446.2 ± 4 Ma for plagioclase-phyric 'diorite' dyke and 447 ± 7 Ma for the vesicular dyke are consistent with geological observations that they cut the Muddy Lake diorite and the mineralisation (Bastrakov, 2000; Strickland, 2005; Table 3.2). It is most likely thus that the final phases of magmatic activity in the CIC occurred at 450 – 446 Ma based on these results (Fig. 3.25). This timing for the cessation of magmatism pre-dates, however, the 440 Ma sericite alteration ages of Perkins et al. (1995), which is problematic. Whether the post-mineralisation dyke ages are from inherited zircons, or whether the sericite ages have been reset, remains unclear. The consistent time bracket (450 – 446 Ma) defined by post-mineralisation dykes from two separate mineral centres (E42 and E46) is concluded here to mark the end of magmatic activity at Cowal.

A sample of K-feldspar + quartz-phyric monzogranite from the northern part of the Cowal district (Fig. 3.23) yielded a $^{206}Pb/^{238}U$ SHRIMP age (zircon) of 474.6 ± 7 Ma (Tosdal, 2008). Crawford et al. (2007b) showed that this rock have similar magmatic affinity to Northparkes intrusive rocks, which were intruded at ~ 440 Ma (Perkins et al., 1990). Earlier magmatic activity occurred in the northern portions of the CIC at ~470 Ma, or dated zircons were inherited from Early Ordovician basement rocks.

Five new $^{206}Pb/^{238}U$ SHRIMP-RG age determinations have been obtained for magmatic zircons from E41 intrusive rocks (Tosdal, 2008; Table 3.3). The samples were chosen for SHRIMP-RG analysis to provide pre- and syn-mineralisation timings, in an attempt to determine absolute age relationships between intrusive rocks and mineralisation. Two intrusive units, the pyroxene-phyric dyke and quartz-monzonite dykelets (Fig. 3.15), were of particular interest for this study as they are inferred to be temporally related to gold mineralisation based on cross-cutting and overprinting relationships. Additionally, brick red-coloured quartz-monzonite dykelets that are scattered throughout the E41 deposit resemble early- and syn-mineralisation monzonite of Cadia and Northparkes intrusive centres, and were also search for zircons. Unfortunately, neither the pyroxene-phyric dykes nor the quartz-monzonite dykelets contained enough zircons for analysis, and consequently the absolute ages of these units remains undetermined.

At E41, the Muddy Lake diorite dips at ~45° to the south and has been cut by many subvertical dykes and by subvertical mafic monzonite intrusion, implying tilting after diorite emplacement. Zircons form three samples of mafic monzonite were subjected to $^{206}Pb/^{238}U$ SHRIMP-RG analysis, returning ages of 458.5 ± 5.2 Ma, 464 ± 5 and 462 ± 5 Ma (Fig. 3.25; Tosdal, 2008). The 464 ± 5 and 462 ± 5 Ma ages are at odds with previously determined ages of the Muddy Lake diorite (Perkins et al., 1995), as they indicate that the mafic monzonite occurred prior to the diorite. Only Tosdal's (2008) zircon ages (461.6 ± 2.3 Ma) for the Muddy Lake diorite and the mafic monzonite (458.5 ± 5.2 Ma) are consistent with the relative ages of these two intrusive phases. It is therefore concluded that the diorite most likely intruded at 461.6 ± 2.3 Ma and the mafic monzonite at 458.5 ± 3.4 Ma, based on zircon data. The Muddy Lake diorite was intruded by a series of dykes prior to the mafic monzonite intrusion. It is therefore concluded that the plagioclase-phyric dykes, blocky-plagioclase-phyric coherent unit ('Robin's lode') and mafic dykes were emplaced between 461.6 and 458 m.y. The $^{206}Pb/^{238}U$ SHRIMP age of 473.4 ± 3.6 Ma for the pre-mineralisation crowded plagioclase-phyric dyke (Tosdal, 2008) remains problematic. Although this age is consistent with a pre-mineralisation timing, it is older than the Muddy Lake diorite. Because the crowded plagioclase-phyric dyke cuts the diorite (DDH: E41D2139) this age cannot be the age of the crowded plagioclase-phyric dyke. The age is interpreted here to be related to zircons inherited from the Early Ordovician volcanic stratigraphy.

An attempt to date the mineralisation was made using adularia crystals from stage 3B gold-bearing veins at E41 (Chapter 5), which were dated using ^{40}Ar-^{39}Ar methods. Results are presented in Table 3.4 and included in Appendix B.3. All analysed samples (Table 3.4) yielded plateau ages of 355.1 ± 1.9 and two ages of 349.8 ± 1.9 Ma. These ages are much younger than the sericite ages from Perkins et al. (1995). They most likely indicate a post-mineralisation thermal event (300 – 150°C) that affected the E41 deposit, resetting the argon isotopic system in adularia. Similar ages were obtained by Henry (2008; Table 3.3) from gold- and adularia-bearing veins from E42. These ages are consistent with the youngest orogenic event to affect the district – the Kanimblan deformation ca. 380 – 320 Ma.

3.6 Summary

Several important conclusions can be drawn from geological observations and geochronological data of the CIC:

- The host stratigraphy at E41 mostly consists of mudstone with local intercalation of sandstone and rare polymictic volcanic breccias. The volcano-sedimentary

sequence is interpreted to be deposited in subaqueous environment distal to a volcanic centre. Proximal volcanic facies are observed at E42 and E46.

- The volcano-sedimentary succession is interpreted to have an early Middle Ordovician timing, and is correlated with Phase 1 magmatism and volcanic activity of the Macquarie Arc (Fig. 3.22).
- During the early Darriwilian (ca. 465 Ma; Fig. 3.22) most of the intrusive rocks of the southern part of the CIC were emplaced. These monzogabbro – monzodiorite suites (Crawford et al., 2007b) appear to be spatially and temporally related to Cu-Au porphyry mineralisation at E43 and E39.
- Absolute age estimates indicate that the Muddy Lake diorite intruded at about 461 Ma. After the emplacement of Muddy Lake diorite, the stratigraphy of the Cowal district was tilted, probably during early Late Ordovician (Fig. 3.22). Following the tilting event, the mafic monzonite intrusion was emplaced at 458 Ma. The Late Darriwilian to Gisbornian timing of Muddy Lake diorite, mafic monzonite and several dykes correspond to Phase 2 magmatism of the Macquarie Arc (Fig. 3.22).
- Monzonites and pyroxene-phyric dykes appear to be temporally and spatially related to gold mineralisation at E41.
- Hornblende – quartz diorite dykes were emplaced during the Bolindian – late Eastonian (ca. 456 – 445 Ma), after mineralisation at E41, E42 and E46. These intrusions marked the cessation of magmatic activity in the CIC.
- It appears that two discrete phases of mineralisation occurred in the CIC: (1) porphyry-style mineralisation in the late Middle Ordovician at E43, E39 (463.5 ± 2.1 Ma), and (2) gold mineralisation in the early Late Ordovician (around 455 Ma) at E46, E42, E41 and E40.

CHAPTER 4
Igneous Geochemistry

4.1 Introduction

Multiphase intrusive activity characterised the Cowal Igneous Complex. Some of the intrusions, although volumetrically minor, are believed to be temporally associated with gold mineralisation. This chapter presents and discusses implications of the whole rock geochemical analyses of least-altered intrusive rocks from E41. These data are used to constrain their compositions and their tectonic setting of emplacement, and to compare with suites of igneous rocks from other Ordovician mineralised districts of NSW. This comparison is used to evaluate whether gold mineralisation at E41 was associated with alkalic magmatism, and whether Cowal has potential for Northparkes- or Cadia- type porphyry copper-gold mineralisation (e.g., Blevin et al., 2002; Holliday et al., 2002; Wilson, 2003; Lickfold et al., 2007).

4.2 Sampling and methodology

A total of 49 intrusive rocks from the E41 deposit were analysed for their major and trace element compositions. This dataset excludes three samples of Crawford et al. (2007b; diorite, cumulate plagioclase wehrlite, and olivine-bearing gabbro) because their sample locations and geological contexts are unknown.

Sampling targeted the least-altered and unweathered intrusive rocks. To allow the geochemical evolution of the intrusive suites to be evaluated, sampling was conducted within the framework of the intrusive history presented in Chapter 3. Representative least-altered samples of each intrusive rock were collected from drill holes shown in Figure 4.1.

All samples were prepared and analysed at CODES, University of Tasmania under the direction of Mr. Phil Robinson in the School of Earth Sciences. Samples were initially crushed using a steel jaw hydraulic crusher to obtain gravel-size fragments. Samples were then ground in a tungsten carbide ring mill for approximately two minutes to produce a rock powder of less than 200 μm. The mill was cleaned with one pass of high purity quartz between each sample run. Approximately 1 gram of each sample was heated, initially at 500ºC for 4 hours and then at 1000ºC overnight. Loss on ignition (LOI) was determined by weighing the samples before and after ignition. Major elements where determined as oxides: SiO_2, TiO_2, Al_2O_3, Fe_2O_3, MnO, MgO,

Whole rock geochemistry - sample locations

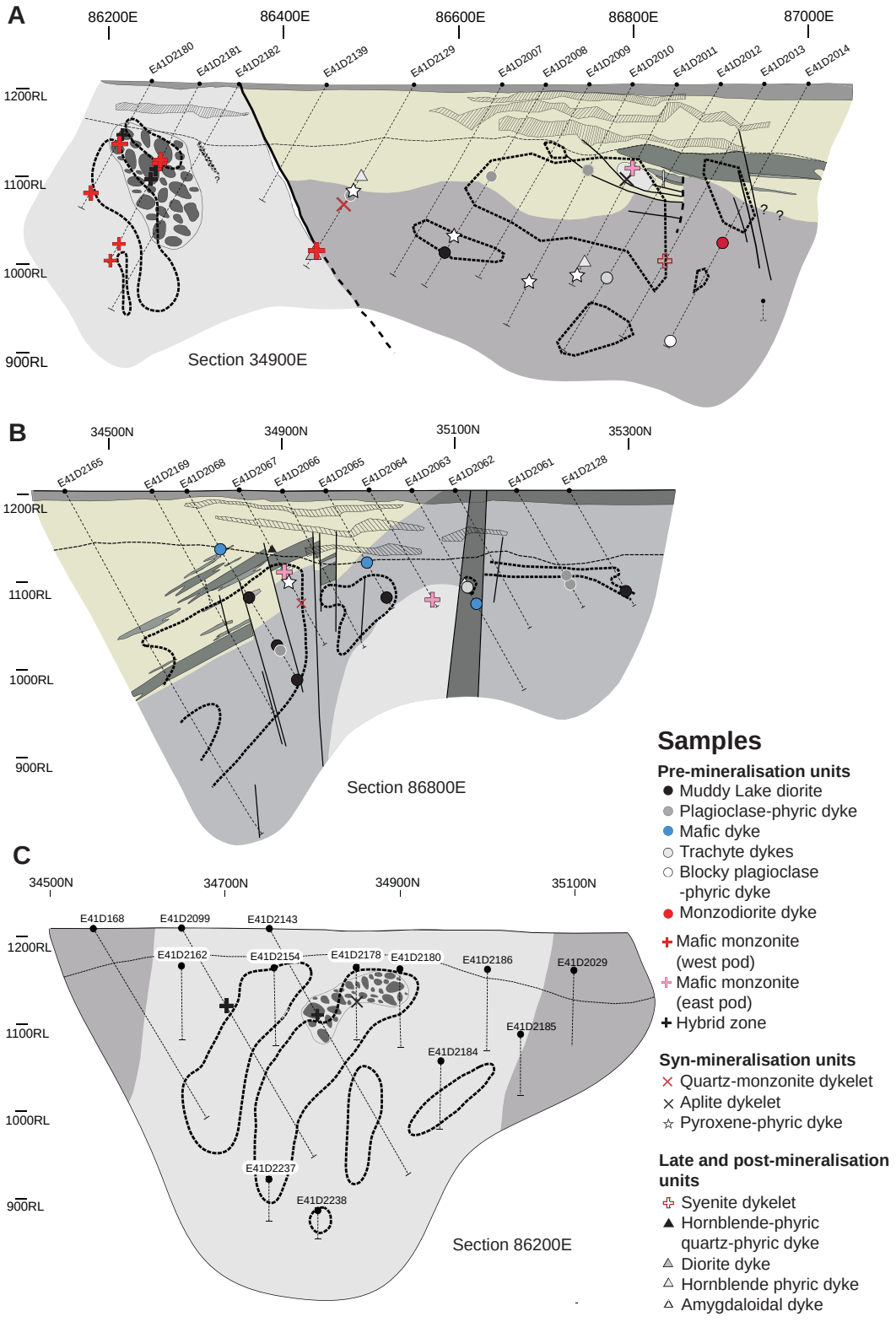

Figure 4.1 Geology of the E41 deposit, showing the location of whole rock geochemical samples. The legend for the rock units and gold grade contours are provided in Figure 3.2. RL=relative level.

CaO, Na_2O, K_2O, P_2O_5 and S using fused disks. Trace elements Nb, Zr, Sr, Cr, Ba, V, La, Y, Rb, U, Th, Pb, As, Bi, Zn, Cu, Ag, Ni and Se were determined using pressed powder pills. Both major and trace elements were analysed using Phillips PW 1480 X-ray Fluorescence Spectrometer (XRF), using standard procedures outlined by Norrish and Chappell (1977) and Robinson et al. (2003). Sample standards were run every 6 to 10 samples to ensure analytical precision. Several splits of the pulverised samples (n=14) were dissolved by the PicoTrace high-pressure HF/H_2SO_4 digestion procedure (Yu et al., 2001), and the solution analysed for trace and rare-earth elements (REE) by inductively-coupled plasma mass spectrometer (ICP-MS) using an Agilent 4500 ICP-MS. The geochemical data obtained in this study are presented in Appendix C.1. Only selected analyses are listed in Table 4.1.

4.3 Hydrothermal alteration effects

Despite every effort to select least altered samples, all samples analysed in this study show at least a moderate degree of hydrothermal alteration. Pre-mineralisation units (e.g., Muddy Lake diorite and mafic monzonite) were collected from the fringes and/or deeper parts of the deposit, away from the mineralised domains, but these samples have been affected by pre-mineralisation Na-Ca-K-bearing alteration facies (Chapters 3 and 5; Table 3.2). Pre-mineralisation dykes are typically spatially associated with faults and host mineralised fractures (Fig. 4.1), whereas syn-mineralisation dykelets commonly occur proximal to mineralised centres (Fig. 4.1), and all these units are typified by multiple pre, syn- to post-mineralisation Ca-K-Na-Mg±P-bearing alteration facies (Chapters 3 and 5; Table 3.2). Mobility of these elements may have strongly affected the major element compositions of analysed rock units. Trace elements such as Ba, Rb and Sr might have also been affected, given their geochemical affinities with K and Ca, respectively. The effects of hydrothermal alteration thus must be assessed prior to using the whole rock data for geochemical classification. To this end, a combination of petrography and bivariate plots has been used to screen all analysed rocks.

The degree of alteration is reflected in part by the loss on ignition (LOI) data. The higher the LOI value, the stronger the effects of hydrothermal alteration. A first approach to evaluate the effects of alteration was to compare the plots of the samples on the mobile-element total alkali-silica diagram (Le Maitre, 1989), and on the immobile-element Zr/TiO_2 versus Nb/Y diagram (Winchester and Floyd, 1977) relative to the loss on ignition (LOI). The total alkali-silica diagram shows a general broad linear trend illustrated by the grey field (Fig. 4.2A). Only a few samples with high LOI (>4 %) appear to deviate from this compositional trend, suggesting that limited secondary remobilisation of the alkali elements occurred at E41.

Although major elements can be mobilised during hydrothermal alteration, some trace elements, including Ti, Zr, Y, Nb and REE, are generally considered to be 'immobile' in low grade hydrothermal and metamorphic environments (Floyd and Winchester, 1975). If bivariate trace element plots for a suite of co-genetic altered rocks show a linear trend that passes through the origin, the elements can be considered immobile. Once immobility has been confirmed, the Zr/TiO_2 and Nb/Y plot can be used to discriminate magma type (Floyd and Winchester, 1975). LOI values for all analysed samples plotted on a Zr/TiO_2 versus Nb/Y diagram again form a roughly linear trend (dark grey field; Fig. 4.2B). Only two samples deviate from this general trend (indicated by lighter grey field on Fig. 4.2B); the aplite dykelet (E41D2011, 121.4 m) and the hornblende-phyric dyke (E41D2129, 123.9 m). Petrographically and in hand specimen these samples appear to be relatively weakly altered and their geochemical analyses are considered to be reliable.

Another screening approach used to assess the effects of hydrothermal alteration involved plotting the mobile large-ion lithophile elements (LILE) against immobile high-field strength lithophile element (HFSE). Since Ba behaves similarly

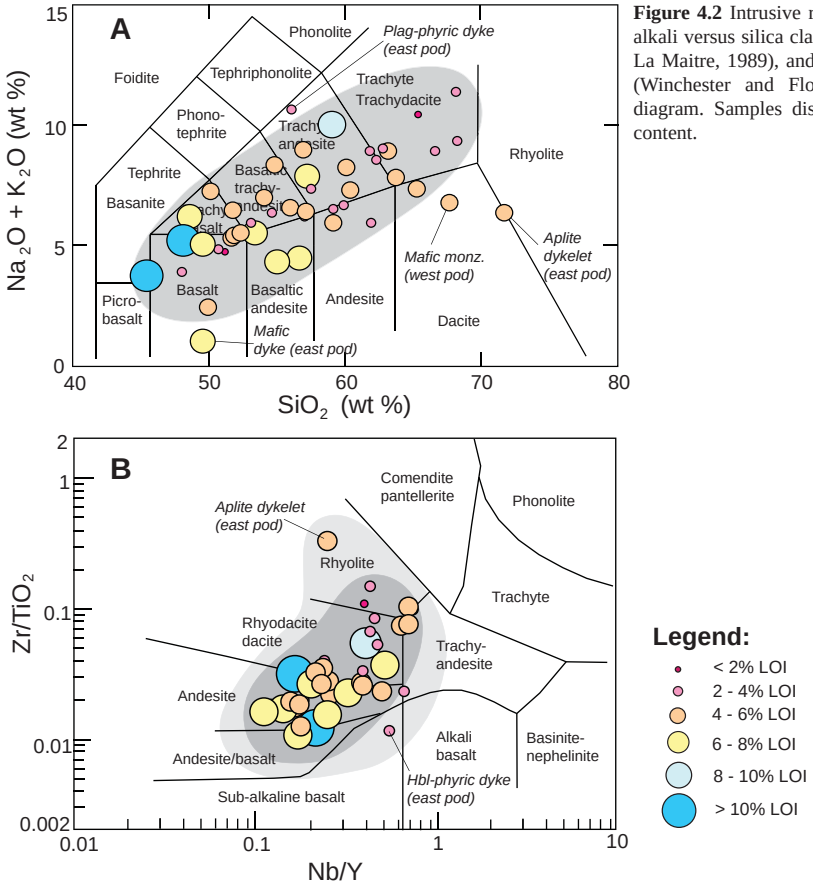

Figure 4.2 Intrusive rocks from E41: (A) total alkali versus silica classification diagram (TAS, La Maitre, 1989), and (B) Nb/Y versus Zr/TiO_2 (Winchester and Floyd, 1977) classification diagram. Samples discriminated by their LOI content.

TABLE 4.1 Selected whole rock major, trace (XRF) and rare earth (solution LA-ICPMS) element analyses of intrusive rocks from E41.

	Sample ID-DDH	E41D2181, 104.8	E41D2180, 148.8	E41D2181, 222.9	E41D2180, 82.8	E41D2181, 102.4	E41D2064, 141.2-3	E41D2011, 107.0	E41D2180, 73.6	E41D2181, 125.2	E41D2181, 110.9	E41D2143, 117.5-6	E41D2099, 96.2	E41D2067, 147.8	E41D2011, 121.4	E41D2178, 99.1-2	E41D2013, 237.3	E41D2010, 256.6
	Lithology	Mafic monzonite	Mafic monzonite	Mafic monzonite	Mafic monzonite	Mafic monzonite	Mafic monzonite	Mafic monzonite	Monzodioritic enclave -hybrid zone	Monzodioritic enclave -hybrid zone	Monzodioritic enclave -hybrid zone	Megacrystic monzodioritic enclave -hybrid zone	Megacrystic monzodioritic enclave -hybrid zone	Quartz monzonite dykelet	Aplite dykelet	Aplite dykelet	Syenite dykelet	Pyroxene-phyric dyke
Major elements#*	SiO_2	67.66	63.11	62.26	66.60	68.27	60.11	57.15	65.27	63.71	56.64	57.54	55.97	60.40	71.67	59.06	68.14	53.10
	TiO_2	0.42	0.64	0.66	0.44	0.44	0.69	0.55	0.49	0.53	0.64	0.71	0.56	0.66	0.09	0.32	0.28	0.79
	Al_2O_3	14.48	16.20	16.83	15.16	15.07	16.58	19.24	14.62	15.64	17.86	17.76	19.67	15.13	11.71	15.26	14.57	14.27
	Fe_2O_3	4.87	5.71	5.96	4.56	3.56	7.13	8.01	6.74	7.04	13.01	8.18	9.10	6.58	2.40	11.36	2.32	10.26
	FeO(t)	4.39	5.14	5.36	4.11	3.20	6.41	7.21	6.07	6.34	11.71	7.36	8.19	5.92	2.16	10.22	2.09	9.24
	MnO	0.07	0.09	0.09	0.07	0.04	0.14	0.15	0.09	0.10	0.10	0.16	0.14	0.12	0.05	0.04	0.04	0.23
	MgO	1.28	1.58	1.76	1.67	1.33	1.80	2.25	1.76	2.17	4.83	3.58	2.49	2.64	0.41	0.46	0.62	6.75
	CaO	4.26	3.41	3.56	2.39	1.80	4.87	5.97	3.45	2.76	2.21	4.37	5.30	6.75	7.25	3.33	2.59	8.78
	Na_2O	1.65	2.27	4.25	3.41	3.32	5.51	4.53	2.86	2.83	0.75	3.96	2.56	3.52	3.31	1.19	1.09	2.37
	K_2O	5.13	6.62	4.26	5.51	5.99	2.73	1.90	4.50	5.00	3.75	3.40	4.00	3.77	3.05	8.81	10.27	3.09
	P_2O_5	0.17	0.37	0.37	0.20	0.17	0.44	0.26	0.21	0.23	0.21	0.34	0.23	0.43	0.04	0.17	0.08	0.34
	Total	100.00	100.00	100.00	100.00	100.00	100.00	100.00	100.00	100.00	100.00	100.00	100.00	100.00	100.00	100.00	100.00	100.00
	Loss inc S-	4.53	4.98	3.66	3.51	2.45	4.90	4.53	4.02	5.18	6.74	3.67	4.12	4.74	4.57	8.05	2.03	4.21
	Total-raw data	99.55	99.87	99.82	99.91	99.66	99.74	99.65	99.80	99.78	99.54	100.12	99.60	99.54	99.68	98.92	99.71	99.98
	S	0.93	1.22	0.50	0.28	0.71	0.18	0.98	0.41	0.58	2.21	0.20	1.29	0.62	0.21	7.93	0.38	0.05
	Y	19.50	22.20	25.10	17.90	21.30	24.60	17.50	18.80	20.00	17.00	24.20	17.60	21.40	16.20	13.65	18.90	18.30
	U	5.10	2.70	3.20	4.70	6.10	<1.5	<1.5	5.00	5.10	2.60	2.20	1.95	1.90	2.35	<1.5	5.40	<1.5
	Rb	83.70	103.50	64.90	68.40	77.10	29.80	24.70	59.90	69.50	97.90	57.00	88.15	30.20	22.35	137.55	103.55	40.40
	Th	8.93	5.80	5.51	7.70	8.84	6.30	1.60	8.84	8.90	5.50	4.80	2.35	4.00	2.40	3.15	10.50	3.00
	Pb	6.95	32.02	3.64	5.42	4.21	3.69	3.64	7.54	7.90	5.82	2.39	5.02	5.91	2.47	10.39	1.99	1.98
	As	26.75	234.80	28.52	33.42	38.51	9.30	24.80	24.60	30.00	32.30	39.90	67.40	110.50	38.70	41.50	14.20	24.00
	Bi	<2		<2	<2	<2			<2									
Trace elements**	Zn	46.30	128.00	71.90	85.40	29.20	54.60	65.10	95.30	67.70	379.50	67.90	91.90	70.80	9.75	14.30	12.50	90.30
	Cu	132.90	176.70	42.00	67.20	187.20	94.73	27.68	78.40	119.72	475.18	131.30	285.70	217.14	60.85	44.45	40.50	21.80
	Ni	4.00	1.70	2.50	5.10	4.30	3.30	2.10	5.20	6.60	28.60	13.05	15.75	6.70	4.55	4.00	3.60	39.00
	Nb	13.40	10.89	10.70	13.00	14.30	5.70	4.40	11.80	13.60	8.70	9.40	6.70	4.30	4.00	5.50	8.00	4.70
	Zr	261.20	90.40	263.70	254.70	252.70	146.14	90.25	216.60	242.29	140.35	139.60	89.70	123.78	189.00	103.10	247.90	105.40
	Sr	166.73	156.38	183.31	124.82	159.49	368.80	531.70	166.53	214.20	60.00	470.80	467.30	752.60	744.80	105.00	358.10	438.30
	Cr	9.50	3.59	3.10	8.20	8.70	2.90	2.60	11.80	12.40	144.00	27.30	40.40	1.70	6.60	3.60	1.30	284.50
	Ba	416.30	550.30	608.30	450.00	580.70	601.20	311.30	761.40	602.00	93.10	416.10	401.90	454.20	554.20	1224.70	764.40	445.50
	Sc	9.70	12.91	15.10	10.40	9.00	17.78	9.46	11.50	11.75	29.74	23.70	20.30	18.41	3.50	10.20	3.90	35.30
	V	64.94	92.99	100.39	83.33	66.96	125.30	116.10	102.92	123.10	243.70	216.00	203.70	178.50	52.70	43.70	25.60	232.90
	La	27.66	24.62	25.27	25.79	30.26	22.41	4.17	30.99	26.77	19.89	23.40	15.90	27.26	13.60	21.10	26.80	26.40
	Ce	55.43	57.84	47.50	46.56	59.80	54.70	21.10	60.58	58.60	42.80	53.90	37.40	63.80	29.10	46.80	61.10	58.90
	Nd	26.69	25.57	26.49	21.74	26.39	32.30	10.77	28.31	26.58	20.86	28.40	18.70	31.82	11.60	20.50	28.60	34.10
REE**	^{139} La		25.86				25.21	28.47			20.69	24.85	17.12	30.53	15.35	17.85	30.13	27.65
	^{140} Ce		53.52				51.29	53.43			41.62	51.75	34.60	53.25	26.15	39.50	59.20	59.89
	^{141} Pr		6.88				7.12	6.57			5.19	6.69	4.45	7.09	3.01	4.92	7.20	8.09
	^{146} Nd		28.49				31.26	25.91			20.63	27.71	18.39	31.73	11.30	19.21	27.09	34.29
	^{147} Sm		5.62				6.52	4.75			3.96	5.61	3.79	6.31	1.89	3.42	4.90	6.37
	^{151} Eu		1.14				1.74	0.85			0.76	1.14	1.70	1.83	0.55	0.95	1.05	1.77
	^{157} Gd		4.69				5.74	3.95			3.22	4.74	3.28	5.36	1.65	2.68	3.89	4.95
	^{159} Tb		0.69				0.84	0.62			0.52	0.72	0.51	0.76	0.30	0.39	0.58	0.67
	^{163} Dy		3.99				4.69	3.59			3.13	4.27	3.00	4.07	2.07	2.27	3.24	3.58
	^{165} Ho		0.81				0.93	0.75			0.66	0.85	0.61	0.78	0.51	0.46	0.65	0.67
	^{166} Er		2.33				2.64	2.35			2.06	2.58	1.81	2.29	1.87	1.42	2.03	1.88
	^{169} Tm		0.36				0.39	0.37			0.31	0.38	0.27	0.34	0.34	0.22	0.32	0.27
	^{172} Yb		2.31				2.56	2.56			2.14	2.54	1.75	2.19	2.60	1.56	2.15	1.75
	^{178} Hf		3.05				3.76	7.22			4.00	4.05	2.42	3.20	4.48	2.67	6.64	2.83
	^{175} Lu		0.35				0.40	0.42			0.33	0.41	0.27	0.35	0.46	0.26	0.36	0.27
	^{181} Ta		1.11				0.49	1.17			0.96	0.70	0.53	0.43	0.69	0.54	0.65	0.36
	^{205} Tl		0.32				0.08	0.28			0.30	0.23	0.33	0.12	<0.1	0.61	0.35	0.21
	Na_2O-2	-0.35	0.27	2.25	1.41	1.32	3.51	2.53	0.86	0.83	-1.25	1.96	0.56	1.52	1.31	-0.81	-0.91	0.37
	Na_2O+K_2O	6.78	8.88	8.52	8.92	9.31	8.24	6.43	7.36	7.83	4.50	7.36	6.55	7.29	6.36	9.99	11.36	5.46
	K_2O/Na_2O	3.10	2.92	1.00	1.61	1.80	0.50	0.42	1.57	1.76	4.99	0.86	1.56	1.07	0.92	7.41	9.47	1.30
	Zr/Y	13.39	4.07	10.51	14.23	11.86	5.94	5.16	11.52	12.11	8.26	5.77	5.10	5.78	11.67	7.55	13.12	5.76
	Ce/Yb		25.08				21.33	8.23			20.03	21.23	21.41	29.14	11.17	30.03	28.43	33.68
	Ta/Yb		0.48				0.19	0.46			0.45	0.28	0.31	0.20	0.26	0.34	0.30	0.21

Major elements normalized to 100 percent on a volatile free basis
* Major element analyses and S reported as weight percent
**Trace element and REE analyses reported as ppm

to K, the LOI versus Ba diagram also shows the effect of K-metasomatism (Fig. 4.3A). Regardless of the rock type, most samples cluster on the LOI vs Ba diagram. Four samples deviate from this cluster: the trachyte dyke, aplite dykelet and two plagioclase-phyric dyke samples. The latter appear to have been significantly enriched in Ba, most likely reflecting strong phyllic alteration. The aplite dykelet has elevated Ba (1225 ppm) compared to another aplite sample (Ba=554 ppm). The sample with elevated Ba is interpreted with caution, as it is not clear whether the high Ba concentration resulted from alteration, or is indicative of the primary Ba content substituted into feldspar.

As indicated on Figure 4.3B, Zr has not been hydrothermally affected in most of the samples and the variations in Zr values reflect fractionation across the intrusive sequence (described below). Plots of Zr versus HFSE (Ti, Nb, Y; Fig. 4.3C-H) display two broadly coherent trends indicated by the green and white fields. The white field contains mafic monzonite samples (average SiO_2 = 62 wt. %) and other rock units that are inferred to be broadly co-genetic with the mafic monzonite. The green field highlights the Muddy Lake diorite (average SiO_2 =52 wt. %) and its co-genetic and/or compositionally similar dioritic counterparts. Two plagioclase-phyric dykes (Fig. 4.3C-H) have lower Ti than the other samples and clearly deviate from the field defined by the dioritic suite. This is consistent with the petrographic examination of these samples, which indicates the strong propylitic and phyllic alteration (Table 3.2). Consequently, these two plagioclase-phyric dykes (E41D2010-113.4 and E41D2068-211.3) have been excluded from the dataset. Because the trachyte dyke (E41D2063-126.6) has a very high LOI value (~12%; Figs. 4.3 A and B), this sample has also been excluded from the dataset. Although the amygdaloidal dyke and aplite dykelet have high LOI values (Figs. 4.3A and B), their HFSE compositions appear to be undisturbed, as they plot together with their co-genetic rock suites, and are therefore retained in the dataset.

The screening procedure excluded three samples (noted in Appendix C.1), and the following description and discussion of whole rock geochemical dataset is therefore based on 46 least-altered samples.

4.4 Intrusions

Many intrusive centres are characterised by increasing SiO_2 content with time (e.g., Lang and Titley, 1998). As has been demonstrated in Chapter 3, this is clearly not the case at E41, where hornblende- and pyroxene-phyric dykes are younger than the quartz-monzonite and aplite dykelets. Figure 4.4 compares the interpreted sequence of intrusive activity with SiO_2, total alkalis, Zr and MgO concentrations. SiO_2 values range from relatively low ($\leq$ 50 wt. %) for pre-mineralisation intrusions, through higher

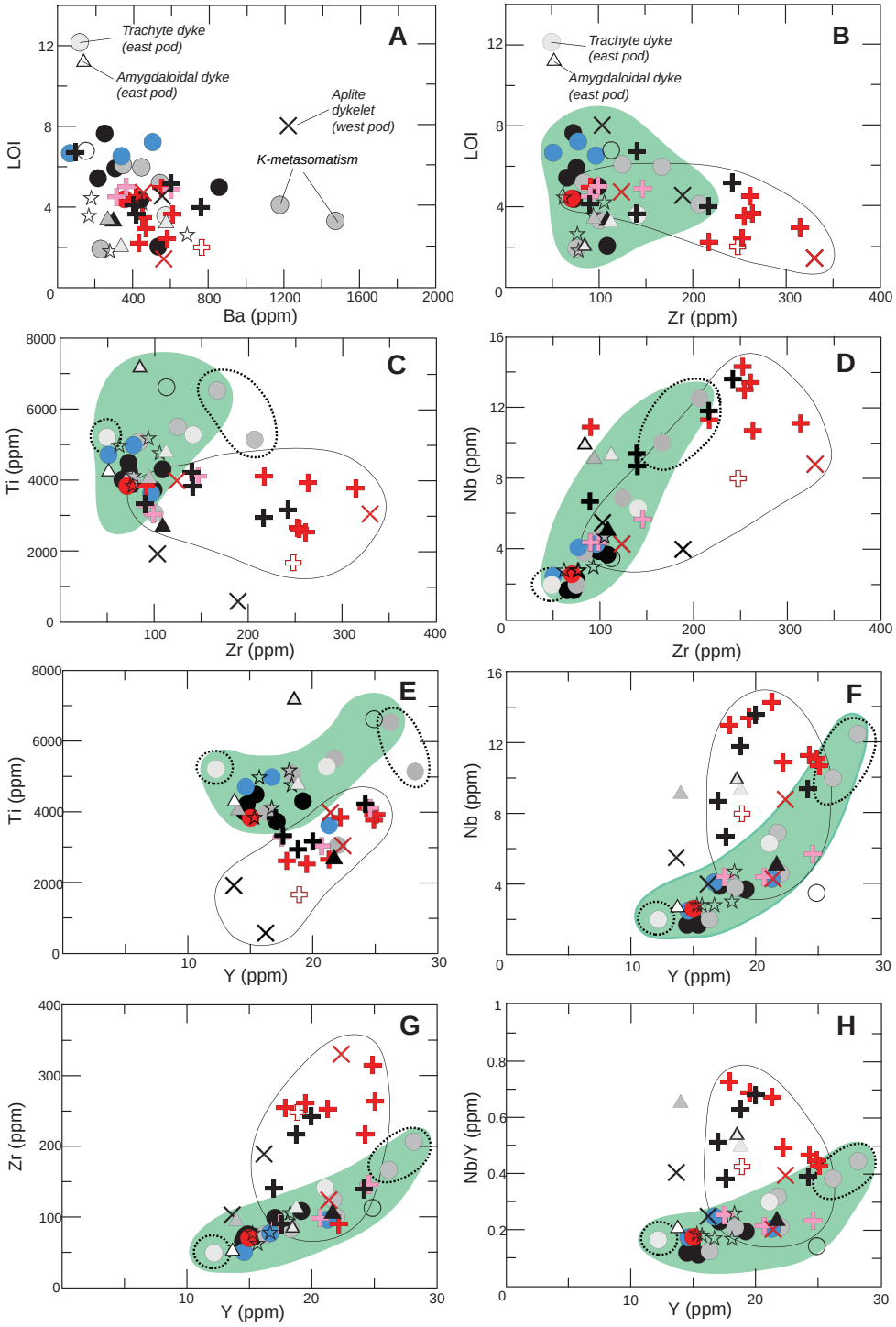

Legend

Pre-mineralisation ~461 - 458 Ma

- Diorite
- Plagioclase-phyric dyke
- Mafic dyke
- Trachyte dykes
- Blocky plagioclase -phyric dyke
- Monzodiorite dyke
- Mafic monzonite (west pod)
- Mafic monzonite (east pod)
- Monzodioritic enclaves - hybrid zone

Syn-mineralisation ~455 Ma

- Quartz-monzonite dykelet
- Aplite dykelet
- Pyroxene-phyric dyke
- monzonitic rocks
- dioritic rocks
- excluded samples

Late-post-mineralisation <455 Ma

- Syenite dykelet
- Hornblende-phyric quartz-phyric dyke
- Diorite dyke
- Hornblende phyric dyke
- Amygdaloidal dyke

Figure 4.3 Variation diagrams of LOI vs Ba and Zr and selected immobile elements for the igneous rocks of the E41 deposit. **A.** LOI vs Ba. **B.** LOI vs Zr. **C.** Ti vs Zr. **D.** Nb vs Zr. **E.** Ti vs Y. **F.** Nb vs Y. **G.** Zr vs Y. **H.** Nb/Y vs Y. Green fields indicate Muddy Lake diorite and pre-mineralisation dykes (Figs. C-H), whereas white fields indicate mafic monzonite with its hybrid zone and dykelets that are inferred to be genetically related to mafic monzonite.

values (>50 to 70 wt. % SiO_2) for the mafic monzonite and several other syn- to late-mineralisation rocks, to as low as 45 wt. % in post-mineralisation dykes. As expected, Zr mimics SiO_2 behaviour, whereas MgO behaves in an opposite fashion, showing higher concentration in the mafic rocks (> 2 wt. % MgO) and lower in the more silicic units (< 3 wt. % MgO). Based on these variations, the E41 intrusive sequence has been separated into four geochemical suites: (1) pre-mineralisation diorites; (2) monzonitic rocks, including the pre-mineralisation mafic monzonite, syn- and late-mineralisation quartz-monzonite, aplite and syenite dykelets; (3) syn-mineralisation pyroxene-phyric dykes; and (4) post-mineralisation diorites (Fig. 4.4).

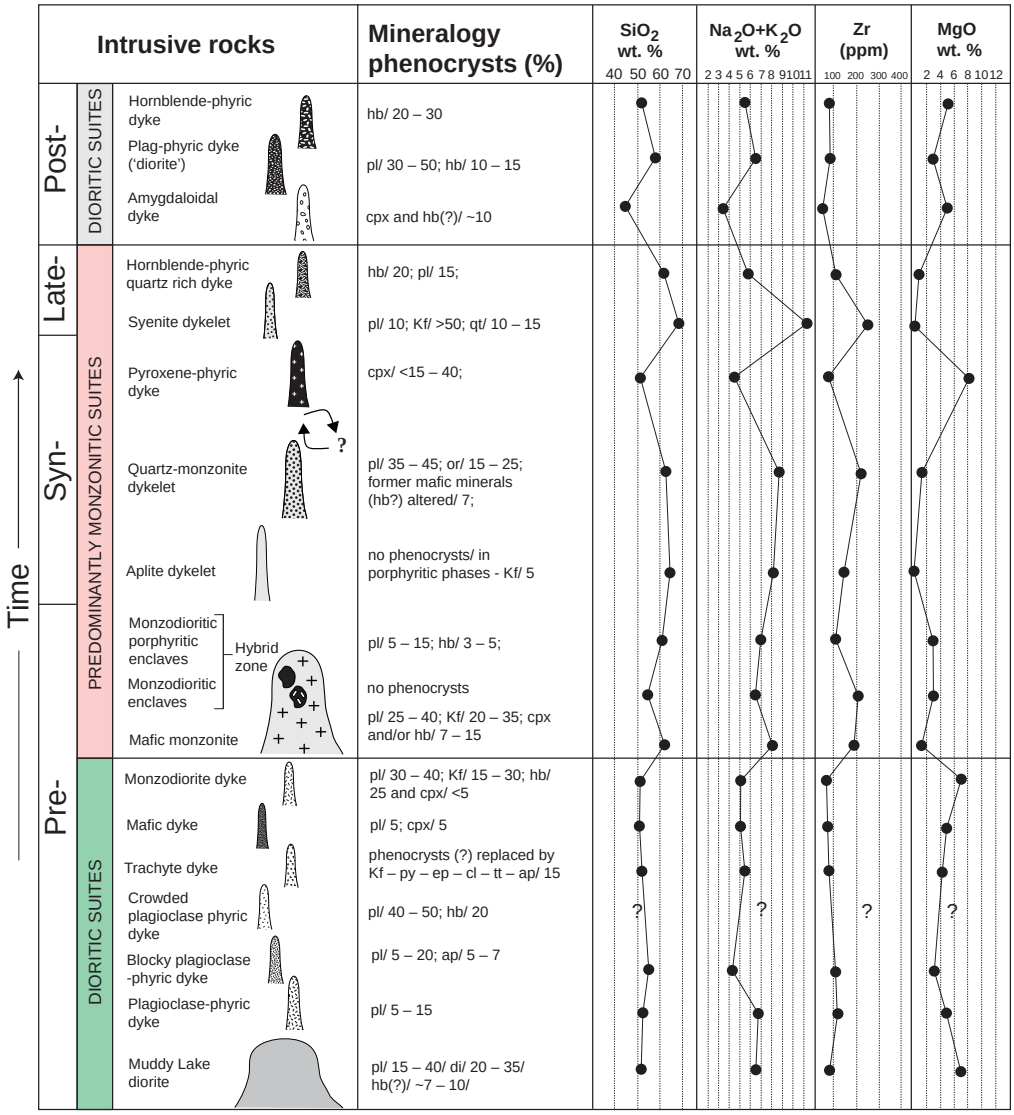

Figure 4.4 Synthesis of igneous evolution of the E41 deposit, Cowal district. Geochemical data from Table 4.1 and Appendix C.1. Abbreviations: ap=apatite, bt=biotite, ch=chlorite, cl=calcite, cpx=clinopyroxene, di=diopside, ep=epidote, hb=hornblende, Kf=K-feldspar, lx=leucoxene, mt=magnetite, pl=plagioclase, qt=quartz, sh=sphene, tt=titanite.

4.4.1 Major element geochemistry

The E41 intrusive rocks straddle the alkalic-subalkalic dividing line of Irvine and Baragar (1971) on the total alkali-silica (TAS) diagram of Le Maitre (1989; Fig. 4.5A and B). The Muddy Lake diorite and pre-mineralisation diorites plot in the trachybasalt, basaltic trachyandesite and trachyandesite fields. The mafic monzonite ranges in composition from trachyandesite (east pod) to trachyte-trachydacite (most of the west pod samples). The syn-mineralisation quartz-monzonite and aplites range from trachyandesite and trachydacite to rhyolitic compositions. The pyroxene-phyric dykes are basaltic to basalt-trachyandesitic. Late syenite plots in the trachyte-trachydacite field and the hornblende-phyric quartz-rich dyke has andesitic composition. The post-mineralisation diorites have trachyandesite to andesitic compositions. Although considerable variations in compositions are apparent in Figure 4.5A, there are considerably fewer variations on the Zr/TiO_2 vs Nb/Y plot of Winchester and Floyd (1977; Fig. 4.5C), and Winchester and Floyd modified by Pearce (1996; Fig. 4.5D), with only a few samples of mafic monzonite plotting in the alkaline trachyandesite field.

The E41 intrusions define two distinctive groups on Figure 4.5E. One contains the pre-mineralisation and post-mineralisation diorite rocks, and the syn-mineralisation pyroxene-phyric dyke. The second group is defined by the mafic monzonite, quartz-monzonite and some of the monzodioritic enclaves from the hybrid zone (Fig. 4.5E). The syenite and one aplite dykelet have extreme K_2O contents, possibly due to secondary K-bearing hydrothermal alteration. In thin section, syenite does not show obvious alteration, whereas the aplite dykelet shows a moderate carbonate – chlorite – illite ± muscovite alteration assemblage. The pre-mineralisation and post-mineralisation dioritic suites have medium- to high-K calc-alkaline affinities, whereas the mafic monzonite and syn-mineralisation monzonitic units are high-K calc-alkaline to shoshonitic (Fig. 4.5E). The monzodioritic enclaves of the hybrid zone are also shoshonitic (Fig. 4.5E). Syn-mineralisation pyroxene-phyric dykes span compositions from medium-K through high-K calc-alkaline to shoshonitic (Fig. 4.5E). One sample of pyroxene-phyric dyke (E41D2010-256.6) falls clearly into shoshonitic spectrum.

In the Ce/Yb vs Ta/Yb diagram (Fig. 4.5F), which claims to discriminate between tholeiitic, calc-alkalic and shoshonitic magmatic affinities, E41 intrusive rocks have transitional high-K calc-alkaline to shoshonitic compositions (Pearce, 1982; Fig. 4.5F). This diagram confirms the shoshonitic nature of the pyroxene-phyric dykes.

The Cowal intrusions plot along linear trends on Harker discrimination diagrams, from Muddy Lake diorite through mafic monzonite to aplites and syenite. Figures 4.5E and 4.6A-H show increasing K_2O and Na_2O, and decreasing TiO_2, Fe_2O_3,

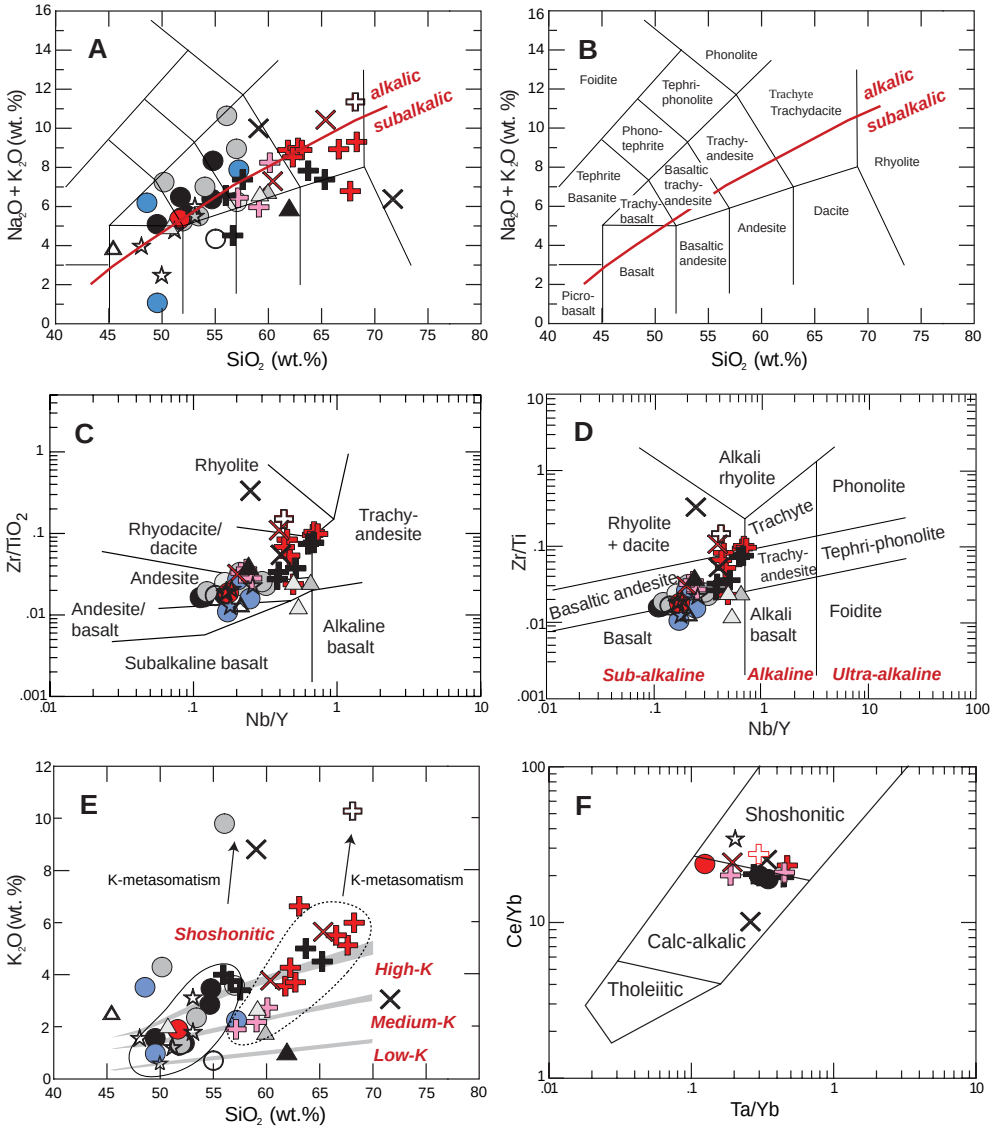

Legend

Pre-mineralisation ~461 - 458 Ma

- Diorite
- Plagioclase-phyric dyke
- Mafic dyke
- Trachyte dykes
- Blocky plagioclase -phyric dyke
- Monzodiorite dyke
- Mafic monzonite (west pod)
- Mafic monzonite (east pod)
- Monzodioritic enclaves - hybrid zone

Syn-mineralisation ~455 Ma

- Quartz-monzonite dykelet
- Aplite dykelet
- Pyroxene-phyric dykes

Late-post-mineralisation <455 Ma

- Syenite dykelet
- Hornblende-phyric quartz-phyric dyke
- Diorite dyke
- Hornblende phyric dyke
- Amygdaloidal dyke

Figure 4.5 Major and trace element discrimination diagrams for intrusions from E41. **A.** Classification of E41 intrusive rocks on the TAS diagram. The alkalic and subalkalic dividing line is from Irvine and Baragar (1971). **B.** Total alkali-silica (TAS) diagram of Le Maitre (1989), showing rock fields defined on the basis of $Na_2O + K_2O$ vs SiO_2. **C.** Zr/Ti vs Nb/Y trace element discrimination plot, after Winchester and Floyd (1977). **D.** Winchester and Floyd (1977) diagram with fields of Pearce (1996). **E.** K_2O vs SiO_2 diagram with fields after Peccerillo and Taylor (1976) and Rickwood (1989). **F.** Ce/Yb vs Ta/Yb immobile element plot (Pearce, 1982). Data listed in Appendix C.1.

MgO and CaO with increasing SiO_2. Significant scatter in Na_2O probably relates to sodium mobility during hydrothermal alteration. Specifically, the Muddy Lake diorite and mafic monzonite have high Na_2O content due to albite alteration (Table 3.2). In general, the pre- and post-mineralisation dioritic rocks and the pyroxene-phyric dykes are enriched in TiO_2, Fe_2O_3, CaO, Al_2O_3, MnO, CaO, MgO and P_2O_5 compared to monzonitic rocks (Figs. 4.6A-F and H).

The Al_2O_3 contents of the E41 intrusions slightly increase with increasing SiO_2 up to ~ 58 wt. % SiO_2 and then decrease with further fractionation (Fig. 4.6C). The trend to lower Al_2O_3 defined by monzonites (Fig. 4.6C) may indicate removal and retention of some plagioclase in the magma chamber.

The P_2O_5 concentration increases in dioritic suites up to ~ 58 wt. % SiO_2 (Fig. 4.6H). It varies from ~ 0.2 to 0.4 wt. % P_2O_5 in the mafic monzonite and decreases with increasing SiO_2, reflecting effective removal of apatite. The aplite and syenite dykelets have the lowest P_2O_5 concentrations. The highest P_2O_5 content was detected in the blocky plagioclase-phyric dyke (Fig. 4.6H), which contains abundant apatite phenocrysts.

The east pod mafic monzonite and the monzodioritic enclaves of the hybrid zone are less evolved than the west pod mafic monzonite. Plots of TiO_2, Fe_2O_3, CaO, Al_2O_3, MnO, CaO, MgO and P_2O_5 versus SiO_2 indicate that there may be several generations of mafic monzonite or that there are spatial variations in compositions within the intrusion. The monzodioritic enclaves of the hybrid zone are interpreted to record injections of more mafic (dioritic – monzodioritic – quartz-dioritic) magmas into mafic monzonite.

4.4.2 Trace and rare earth element geochemistry

Trace element data are shown on Figures 4.7A-L and listed in Appendix C.1. With increasing fractionation there are general trends of decreasing concentrations of Ni, Cr, Sc, Sr and V, and increasing abundances of HFSE (Nb, Zr), LREE (La, Ce) and LILE (Rb and Ba). The pre- and post-mineralisation diorites are enriched in Ni, Cr, Sr, Sc and V and depleted in Nb, Zr, Ba compared to the monzonites. The pyroxene-phyric dykes have trace element characteristics similar to the pre- and post-mineralisation diorites except for a distinctively higher concentration of Ni and Cr (Figs. 4.7A and B). In contrast, monzonites are characterised by pronounced depletions in Ni and Cr. The monzonites are enriched in HFSE (Nb, Zr), and have elevated Rb and Ba relative to the diorites. Mobile elements (e.g., Sr, Rb) are scattered on Figures 4.7E and 4.7G due to epidote, calcite, orthoclase and illite alteration.

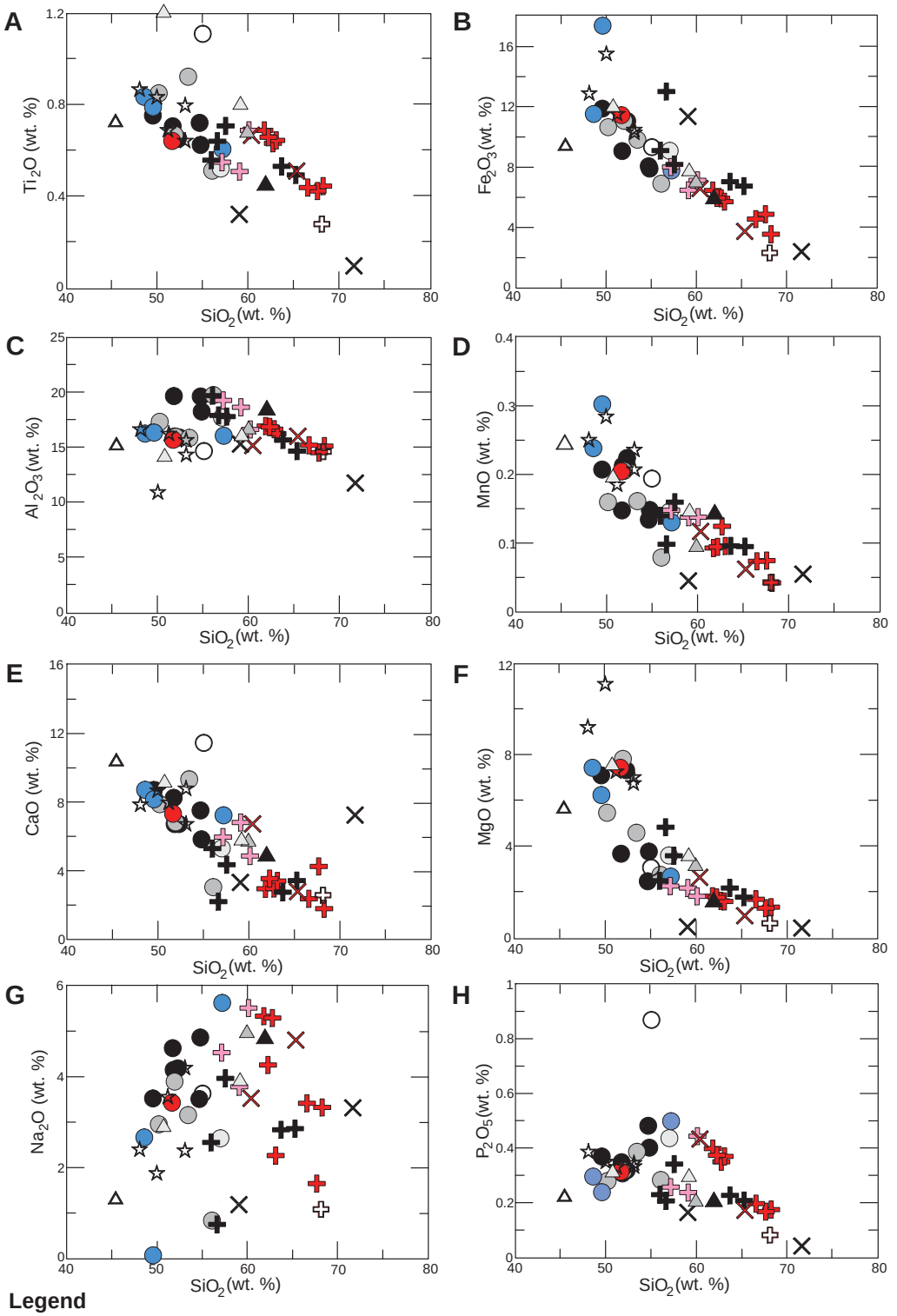

Figure 4.6 Harker variation diagrams showing major element chemistry of intrusive rocks of the E41 deposit. **A.** Ti_2O vs SiO_2 **B.** Fe_2O_3 vs SiO_2. **C.** Al_2O_3 vs SiO_2. **D.** MnO vs SiO_2. **E.** CaO vs SiO_2. **F.** Na_2O vs SiO_2. **G.** P_2O_5 vs SiO_2. Data listed in Appendix C.1.

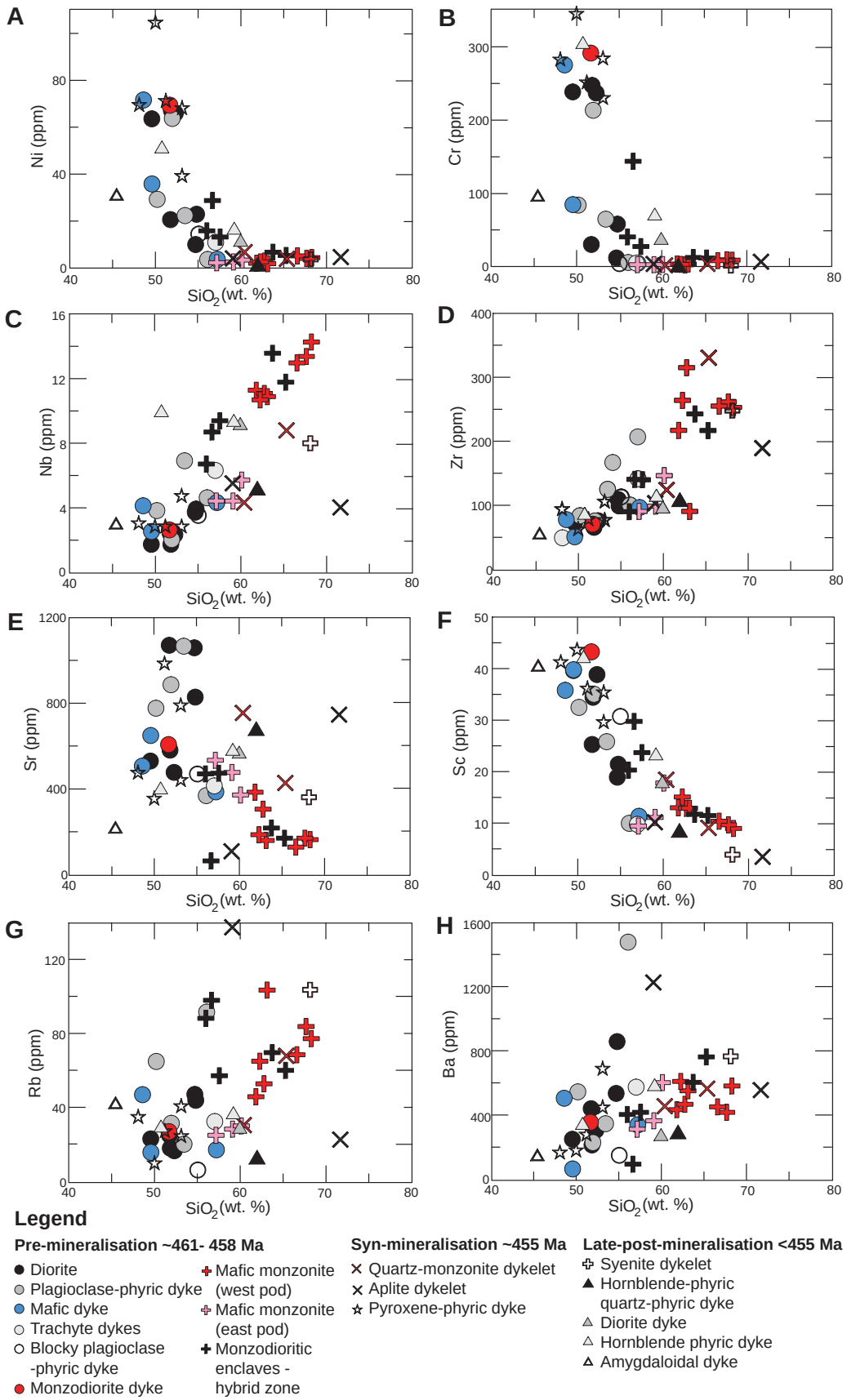

Figure 4.7 Trace element Harker diagrams for intrusive rocks of the E41 deposit. **A.** Ni vs SiO_2. **B.** Cr vs SiO_2. **C.** Nb vs SiO_2. **D.** Zr vs SiO_2. **E.** Sr vs SiO_2. **F.** Sc vs SiO_2. **G.** Rb vs SiO_2. **H.** Ba vs SiO_2. Data listed in Appendix C.1.

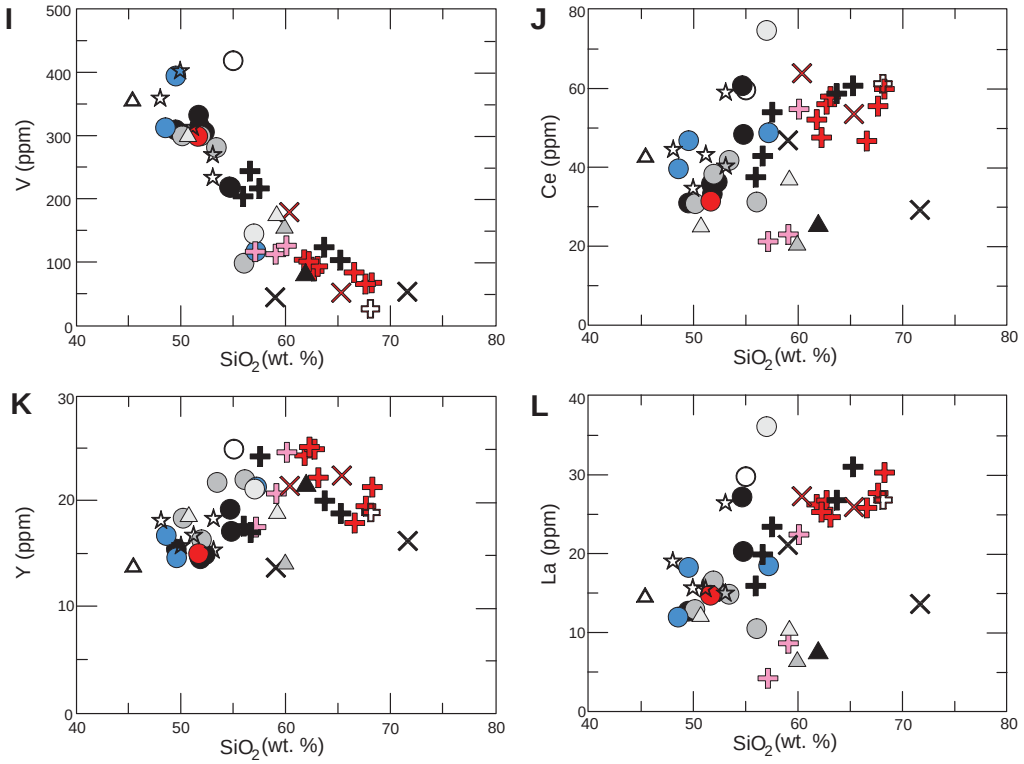

Figure 4.7 (Cont.) **I.** V vs SiO_2. **J.** Ce vs SiO_2. **K.** Y vs SiO_2. **L.** La vs SiO_2. Data listed in Appendix C.1.

N-MORB normalised trace element plots are shown in Figure 4.8 (N-MORB; Sun and McDonough, 1989). On such plots, arc-type magmas are typically enriched in large ion lithophile elements (LILE) such as Rb, Ba, Sr, Th and light earth elements (LREE) relative to MORB. They also show pronounced negative Nb anomalies relative to K and La and Ce and positive Sr and Pb anomalies relative to Ce and Pr (Sun and McDonough, 1989; Wilson, 1989). The E41 intrusive rocks clearly have these anomalies (Fig. 4.8) that are characteristic of island arc rocks.

The Muddy Lake diorite and pre-mineralisation dykes have similar profiles on Figure 4.8B. There are apparent variations in LILE, K and Pb, which probably reflect Ca and K being affected by hydrothermal alteration. Figure 4.8C shows that the mafic monzonite has remarkably similar multi-element profiles to the Muddy Lake diorite. The only major difference is that the Muddy Lake diorite has a positive Sr anomaly, whereas the mafic monzonite is characterised by a negative Sr anomaly, reflecting plagioclase enrichment (diorite) and removal (monzonite).

Chondrite-normalised (Sun and McDonough, 1989) whole rock REE profiles for all analysed samples show broadly similar patterns (Figs. 4.9A-H). Most of the REE profiles have moderate to strong LREE enrichment. The REE profiles are typically steeply dipping from the LREE to the MREE, and are flat from the MREE to the HREE.

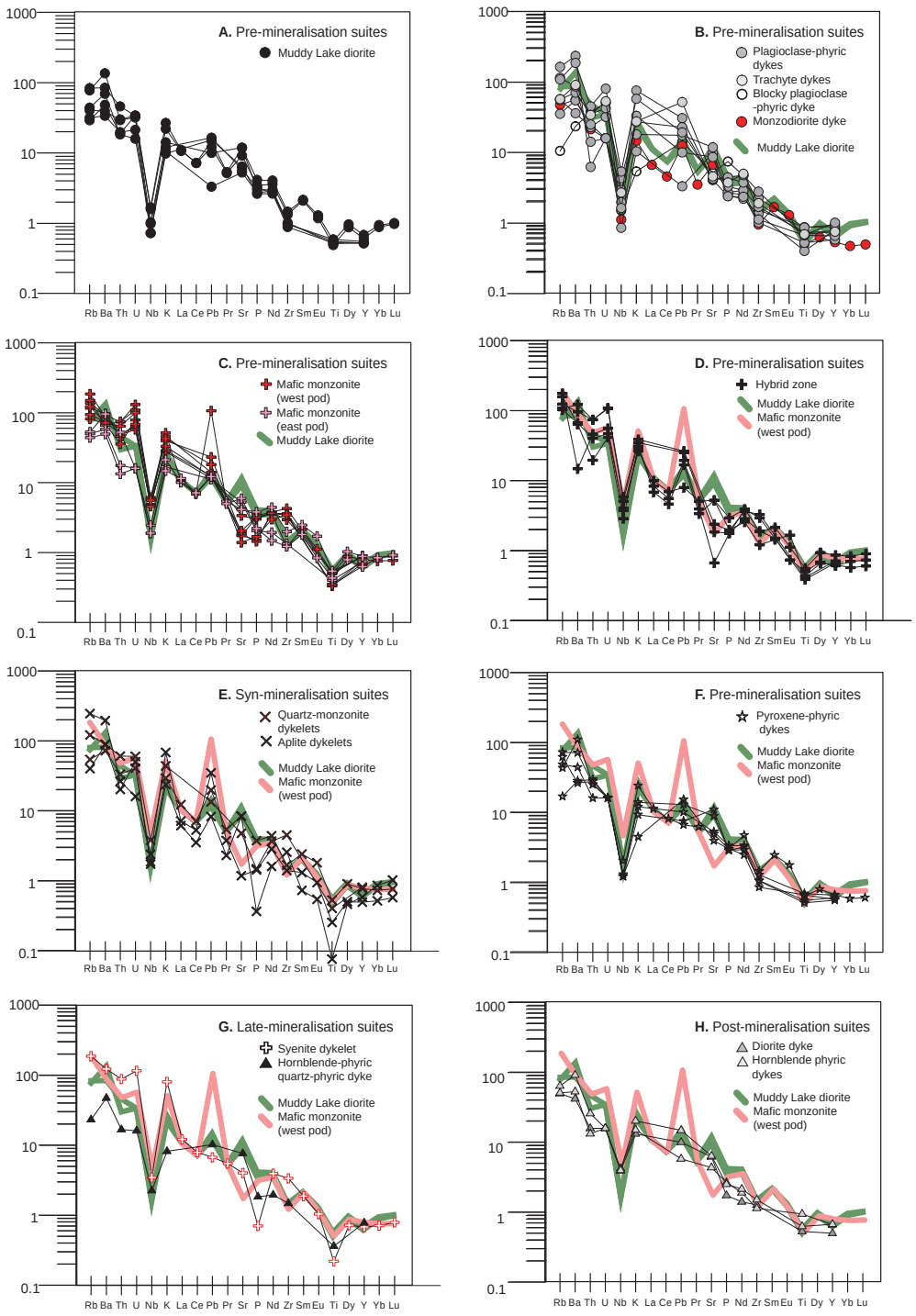

Figure 4.8 Normalised trace element plots of E41 intrusive rocks. Data are normalised to N-MORB values of Sun and McDonough (1989). Data are presented in order of interpreted sequence of emplacement from pre-mineralisation to post-mineralisation intrusions. Intrusive rocks are plotted relative to representative samples of Muddy Lake diorite and mafic monzonite. Data listed in Appendix C.1.

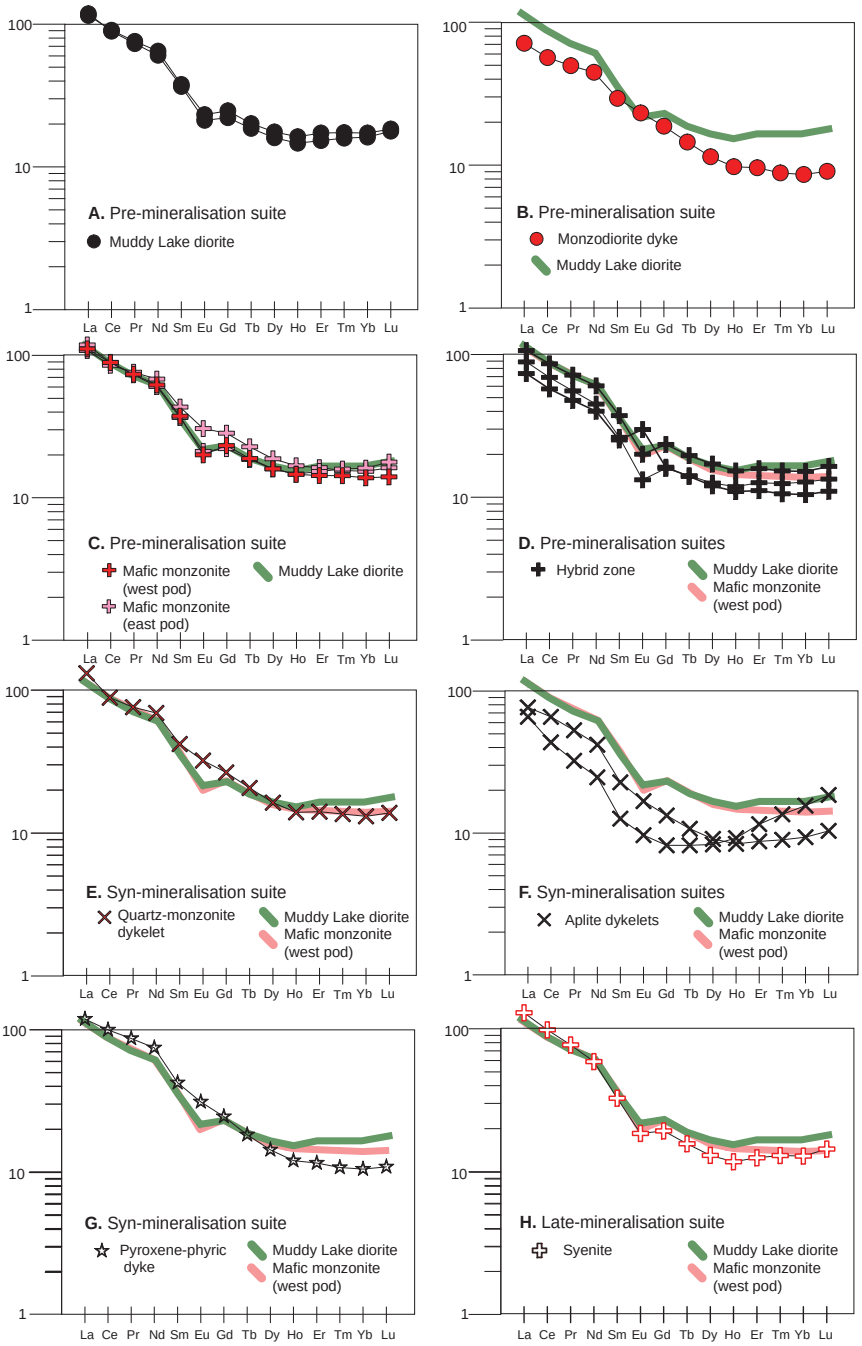

Figure 4.9 Chondrite-normalised (Sun and McDonough, 1989) REE diagrams for selected intrusive suites from E41. The REE plots presented in the interpreted sequence of emplacement from oldest to youngest. **A.** Muddy Lake diorite. **B.** Pre-mineralisation monzodiorite dyke. **C.** Pre-mineralisation mafic monzonite. **D.** Hybrid zone with monzodiorite enclaves. **E.** Quartz-monzonite dykelet. **F.** Aplite dykelet. **G.** Pyroxene-phyric dyke. **H.** Late-mineralisation syenite dykelet. Intrusive rocks are plotted relative to representative samples of Muddy Lake diorite and mafic monzonite. Data listed in Appendix C.1.

Only the aplite dykelets and monzodiorite dyke show REE patterns significantly below that of the Muddy Lake diorite (Figs. 4.9B and F). For the aplite this reflects significant prior apatite fractionation (reflected in its low P_2O_5; Fig. 4.6H).

The Muddy Lake diorite and mafic monzonite have similar REE patterns

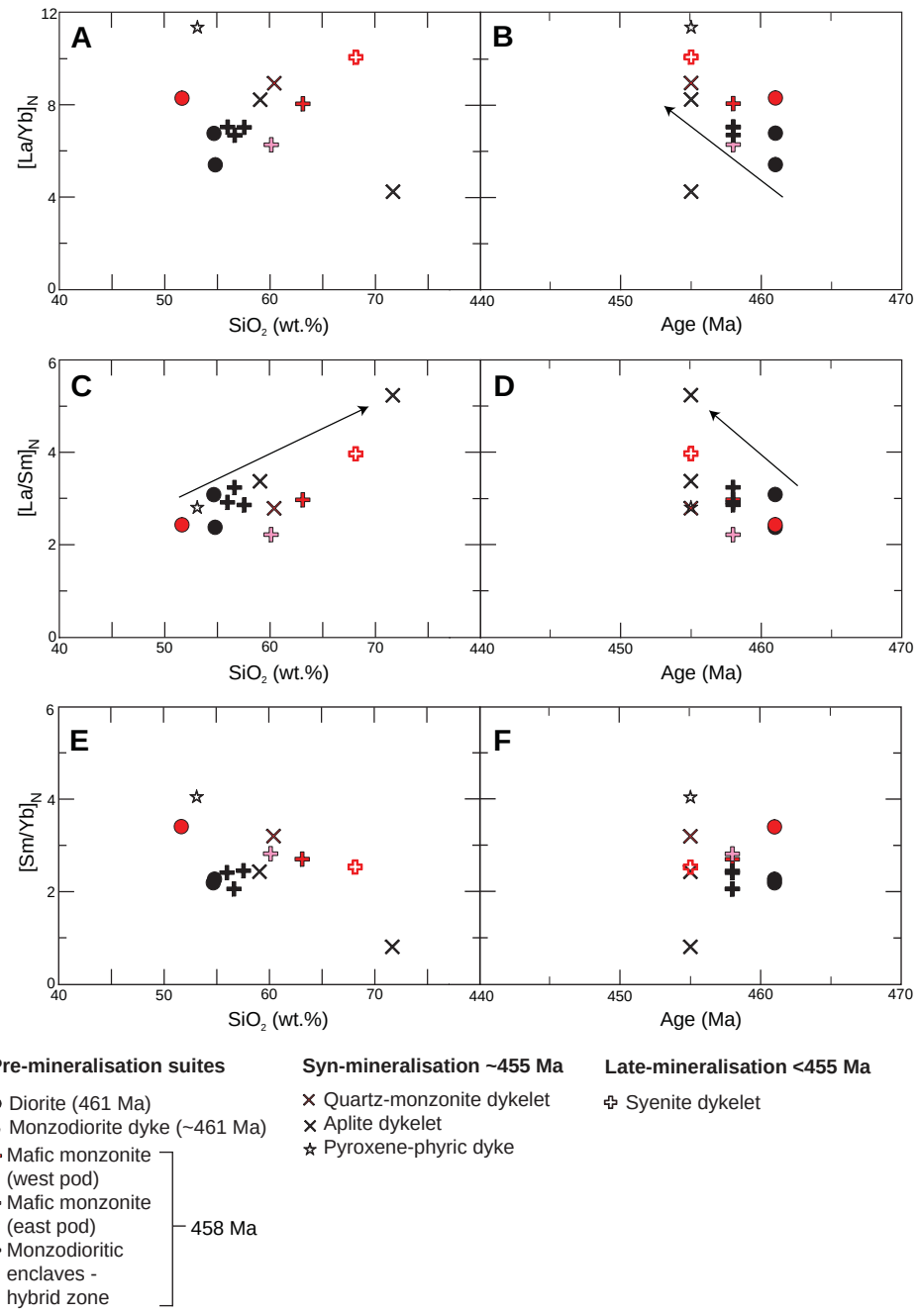

Figure 4.10 Variation in rare earth element (REE) concentrations with respect to silica abundances and absolute age data. **A&B.** $[La/Yb]_N$ show total REE variation as a function of silica (A) and age (B). **B&C.** $[La/Sm]_N$ show light REE variations. **D&E.** $[Sm/Yb]_N$ show heavy REE variation. Absolute age determinations are presented in Table 3.3. Estimates of the ages of other intrusions in the E41 deposit are inferred from geological relationships and from dating post-mineralisation intrusive rocks. Data listed in Appendix C.1.

(compare Figs. 4.9A and C). The monzodiorite dyke has lower REE concentrations than the Muddy Lake diorite (Fig. 4.9B). The monzodioritic enclaves of the hybrid zone, quartz-monzonite dyke and the syenite have REE patterns that mimic the Muddy Lake diorite and mafic monzonite patterns (Figs. 4.9 D,E, H). The weak Eu

anomaly that characterises the Muddy Lake diorite and the mafic monzonite is not a feature of the monzodiorite, quartz-monzonite, aplite and pyroxene-phyric dykes. One monzodioritic enclave has a positive Eu anomaly (Fig. 4.9D).

The aplite dykelet has a distinctive REE-profile typified by a 'u-shaped' pattern (Fig. 4.9F). A trough in MREE values is particularly apparent between Eu and Ho, indicating relative depletion of the middle REE and enrichment of heavy REE. Similar 'u-shaped' REE patterns have been documented for the mineralising intrusions at the Northparkes porphyry Cu-Au deposits (Lickfold et al., 2007).

The sequence from Muddy Lake diorite to mafic monzonite to quartz-monzonite and syenite is characterised by increasing fractionation of REE with increasing magmatic differentiation ($[La/Yb]_N$ = 5.4 – 10.0; Fig. 4.10A). The aplite dykelet is not consistent with this trend, having a lower $[La/Yb]_N$ value (4.2) at high SiO_2 content. In detail, LREE increases with fractionation ($[La/Sm]_N$ = 2.4 – 5.2; Fig. 4.10C) and the HREE component generally decreases with fractionation ($[Sm/Yb]_N$ = 4.0 – 0.8; Fig. 4.10E), the latter usually is a feature of magmatic systems involving significant apatite and hornblende removal (Lickfold et al., 2007). The highest degrees of LREE enrichment occur in the aplite and in the syenite dykelet ($[La/Sm]_N$ = 5.2 and 3.9, respectively; Fig. 4.10C). HREE are most enriched in the pyroxene-phyric dyke and the monzodiorite dyke ($[Sm/Yb]_N$ = 4.0 and 3.4, respectively; Fig. 4.10E). The aplite dykelet has the lowest HREE concentrations ($[Sm/Yb]_N$ = 0.8; Fig. 4.10E). Overall, the syn-mineralisation pyroxene-phyric dyke is the most REE-enriched intrusion at E41 ($[La/Yb]_N$ = 11.3; Fig. 4.10A).

With respect to absolute age estimates, there is a general enrichment in absolute REE concentration from pre-mineralisation intrusions to syn-mineralisation dykes (Fig. 4.10B). Figures 4.10D and 4.10F show an increase in LREE and HREE from older to younger intrusions, respectively.

4.5 Discussion

This section characterises the CIC intrusions, compares the E41 intrusions with the data from CIC (Crawford et al., 2007b; Bissig, unpublished data; Appendix C.1), and with the shoshonitic Macquarie Arc rocks of the Northparkes and Cadia district (Lickfold, 2002; Wilson, 2003; Lickfold et al., 2007).

4.5.1 Cowal Igneous Complex

The geochemistry of volcanic and intrusive rocks of the CIC was investigated by Crawford (1999) and Crawford et al. (2007a and b) as part of a broader study of the Macquarie Arc. These workers concluded that the CIC consists of a basement sequence of

Early Ordovician high-K calc-alkaline to shoshonitic lavas and volcaniclastic rocks that compositionally range from basaltic through trachyandesitic to trachytic compositions (~470 – 465 Ma; Phase 1 magmatism). The high-K calc-alkaline trachybasalts, andesites and trachytes Phase 1 rocks appear to be volumetrically abundant in the central and northern portions of the CIC. Crawford et al. (2007b) showed also that Phase 2 (central part of the CIC) and Phase 3 (southern part of the CIC) have also contributed to the igneous development of the CIC. According to Crawford et al. (2007b) Macquarie Arc Phase 4 shoshonitic magmatism is represented in the northern part of the district by high-level monzogranitic intrusions.

Several geochemical features for each magmatic phase are listed in Table 4.2. Figure 4.11 compares the CIC volcanic and intrusive units in terms of compositions and ages. The E41 intrusions are more enriched in LREE than intrusive rocks from E42, E43 and E35 (Fig. 4.11A). Most of the E43 rocks, some North Cowal samples, and the E35 granodiorite are characterised by $[La/Sm]_N$ = <2 values whereas most of the E41 samples have $[La/Sm]_N$ ratios >2. A strong geochemical difference between intrusives of the southern part of the CIC (i.e., E43, E35) is also apparent on the Zr/Nb versus $[La/Sm]_N$ diagram (Fig. 4.11B), which shows that the E41 intrusives, E40 lamprophyre, Muddy Lake diorite, E42 lava and the E43 quartz-feldspar porphyry have Zr/Nb values between 10 to 30 and $[La/Sm]_N$ ratios between 2 to 5. Crawford et al. (2007a) showed that these geochemical differences may reflect a spatial and temporal relationship within the arc, with the most arc-like rocks having high Zr/Nb and lowest $[La/Sm]_N$. These high Zr/Nb and lowest $[La/Sm]_N$ values are characteristic of Phase 2 Macquarie magmatism (Table 4.2). In contrast, Phase 4 magmatism has much higher $[La/Sm]_N$ and lower Zr/Nb ratios (Table 4.2), similar to those observed at E41 and it might be that Phase 4 type magmatic activity of the Macquarie Arc is actually represented at E41.

With respect to absolute age constraints, there is a general increase in LREE contents with decreasing time for the CIC intrusives (Fig. 4.11C), with the E41 intrusives

TABLE 4.2 Geochemical characteristics of magmatic phases that have contributed to the evolution of the Macquarie Arc (sourced from Crawford et al., 2007a).

Magmatic Phase	Compositions	Geochemical features
Phase 1	High-K calc-alkaline	Al_2O_3 vs SiO_2 ~1-3; high Sc/Y=~2-3; Zr/Nb=5-25; $[La/Sm]_N$=1.5-2.5; $[Gd/Yb]_N$=1.5-2.5
Phase 2	Medium-K; high-K calc-alkaline to shoshonitic	High Zr/Nb (arc-like: 40-60 and transitional: around 20), flattest LREE (lowest $[La/Sm]_N$=1-2.5)
Phase 3	Medium-K calc-alkaline	Low MgO, TiO_2; less enriched in LILE than Phase 2 or the Phase 4; high Sr/Y but no HREE depletion
Phase 4	Shoshonitic	Lower than Phase 2 Zr/Nb values; steeper LREE $[La/Sm]_N$=2-5) at $[Gd/Yb]_N$=1-2

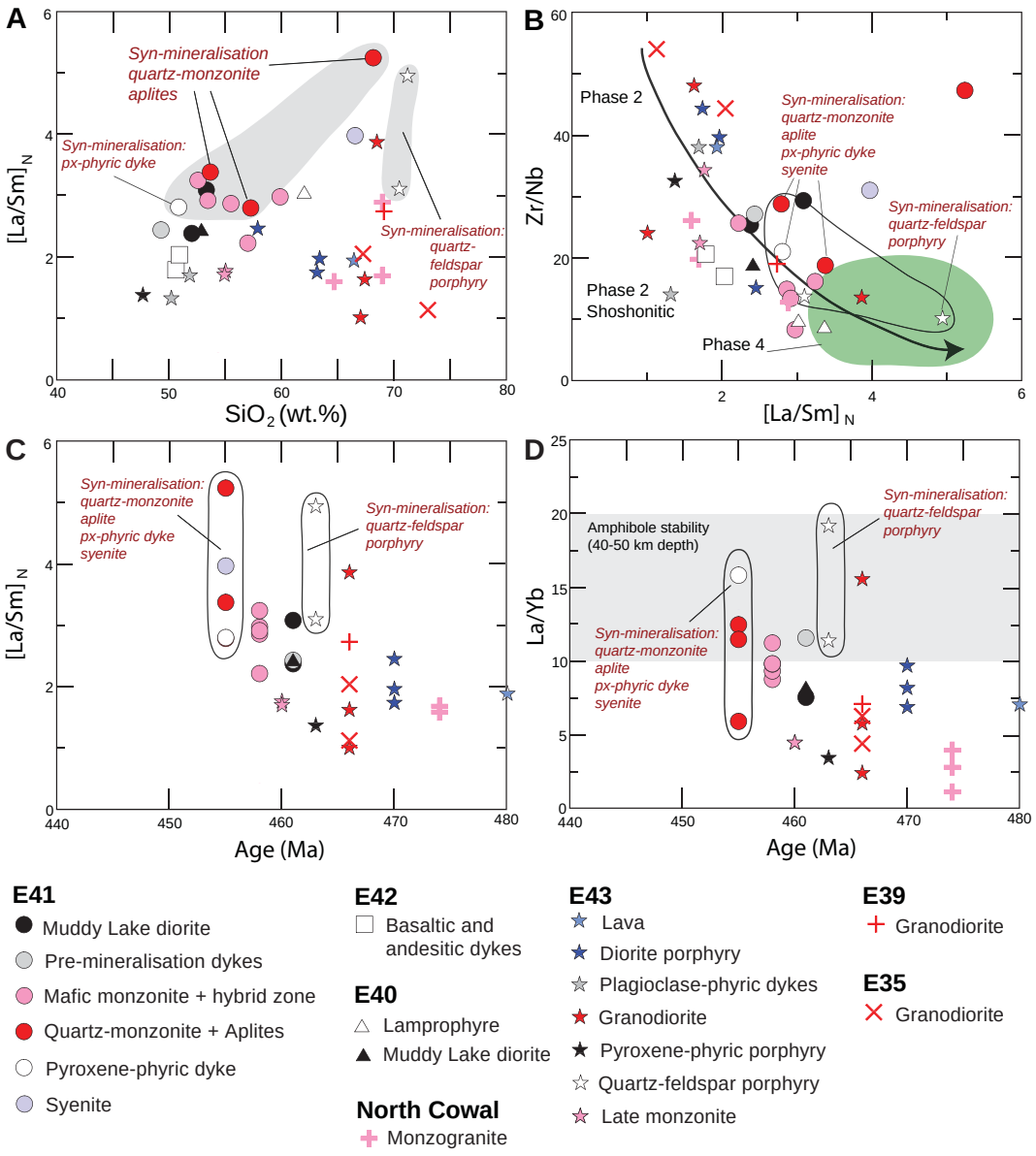

Figure 4.11 Variation in rare earth element (REE) concentrations of intrusive rocks of the CIC. **A.** $[La/Sm]_N$ vs SiO_2 shows light REE variations. **B.** Zr/Nb vs $[La/Sm]_N$. **C.** $[La/Sm]_N$ vs age (Ma). **D.** La/Yb vs age (Ma). Absolute age determinations are presented in Table 3.3. Estimates of the ages of other intrusions at E41 deposit are inferred from geological relationships and from dating post-mineralisation intrusive rocks (Table 3.3). Note a general increase of light REE with fractionation for the CIC intrusive rocks. Also note that some syn-mineralisation rocks (i.e., quartz-monzonite: E41; aplites: E41; pyroxene-phyric dykes: E41; quartz-feldspar porphyry: E43) are characterised by high $[La/Sm]_N$ and La/Yb ratios and lower Zr/Nb ratio (at higher $[La/Sm]_N$). Amphibole stability field taken from Kay and Kurtz (1995). Phase 4 field taken from Crawford et al. (2007a). Data listed in Appendix C.1.

typified by highest $[La/Sm]_N$ ratios. Importantly, regardless of their age, rocks that are associated with epithermal gold (i.e., quartz-monzonite, aplite, pyroxene-phyric dyke; E41) or porphyry-copper mineralisation (quartz-feldspar porphyry, E43; Zukowski, 2009) have distinctively high $[La/Sm]_N$ and La/Yb ratios relative to rocks that are unrelated to mineralisation (Figs. 4.11C and D).

4.5.2 Interpretation of E41 intrusive sequence

4.5.2.1 Major elements

E41 intrusives were emplaced between 461 and ~447 Ma and have medium- to high-K calc-alkaline and shoshonitic magmatic affinities. Although the E41 intrusive rock samples form a coherent linear trend on Harker diagrams (SiO_2 vs K_2O, Fe_2O_3, TiO_2 and MgO) with a positive variation of K_2O and antithetic variation of TiO_2, MgO, CaO and Fe_2O_3 with respect to SiO_2, they are interpreted to have been generated from at least two, if not more, different parental magmas. The elevated Cr, Ni and V concentrations of the Muddy Lake diorite are consistent with a relatively primitive parental melt of basaltic to andesite composition. The sequence: plagioclase-phyric dykes → mafic dykes → trachyte dykes → blocky plagioclase-phyric dyke → monzodiorite dyke → mafic monzonite + monzodioritic enclaves → quartz-monzonite dykelets → aplite dykelets → syenite dykelet forms a coherent trend on Harker diagrams from basaltic through to trachyte-trachydacite that is consistent with fractional crystallisation processes. This trend also reflects the broadly comagmatic nature of this sequence of intrusive rocks from the evolving high-K calc-alkaline to shoshonitic magma chamber. It appears that monzonites were generated from melts that had already undergone considerable fractionation, as indicated by their low Ni, Cr and V concentrations. No reasonable fractionation scheme, however, can explain the similar timing of the pyroxene-phyric dykes and the quartz monzonites and aplites, and an alternative explanation is required for the coexistence of the mafic and silicic rocks.

4.5.2.2 Trace element and REE patterns

The similar trace element patterns for the E41 intrusions (Fig. 4.8) are consistent with the rocks forming in similar tectonic settings. The intrusions are all enriched in LILE and LREE and are depleted in HFSE (Nb/La < 1), features typical of a subduction zone setting (Wilson, 1989; Pearce and Peate, 1995). Similar REE patterns for most of the analysed samples (Fig. 4.9) indicate derivation from broadly similar parental magmas. Variations in REE patterns may reflect small changes in magma generation processes, such as the relative extent of melting of the source, extent of fractionation, and the degree of magma mixing or crustal contamination.

Because LREE are incompatible elements, their absolute concentrations typically increase with SiO_2 content due to fractional crystallisation (Winter, 2001). The opposite relationship has been detected for several samples from E41. Decreasing total concentration of REE with increasing fractionation characterises the monzodioritic enclaves of the hybrid zone and syn-mineralisation aplite dykelets. This progressive extraction of REE with increasing fractionation may relate to significant amphibole-

and also REE-bearing phases such as apatite, titanite and zircon being removed during crystallisation of these rocks (Rollinson, 1993; Davidson et al., 2007). The 'u-shaped' REE pattern of the aplite dykelet is distinctive from the other REE from E41 (Fig. 4.9). Similar REE patterns have been documented from the most fractionated intrusions of Laramide porphyry copper deposits in Arizona (Lang and Titley, 1998) and the Ordovician porphyry Cu-Au deposits in Northparkes (Lickfold et al., 2007), and has been explained by significant hornblende + apatite fractionation (Lickfold et al., 2007). Hornblende fractionation thus is thought to be responsible for MREE depletion in the E41 aplite.

4.5.2.3 Eu anomaly and magma oxidation state

The lack of negative Eu anomalies in the pre-mineralisation monzodiorite dyke and syn-mineralisation quartz-monzonite, aplites and pyroxene-phyric rocks may suggest that significant plagioclase fractionation did not occur in those units (e.g., Green, 1980). In contrast, the Muddy Lake diorite, the mafic monzonite, the monzodioritic enclaves and the late syenite are all characterised by a weak negative Eu anomaly. Petrographic examination indicates that plagioclase phenocrysts are present in all analysed rocks, suggesting that plagioclase fractionation did, in fact, occur during crystallisation throughout the E41 intrusive sequence. The lack of an Eu anomaly has been also documented from Cadia intrusives (Wilson, 2003) and volcanic rocks at Northparkes (Lickfold; 2003; Lickfold et al., 2007). In addition, the weak development or absence of Eu anomalies has been reported from Cripple Creek's evolved alkalic rocks (Jansen, 2003). Blevin (2002) argued that only Eu^{2+} commonly substitutes into plagioclase and the lack of Eu anomaly may indicate that only Eu^{3+} was present in Cadia and Northparkes shoshonites, and therefore it did not get included into plagioclase phenocrysts. Based on the observations made for Cadia and Northparkes it is interpreted that Eu was incorporated into E41 rocks as the oxidised trivalent state, indicating high oxidation state for the monzodiorite, quartz-monzonite, aplites and pyroxene-phyric dykes. The oxidised nature of these units is also supported by high Fe_2O_3/FeO ratios (>1; Table 4.1).

4.5.2.4 Shoshonitic signature at E41 intrusive complex

This section evaluate whether some of the intrusive rocks at E41 have shoshonitic affinities. Appendix C.2 shows selected samples that have been stained with sodium-cobaltinitrite in order to highlight primary K-feldspar component in these rocks. The International Union of Geological Sciences defines shoshonite as 'a potassic variety of basaltic trachyandesite (~50 to ~ 55 % SiO_2), in which Na_2O-2 ≤ K_2O (Le Maitre, 1989).

However, not all igneous rocks that have been called shoshonites fit this description. Joplin (1968) defined the absarokite-shoshonite-banakite K-rich basaltic series as a shoshonite association in which SiO_2 varies from 48 wt.% to >63 wt. %. Morrison (1980) redefined shoshonite, providing a coherent series of textural and chemical characteristics including: low or no iron enrichment, high total alkalies ($Na_2O + K_2O$ > 5%), high K_2O/Na_2O (>0.6 at 50% SiO_2, >1.0 at 55% SiO_2), low TiO_2 (<1.3%), high but variable Al_2O_3 (14-19%), high Fe_2O_3/FeO (>0.5) and enrichment in P, Rb, Sr, Ba, Pb and LREE, in accord with K_2O enrichment. The shoshonite association has higher Th, U, V and Cu, and lower Y and Zr than other igneous associations. Cr, Ni, Co and Sc are higher for shoshonites than in the island arc tholeiites or calc-alkaline rocks at similar SiO_2 levels. Within the shoshonite association, Rb, Ba, Sr, Pb, Th, U, Y and Zr increase, and Cu, Ni, Co, V and Cr decrease, with increasing SiO_2 (Morrison, 1980).

Coexisting groundmass plagioclase and sanidine characterise shoshonites, as do K-feldspar rims on plagioclase phenocrysts. Clinopyroxenes have low TiO_2 concentrations and lack iron enrichment. Morrison (1980) and Crawford et al. (1992) noted that shoshonites are commonly typified by apatite microphenocrysts.

Figures 4.5E and F show that several intrusive rocks from the E41 deposit plot in the 'shoshonitic association' field. The shoshonite rocks are monzodioritic enclaves from the hybrid zone and the pyroxene-phyric dykes (Fig. 4.5E; 52-56 wt. % SiO_2), whereas the mafic monzonite, quartz-monzonite, aplites and syenite dykelets cluster in the banakite field (Fig. 4.5E; Peccerillo and Taylor, 1976). All of these rocks thus can be classified as having a shoshonitic signature.

The monzodiorite enclaves have low TiO_2 (0.49-0.71 wt. %), high Al_2O_3 (14.62-19.67 wt.%), high total alkalies (4.5-7.8 wt. % K_2O+Na_2O) and high K_2O/Na_2O (2.5 wt. % at >55 wt.% SiO_2). These chemical features are consistent with shoshonitic compositions, according to the criteria of Joplin (1968) and Morrison (1980). The monzodioritic enclaves are mingled with more SiO_2-rich shoshonitic mafic monzonite characterised by higher K_2O and total alkali concentrations, and lower K_2O/Na_2O, TiO_2, Al_2O_3 and Na_2O-2 values (Table 4.1).

The syn-mineralisation quartz-monzonite dykelet, aplite dyklets and late-mineralisation syenite dykelet also have shoshonitic chemical characteristics based on the criteria of Morrison (1980; Table 4.1). Classification of these rocks should be treated with particular caution, as all were affected by various degrees of secondary K-metasomatism (Fig. 4.5E). These rocks, however, contain apatite microphenocrysts, which is consistent with a shoshonitic nature.

The pyroxene-phyric dykes have high K_2O and K_2O+Na_2O (3.09 and 5.5 wt. %, respectively), more than >1.0 at ~55% SiO_2 of K_2O/Na_2O and low TiO_2 (0.79 wt

%), consistent with a shoshonitic affinity. High MgO values at about 0.4 P_2O_5 as well as high P_2O_5/Al_2O_3 and K_2O/Al_2O_3 ratios (Figs. 4.13A and B) are also consistent with shoshonitic compositions. Rogers and Setterfield (1994) and Verbeeten (1996) showed that high-K calc-alkaline to shoshonitic Fijian lava suites typically have Zr/Nb values mainly between 20 and 25, a range that is broadly consistent with the E41 pyroxene-phyric dykes, which range between 22.2 and 31.1 (average=26.1; Fig. 4.12B).

4.5.2.5 Discrimination of tectonic setting

All volcanic and intrusive rocks of the CIC have geochemical signatures consistent with a subduction-related post-collisional setting, which is in agreement with models proposed by Glen et al. (1998), Crawford at al. (2001), and Crawford et al. (2007b). On immobile element discrimination diagrams (Fig. 4.12A), a late intra oceanic arc tectonic setting is inferred for the E41 intrusive rocks. Many of the samples plot in the continental arc + post-collisional arc on Figure 4.12A, whereas most samples plot in the late oceanic field on Figure 4.12B. A late oceanic arc tectonic setting, rather than a continental arc setting is supported by relatively high LILE and low LREE and HFSE of the E41 intrusive rocks.

4.5.2.6 Interaction of mafic and silicic magmas

The temporal relationship of alkalic mafic magmas with Cu-Au mineralisation has been highlighted as an important factor for the genesis of porphyry deposits (Keith et al., 1998; Hattori and Keith, 2001; Maughan et al., 2002; Lickfold et al., 2007). Based on igneous geochemistry, textural characteristics and mass balance constraints, it has been suggested that a large proportion of the sulfur and chalcophile elements in porphyry systems may have been derived from mafic alkaline melts that were episodically injected into the crystallising felsic magma chamber (Keith et al., 1998).

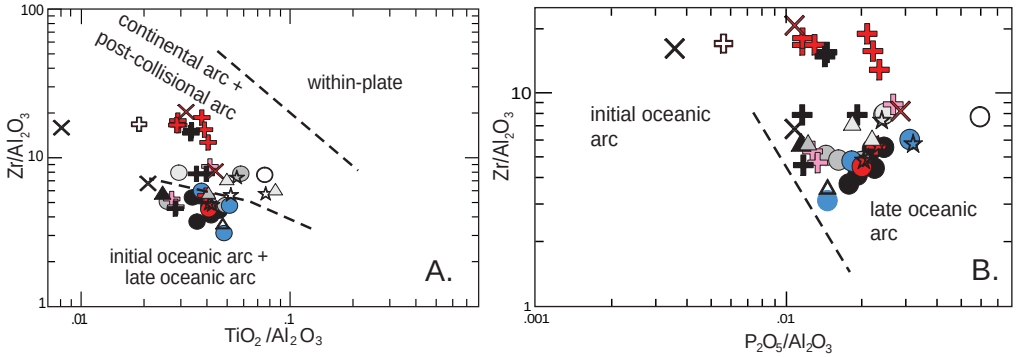

Figure 4.12 Tectonic setting discrimination diagrams. **A.** Zr/Al_2O_3 vs TiO_2/Al_2O_3 diagram discriminates between within-plate, continental arc and island arc (Muller et al., 1992). **B.** Zr/Al_2O_3 vs P_2O_5/Al_2O_3 discriminates between initial oceanic arc and late oceanic arc (Muller et al., 1992). Symbols are same as in Figure 4.6. Geochemical data listed in Appendix C.1.

Cooling and quenching of the hot mafic magmas on the contact with the cooler, crystallising felsic melt is thought to be responsible for release of volatile- and metal-charged aqueous fluids. The involvement of these fluids sourced from mafic melts may contribute significantly to the overall mineralisation of the magmatic-hydrothermal system (Hattori and Keith, 2001, Maughan et al., 2002). Intrusion of mafic magma into a silicic magma chamber has been proposed as a trigger for the formation of the Northparkes deposits by Lickfold et al. (2007), and for the Bingham Canyon porphyry deposits by Keith et al. (1998). At E41, the synchronicity of pyroxene-phyric dykes and Au mineralisation suggests that similar processes of interaction between silicic and mafic magmas may have been operating during mineralisation at E41 and possibly in other gold epithermal centres at Cowal. The monzodioritic enclaves within the mafic monzonite intrusion also suggest that the mafic melts were injected into a more felsic magma chamber prior to mineralisation at E41.

4.5.3 Macquarie Arc magmatism

Figure 4.13 integrates geochemical data from the CIC, Northparkes and Cadia districts. The P_2O_5 versus MgO diagram (Fig. 4.13A) shows strong high-K calc-alkaline to shoshonitic signature for the E42 lava and the E41 pyroxene-phyric dykes. A shoshonitic magmatic affinity for the E42 lava and the E41 pyroxene-phyric dykes is also apparent on the P_2O_5/Al_2O_3 versus K_2O/Al_2O_3 diagram (Fig. 4.13B). On both diagrams the E41 intrusive rocks overlap with the Cadia and Northparkes rocks. Most intrusives from CIC, Northparkes and Cadia are characterised by similar fractionation trends related to late apatite crystallisation (Fig. 4.13A).

The Ce/Yb versus Ta/Yb diagram (Fig. 4.13C) discriminates between tholeiitic, calc-alkalic and shoshonitic magmatic affinities (Pearce, 1982). The E41 intrusions overlap the field defined by rocks from Northparkes and Cadia, and have high-K to shoshonitic compositions (Fig. 4.13C). On the Th/Yb versus Ta/Yb diagram (Fig. 4.13D), all of the intrusions from E41, Northparkes and Cadia straddle the boundary between high-K and shoshonitic. The E43 and E35 intrusions are characterised by much lower Ta/Yb ratios and deviate from the cluster defined by the E41, Northparkes and Cadia, consistent with a calc-alkaline magmatic affinity for E43 and E35, as proposed by Crawford et al. (2007b).

The ratios of $[Gd/Yb]_N$ versus $[La/Sm]_N$ (Fig. 6.13E) are relatively insensitive to fractionation. On this diagram, the E43 and E39 intrusive rocks (Phase 2) are clearly discriminated from the fields defined by Northparkes and Cadia (Phase 4; Fig. 4.13E). In contrast, the E41 rocks have low $[Gd/Yb]_N$ values at high $[La/Sm]_N$ concentrations and overlap the Northparkes and Cadia data. The Goonumbla and Wombin Volcanics

Geochemical synthesis of the Macquarie Arc;
Cowal Igneous Complex, Northparkes and Cadia

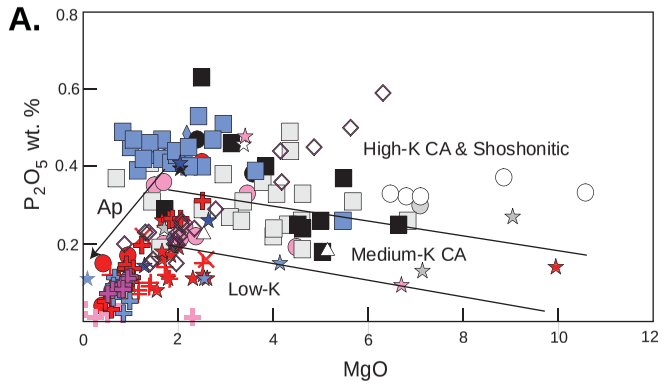

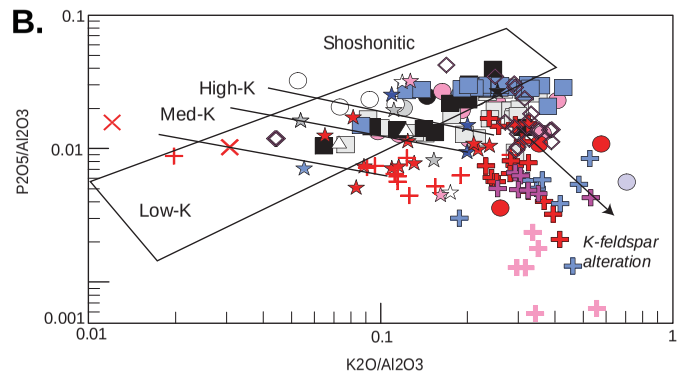

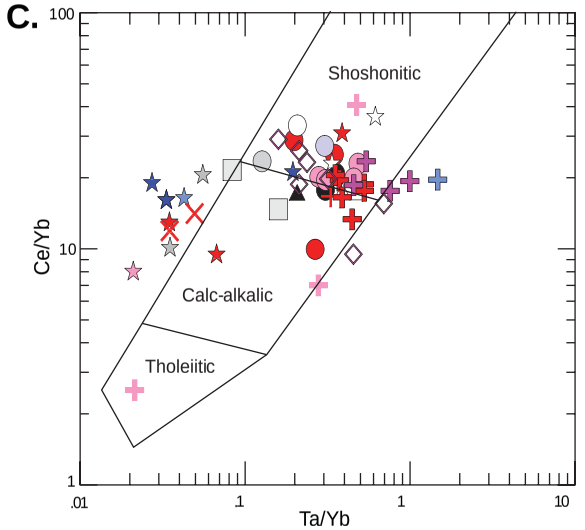

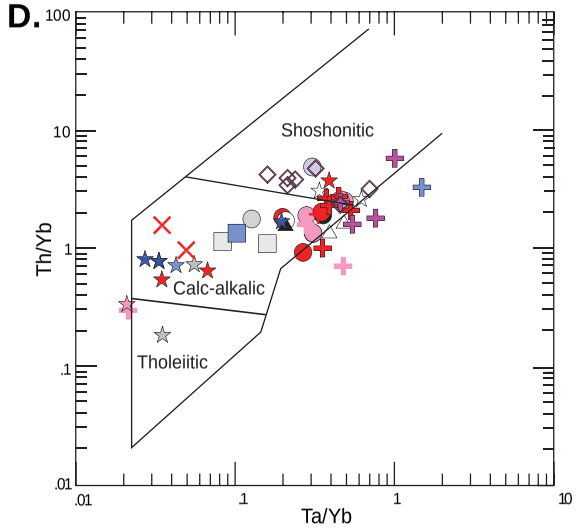

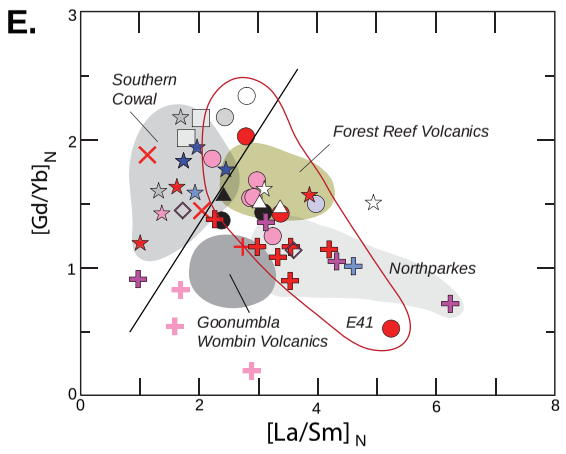

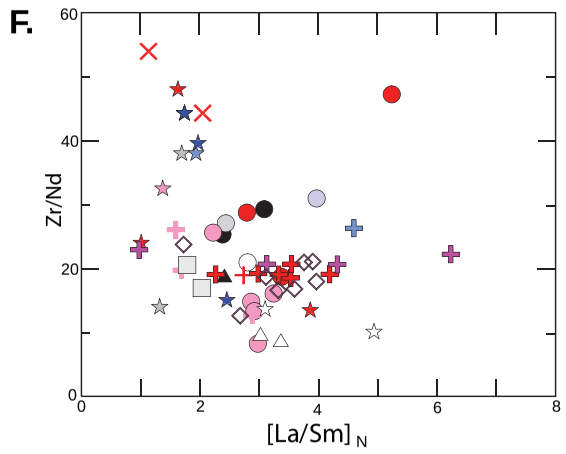

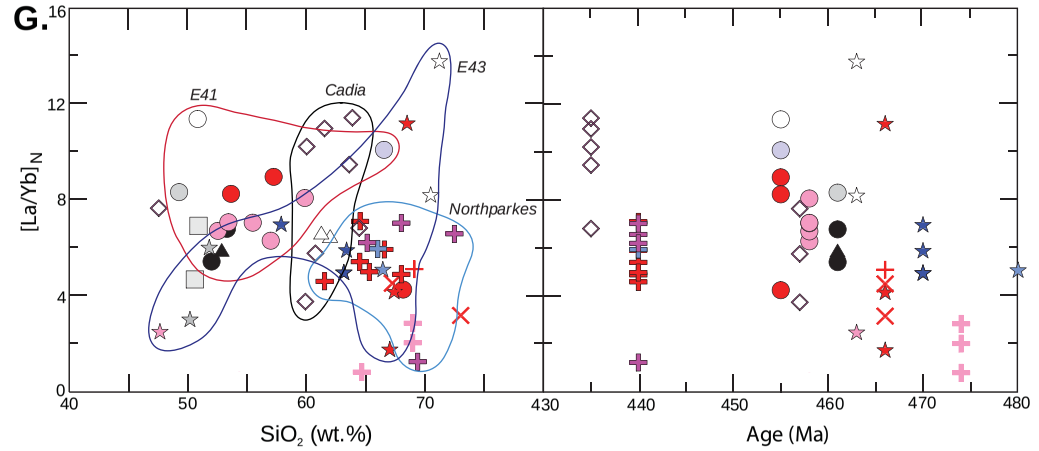

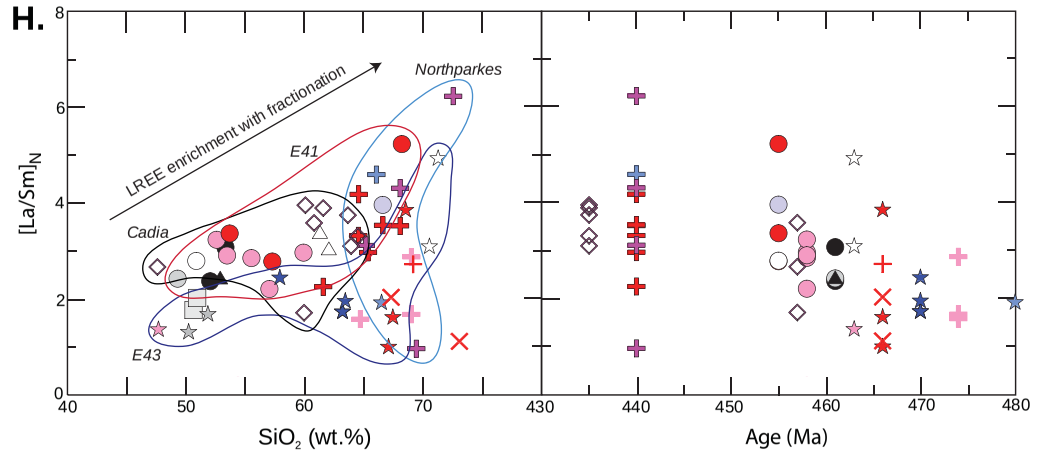

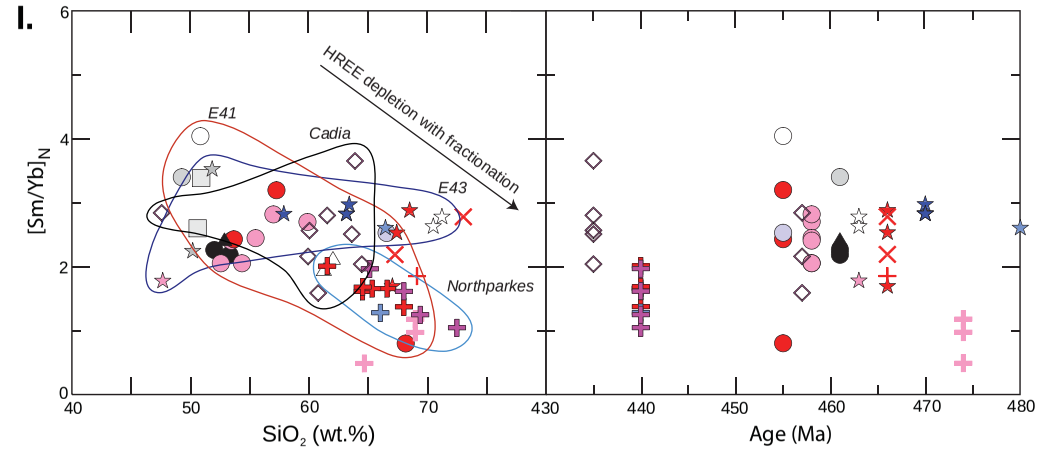

Figure 4.13 Geochemical synthesis of the Macquarie Arc. **A.** P_2O_5 vs MgO (after Crawford et al., 2007a). **B.** P_2O_5/Al_2O_3 vs K_2O/Al_2O_3 (after Crawford et al., 2007a). **C.** Ce/Yb vs Ta/Yb (Pearce, 1982). **D.** Th/Yb vs Ta/Yb (Pearce, 1982). **E.** $[Gd/Yb]_N$ vs $[La/Sm]_N$. **F.** Zr/Nd vs $[La/Sm]_N$. **G.** $[La/Yb]_N$ shows total REE variations and their changes with time. **H.** $[La/Sm]_N$shows light REE variations and their changes with time. **I.** $[Sm/Yb]_N$ shows heavy REE variation and their changes with time. Absolute age determinations are presented in Table 3.3 for CIC intrusive rocks. The geochronological data for intrusives of Northparkes and Cadia are taken from Lickfold (2002; Appendix C.1) and Wilson (2003 and sources therein; Appendix C.1), respectively.

Legend

North Cowal
- Monzogranite

E46
- Lava

E42
- Muddy Lake diorite
- Basaltic and andesitic dykes
- Lava

E41
- Muddy Lake diorite
- Pre-mineralisation dykes
- Mafic monzonite + hybrid zone
- Quartz-monzonite + Aplites
- Pyroxene-phyric dyke
- Syenite

E40
- Lamprophyre
- Muddy Lake diorite

E43
- Lava
- Diorite porphyry
- Plagioclase-phyric dykes
- Granodiorite
- Pyroxene-phyric porphyry
- Quartz-feldspar porphyry
- Late monzonite

E35
- Granodiorite

E39
- Granodiorite

Northparkes
- Biotite-quartz monzonite and biotite-quartz monzonite porphyry (early-mineralisation)
- K-feldspar-phyric quartz monzonite porphyry (syn-mineralisation)
- Augite-biotite-K-feldspar-quartz monzonite porphyry (late-mineralisation)

Cadia
- monzonites (Cadia Far East, Cadia Hill, Cadia Quarry) and mafic monzonite (Ridgeway)

(Northparkes district) and the Forest Reef Volcanics (Cadia district; Fig. 4.13E; fields taken from Crawford, 1999) are temporally and spatially associated with mineralising intrusions at Northparkes and Cadia, respectively. These rocks are characterised by low MREE and high LREE, and these geochemical fields overlap with some of the E41 samples (Fig. 4.13E). Similar geochemical signature for E41 intrusive rocks and the Northparkes and Cadia suites are also apparent on the Zr/Nd versus $[La/Sm]_N$ diagram (Fig. 4.13F).

The Northparkes and Cadia intrusions are generally more evolved compositions than the E41 intrusives (Fig. 4.13G). They have higher SiO_2 contents, and abundant biotite phenocrysts (Wilson et al., 2003; Lickfold et al., 2003). Biotite does not occur in the E41 intrusions. Although SiO_2-rich, the Northparkes intrusions have lower overall REE enrichment ($[La/Yb]_N$ =1.2-7.0; Fig. 4.13G) relative to the E41 rocks and Cadia ($[La/Yb]_N$ =5-12). The E41 and Cadia have very similar absolute REE concentrations. In general, the LREE increases with fractionation from E41, through Cadia to Northparkes (Fig. 4.13H) and the HREE component generally decreases with fractionation for E41, Cadia and Northparkes, respectively (Fig. 4.13I). With respect to absolute age estimates, it appears that there is a general increase of overall REE with time for both in the CIC to Cadia district.

As has been shown above, the E41 intrusives have several geochemical features similar to those at Northparkes and Cadia districts, which likely indicate similar source compositions and partial melting regimes. Their different ages, however, suggest that the mineralising intrusives at E41, Northparkes and Cadia were produced at least 15 m.y. apart from each other and/or the shoshonitic intrusives were intruded episodically over that period of time. In addition to their similar geochemical features, their intrusive sequences are also comparable. In all three districts, the intrusive sequence returns to mafic compositions (Lickfold, 2002; Wilson, 2003; Lickfold et al., 2007) with Northparkes porphyry mineralisation being specifically attributed to the involvement of mafic melts during mineralisation (Lickfold et al., 2007).

Given that both E41 and the genesis of the Northparkes Cu-Au porphyries have been linked to the involvement of mafic alkalic melts during mineralisation, it maybe that these processes of injection of mafic melts into shallow-mid(?) crustal magma chambers were episodically occurring across the Macquarie Arc, producing various styles of mineralisation. If these processes operated from Late Ordovician (Cowal) to Early Silurian (Northparkes), then this implies that the tectonic setting necessary for the tapping of shoshonitic melts from a subduction-modified mantle source was sustained for a prolonged period or was episodically re-created.

4.5.3.1 Partial melting regime

The thickness of the crust influences the mineralogy of the partial melting regime, and can therefore influence REE contents (Kay et al., 1999). Garnet is stable in thickened crust (60-70 km) and accommodates heavy REE. Melts crystallising in deep crustal settings are typically HREE-depleted and have high La/Yb ratios (Kay et al., 1999). In contrast, MREE are in amphibole and clinopyroxene, which are stable in thinner crust (Kay et al., 1999; Davidson et al., 2007). The HREE portions of all of the E41 spidergrams (Fig. 4.9) are relatively flat, implying that garnet was not in equilibrium with the melt during partial melting or crystallisation (Winter, 2001; Richards and Kerrich, 2007). It is therefore concluded that the E41 intrusions did not undergo early fractionation in a garnet-stable regime. Instead, amphiboles are assumed to have been the stable mafic minerals crystallising. Major and trace element compositions of the diorites and monzonites are interpreted to be consistent with early low-pressure fractionation of clinopyroxene, followed by later fractionation of amphibole, plagioclase, Fe-Ti oxide and apatite (Gill, 1981). The pyroxene-phyric dyke has a distinctively high $[La/Yb]_N$ value (Fig. 4.13G) when compared with other E41 intrusives. The alkalic pyroxene-phyric dyke also has higher HREE and LREE than the mafic monzonite and is inferred to have been sourced from greater depths.

It is concluded that mineralising intrusive rocks of the CIC (regardless of age and the style of mineralisation) were generated via mid-deep (40-50 km depth) 'wet' amphibole-bearing crystallisation of parental basalts derived from subduction-modified upper mantle. The rocks generated from amphibole-stable melts intruded into Phase 2 rocks (i.e., the majority of the E43 rocks, except the quartz-feldspar porphyry and the E35 granodiorite) that were likely produced at shallower low-pressure crustal levels (<35 km) via a dry pyroxene + plagioclase-bearing fractionation assemblage.

4.6 Summary

Major conclusions from this whole-rock geochemical study of the E41 intrusive complex and the CIC are that:

- E41 is associated with an intrusive complex that evolved from mafic towards felsic and then back to mafic compositions, with evidence for both mafic and felsic magmatism at the time of mineralisation.
- The E41 intrusive complex had high-K calc-alkaline to shoshonitic magmatic affinities around the time of gold mineralisation, consistent with an alkalic association for gold mineralisation.
- The upper crustal magma chamber that initially generated medium- to high-K calc-alkaline dioritic suites and subsequently high-K calc-alkaline to shoshonitic

mafic monzonite and more fractionated, SiO_2-rich dykelets was episodically recharged with shoshonitic mafic melts and the addition of mafic melts into the magma chamber contributed to mineralisation at E41.

- The E41 intrusives have trace element and REE characteristics similar to the alkalic mineralising intrusions of Cadia and Northparkes.
- The syn-mineralisation intrusions of the CIC (at epithermal and porphyry centres) are characterised by high absolute REE concentrations with LREE enrichment, which discriminates them from the weakly or non-mineralised intrusions.
- Trace element and REE compositions of the CIC are consistent with derivation from an isotopically primitive, but chemically enriched, mantle source region.

CHAPTER 5
Veins and Altered Rocks

5.1 Introduction

Mineralised domains of altered rocks that occur between the classic epithermal and porphyry end-member environments have only been documented by a few workers (e.g., Corbett and Leach, 1998) and can be difficult to categorise genetically. It is important, however, to recognise their significance as they may be vectors that point towards the center of magmatic-hydrothermal activity. Careful reconstruction of their original geometries and detailed analysis of temporal and spatial relationships between hydrothermal events are the fundamental keys to understand the evolution of the fluids responsible for mineralisation in such systems.

This chapter describes the hydrothermal alteration facies and mineralisation assemblages, including the varying styles of precious and base metal occurrences and their paragenetic relationships from E41.

5.2 Previous work

Prior to this study, no detailed analysis of hydrothermal alteration assemblages and vein mineralisation at E41 had been undertaken. Previous studies were restricted to internal unpublished reports to Barrick Gold of Australia Ltd. Several petrological descriptions from Barrick reports (Ashley, 2004; 2005) described samples located on the cross sections studied here, and these data are incorporated with citation into this chapter.

More comprehensive previous studies have been undertaken for the E42 deposit (McInnes, 1998; 2003; Miles and Brooker, 1998; Bastrakov, 2000; Borthwick, 2004; Strickland, 2005). Although E41 and E42 are only separated by ~1 km (Fig. 2.5) they have some hydrothermal features that distinguish them from each other, in addition to many common features. The most important hydrothermal characteristics of the E42 deposit are summarised in Table 5.1. The E46 and E40 prospects have been the subject of limited investigations (e.g., McInnes, 1997; Simpson and Cooke, 2006; Simpson, 2008; Table 5.1), and the relevant information from these studies is cited where appropriate.

The E46, E42 and E40 systems consists of Au-rich, quartz – carbonate – pyrite-base metal sulfide veins. Most of the Au mineralisation is hosted in quartz – pyrite – sphalerite ± carbonate ± adularia ± chlorite ± galena ± chalcopyrite veins (Table

TABLE 5.1 Hydrothermal alteration and mineralisation characteristics of E42, E46 and E40.

Endeavour 42

Hydrothermal alteration

Alteration phase	*Mineral assemblage*	*Style*	*Characteristics*	*Relation to mineralisation*	*Host Rock*	*References*
Propylitic alteration	Albite – chlorite ± epidote ± hematite/magnetite ± carbonate (calcite) ± actinolite ± biotite ± prehnite ± K-feldspar	Selective pervasive; epidote as aggregates and associated with veins	Replacement of phenocrysts and groundmass plagioclase to albite and mafic minerals to chlorite, and/or biotite, actinolite, magnetite	Pre-mineralisation	All rock types; epidote rare or absent from lava	Miles and Brooker, 1998; McInnes, 1998; Bastrakov, 2000; McInnes, 2003; Bywater et al., 2004
'Advanced' propylitic alteration	Chlorite – carbonate (calcite) – pyrite ± hematite ± leucoxene ± K-feldspar ± sericite	Selective pervasive to vein/veinlet style; clots and dissemination	Pyrite occurs as disseminations, blebs and stringers and halos around gold bearing and veins; leucoxene is abundant close to shear zones; hematite and pyrite formed from alteration of Fe Ti oxides; mafic minerals are altered to black coloured chlorite ± carbonate ± quartz ± leucoxene ± pyrite	Low gold grades (0.1-0.3g/t); syn-mineralisation	Diorite; trachyandesite lava; lower volcaniclastic unit; absent from post -mineralisation dykes	
K-feldspar – quartz alteration	K-feldspar – quartz	Patchy, blebs, halos around mineralised veins	This alteration has overprinted and is best developed in 'advanced' propylitic alteration; pink colour has been attributed to hematite dusted plagioclase and K-feldspar	Associated with mineralised veins; syn-mineralisation	Restricted to trachyandesite lava; locally within volcaniclastic and diorite	
Phyllic alteration	Sericite ± quartz ± carbonate (ankerite) ± pyrite ± leucoxene ± albite ± chlorite ± tourmaline ±	Pervasive bleaching (yellow to green), texturally destructive; halos around veins, faults and tectonic and hydrothermal vein breccias	Well developed in the upper part of the deposit, moderate and weaker at deeper levels; locally appears to be coeval with 'advanced' propylitic alteration; strongly developed around faults and breccias, weakly developed away from fractures; several generations of phyllic alteration had affected the deposit	Barren or intimately associated with mineralisation; early-, syn- to post mineralisation	All host rocks, most prominent within the upper volcaniclastics	

Mineralisation features

Stage	*Vein assemblages*	*Style*	*Characteristics*	*Host Rock*	*Structural control*	*References*
Pyrite-gold mineralisation	Quartz ± carbonate ± sulfides (pyrite) ± adularia	Straight-sided ('dilational') veins	Comb textures present locally; commonly sericite – adularia halos associated with these veins, associated with the 'advanced' propylitic alteration;	Greatest density in trachyandesite unit, veins are thicker and generally less common in diorite	Two major structural sets control mineralisation: (1) steep fractures: 331/73 NE, 069/76 SE; and (2) inclined fractures: 101/42 SW, 185/39 W	McInnes,2003; Henry, 2008
Base metal-gold mineralisation	Quartz – carbonate – chlorite – pyrite - chalcopyrite - Fe-poor sphalerite - galena ± hematite ± tetrahedrite-tenantite ± gold-electrum	Veins, infill in pyrite-bearing straight-walled veins, and infill in breccias and shears	Galena – sphalerite – chalcopyrite – gold commonly occur in fractured pyrite, pyrite from the early stage mineralisation appears to be intimately associated with gold occurrences	All host rocks		

TABLE 5.1 (Cont.)

Alteration phase	*Mineral assemblage*	*Style*	*Characteristics*	*Comments/host rock and relation to mineralisation/ structural control on mineralisation*	*References*
Endeavour 46					
Hydrothermal alteration					
Phyllic alteration	Sericite ± chlorite ± carbonate; K-feldspar; minor epidote and ankerite	Pervasive, selective pervasive, vein halos	Pervasive chlorite, sericite (muscovite-illite) and selective replacement of aphyric and feldspar-phyric clasts; K-feldspar forms halo and locally clots; sericite ± chlorite ± carbonate alteration halos associated with mineralised veins	Bleached zones of sericite and chlorite alteration mark mineralised zones; volcano-sedimentary succession with volcanic and volcaniclastic breccias/ sandstones/ mudstones; lava; diorite-gabbro sill (Muddy Lake diorite)	Munroe et al., 2005, Simpson and Cooke, 2006
Mineralisation features					
Vein stages: broadly analogous to major mineralisation stage at E42 deposit	(1) Quartz – carbonate – pyrite – sphalerite ± galena ± chalcopyrite; (2) quartz – carbonate – pyrite; (3) monomineralic pyrite stringers; (4) Quartz – carbonate – pyrite – chlorite – chalcopyrite	Vein, veinlets and minor dissemination	Mineralisation commonly related to shear zones, irregular vein and veinlets scattered throughout;	Mineralisation strongly developed in volcanic and volcaniclastic units, weak mineralisation in coherent facies; no apparent lithologic control on mineralisation; two pods of mineralisation aligned roughly to the north	
Endeavour 40					
Hydrothermal alteration					
Silicification	Quartz	Pervasive	Imparts bleached occurrence to the host rock, local pink colour of sericitic alteration may is attributed to hematite dusted K-feldspar	Syn-mineralisation; volcano-sedimentary succession dominated by mudstone and local sandstone	McInnes et al., 1998; Munroe et al., 2005
Sericitisation	Sericite – carbonate – pyrite – chlorite	Halos associated with veins			
Mineralisation features					
Poorly developed mineralised system; analogous to major vein stages at E42	Quartz – pyrite – chlorite – hematite – K-feldspar – pyrrhotite ± Au; minor epidote veins	Common thin-pyritic stringer veinlets; dissemination; rare parallel-sided veins	Quartz parallel-sided veins are rare and well mineralised; common pyrite stringers veinlets associated with sericite haloes	Mudstone; l shallow - moderate dip, with northwest and north trends	

5.1). Locally significant mineralisation has also been encountered in quartz – sulfide-cemented hydrothermal breccias ('QSB'), and pyrite 'stringer' veins and quartz- and sulfide-rich 'shear' veins (McInnes, 2003; Bywater et al., 2004). McInnes (2003) proposed that gold mineralisation formed during two main stages at each deposit.

5.3 E41 hydrothermal system

5.3.1 Terminology

The alteration terminology used in this thesis is largely based on Titley (1982). Definitions of terms used herein to describe various alteration facies and mineralisation features are listed in Table 5.2.

TABLE 5.2 Definition of alteration and mineralisation terminology used in this thesis, based on Titley (1982).

Term	Definition
Alteration facies	Equilibrium mineral assemblage that has formed by alteration of pre-existing minerals
Pervasive alteration	Alteration of the rock that has resulted in the complete change of rock compositions, minerals and textures
Selectively pervasive alteration	Alteration in which only specific minerals in the host rock have been altered. This alteration typically preserves or enhances the rock texture
Vein	A fracture >5mm wide that is partially or totally infilled by secondary minerals
Veinlet	A fracture <5mm wide that is partially or totally infilled by secondary minerals
Stringer	A discontinuous wavy fracture (≤ 5mm) that is partially infilled by secondary minerals
Multi-stage vein	A fracture (vein) that has undergone reopening which has resulted in secondary hydrothermal infill
Vein halo/alteration envelope	Alteration (pervasive or selective pervasive) that occurs in the wall-rock immediately adjacent to a vein or veinlet
Weak, moderate, intense	Describes the relative intensity of alteration based on visual examination

5.3.2 General characteristics

E41 contains a complex array of alteration and mineralisation features. Two gold-mineralised zones, known as west and east pod, have been identified at E41. These zones of mineralisation have largely been defined on the basis of assay data but also partly on mineralogical and structural criteria (presence and absence of fracture sets). The ore zones are outlined by >0.4 g/t Au grade contours on Figure 3.2. Some mineralised veins identified during this study were observed outside of the two ore zones (illustrated below).

E41 is characterised mainly by vein-style mineralisation. Significant Au grades are also associated with faults, shear zones and reactivated fractures. Some pyrite disseminations in the altered wallrocks are highly mineralised. Vein morphologies and shapes vary across the deposit with the most common vein type being straight-walled and parallel-sided. Multi stage veins (locally with banded textures) are the second

Idealised paragenetic sequence for the Endeavour 41 deposit, east and west pod

East pod

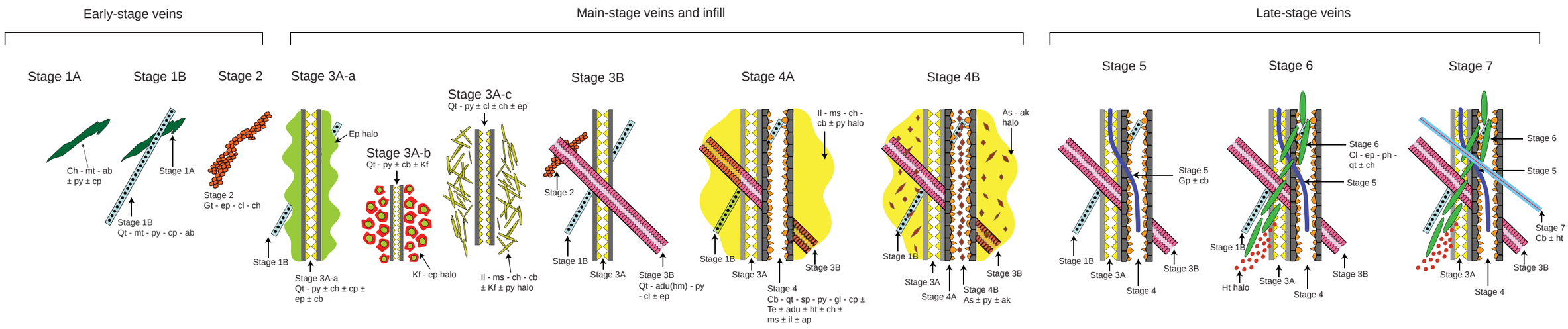

West pod

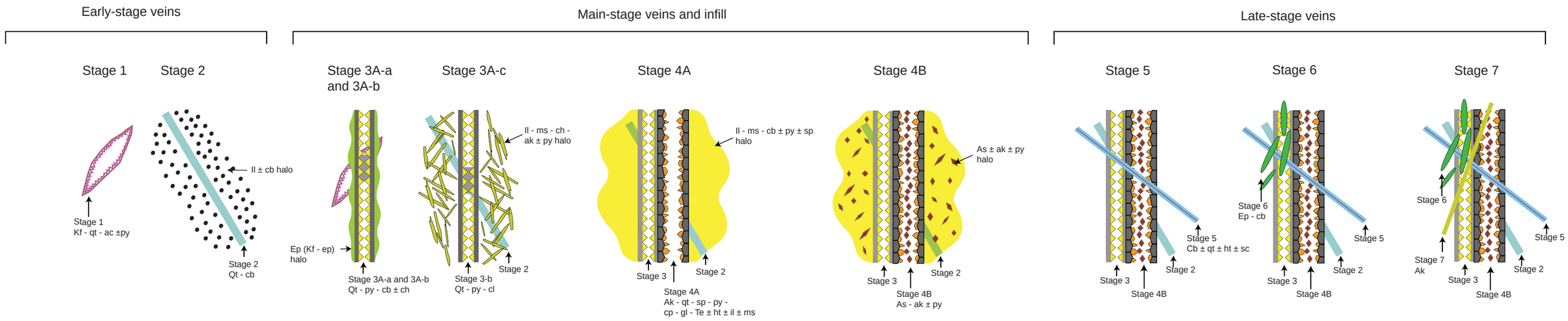

Figure 5.1 Paragenetic sequence for both pods of gold mineralisation at Endeavour 41, showing vein stages from oldest to youngest (left to right). Detailed descriptions are provided in Table 5.4 and 5.6. Abbreviations: ab=albite, ac=actinolite, adu=adularia, ak=ankerite, ap=apatite, as=arsenopyrite, cb=carbonate, ch=chlorite, cp=chalcopyrite, ep=epidote, gt=garnet, gl=galena, gp=gypsum, ht=hematite, il=illite, Kf=K-feldspar, ms=muscovite, sc=specularite, sp=sphalerite, qt=quartz, sc=specularite, Te=tellurides, ph=prehnite, py=pyrite

most abundant vein type. They record complicated histories of vein reactivation and reopening. Veins that have undergone brecciation and multiple hydrothermal infill events are the third major category of veins.

Barrick geologists have documented three major vein types based on morphological and compositional features, namely: 'dilational' veins, 'shear' veins and 'quartz sulfide breccia-('QSB') veins (Smolonogov, 2003). This terminology has been used in later research projects and company reports (e.g., McInnes, 2003; Borthwick, 2004; Strickland, 2005). Because some veins at E41 do not conform to this classification scheme readily, in this thesis, all vein types are described and classified on the basis of their mineralogy, rather than their morphology.

An alteration and mineralisation paragenesis for E41 has been established through detailed observations of crosscutting and overprinting relationships. Figure 5.1 shows simplified vein paragenesis for east and west pod. The alteration facies and vein stages have been classified into three major groups: 'early-stage' (pre-mineralisation), 'main-stage' (syn-mineralisation), and 'late-stage' (post-mineralisation). Where possible, the temporal relationships between alteration facies and vein assemblages have been constrained primarily on the presence or absence of vein halos. Relationships between alteration facies and the intrusive history have also been considered.

The host rock and hydrothermal features of east and west pods are different in several ways. Therefore, the veins and altered rocks from the two pods are described separately.

5.3.3 Short wave infrared spectroscopy

Illite and muscovite were initially logged as 'sericite'. SWIR infrared spectroscopy was then applied to define the mineralogical composition of 'sericite'. SWIR spectrometry was conducted using a portable infrared mineral analyser (PIMA). A total of 566 analyses were carried out on pervasive sericite and on sericite alteration halos (Appendix D.1). The obtained data show that most of the sericite is illite with subordinate muscovite (Fig. 5.2). Because both illite and muscovite typically occur together in each sample, this alteration type is referred to as illite – muscovite.

5.4 East pod

The east pod has produced an embayment in the magnetic high defined by the Muddy Lake diorite on the eastern side of the geophysical image of the Cowal 'gold corridor' (Fig. 3.1). Within this embayment, hypogene gold is associated with several vein assemblages and minor sulfides disseminations. Gold mineralisation was localised at the contact between volcaniclastic units and the diorite sill, and is located less

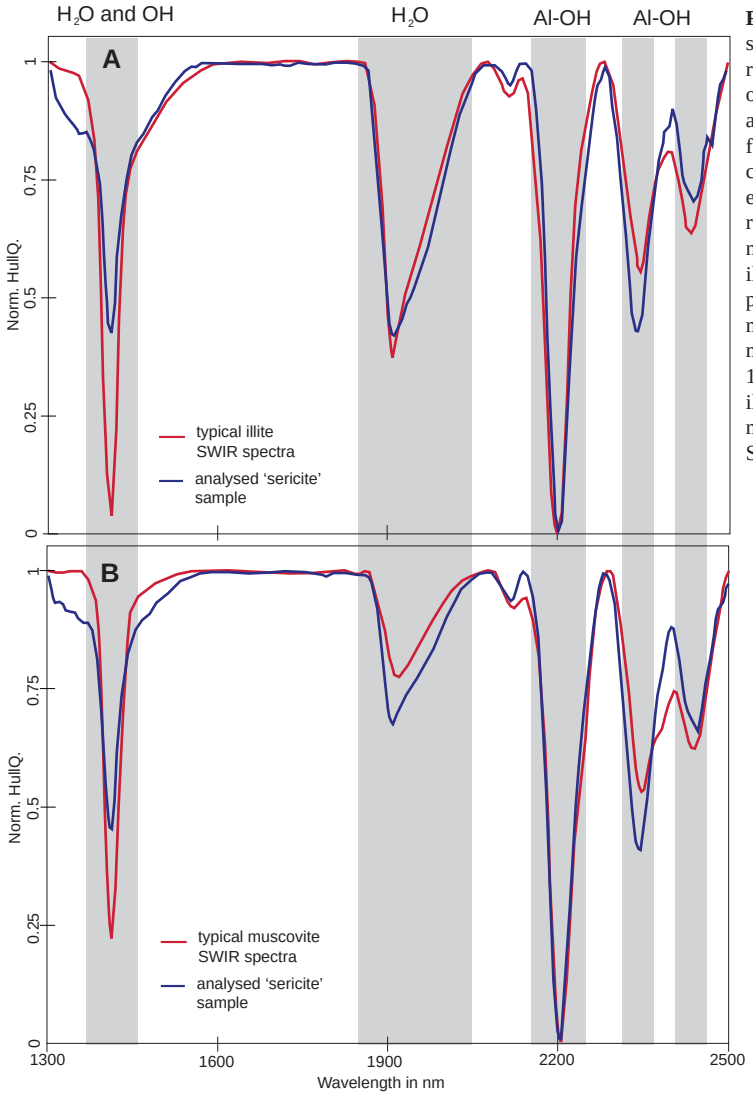

Figure 5.2 Representative PIMA spectra for 'sericite'. **A.** Blue line shows representative spectral signature typical of that obtained from most of the analysed samples. The 'sericite' spectra fits with absorption bands that are characteristic for illite (red line; Pontual et al., 1997). **B.** Blue spectrum represents a less commonly observed muscovite that typically coexists with illite. Shaded areas highlight the principal absorption bands for illite. The major difference between illite and muscovite spectra is that the water 1900 nm absorption band is deeper in illite. Reference spectra of illite and muscovite were taken from The Spectral Geologist V.2.0 (TSG) library.

than 200 m below the present-day surface (Figs. 5.3 and 5.4). The hypogene zone of mineralisation is approximately 250 m in diameter, and up to 200 m thick. Apart from the main mineralised zone, volumetrically smaller domains of gold mineralisation are distributed randomly throughout east pod. Supergene gold occurs in the weathering profile, above the hypogene zone. The weathering profile is up to 120 m thick (Figs. 5.3 and 5.4).

Two main vein stages are associated with hypogene gold in east pod: quartz – pyrite veins and veinlets that contain minor carbonate and chlorite, and sphalerite-, galena-, pyrite-, and telluride-bearing 'carbonate-base metal sulfides' veins. Many of the mineralised fractures are closely associated with fault zones. Primary gold grades are between 1 - 1.2 g/t Au (McInnes, 2006). The grade of oxide gold mineralisation at east pod averages between 1.2 – 1.5 g/t, similar to the hypogene grades.

Alteration facies distribution - cross section 34900N

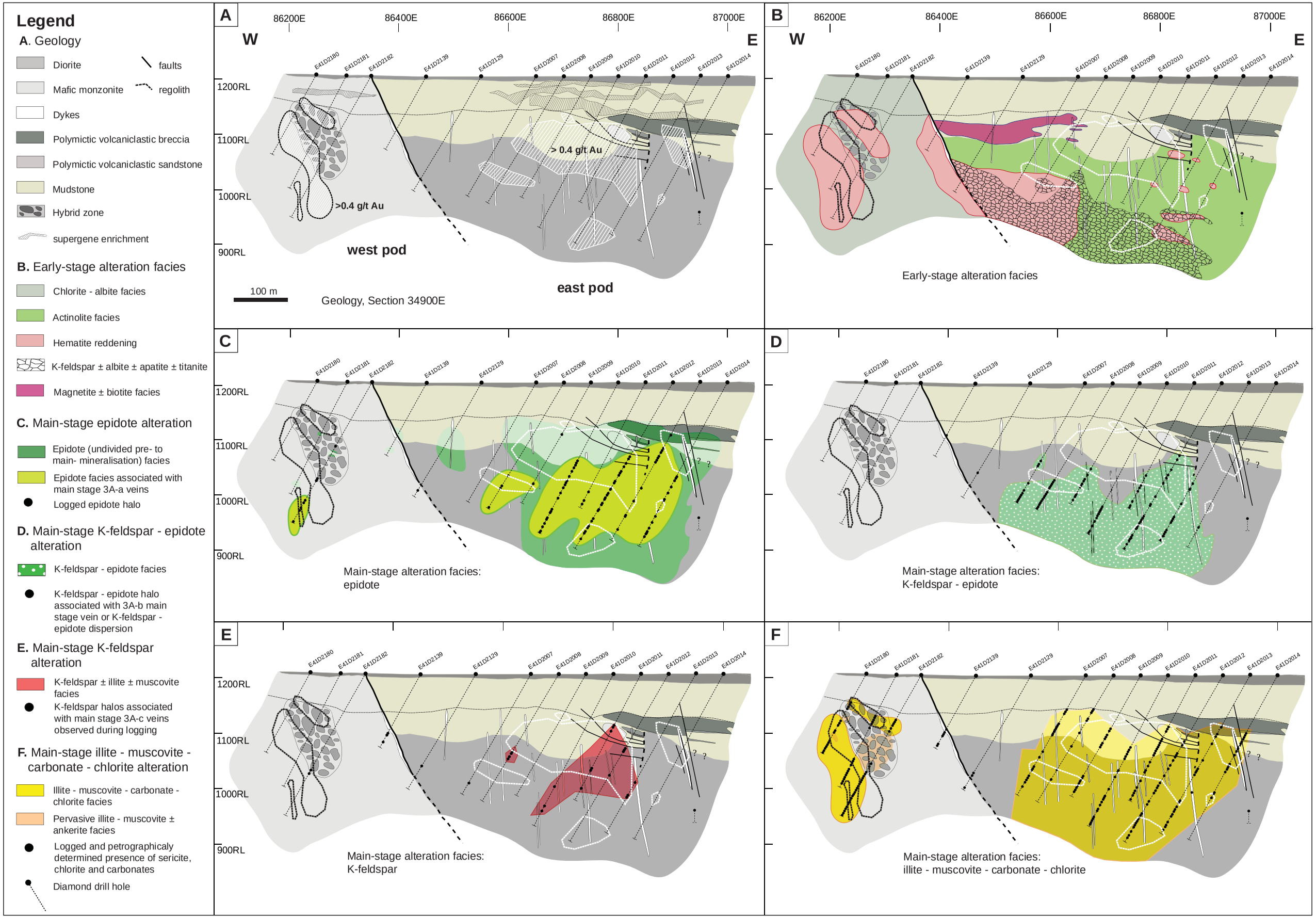

Figure 5.3 Alteration and gold grade distribution on cross section 84900N through both east and west pods. Alteration facies have been delineated in paragenetic order from oldest to youngest. **A.** Geology of section 84900N. **B.** Distribution of early-stage alteration assemblages. **C.** Undivided epidote alteration. Some of the epidote delineated on the section forms part of the pre-mineralisation actinolite facies. Main stage epidote forms zones that follow distribution of stage 3A-a veins. **D.** K-feldspar-epidote alteration facies distribution has been based on random dispersion and alteration halos associated with stage 3A-b. Green pattern illustrates the interpreted K-feldspar-epidote facies zone. **E.** K-feldspar alteration halos associated with stage 3A-c and 3B, locally K-feldspar is dusted by hematite. Red pattern shows the interpreted distribution of this facies. **F.** Illite - muscovite - chlorie - carbonate associated with mineralised veins 3A-c, 4A, and 4C. The light brown colour in west pod represents pre- to early mineralisation occurrence of sericite. The yellow broad zone illustrates interpreted the main gold-related assemblage distribution.

Alteration facies distribution - cross section 86800E

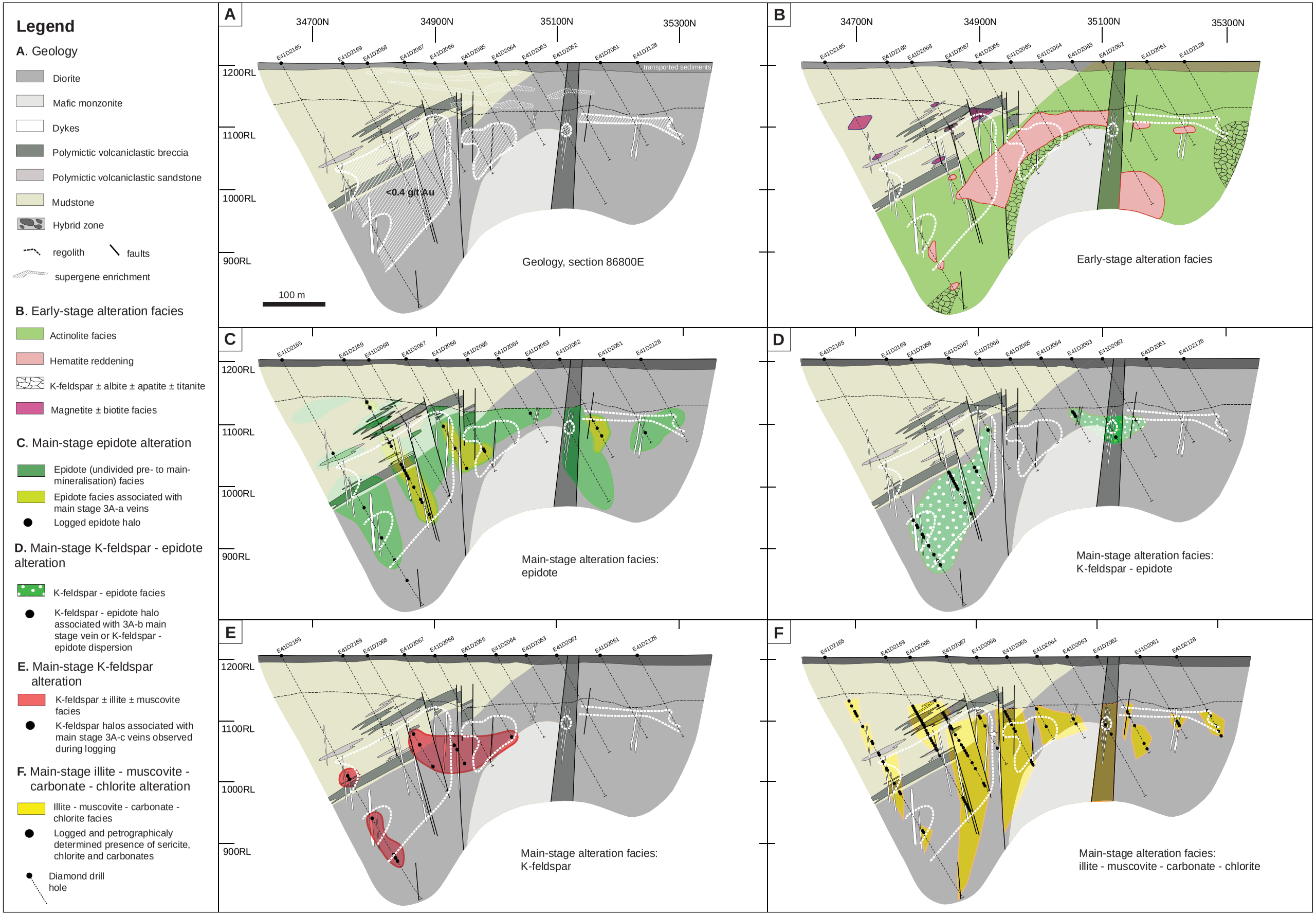

Figure 5.4 Alteration and gold grade distribution on cross section 86800E through the east pod. Alteration facies have been delineated in paragenetic order from oldest to youngest. **A.** Geology of section 86800E. **B.** Distribution of major early-stage alteration assemblages. **C.** Undivided epidote alteration. Some of the epidote delineated on the section forms part of the pre-mineralisation actinolite facies. Main mineralisation epidote zones follow distribution of stage 3A-a veins. **D.** K-feldspar - epidote alteration facies distribution has been based on dispersion and alteration halos associated with stage 3A-b. Green pattern illustrates the interpreted K-feldspar - epidote facies zone. **E.** K-feldspar alteration envelopes associated with stage 3A-c and 3B, locally K-feldspar dusted by hematite. Red pattern shows the interpreted distribution of this facies. **F.** Illite - muscovite - chlorie - carbonate associated with mineralised veins 3A-c, 4A, and 4C. The yellow broad zone illustrates the interpreted assemblage distribution.

Tables 5.3 and 5.4 summarise the alteration facies and vein stages of east pod. Seven vein stages and 11 hydrothermal alteration facies have been recognised. Alteration styles are typically pervasive, and commonly have completely obscured primary textures and mineralogies. Alteration facies are described below according to the paragenetic sequence established during the current study (Fig. 5.1), and overprinting relationships are illustrated schematically in a series of cross sections presented on Figures 5.3 and 5.4.

5.4.1 Early stage alteration facies and veins

5.4.1.1 Magnetite alteration facies

The volcano-sedimentary units of the east pod have been altered to a moderate to intensely developed pervasive magnetite – chlorite – albite ± biotite ± K-feldspar ± epidote ± pyrite assemblage (Table 5.3). The magnetite alteration facies typically occurs as massive zones or clot-like domains that have overprinted primary features within the mudstones. Magnetite and chlorite are dominant and pyrite is minor. Magnetite has selectively replaced coarser bands within the mudstone. Some patchy occurrences of magnetite – chlorite alteration have pale grey to green selvages of albite. Albite also occurs as halos around monomineralic magnetite veinlets (Figs. 5.5A, B and 5.6A) and is intergrown with magnetite in elongated patches (Fig. 5.5A). Biotite is also intergrown with magnetite and has locally formed clots (Figs. 5.5B and F). The biotite clots are fine-grained (~40 μm) and virtually impossible to recognise in hand specimen. The presence of biotite was confirmed by EDS analysis. Locally, epidote of uncertain timing occurs in the distal parts of the selvages around chlorite – magnetite veins. Sodium cobaltinitrite staining has revealed the presence of K-feldspar in albitic patches. K-feldspar occurs as both an early- and main-stage alteration phase, therefore its exact timing is difficult to constrain.

Well-preserved magnetite alteration was identified in three drill holes on the western flank of east pod (strong alteration in DDH: E41D2129, E41D2007 and weaker at DDH: E41D2008; Fig. 5.3B). Magnetite alteration also occurs locally to the south of the mineralised centre (Fig. 5.4B). Biotite – magnetite alteration clots were detected only in drill hole E41D2129. Towards the centre of the ore body, magnetite-altered rocks have undergone pyrite alteration during main-stage illite – muscovite – carbonate – chlorite alteration. Although magnetite is best preserved away from the mineralised zones, moderate to strong magnetite alteration of the polymictic volcaniclastic breccia has been recognised near mineralised domains (e.g., DDH: E41D2067; Fig. 5.4B).

The exact timing of magnetite alteration is uncertain. It may have occurred during intrusion of the diorite, or it may have been synchronous with the actinolite

TABLE 5.3 Styles of alteration and the spatial and temporal distribution of alteration facies at east pod, E41.

Alteration assemblage/facies[1]	Major minerals	Minor minerals	Alteration intensity and styles	Spatial and temporal association
Early – stage alteration facies				
	Magnetite, albite, chlorite	± biotite ± K-feldspar ± titanite ± epidote	Moderate to intense pervasive and selectively pervasive alteration, localized in specific beds or patchy, irregular blobs; commonly albite has formed narrow halos around monomineralic magnetite veinlets; biotite together with magnetite occurs as clots; and as alteration envelopes around 1A veins	Occurs in mudstone on the western flank of the east pod and between east and west pod, 150 meters away from the known centre of gold mineralisation; temporally related to intrusion of diorite (?)
	Actinolite, magnetite, albite, chlorite	K-feldspar ± titanite ± epidote ± hematite ± chalcopyrite	Moderate to intense selectively pervasive alteration of diorite; actinolite together with magnetite replaced former clinopyroxene and hornblende phenocrysts; albite occurs as pseudomorphs of plagioclase and possibly K-feldspar phenocrysts; chlorite has locally replaced actinolite; magnetite and chalcopyrite occur in former mafic sites; locally ubiquitous strong reddening due to hematite dusting of feldspar component	Restricted to the diorite sill and some dyke suites including mafic and plagioclase-phyric dykes; actinolite has been partially to completely replaced by chlorite and carbonate in the mineralised zone
	K-feldspar, albite	Hematite (dusting of K-feldspar), apatite, titanomagnetite	'Patchy texture' intensely developed, selectively pervasive to pervasive alteration; K-feldspar has replaced the primary feldspar component and has partially pseudomorphed primary ferromagnesian minerals; albite is also present and occurs as cluster around actinolite-magnetite-chlorite domains, albite commonly has K-feldspar rims; this alteration facies is either pale-cream or pink coloured due to hematite dusted K-feldspar	This alteration facies occurs in the diorite sill at depths below 100 m (N-S section) and 200m (E-W section); K-feldspar – albite alteration assemblage occurs in the diorite near the mafic monzonite contact and extends laterally over 450 metres east (E-W section) from that contact
Main – stage alteration facies				
	Epidote	± pyrite ± carbonate ± leucoxene ± chlorite	Strong, texturally destructive alteration halos around 3A-a veins; pervasive throughout the deposit, with epidote locally overprinting the entire host rock	Related to 3A-a stage veins; occurs in the diorite and pre-mineral dykes suites, and clastic intervals; has overprinted early alteration; strong association of epidote with steep fault zones where epidote has altered pre-mineralisation dykes
	K-feldspar, epidote	Hematite (dusting K-feldspar) ± apatite ± titanite ± chlorite ± calcite	Weak to strong, selectively pervasive alteration or halos around 3A-b vein stage; has commonly overprinted 'patchy' texture where epidote clots have replaced actinolite – magnetite – chlorite domains and feldspars are pseudomorphed to strongly hematite dusted K-feldspar; this alteration facies is particularly distinctive due to its intensive apple green-red colouration and clotty appearance	Occurs at depth in diorite, only locally extends vertically up to 140 meters (E-W section) affecting actinolite – magnetite – albite altered diorite; in places traces of this facies occur randomly in dykes (e.g., trachyte dyke); and are associated with 3A-b veins

TABLE 5.3 (Cont.)

	Illite - muscovite, chlorite, carbonate	± pyrite ± leucoxene	Weak to strong, pervasive, selectively pervasive and/or alteration halos; commonly texturally destructive; in actinolite – magnetite –albite altered diorite this assemblage pseudomorphed secondary actinolite and epidote; illite – muscovite together with carbonate has replaced feldspars; leucoxene is randomly dispersed or formed halos (occurs up to 10 cm away from veins); the alteration facies is more intensely developed in carbonate when associated with carbonate base metal sulfide veins (stage 4)	This alteration is spatially and temporally related to stage 3A-c, 3B, 4A and 4C veins; locally difficult to recognize, particularly in dark green diorite but obvious in thin section; some veins of 3A-c and 3B stage lack illite – muscovite halos, as crystals of actinolite cut by these veins are still well preserved
	K-feldspar	± illite-muscovite, hematite (dusting K-feldspar)	Rare alteration halos associated with mineralised veins; K-feldspar has pseudomorphed plagioclase and albite; K-feldspar typically dusted by hematite	Temporally related to stage 3B veins and rarely to stage 3A-c
	Ankerite, arsenopyrite	± pyrite ± illite-muscovite	Weak to moderate selectively pervasive alteration, typically restricted to vein halos; brown ankerite commonly occurs with arsenopyrite and minor pyrite; locally, arsenopyrite has pseudomorphed clinopyroxenes; illite – muscovite replaced feldspars, in places fragments of wall rock are replaced by arsenopyrite	This alteration facies occurs as halos around hybrid veins (e.g., reopened 3A-c stage and filled with 4A and 4B) and some stage 4C veins
Post – mineralisation alteration facies				
	Albite, epidote	Chlorite, carbonate	Weak to moderate, selectively pervasive alteration; plagioclase replaced by albite and carbonate, ferromagnesian minerals altered to chlorite and carbonate, epidote disseminated in mafic sites and weak selectively pervasive replacement on plagioclase	Associated with post-mineralisation plagioclase-phyric (‘diorite’) dyke, locally abundant in post-mineralisation shear zones
	Carbonate, hematite		Selectively pervasive alteration, weakly developed, occurs as an infill of amygdules where carbonate clots are surrounded by hematite rims	Amygdaloidal dyke
	Illite, muscovite, carbonate, chlorite	Pyrite, clays	Strong pervasive alteration associated with faults; weak pervasive alteration of late dykes with mafic minerals altered to chlorite and carbonate and feldspars pseudomorphed to illite, muscovite, carbonates and clays	Associated with faults and post-mineralisation dykes; has overprinted early and main stage alteration facies

[1] Alteration facies are listed from oldest to youngest otherwise stated in text.

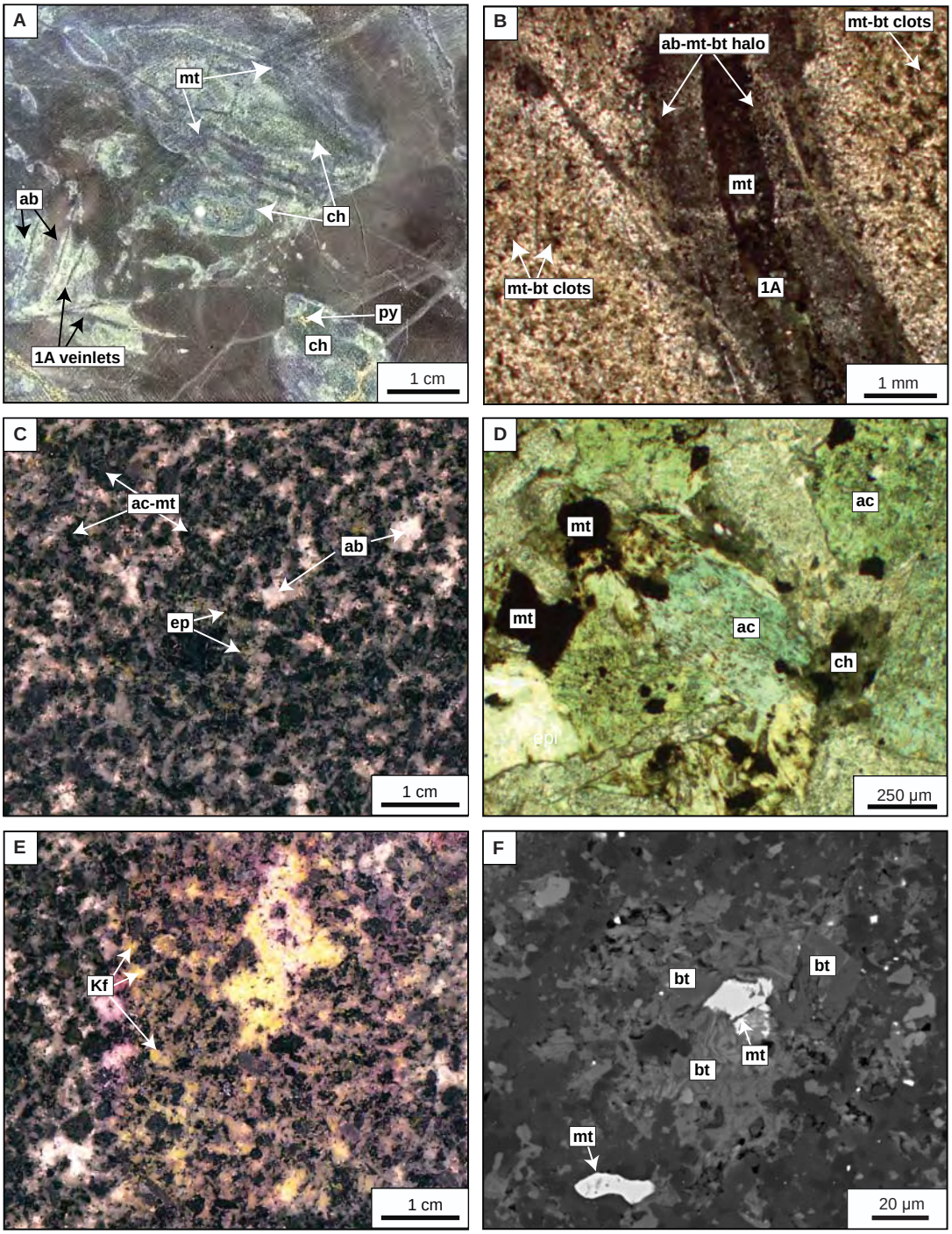

Figure 5.5 Early stage alteration facies. **A.** Magnetite - chlorite ± albite alteration of mudstone with thin monomineralic magnetite veinlets (stage 1A) associated with albite alteration halos (E41D2129; 135.1m). **B.** Photomicrograph (ppl) of magnetite - biotite - albite alteration in mudstone. The stage 1A veinlet has an albite - magnetite - biotite alteration halo (E41D2129; 132.7 m). **C.** Early actinolite - magnetite - albite ± K-feldspar ± titanite ± epidote ± chalcopyrite ± hematite alteration of diorite (E41D2010, 204.1m). **D.** Photomicrograph (ppl) of diorite showing actinolite - magnetite and epidote in former clinopyroxene and hornblende sites (E41D2062, 177.1m). **E.** K-feldspar stained sample of diorite showing that some former plagioclase crystals are altered to K-feldspar (E41D2010, 204.1m). **F.** BSE image of biotite - magnetite alteration facies in mudstone. Magnetite crystals are intercalated within biotite clots (E41D2129, 132.7m). Abbreviations: ac=actinolite, ab=albite, bt=biotite, ch=chlorite, ep=epidote, Kf=K-feldspar, mt=magnetite, py=pyrite, BSE=back scattered electron imaging.

TABLE 5.4 East pod vein stages, E41.

Vein[1] stage	Major minerals	Minor minerals	Alteration Halos / width	Average[A] Au grade (g/t)	Average[A] grade Cu (ppm)	Thickness	Form, mineral associations, internal vein texture and occurrence	Orientation
Early – stage veins								
Stage 1A	Chlorite, magnetite,	Albite, pyrite, chalcopyrite	Epidote, albite-chlorite; 2 – 40 mm wide; when with albite and chlorite, epidote occurs in the more distal parts of halos; distinctive halos have not been observed in diorite	0.4 (n=4)	550 (n=4)	≤ 1 – 30 mm	Irregular, diffuse vein walls, wispy and clotty veins and veinlets dominated by chlorite and magnetite; locally magnetite occurs as blobs (10 mm across) intergrown with pyrite; there are some monomineralic magnetite veins; magnetite absent towards the centre of mineralisation; this stage formed synchronous with early magnetite ± biotite alteration facies	Various orientations
Stage 1B	Quartz, magnetite	Pyrite, chalcopyrite, albite	Albite, chlorite; ≤ 10 mm wide	0.9 (n=1)	1600 (n=1)	2 - 5 mm	Continuous, sub-parallel, sharp-vein walls, wavy to straight-sided; pyrite occurs either in vein centre or on vein margins; magnetite randomly dispersed throughout veins, locally occurring as stringers along the vein axis; chlorite occurs in vein margins or is associated with pyrite	Associated with steep fractures and minor shallow fracture sets [2]
Stage 2	Andradite, epidote, calcite	Quartz, chlorite ± grossular	None or epidote; 2 - 3 mm wide	No data	No data	≤ 1-10 mm	Discontinuous or continuous, irregular blebby veins, wavy-sided, local clots; quartz and epidote are intergrown with each other; locally, garnet veinlets surrounded by epidote; this vein stage is restricted to volcaniclastic breccia and sandstone	Various orientations
Main – stage veins								
Stage 3A	a Quartz, pyrite	Chalcopyrite, chlorite ± carbonates	Epidote; 10 - 50 mm wide, strongly developed halos, locally with pyrite	0.8 (n=5)	638 (n=5)	2 - 30 mm	Continuous to discontinuous (terminate in 40 mm), irregular veins, locally massive, diffuse vein margins merge with epidote outer alteration halos; these veins generally lack quartz in the mudstone and the stage is dominated by pyrite; cross-cutting relationships with sub-stage 3A-b undetermined, cut by 3A-c	Typically associated with steep dipping fractures - generally NE striking, (75° SE dip); only locally rare discontinuous shallow dipping (~50° SE)
	b Quartz, pyrite	Carbonates, K-feldspar	K-feldspar-epidote; 30 - 40 mm wide, intensive and very distinctive apple green-red coloured halos	0.5 (n=5)	270 (n=5)	2 ≤ 10 mm	The morphology of these sub-stage veins is similar to stage 3A-a, they can be more irregular locally; some veins lack quartz and are dominated by epidote and pyrite; No cross-cutting relationships determined with sub-stage 3A-a as they are both commonly associated with steeply dipping fractures	Associated with steep fractures – generally NE striking and dip ~75ºSE
	c Quartz, pyrite	Calcite, chlorite ± epidote ± illite-muscovite	Illite-muscovite, chlorite or K-feldspar, ± pyrite; 10-30 mm wide	0.4 (n=5)	179 (n=5)	5 – 100 mm	Continuous, parallel straight-sided veins; quartz is typically the most abundant mineral; locally, comb quartz typically constitutes the first phase of vein infill; pyrite occurs as elongate wisps or along vein margins; epidote is attached to vein walls, and is most common in 3A-c veins hosted in clastic units; in places this sub-stage has been reopened; some wall rock fragments are present; locally reactivated veins have been filled by later stages (mineralised and barren)	Inclined, moderately to steep dipping fractures – generally ENE-striking 56ºSE dipping, and 2nd population E-striking 47º S to SE dipping
Stage 3B	Quartz-pyrite-K-feldspar (adularia)	Carbonate, hematite (dusting adularia) ± epidote	None, or K-feldspar or illite-muscovite ± pyrite; up to 30 mm wide	3.0 (n=7)	388 (n=7)	2 - 50 mm	Continuous, parallel sided vein walls, rarely wavy vein walls; red-pink adularia crystals typically occur in vein selvages and are locally dispersed throughout veins or in quartz overgrowths	Generally ENE-striking 65º SE (dipping); 2nd population ENE-striking 50º S (dipping)
Stage 4A	Calcite, ankerite, quartz	Pyrite, sphalerite, galena, chalcopyrite, adularia, tetrahedrite, hematite, apatite, Ag-Au-tellurides, Bi-tellurides, illite-muscovite, chlorite	Illite-muscovite, carbonate, black chlorite; up to 100 mm wide; in places halos are dominated by chlorite and sericite over carbonate	2.0 (n=13)	703 (n=13)	≤ 1 - 5 mm, up to 50 mm	Irregular, wispy-shaped and locally sheared veins or infill in pre-existed vein stages; veins are rarely parallel-sided; locally purple coloration of these veins due to fine grained sulfides and hematite incorporated into carbonates; some carbonates are pale-cream to white coloured; parallel-sided vein types are characterised by fine grained sugary pyrite; white carbonate intergrown with pyrite.	Shallow, moderate to steep dipping [2]
Stage 4B	Arsenopyrite	Ankerite ± pyrite, Bi-tellurides	Ankerite, arsenopyrite, pyrite, ± fuchsite; 60 mm wide	No data	No data	Infill	Occurs as infill in stage 4A veins and veins that have been reopened (associated with faults); arsenopyrite is fine grained occurring in irregular aggregates or course grains and euhedral associated with pyrite crystals	No data
Stage 4C	Quartz, pyrite, carbonate, galena, sphalerite	Chalcopyrite, arsenopyrite, illite-muscovite, chlorite, tellurides, tetrahedrite	Illite-muscovite, chlorite, leucoxene, carbonate, ankerite, arsenopyrite, pyrite; up to 1m wide	5.2 (n=12)	1346 (n=12)	20 mm - 3 m	('Quartz sulfide breccia') consists of stage 3A, 3B and 4A and 4B; this stage is typically associated with faults and fractures, commonly irregular, chaotic, brecciated and strongly altered; typically comprises fractured 3A and 3B quartz and pyrite which have been cemented by stage 4 carbonate, quartz, galena, chalcopyrite, sphalerite, tellurides and tetrahedrite, needle-like arsenopyrite crystals are scattered throughout the brecciated veins	Associated with steep faults and shear zones; ENE-striking 70º SE dipping; 2nd population NNE-striking 70º E dipping
Late – stage veins								
Stage 5	Gypsum	Calcite	None	None	None	2 – 5 mm	Continuous, wavy veins and massive coarse grained gypsum infill in faults; locally occurs as infill in mineralised multi stage opening veins	Various orientations, often associated with steep faults and shear zones[2]
Stage 6	Calcite, epidote	Prehnite, quartz ± chlorite	Red hematite halos (dusting feldspars) occur around some epidote veinlets; 50 mm wide	None	None	1 - 40 mm	Irregular, wavy, sinuous-shaped, randomly oriented veinlets; commonly have cross-cut each other to form erratic net veinlet systems; this stage occurs as a late infill in mineralised veins – particularly prehnite crystals; abundant wisps of white carbonate veinlets	Various orientations, in places tend to follow steep structures; e.g., ~ NE-striking 45ºNW dipping
Stage 7	Carbonate	± hematite ± quartz ± chlorite	None	None	None	1 - 10mm	Morphological nature and style is similar to stage 6; hematite colours range from purple through dark red to blood red; genetically associated with carbonate-hematite alteration facies; observed in post-mineral vesicular dyke	Various orientations

[1] Vein stage from oldest to youngest
[2] No structural measurements available for this stage due to lack of core orientation or broken core
* Structural data sourced from Barrick Gold Limited (unpublished data)
[A] Average grades determined by LA-ICPMS analyses of individual veins
n =number of analyses per vein stage

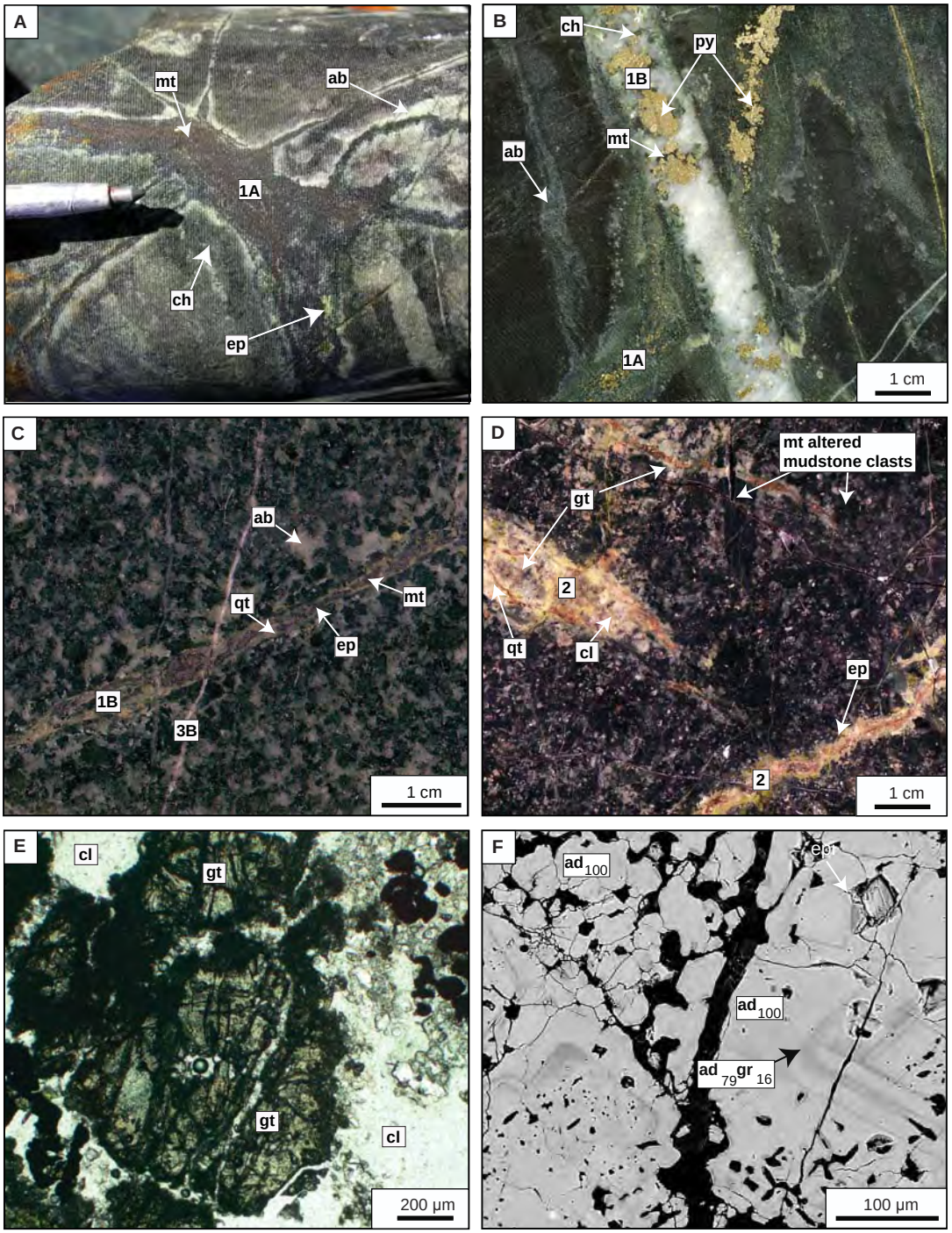

Figure 5.6 Early mineralisation veins in the east pod. **A.** Stage 1A, monomineralic magnetite veinlets with albite halos in chlorite - magnetite-altered mudstone (E41D2129, 135.8m). **B.** Magnetite - chlorite-altered mudstone with stage 1A vein minerals cut by stage 1B quartz - pyrite - chlorite ± chalcopyrite (E41D2007, 88.2m). **C.** Stage 1A vein with weak albite alteration halo cross-cut by stage 3B veinlet. These veins are hosted in actinolite - magnetite - albite - chlorite ± chalcopyrite altered diorite (E41D2067, 197.5m). **D.** Stage 2 veinlets and lenses filled with quartz - garnet - epidote and calcite. Garnet veinlet in the right corner has a weakly developed epidote alteration halo. The host rock is magnetite - chlorite - carbonate ± epidote ± K-feldspar altered polymictic volcaniclastic sandstone (E41D2067, 91.4m). **E.** Photomicrograph (ppl) of garnet from stage 2 vein. Euhedral garnet occurs along with calcite and epidote (E41D2011, 97.7m). **F.** BSE image of andradite showing differences in compositions. Grey bands are dominated by andradite-grossular isomorphic members (E41D2067, 91.4m). Abbreviations: ab=albite, ad=andradite, cl=calcite, ch=chlorite, ep=epidote, gr=grossular, gt=garnet, mt=magnetite, py=pyrite, qt=quartz, BSE=back scattered electron imaging.

alteration facies that has overprinted the diorite as described below. The magnetite alteration facies is spatially related to stage 1A veins.

5.4.1.2 Stage 1A veins

Stage 1A veins consist of chlorite – magnetite – albite – pyrite ± chalcopyrite ± epidote (Figs. 5.5B and 5.6A, B). The characteristics of this stage are described in detail in Table 5.4. Stage 1A is the earliest-formed veins at E41, and they are best observed away from the mineralised centre, where the vein assemblage has not been altered or obscured by later hydrothermal activity. These early veins commonly occur in mudstone, as chlorite- and magnetite-dominated veinlets with minor pyrite and chalcopyrite. They are weakly gold mineralised (Table 5.4). Chlorite alteration halos surround stage 1A veins, with epidote present locally in the more distal part of the alteration halos. Monomineralic magnetite veinlets are common locally (Fig. 5.6A). These early stage veins are restricted to the western part of east pod (Fig. 5.7A). They have not been observed closer to the centre of mineralisation. Rare examples of stage 1A veins have been recognised in the diorite, where they consist of magnetite and red K-feldspar and lack obvious alteration halos.

5.4.1.3 Actinolite alteration facies

Early hydrothermal alteration of the diorite at E41 produced an assemblage of secondary actinolite – magnetite – albite ± chalcopyrite ± apatite ± titanite ± epidote (Fig. 5.5C; Table 5.3). The actinolite alteration facies is selectively pervasive and is restricted spatially to the diorite sill of the east pod (Figs. 5.3B and 5.4B). The colour of the diorite varies as a function of the alteration mineralogy, with actinolite + magnetite typically rendering it dark-green.

Secondary actinolite and magnetite have replaced primary clinopyroxene (diopside) and hornblende phenocrysts. In thin section, anhedral, slightly fibrous crystals of actinolite are characterised by a green-bluish pleochroism, typically mimicking habits of mafic minerals (Fig. 5.5D). Because it typically occurs as fine-grained aggregates, actinolite can be difficult to identify in hand specimen or petrographically. Its presence has been confirmed with XRD analyses (Appendix D.2). Secondary actinolite is best preserved away from the mineralised zones (e.g., DDH: E41D2062). Actinolite has been totally replaced by chlorite – carbonate close to the mineralised domains. Secondary magnetite crystals are commonly euhedral to subhedral and occur together with actinolite, forming distinctive black magnetic domains when examined in hand specimen (Fig. 5.5C). Minor chalcopyrite has been observed intergrown with actinolite, along cleavage planes and as irregular pods. Fine-grained albite occurs as

pseudomorphs of feldspar (plagioclase and possibly K-feldspar) phenocrysts (Fig. 4.5C). The presence of albite has been confirmed using XRD (Appendix D.2). Titanite occurs locally in areas where the diorite has been strongly sheared, and also proximal to faults. The presence of secondary K-feldspar in the actinolite-altered rocks has been confirmed using sodium cobaltinitrite staining (Fig. 5.5E). It is unclear whether the K-feldspar is part of a separate alteration facies or is coeval with the actinolite assemblage. Epidote also occurs with actinolite, magnetite and may be coeval with the actinolite assemblage (at least in part). Epidote has partially replaced former ferromagnesian minerals and plagioclase crystals.

The actinolite alteration facies has not been recognised in any of the coherent units apart from the diorite in east pod. This suggests that actinolite alteration occurred prior to the intrusion of the mafic monzonite and/or was induced by the intrusion of mafic monzonite. It is unclear if this alteration was present in some of the pre-mineralisation dykes. This is because of the pre-mineralisation dykes have been strongly altered by chlorite – carbonate – illite – muscovite, preventing recognition of actinolite.

The actinolite alteration facies in the diorite is interpreted to have developed synchronously with magnetite alteration in the volcano-sedimentary units. The mineralogical differences between the two facies are interpreted to relate to the primary compositions of the host rocks.

5.4.1.4 Stage 1B veins

Magnetite – quartz – pyrite – chalcopyrite ± epidote ± albite constitute stage 1B veins (Fig. 5.6C). These veins have cross-cut the diorite locally. They have also cut the grey mudstone between east and west pods (Figs. 5.7A and 5.8A). Within the diorite, stage 1B veins mainly consist of elongate aggregates of magnetite and milky-coloured quartz. When present, pyrite is associated with minor fine-grained chalcopyrite. Morphological features are listed in Table 5.4. Weak albite and intense magnetite alteration produced 2 cm wide halos in the adjacent diorite, indicating a temporal association of stage 1B veins with pre-mineralisation actinolite alteration.

Stage 1B veins in the mudstones are up to 40 mm wide and are dominated by white quartz with disseminated fine magnetite. Minor fine grained pyrite and chalcopyrite are irregularly dispersed throughout the veins. Locally, chlorite, epidote and fragments of chlorite-altered wall rock also occur within stage 1B veins, which have weak pale green chlorite alteration halos.

Stage 1B is cut by stage 3B quartz – adularia – pyrite ± carbonate gold-mineralised veins (Fig. 5.6C), indicating a pre- main stage mineralisation timing for stage 1B.

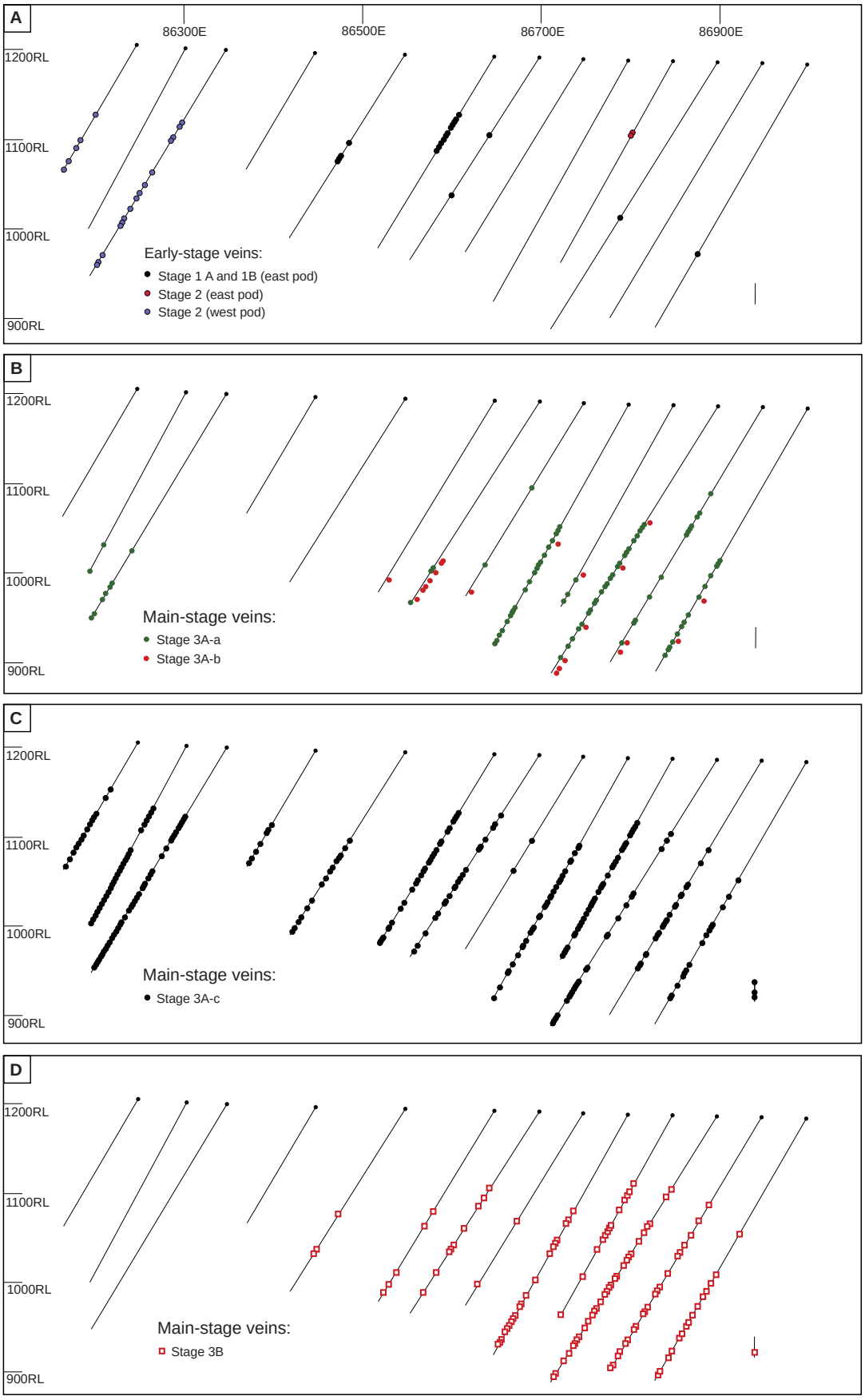

Figure 5.7 Cross section 34900N showing the observed spatial distribution of vein stages. **A.** Early-stage veins. **B.** Main-stage veins 3A-a and 3A-b. **C.** Main-stage veins 3A-c. **D.** Main-stage 3B. **E.** Main-stage veins 4A. **F.** Late-stage veins 5, 6 and stage 7. Detailed descriptions of vein stages are provided in Table 5.4 and 5.6.

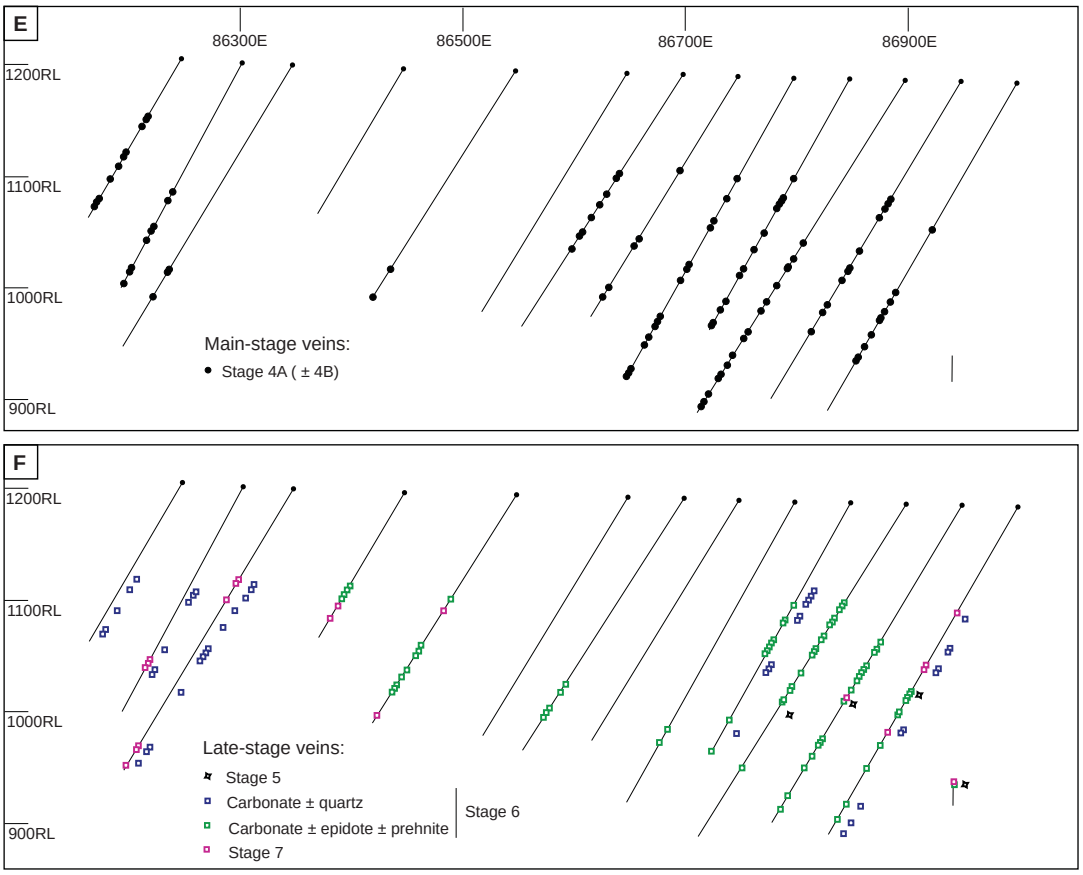

Figure 5.7 (Cont.)

5.4.1.5 K-feldspar – albite alteration facies ('patchy' texture)

A distinctive early alteration facies is characterised by the occurrence of weakly to strongly hematite-dusted K-feldspar, giving the rock a 'patchy' pink- to cream and black coloured texture (Figs. 5.9A and B; Table 5.3). This style of alteration is interpreted to have resulted from the partial replacement of the coarse-grained diorite, and caused a radical mineralogical transition. More than 40% of the mafic minerals within the most mafic-member of the diorite suite and about 25% of the primary ferromagnesian minerals in the 'intermediate' phase of the diorite have been altered to K-feldspar and albite. Black 'patchy' domains contain residual actinolite – magnetite, and have been enriched in apatite and titanomagnetite (Figs. 5.9C and D). The pink to cream-coloured domains within this 'patchy' alteration react very strongly to sodium cobaltinitrite staining, indicating abundant K-feldspar (Fig. 5.9B). Albite occurs as rinds around the dark-coloured actinolite – magnetite aggregates (Fig. 5.9B). Albite commonly has K-feldspar rims.

The 'patchy' texture is best-developed in diorite near its contact with the mafic monzonite (Figs. 5.3B and 5.4B). Volumetrically minor occurrences have also been

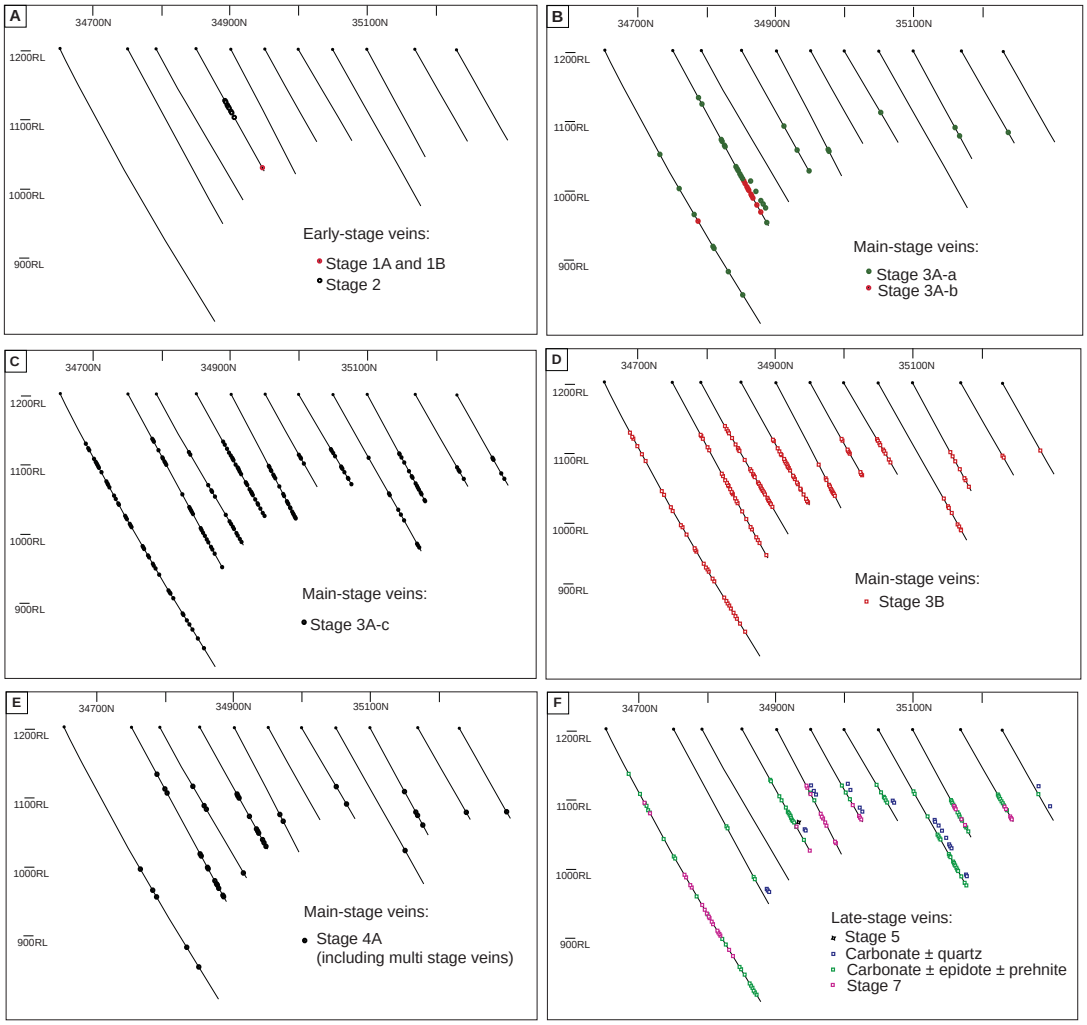

Figure 5.8 Cross section 86800E illustrates the distribution of vein stages in paragenetic order. **A.** Early-stage veins. **B.** Main-stage veins 3A-a and 3A-b. **C.** Main-stage veins 3A-c. **D.** Main-stage 3B. **E.** Main-stage veins 4A. **F.** Late-stage veins 5, 6 and stage 7. Detailed vein descriptions are provided in Table 5.4.

identified in the lower portion of the diorite sill at the eastern part of the east pod on long section 34900N (Fig. 5.3B). Scattered domains of this alteration facies are also present at depth and to the north on section 86800E (Fig. 5.4B), possibly indicating the presence of mafic monzonite. Based on the observed spatial association, the 'patchy' texture is interpreted to be a direct consequence of potassium metasomatism induced by intrusion of the mafic monzonite into the diorite.

5.4.1.6 Hematite ('red rock') alteration

'Red rock' alteration occurs at several locations across the E41 deposit. It has been recognised mainly in the diorite. Several weakly developed occurrences were observed in some of the dyke suites. This alteration imparted a red to pink coloration to the rocks due to sub-micron hematite inclusions within feldspar (Fig. 5.9E). In thin section, hematite dusting results in a distinctive turbid, brownish appearance to feldspar

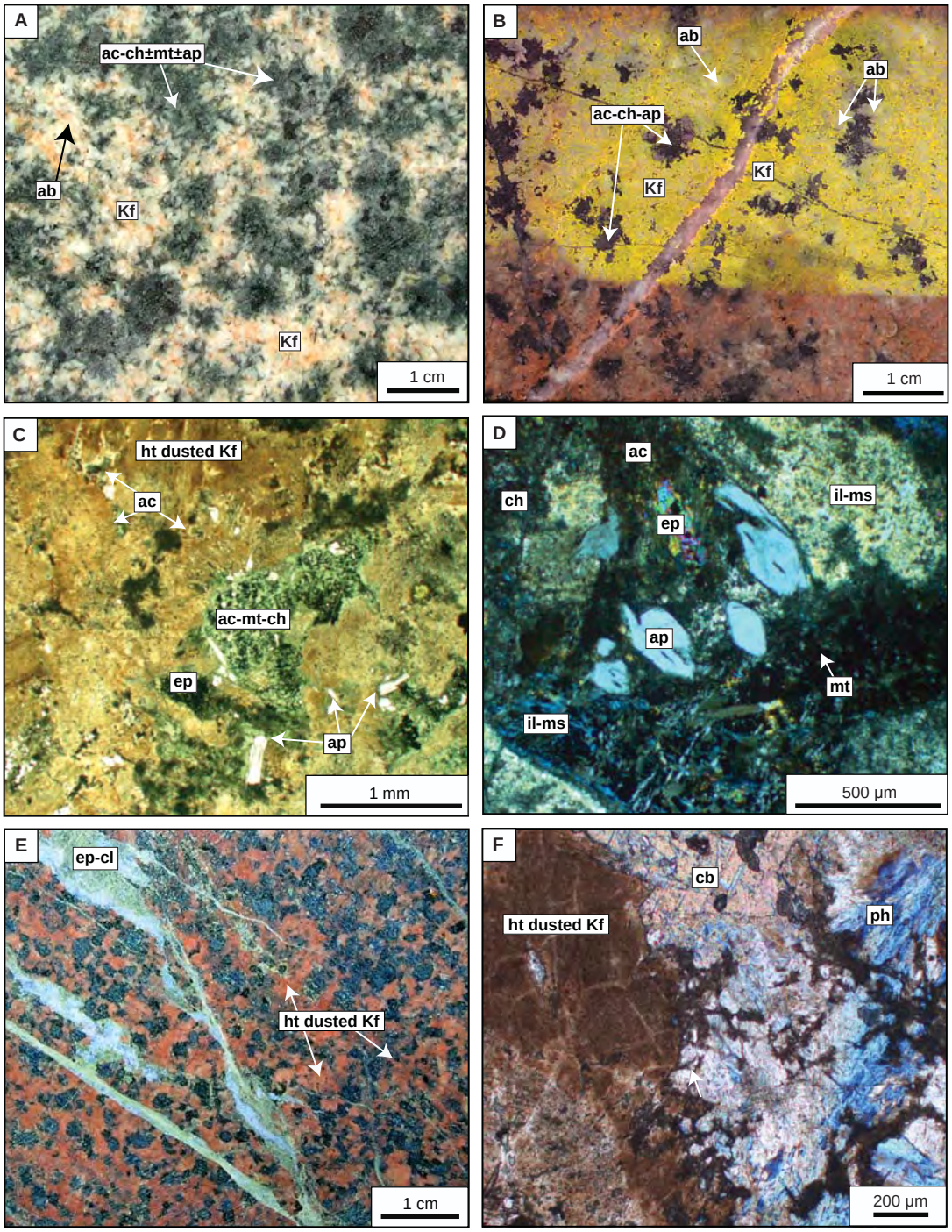

Figure 5.9 Pre-mineralisation alteration facies. **A.** K-feldspar-albite 'patchy texture' with cream to pink coloured feldspathic domains and black-green coloured actinolite - chlorite ± apatite ± titanite domains in diorite (E41D2008, 228.9m). **B.** K-feldspar stained 'patchy texture' shows abundant secondary K-feldspar in diorite (E41D2014, 284.2m). **C.** Photomicrograph (ppl) of 'patchy texture' showing turbid occurrence of feldspars together with actinolite - chlorite - magnetite domains (E41D2007; 248.6m). **D.** Photomicrograph (xpl) of an actinolite - chlorite - magnetite domain in 'patchy texture' enriched in apatite crystals (E41D2007; 248.6m). **E.** Actinolite - magnetite - chlorite - albite altered diorite with strong red coloration imparted by hematite dusting of feldspar components (E41D2012, 159.4m). **F.** Photomicrograph (xpl) showing turbid nature of K-feldspar resulated from microinclusions of hematite. Hosted by diorite (E41D2008, 173.8m). Abbreviations: ac=actinolite, ab=albite, ap=apatite, ch=chlorite, cl=calcite, ep=epidote, ht=hematite, il-ms=illite-muscovite, Kf=K-feldspar, mt-magnetite, ph=prehnite.

crystals (Fig. 5.9F). K-feldspar appears to be especially susceptible to the hematite dusting. Hematite only locally occurs in albite and plagioclase. On section 86800E, intense hematite alteration defines an aureole around the mafic monzonite and locally grades into the 'patchy' texture around the upper part of the mafic monzonite intrusion (Fig. 5.4B). Pervasive hematite alteration extends for approximately 100 m up section and 150 m laterally, resulting in a discontinuous zone of red rock alteration within the diorite (Fig. 5.3B).

5.4.1.7 Stage 2 veinlets

Stage 2 veinlets are composed of garnet – calcite – epidote ± quartz. This stage is restricted to the pervasively magnetite-altered volcaniclastic breccia unit above the main mineralised centre in east pod (Figs. 5.7A and 5.8A). Based on vein morphology and mineral assemblages, two generations of stage 2 veins have been recognised: (1) irregular wispy veinlets or aggregates dominated by garnet with subordinate epidote; and (2) parallel-sided veins and lenses composed of calcite, epidote and quartz with minor garnet. The irregular, wispy veinlets are typically 2-3 mm wide and rarely continue for more than a few centimetres (Fig. 5.6D). Within these veinlets, epidote typically occurs as a vein selvage or forms a halo around garnet. The parallel-sided veins are dominated by calcite and epidote intergrown with quartz. Thicker (15 mm wide) parallel-sided veins consist of alternating bands of calcite and epidote with later euhedral garnet, filling areas between the bands. In both vein stages, garnet is typically dark brown to dusky red-coloured. Thin section observation reveals that garnet crystals range from euhedral to anhedral (Fig. 5.6E) with the majority being very poorly crystallised. Garnet commonly forms elongated aggregates and can be difficult to identify. Electron microprobe imagining (BSE) of these crystals (Fig. 5.6F) identified the presence of growth bands which reflect varying garnet compositions. Microprobe analyses of these bands indicate compositions varying from andraditic to grossularic end-members ($Ad_{79}Gr_{16}$). The garnet crystals are dominated by andradite (Ad_{100}; Appendix D.3).

No cross-cutting relationships were observed between stage 2 and stage 1A and 1B veins. However, since the magnetite veins are spatially associated with early magnetite alteration and the pervasive magnetite alteration is cut by garnet, it is inferred that the garnet veins post date stage 1A and 1B veins.

5.4.2 Main stage alteration facies and veins

5.4.2.1 Epidote alteration

Epidote alteration is ubiquitous in east pod (Figs 5.3C and 5.4C). Epidote has been separated into two subfacies – pervasive epidote of unknown timing and epidote intimately associated with stage 3A-a veins.

Multiple generations of epidote have made it difficult to determine the exact timing of this alteration mineral in many cases. However, based on overprinting relationships, it is interpreted that some epidote was introduced into the system during the early phases of gold mineralisation, associated with stage 3A-a vein stage (Fig. 5.10A). The syn-mineralisation epidote occurs as vein envelopes to stage 3A-a veins and has a selectively pervasive to pervasive character. It typically occurs as monomineralic, irregular halos and locally with subordinate carbonate and pyrite. Intensely developed epidote alteration halos have obscured primary diorite textures. Epidote has selectively overprinted actinolite - magnetite domains in actinolite-altered diorite and has also selectively replaced plagioclase phenocrysts. Stage 3A-c and 3B veins have cut stage 3A-a epidote halos.

Domains of pervasive epidote alteration in the diorite, and mafic dykes and plagioclase-phyric dykes are particularly difficult to constrain paragenetically. There are locations where intensely epidote-altered rocks have no obvious spatial or temporal association with any vein stages but are correlated with elevated gold grades (e.g., DDH: E41D2012, 200.4m; 94.8 g/t Au; Fig. 5.11). Such relationships lead to the interpretation that epidote is at least partially associated with gold mineralisation, particularly in mafic and plagioclase-phyric dykes, and that some gold was deposited during pervasive epidote alteration.

5.4.2.2 Stage 3A-a veins

Quartz – pyrite ± chalcopyrite ± chlorite ± carbonate veins are the earliest-forming gold-mineralised structures at E41 (Table 5.4; Fig. 5.11). They have a wide spatial distribution, but appear to be confined to the diorite sill (Figs. 5.7B and 5.8B). Stage 3A-a veins occur in steeply-dipping fractures and have alteration halos up to 50 mm wide that contain clotty and massive epidote (Fig. 5.10A). The veins are commonly straight-sided to wavy. Some are sheared, especially where associated with faults. Stage 3A-a is dominated by quartz and pyrite with minor chalcopyrite. Carbonate is present locally, whereas chlorite is scarce. Rare monomineralic pyrite veinlets with epidote halos have been assigned to this stage. Stage 3A-a veins occur in both volcaniclastic and coherent units. They are particularly common in the mafic dykes and plagioclase-phyric dykes. Many stage 3A-a veins have been reopened, and have

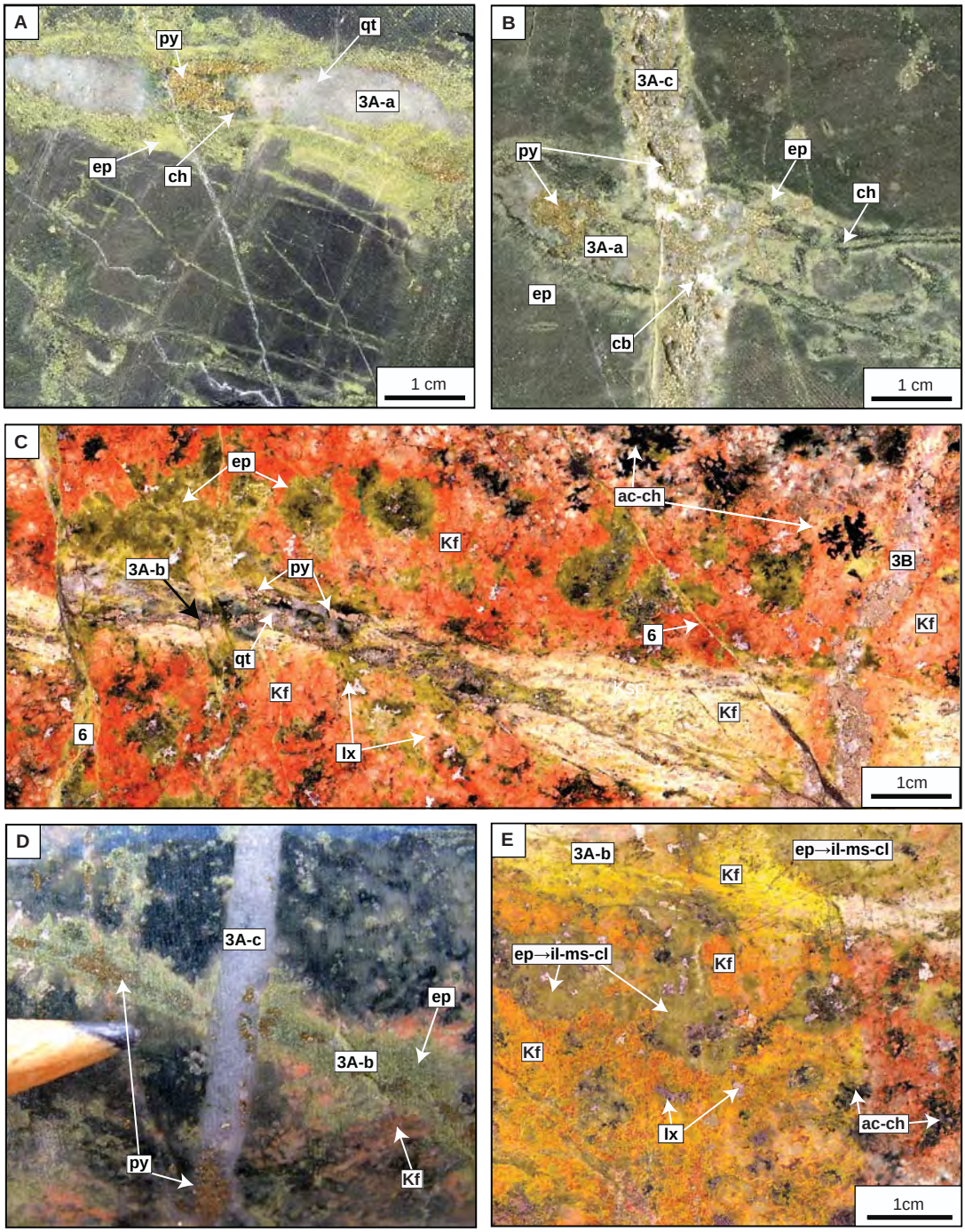

Figure 5.10 Main-stage veins. **A.** Stage 3A-a vein with epidote halo in chlorite ± magnetite altered mudstone. Vein is perpendicular to bedding (E41D2009, 111.6m). **B.** Stage 3A-a cut by stage 3A-c. Veins hosted in chlorite - illite - pyrite altered mudstone (E41D2009, 111.4m). **C.** Stage 3A-b vein with K-feldspar - epidote alteration halo cut by stage 3B and stage 6 veins in K-feldspar - albite - actinolite - chlorite ± apatite ± titanite altered diorite (E41D2008, 222.8-9 m). **D.** Stage 3A-b veinlet cut by stage 3A-c in diorite (E412009, 202.9m). **E.** K-feldspar stained halo of stage 3A-b vein highlighting the intense K-feldspar alteration around this vein (E41D2008, 222.8-9m). Abbreviations: ac=actinolite, cl=calcite, ch=chlorite, ep=epidote, Kf=K-feldsar, lx=leucoxene, mt=magnetite, py=pyrite, qt=quartz, tn=titanite.

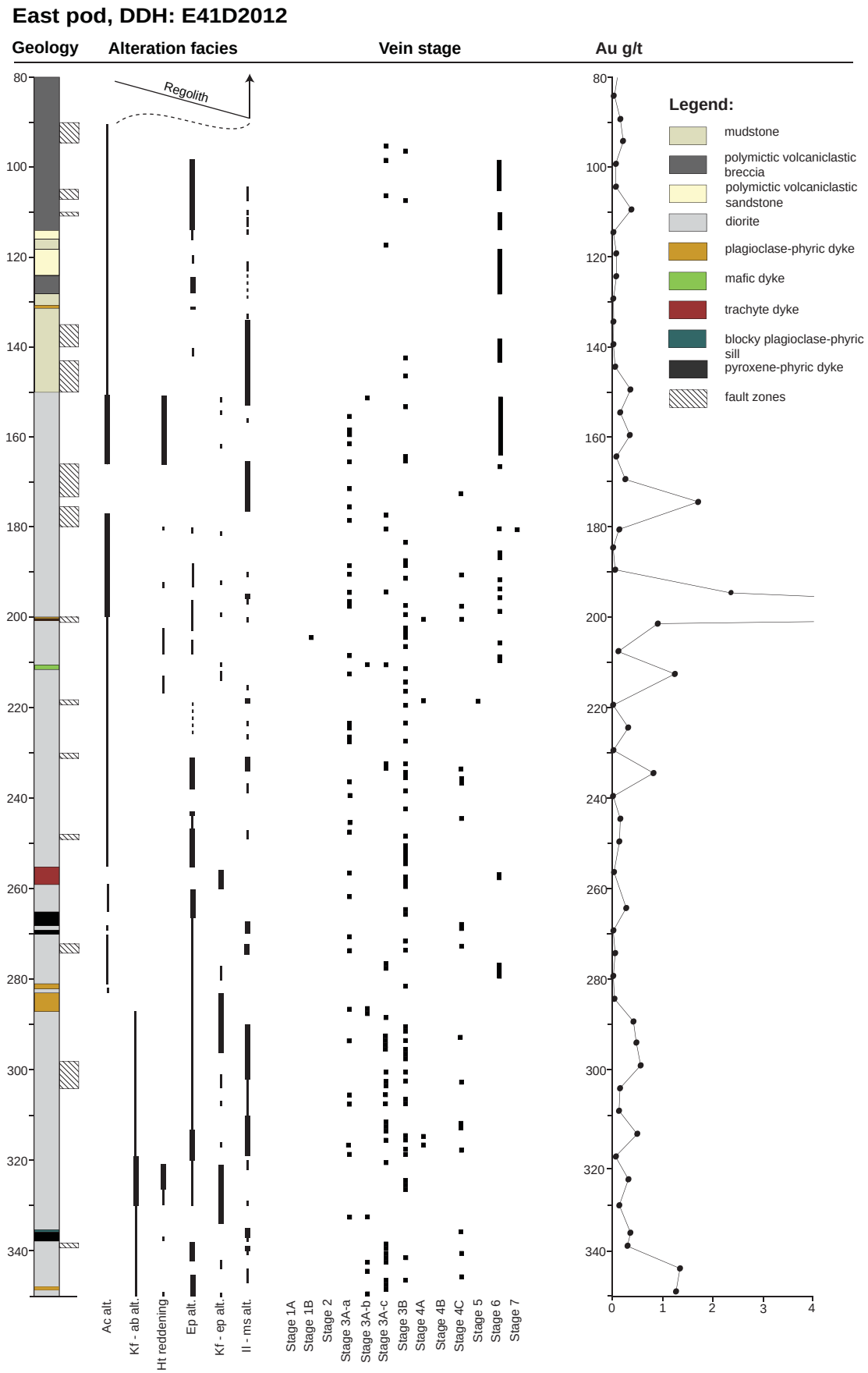

Figure 5.11 Representative drill hole log (DDH: E41D2012) with lithology, alteration facies and vein stages in paragenetic order. Abbreviations: ab=albite, ac=actinolite, ep=epidote, ht=hematite, il-ms=illite-muscovite, Kf=K-feldspar.

been cut by later vein stages. Illite – muscovite-bearing alteration halos associated with highly-mineralised stage 3A-c and 4A have overprinted epidote alteration halos of stage 3A-a veins.

5.4.2.3 K-feldspar – epidote alteration

This alteration facies occurs within the diorite, and also in the plagioclase-phyric and trachyte dyke. It has a selectively pervasive nature and is characterised by patchy occurrences of apple green epidote surrounded by irregular K-feldspar rims (Figs. 5.12A; Table 5.3). K-feldspar – epidote alteration facies were recognised in a single broad zone on the north-south section (86800E; Fig. 5.4D). A wide domain of this alteration assemblage was encountered on the long section (34900N), mostly at depth flanking the mafic monzonite underling east pod (Fig. 5.3D). The interpreted zones of this facies appear to be enclosed within the mineralised domain on north-south section (Fig. 5.4D). On long section 34900N K-feldspar – epidote alteration zones overlap with the lower portion of the >0.4 g/t gold contour, and also partially overlap minor gold-mineralised patches (Fig. 5.3D).

At least three distinctive styles of K-feldspar – epidote alteration facies have been recognised: (1) halos associated with stage 3A-b veins (Fig. 5.10C); (2) pervasive alteration of diorite (Fig. 5.12A); and (3) selective replacement of phenocrysts in plagioclase-phyric and trachyte dyke suites (Figs. 5.12B and D). The latter style is locally accompanied by apatite, pyrite, chlorite, titanite and calcite. Fine grained apatite ($\leq$20 μm) is either intergrown with calcite, chlorite and K-feldspar in the central part of the clots, or occurs in the epidote-dominated rims (Fig. 5.12C).

K-feldspar – epidote alteration is inferred to have occurred during the main stage of gold mineralisation, as it occurs as halos around moderately mineralised stage 3A-b veins (Table 5.4; Fig. 5.11) and is cut by stage 3B veins (Figs. 5.10C and 5.12E). The K-feldspar – epidote alteration facies has overprinted the ‘patchy’ K-feldspar – albite alteration assemblage. Timing relationships between K-feldspar – epidote alteration and epidote halos around 3A-a stage veins remain undetermined, as these steep structures do not cross cut each other. It may be that epidote and K-feldspar – epidote alteration facies may have formed at the same time, with the differences in mineralogy being a function of the depth of formation and/or host rock compositions. K-feldspar – epidote alteration is thought to be particularly important as it appears that it decorated zones and fractures that were later used by gold-rich fluids (during stage 3A-c and 4A veining events).

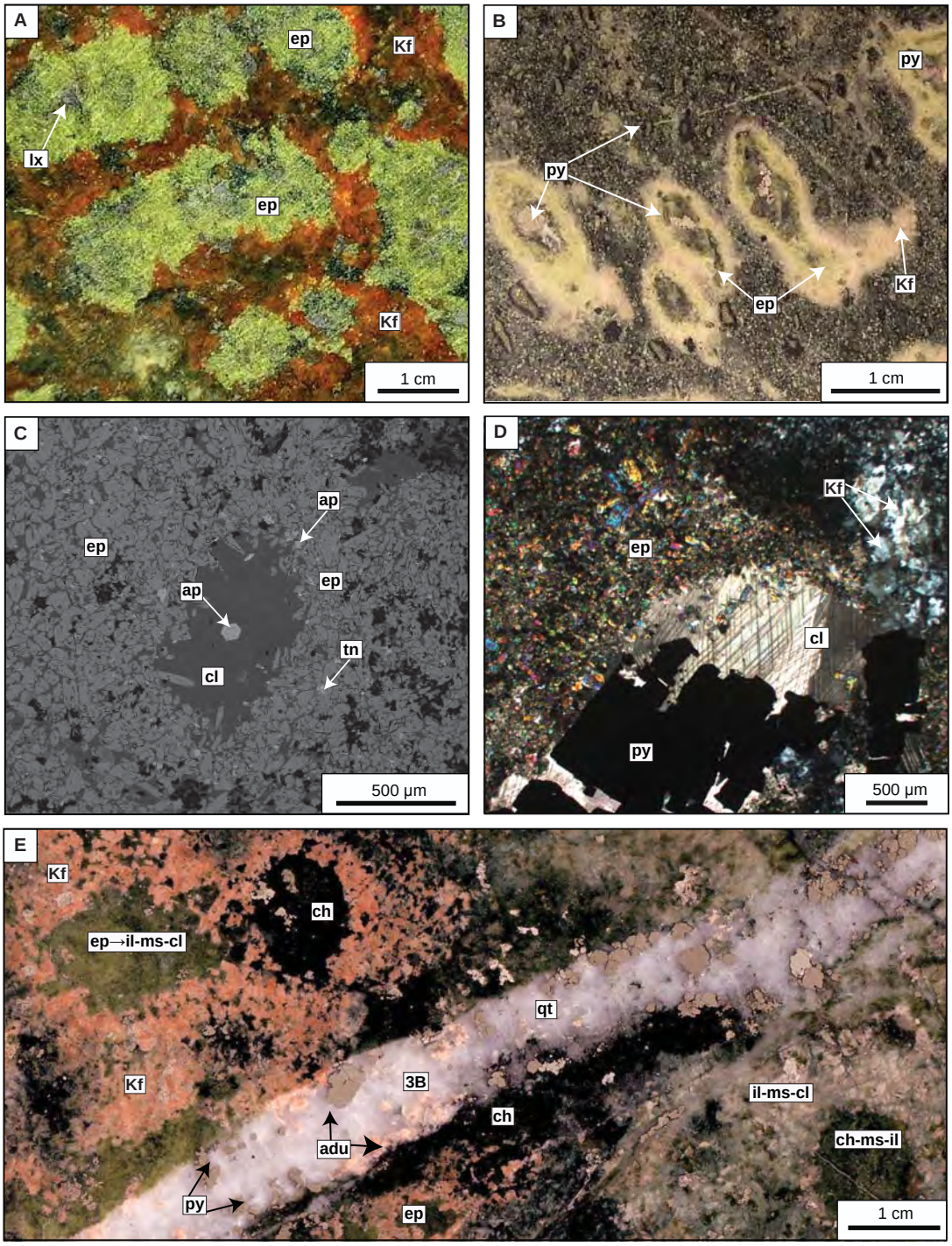

Figure 5.12 Main-stage alteration facies. **A.** Selective pervasive K-feldspar - epidote alteration randomly dispersed throughout the diorite. Epidote has replaced actinolite - chlorite - magnetite domains. Hematite dusted K-feldspar has pseudomorphed feldspars (E41D2008, 214.1m). **B.** K-feldspar - epidote alteration facies in trachyte dyke with additional calcite, pyrite and chlorite. Pyrite has replaced the central portion of the plagioclase and/or amygdule with a strong developed epidote rim (E41D2012, 256.0m). **C.** BSE image of K-feldspar - epidote altered trachyte dyke with epidote clot replacing former amygdule. Note apatite in the centre of the clot (E41D2012, 256.0m). **D.** Photomicrograph (xpl) of epidote and K-feldspar rim around pyrite - calcite (E41D2012, 256.0m). **E.** Stage 3B vein. There is a front of illite - muscovite - chlorite - carbonate alteration (left) that has overprinted pre-existing K-feldspar - epidote alteration facies (right). Chlorite has replaced epidote and K-feldspar has been pseudomorphed by illite - carbonate ± pyrite (E41D2010, 262.5m). Abbreviations: adu=adularia, ap=apatite, ch=chlorite, cl=calcite, ep=epidote, ep→il-ms-cl=epidote altered to illite - muscovite - calcite, il-ms=illite-muscovite, Kf=K-feldspar, py=pyrite, tn=titanite, BSE=back scattered electron imaging.

5.4.2.4 Stage 3A-b veins

Figures 5.7B and 5.8B show the distribution of stage 3A-b veins, which are restricted to the deeper parts of east pod and overlap with zones rich in stage 3A-a veins. Mineralogically, stage 3A-b veins are similar to stage 3A-a (Table 5.4). They consist of quartz – pyrite ± K-feldspar ± carbonates. Stage 3A-b veins are discriminated on the basis of their association with strongly developed, selective pervasive K-feldspar – epidote halos (Figs. 5.10C and E). The veins have been reopened locally, and infill with later stages (e.g., 3B, 4A). Some stage 3A-b veins are dominated by pyrite. Stage 3A-b has been cut by stage 3B (Fig. 5.10D).

5.4.2.5 Illite – muscovite – chlorite – carbonate ± pyrite alteration facies

Illite – muscovite (determined by PIMA; section 5.3.3), chlorite, carbonate and pyrite are the principal alteration minerals associated with the 'main-stage' mineralisation events in the east pod. This alteration varies in both intensity and style, due to variable rock types and pre-existing alteration assemblages (Table 5.3). Alteration styles include pervasive or selectively pervasive replacement of the wall-rocks, and (most typically) halos around stage 3A-c, 4A, 4B and 4C. This alteration facies commonly indicates proximity to mineralised zones (Figs. 5.3F, 5.4F and 5.11).

In clastic units, illite – muscovite, carbonate and pyrite occur in bleached zones that are spatially associated with gold-rich veins. Pyrite occurs as fine disseminations in the alteration halos of illite – muscovite where it has replaced secondary magnetite. It is difficult to determine the amount of secondary chlorite produced during illite – muscovite – carbonate alteration.

Within mineralised zones of diorite, the illite – muscovite – chlorite – carbonate alteration assemblage has overprinted earlier-formed K-feldspar – albite ('patchy') alteration (Figs. 5.13A and B), actinolite alteration, epidote, and also K-feldspar – epidote alteration facies (Fig. 4.12E). The illite – muscovite – chlorite – carbonate assemblage is most conspicuous where it occurs as vein halos (Fig. 5.13B), otherwise it is difficult to recognise in hand specimen. In the K-feldspar – epidote-altered diorite, black chlorite has replaced green epidote, and illite - muscovite and carbonate have replaced K-feldspar (Figs. 5.12E and 5.13B). Secondary actinolite has been partially to completely altered to chlorite – illite – muscovite – carbonate aggregates. Illite – muscovite has also preferentially replaced albite- altered plagioclase crystals (Fig. 5.13D).

There are slight differences between the alteration halos that surround stage 3A-c, 4A and 4C veins. Stage 3A-c veins have typically weak illite – muscovite – carbonate ± pyrite halos (Fig. 5.14A), that are only recognisable in thin section. Some

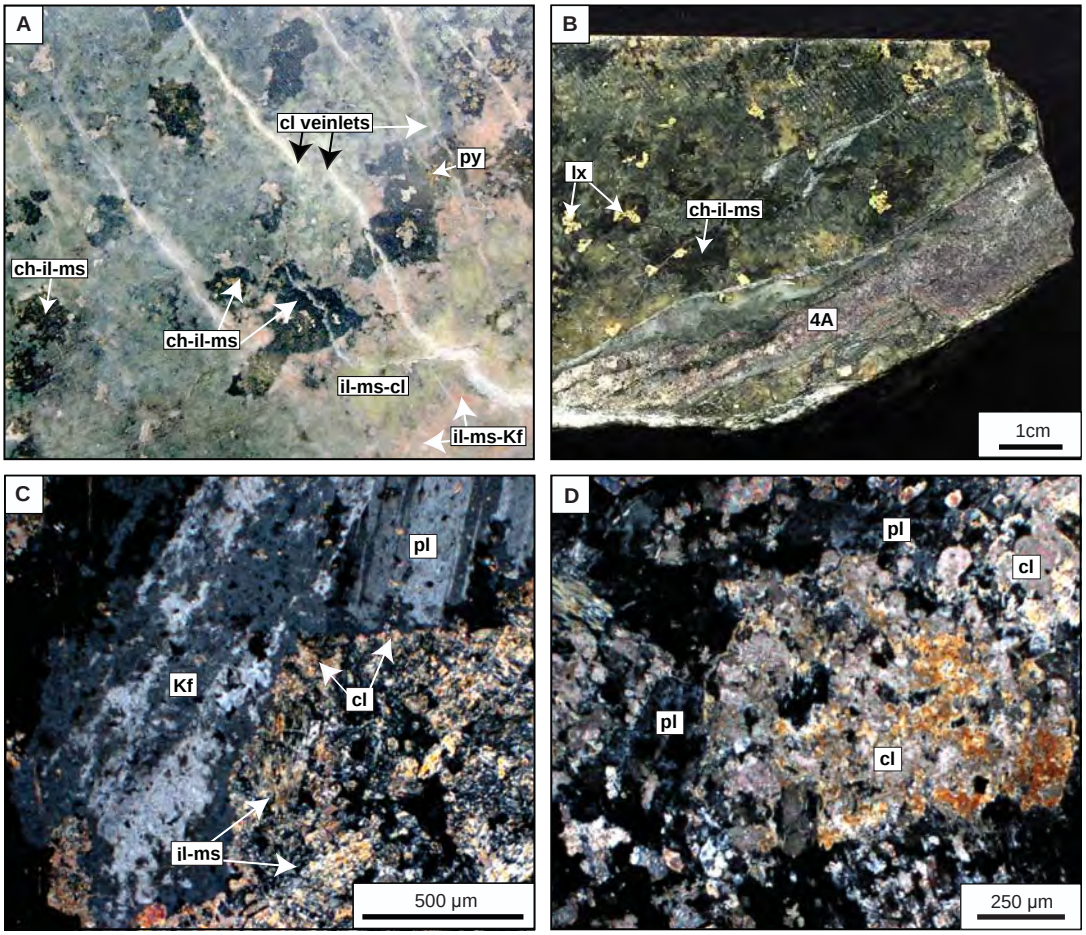

Figure 5.13 Main-stage alteration facies. **A.** Main-stage chlorite - illite - muscovite - carbonate alteration of diorite from a well-mineralised zone (east pod). Chlorite - illite - muscovite has replaced pre-existed epidote clots. Hematite has dusted feldspars which have been overprinted by illite and carbonate. Pale pink coloration is still preserved. Late carbonate veins (stage 6) have cut altered rock (E41D2009, 234.6m). **B.** Stage 4A vein with a strongly developed chlorite - illite - carbonate alteration halo hosted in actinolite - magnetite - albite - K-feldspar - epidote altered diorite (E41D2010, 255.2m). **C.** Photomicrograph (plx) of selective pervasive illite - muscovite - K-feldspar alteration hosted in diorite. Illite - muscovite has selectively pervasively replaced prexisted epidote crystals of K-feldspar - epidote facies. K-feldspar has partially pseudomorphed plagioclase crystals (E41D2012, 262.5m). **D.** Photomicrograph (plx) showing carbonate that has completely replaced plagioclase crystals (E41D2068, 219.4m). Abbreviations: ch=chlorite, cl=calcite, il-ms=illite-muscovite, Kf=K-feldspar, pl=plagioclase, py=pyrite, lx=leucoxene, py=pyrite, qt=quartz.

stage 3B mineralised veins lack obvious alteration envelopes (Fig. 5.14B). In contrast, stage 4A alteration halos are distinctive in hand specimen (Figs. 5.15B and C). They are intensely developed with abundant black chlorite and carbonate. Some alteration halos associated with stage 4A mineralisation may lack pyrite, whereas others contain arsenopyrite and brown-coloured ankerite (typically associated with stage 4B infill).

Intensely developed, texturally destructive illite – muscovite – carbonate alteration halos are spatially associated with brecciated and multi stage veins (stage 4C). These alteration halos can extend up to 1 m away from the veins and/or breccias, making them a very distinctive alteration features. The illite – muscovite assemblage is typically green-coloured, and is associated with highly crystalline illite – muscovite as observed petrographically. Dark green to black chlorite and pyrite are common

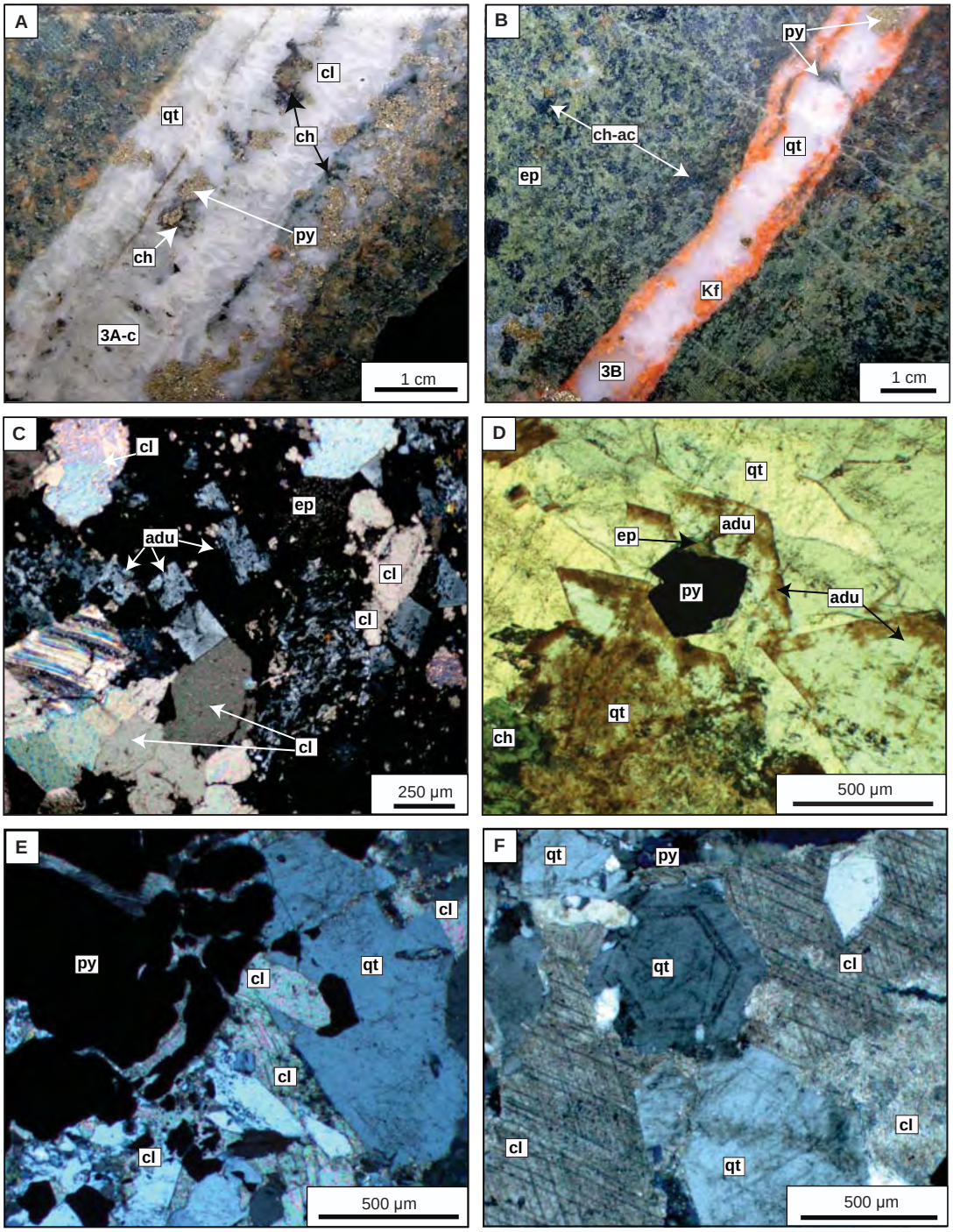

Figure 5.14 Main-stage veins hosted by diorite in the east pod. **A.** Typical parallel-sided stage 3A-c vein with weak illite - muscovite - carbonate - pyrite alteration halo (E41D2165, 363.6m). **B.** Parallel-sided stage 3B vein lined by red hematite-dusted adularia (E41D2065, 111.2m). **C.** Photomicrograph (xpl) of stage 3B carbonate - quartz - illite - muscovite - pyrite vein. Rombic adularia crystals are dispersed throughout the vein (E41D2068, 222.3m). **D.** Photomicrograph (ppl) of stage 3B vein with euhedral adularia crystals lining the vein margins (E41D2065, 111.2m). **E.** Photomicrograph (xpl) of stage 3A-c vein showing pyrite and carbonate intergrowths (E41D2010, 262.5m). **F.** Photomicrograph (xpl) of stage 3A-c vein with interlocking euhedral quartz and massive carbonate infill (E41D2067, 166.7m). Abbreviations: ac=actinolite, adu=adularia, cl=calcite, cb=carbonate, ch=chlorite, ep=epidote, mt=magnetite, py=pyrite, qt=quartz.

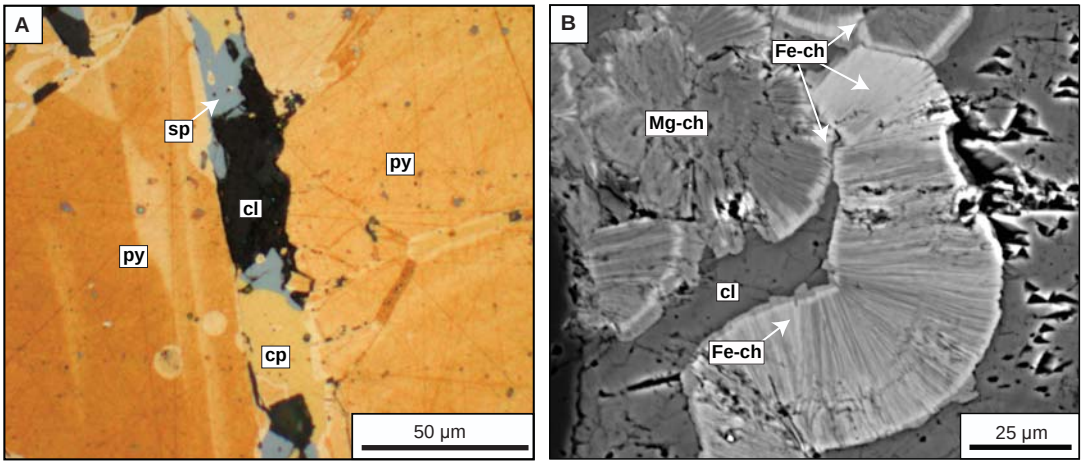

Figure 5.15 Stage 3A-c and 4A infill characteristics. **A.** Photomicrograph (reflected light) of pyrite from 3A-c vein. Fracture in pyrite is filled with stage 4A sphalerite - calcite - chalcopyrite (E41D2010, 196.4m). **B.** BSE image showing calcite and chlorite crystals of stage 3A-c. Calcite appears to be paragenetically earlier than chlorite. Chlorite is typically Mg-rich and its rinds are enriched in iron (E41D2011, 200.7m). Abbreviations: cl=calcite, cp=chalcopyrite, Fe-ch=iron rich chlorite, Mg-ch=magnesium rich chlorite, sp=sphalerite, py=pyrite, BSE= back scattered electron imaging.

alteration products around brecciated multi stage veins, and leucoxene is also a characteristic feature.

The illite – muscovite – carbonate – chlorite ± pyrite assemblage has been delineated spatially and is presented in Figures 5.3F and 5.4F. It appears that these alteration facies formed zones spatially related to faults and closely-spaced fractures.

5.4.2.6 K-feldspar alteration facies

Selectively pervasive K-feldspar alteration has produced halos around some stage 3A-c and 3B veins. Strongly-hematite dusted K-feldspar typically formed monomineralic alteration halos around those veins. Some alteration halos in the diorite are composed of K-feldspar – illite – muscovite ± carbonates that have selectively pervasively replaced plagioclase crystals (Fig. 5.13C). The alteration intensity of the K-feldspar facies varies from moderate to intense. Pervasive K-feldspar alteration has affected most of the coherent rock units, comprising up to 30% by volume locally. K-feldspar halos with minor illite – muscovite and chlorite have been mapped out and the interpreted zones of this main stage alteration facies are shown on Figures 5.3 and 5.4. Zones of this alteration facies partially overlap with mineralised domains.

It is difficult to ascertain the relative proportions of syn- and early-mineralisation K-feldspar alteration. The fact that it is associated with mineralised veins is consistent with its main stage timing. Intense K-feldspar alteration has been detected in a late-mineralisation syenitic dykelet that appears to be washed with K-feldspar (Fig. 3.14A). This is consistent with K-feldspar alteration occurring several times during hydrothermal activity at E41.

5.4.2.7 Stage 3A-c veins

Stage 3A-c veins are composed of quartz – pyrite – calcite – chlorite ± epidote. These are the most abundant mineralised veins in east pod. Their distribution is illustrated on Figures 5.7C and 5.8C. Stage 3A-c veins are typically planar and range from 1 mm to > 10 cm wide. Sheared irregular stage 3A-c veins and/or veinlets are commonly associated with fault zones. Stage 3A-c veins hosted in diorite are characterised by abundant quartz, locally intergrown with calcite (Figs. 5.14A, E and F) and chlorite. Quartz is commonly massive and milky (Fig. 5.14A). Where observed, comb quartz typically occurs as the first phase of vein infill and occupies vein margins (Fig. 5.14A). Rare euhedral zoned quartz crystals are associated with up to 70% massive to euhedral pyrite (Fig. 5.14F). Chlorite is typically subordinate, anhedral and occurs as crystals tightly interlocked with calcite and quartz (Fig. 5.15B). EDS analyses showed that chlorite compositions vary internally with iron-rims and Mg-rich cores (Fig. 5.15B). Epidote tends to be more common in 3A-c stage veins hosted by volcaniclastics.

Typically stage 3A-c veins were reopened during later hydrothermal activity (Fig. 5.14A). This has produced laminated textures in the veins, which are defined by thin fractures that are most obvious in thin section. Stage 4A sphalerite, chalcopyrite and galena are the most common fracture-fill minerals within fractured pyrite of stage 3A-c veins (Fig. 5.15A).

5.4.2.8 Stage 3B veins

Figures 5.7D and 5.8D show the spatial distributions of stage 3B veins. These typically well-mineralised veins (Table 5.4; Fig. 5.11) are similar to stage 3A-c, but are distinguished by the presence of adularia on the vein margins (Figs. 5.12E, 5.14B and D). Fine- to medium-grained adularia is typically euhedral (rhombic) and comprises 10-20% of the veins. There are rare examples where adularia is dispersed throughout the veins (Fig. 5.14C). Adularia has a distinctive brown-yellow colour and turbid appearance in thin section due to abundant hematite inclusions.

Stage 3B veins have typically truncated stage 3A-c veins, but some examples of opposite relationships have also been observed, indicating that these two stages formed at similar times or that conditions fluctuated back and forth during stage 3. Locally both stages have undergone re-opening and subsequent infilling with stage 4A minerals (carbonates and base-metal sulfides) and late-stage carbonates, epidote and prehnite. Stage 3B veins have been cut by stage 4A veins (Fig. 5.16A).

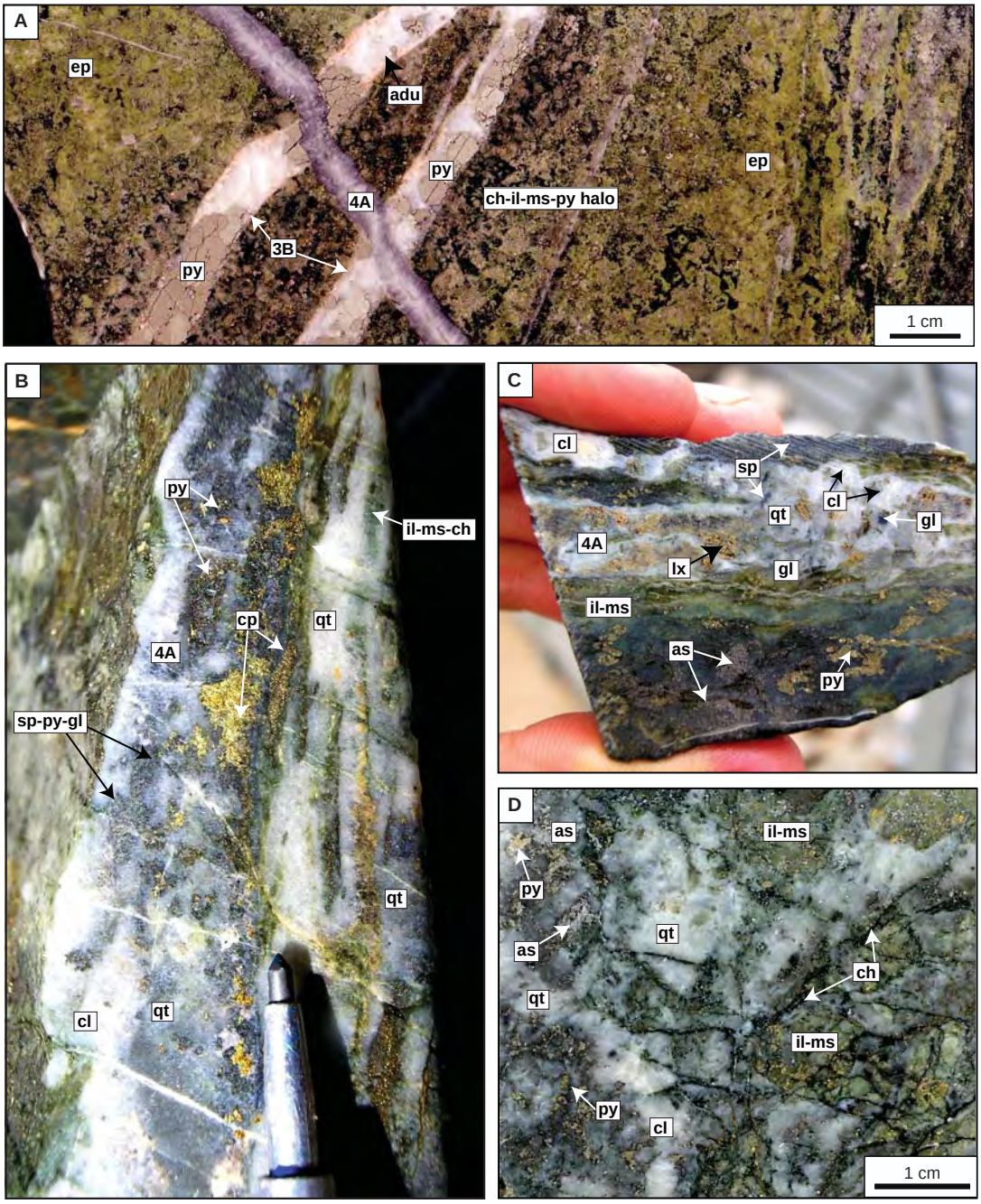

Figure 5.16 Main-stage mineralisation in the east pod. **A.** Stage 3B veins cut by purple-coloured stage 4A vein of carbonate - pyrite - hematite - chalcopyrite - apatite. The illite - muscovite - chlorite - pyrite alteration halo associated with this vein has overprinted epidote-altered diorite (E41D2012, 247.5m). **B.** Steeply dipping multi stage vein (4A) associated with a fault zone. Infill consists of quartz - carbonate - chalcopyrite - pyrite and fine grained sphalerite - galena - pyrite. Vein associated with illite - muscovite - chlorite halo. Illite - muscovite - chlorite formed elongated layers within the vein (E41D2069, 279.8m). **C.** Multi stage (4A), well-mineralised vein (4.45 Au ppm) composed of quartz - carbonate - sphalerite - galena and leucoxene. Halo of illite - muscovite is associated with this vein. Aggregates of arsenopyrite (stage 4B) has overprinted illite - muscovite alteration halo (E41D2012, 335.9m). **D.** Strongly brecciated vein ('QSB') associated with a fault zone. Quartz - carbonate - pyrite - arsenopyrite - illite - muscovite - chlorite are the infill minerals in this highly-mineralised occurrence (E41D2166, 367.8m). Abbreviations: adu=adularia, as=arsenopyrite, ch=chlorite, cl=calcite, gl=galena, il-ms=illite-muscovite, lx=leucoxene, py=pyrite, qt=quartz, sp=sphalerite.

5.4.2.9 Stage 4A veins and infill

Stage 4A veins formed during the second major mineralising event at E41. This stage is characterised by abundant carbonate species, quartz, chlorite, illite - muscovite, sulfides ± hematite ± apatite. Sulfides include pyrite, sphalerite, galena, chalcopyrite, tetrahedrite and Ag-Au- and Bi-tellurides. Silver tellurides have been reported from similar veins at E42 (Bastrakov, 2000). This vein stage contributed significantly to the mineralisation at E41. Stage 4A veins are typically highly-mineralised (Table 5.4). Their distribution is shown in Figures 5.7E and 5.8E.

Stage 4A veins have typically reopened and infilled stage 3A-c or 3B veins. Thin section petrography has revealed fractures in stage 3 pyrite are filled with stage 4A galena, chalcopyrite, calcite, tetrahedrite and tellurides (Figs. 5.15A and 5.16C, D). Morphologies of discrete stage 4A veins vary from parallel-sided, wispy, locally 'shear-like' to massive.

Sphalerite is typically fine-grained (<1 up to 5 mm) and dark grey or black-coloured. Sphalerite occurs as aggregates, clots or individual crystals dispersed throughout stage 4A veins. Chalcopyrite is typically associated with sphalerite occurring as fine inclusions within coarser sphalerite grains. Galena is commonly intergrown with sphalerite. Carbonates are abundant. PIMA and microprobe analyses (Appendix D.3) have detected ankerite as a common carbonate phase in stage 4A veins. But EDS analyses have revealed that some of the well-mineralised stage 4A veins are dominated by calcite, indicating variable carbonate components during stage 4A. Some stage 4A veins have a purple colour due to local hematite dusting of carbonates. Pyrite is fine-grained and heterogeneous compared to stage 3 pyrite.

Apatite occurs in some of the strongly mineralised stage 4A veins, where it is intergrown with illite – muscovite and calcite. Locally micas are REE-enriched (Fig. 5.17A) These apatite-bearing veins are locally enriched in chalcopyrite, arsenopyrite and Bi-tellurides. Specs of Ti-bearing phases also occur along with apatite, illite and muscovite. EDS analyses have revealed that some apatite crystals have elevated La, Ce, Nd and Sm contents, that produce discrete 1-2 μm wide bright domains within apatite crystals when viewed as a BSE image (Fig. 5.17B). Apatite-bearing veins are associated with intensely developed illite – muscovite – chlorite – carbonate alteration halos.

Gold occurs in stage 4A veins as Ag-Au-tellurides or as electrum. Tellurides are associated with chalcopyrite and sphalerite crystals or between pyrite crystals (Fig. 5.17D). Electrum is associated with chalcopyrite locally (Fig. 5.17C).

Selective assay data of individual veins of stage 4A show that the high gold grades (up to 12.5 g/t; Table 5.4) appear to correlate with the occurrence of carbonates and base metal sulfides.

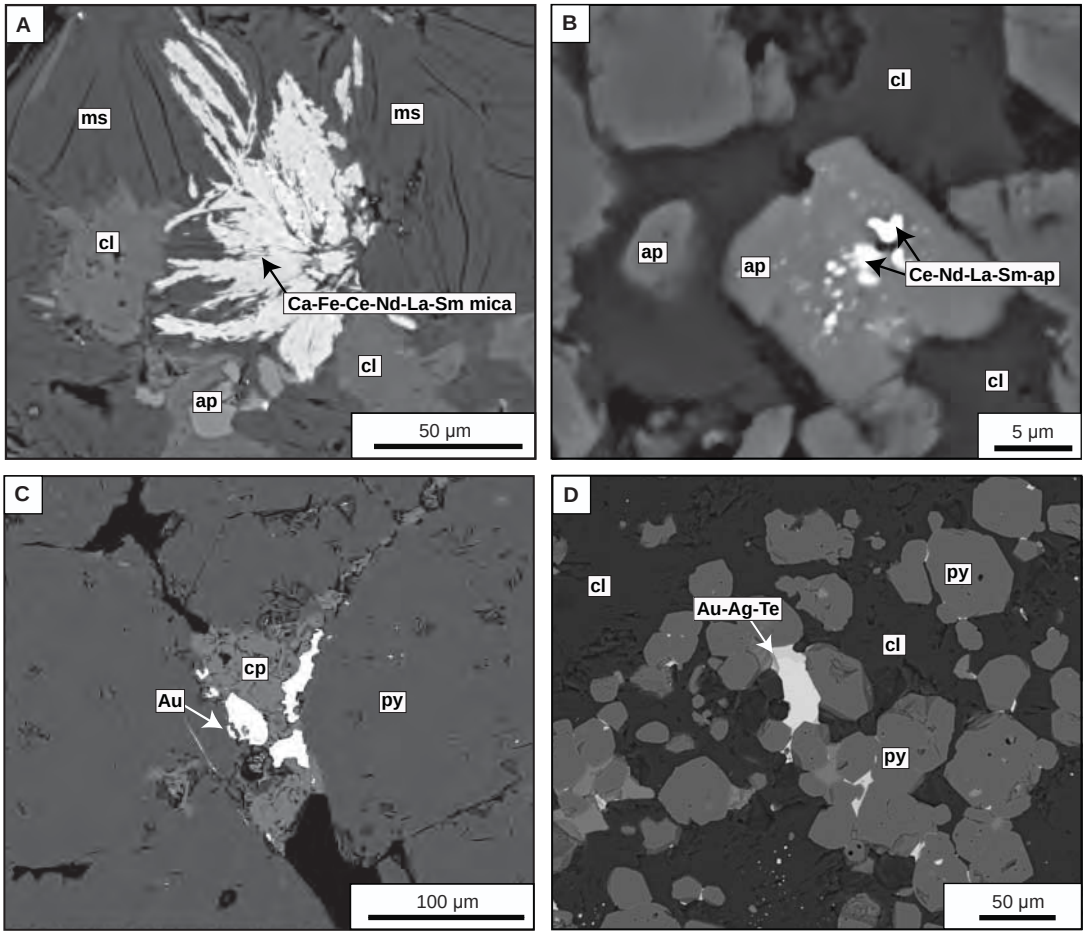

Figure 5.17 BSE imaging of stage 4A vein infill characteristics. **A.** Stage 4A vein dominated by calcite and domains of muscovite - apatite and rare arsenopyrite. REE-enriched Ca-Fe-mica is intergrown with muscovite and apatite (E41D2010, 197. 0m). **B.** REE-enriched apatite crystals in 4A stage infill (E41D2010, 197.0m). **C.** Stage 3A-c pyrite cut by stage 4A chalcopyrite - electrum (E41D2010, 197.0m). **D.** Stage 4A infill of calcite, euhedral pyrite and Ag-Au-tellurides (E41D2010, 197.0m). Abbreviations: ap=apatite, cl=calcite, Au-Ag-Te= Au-Ag-tellurides, cp=chalcopyrite, gl=galena, py=pyrite, BSE=back scattered electron imaging.

5.4.2.10 Arsenopyrite – ankerite alteration facies

Arsenopyrite alteration (Table 5.3) is temporally and spatially related to stage 4B. It has typically overprinted illite – muscovite alteration halos associated with stage 4A veins (Fig. 5.16C). Arsenopyrite locally occurs as part of the alteration halos around multi stage veins, pseudomorphing clinopyroxene in diorite (Fig. 5.18D). Ankerite and grass green-coloured mica were also observed as alteration halos associated with some arsenopyrite-bearing fractures.

5.4.2.11 Stage 4B infill

Stage 4B consists of arsenopyrite – ankerite ± pyrite ± Bi-tellurides. Detailed characteristics of stage 4B are presented in Table 5.4. The stage 4B arsenopyrite is typically spatially related to reactivated stage 4A veins, where it has cut pre-existing stage 4A sulfides and associated silicate and carbonate minerals (Figs. 5.18A and C).

BSE imaging together with EDS analysis revealed that some stage 4B arsenopyrites are associated with Bi-tellurides.

5.4.2.12 Stage 4C ('QSB')

Stage 4C contains fragments of stage 3A and 3B veins cemented by stage 4A minerals. Detailed characteristics of stage 4C are provided in Table 5.4. This stage is typically associated with steep-dipping faults and fractures and it is commonly irregular, chaotic, brecciated and intensely altered (Fig. 5.16C). Pervasively illite – muscovite – chlorite-altered wall rock fragments commonly occur in brecciated 4C stage. The stage 4C cement typically has a massive texture. It is also evident that brecciated veins are strongly mineralised (Fig. 5.11; Table 5.4). Based on observed mineral relationships in

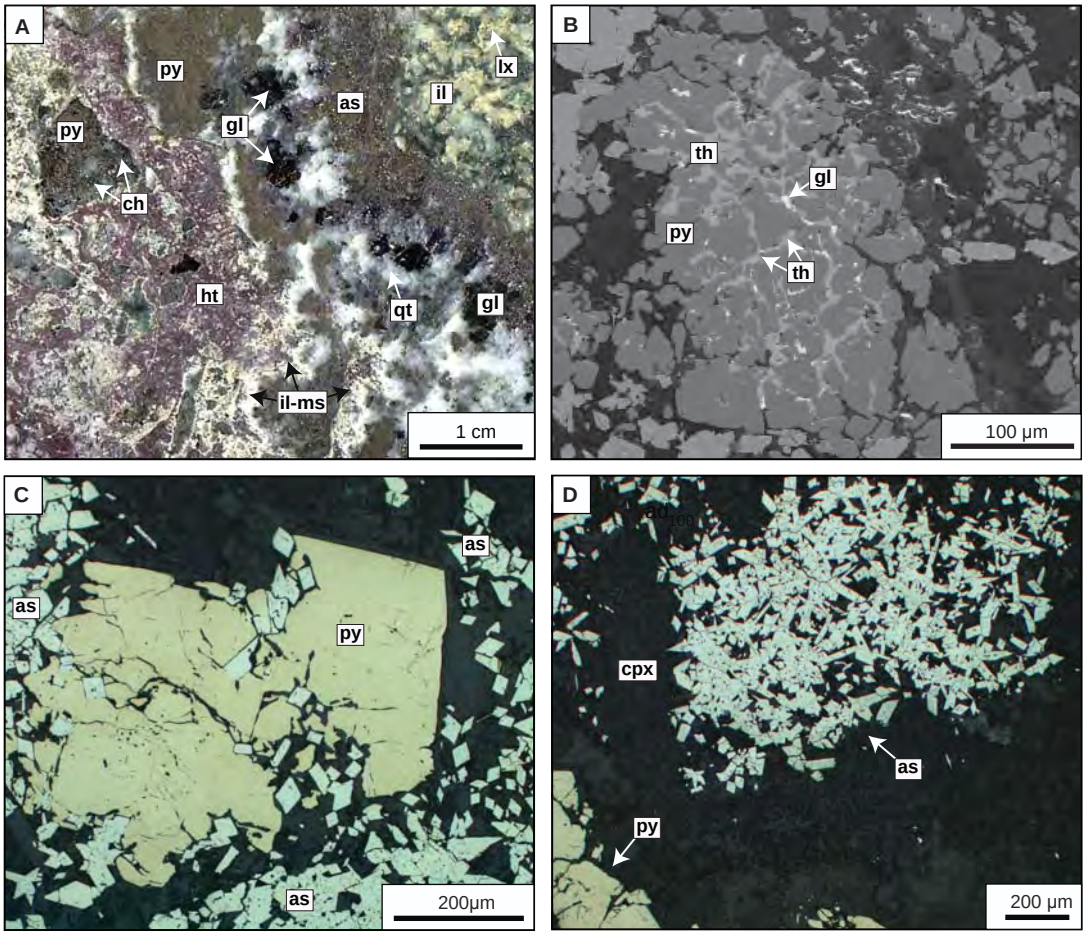

Figure 5.18 Main stage 4B infill characteristics. **A.** Diorite hosted stage 3A-c vein (?) reopened and filled by stage 4A minerals including galena, chalcopyrite, sphalerite, tetetrahedrite and hematite, and stage 4B arsenopyrite. There is a strongly developed illite - muscovite - leucoxene - carbonate(ankerite) - arsenopyrite halo associated with the vein (E41D2011, 195.5m). **B.** BSE image from multi stage vein (stage 3A-c, 4A and 4B) showing stage 4A galena and tetrahedrite within a stage 3A-c pyrite crystal (E41D2011, 195.5m). **C.** Photomicrograph (reflected light) of stage 3 pyrite cut by stage 4B arsenopyrite. Arsenopyrite filled cracks within the pyrite (E41D2011, 195.3m). **D.** Photomicrograph (reflected light) of sample from halo of multistage opening vein from Figure 13.C. Arsenopyrite has pseudomorphed clinopyroxene (E41D2011, 195.3m). Abbreviations: as=arsenopyrite, cb=carbonate, ch=chlorite, cpx=clinopyroxene, gl=galena, ht=hematite, il-ms=illite-muscovite, lx=leucoxene, py=pyrite, qt=quartz, th=tetrahedrite, BSE=back scattered electron imaging.

stage 4C, it is interpreted that these mineralised veins ('QSB') were formed during the carbonate-base metal event.

Similar vein occurrences have been recognised at E42, where they occupy highly mineralised fractures (Smolonogov, 2003; Bywater et al., 2004; Henry, 2008). Most brecciated intervals are spatially associated with major faults in the E42 deposit and are discontinuous both laterally and vertically on decimeter to meter scales (Henry, 2008). The occurrence of QSBs at E41 and E42 indicates that similar processes of mineralisation were operating in both epithermal centres.

5.4.3 Late stage alteration facies and veins

5.4.3.1 Post-mineralisation alteration facies

Late stage alteration in the east pod is characterised by epidote, hematite – calcite and pervasive fault related clay and mica-bearing mineral assemblages (Table 5.3). Epidote occurs as weakly developed replacements of plagioclase crystals and groundmass in some post-mineralisation dykes (i.e., the 'diorite' dyke and hornblende-phyric dyke; Figs. 3.18D and C). Late stage epidote is most abundant in post-mineralisation shear zones. Hematite – calcite alteration has altered the post-mineralisation amygdaloidal dyke (Figs. 5.19F and G). Ankerite occurs together with other carbonate species as a late alteration overprint at E41. Ankerite is easily distinguished by a brown oxidation staining of weathered drill core. Weak selective pervasive to locally pervasive illite – muscovite, chlorite and carbonate alteration is present in all post-mineralisation dykes.

5.4.3.2 Stage 5 veins

Gypsum veins are rare at E41. They are narrow (up to 5 mm) and parallel-sided to sinuous (Figs. 5.19A and B; Table 5.4). Gypsum occurs in multi stage veins as a post-mineralisation infill. Cream-coloured carbonate also occurs with the gypsum as discrete bands. The distribution of gypsum veins is shown on Figures 5.7F and 5.8F. A post-mineralisation timing of these veins has been inferred based on their cross-cutting relationships with a syn-mineralisation pyroxene dyke (Fig. 5.19A), and also because stage 5 constitutes a late infill in main stage veins. Epidote – carbonate veins have cut gypsum veins (Fig. 5.19B), evidence for stage 5 forming prior to stage 6 epidote – carbonate veins. Gypsum also occurs as infill within reopened stage 7 carbonate ± hematite veins which complicates the paragenetic sequence or indicates several generation of gypsum veining. There is no obvious evidence for gypsum replacing anhydrite at E41.

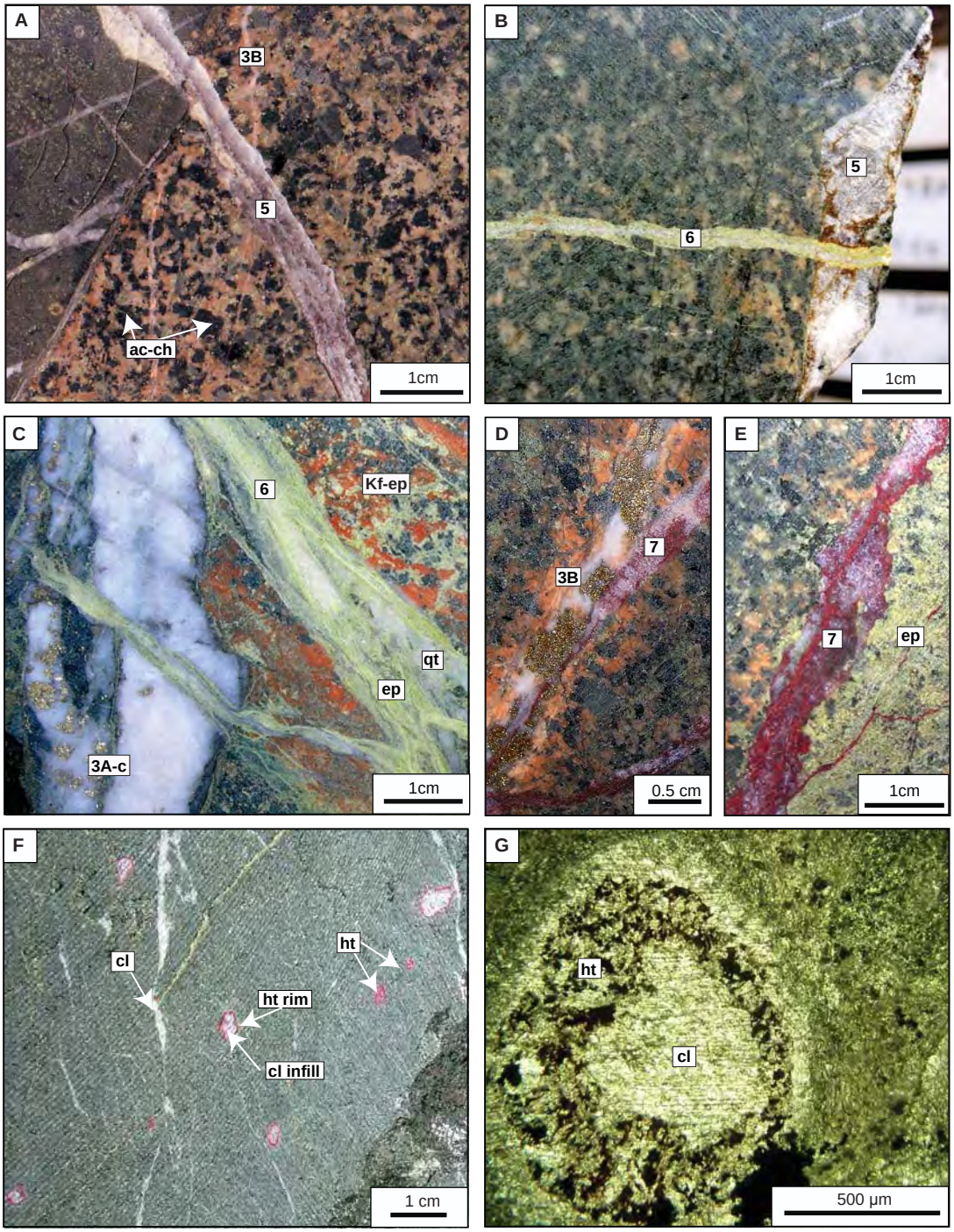

Figure 5.19 Post mineralisation vein stages and alteration facies. **A.** Stage 5 gypsum - calcite vein cutting pyroxene-phyric dyke and stage 3B vein. Hosted in diorite (E41D2067, 159.5m). **B.** Stage 6 vein cutting stage 5 vein in diorite (E41D2013, 204.0m). **C.** Stage 3A-c vein cut by wispy stage 6. Stage 6 vein in this sample has also cut the K-feldspar - epidote alteration in diorite (E41D2014, 213.8m). **D.** Stage 3B quartz - pyrite - calcite - K-feldspar vein with hematite-dusted K-feldspar alteration halo cut by carbonate - hematite-bearing stage 7 vein. Hosted in diorite (E41D2165, 336.2 m). **E.** Stage 6 veining with weak hematite alteration halo cut by stage 7 vein hosted in diorite (E41D2165, 306.1m). **F.** Post-mineralisation amygdaloidal dyke altered by late hematite - calcite facies. Late calcite veinlets have cut the dyke sample (E41D2063, 117.4m). **G.** Photomicrograph (ppl) of hematite - calcite infill of amygdale. Hematite occupies rim of amygdale whereas calcite has filled its central part. Groundmass is altered to chlorite - clays. Hosted in amygdaloidal dyke (E41D2063, 117.4m). Abbreviations: ac=actinolite, ab=albite, ch=chlorite, cl=calcite, ep=epidote, ht=hematite, Kf=K-feldspar, qt=quartz.

5.4.3.3 Stage 6 veins

Stage 6 veins consist of epidote, carbonate and subordinate quartz, prehnite ± minor pyrite (Table 5.4). The veins and veinlets are irregular to wispy shaped, and can occur in erratic nets that completely obscure the primary texture of the rock. Locally red hematitic alteration envelopes are best-developed around epidote ± carbonate veinlets. Stage 6 veins cross-cut all previous vein stages (e.g., 3A-c; Fig. 5.19C). Epidote – carbonate veinlets are found mutually cross cutting each other. All barren carbonate ± quartz ± chlorite or monomineralic carbonate veins and veinlets have been tentatively included within this stage.

The distribution of stage 6 veins is shown on Figures 5.7F and 5.8F. Since carbonate – quartz and epidote – carbonate – prehnite veinlets were discriminated during logging, their distributions are indicated individually on Figure 5.7F. A strong network of white carbonate veinlets occurs in the eastern part of east pod (Fig. 5.7F). They are localised near a major east-dipping fault which flanks east pod. An increased density of carbonate – epidote – prehnite veinlets has been noted adjacent to the mineralised zones (Fig. 5.7F). They are also more abundant in shallower levels (Fig. 5.11). Precise temporal relationships between epidote – carbonate ± prehnite veins and carbonate ± quartz veins remains undetermined.

5.4.3.4 Stage 7 veins

Stage 7 consists of hematite – carbonate veins that occur throughout E41. They are typically narrow (up to 10 mm wide), wavy and discontinuous veins (Figs. 5.19D and E; Table 5.4). Stage 7 veins cross-cut stage 3A, stage 3B and stage 4 veins, and also occurs as late infill in reopened-stage 3 and 4 veins. In places, stage 7 hematite – carbonate veins can be easily mistaken for hematite-bearing stage 4A veins. Stage 4A, however, exhibits intensely-developed illite – muscovite – chlorite – carbonate alteration halos, which are absent from stage 7 veins. The distribution of stage 7 veins is shown on Figures 5.7F and 5.8F. As for stage 6, these veins appear to flanked mineralised zones.

5.5 West pod

The nature of mineralisation and alteration in west pod differs from the eastern part of the deposit. Two major zones of hypogene gold mineralisation have been recognised in the mafic monzonite intrusion (Figs. 3.2A and 5.3). Both zones strike north to north-northeast and dip moderately steeply (60˚) to the east. They are elongate and localised on the margins of the hybrid zone (Fig. 5.3A). Main stage mineralisation veins are either rare or absent from the hybrid zone. Supergene gold mineralisation at west pod of E41 is intersected within 10 m of the surface (Fig. 5.3A).

The styles of alteration in west pod range from pervasive to selectively pervasive as well as vein halos. Unlike in the east pod diorite, the primary mineralogy and equigranular texture of the west pod mafic monzonite is well-preserved. The overall vein paragenetic sequence and alteration facies show less variability than in the east pod (Fig. 5.1; Tables 5.5 and 5.6). Seven major alteration facies and seven vein stages (Fig. 5.1; Table 5.6) have been recognised at west pod. Their characteristics are described in the following sections.

5.5.1 Early stage alteration facies and veins

5.5.1.1 Albite – chlorite ± (hematite-dusted) K-feldspar alteration

Early pervasive alteration at west pod comprises albite and chlorite and occurs throughout the mafic monzonite intrusion (Figs. 5.3B and 5.20B). Albite has replaced plagioclase whereas chlorite occurs as pseudomorphs after ferromagnesian minerals, most likely former hornblende and pyroxene. The altered mafic monzonite has a characteristic red coloration which has overprinted early formed chlorite – albite (Fig. 5.21A). The 'red rock' alteration relates to hematite-dusted feldspar (Figs. 5.21A, B, C, F and G). Hematite reddening of the mafic monzonite is indicated on Figures 5.3B and 5.20B. Sodium cobaltinitrite staining indicates a moderate to intense K-feldspar content in the mafic monzonite. Giving that primary K-feldspar is present in the mafic monzonite it is difficult to assess with confidence the volume and degree of K-feldspar alteration. It also remains unclear whether or not hematite dusting occurred coeval with K-feldspar alteration.

5.5.1.2 Stage 1A 'vein dykes'

Stage 1A 'vein dykes' (Figs. 5.21B and C) occur locally within the mafic monzonite. They are composed of fine grained, pink or red-coloured K-feldspar that is intimately intergrown with quartz and actinolite. Myrmekitic texture characterises intergrowths of K-feldspar and quartz and can be observed using a hand lens. Quartz locally shows radial growth bands and occurs in the central part of the vein dykes. K-feldspar typically forms a 2 – 4 mm wide coherent mass along the vein dyke margins. Some vein dykes consist entirely of K-feldspar and quartz. Euhedral pyrite crystals are the only sulfides associated with vein dykes and they commonly occur in the centre. Actinolite is fibrous and well crystallised (Figs. 5.21C and D) and locally it has been replaced completely by muscovite (Fig. 5.21E). Vein dykes morphologies are described in Table 5.6. No obvious alteration envelopes were recognised. Similar magmatic-hydrothermal features have been described at Northparkes (Lickfold et al., 2003) and Cadia (Wilson et al., 2003). At west pod, it does not appear that these magmatic-hydrothermal features (vein dykes) are spatially confined to any particular part of the mineralised zones.

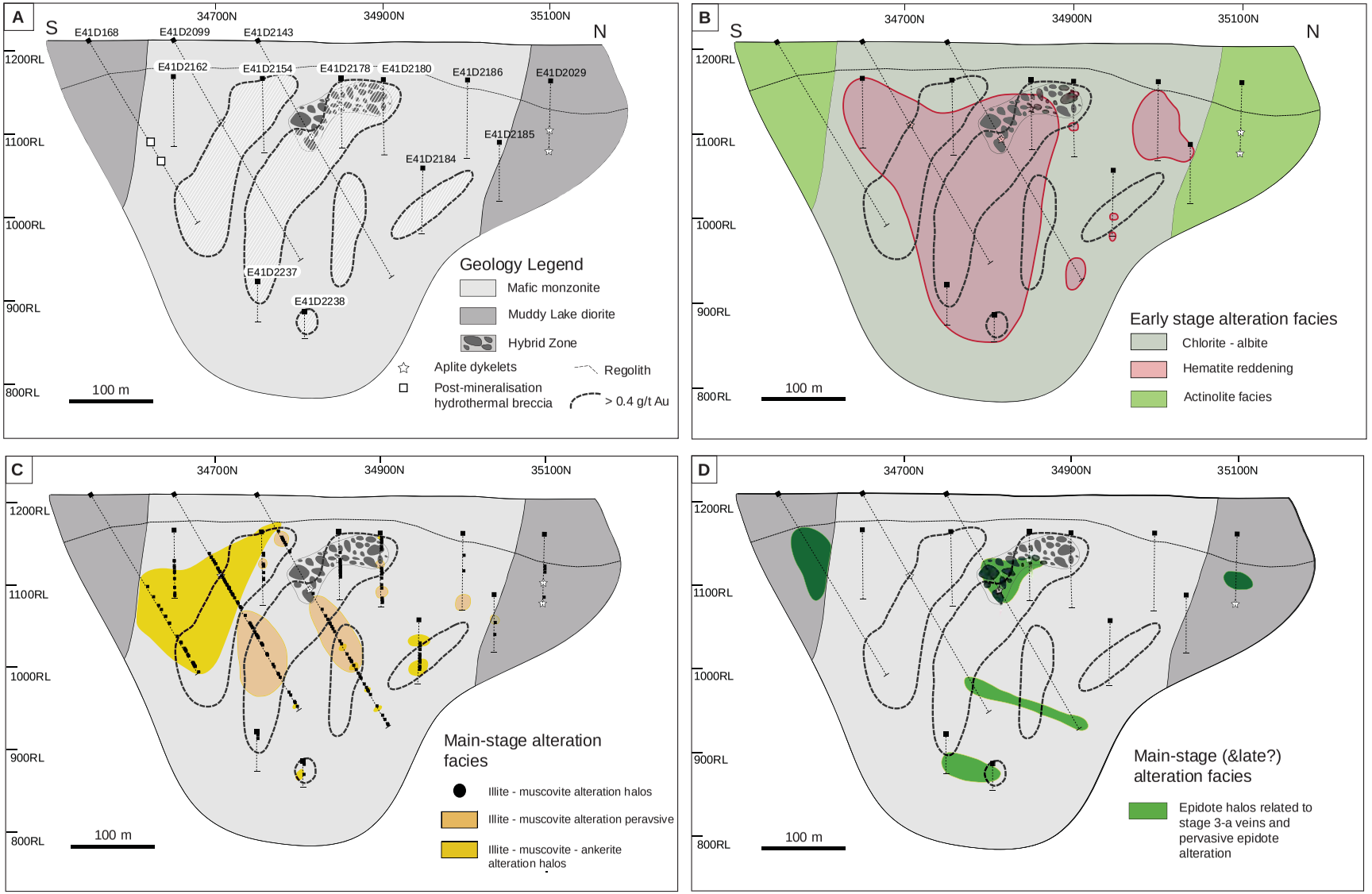

Figure 5.20 Alteration and gold distribution on cross section 86200E through the west pod. **A.** Geology of section 86200E. **B.** Distribution of early stage alteration facies. **C.** Distribution of main-stage illite – muscovite ± ankerite alteration facies. **D.** Distribution of main-stage (and late ?) epidote alteration facies.

TABLE 5.5 Styles of alteration and the spatial and temporal distribution of alteration facies at west pod, E41.

Alteration assemblage/facies	Major minerals	Minor minerals	Alteration intensity and styles	Spatial and temporal association
Early – stage alteration facies				
	Albite, chlorite	± K-feldspar ± hematite ± pyrite	Weak, selectively pervasive alteration; primary mafic minerals have been replaced by chlorite; plagioclase altered to albite and K-feldspar; characteristic common reddening relates to hematite-dusted feldspar component	Occurs in the mafic monzonite and monzonite dykes; this assemblage together with hematite occurs as a broad zone in the centre of the west pod extending up to 300 meters vertically and 200 wide laterally, narrowing downward and weakening towards the north
	Illite-muscovite, ankerite	± pyrite	Moderate to strong pervasive, typically texturally destructive alteration, locally occurs as alteration halos; this assemblage has overprinted primary minerals in the mafic monzonite	Strongly developed in central parts of the mafic monzonite and extends to the south of the deposit, weak towards the north; not related to mineralised zones
Main – stage alteration facies				
	Epidote	± K-feldspar	Weak, selectively pervasive, typically restricted to vein envelopes, original rock textures preserved; epidote preferentially altered primary mafic minerals and plagioclase crystals	Temporally, epidote and rare K-feldspar are partially related to the stage 3A-c veins. Spatially, two major domains of epidote are recognised: (1) within the hybrid zone of the mafic monzonite, (2) rare disseminations at depth in the same intrusion
	Illite-muscovite, calcite, ankerite	± pyrite ± chlorite ± sphalerite	Moderate to intensive alteration halos; well mineralised illite – muscovite has a waxy green appearance, has replaced primary K-feldspar phenocrysts and plagioclase, intensely developed alteration halos commonly pseudomorphed ferromagnesian minerals; halos more intensely developed around stage 4 veins	Associated with stage 3 and stage 4 veins and infill and multi stage veins; pyrite, sphalerite and gold locally occur in halos that are associated with stage 4 veins
	Arsenopyrite	Ankerite	Weak alteration halos, where euhedral arsenopyrite crystals have overprinted the illite – muscovite alteration facies	Associated with stage 4 veins and reopened veins (e.g., stages 3-4 stage)
Post – mineralisation alteration facies				
	Illite-muscovite, ankerite	± pyrite	Intensely developed, pervasive alteration of matrix, clasts and cement in post-mineralisation hydrothermal breccia	Temporally associated with hydrothermal breccia in the southern part of the deposit (ankerite-dominated alteration facies); and on the eastern flank of west pod (34900N section) illite – muscovite dominated alteration facies
	Illite, muscovite, carbonate, clays	± pyrite	Moderate, pervasive, texturally destructive alteration halos around late faults	Associated with late fault zones and has infilled fractures which have cut post-mineralisation hydrothermal breccia

[1] Alteration facies are listed from oldest to youngest

TABLE 5.6. Vein stages of west pod, E41.

Vein stage[1]	Major minerals	Minor minerals	Alteration halos/average width	Average[A] Au grade (g/t)	Average[A] Cu grade (ppm)	Thickness	Form, mineral associations, internal vein textures and occurrences	Orientation
Early – stage veins								
Stage 1 vein dykes	Quartz, K-feldspar, actinolite	Pyrite	None	No data	No data	2-10 mm	Quartz lenses surrounded by euhedral K-feldspar crystals; typically K-feldspar with myrmekitic texture; some contain course fibrous actinolite crystals partially overprinted by muscovite and chlorite	No data
Stage 2	Quartz, carbonate	None	Fine grained illite ± ankerite; slightly green, pink to pale brown coloured; up 50 mm wide	No data	No data	≤ 1 - 5 mm	Continuous veins, parallel to sub-parallel or hair-like veinlets; quartz and white carbonate intergrown with each other; quartz commonly dominates this stage	Flat to moderately inclined vein sets[2]
Main – stage veins								
Stage 3A-a and 3A-b	Quartz, pyrite	Chlorite ± pyrite	(1) Epidote; (2) K-feldspar-epidote; up to 5 – 10 mm wide	No data	No data	2 - 3 mm	Rare continuous, straight-sided vein walls; this stage has only been observed at depth	Generally E striking 65º S to SE dipping
Stage 3A-c	Quartz, pyrite	Carbonates, illite	Illite (1): waxy green illite ± carbonate; 10 -15 mm; (2) cream to light pink-coloured halo of illite; 10 -60 mm; (3) illite – chlorite – pyrite ± carbonate; 10 mm; (4) illite – ankerite; 10-15 mm	0.6 (n=8)	167 (n=8)	2 – 10 mm	Continuous, parallel-sided vein walls; pyrite is fine grained euhedral to subhedral, or fractured, and dispersed throughout veins; occasionally pyrite occurs as stringers within the vein; chlorite occurs usually at depth; stage 3A-c is the most common stage at west pod	Generally E- and NNE striking vein orientation 57º S dipping and 60º E dipping, respectively*
Stage 4A	Carbonates (ankerite), sphalerite, quartz	Calcite, pyrite, quartz, chalcopyrite, galena, tellurides, Au ± hematite	(1) Illite (green waxy, well crystallized) ± carbonate ± pyrite ± sphalerite; 40 mm wide (2) Illite; ~ 40 mm wide - white-to cream coloured	0.4 (n=4)	225 (n=4)	≤ 5 - 10 mm	Continuous, parallel-sided vein walls; locally slightly irregular/or wavy margins; quartz intergrown with white-cream carbonate; carbonate crystals are euhedral, some are sugary textured; sphalerite (honey coloured or rarely black) have formed chains and/ or aggregates along the margins; this stage commonly constitutes a second infill in stage 3A-c veins	Generally ENE-striking (70º SE dipping); 2nd population NE –striking 70º NW (dipping)

TABLE 5.6 (Cont.)

Stage 4C	Quartz, pyrite, carbonate	Sphalerite, galena, illite, arsenopyrite, pyrite, tellurides, ankerite, chlorite	Green, waxy illite ± carbonate ± pyrite ± ankerite; 50 cm	2.9 (n=8)	288 (n=8)	Up to 3m	'Quartz sulfide breccia', irregular, multi-stage veins, typically brecciated; brownish colour is imparted by ankerite; sulfides are fine (sphalerite, galena) to coarse grained (pyrite); pervasively illite – muscovite-altered fragments of wall rock are common	Associated with faults [2]; this stage has filled fractures in stage 3A-c veins, and is oriented parallel to stage 3A-c veins
Late – stage veins								
Stage 5	Carbonate, quartz	± hematite ± specularite	Weak cream illite halos occur locally; up to 30 mm wide	None	None	2-5 mm	Continuous, straight-sided to wispy and typically thin, sugary textured, white carbonate intergrown with minor quartz; grains of specularite are dispersed throughout the vein; locally sheeted vein sets	Various orientations
Stage 6	Epidote, carbonate	Pyrite	None	None	None	1-40 mm	Irregular, wavy, sinuous-shaped; randomly oriented veinlets mutually cross-cutting have formed erratic net veinlet systems in the diorite	Various orientations
Stage 7	Ankerite	None	None	None	None	2-40 mm	Continuous to discontinuous veinlets; strongly brown coloured, occur throughout the pod; cut all the previous stages constituting late stages and cutting faults	Various orientations

[1] Vein stages listed from oldest to youngest
[2] No structural measurements available for this stage due to lack of an oriented core, or due to broken core
* Structural data sourced from Barrick Gold Limited (unpublished data)
[A] Average grades determined by ICP-MS analyses of individual veins.
n =number of analyses per vein stage

5.5.1.3 Stage 2 veins

Stage 2 veins (Fig. 5.21F) and veinlets are developed throughout the mafic monzonite of west pod. Some of their characteristics are presented in Table 5.6. The veins are composed of quartz and white to cream-coloured carbonate. This stage lacks sulfides. Quartz and carbonate are fine grained. Shear features are apparent when examined in thin section. There is a strong spatial association of stage 2 veins with weak to moderate illite – muscovite ± ankerite alteration halos (Fig. 5.21F). Locally well crystallised illite – muscovite has a green coloration.

5.5.2 Main stage alteration facies and veins

5.5.2.1 Illite – muscovite – carbonate ± sulfides alteration

In west pod main stage alteration facies are predominantly represented by illite – muscovite, carbonate and minor sulfides. The complex nature and multiple generations of illite – muscovite alteration make it difficult to assess paragenetically. No significant vertical variations in illite crystallinity have been detected in west pod (illite crystallinity was qualitatively illustrated by determining the ratio of the depths of the 2200 nm to the 1900 nm absorption features; Fig. 5.24). Based on field observations two distinctive illite – muscovite sub-facies have been defined: (1) pervasive, texturally destructive illite – muscovite – ankerite alteration; and (2) green, waxy to pale - yellow alteration envelopes dominated by illite – muscovite.

The pervasive, texturally destructive illite – muscovite – ankerite alteration has affected rocks in the west pod, altering mafic monzonite and the ‘hybrid zone’ (Figs. 5.22E and F). The exact timing of this pervasive alteration is ambiguous. Several examples of mineralised veins cross cut the pervasive pale yellow to brown-coloured alteration, indicating that at least in part this alteration stage pre-dates the main gold-bearing veins. Illite – muscovite – ankerite halos around pre-mineralisation stage 2 quartz – carbonate veins provide evidence for a relatively early development of this assemblage. Furthermore, illite – muscovite – ankerite altered clasts, which occur together with illite-altered clasts and quartz – carbonate vein-bearing clasts in a post-mineralisation ankerite-cemented hydrothermal breccia (described below) also indicate an early timing of illite – muscovite – ankerite hydrothermal alteration.

The pervasive green illite has also selectively replaced plagioclase megacrysts (up to 1 mm laths) that are randomly distributed throughout the body of mafic monzonite. The origin of these pseudomorphed megacrysts is uncertain. However, given the fact that some megacryst-bearing monzodioritic enclaves occur locally in the hybrid zone, these altered laths are interpreted to possibly be a residuum of those megacrysts. The distribution of the illite – muscovite – carbonate alteration facies is

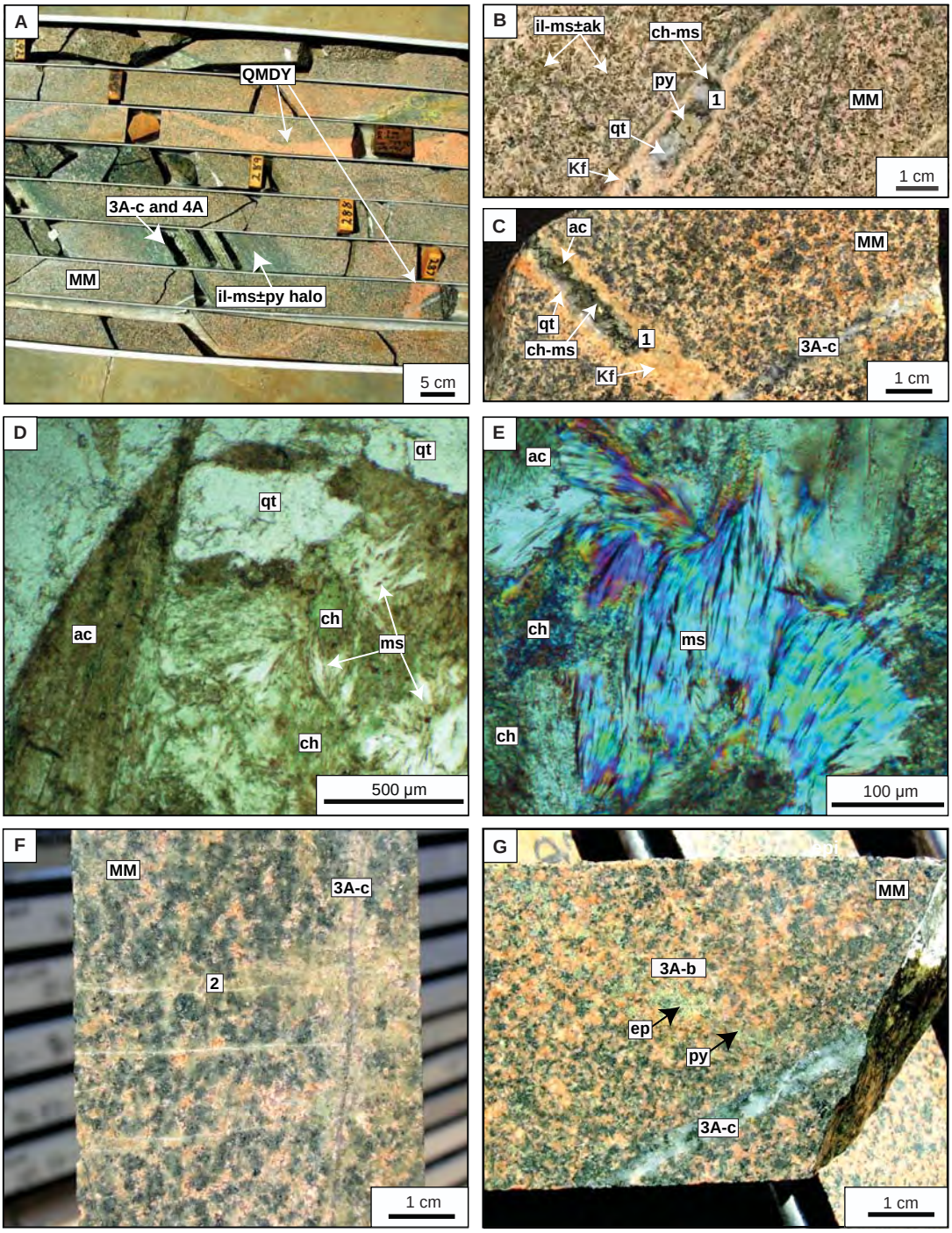

Figure 5.21 Early- and main-stage alteration assemblages and veins in the west pod mafic monzonite. **A.** Equigranular mafic monzonite with former mafic minerals altered to chlorite and plagioclase crystals altered to albite. Hematite reddening is widespread throughout the core. The early pervasive alteration is cut by mineralised veins associated with intensely developed illite - muscovite alteration halos (E41D2182, 285.17-292.30m). **B.** Example of vein dyke hosted in mafic monzonite. Hematite dusted K-feldspar on margins of the vein dyke (E41D2099, 213. 1-2m). **C.** Vein dyke cut by stage 3A-c vein (E41D2099, 265.2m). **D.** Photomicrograph (ppl) of vein dyke infill with course fibrous crystals of actinolite overprinted by chlorite and muscovite (E41D2099, 265.2m). **E.** Photomicrograph (xpl) of muscovite crystals within a vein dyke that have developed on actinolite. In places muscovite occurs together with chlorite (E41D2099, 265.2m). **F.** Stage 3A-c quartz - pyrite vein cutting stage 2 carbonate veins. Stage 2 veins have weak illite - muscovite alteration halos (E41D2162, 81.8m). **G.** Weakly developed stage 3A-b vein consists of stringer pyrite veinlet with epidote - K-feldspar halo that has been cut by stage 3A-c vein composed of quartz - pyrite and chlorite (E412237, 345.5m). Abbreviations: ac=actinolite, ch=chlorite, ep=epidote, il=illite, ms=muscovite, Kf=K-feldspar, qt=quartz, py=pyrite.

illustrated on Figures 5.3F and 5.20C. Note that illite – muscovite – ankerite alteration zones might have formed during the main- and /or post-mineralisation hydrothermal activity and cannot be better constrained temporally due to a lack of cross-cutting relationships. The domain of pervasive illite – muscovite – ankerite alteration does not appear to correlate spatially with the mineralised domains (Fig. 5.3F).

Green, waxy to pale - yellow alteration envelopes dominated by illite – muscovite, carbonate and locally sulfides occur around mineralised stage 3A-c and 4A veins (Figs. 5.21A, 5.22A, D and 5.23A). The halos around 3A-c veins are composed of green illite – muscovite close to the vein. The illite grainsize decreases away from the vein (Fig. 5.22D). Intensely developed, waxy-green alteration halos occur around stage 4A veins (Figs. 5.22A and 5.23A). They have a pervasive texturally destructive nature. Illite – muscovite has typically replaced all primary minerals, including feldspar, but also locally overprinted secondary chlorite after hornblende. In thin section, 5-10 μm occurrences of gold have been observed that are dispersed in, or attached to sphalerite in the alteration halos (Fig. 5.23G). Locally arsenopyrite occurs in halos associated with stage 4A veins and post-dates the green-coloured, well crystallised illite (Fig. 5.23H).

Green, waxy to pale - yellow alteration envelopes dominated by illite – muscovite, carbonate type of alteration forms two zones which are spatially associated with mineralisation on 34900N cross section (Fig. 5.3F). Intimate spatial relationship of waxy illite – muscovite facies to mineralisation is also obvious on Figure 5.24. On the north-south section distribution of this facies appears more chaotic and cannot always be well-correlated with mineralisation (Fig. 5.20C).

5.5.2.2 Stage 3A-a and 3A-b veins

Stages 3A-a and 3A-b are composed predominately of quartz and pyrite with minor carbonate and chlorite and they have epidote or K-feldspar – epidote halos (Table 5.6; Fig. 5.21G). Stage 3A-a and 3A-b veins at west pod are equivalent to stage 3A-a and 3A-b veins in the east pod (Fig. 5.1). Quartz – pyrite veins with epidote and with K-feldspar – epidote halos are rare in west pod and cross-cutting relationships are uncommon, however, they are thought to have formed at similar times and are combined here as stage 3A-a and 3A-b. Quartz is commonly euhedral and carbonate is in places associated with interstitial anhedral chlorite. Typically, carbonate and chlorite are intimately associated with pyrite. Stage 3A-a and 3A-b appears to be limited to the deeper parts of the deposit (Fig. 5.7B). The distribution of epidote and K-feldspar – epidote alteration halos associated with this vein stage are presented on Figures 5.3C and 5.20C. They are restricted to the deeper portions of west pod.

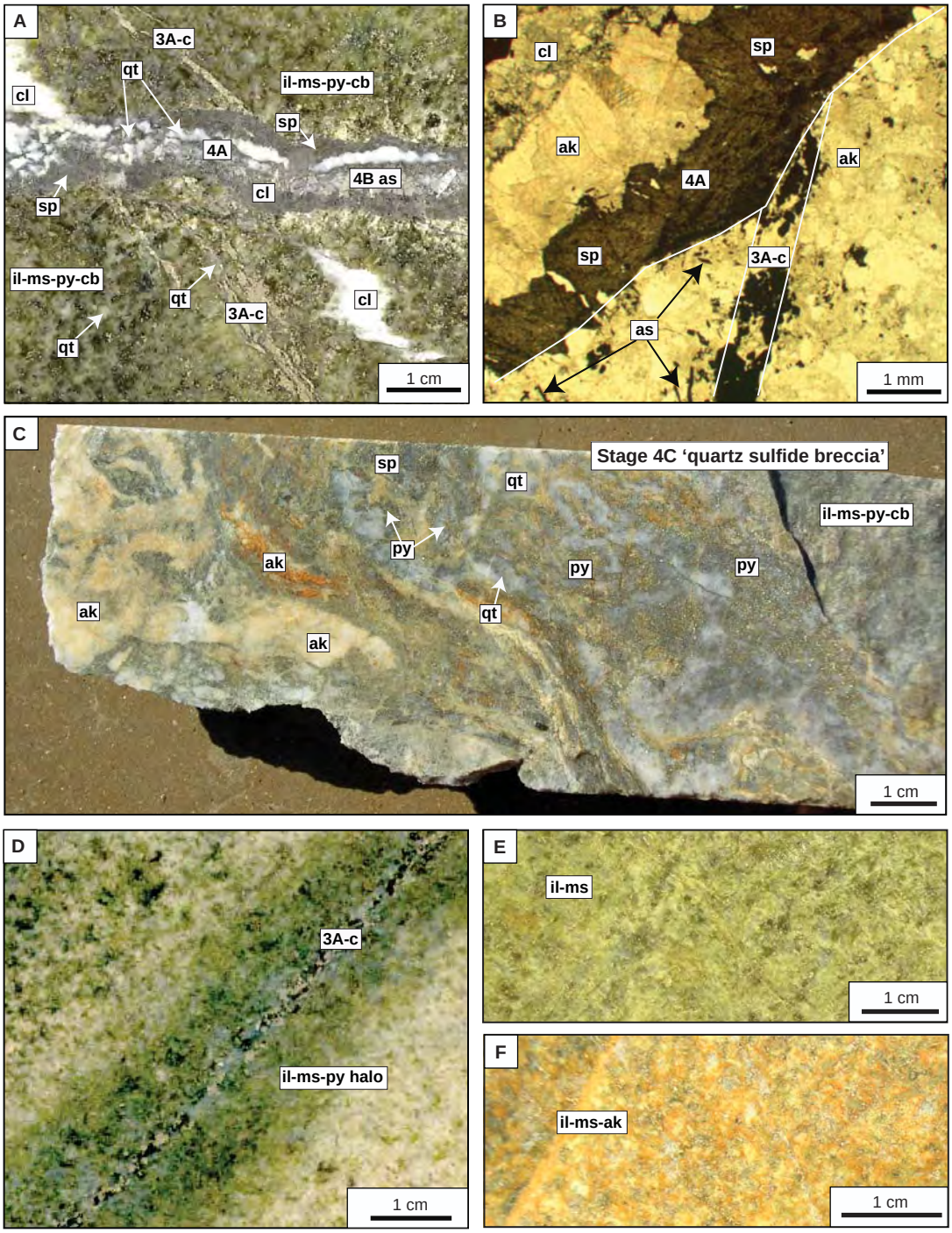

Figure 5.22 Main-stage veins and alteration facies hosted in mafic monzonite. **A.** Stage 3A-c quartz - pyrite vein cut by stage 4A carbonates (ankerite and calcite) - pyrite - sphalerite - quartz - galena, and stage 4B arsenopyrite. Euhedral crystals of arsenopyrite (stage 4B) constitute the central part of the vein, post-dating the formation of sphalerite and carbonate (E41D2180, 104.2m). **B.** Photomicrograph (ppl) of stage 4A and 4B veins that have cut a stage 3A-c quartz - pyrite vein (E41D2180, 104.2m). **C.** Stage 4C 'quartz sulfide breccia'. Highly mineralised (11.5 ppm Au) brecciated vein (E41D168, 225.8m). **D.** Stage 3A-c vein with strong waxy green illite - muscovite - pyrite alteration halo (E41D2143, 179. 1m). **E.** Pervasive illite - muscovite ± pyrite alteration facies (E41D2143, 75.2m). **F.** Peravsive illite - muscovite - ankerite ± pyrite alteration facies (E41D2143, 64.9m). Abbreviations: ak=ankerite, as=arsenopyrite, cb=carbonate, cl=calcite, ch=chlorite, ep=epidote, py=pyrite, sp=sphalerite, il-ms=illite-muscovite, qt=quartz.

5.5.2.3 Stage 3A-c veins

Stage 3A-c (Figs. 5.22A and D) is the most common gold-bearing vein stage in west pod (Fig. 5.7C). It appears that the hybrid zone has a lower density of this vein stage (Fig. 5.24). This stage corresponds to stage 3A-c veins in east pod (Fig. 5.1). The mineralogy, style and morphological features of 3A-c stage are listed in Table 5.6. Several generations of stage 3A-c veins have been observed that mutually crosscut each other. Some of the 3A-c veins are distinguished by abundant sugary white carbonate. Stage 3A-c veins are commonly associated with distinctive illite – muscovite halos (Fig. 5.22D), but some veins lack obvious alteration envelopes (Figs. 5.21C and G), suggesting that they formed in chemical equilibrium with the previously altered wall rocks.

5.5.2.4 Stage 4A veins

This stage is composed of carbonate and base-metal sulfide-bearing veins and is mineralogically equivalent to stage 4A veins from east pod (Fig. 5.1). As for east pod, stage 4A veins at west pod are associated with high gold grades (Table 5.6 and Fig.5.24). The characteristics of stage 4A veins are provided in Table 5.6. Stage 4A veins (Fig. 5.23A) are characterised by the presence of a white to cream-coloured carbonate (ankerite), minor euhedral quartz and sulfides. Ankerite crystals are euhedral, have growth bands and grow into the centre of the vein (Fig. 5.23C). They were an early vein infill and occupy the vein margins. A second generation of carbonates that are more calcitic occurs in the central parts of the vein together with sulfides (Figs. 5.23C and D). The sulfides, predominately sphalerite (with abundant chalcopyrite inclusions; Fig. 5.23B), galena and pyrite also occur as continuous bands along vein margins. The sulfides have an intimate association with gold and tellurides, as determined by electron microprobe. Fine-grained Ag-telluride crystals are typically 1-2 μm in diameter and are hosted in sphalerite, generally adjacent to gold grains (Fig. 5.23F). Individual gold grains occur within sphalerite crystals and also within illite – muscovite – carbonate vein halos associated with finely crystalline sphalerite (Fig. 5.23G). Gold grains are ~ 20 μm in size.

In east pod it is difficult to see crosscutting relationships between stage 3A-c quartz – pyrite and stage 4A carbonate-base metal veins. In west pod, these relationships are clearly evident, with examples of stage 4A veins cutting stage 3A-c quartz – pyrite veins (Fig. 5.22A and B).

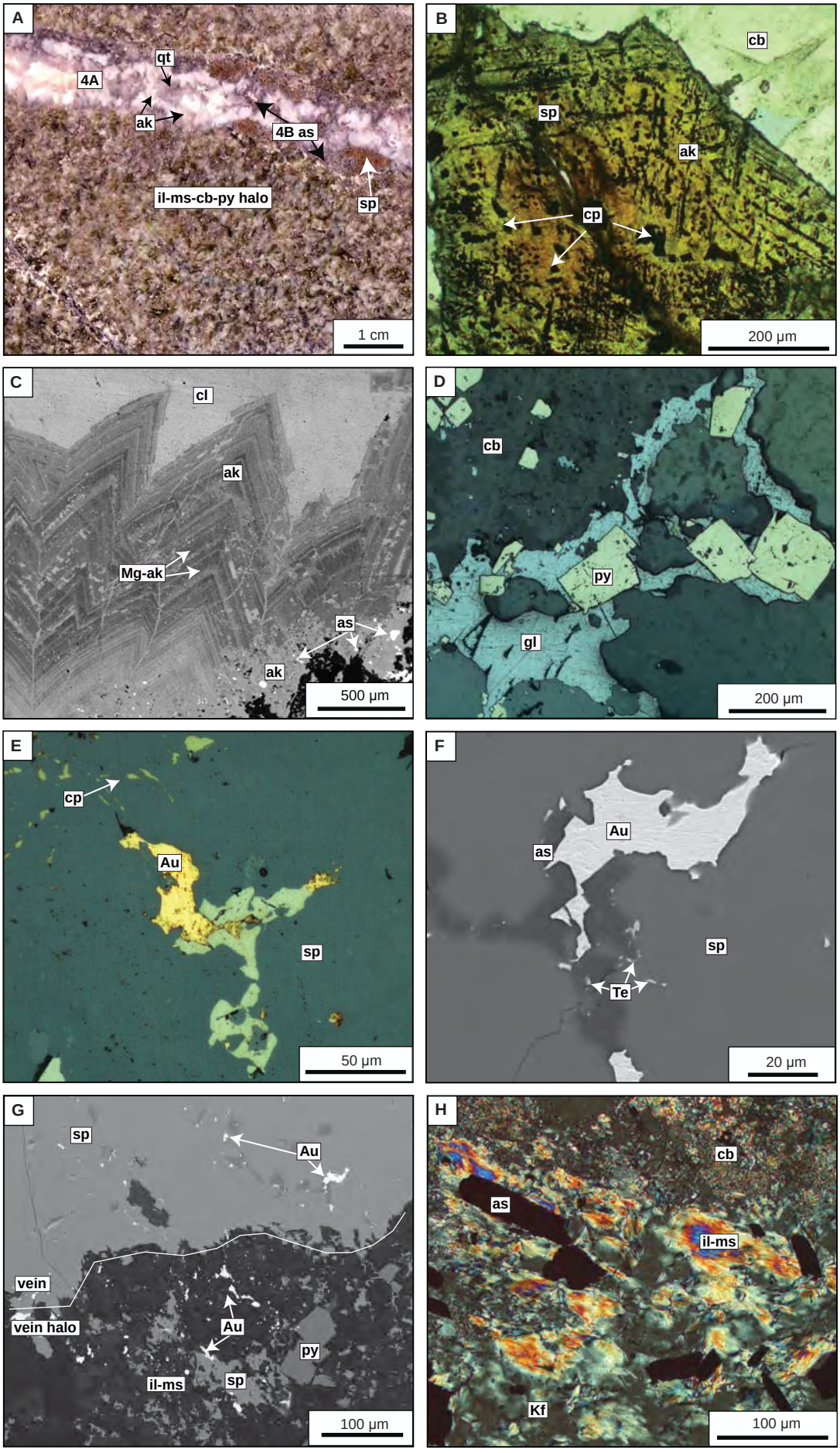

Figure 5.23 Stage 4A and 4B infill in the west pod.

5.5.2.5 Arsenopyrite – ankerite alteration facies

Arsenopyrite alteration (Table 5.5) is temporally and spatially related to stage 4B. This alteration is temporally equivalent to the arsenopyrite – ankerite assemblage at east pod (Fig. 5.1). In west pod euhedral arsenopyrite crystals occur in alteration envelopes associated with stage 4A that have been reactivated and filled with 4B stage. Arsenopyrite appears to have overgrown illite (Fig. 5.23H).

5.5.2.6 Stage 4B infill

Stage 4B arsenopyrite is commonly spatially related to stage 4A veins, and only locally forms individual veins with ankerite. Stage 4B infill features are listed in Table 5.6. Arsenopyrite is typically observed in vein margins together with ankerite or occupies a central part of the vein (Fig. 5.22A). Crystals of arsenopyrite are up to 2 mm, euhedral with a needle-like habit. Arsenopyrite is interpreted to have formed shortly after precipitation of the major phase of stage 4A, as it post-dates sphalerite, galena, pyrite, chalcopyrite and tellurides (Fig. 5.22A). Some ankerite is interpreted to have been deposited synchronous with arsenopyrite based on their mutual intergrowths.

5.5.2.7 Stage 4C

Stage 4C in west pod have similar characteristics as in east pod (Table 5.6). It typically shows evidence for reactivation and multi stage infill. The minerals of stage 4C are massive with abundant carbonates (ankerite) and intensely fractured pyrite. Stage 4C has been intersected only in two locations in west pod (DDH: E41D2180, 63-64 m interval and E41D168, 225.8m; Fig. 5.22C). In both areas the 4C occurrences have marked highly mineralised domains (e.g., sample E41D2180; Fig. 5.24). This stage is spatially and temporally associated with strong green waxy illite – muscovite alteration.

Figure 5.23 Main stage 4A and 4B veins hosted in mafic monzonite from west pod. **A.** Stage 4A vein with secondary infill of arsenopyrite and ankerite (stage 4B). The milky coloured crystals in vein margins are ankerite. The white anhedral minor mineral in the central part of the vein is calcite. Sphalerite occupies vein margins. The vein has a intense illite - muscovite - carbonate - pyrite - arsenopyrite alteration halo (E41D2180, 103.9m). **B.** Stage 4A vein with honey-coloured sphalerite that contains numerous chalcopyrite inclusions (chalcopyrite disease). Vein hosted in mafic monzonite (E41D2180, 102.6m). **C.** BSE image of euhedral ankerite crystals from the 4A stage vein margin. Individual ankerite crystals have distinctive black-grey Mg-rich layers. Photograph also shows vein centre (top of the picture) which has been filled with calcite. Marginal part of the vein is occupied by a fine grained mass of ankerite which occur together with stage 4B arsenopyrite (E41D2180, 103.9m). **D.** Photomicrograph (reflected light) showing association of galena and euhedral pyrite of stage 4A (E41D2143, 289.9m). **E.** Photomicrograph (reflected light) of gold occurrence within sphalerite crystal of stage 4A vein. Minor chalcopyrite specs are also present in sphalerite (E41D2180, 103.9m). **F.** BSE image of Au grain hosted in sphalerite. Occurrence of Au is intimately associated with fine Ag-tellurides (E41D2180, 103.9m). **G.** BSE image of rare occurrences of gold grains in vein halos. In this sample gold is dispersed throughout the alteration halo of the 4A vein stage. It occurs together with carbonate - illite - muscovite (E41D2180, 103.9m). **H.** Photomicrograph (xpl) showing a relationship between illite - muscovite and arsenopyrite with the latter cutting illite - muscovite crystals. Illite - muscovite and arsenopyrite occur as an alteration halo associated with multi stage vein (4A + 4B; E41D2180, 103.9m). Abbreviations: ak=ankerite, as=arsenopyrite, cl=calcite, cp=chalcopyrite, gl=galena, il=illite, Kf=K-feldspar, Mg-ak=magnesium-rich ankerite, ms=muscovite, mt=magnetite, py=pyrite, sp=sphalerite, Te=tellurides, BSE=back scattered electron imaging.

5.5.3 Late stage alteration facies, veins and breccias

5.5.3.1 Late stage alteration

Late stage hydrothermal alteration in west pod has proven to be difficult to identify unambiguously. Ankerite occurs together with other carbonates as a late alteration overprint based on the brown oxidation stain of weathered core.

Late faults that have cut post-mineral ankerite-cemented hydrothermal breccia helped to constrained the character of the late alteration assemblages (Fig. 5.25F). The late faults are typically infilled with clay minerals, illite and carbonates. Locally, 1 mm veinlets of pyrite define a tectonic fabric aligned subparallel to the late faults, which suggests that some sulfides were precipitated from the late fluids.

In west pod, weakly-developed epidote alteration has altered earlier-formed alteration facies. Epidote has altered the black monzodioritic enclaves and also locally the mafic monzonite within the 'hybrid zone'. Zones of pervasive epidote have been mapped (Fig. 5.20D). The upper zones of epidote alteration on 86200E section are interpreted to represent late epidote occurrences whereas the lower domains of epidote are related to stage 3A-a and 3A-b veins.

5.5.3.2 Stage 5 veins

This stage is composed of ankerite, some calcite, quartz with hematite and specularite occurring locally. Veins are straight-sided to wispy and typically thin, 2-5 mm. The carbonates are intergrown with white quartz in most veins. In others, carbonate and quartz occur in discrete bands. Ankerite has a distinctive brown to orange coloration. Specularite occurs either in elongated wispy ribbons, as a massive 5 mm infill, or as specks dispersed throughout the veins (Fig. 5.25B). Because stage 5 veins commonly crosscut stage 3A-c veins (Fig. 5.25B) and also cut post-mineralisation ankerite-cemented hydrothermal breccia and clasts (Fig. 5.25E), a post-mineralisation timing has been interpreted for this stage.

5.5.3.3 Stage 6 veins

Stage 6 veins in west pod have the same characteristics as those in east pod (Fig. 5.1), as described in Table 5.6. Stage 6 veins in the west pod are restricted to the diorite to the north and south of the mafic monzonite intrusion.

5.5.3.4 Stage 7 veins

Stage 7 consists of ankerite veins. Fine ($\leq$ 1 mm) brown ankeritic veinlets are ubiquitous at west pod. Late stage ankerite veins and veinlets have irregular shapes. Some are continuous within individual drill core whereas others are discontinuous. Ankerite has

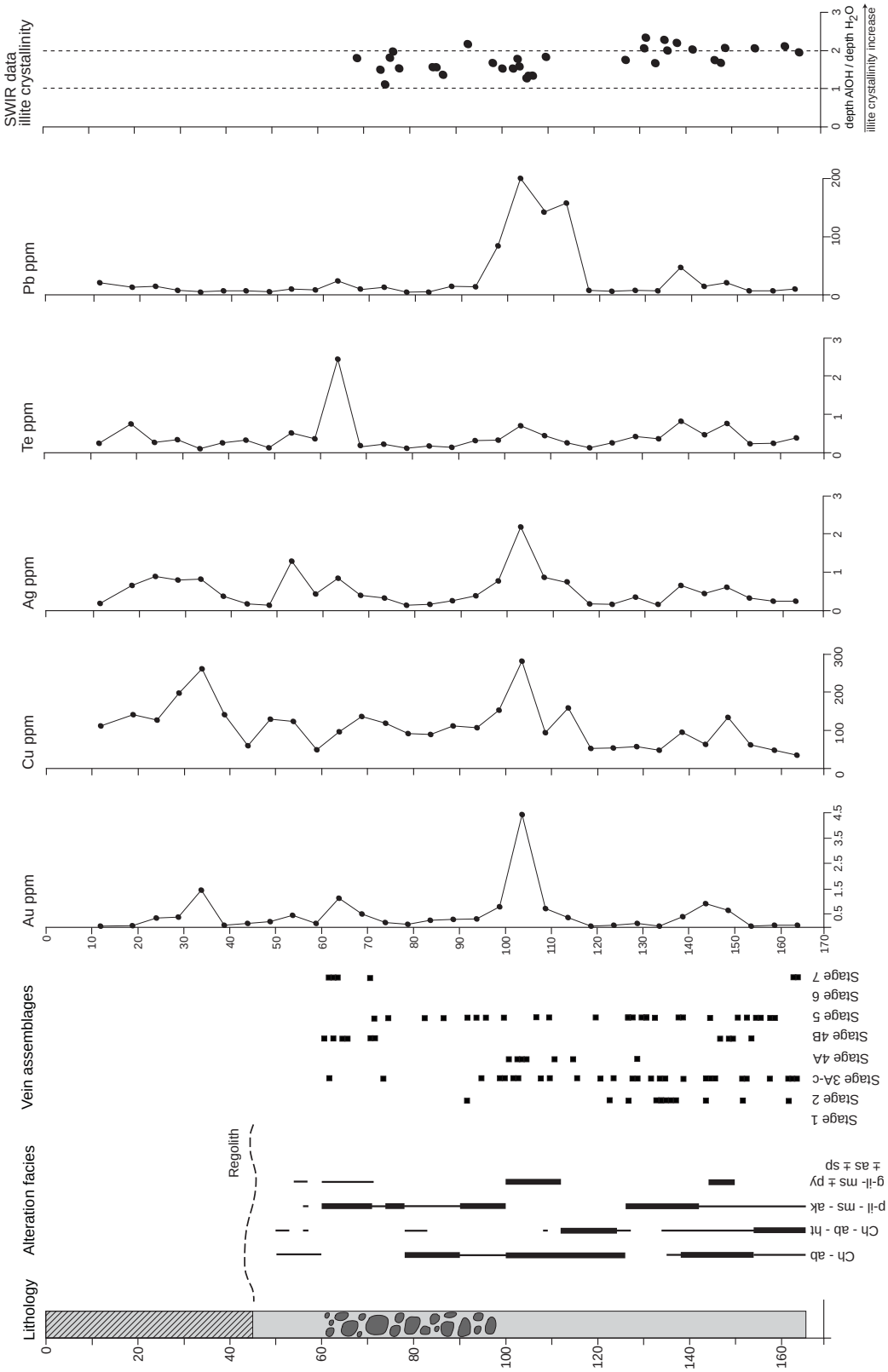

Figure 5.24 Representative summary log (DDH: E41D2180, west pod) with lithology, alteration facies and vein stages in paragenetic order. SWIR downhole data are illustrated here showing the calculated crystallinity index of illite determined based on the ratio of the depth of AlOH (2200 nm) to the H_2O (1900 nm) absorption features. The crystallinity above 2 typically indicates highly crystalline illite. Abbreviations: ab=albite, ak=ankerite, as=arsenopyrite, ch=chlorite, ht=hematite, p-il-ms=pervasive illite-muscovite, g-il=green waxy illite-muscovite, py=pyrite,

also filled reopened mineralised veins, where it has cut quartz and pyrite. Ankerite is particularly common as a late infill in the multi-stage veins.

5.5.3.5 Post mineralisation polymictic matrix-supported hydrothermal breccia

In west pod, a narrow (2 m wide) polymictic matrix-supported breccia body has been identified in two locations (Fig. 3.2B and 3.2C). The breccia contain clasts that are 2 mm to 10 cm in diameter, and are angular to subrounded. Several clast populations have been recognised: (1) strongly illite – muscovite – carbonate altered mafic monzonite; (2) polymictic breccia clasts with pyrite cement; (3) fragments of quartz veins (Fig. 5.25D), some of which are grey and contain fine-grained sulfides; (4) fine-grained lithic clasts of aphyric volcanics; truncated veins within those clasts; (5) ragged and irregular coherent equigranular clasts of monzonite; and (6) rounded clasts of feldspar-porphyry (Fig. 5.26). The matrix is characterised by intensely illite – muscovite – carbonate altered fine-grained rock fragments and crystals (Fig. 5.25C).

In the southern part of west pod, a similar breccia facies has been intersected. The southern breccia is essentially monomictic, with angular clasts of mafic monzonite ranging from 2-5 mm to 20 cm. Locally, the breccia lacks matrix and is cemented by brown to dark yellow ankerite (Figs. 5.25D, E and F). In addition, in the polymictic matrix supported hydrothermal breccia, illite has altered the matrix and locally occurs as alteration rinds on some clasts (Fig. 5.25C). The latter is interpreted as a syn-brecciation alteration feature. The ankerite ± illite alteration extends latterly and vertically over 150 m from the breccia occurrence and weakens towards the north (Fig. 5.20C).

These polymictic and monomictic matrix-supported breccia bodies have many features characteristic of hydrothermal breccias (e.g., Sillitoe, 1985) including: (1) alteration rinds on some clasts; (2) mineralised clasts; (3) truncated veins within clasts; (4) polymictic breccia clasts (possible evidence for multiple brecciation events); (5) hydrothermal cement; and (6) a pipe-like geometry. Thus the breccia body at the west pod is interpreted to be hydrothermal in nature. It contains no gold mineralisation, and is interpreted to be the last hydrothermal event at west pod.

5.6 Metal zonation

Geochemical trends from section 34900N are presented on Figure 5.27. Multielements contours have been interpreted from an unpublished geochemical data set provided by Barrick Gold of Australia Ltd. (Appendix D.4). Geologic and structural data were considered when making the interpretations.

The gold grades (>0.4 ppm) illustrated on the geological cross sections were adapted from Barrick (Figs. 5.3 and 5.4). However, in order to better characterise and

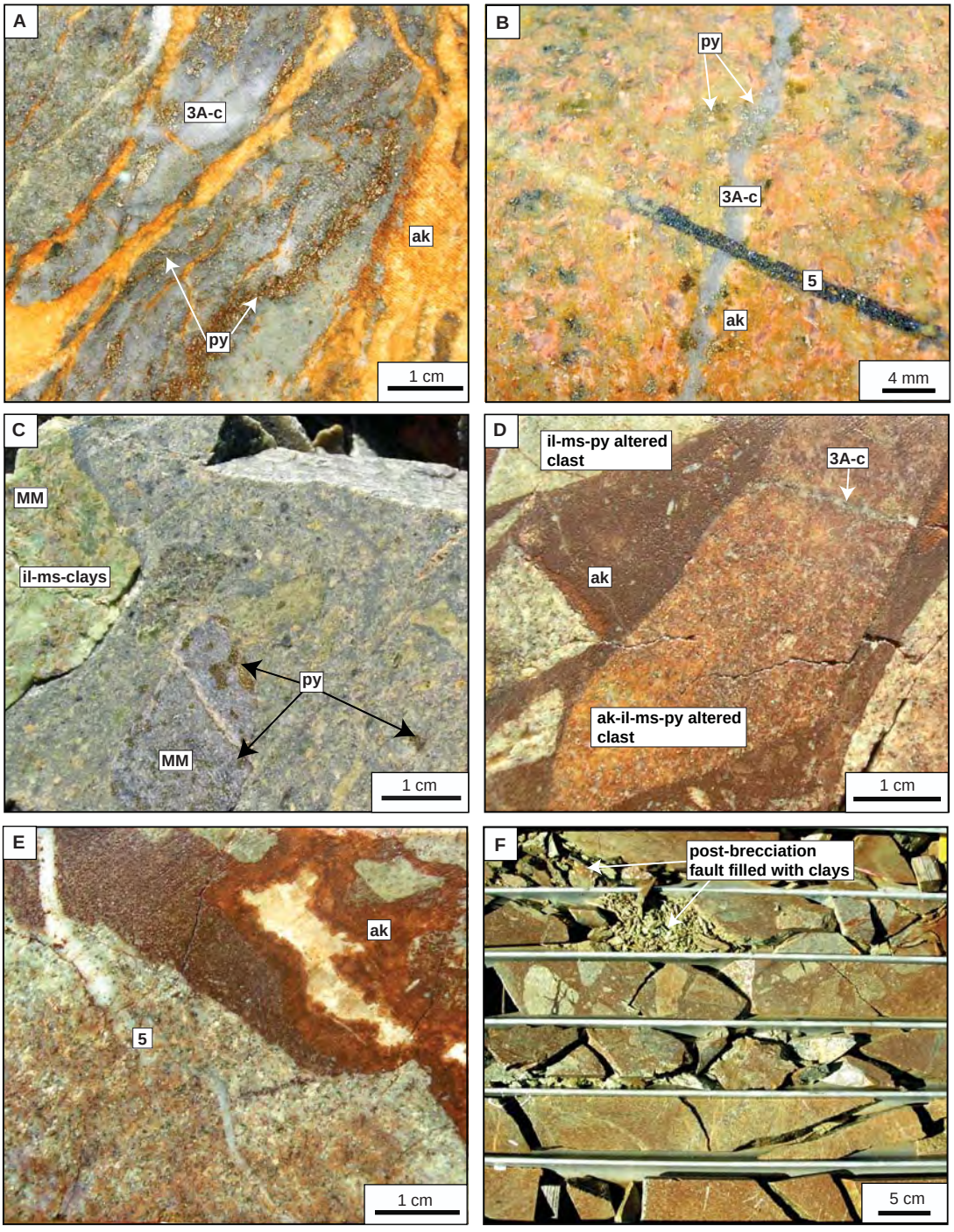

Figure 5.25 Post mineralisation veins and alteration facies in the west pod. **A.** Mafic monzonite-hosted stage 3A-c multi stage vein cut by stage 7 ankerite veins (E41D2143, 69.2m). **B.** Illite - muscovite - ankerite altered mafic monzonite with a stage 3A-c vein cut by stage 5 quartz - carbonate - specularite (E41D168, 206.0m). **C.** Hydrothermal breccia with matrix altered to illite - muscovite and clay minerals. Mafic monzonite clasts are variably altered with some entirely altered to illite - muscovite, and other altered to illite - muscovite - carbonate and pyrite (E41D2182, 89.8m). **D.** Polymictic hydrothermal breccia with ankerite cement. Photo is showing two distinctive clasts which have been altered to (1) illite - muscovite - pyrite and (2) ankerite - illite - muscovite - pyrite. The latter contains truncated stage 3A-c veins (E41D168, 138.9m). **E.** Stage 5 quartz-ankerite cutting hydrothermal breccia (E41D168, 139.4m). **F.** Photo shows late faults filled with clay minerals cutting post-mineralisation breccia (E41D168, 166.25 - 171.35m). Abbreviations: ak=ankerite, il-ms=illite-muscovite, MM=mafic monzonite, py=pyrite.

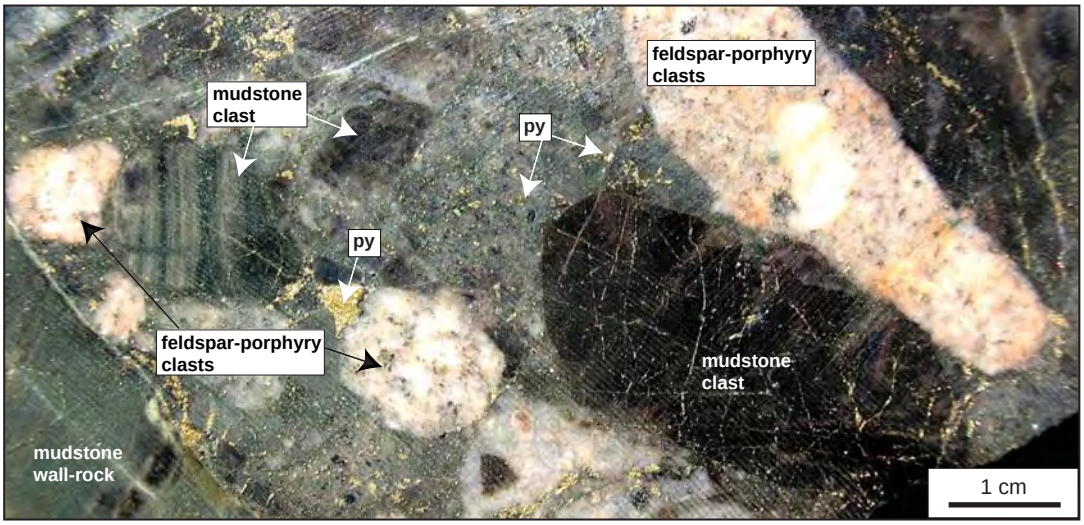

Figure 5.26 Polymictic hydrothermal breccia. Photo is showing two distinctive clasts: (a) rounded feldspar-porphyry clasts, and (b) rounded mudstone clasts. Clasts are supported in illite - chlorite - pyrite altered matrix (E41D2129, 91.1m).

understand gold mineralisation patterns in the E41 deposit, gold values were divided into four ranges that were confined using a normal distribution method. Gold patterns (Fig. 5.27A) in the east pod are generally patchy with the widest ore zones (hypogene and supergene zones) occurring along east-trending (south-dipping) fractures. Patches of gold appear to be also associated spatially with northeast-trending fractures. Similarly, in the west pod, the gold zones are predominantly related to relatively steep east-dipping and northeast-trending fractures, broadly forming two zones (Fig. 5.27A).

Copper values in east pod (> 500 ppm) are distinctively higher than in west pod (up to 250 ppm; Fig. 5.27B). Given that the east pod is dominated by mafic rocks, it may be that the copper anomalies relate to a greater potential for the replacement of mafic minerals by chalcopyrite. Chalcopyrite partially pseudomorphing some ferromagnesian minerals has been observed in the actinolite alteration facies (section 5.4.1.3). Several domains of elevated copper in the east pod roughly overlap with gold zones (compare Fig. 5.27A and Fig 5.27B). In addition, a broad zone of anomalous copper occurs at depth, overlaying early 'patchy' alteration domain and K-feldspar – epidote alteration facies (compare Fig. 5.3 and Fig. 5.27B).

Within the gold ore zones, anomalous concentrations of Te (>4 ppm), Ag (>2 ppm), As (>500 ppm), Zn (>500 ppm), Pb (>200 ppm) and P (up to 2000 ppm) have been detected (Figs. 5.27C, D, E, F and G). They correlate moderately to strongly with gold, with the concentration of Te, Ag and As having the most obvious positive correlation (compare Fig.5.27A with Figs. 5.27C, D and E). The positive correlation of Au with Cu, Ag, Te and Pb is also apparent on Figure 5.24. Elevated zinc (>500 ppm) occurs in two broad zones in east pod (Fig. 5.27F). In east pod, the lower zone of zinc anomaly weakly correlates with gold, while the upper sub-horizontal elongated

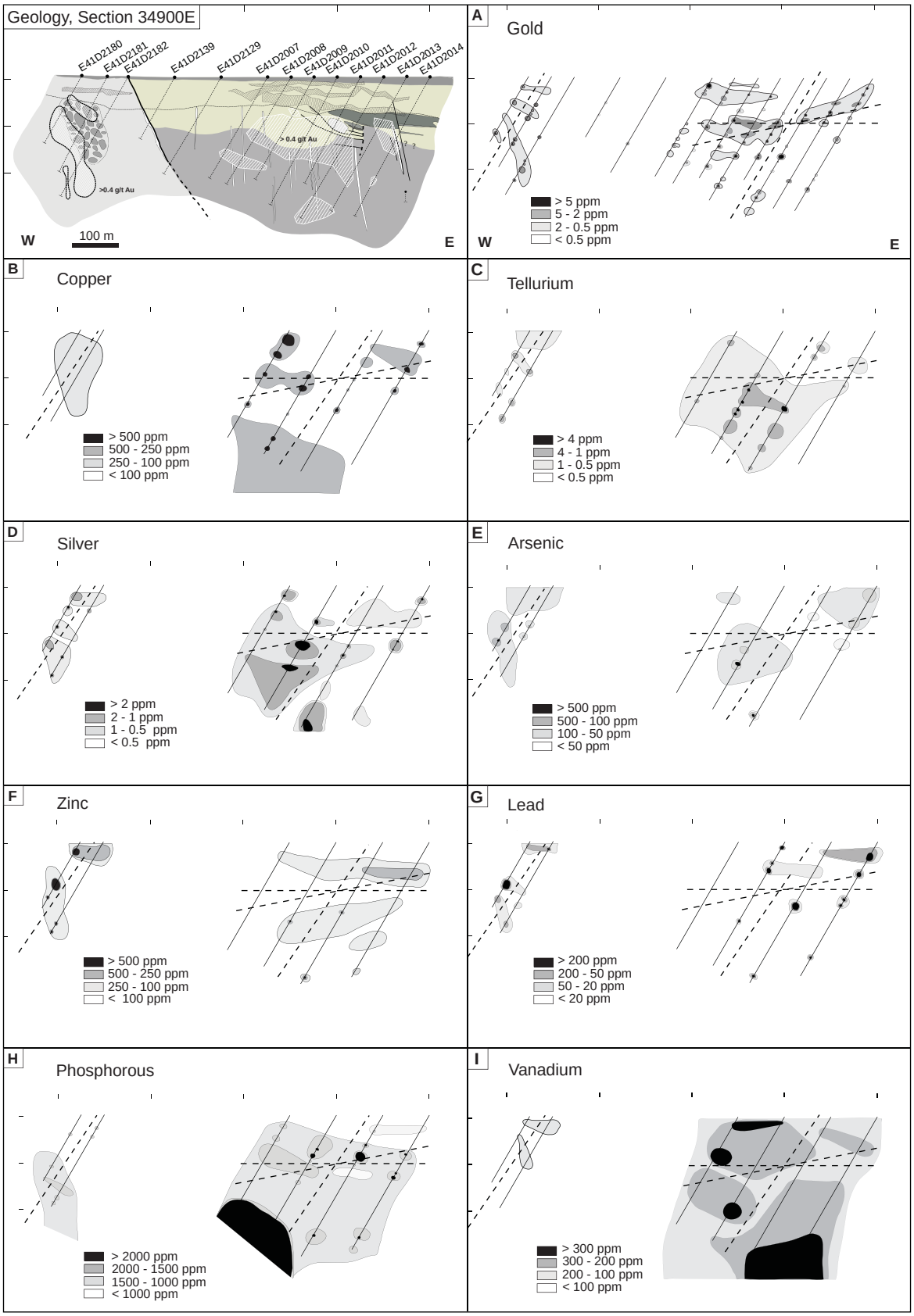

Figure 5.27 Contoured multi-element distribution for the 34900N cross section. Samples of drill core were collected every 5 metres down hole from six drill holes. Gold values are contoured based on assay data collected from each metre down hole. Dashed lines indicate major structures (based on vein orientations) that were associated with mineralised veins. These are east-, east-northeast, and north-northeast trending fractures.

domain shows obvious spatial correlations with Au patches (compare Fig. 5.27F and Fig. 5.27A). The zinc anomaly readily correlates with elevated gold in west pod (compare Fig. 5.27F and Fig. 5.27A).

In the lower portion of east pod, a strong phosphorous anomaly (> 2000 ppm; Fig. 5.27H) defines an aureole around the mafic monzonite intrusion. This phosphorous anomaly essentially mimics zones of 'patchy' alteration and reflects the presence of hydrothermal apatite in this alteration zone (compare Fig. 5.3B and Fig. 5.27H). Randomly dispersed domains of elevated phosphorous are correlated with elevated gold grades (compare Fig. 5.27H and Fig. 5.27A). This is consistent with an intimate association between apatite and gold-bearing main-stage veins (Table 5.4). Weaker than in east pod, the anomalous phosphorous zones (up to 2000 ppm) are restricted to deeper portion of west pod (Fig. 5.27H).

Figure 5.27I shows contoured vanadium concentrations. West pod is deficient in vanadium (<200 ppm), whereas at least three zones of vanadium enrichment have been defined in east pod (up to >300 ppm). The strongest anomaly is present in the deeper parts on the eastern edge of east pod (Fig. 5.27I). This vanadium zone extends up section, but doesn't appear to be associated with mineralised domains. Two other vanadium zones located in the central part of east pod have a weak spatial relationship with anomalous gold concentrations (compare Fig. 6.27A and Fig.6.27I). Although no roscoelite (vanadium-bearing mica) has been identified from veins and alteration halos at E41, there is vanadium-bearing illite associated with some main stage veins (Chapter 6). This may explain the local spatial relationship of vanadium and gold. Alternatively, the anomalous vanadium may be related to common mafic host rocks in east pod that are characterised by high primary concentration of vanadium (Chapter 4).

5.7 Structural controls on mineralisation

This section summarises the results of structural measurements of vein orientations. The principal goals are to identify the key mineralised structural elements of the deposit and to establish a structural paragenesis. All the data are presented as "strike/dip dip direction" for planes. The collected data are listed in Appendix D.5.

Vein orientations were collected from drill core using the paragenetic framework outlined in Figure 5.1. Due to a lack of oriented drill core in some locations, it was not possible to obtain measurements of some vein stages. Figure 5.28 shows stereoplots generated for four principal stages of main-stage veins from the east and west pods. The structural data for stage 3A-a and 3A-b (east pod) have been combined and show that the veins occupy relatively steeply dipping structures (71º SE) and are generally northeast-striking (Fig. 4.28A).

Stage 3A-c veins (Fig. 5.28B) are the dominant population of gold-bearing veins at E41. The stage 3A-c veins are inclined, moderately south-dipping, and generally east-striking. These gently dipping fractures have cut the steeper structures occupied by stage 3A-a and 3A-b veins. Stereoplots for stage 3A-c veins from west pod show at least three distinctive clusters (Fig. 5.28B), with the major cluster being characterised by east-striking and moderately 57º S dipping fractures. Stage 3B infill occurs in steep and inclined fractures (Fig. 5.28C). The stage 3B veins are generally east-northeast-striking and dip 65º SE.

Only a few measurements were collected for stage 4A and 4B (Fig. 5.28D). The data are scattered, with a cluster defining a north-northeast-striking and relatively steeply dipping (70º S-SE) orientation. Data for stage 4A and 4B veins from west pod are characterised by two clusters: (1) east-striking, dipping 78° S and (2) northeast-striking, with a dip of 61° NW.

Additional to the structural data collected during this study, several hundred vein orientation measurements (n=706) were extracted from Barrick's dataset for the entire E41 deposit (Fig. 5.28G-J). The structural data were assigned to the vein stages defined by the current study, using the vein descriptions from Barrick's database. Measurements obtained for stage 3A-a and 3A-b veins define an east-striking cluster (Fig. 5.28G), with an average dip of 62º S. This result is not consistent with the northeast-striking data obtained by the author (Fig. 5.28A). This discrepancy may result either from incorrectly identified vein stages or may indicate another structural trend for stage 3A-a and 3A-b veins. A cluster of data for stage 3A-c defines an east-striking population, which range from steeply to gently dipping vein sets (Fig. 5.28I). A similar trend is defined by stage 3B veins, ranging from steeply dipping to inclined towards to south and southeast (Fig. 5.28H). The stereoplot for stage 4A and 4B veins (Fig. 5.28J) shows a distinctive cluster of steeply south- to southeast- dipping veins. These veins are commonly described by Barrick geologists as 'shear veins'.

Structural analysis of main-stage veins has shown that a major east-trending structure controlled main stage gold mineralisation at E41. Most of the stage 3A-a and 3A-b veins occupy steeply south- and southeast-dipping fractures. Stage 3A-c occupy inclined fractures that have cut the steep veins. Although stage 3A-c and 3B mineralogies have typically filled the inclined fractures, there are several examples where 3A-c and 3B minerals have infilled steep fractures as well. This suggests that the steep structures may have been reactivated locally during stages 3A-c and 3B. Common mineral laminae defined by chlorite and pyrite 'chains' along veins axes have been observed during this study as well as reported by Barrick support this hypothesis. Furthermore, an overprint of illite ± muscovite (associated with stage 3A-c and 3B)

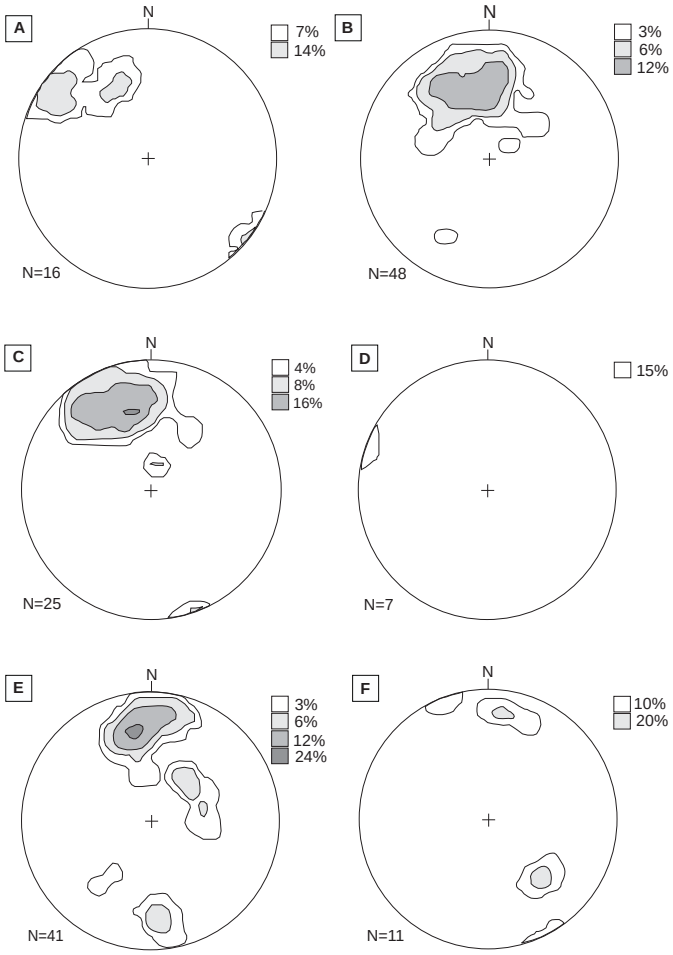

Figure 5.28 Stereoplots of measurements collected as part of this study from main-mineralisation vein stages. Orientation features are plotted onto contoured pole-to-bedding stereoplot. Stereoplots G-J of measurements from the main - stage mineralisation vein stages extracted from Barrick's unpublished database (data collected from both east and west pod). **A.** Stage 3A-a and 3A-b veins, east pod. **B.** Stage 3A-c veins, west pod. **C.** Stage 3B veins, east pod. **D.** Stage 4A and 4B veins, east pod. **E.** Stage 3-b veins, west pod. **F.** Stage 4A and 4B veins, west pod. **G.** Stage 3A-a veins. H. Stage 3B veins. **I.** Stage 3A-c veins. **J.** Stage 4A and 4B veins.

Barrick's data

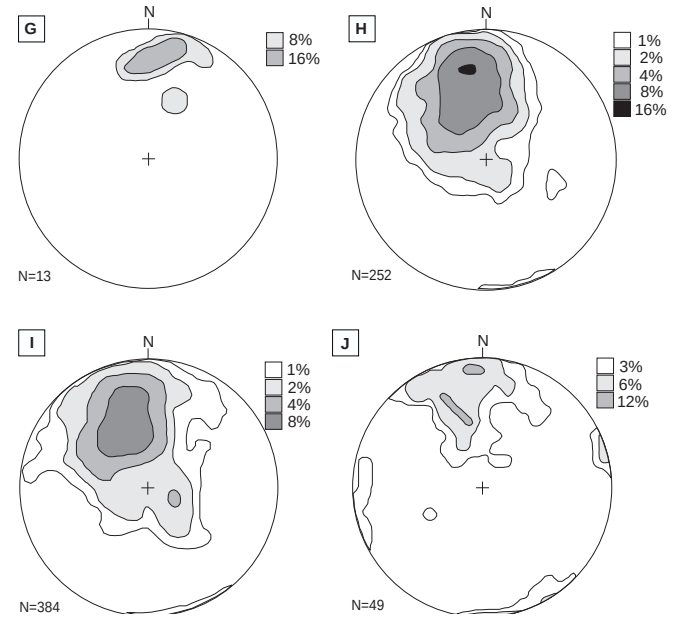

over epidote (associated with stage 3A-a) also indicates reactivation and a change of fluid composition.

Stage 4 carbonate-base metal sulfide mineralisation has been recognised in both steeply dipping and inclined vein sets. In west pod stage 4A and 4B are dominantly associated with steep fractures, and have cut inclined stage 3A-c veins (Fig. 5.22A). Stage 4C ('quartz sulfide breccias') occurrences are typically associated with steep structures (Fig. 5.16B).

In summary, stage 3A-a and 3A-b vein have predominantly formed along steep dipping structures. These sets of steep fractures were cut by inclined stage 3A-c and 3B fractures. Although the mineral assemblages are slightly different between the gold-mineralised centres, similar structural paragenesis have been recognised at E42, where the inclined veins have cut the pre-existing steep dipping veins (Henry, 2008). The early gold-bearing veins were interpreted as forming within a tensional stress regime. Because brecciated 'quartz sulfide breccias' (Stage 4C at E41) are spatially related to steep faults at E42 their formation has been included temporally with early gold-bearing veins (Henry, 2008). Crosscutting the early steep gold-bearing vein sets are the inclined gold-veins, which have been interpreted to form in a compressional stress regime with tension directed subvertically (Henry, 2008). Although vein orientations vary across the district, the similar structural vein paragenesis suggests that the gold-bearing vein could have been formed under similar stress regimes within the Cowal 'gold corridor'. The only difference is that at E41 there is evidence for steeply dipping veins with carbonate-base metal sulfides cutting inclined quartz-pyrite (stage 3A-c) veins, which is consistent with the established mineral paragenesis. It is concluded thus that fault- related, typically brecciated stage 4C veins formed predominately along steep fractures that were originally filled by stage 3A-a and 3A-b vein material, but were reactivated during carbonate-base metal mineralising event. These steep fractures acted as feeders to the inclined vein sets resulting in precipitation of stage 4A infills in the pre-existing vein stages.

5.8 Discussion

Several hydrothermal events, including two stages of gold mineralisation produced the E41 gold deposit. Figure 5.29 summarises the temporal and spatial relationships of hydrothermal and intrusive features. It appears that E41 evolved from early porphyry-style to later epithermal-style conditions. Gold mineralisation was associated with epithermal activity (Table 5.7).

5.8.1 High-temperature porphyry-style alteration

The Muddy Lake diorite, pre-mineralisation dykes and volcano-sedimentary units have been affected by early potassic and high-temperature propylitic and transitional propylitic-potassic assemblages, comparable to alteration in porphyry copper deposits. Potassic alteration in both calc-alkalic and alkalic porphyry systems is typically associated with mineralisation (Meyer and Hemley, 1967; Gustafson and Hunt, 1975; Titley et al., 1981; Sillitoe, 2000; Wilson et al., 2003; Seedorff et al., 2005). Weak magnetite ± biotite alteration at E41 is preserved in mudstone away from the centre of gold mineralisation, but is not associated with any known areas of copper mineralisation or stockwork veining. The magnetite ± biotite alteration assemblage could have initially been more widespread, and overprinting by later alteration facies related to gold mineralisation may have obscured it. The presence of biotite-bearing alteration assemblage, however, implies that early fluids had temperature of up to 550ºC (e.g., Beane, 1974).

TABLE 5.7 Proposed genetic classification of alteration facies of the Endeavour 41 deposit.

Alteration assemblage/facies	Major minerals	Minor minerals
Early – stage alteration facies		
Potassic	Magnetite, albite, chlorite ± biotite	± K-feldspar ± titanite ± epidote
Propylitic	Actinolite, magnetite, albite	K-feldspar ± titanite ± epidote ± hematite, ± chalcopyrite
Potassic	K-feldspar, albite	Hematite (dusting feldspar), apatite, titanomagnetite
Phyllic (west pod)	Illite – muscovite ± ankerite	
Main – stage alteration facies		
	Epidote	± pyrite ± calcite ± leucoxene
Transitional propylitic - potassic	K-feldspar, epidote	Hematite (dusting K-feldspar) ± apatite ± titanite ± chlorite ± calcite
Phyllic (east pod)	Illite – muscovite, chlorite, carbonate	Pyrite ± leucoxene ± hematite ± sphalerite ± gold ± ankerite ± arsenopyrite
	K-feldspar	Illite - muscovite, hematite (dusted K-feldspar)
Phyllic (west pod)	Illite – muscovite – pyrite	Carbonates
Late – stage alteration facies		
Propylitic	Albite, epidote, chlorite Calcite, hematite	Carbonates
Phyllic	Illite, muscovite, carbonates, chlorite	Pyrite, clays

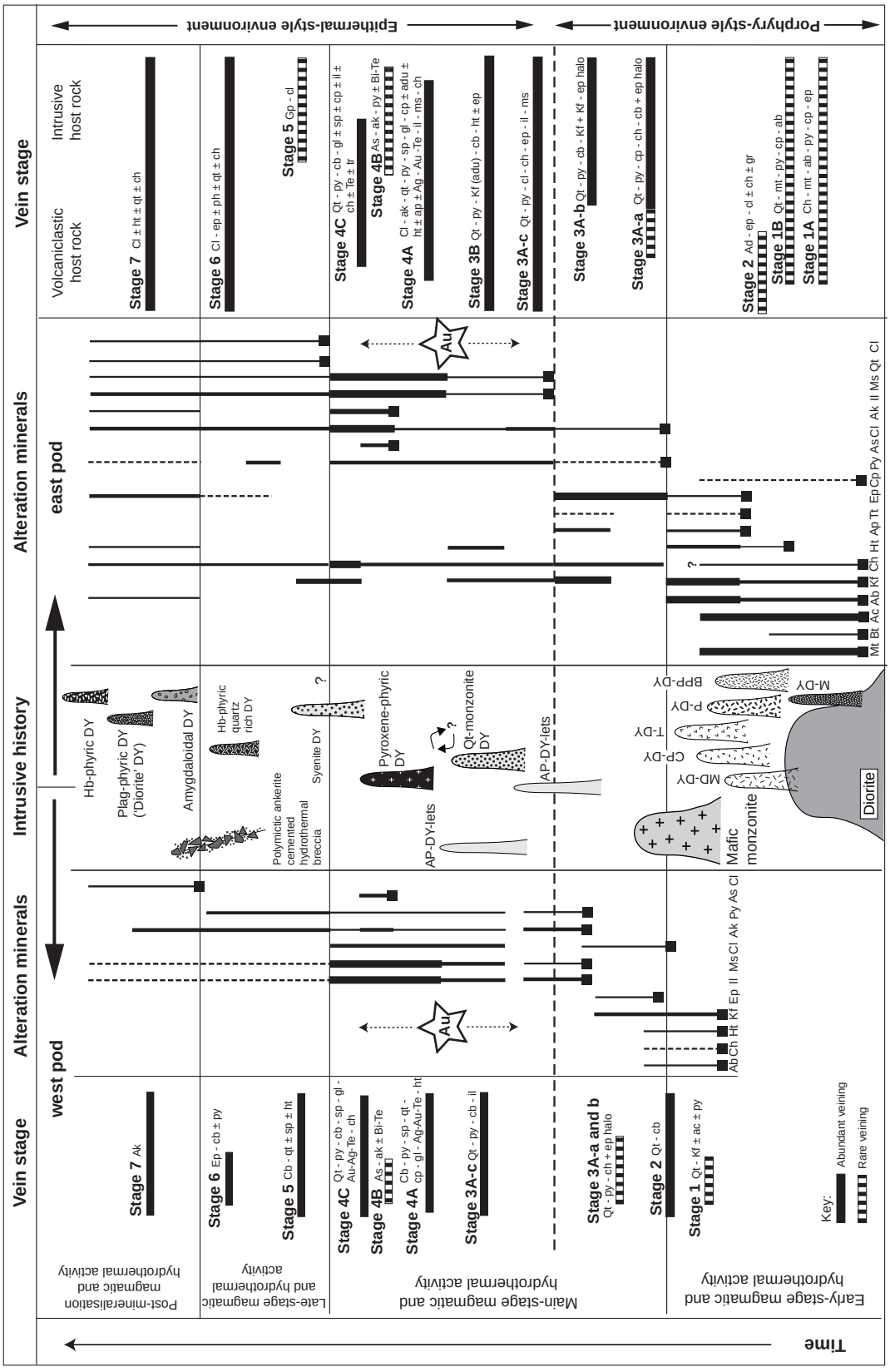

Figure 5.29 Schematic space-time diagram of alteration and vein stages relative to the intrusive history of E41. Abbreviations: DY-dyke, MD-DY - monzodiorite dyke, P-DY - plagioclase-phyric dyke, BPP-DY - blocky plagioclase-phyric dyke, T-DY - trachytic dyke, M-DY - mafic dyke, CP-DY - crowded plagioclase dyke, AP-DY - aplite dykelet, Hb-phyric DY - hornblende-phyric dyke, plag-phyric DY ('diorite' DY) = plagioclase-phyric dyke. Abbreviations: ab=albite, ac=actinolite, ad=andradite, adu=adularia, Ag-Au-Te=Ag-Au-telllurides, ak=ankerite, ap=apatite, as=arsenopyrite, Bi-Te=bismut tellurides, bt=biotite, cb=carbonate, cl=calcite, cp=chalcopyrite, ch=chlorite, ep=epidote, gl=galena, gr=grossular, gp=gypsum, ht=hematite, il=illite, Kf=K-feldspar, mt=magnetite, ms=muscovite, py=pyrite, sp=sphalerite, Te=tellurides, tt=titanite, tr=tetrahedrite, qt=quartz.

Propylitic alteration assemblages are characteristic of the distal portions of porphyry systems (e.g., Meyer and Hemley, 1967; Lowell and Guilbert, 1970; Gustafson and Hunt, 1975; Seedorff et al., 2005) and are thought to develop synchronous with the proximal, highly mineralised portions of porphyries (e.g., Sillitoe, 2000; Wilson et al., 2003; Cooke et al., 2004; Cooke et al., 2005). At E41, early high temperature alteration of intrusive units produced actinolite, magnetite, albite and epidote. Actinolite is not typical of epithermal environments, and its presence, along with epidote, indicates that high temperature fluids (~ >400ºC and ~ >300ºC, respectively) were involved in the early stages of the E41 hydrothermal system (Reyes, 1990; Deer et al., 1997). Actinolite characterises the highest temperature subzone of propylitic alteration halos adjacent to the mineralised potassic centres of several porphyry copper deposits and geothermal fields, including Tintic (Norman et al., 1991), Batu Hijau, (Garwin, 2002) and Palinpinon, (Rae et al., 2004). Actinolite can also be a component of metamorphic assemblages (Deer et al., 1992). Since no metamorphic textures such as triple junctions or foliation have been observed, it is interpreted that actinolite from E41 is hydrothermal in origin. The presence of secondary magnetite is also consistent with high temperature fluids during early hydrothermal activity at E41. Abundant hydrothermal magnetite is common in the core of many gold-rich porphyry copper deposits, irrespective as to whether they are associated with alkalic or calc-alkalic magmatism (e.g., Sillitoe, 1979; Pollard and Taylor et al., 2002; Harris et al., 2005; Seedorff et al., 2005).

At Ridgeway, Wilson et al. (2003; 2005) recognised two phases of propylitic alteration: outer propylitic, distal to the core of porphyry; and inner propylitic which formed a shell between the potassic and outer propylitic alteration zone (Fig. 1.5A). The inner propylitic alteration assemblage at Ridgeway contains hematite, chlorite, albite, actinolite and magnetite and is consistent with the propylitic assemblage identified at E41. Although hematite is much less ubiquitous at E41 than it is at Ridgeway, it may be that the domains of hematite reddening marked zones that are analogous to those proximal to the mineralised core of Ridgeway deposit (Fig. 1.5A). In fact, not only the Ridgeway deposit is characterised by zones of intense hematite reddening. In many alkalic porphyry systems hematite alteration occurs close to, or it is spatially and temporally associated with domains of Cu-Au mineralisation (e.g., Mt Polley: Pass et al., 2008; Northparkes: Lickfold et al., 2003). Whether the ‘red-rock’ hematite alteration at E41 points toward an alkalic-porphyry centre at depth remains unknown, but the presence of hematite indicates the involvement of oxidised fluids at E41, which is consistent with the alkalic porphyry systems (e.g., Wilson et al., 2007a).

Additional evidence for the involvement of high temperature oxidised fluids is provided by the presence of andradite stage 2 veinlets (e.g., Einaudi et al., 1981),

which formed prior to gold mineralisation. In skarn deposits, garnet forms during prograde alteration at relatively high-temperatures from hypersaline, magmatically-derived fluids (e.g., Meinert et al., 2003). In gold skarns, the garnet stage of alteration is then overprinted by a retrograde stage of gold mineralisation, typically associated with illite – muscovite alteration. At the Porgera alkalic epithermal deposit, garnet and actinolite are temporally and spatially related (Richards and Kerrich, 1993). It is possible that garnet at E41 is genetically related to the actinolite – magnetite alteration assemblage.

At E41 transitional propylitic-potassic alteration produced epidote that is associated with strongly hematite dusted K-feldspar. This alteration event overprinted the propylitic and potassic alteration facies (Fig. 5.29). Similar K-feldspar – epidote assemblages have been noted at the Lorraine deposit in British Columbia, where clots of epidote are rimmed by pink K-feldspar (Bath, 2009). The transitional propylitic-potassic assemblage at E41 is interpreted to indicate that relatively high temperature (~350°C) fluids were involved in the early phases of main-stage gold mineralisation. These fluids were oxidising based on the abundance of Fe^{3+}-bearing minerals (hematite, epidote). In addition, the spatial distribution of the transitional propylitic-potassic assemblage defines patterns that partially overlap with the mineralised zones defined by >0.4 g/t gold contours (Fig. 5.3 and 5.4). The pyrite-bearing veins (stage 3A-a and 3A-b) contain some gold (0.4 g/t Au; Table 5.4) and this implies that the transitional propylitic-potassic alteration facies could be used as a mineralogical vector to trace mineralised fluid paths and as an indicator of upflow zones from an underlying magmatic-hydrothermal centre.

5.8.2 Low-temperature epithermal style alteration

Most of the gold at E41 is hosted in stage 3 quartz – sulfide veins and stage 4 carbonate base-metal sulfide veins. Both stages are associated with illite – muscovite – chlorite – carbonate – K-feldspar ± pyrite ± arsenopyrite alteration. These mineral assemblages are consistent with a low-sulfidation epithermal environment (Cooke and Simmons, 2000; Einaudi et al., 2003; Simmons et al., 2005). The formation of illite – muscovite and adularia alteration implies lower temperature condition (200-300°C; Reyes, 1990) than for the propylitic and transitional propylitic-potassic alteration facies. Diagnostic minerals such as chalcedony and textures such as bladed calcite or colloform banding (e.g., White and Hedenquist, 1990) were not observed during this study. Brecciated veins, illite – muscovite, adularia and carbonate alteration are the only ‘classic’ epithermal features that characterise E41.

The fluids that produced low-temperature alteration minerals in alkalic epithermal systems appear to be oxidised with near-neutral pH due to the presence of roscoelite, carbonates, illite, adularia and hematite (Richards, 1995; Jensen and Barton, 2000). Evidence for oxidised fluids during gold mineralisation at E41 comes from sulfur isotopic analyses of sulfides (Chapter 6), and is also supported by local hematite occurrences either as alteration halos around mineralised stage 3 veins or as a vein infill in some stage 4 veins. The presence of illite – muscovite, adularia and carbonate minerals at E41 indicates near-neutral pH conditions during gold precipitation. In contrast, the involvement of reduced fluids at E41 is manifested by the presence of arsenopyrite during stage 4B.

An intimate association between illite, carbonates, K-feldspar and gold has been reported from several alkalic porphyry and epithermal systems (e.g., Ridgeway: Wilson et al., 2005, Northparkes: Kolkert, 1998; Lickfold, 2002; Lickfold et al., 2003; Mt Polley: Pass et al., 2008; Cripple Creek: Jensen and Barton, 2000; Jensen, 2003; Lihir: Carman, 1994; Porgera: Richards and Kerrich, 1993; Ronacher et al., 2004; Emperor: Ahmad et al., 1987; Gies: Zhang and Spry, 1994). In most cases, lower-temperature mineral assemblages have directly overprinted much higher temperatures style of alteration and mineralisation (e.g., Lihir, Cripple Creek; Carman, 2003; Jensen and Barton, 2000; Jensen, 2003). This superpositioning of low-temperature illite-bearing assemblages in alkalic epithermal and porphyry deposits is consistent with the observed sequence of hydrothermal events at E41, where the bulk of the gold mineralisation and related illite – muscovite alteration have cross-cut and overprinted pre-existing potassic, propylitic and transitional propylitic-potassic alteration assemblages (Fig. 5.29). Telescoping of epithermal environments into porphyry systems occurs relatively late in the life of magmatic-hydrothermal system (e.g., Sillitoe, 1994; Masterman et al., 2005), when phyllic alteration, commonly associated with faults, cuts earlier-formed potassic alteration facies associated with copper-gold mineralisation.

Low-temperature phyllic alteration in alkalic porphyry systems typically form narrow halos around faults and late-stage veining that locally contain carbonate-base-metal sulfide mineralisation (Cadia: Wilson et al., 2003; Northparkes: Kolkert, 1998; Lickfold et al., 2003; Mt Polley: Pass et al., 2008; Mt Milligan: Jago, 2008). At E41 domains of pervasive phyllic alteration are lacking and the intense phyllic alteration is limited to alteration halos around mineralised veins that do not exceed few cm (most commonly up to 5 cm). Only brecciated veins have wider phyllic alteration halos (up to 2 m). Because of the weak phyllic alteration, pre-existing high-temperature alteration facies are remarkable well-preserved at E41. The lack of pervasive phyllic alteration at E41 is interpreted to indicate that water/rock ratios were small during the

phyllic alteration and that the involved fluids were relatively H^+-depleted, preventing the development of widespread phyllic alteration. Alternatively, high $(K^+ + Ca^{2+} + Na^+)/H^+$ fluid composition with additional presence of CO_2 and other carbonate species may have buffered the H^+-bearing fluids (Lang et al., 1995b; Jensen and Barton, 2000), precluding the formation of intense acidic alteration at E41.

It is interpreted that illite-bearing (phyllic) alteration related to faults and late veins in alkalic porphyry systems are possibly analogous to the gold-mineralised epithermal veins at E41 deposit. This hypothesis will be tested with isotopic data in Chapter 6.

CHAPTER 6
Mineral and Hydrothermal Geochemistry

6.1. Introduction

Geological relationships between intrusions, veins and alteration assemblages at E41 reveal a complex paragenetic sequence of discrete magmatic-hydrothermal events. The sulfides and associated carbonates and K-silicate alteration minerals that formed during hydrothermal activity at E41 provide an opportunity to investigate the chemical nature of evolving magmatic-hydrothermal fluids. This chapter investigates the mineral, isotopic and fluid chemistry of several paragenetic stages at E41 in order to define the physicochemical environments and processes of gold deposition.

6.2 Sulfide mineral chemistry

Laser ablation-ICPMS analyses of sulfide grains from E41 have been undertaken to determine their trace metal concentrations. Chemical mapping using LA-ICPMS has also been carried out in order to identify the locations of gold and trace metals in the sulfide grains (i.e., as discrete inclusions or evenly distributed in the crystal lattice).

6.2.1 Methodology

Concentrations of trace elements in pyrite, sphalerite and arsenopyrite were determined by laser-ablation inductively coupled plasma mass-spectrometry (LA-ICPMS) at CODES, University of Tasmania, using a 213-nm New Wave UP213 solid state Nd-YAG laser microprobe coupled with an Agilent 4500 quadrupole mass spectrometer. Detailed descriptions of the LA-ICPMS methodology have been provided in Large et al. (2007), Large et al. (2009) and Danyushevsky et al. (in press).

LA-ICPMS imaging was performed by ablating sets of parallel lines in a grid across the samples. Lines were ablated with a beam size at 15 μm. Spacing between the lines was kept constant, at the same size as the laser beam. The lines were ablated with a repetition rate at 10 Hz. Every line sweep recorded in the mass spectrometer forms a separate pixel in the chemical maps shown in Figures 6.1 to 6.5. A set of 26 elements was analysed with acquisition time for most masses set to 0.002 s. In order to improve their detection limits, Ag, Te and Au were measured for 0.04 s. Background levels and the primary sulfide standard (Danyushevsky et al., in press) were measured before and after each map was generated.

LA-ICPMS spot (n=10) and line analyses (n=7) were also obtained from mapped sulfides in order to quantify element concentrations. Analyses in spot mode

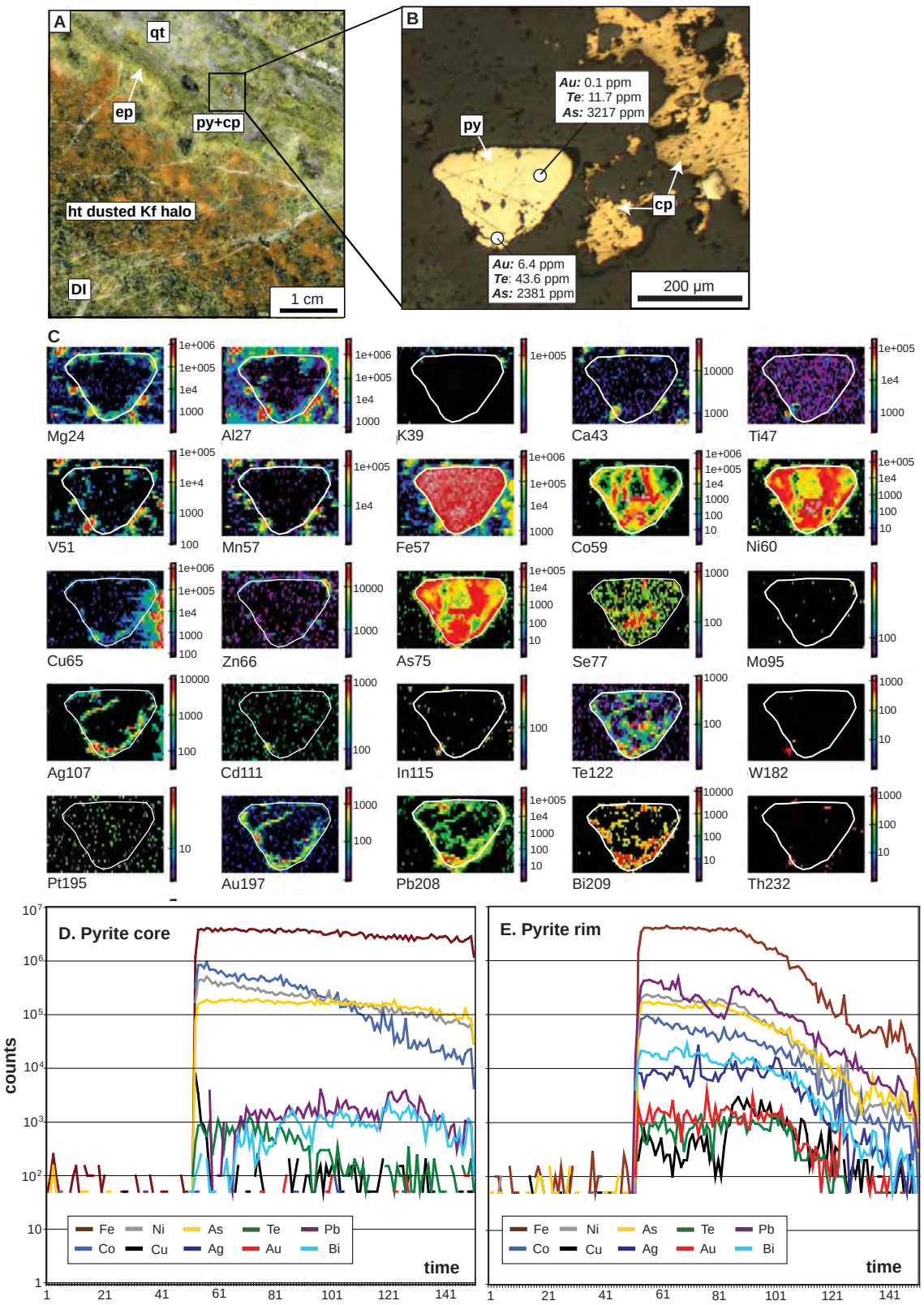

Figure 6.1 A. Stage 3A-b vein with strong K-feldspar - epidote alteration halo (E41D2064, 112.7 m). **B.** Photomicrograph (reflected light) of stage 3A-b pyrite. Pyrite 3A-b is typically homogenous and subhedral. Spots indicate location of LA-ICPMS analyses. Note the pyrite rim has higher Au and Te and lower As concentrations than the core. **C.** Laser-ablation ICP-MS trace element maps of 3A-b pyrite. The element maps show high (hot colours) and low concentrations (cool colours) of various elements substituted within pyrite. White line traces crystal boundary. The pyrite is enriched in Co, Ni and As. The rind is Au-, Ag-, Pb-, Bi-enriched. Se appears to mimic distribution of Te. **D.** LA-ICPMS output for stage 3A-b pyrite: core and rim have been analysed. Note variations in metal abundances between rim and core. Abbreviations: qt=quartz, py=pyrite, cp=chalcopyrite, ep=epidote, ht=hematite, Kf=K-feldspar, DI=diorite.

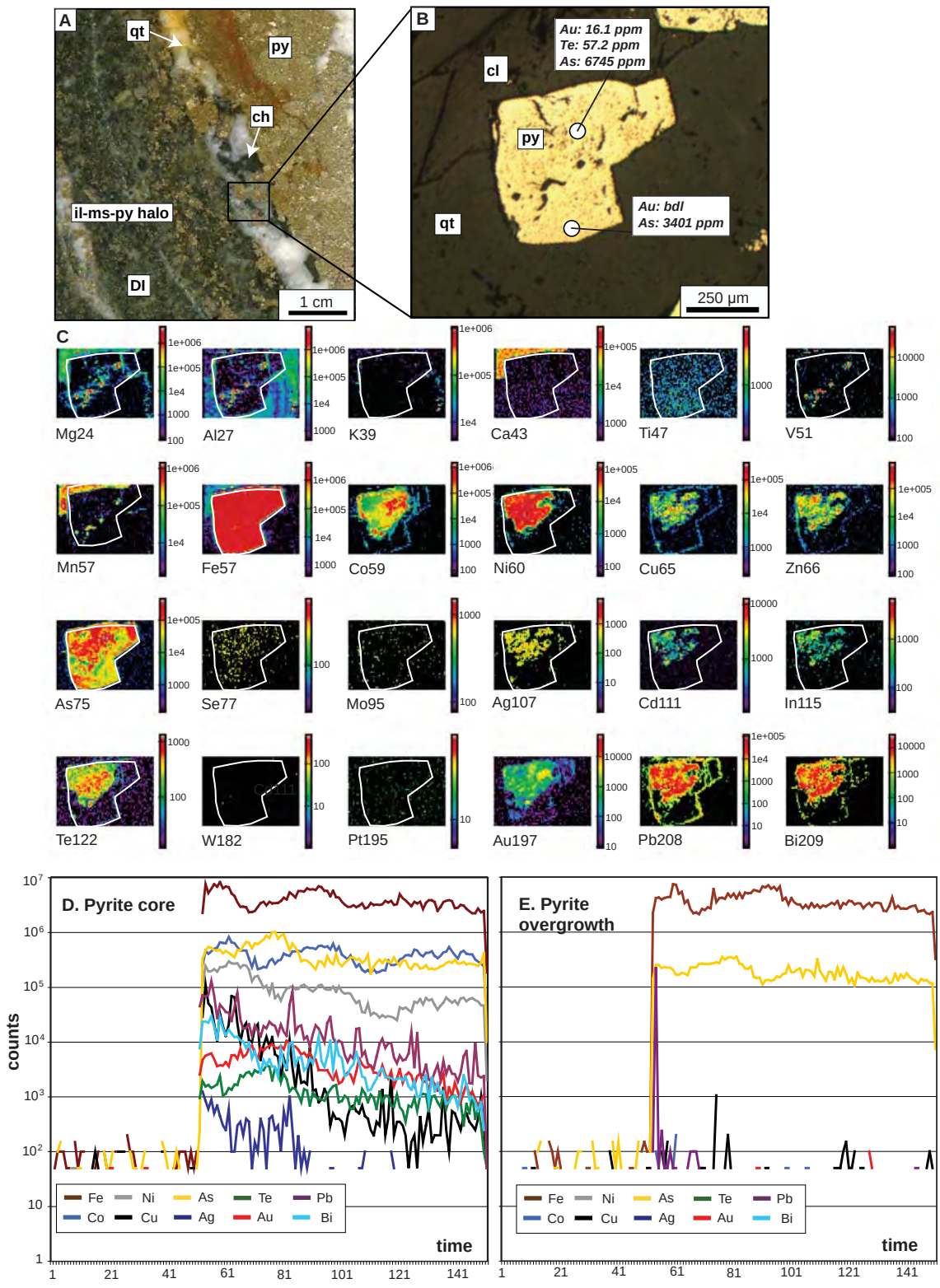

Figure 6.2 A. Stage 3A-c vein with illite - muscovite - pyrite alteration halo (E41D2011, 200.7 m). **B.** Photomicrograph (reflected light) of stage 3A-c pyrite. Pyrite 3A-c is typically euhedral, locally drusy and heterogenous. Spots indicate LA-ICPMS analyses. Note the pyrite core has higher concentrations of Au, Te and As compared with the overgrowth. **C.** Laser-ablation LA-ICPMS trace element maps of 3A-c pyrite. The element maps show high (hot colours) and low concentrations (cool colours) of various elements substituted within pyrite. White line traces crystal boundary. The core and top left corner of pyrite shows Co-, Ni-, Cu-, Zn-, Ag-, Cd-, In-, Te-, Au-, Pb- and Bi- enrichment. As appears to be evenly distributed throughout the early pyrite. Note inclusions of carbonates and possibly silicates rimming the metal-enriched domain in the pyrite. **D.** LA-ICPMS output for stage 3A-c pyrite showing trace element enriched in Co, As, Ni, Pb, Bi and Te in early pyrite and a virtually barren overgrowth (top right and bottom right-E). Abbreviations: cl=calcite, qt=quartz, py=pyrite, ch=chlorite, il=illite, ms=muscovite, DI=diorite.

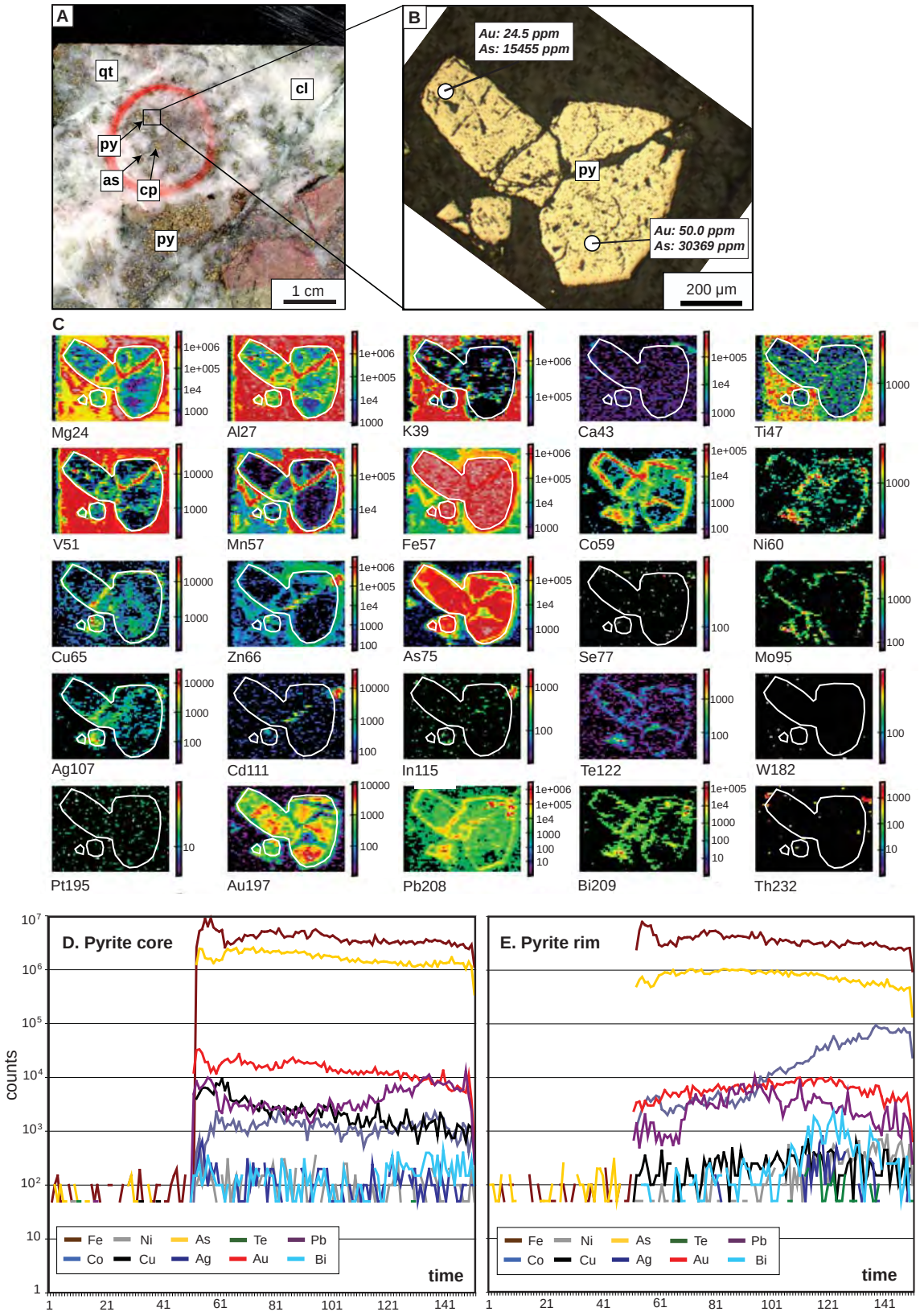

Figure 6.3 A. Pyrite-bearing stage 4A vein (E41D2068, 130.5 m). **B.** Photomicrograph (reflected light) of stage 4A pyrite. The 4A pyrite is typically subhedral and has a heterogenous texture. Spots indicate LA-ICPMS analyses. **C.** Laser-ablation ICP-MS trace element maps of 4A pyrite. The element maps show high (hot colours) and low concentrations (cool colours) of various elements substituted within pyrite. White line traces crystal boundary. The 4A pyrite is strongly enriched in As. Au-rich domains occur throughout the fractured pyrite. The pyrite has a Co-, Ni-, Mo-, Te-, Bi- and Pb-enriched rind. Note also abundant inclusions of K-bearing silicates. **D.** LA-ICPMS output for stage 4A pyrite. Note relatively consistent Au-, As-, Co-, Pb-, Cu-enrichment of trace elements throughout the 4A pyrite crystal. Only the pyrite core appears to be slightly more enriched in Cu than its rim. Abbreviations: as=arsenopyrite, cl=calcite, cp=chalcopyrite, py=pyrite, qt=pyrite.

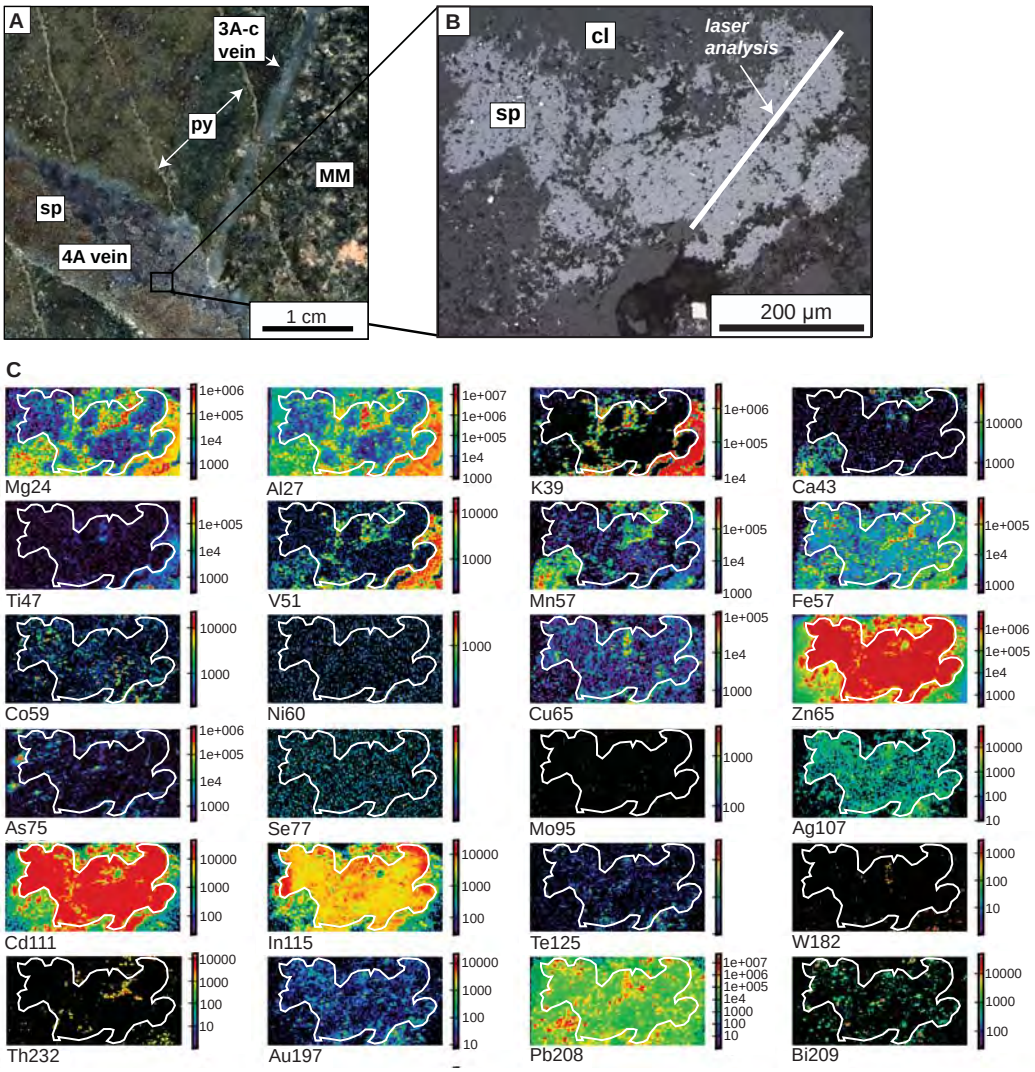

Figure 6.4 A. Stage 3A-c vein crosscut by stage 4A vein (E41D2143, 289.9 m). Both veins are associated with illite - muscovite alteration. **B.** Photomicrograph (reflected light) of stage 4A sphalerite. The sphalerite is irregular with abundant chalcopyrite inclusions. Sphalerite is intergrown with quartz, carbonates and illite. White line indicates the location of the LA-ICPMS line analysis. **C.** Laser-ablation ICP-MS trace element maps of 4A sphalerite. White line traces the crystal boundary. The element maps show high (hot colours) and low concentrations (cool colours) of various elements substituted within sphalerite. The sphalerite shows apparent enrichment in Cd and In. Weak Au anomaly appears to be evenly distributed throughout the sphalerite crystal. Ag mimics Au behaviour. Pb occurs in anomalous domains in and outside the sphalerite crystal. Note abundant inclusions of K-silicate minerals within the sphalerite. Note also anomalous V-enriched illite intergrown with sphalerite. **D.** Laser ablation traverse across stage 4A sphalerite. Au counts are low. Note Cu-, Fe-, Pb-bearing inclusions in the sphalerite. Abbreviations: py=pyrite, cl=Mn-Fe-calcite, sp=sphalerite, cp=chalcopyrite, gl=galena, MM=mafic monzonite.

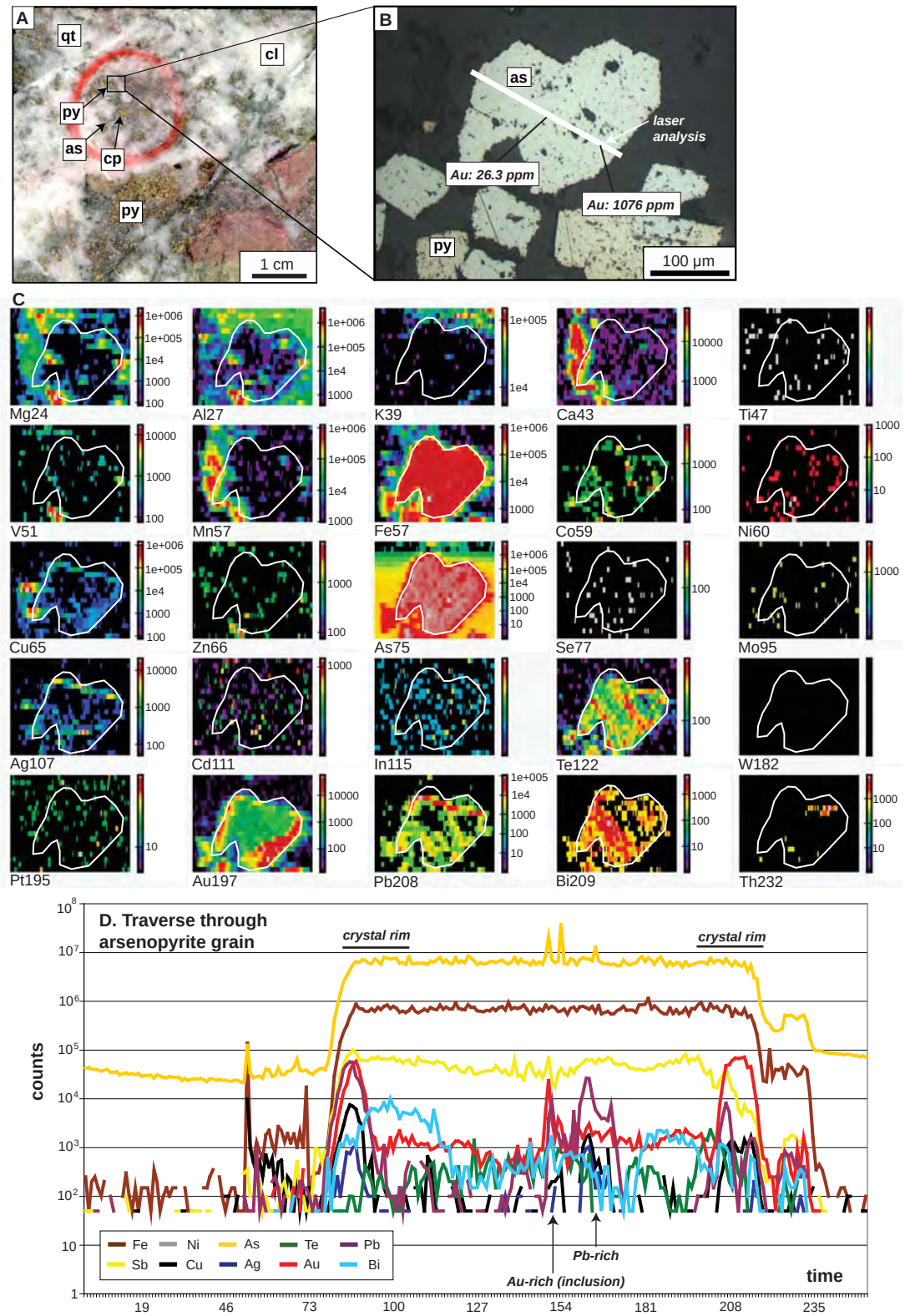

Figure 6.5 A. Stage 4A vein cut by arsenopyrite-bearing stage 4B (E41D2068, 130.5 m). **B.** Photomicrograph (reflected light) of stage 4B arsenopyrite. 4B arsenopyrite is euhedral and displays abundant pits throughout the crystal. White line indicates LA-ICPMS analysis. **C.** Laser-ablation LA-ICPMS trace element maps of 4B arsenopyrite. White line traces the crystal boundary. The element maps show high (hot colours) and low concentrations (cool colours) of various elements substituted within arsenopyrite. An Au-enriched rind is apparent in arsenopyrite. Pb, Bi and Te appear to be anomalous throughout the arsenopyrite grain. Note also Mn-bearing carbonate associated with arsenopyrite. **D.** Laser ablation traverse across stage 4B arsenopyrite. The core of the crystal is characterised by elevated Sb. Au-Pb and Pb inclusions are present in the core of the arsenopyrite. Arsenopyrite rinds are typified by Au-, Cu-, Pb- and Ag-enrichment. Abbreviations: as=arsenopyrite, cl=calcite, cp=chalcopyrite, qt=pyrite, py=pyrite.

were carried out using a laser beam of 40 μm, a repetition rate of 5 Hz and laser energy of ~6 J/cm^2. Data were collected in time-resolved mode. Each analysis time was 90 s, including a 30-s pre-ablation background measurement. All analyses were quantified against the STDGL2b2 standard (Danyushevsky et al., 2003), following the procedure of Longerich et al. (1996) and using Fe (or Zn for sphalerite) as the internal standard.

6.2.2 Results

Pyrite grains from three vein stages were selected for LA-ICPMS mapping and chemical analyses: stages 3A-b, 3A-c and 4A. Chalcopyrite and sphalerite crystals associated with stage 4A pyrite were also chemically mapped and analysed. Chemical analysis of one sample of stage 4B arsenopyrite was also completed. Table 6.1 presents LA-ICPMS results from analysed sulfide samples. Figures 6.1-6.5 show examples of chemical maps generated for each of the investigated paragenetic stage. Appendix E.1 shows additional LA-ICPMS chemical maps of sulfides generated as part of this study.

6.2.2.1 Stage 3A-b pyrite

Stage 3A-b veins (Fig. 6.1A) contain pyrite that is typically fine grained and homogeneous (Fig. 6.1B). These euhedral to subhedral crystals only have corroded edges locally. Chemical mapping highlights strong As- and Ni-enrichment (326 ppm and 2011 ppm, respectively). Co, Se, Te, Bi, Pb, Ag and Au exhibit zonation patterns, with Au best correlated with Bi, Pb and Ag (Fig. 6.1C). It is uncertain whether Au occurs as inclusions or occurs within the pyrite lattice (Fig. 6.1C; Table 6.2). Trace element associations with Au are shown in Figure 6.1E and are summarised in Table 6.2.

Gold was below detection limit in the core of the stage 3A-b pyrite crystal (Table 6.1). Rims of analysed 3A-b pyrite have elevated Au (up to 6.4 ppm). The 3A-b pyrite rim is also characterised by higher Bi (19.3 ppm), Pb (376.2 ppm) and Te (43.6 ppm) levels. Copper, silver and arsenic concentrations are comparable with those from stage 3A-c and 4A pyrite (Table 6.1).

6.2.2.2 Stage 3A-c pyrite

Stage 3A-c pyrite occurs as isolated grains or in clusters. It is typically euhedral to subhedral, locally massive with common inclusions and fractures (Fig. 6.2B). The analysed sample of stage 3A-c pyrite was coarser grained than the 3A-b pyrite (compare Fig. 6.1B and Fig. 6.2B). The core of the stage 3A-c pyrite (Figs. 6.2B and C) is surrounded by wispy microfractures, which possibly mark two generations of pyrite growth.

TABLE 6.1 LA-ICPMS analyses of pyrite, sphalerite and arsenopyrite from E41. Samples are presented in paragenetic order from oldest to youngest.

Sample ID/ paragenetic stage	Mineral	Spot /line	Au (ppm)	Al (ppm)	Ti (ppm)	V (ppm)	Cr (ppm)	Mn (ppm)	Fe (ppm)	Co (ppm)	Ni (ppm)	Cu (ppm)	Zn (ppm)	As (ppm)	Se (ppm)	Mo (ppm)	Ag (ppm)
Stage 3A-b																	
E41D2064_112.7	pyrite	spot-rim	6.35	213.5	3.36	2.27	<1.48	1.63	465000	159.3	2863.9	13.99	<1.23	2381.3	82.6	<0.15	48.41
E41D2064_112.7	pyrite	spot-core	0.06	723.0	10.82	6.80	5.32	16.37	465000	650.1	3313.1	0.97	6.01	3217.6	92.3	<0.08	0.07
E41D2064_112.7	pyrite	line	<0.04	4.10	1.89	<0.07	<2.75	<0.88	465000	606.2	2011.5	196.7	1248.1	236.5	114.0	<0.15	1.69
Stage 3A-c																	
E41D2011_200.7	pyrite	spot-core	16.08	28.15	3.39	0.28	<1.27	15.20	465000	1146.0	1375.7	58.51	59.43	6745.9	27.21	<0.05	0.48
E41D2011_200.7	pyrite	spot-overgrowth	<0.02	0.44	1.98	<0.04	<1.45	<0.35	465000	<0.03	0.16	0.39	<0.71	3401.2	7.74	<0.05	<0.05
E41D2011_200.7	pyrite	line	3.29	296.6	22.33	0.45	2.02	97.58	465000	164.5	1.46	16.34	100.20	4440.1	11.18	1.35	0.80
Stage 4A																	
E41D2068_130.5	pyrite	spot-core	50.04	11.99	1.83	<0.04	<1.14	<0.40	465000	3.99	1.52	30.19	<0.74	30369.7	<1.47	<0.07	0.41
E41D2068_130.5	pyrite	spot-rim	24.45	15.38	1.72	0.07	<1.25	<0.39	465000	66.40	2.60	3.42	<0.73	15455.0	2.79	<0.08	0.41
E41D2068_130.5	pyrite	line	17.23	2336.0	9.96	2.37	<1.91	116.82	465000	34.68	17.74	5090.8	216.16	12059.0	<2.63	1.19	41.75
E41D2143_289.9	sphalerite	line	0.39	88.40	5.19	0.08	3.18	138.25	10565.1	6.66	0.82	312.9	671000	9.24	24.86	0.13	12.90
E41D2143_289.9	sphalerite	line	0.52	132.10	4.30	0.09	3.34	46.91	7980	3.86	0.87	111.6	671000	18.89	61.82	0.17	13.79
E41D2143_289.9	sphalerite	line	0.51	393.06	1.81	0.10	2.66	213.25	56440	13.23	0.61	3278.0	671000	16.07	9.84	0.15	9.42
E41D2068_130.5	sphalerite	line	0.30	7.89	1.93	0.07	2.23	50.91	22766	2.84	0.37	23102.3	671000	9.59	17.36	1.91	31.86
Stage 4B																	
E41D2068_130.5	arsenopyrite	line-core	26.33	4.23	<2.26	0.26	<5.67	<1.85	343000	1.51	2.13	6.50	<2.02	629042.2	11.41	2.73	1.08
E41D2068_130.5	arsenopyrite	line-rim	1076.2	9.64	7.48	<0.42	<15.15	<4.67	343000	10.74	9.67	55.38	<5.29	578434.2	29.68	1.39	<0.43
E41D2068_130.5	arsenopyrite	line-core	23.09	1510.7	<2.83	4.07	<6.32	62.52	343000	2.12	2.84	11.38	16.3	618991.6	17.80	1.44	4.04
E41D2068_130.5	arsenopyrite	line-rim	982.7	1.38	<4.09	<0.21	<8.96	<3.19	343000	7.11	7.54	58.87	<3.65	648273.3	<15.09	0.92	3.59

Sample ID/ paragenetic stage	Mineral	Spot /line	Cd (ppm)	In (ppm)	Sn (ppm)	Sb (ppm)	Te (ppm)	Pt (ppm)	Pb (ppm)	Bi (ppm)	Th (ppm)
Stage 3A-b											
E41D2064_112.7	pyrite	spot-rim	1.91	<0.01	0.54	0.40	43.61	<0.03	376.2	19.25	0.01
E41D2064_112.7	pyrite	spot-core	0.02	<0.02	0.24	<0.10	11.69	<0.03	3.17	1.44	0.12
E41D2064_112.7	pyrite	line	14.94	<0.03	1.64	0.20	7.68	<0.06	5.20	1.24	<0.01
Stage 3A-c											
E41D2011_200.7	pyrite	spot-core	1.52	0.04	0.09	1.31	57.16	<0.03	18.96	4.32	0.00
E41D2011_200.7	pyrite	spot-overgrowth	<0.34	<0.01	<0.09	<0.04	<0.21	<0.06	<0.02	<0.01	0.00
E41D2011_200.7	pyrite	line	0.38	0.04	4.90	0.42	18.86	<0.06	18.29	5.33	0.01
Stage 4A											
E41D2068_130.5	pyrite	spot-core	0.07	0.01	0.09	1.21	<0.36	<0.05	5.24	0.14	<0.01
E41D2068_130.5	pyrite	spot-rim	<0.41	<0.01	0.14	0.78	1.34	<0.04	5.03	0.42	<0.01
E41D2068_130.5	pyrite	line	1.65	0.15	5.98	130.64	22.55	<0.04	1524.5	12.46	<0.01
E41D2143_289.9	sphalerite	line	7264.1	67.15	4.57	8.14	0.35	0.07	65.76	0.25	0.01
E41D2143_289.9	sphalerite	line	7391.0	61.34	1.75	12.47	1.14	0.08	885.0	1.59	0.03
E41D2143_289.9	sphalerite	line	6858.5	53.91	1.04	14.86	0.69	0.02	271.7	0.09	0.01
E41D2068_130.5	sphalerite	line	12536.3	8.97	0.96	9.54	0.62	0.06	49.52	1.35	0.00
Stage 4B											
E41D2068_130.5	arsenopyrite	line-core	<0.86	0.15	<2.38	888.90	77.72	<0.17	10.04	4.40	0.21
E41D2068_130.5	arsenopyrite	line-rim	<2.32	<0.18	<6.02	321.03	78.41	<0.45	13.94	1.39	<0.05
E41D2068_130.5	arsenopyrite	line-core	<0.68	0.15	<2.54	1283.2	86.15	<0.21	20.80	25.22	<0.02
E41D2068_130.5	arsenopyrite	line-rim	<0.98	0.26	<3.66	467.70	159.68	<0.30	109.20	6.03	<0.03

The chemical map shows that the core of the 3A-c pyrite and the top left part of the crystal are enriched in Co, Ni, Cu, Zn, Ag, Cd, In, Te and Pb (Fig. 6.2C; Table 6.1). The gold content of the pyrite core is high (16.1 ppm). Arsenic is evenly distributed throughout the 3A-c pyrite grain (compare rim and overgrowth in Table 6.1 and Fig. 6.2C). The chemical maps also indicate V-bearing silicate inclusions in the 3A-c pyrite microfractures (Fig. 6.2C). The chemical mapping combined with line and spots analyses, show that Au is hosted in the crystal lattice of stage 3A-c pyrite and has positive correlations with As, Ag, Ni, Pb and Bi (Figure 6.2D; Table 6.2). Modes of occurrences for other analysed metals are summarised in Table 6.2.

6.2.2.3 Stage 4A pyrite, sphalerite and chalcopyrite

Grains of pyrite, sphalerite and chalcopyrite from stage 4A veins (Figs. 6.3A and 6.4A) were subjected to chemical mapping and selected crystals were analysed quantitatively by spot and line analyses using the LA-ICPMS. Stage 4A pyrite has the most complex and variable textures, commonly occurring as heterogeneous, irregular and intensely fractured anhedral grains (Fig. 6.3B; Table 6.2). This type of pyrite also forms clusters

TABLE 6.2 Summary of sulfides textures, gold content, metal association with gold and mode of occurrence of the trace elements.

Stage	Textural characteristic	Metal association with gold		Au ppm#	Trace element occurrence mode		
		Rim	*Core*		*Structure*	*Inclusions*	*Uncertain*
3A-b pyrite	fine-grained, homogenous	Pb, Ni, As, Co, Bi, Ag, Pb, Te; weak: Cu	No Au detected	bdl	As, Co, Ni,	Zn, Cu, Pb	Au, Ag, Bi, Te, Se
3A-c pyrite	fine-, coarse-grained, common micro-pores and microfractures	No Au detected	strong: As, Ni, Pb, Bi, Te, Cu; weak: Zn, Ag Cd, In,	3.3 ppm	As, Co, Au, Ni, Bi	Au (?), Cu, Te, Zn	Ag, Pb, In, Cd
4A pyrite	complex textures; fine-coarse-grained, heterogeneous, irregular, porous and intensely fractured anhedral grains	As, Co, Pb; weak: Bi, Te	As, Pb, Cu, Co	17.23 ppm	Au, As, Pb, Ag, Co, Zn, Sb, Bi	Te (?), Pb, Bi	Cu, Ni
4A sphalerite	massive, fine-grained	Au mimics patterns of trace elements in inclusions	Au mimics patterns of trace elements in inclusions	0.43 ppm*	In, Cd, Hg	Au, Te, Pb, Bi, Ag, Cu, Co	-
4A chalcopyrite	fine-grained, flaky textured	Bi, Ag, Te, Pb, Zn	Pb, Bi, As, Co, Ni, Zn	No data	In, Bi, Pb, Co, Ni	Au, Te, Ag, Zn, Cd	As
4B arsenopyrite	fine-grained; needle-shaped	Sb, Pb, Cu, Bi, Ag	Bi, Te, Pb	24.71 ppm**	Au, Sb, Bi, Te	Au, Pb, Cu, Ag	Co

* average of two line analyses (Au rim excluded)
**average of four line analyses
bdl=below detection limit
# bulk analysis (line)

of euhedral fine-grained crystals (Appendix E.1) and most commonly occurs with chalcopyrite, sphalerite, carbonates and hematite.

Chemical mapping has shown that stage 4A pyrites are compositionally zoned (Fig. 6.3C). Analysed stage 4 pyrite samples are As-rich and have Co-, Ni-, Mo-, and Te-rich rims. Bi is also enriched in the pyrite rim and may have substituted throughout the pyrite structure. Pb occurs as a thin rind at the edge of the pyrite grain but locally also displays strongly anomalous domains possibly indicating the presence of galena inclusions (Fig. 6.3C). Abundant K-silicate inclusions have been incorporated into stage 4 pyrite (Fig. 6.3C).

Gold is distributed throughout stage 4A pyrite (core: 50.0 ppm; rim: 24.5 ppm), suggesting that it occurs within the pyrite lattice. Results from spot and line analyses support this interpretation, however, there may also be some Au occurring as micro-nuggets (Appendix E.1). Stage 4A pyrite is relatively depleted in Ni compared to pyrite from stages 3A-b and 3A-c (Tables 6.1 and 6.2). Stage 4A pyrite has the highest level of Cu (5090.8 ppm), Ag (41.7 ppm), Sb (130.64 ppm), Te (22.5 ppm), Pb (1524.5 pmm) and Bi (12.5 ppm). Stage 4A pyrite contains lower As than 3A-b and 3A-c pyrite (Table 6.1).

Irregular-shaped stage 4A sphalerite crystals commonly occur in aggregates (Figs. 6.4A and B). Sphalerite crystals can be massive (Fig. 6.4A) or can form fine-grained specks. Sphalerite contains abundant chalcopyrite inclusions. Chemical maps have shown that sphalerite from west pod is depleted in Fe (Fig. 6.4C) compared with the east pod sphalerite (Appendix E.1). Overall, stage 4A sphalerite is characterised by strong Cd and In enrichment (Table 6.1). The Au content (average 0.5 ppm) is lower than for stage 4A pyrite (Table 6.1). Stage 4A sphalerite is also enriched in Ag (Table 6.1) and appears to have abundant Pb-bearing micro-inclusions dispersed throughout the grain (Fig. 6.4D). In addition to Pb-rich inclusions, there are domains relatively enriched in Au-, Cu-, Te- and Bi in stage 4A sphalerite; these elements probably occur as mineral inclusions. The presence of Te, Au and Bi-rich areas is consistent with petrographic observations of Ag-Au-Bi-tellurides disseminated within sphalerite (Chapter 5). V-bearing K-silicate inclusions appear to be intergrown with sphalerite (Fig. 6.4C).

One sample of chalcopyrite from a stage 4A vein was selected for chemical mapping. There is a moderate to strong association of Au with Te, Ag, Zn and Cd in the chalcopyrite. These elements appear to be occurring as inclusions randomly distributed throughout the chalcopyrite grain (Appendix E.1).

6.2.2.4 Stage 4B arsenopyrite

Arsenopyrite crystals, which are not common at E41, are typically fine-grained and locally have well-developed needle-shapes. The arsenopyrite ranges from mostly inclusion-free to strongly inclusion-rich (Fig. 6.5B). Laser mapping reveals that the analysed stage 4B arsenopyrite crystal has a strongly Au-enriched rim (Figs. 6.5C). Te, Bi and Pb have similar patterns, partially overlapping with some areas of Au enrichment (Fig. 6.5C). There are also Ca- and Mn-rich domains, most likely indicating that Mn-bearing calcite is intergrown with arsenopyrite.

Two LA-ICPMS analyses were performed on arsenopyrite (Fig. 6.5D). The arsenopyrite rims have the highest gold concentrations detected in the analysed sulfides (up to 1076.2 ppm in the crystal rim; Table 6.1). Stage 4B arsenopyrite has also the highest concentrations of Sb and Te compared to pyrite samples from stages 3A-b, 3A-c and 4A (Table 6.1). The combination of mapping and line analyses indicate that Au in arsenopyrite is hosted both within the crystal lattice and as inclusions (Figure 6.5D). The mode of occurrence of other trace elements and their association with Au are listed in Table 6.2. It appears that Au in stage 4B arsenopyrite is positively correlated with Sb and Pb.

6.2.2.5 Discussion

Petrographic and LA-ICPMS analyses of sulfides have highlighted several important paragenetic features at E41. The carbonate-base metal sulfide stage (4A) and arsenopyrite-bearing stage (4B) have the most gold-enriched sulfides at E41. Gold in stage 4A occurs as inclusions in sphalerite, pyrite and chalcopyrite, but is more common in the crystal lattice of pyrite. Similarly, stage 4B arsenopyrite contains gold in the crystal lattice and also as minor inclusions (Fig. 6.5). Stage 3A-c pyrite also has gold predominantly incorporated into its structure (Fig.6.2). Stage 3A-b has a Au-depleted core and Au-enriched rind (Fig. 6.1). Free gold has been observed in stage 4A and 4C (Chapter 5). More systematic work needs to be undertaken to investigate processes that have controlled gold mode variations in sulfides at E41. Because the highest gold grades occur in stage 4, it would be also interesting to test whether gold inclusions in stage 4A pyrite formed in response to deformation-induced recrystallisation of Au-enriched pyrite (i.e., stage 3A-c).

Gold as inclusions in late paragenetic stages has been reported from several deposits, particularly of orogenic type (Large et al., 2007). The gold inclusions have been interpreted as being a product of remobilization from pre-existing structurally gold-hosted sulfides via deformational events or metamorphism (Large et al., 2007). Metamorphism appears not to be important at E41, based on the sub-greenshist facies

mineralogy preserved (illite, prehnite). Instead, magmatic events are inferred to have contributed gold at several times during the paragenetic evolution of the deposit. The Au-Ag-Zn-Pb-Te metal association at E41 is consistent with a low sulfidation epithermal origin (e.g., White and Hedenquist, 1990), and contrasts with orogenic gold deposits which are typically characterised by high Au-Ag-As metal contents (e.g., Groves et al., 2003).

6.3 Fluid inclusions

6.3.1 Introduction and methods

Fluid inclusions from E41 have been analysed in order to provide estimates of fluid temperatures and salinities that prevailed during hydrothermal activity. Data from the fluid inclusion assemblages are used to constrained likely depths and pressures that prevailed during deposition of gold-bearing veins.

Microthermometry was conducted using a Linkam MDS600 (operating temperatures between -80 and 590ºC) at CODES, University of Tasmania. Detailed descriptions of heating and freezing procedures are provided in Roedder (1984). Heating and freezing temperatures were calibrated using synthetic fluid inclusions supplied by Synflinc Inc. The precision of measured temperatures are ± 1.0ºC for heating experiments and ± 0.3ºC for freezing. Salinities were determined as NaCl equivalent weight percent (eq. wt. NaCl).

6.3.2 Petrography and classification

Twenty five doubly polished 150 μm-thick fluid inclusion wafers from stages 1, 2, 3A-a, 3A-b, 3A-c and 4A were examined petrographically in order to identify fluid inclusions and assemblages. Workable fluid inclusions were found only in quartz, calcite and garnet crystals. Hydrothermal quartz crystals from stage 1 (west pod) and 3A-c (east pod) were subjected to scanning electron microprobe-cathodoluminscence (SEM-CL) at the Central Science Laboratory, University of Tasmania in order to identify primary growth zones. SEM-CL photographs (n=853) revealed zones in quartz crystals that are free of fractures (e.g., Fig. 6.6A). Some of these fracture-free zones were also apparent in transmitted light (Fig. 6.7B). Zoned quartz crystals typically have cloudy appearances as they host numerous fluid inclusions, some of which are well-preserved (Fig. 6.6B). Locally, only fragments of crystals or certain zones, typically in the pressure shadows of sulfides, contain well- preserved fluid inclusions.

Fluid inclusions range from < 5 - 20 μm in diameter with most between 5 and 8 μm. They typically occur in elongated clusters (Figs. 6.6B, D and 6.7C). Shapes are elongated (Fig. 6.6C), circular (Fig. 6.6D) and ellipsoidal (Figs. 6.7D, E) or irregular

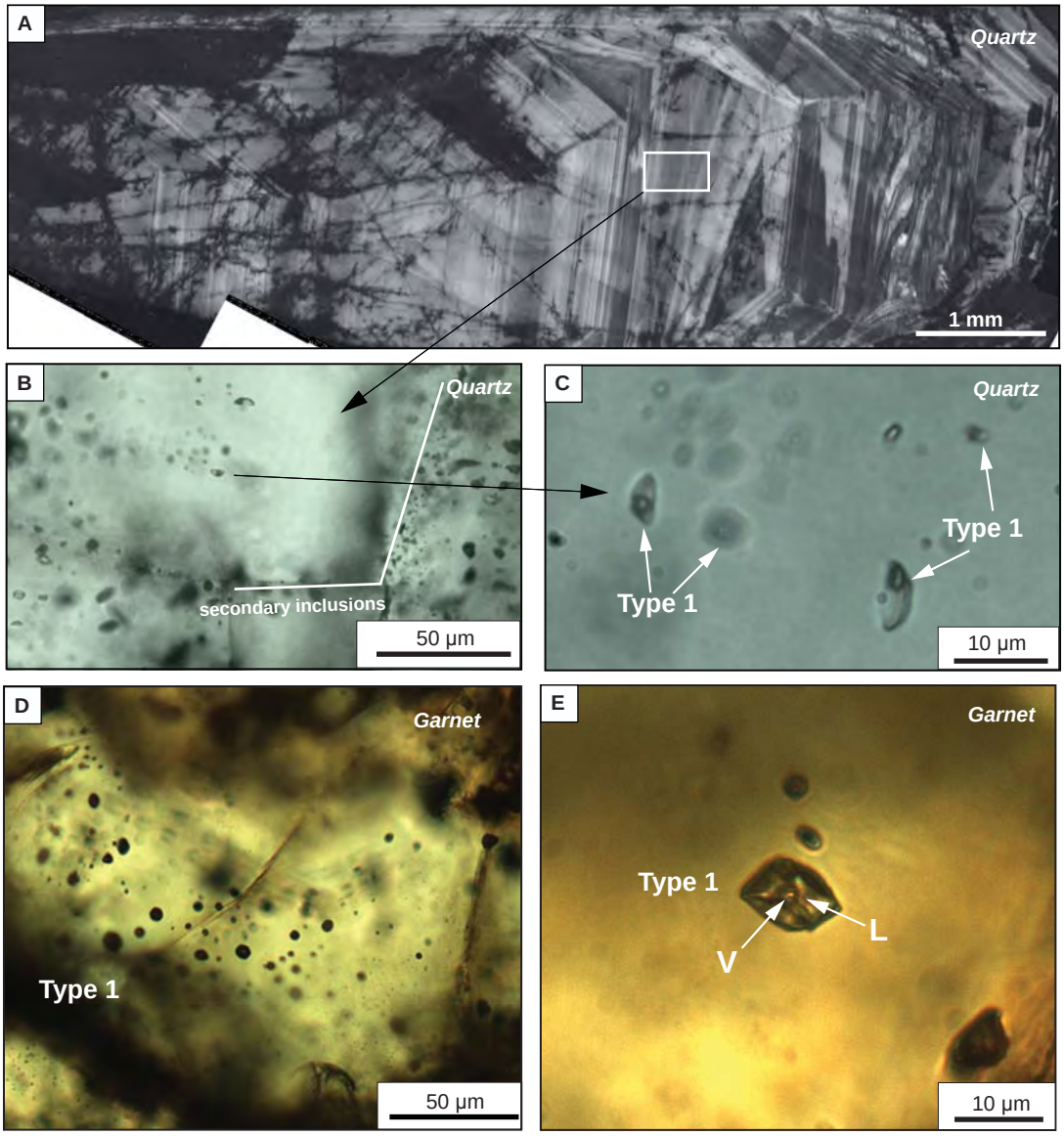

Figure 6.6 Fluid inclusions from stage 1 and 2. **A.** Cathodoluminescence image of stage 1 quartz. The image shows quartz growth zones that appear to be free of fractures. Locally only minor fractures are present and these are associated with secondary inclusion trails (E412099, 213.1m). **B-C**. Isolated Type 1 primary inclusions in stage 1 quartz (E41D2099, 213.1m). **D.** Fluid inclusions hosted in a stage 2 garnet crystal. This fluid inclusion population (Type 1) is associated with garnet growth zones (E41D2011, 97.7m). **E.** Type 1 isolated liquid-rich inclusion hosted in stage 2 garnet (E41D2011, 97.7m).

(Figs. 6.7D, F). Locally isolated fluid inclusions are also present (Fig. 6.6E). All identified fluid inclusions typically have smooth walls and occur in fracture-free zones. These were the main factors that established the inclusions as primary in origin, using the criteria of Roedder (1984). In contrast, irregular extended morphologies and strong relationships to fractures that cross cut grain boundaries typify secondary inclusions (Fig. 6.6B). Secondary inclusions, although common, were avoided in this study. The best primary inclusions were recognised in quartz crystals (stage 3A-c: Fig. 6.7). Several fluid inclusions in calcite (stage 1) were also identified. These have irregular

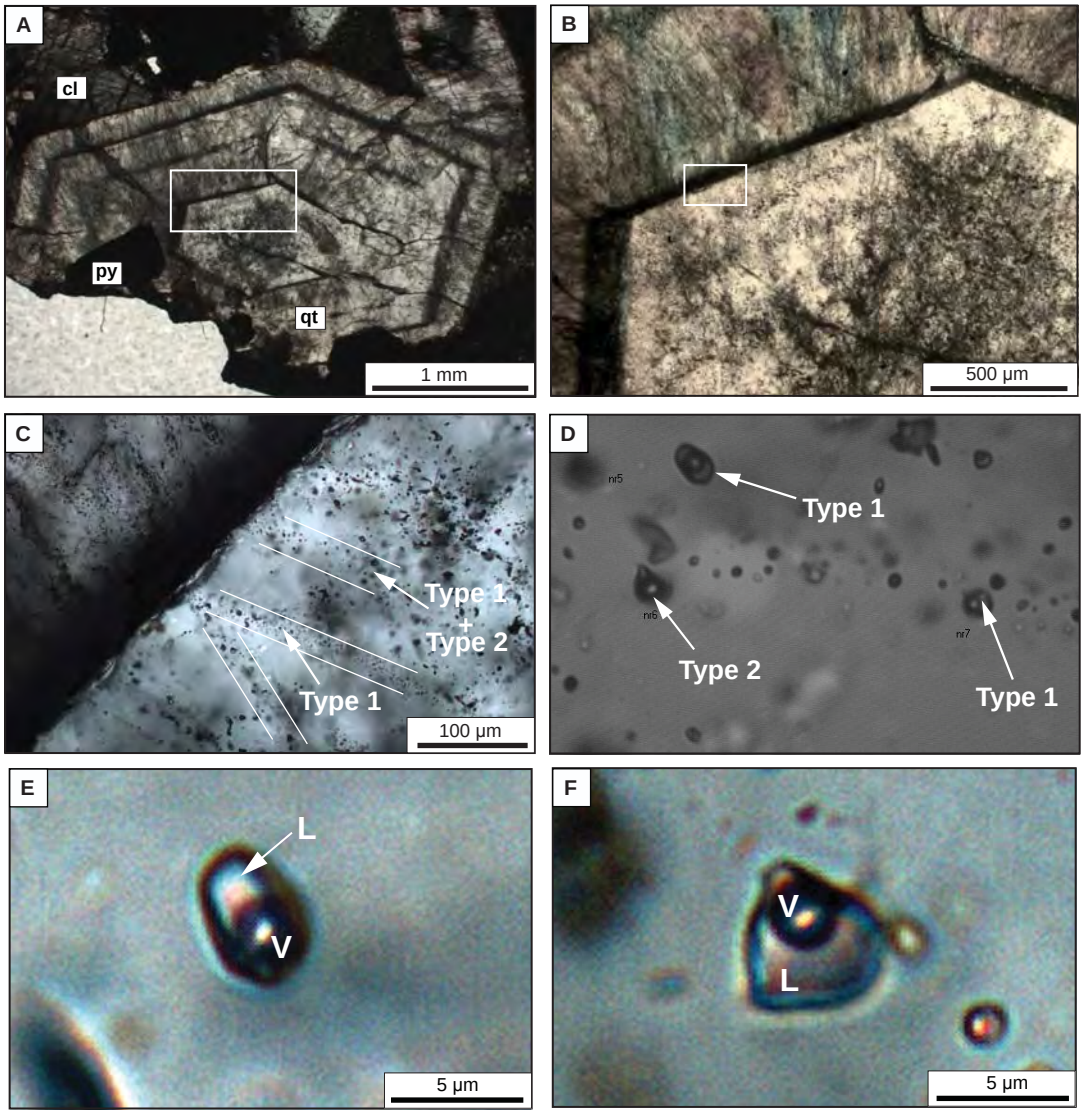

Figure 6.7 Occurrence and types of fluid inclusions in quartz - pyrite veins in the E41 deposit (E41D2011, 200.7 m). **A.** Photomicrograph (ppl) of zoned quartz crystal from stage 3A-c vein. Quartz is adjacent to a pyrite grain. Note numerous fractures that have cut the quartz crystals. **B.** Strongly dusted quartz growth zones associated with abundant fluid inclusions. This central part of the quartz crystal is free of fractures. **C.** Photomicrograph (ppl) of quartz with Type 1 and Type 2 inclusions that formed trails perpendicular to growth zones. **D.** Coexisting Type 1 liquid-rich inclusion with Type 2 vapour-rich inclusions. Inclusions are hosted in growth zones in quartz. **E-F**. Images of the most common liquid-rich (Type 1) inclusions at E41 with oval- (E) and irregular (F) shapes.

shapes but commonly occur in growth zones of calcite crystals; they are interpreted to be primary inclusions. Garnet from E41 contains only a few workable fluid inclusions (e.g., Fig. 6.6D).

Two types of fluid inclusions have been identified at E41 based on their phase relationships at room temperature: type 1 – liquid-rich, two-phase inclusions; and type 2 – vapour-rich, two phase inclusions. Microthermometric measurements were made on fluid inclusions in quartz, calcite and garnet. Type 1 inclusions are liquid-rich (Figs. 6.6C, E and 6.7D, E and F), low-salinity, lack daughter salts, and are the most abundant volumetrically. They contain approximately 30 to 40 percent vapour by volume and

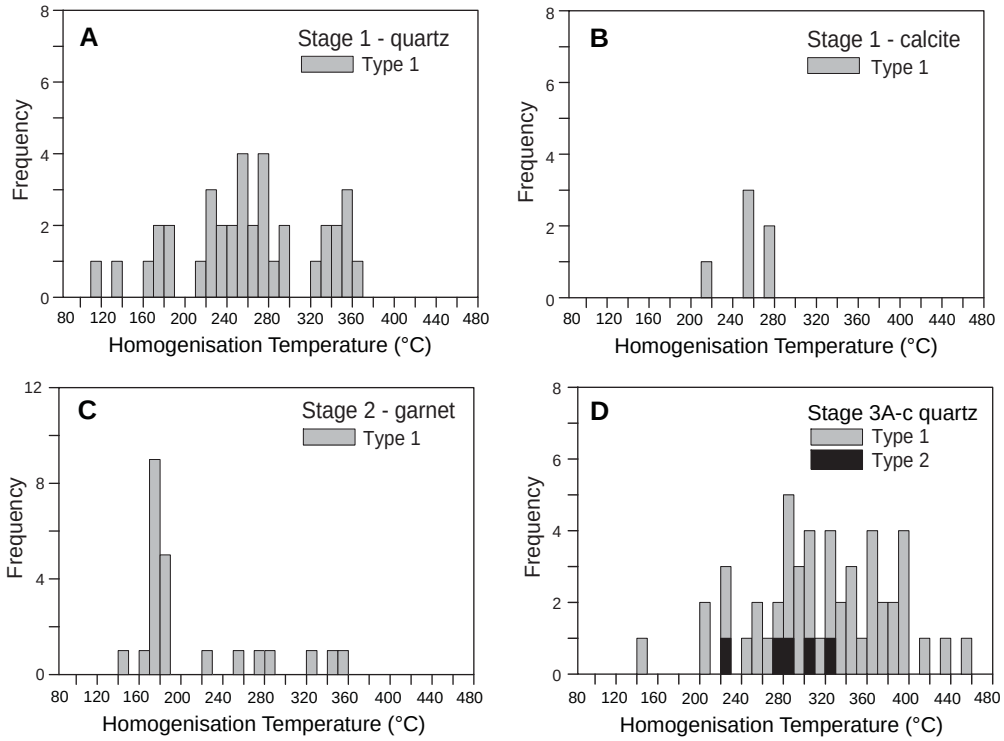

Figure 6.8 Cumulative frequency summarising microthermometric results. **A.** Homogenisation temperature measurements for stage 1 quartz. **B.** Homogenisation temperature measurements for stage 1 calcite. **C.** Homogenisation temperature measurements for stage 2 garnet. **D.** Homogenisation temperatures for stage 3A-c quartz.

homogenise to a liquid phase. Type 2 inclusions (Fig. 6.7D) are two-phase, contain approximately 20 volume percent liquid, lack daughter minerals, and homogenise to vapour. The liquid phase typically occurs as a thin film around the vapour phase. Type 2 inclusions are less common than type 1; both coexist in some primary growth zones in stage 3A-c quartz (Figs. 6.7C and D). Type 3 fluid inclusions were described from E41 by Bastrakov (2000), they are three-phase high-density inclusions that homogenise at ~180°C and typically contain daughter crystals in addition to vapour and liquid. Type 3 inclusions were not observed in the current study. Secondary type 3 inclusions with red hematite crystals and rare opaque minerals were observed but were not analysed due to their small sizes.

6.3.3 Heating and freezing experiments

A total of 119 fluid inclusions were subjected to heating experiments. All microthermometry data gathered from fluid inclusion assemblages [FIAs] are presented in Appendix E.2 and summarised in Table 6.3. Inclusions in FIA are inferred to have been trapped ‘simultaneously’ from the same fluid, representing a population of inclusions representative of that fluid event (Goldstein and Reynolds, 1994). Two types of homogenisation behaviour were recognised: homogenisation to liquid, and to vapour.

A total of 37 homogenisation temperatures were measured from type 1 fluids identified in stage 1 quartz (Figs. 6.6B and C). The temperatures range from 120º to 362ºC, with an average of 260ºC (Fig. 6.8A). Six fluid inclusions from zoned calcite crystals of the same vein stage 1 yielded a temperature range of 211º to 272ºC (average: 253ºC; Fig. 6.8B). Homogenisation temperatures of garnet-hosted type 1 fluid inclusions (n=23) range from 167º to 351ºC (average: 212ºC; Fig. 6.8C). Fluid inclusions from a growth zone in garnet had an average temperature of 208ºC and range of 149º to 351ºC. Isolated fluid inclusions in garnet homogenised at slightly higher temperatures, from 174º to 341ºC (average: 221ºC). Fluid inclusion assemblages (FIAs) that were recognised in stage 3A-c quartz are listed in Appendix E.2. Stage 3A-c quartz is characterised by fluid inclusion assemblages from growth zones and isolated fluid inclusions (n = 53) that homogenised between 110º and 450ºC (average: 310ºC; Fig. 6.7D) with FIAs being typified by range of temperatures between 300-350ºC.

Freezing experiments were conducted on 48 fluid inclusions from quartz, calcite and garnet (Table 6.3). Salinities were calculated from measured final ice-melting temperatures using the algorithm of Bodnar et al. (1993).

Type 1 fluid inclusion in stage 1 quartz had final ice-melting temperature (n=27) ranging from -14.5 to -4.2 (average: -7.6). These temperatures correspond to calculated range of salinities from 6.7 to 16.9 eq. wt. % NaCl with an average of 11.0 eq. wt. % NaCl. Only one measurement of final ice-melting temperature was taken from stage 1 calcite; -6.9, which indicates a salinity of 10.4 eq. wt. % NaCl. Stage 2 garnet (n=6) showed final ice-melting at average temperature of -4.5, corresponding to a salinity of 7.0 eq. wt. % NaCl. Ice-melting temperatures of stage 3A-c quartz (n=14) were measured from -12.9 to -3.2 (average: -6.3). Calculated salinities for stage 3A-c quartz range from 5.3 to 16.8 eq. wt. % NaCl, with an average of 9.5 eq. wt. % NaCl.

The study of fluid inclusions from the ~455 Ma Ordovician E41 gold deposit has proven particularly challenging due to recrystallization effects, most likely related to post-mineralization deformation (Chapter 2). Although no obvious fluid inclusion re-equilibration textures have been identified at E41 (c.f. Ayllon et al., 2003), the deposit has potentially been deformed during the Devonian Tabberrabberan and/or Carboniferous Kanimblan orogenies (Henry, 2008). Re-equilibration of fluid inclusions typically creates a wide range of homogenization temperatures (Vityk and Bodnar, 1998), which may be the case with the data obtained from stage 1 and 2 fluids at E41 (Fig. 6.8).

6.3.4 Discussion

Fluid inclusion microthermometry experiments have revealed that type 1 and type 2 fluid inclusions from early- and main-mineralisation stages have relatively similar

TABLE 6.3 Summary of fluid inclusions microthermometry results.

Stage	Mineral	Number of analyses	Inclusion Types	Homogenisation temperature (ºC) min/max/avg	Final ice melting (ºC) min/max/avg	Salinity (wt % NaCl equiv) min/max/avg	Style of homogenisation
1	Quartz	37	T-1	120/ 362/ 259	-14.5/ -4.2/ -7.6	6.7/ 17.8/ 11.0	V-disappearance
1	Calcite	6	T-1	211/ 272/ 253	-.6.9 (n=1)	10.36 (n=1)	V-disappearance
2	Garnet	23	T-1	149/ 351/ 212	-9.1/ -3.0/ -4.5	4.9/ 12.9/ 7.0	V-disappearance
3A-c	Quartz	53	T-1+T-2	110/ 450/ 311	-12.9/ -3.2/ -6.3	5.26/ 16.8/ 9.5	V-disappearance V-expansion

homogenisation temperatures (Table 6.3). While the temperature of 310ºC for 3A-c quartz veins appears to be consistent with associated illite – muscovite-bearing alteration halos, the temperatures obtained for stage 1 and 2 veins appear to be too low. Stage 1 quartz is in equilibrium with orthoclase and actinolite, implying the involvement of much higher temperatures (>450ºC; Deer et al., 1992) than measured from type 1 fluid inclusions (~260ºC). Similarly, fluid inclusions in andradite that homogenised at 212ºC cannot be representative of garnet formation. Andradite is stable at temperature around 550ºC (Gustafson, 1974; Taylor and Liou, 1978). It may be that the fluid inclusions at E41 from actinolite-bearing stage 1 and andradite-bearing stage 2 veins have re-equilibrated after entrapment, or that they were trapped at higher pressures and a pressure correction is required to convert homogenisation temperatures to trapping temperatures (Roedder, 1984). Using the pressure correction diagram of Potter (1977; Fig. 6.9) for 5 wt. NaCl % fluids, a temperature correction of ~80ºC is required if stage 1 and 2 fluid inclusions were trapped at ~1 kbar. This corrects homogenisation temperatures of ~250ºC to trapping temperatures of ~330ºC, more consistent with the observed epidote and chlorite that occurs in andradite-bearing veins. Although the confining pressures during stage 1 and 2 remain unknown, trapping of fluid inclusions under pressures higher than L-V saturation could at least partially explain the discrepancy between homogenisation temperatures and the temperature of entrapment.

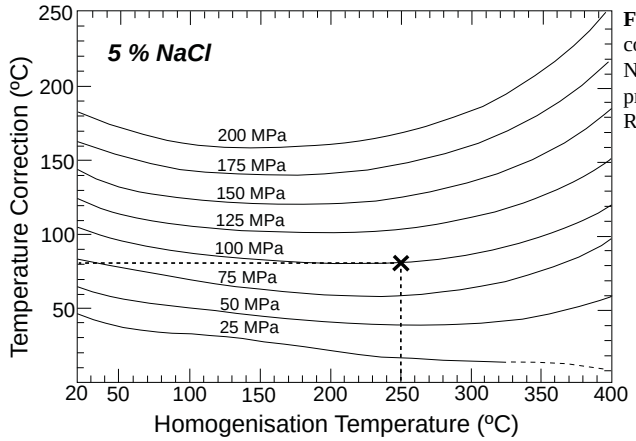

Figure 6.9 Pressure correction for inclusions containing NaCl solutions of the weight percent NaCl indicated, as a function of temperature and pressure in megapascals (i.e., bars × 0.1), from Roedder (1984, after Potter 1977).

Fluid sources and ore-forming processes

Homogenisation temperatures that range from 150º to 300ºC and dilute fluids (less than 3.5 eq. wt. % NaCl) characterise epithermal style deposits (Cooke and Simmons, 2000; Simmons, 2005). Fluid inclusion data obtained in this study are somewhat atypical for an epithermal environment because of their higher salinities, but high salinities have been documented from some epithermal deposits (e.g., Santa Nino, Mexico; Simmons et al., 1988; Rosita Hills, Colorado: McEwan et al., 1996; Porgera, PNG; Richards and Kerrich, 1993; Kelian, Davies et al., 2008), where they were attributed to the involvement of saline magmatic-hydrothermal fluids. Alternatively, if there is no obvious source of saline fluids in the vicinity of the deposit, higher salinities in the epithermal environment can be achieved by boiling to dryness in an open system environment (Simmons and Browne, 1997). Sulfur and carbon-oxygen isotopic compositions of sulfides and carbonates from early vein stages (up to stage 3A-c), indicate a magmatic fluid component prior- to and during mineralisation at E41 (section 6.4), supporting the interpretation that the elevated salinities at E41 relate to a contribution from magmatic fluids.

Co-existing liquid- and vapour-rich inclusions have only been identified in stage 3A-c quartz crystals (Fig. 6.7D). Their occurrence together in the same growth zone indicates that the quartz precipitated from a fluid that had undergone boiling either at the site of entrapment and/or at greater depth (Roedder, 1984; Bodnar et al., 1985a). Boiling is therefore inferred as a depositional process for stage 3A-c veins, consistent with the presence of adularia (Spycher and Reed, 1989; Cooke and McPhail, 2001).

Although fluid inclusions from stages 1 and 2 may have re-equilibrated after entrapment, their salinities and homogenisation temperatures define weak arrays on Figure 6.10 that are consistent with boiling during stage 1 (Fig. 6.10A), and mixing of

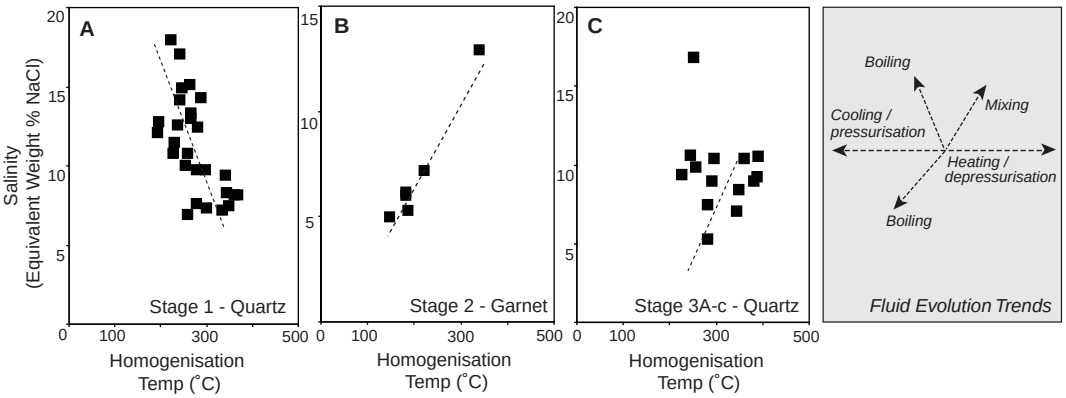

Figure 6.10 Homogenisation temperature versus salinity for stage 1 quartz, stage 2 garnet and stage 3A-c quartz fluid inclusions. Salinities are recorded as eq. wt. % NaCl. Lines on each of the salinity-homogenisation temperature plots represent fluid evolution trends, with the interpreted significance of these trends highlighted in grey box modified from Davies et al., 2008.

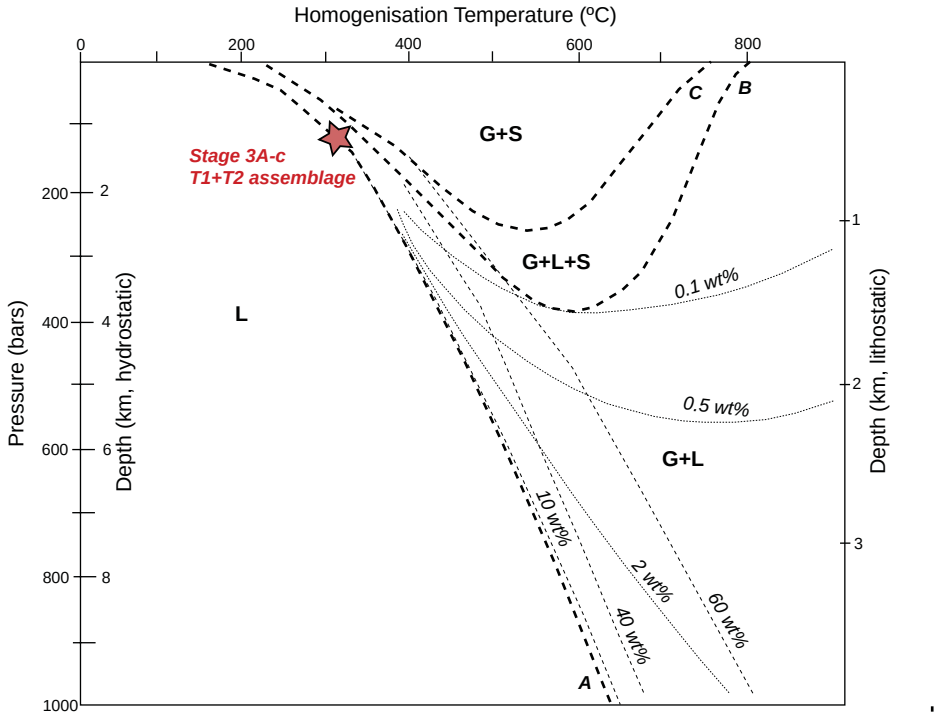

Figure 6.11 Temperature vs depth diagram in the NaCl-H_2O system based on Bodnar et al. (1985b), Fournier (1999) and modified from Muntean and Einaudi (2001). The diagram shows the predominance field for liquid (L), gas+liquid (G+L) and gas+halite (G+S). Curve A is the boiling point for a 10 wt. % NaCl solution. Curve B separates the G+L field from a three phase field (G+L+S) for the NaCl-H_2O system. Curve C is the liquid saturation curve for the NaCl-KCl-H_2O system. Contours of constant NaCl (wt.%) in the G+L field are shown for liquid (thin dash line) and gas (thin dotted lines). The diagram illustrates the proposed characteristic for fluids that produced stage 3A-c gold-bearing veins - show by star.

two fluids during stage 2. Specifically, high-temperature, high salinity fluids are inferred to have mixed with low-temperature, low salinity water (Fig. 6.10B). These trends, however, should be treated with caution as they are based on all analysed samples i.e. both isolated fluid inclusions and fluid inclusion assemblages from growth zones, and those populations that homogenised over a wide range of temperatures (Appendix E.2), and therefore some ambiguity exists regarding the correlation of the various data sets. More fluid inclusion analyses of well-constrained of FIAs are required to test whether these processes played an important role during early hydrothermal activity at E41.

The co-existing low- and higher-density inclusions present in stage 3A-c (Fig. 6.10C) imply that phase separation was typical of the magmatic-hydrothermal event.

Pressure and depth constraints

Boiling assemblages have been identified only in stage 3A-c. Samples that contain such textural evidence of boiling are assumed to have been trapped under hydrostatic pressure on the two-phase (liquid-vapour) saturation curve (Fig. 6.11). Thus, these inclusions can be used to determine pressure at the time of fluid entrapment and hence the depth of mineral deposition below paleowater table (Roedder and Bodnar, 1980).

Estimation of the depths of formation for the boiling fluid inclusions assemblages of stage 3A-c veins can be obtained by using phase relations in the NaCl-H_2O system (Bodnar et al., 1985b; Fournier, 1987; 1999) and a pressure versus temperature diagram (Fig. 6.11); modified from Muntean and Einaudi (2001). Depths are shown assuming densities of 1g/cm^3 hydrostatic pressure and 2.5g/cm^3 for lithostatic pressures. Within the two phase gas + liquid (G+L) field, contours of constant weight % NaCl dissolved in the liquid and gas are represented. In order to estimate the pressure, and hence the depth of formation, the 3A-c fluid inclusions data has been plotted in terms of homogenisation temperatures and salinities (Fig. 6.11). There are uncertainties of approximately 100-200 bars with regards to the pressure estimates (Muntean and Einaudi, 2001).

The stage 3A-c boiling fluid inclusions assemblages plot on the L-V saturation curve at depth of ~1.2 km, which corresponds to a hydrostatic pressure of 110 bars (Fig. 6.11). Using the equations of Haas (1971), 310ºC, the 9.5 wt. % NaCl boiling fluid 3A-c was trapped at approximately 90 bars and a depth of ~1 km under hydrostatic load. The abundant open space fill textures throughout the deposit are consistent with hydrostatic pressure conditions (e.g., Ayllon et al., 2003).

CO_2 concentrations

Although no CO_2 was detected in fluid inclusions at E41, the presence of calcite and ankerite as vein and alteration minerals throughout the paragenesis suggest that CO_2 was a component in the gold-bearing fluids. The lack of visible CO_2 in quartz-hosted fluid inclusions indicates that its concentration was below 4.4 wt. % (Cooke and Bloom, 1990). The amount of CO_2 dissolved in water increases the pressure (and therefore depth) at which phase separation will begin to occur at a given temperature (Takenouchi and Kennedy, 1965; Bodnar et al., 1985a; Hedenquist and Henley, 1985). The presence of CO_2 in mineralising fluids have been suggested as a key element for the formation of several epithermal-style deposits that are interpreted to form at depths greater than 1 km, including Porgera (Ronacher et al., 2000) and Cripple Creek (Thompson et al., 1985). A similar scenario may apply to E41.

6.4 Stable isotopes

Investigations into the stable isotope geochemistry of hydrothermal minerals at E41 were conducted to constrain fluid sources and processes responsible for mineral deposition. A combination of S, C-O and O-D isotopes have been analysed from veins and alteration minerals from several paragenetic stages. In addition, S isotopic compositions of sulfides are used to determine whether any sulfur isotopic zonation

pattern exists at E41, and if so whether this pattern can be used as a proxy for fluid flow, helping to define the centre(s) of magmatic-hydrothermal activity at E41.

This is the first systematic stable isotope investigation of E41. Prior to this study, limited stable isotopic data were available for E42 (Bastrakov, 2000; Strickland, 2005) and E43 (Zukowski, 2009). Only two pyrite samples of uncertain paragenesis from E41 have been previously analysed for their sulfur isotopic compositions (-3.0 and -3.3‰; Bastrakov, 2000).

6.4.1 Sulfur isotopes

6.4.1.1 Introduction

In the current study, sulfide and sulfate minerals have been analysed for their sulfur isotopic compositions to determine potential sources of sulfur and sulfur speciation in the ore forming fluids (e.g., Ohmoto and Rye, 1979; Ohmoto and Goldhaber, 1997). In addition, paragenetically constrained samples were used to investigate spatial and temporal variations in sulfur isotopic compositions, in order to help infer fluid evolution and to trace potential fluid pathways at E41.

6.4.1.2 Methodology

Sulfur isotopic analyses involved conventional and laser ablation techniques. Medium- to coarse-grained sulfide material was extracted manually using a hand-held drill (Dremel tool) at CODES, University of Tasmania. Care was taken to ensure that pure mineral separates were prepared, although in the case of very fine-grained samples with intergrowths of sulfides, some contamination could not be avoided. Sulfur isotopic analyses were completed at the University of Tasmania Central Science Laboratory in Hobart, using the conventional sulfur isotope analytical techniques of Robinson and Kusakabe (1975). Measurements were performed on a VG Sira Series II mass spectrometer. Analytical uncertainties for the technique are estimated at ±0.1 per mil (‰).

Samples of finely intergrown sulfides (<1 mm) could not be hand drilled. Six samples of fine-grained sulfides were therefore analysed using the laser ablation method of Huston et al. (1995) on ~200 μm thick polished sections (Table 6.4). Ablations were conducted using an 18W Quantronix 117Nd:YAG model laser in an oxidising atmosphere (at 25 torr oxygen pressure) and a ~35mA current for 2 seconds on single or multiple sites (up to 5) to yield sufficient SO_2 for analysis. The total gas was passed from the sample chamber through two different purification circuits (H_2O and CO_2) before SO_2 gas was collected and analysed using a VG Sira Series II mass spectrometer.

TABLE 6.4 $\delta^{34}S_{CDT}$ values of sulfide minerals from E41. Data listed in paragenetic order.

Drill hole	Depth (m)	Paragenetic stage	Mineral	Alteration halo	Alteration zone	d ^{34}S (‰)	Analytical method
E41D2007	88.2	1A	pyrite	magnetite - chalorite ± biotite	Potassic	-0.5	C
E41D2007	93.6	1A	pyrite	magnetite - chlorite - albite	Potassic	-2.0	C
E41D2067	197.5	1B	chalcopyrite	weak albite	Propylitic	-4.9	L
E41D2009	236.9	3A-a	pyrite	epidote	Transitional propylitic - potassic	-2.9	C
E41D2009	111.4	3A-a	pyrite	epidote	Transitional propylitic - potassic	-2.6	C
E41D2009	223	3A-a	pyrite	epidote and traces of red K-feldspar	Transitional propylitic - potassic	-4.2	C
E41D2014	251.7	3A-a	pyrite	epidote	Transitional propylitic - potassic	-2.4	C
E41D2014	310.2	3A-a	pyrite	epidote	Transitional propylitic - potassic	-3.2	C
E41D2013	152.3	3A-a	pyrite	epidote	Transitional propylitic - potassic	-3.4	C
E41D2014	213.8	3A-b	pyrite	K-feldspar - epidote	Transitional propylitic - potassic	-1.6	C
E41D2007	195.7	3A-c	pyrite	chlorite - pyrite - illite - muscovite	Phyllic facies overprinting propylitic	-3.4	C
E41D2007	170.9	3A-c	pyrite	illite - muscovite	Phyllic	-3.7	C
E41D2007	150.9	3A-c	pyrite	chlorite - carbonate - pyrite - illite - muscovite	Phyllic facies overprinting propylitic	-2.7	C
E41D2007	108.7	3A-c	pyrite	illite - muscovite	Phyllic	-2.4	C
E41D2008	131.6	3A-c	pyrite	*no obvious halo*	Phyllic overprining weak epidote facies	-2.6	C
E41D2009	184.1	3A-c	pyrite	*no obvious halo*	Propylitic and weak transitional propylitic - potassic	-5.2	C
E41D2009	157.1	3A-c	pyrite	*no obvious halo*	Phyllic (bleached mudstone)	-4.9	C
E41D2009	132.8	3A-c	pyrite	*no obvious halo*	Phyllic (bleached mudstone)	-2.7	C
E41D2009	111.4	3A-c	pyrite	*no obvious halo*	Transitional propylitic - potassic	-3.0	C
E41D2010	195.3	3A-c	pyrite	illite - muscovite	Phyllic (bleached mudstone)	-1.2	C
E41D2011	123.1	3A-c	pyrite	*no obvious halo*	Propylitic and weak transitional propylitic - potassic	-1.4	C
E41D2011	199.6	3A-c	pyrite	illite - muscovite	Phyllic overprinting transitional propylitic - potassic	-2.5	C
E41D2011	95.6	3A-c	pyrite	illite - muscovite	Phyllic	-3.2	C
E41D2011	242.7	3A-c	pyrite	epidote - illite - muscovite	Propylitic	-2.5	C
E41D2013	137.6	3A-c	pyrite	*no obvious halo*	Propylitic	-3.5	C
E41D2013	114.3	3A-c	pyrite	illite - muscovite	Propylitic	-3.1	C
E41D2014	278.6	3A-c	pyrite	weak illite - muscovite	Propylitic	-3.6	C
E41D2014	232.3	3A-c	pyrite	weak chlorite - illite - muscovite	Phyllic overprinting propylitic	-3.5	C
E41D2114	287.2	3A-c	pyrite	chlorite - illite - muscovite	Phyllic	-3.5	C
E41D2114	301.9	3A-c	pyrite	K-feldspar - pyrite - illite - muscovite	Phyllic	-3.0	C
E41D2129	90.4	3A-c	pyrite	carbonate - illite - muscovite	Phyllic overprinting potassic	-1.8	C
E41D2129	167.8	3A-c	pyrite	K-feldpsar - chlorite - illite - muscovite	Phyllic overprinting propylitic	0.5	C
E41D2139	122.1-2	3A-c	pyrite	illite - muscovite	Phyllic	-1.6	C
E41D2139	141.1	3A-c	pyrite	illite - muscovite	Phyllic	0.8	C
E41D2180	108	3A-c	pyrite	illite - muscovite	Phyllic	-2.6	C
E41D2180	77.8	3A-c	pyrite	illite - muscovite	Phyllic	-0.9	C
E41D2180	127.3	3A-c	pyrite	illite - muscovite	Phyllic	-4.4	C
E41D2181	132	3A-c	pyrite	illite - muscovite	Phyllic	-3.9	C

TABLE 6.4 $\delta^{34}S_{CDT}$ values of sulfide minerals from E41. Data listed in paragenetic order.

E41D2181	154.5	3A-c	pyrite	illite - muscovite	Phyllic	-2.1	C
E41D2181	195.2	3A-c	pyrite	waxy green illite - muscovite	Phyllic	-2.7	C
E41D2181	71	3A-c	pyrite	carbonate - illite - muscovite	Phyllic	-0.7	C
E41D2182	221.7	3A-c	pyrite	illite - muscovite	Phyllic	-2.7	C
E41D2182	230.9	3A-c	pyrite	illite - muscovite	Phyllic	-3	C
E41D2182	97.9	3A-c	pyrite	illite - muscovite	Phyllic	-1.9	C
E41D2182	195.6	3A-c	pyrite	illite - muscovite	Phyllic	-1.1	C
E41D2011	110.1	3A-c	pyrite	illite - muscovite	Phyllic	-3.4	C
E41D2011	200.7	3A-c	pyrite	illite - muscovite	Phyllic overprinting propylitic	-2.5	C
E41D2012	292.8	3A-c	pyrite	chlorite - illite - muscovite	Propylitic	-3.6	C
E41D2014	257.9	3A-c	pyrite	weak illite - muscovite - pyrite	Phyllic overprinting propylitic	-1.5	C
E41D2014	204.6	3A-c	pyrite	*no obvious halo*	Phyllic overprinting propylitic	-3.1	C
E41D2180a	146.9	3A-c	pyrite	illite - muscovite	Phyllic	-2.5	C
E41D2181	85.7	3A-c	pyrite	illite - muscovite - pyrite - chlorite	Phyllic	-4.0	C
E41D2007	242	3B	pyrite	carbonate - illite - muscovite	Phyllic overprinting potassic	-2.9	C
E41D2007	176.1	3B	pyrite	weak illite - muscovite	Propylitic and traces of transitional propylitic - potassic	-3.6	C
E41D2007	123.7	3B	pyrite	illite - muscovite	Phyllic	-2.7	C
E41D2008	187.8	3B	pyrite	*no obvious halo*	Propylitic	-3.3	C
E41D2008	234.7	3B	pyrite	weak hematite dusted K-feldspar	Potassic	-3.8	C
E41D2009	98.9	3B	pyrite	illite - muscovite - pyrite	Phyllic (bleached mudstone)	-3.0	C
E41D2009	122.8	3B	pyrite	illite - K-feldspar	Phyllic	-5.0	C
E41D2009	236.9	3B	pyrite	illite - calcite - muscovite	Phyllic overprinting transitional propylitic - potassic	-3.7	C
E41D2010	160.3	3B	pyrite	weal chlorite - illite - muscovite	Phyllic	-3.4	C
E41D2010	118.1	3B	pyrite	*no obvious halo*	Phyllic	-3.3	C
E41D2010	269.9	3B	pyrite	hematite	Phyllic alteration overprinting transitional propylitic - potassic	-1.53	C
E41D2012	199.0-1	3B	pyrite	weak illite - muscovite	Propylitic and transitional propylitic - potassic	-2.9	C
E41D2012	247.5	3B	pyrite	weak illite - muscovite	Phyllic overprinting propylitic and transitional propylitic - potassic	-4.0	C
E41D2013	137.6	3B	pyrite	weak chlorite - illite - muscovite	Phyllic alteration overprinting propylitic	-4.0	C
E41D2013	256.9	3B	pyrite	weak hematite dusted K-feldspar	Propylitic	-3.0	C
E41D2013	196.4	3B	pyrite	weak chlorite - illite - muscovite	Phyllic alteration overprinting propylitic	-3.0	C
E41D2014	310.2	3B	pyrite	weak illite - muscovite	Propylitic and transitional propylitic - potassic	-2.9	C
E41D2114	293.1	3B	pyrite	chlorite - illite - muscovite (+clays)	Phyllic (fault related)	-4.1	C
E41D2007	123	4A	sphalerite	carbonate - illite - muscovite	Phyllic	-2.6	C
E41D2011	195.5	4A	galena	ankerite - arsenopyrite - illite - muscovite	Phyllic	-7.5	C
E41D2011	159	4A	sphalerite	illite - muscovite	Phyllic	-4.7	C
E41D2011	132	4A	sphalerite	illite - muscovite	Phyllic	-1.4	C
E41D2012	212.7	4A	pyrite	chlorite - illite - muscovite	Transitional propylitic - potassic	-4.0	C
E41D2012	259.1	4A	galena	chlorite - carbonate - illite - muscovite	Transitional propylitic - potassic	-6.6	C

TABLE 6.4 $\delta^{34}S_{CDT}$ values of sulfide minerals from E41. Data listed in paragenetic order.

Drill hole	Depth (m)	Paragenetic stage	Mineral	Alteration halo	Alteration zone	d ^{34}S (‰)	Analytical method
E41D2012	335.8	4A	galena	illite - muscovite	Phyllic	-2.0	C
E41D2013	330.9	4A	pyrite	weak illite - muscovite	Phyllic alteration overprining potassic	-3.2	C
E41D2013	114.9	4A	galena	carbonate - chlorite - illite - muscovite	Phyllic	-5.1	C
E41D2013	196.4	4A	sphalerite	chlorite - carbonate - pyrite - illite - muscovite	Phyllic overprinting propylitic	-4.4	C
E41D2014	278.6-B	4A	galena	weak illite - muscovite	Propylitic and transitional propylitic-potassic	-5.3	C
E41D2129	215.9	4A	sphalerite	arsenopyrite - pyrite - illite - muscovite	Phyllic	-0.4	C
E41D2180	103.9	4A	sphalerite	arsenopyrite - illite - muscovite	Phyllic	-0.6	C
E41D2180	63.8	4A	sphalerite	illite - muscovite	Phyllic	-1.73	C
E41D2181	104.9	4A	pyrite	waxy illite pyrite - muscovite - pyrite	Phyllic	-3.2	C
E41D2181	224.9	4A	pyrite	waxy illite - muscovite - pyrite	Phyllic	-5.0	C
E41D2182	242	4A	pyrite	illite - muscovite	Phyllic	-4.2	C
E41D2182	268.1-2	4A(?)	chalcopyrite	*no obvious halo*	Phyllic	2.5	C
E41D2007	150.9-A	4A	pyrite	weak illite - muscovite	Propylitic	-2.8	C
E41D2010	197.3	4B	arsenopyrite	carbonate - illite - muscovite	Phyllic (related to fault zone)	-2.1	L
E41D2011	195.5(1)	4B	arsenopyrite	ankerite - arsenopyrite - illite - muscovite	Phyllic	0.8	L
E41D2011	195.5(2)	4B	arsenopyrite	ankerite - arsenopyrite - illite - muscovite	Phyllic	0.3	L
E41D2180	109.9	4B	arsenopyrite	ankerite - illite - muscovite	Phyllic	3.4	L
E41D2010	247.7	4C	galena	illite - muscovite	Phyllic (shear zone)	-5.4	C
E41D2007	220.2	4C	sphalerite	carbonate - illite - muscovite	Phyllic	-2.2	C
E41D2008	152.8	4C	chalcopyrite	illite - muscovite	Phyllic	-2.3	L
E41D2010	197.3	4C	galena	carbonate - illite - muscovite	Phyllic	-3.3	C
E41D2010	155.4	4C	sphalerite	strong carbonate - illite - muscovite	Phyllic	-2.8	C
E41D2014	218.8	4C	galena	chlorite - illite - muscovite	Propylitic	-6.5	C
E41D2181	212.8	4C	sphalerite	carbonate - illite - muscovite	Phyllic	-3.9	C
E41D2067	159.5	5	gypsum	*no obvious halo*	Propylitic	15.7	C

L=laser ablation

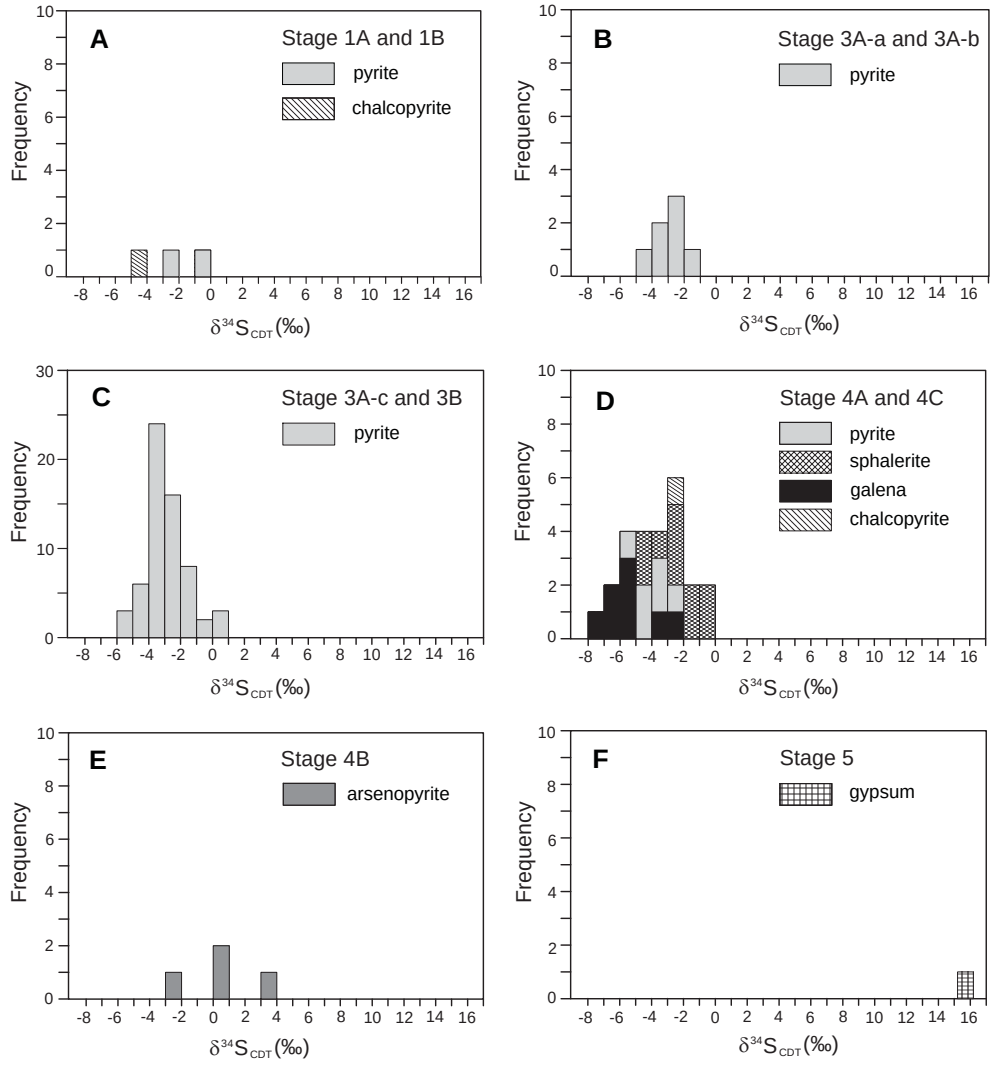

Figure 6.12 Cumulative frequency plots of sulfur isotope values (per mil relative to CDT standard) for sulfides and gypsum from E41. Dataset is listed in Table 6.4.

All measured $\delta^{34}S‰$ values are reported relative to Canyon Diablo Troilite (CDT), and were calculated as follows:

$$\delta^{34}S_{sample}\ (‰) = [(^{34}S/^{32}S)_{standard} \times 1000] / (^{34}S/^{32}S)_{standard}$$

6.4.1.3 Results

Sulfur isotopic compositions of 100 sulfides and one sulfate sample were analysed. Specifically, samples of pyrite, chalcopyrite, galena, sphalerite and arsenopyrite were analysed from stages: 1A, 1B, 3A-a, 3A-b, 3A-c, 3B and 4A, B, C. One sample of stage 5 gypsum was also analysed. Sulfur isotopic results are shown in Figure 6.12 and summarised in Table 6.4.

Sulfur isotope compositions of sulfides from E41 vary according to their paragenetic stage. Only three 1A and 1B sulfides were analysed (Table 6.4), varying

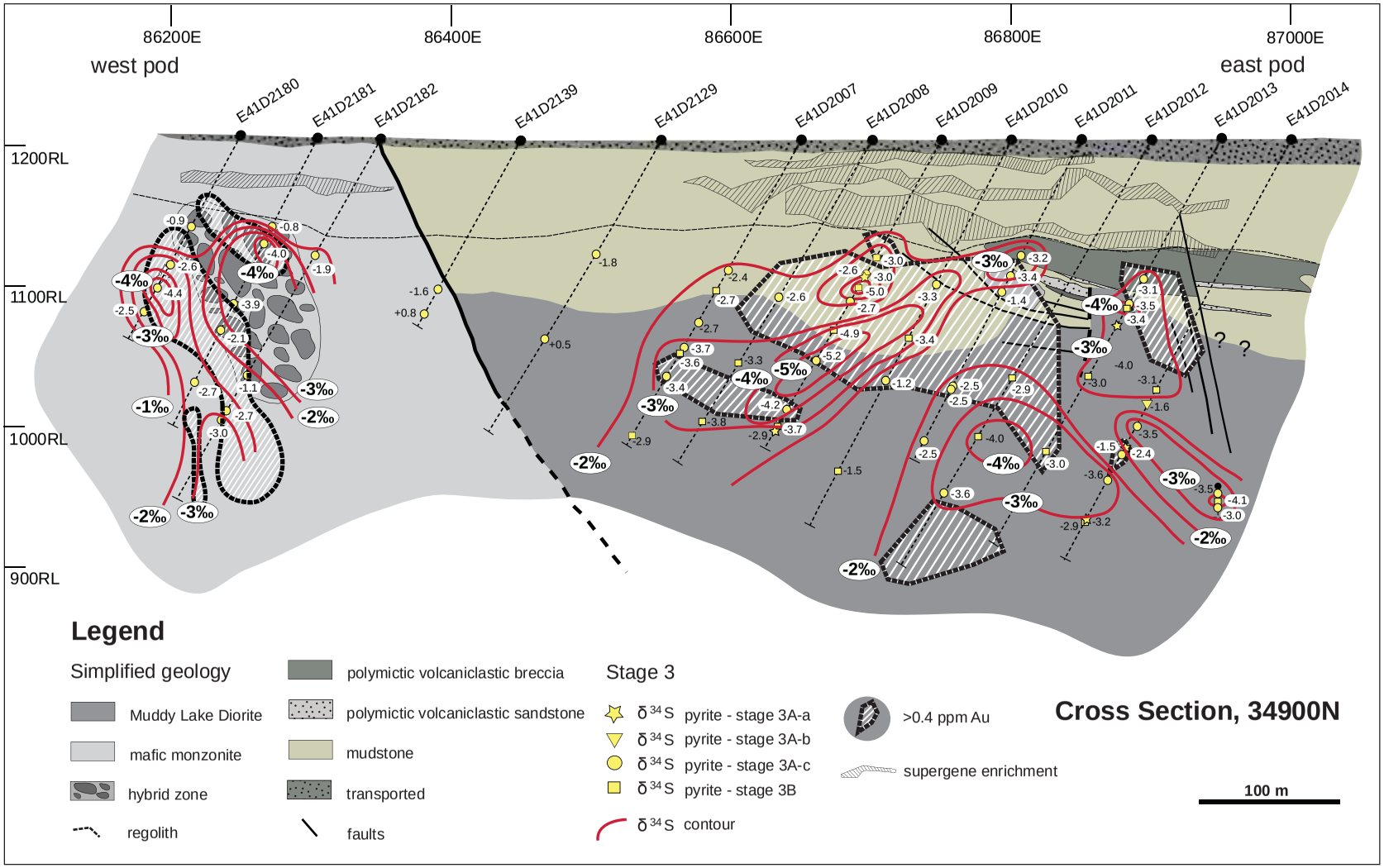

Figure 6.13 Contoured values of $\delta^{34}S$ for stage 3 (quartz-pyrite) mineralisation including stages 3A-a, 3A-b, 3A-c, and 3B. The isotopic values and interpreted contours have been drawn on the geology section from Figure 3.2. RL=relative level.

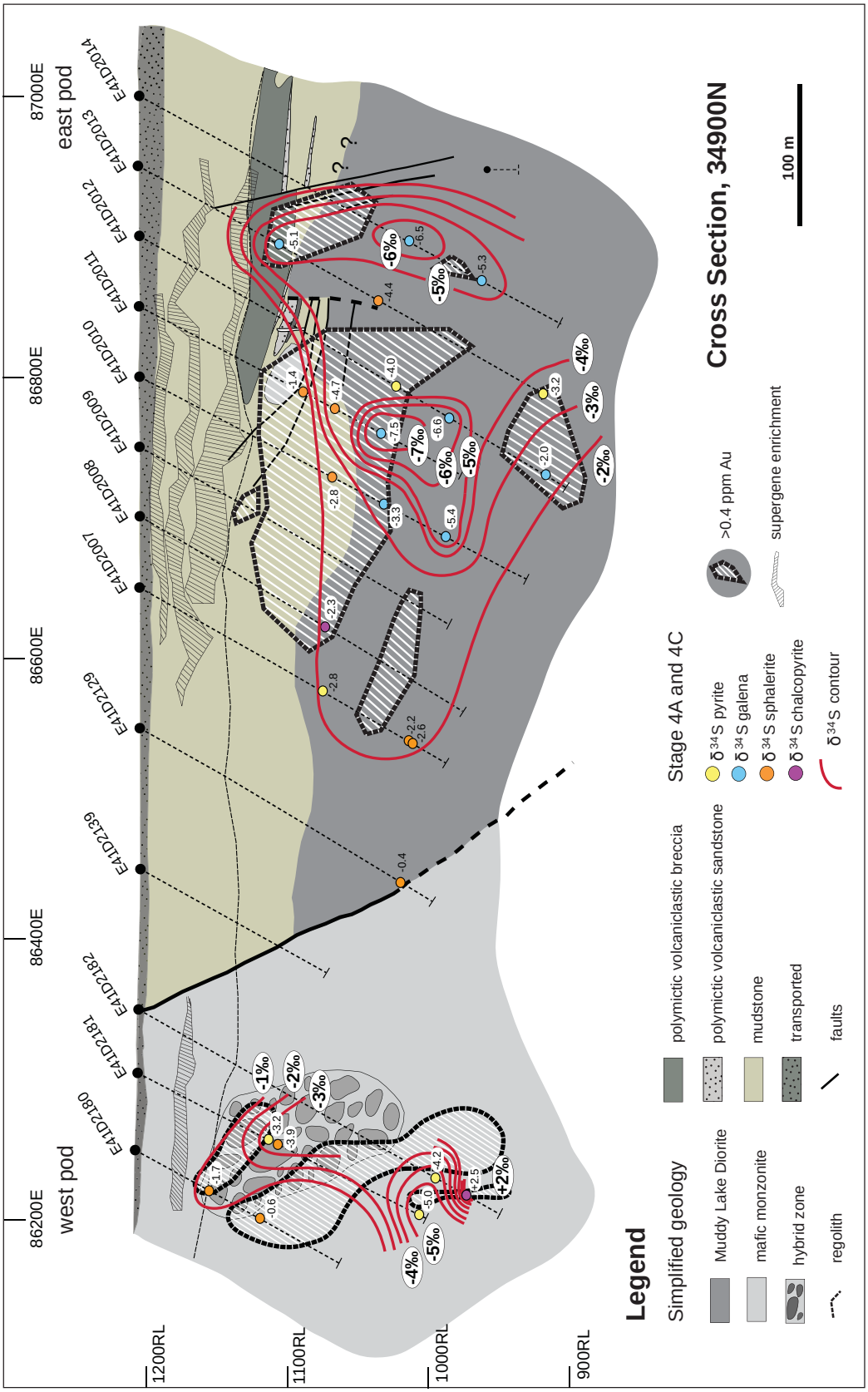

Figure 6.14 Contoured values of $\delta^{34}S$ for stage 4 A and 4C mineralisation. The isotopic values and interpreted contours have been drawn on geology section from Figure 3.2. RL=relative level.

from -4.9 to -0.5‰. Stage 3A-a sulfides (n=6) have $\delta^{34}S$ values ranging from -3.4 to -2.4‰, stage 3A-b (n=1) has a value of -1.6‰, and stage 3A-c (n=49) range from -5.2 to +0.8 ‰. Stage 3B (n=18) sulfides are characterised by -5.0 to -1.5‰ values. Stage 4A (n=19) and 4C (n=7) range from -7.5 to +2.5‰. Galena has the lowest $\delta^{34}S$ detected signature (-7.5‰; Fig. 6.12D). The highest value of $\delta^{34}S$ (+3.4‰) was obtained from stage 4B arsenopyrite, with values that range from -2.1 to +3.4‰. Disseminated pyrite from post-mineralisation hydrothermal breccia yielded -4.9 ‰. A gold-bearing pyrite clot from an aplite dykelet has a $\delta^{34}S$ value of -1.2‰. One stage 5 gypsum vein returned a value of +15.7‰.

Contours of sulfur isotopic values for stages 3A-a, 3A-b, 3A-c, 3B, 4A, 4B and 4C are illustrated on Figures 6.13 and 6.14. A distinctive sulfur isotopic zonation pattern appears to be recorded by both paragenetic stages at E41 with the lowest values occurring close to and/or overlapping with mineralised domains. Because steep northeast-trending fractures are inferred to be the conduits for mineralising fluids at E41 the illustrated contours form closed geometries around those upflow zones at depth on 34900N section. The domains of negative $\delta^{34}S$ values are believed to extend to greater depths along the northeast-trending faults away from this section.

6.4.1.4 Discussion

Fractionation of sulfur isotopes in magmatic-hydrothermal environments is sensitive to any changes in temperature, oxidation potential (redox), pH, and processes such as phase separation (e.g., Ohmoto and Goldhaber, 1997). At high temperatures the SO_2 and H_2S are the predominant aqueous sulfur species (Ohmoto, 1972; Ohmoto and Rye, 1979; Rye, 1993). SO_2 disproportionates to SO_4^{2-} and H_2S at temperatures of approximately 350º to 400ºC according to the following chemical reaction:

$$4SO_2 + 4H_2O \leftrightarrow 3H_2SO_4 + H_2S$$

Under oxidising conditions ^{34}S isotope preferentially fractionates into the oxidised sulfur species (Ohmoto and Goldhaber, 1997) so that sulfate minerals typically have positive and homogeneous $\delta^{34}S$ values. In contrast, sulfide phases deposited from the sulfate-predominant fluids scavenge the available ^{32}S and fractionate strongly to progressively lighter $\delta^{34}S$ values (Rye et al., 1993).

This study has found that systematic sulfur isotopic zonation patterns characterise vein stages 3 and 4 at E41. The patterns broadly correlate with the ore domains (Figs. 6.13 and 6.14). The ^{34}S-depleted zones occur close to and partially overlap with highly mineralised domains, whereas the ^{34}S-enriched zones occur on

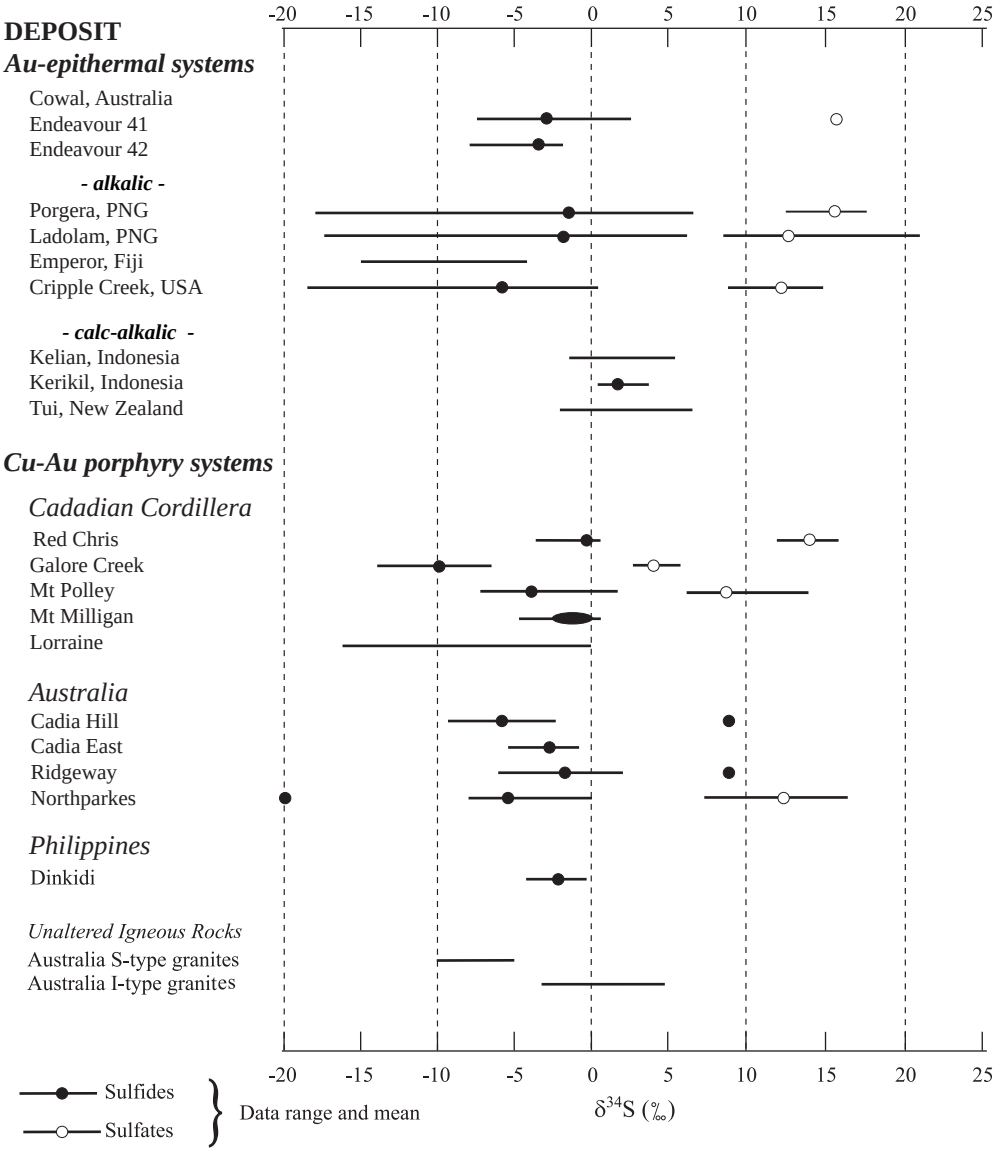

Figure 6.15 Ranges of δ^{34}S sulfides values (‰) determined for sulfides and sulfate minerals associated with epithermal and porphyry copper (-gold) deposits and with granitic rocks. Data for Cowal deposits are from this study and Strickland (2005). Other data sources: Ahmad et al. (1987), Richards and Kerrich (1993), Baker and Thompson (1998), Cameron (1998), Wolfe (2001), Lickfold (2002), Jensen (2003), Gemmell et al. (2004), Ronacher et al. (2004), Wurst (2004), Cooke et al. (2006), Wilson et al. (2007a), Davies et al. (2008), Jago et al. (2008), and Pass et al. (2008).

the peripheries of ore centres. The δ^{34}S contours defined by stage 3 veins overlap both with high-temperature main stage epidote and K-feldspar – epidote assemblages and with domains of phyllic alteration (compare Figs. 5.3C-F and Fig. 6.13). Depleted δ^{34}S sulfide values from stage 4 are spatially associated with zones of phyllic alteration (compare Fig. 5.3F and Fig. 6.14). The negative sulfur values appear to be spatially related to northeast- and east-trending fracture zones (compare zones of mineralisation on Fig. 3.2A with Figs. 6.13 and 6.14) in east and west pods (respectively) that are inferred to have been conduits for mineralising fluids.

Negative sulfur isotopic values for sulfide minerals characterise alkalic porphyry deposits (Fig. 6.15), where the lowest $\delta^{34}S$ values appear to be associated with highly-Cu-Au mineralised potassically altered centres (e.g., Radclyffe 1995, Wilson, 2003, Deyell and Tosdal, 2005; Wilson et al., 2007a). At Ridgeway, the high grade core of the deposit is characterised by strongly depleted $\delta^{34}S$ values for sulfides, with an outer pyritic halo distinguished by more ^{34}S-enriched isotopic compositions (Harper, 2000; Wilson, 2003; Wilson et al., 2007a). Sulfides in the quartz monzonite porphyries at Northparkes have $\delta^{34}S$ values as low as -19.0‰ (Heithersay and Walshe, 1995; Radclyffe, 1995; Lickfold, 2002). Wolfe (2001) documented similar features at Didipio in the Philippines. The Mt. Polley (Deyell and Tosdal, 2005; Deyell et al., 2005; Pass et al., 2008, Lorraine and Afton (Deyell and Tosdal, 2005), Galore Creek (Shannon et al., 1983; Micko et al., 2008), Mt. Milligan (Jago, 2008) and Red Chris (Baker and Thompson, 1998) deposits in British Columbia are characterised by $\delta^{34}S$-delepted sulfide values that exhibit spatially zoned patterns and temporal relationships to Cu-Au mineralisation. The results from E41 are therefore consistent with an alkalic porphyry affiliation, due to the similar zonation patterns and ranges of $\delta^{34}S$ values (Fig. 6.15).

The E41 sulfur isotopic data are also consistent with alkalic epithermal systems (Fig. 6.15). An extensive sulfur isotopic study has been carried out at Porgera in PNG (Richards and Kerrich, 1993; Cameron, 1998; Ronacher et al., 2004; Cooke et al., 2006). The first vein stage at Porgera has isotopic values ranging from -1.0 to +6.0‰ and has been interpreted to indicate the involvement of reducing fluids. The main mineralising stage at Porgera (pyrite – Au – roscoelite) has extremely ^{34}S-depleted sulfides ranging from -18.0 to -11.0‰. This strongly negative sulfur signature has been concluded to be a product of magmatic-hydrothermal sulfate-predominant fluids (Cooke et al., 2006). Similar negative sulfur isotopic signatures have also been reported from other giant alkalic epithermal systems, e.g., Lihir (Carman, 1994; Gemmell et al., 2004), Emperor (Ahmad et al., 1987; Begg, 1996) and Cripple Creek (Jensen, 2003).

Alternatively to a magmatic-hydrothermal source of oxidised sulfur, the ^{34}S-depleted sulfides could be produced by: (a) incorporation of external, isotopically light biogenic sulfur; or (b) the involvement of SO_4^{2-} complexes sourced from evaporate-rich host rocks (Ohmoto and Rye, 1979). Neither of these sources appear plausible for E41 as the there is no organic material or evaporates available in the stratigraphy of the E41 deposit.

It is interpreted that most of the gold-bearing vein stages at E41 (stages 3A-a, 3A-b, 3A-c, 3B, 4A and 4C) formed from oxidised, sulfate-rich predominantly magmatic fluids that are typical of alkalic porphyry and epithermal systems. Sulfur

isotopic zonation patterns at E41 are spatially related to mineralised zones and associated alteration facies. This zonation is inferred to indicate upflow of oxidised magmatic-hydrothermal fluids to the site of mineralisation, with domains of $\delta^{34}S$ depletion at the core of the upflow zone, potentially providing a vector towards a magmatic (porphyry-style) mineralised centre below the current level of exposure of epithermal gold mineralisation at E41.

Stage 4B arsenopyrite from E41 has positive $\delta^{34}S$ values, which are inconsistent with all other E41 sulfides (Fig. 6.12F; Table 6.4). This is consistent with reducing conditions at the time of stage 4B sulfide precipitation. A reducing environment is also inferred from the presence of green-coloured (Cr-bearing) micas that are related temporally and spatially to arsenopyrite. Arsenopyrite appears to be spatially associated with highly mineralised stage 4A veins, occurring as an infill that has cut stage 4A sphalerite, pyrite and illite. The change from stage 4A to 4B is interpreted to relate to a shift from oxidising (sulfate-predominant) to reducing (H_2S-predominant) conditions. This shift from oxidising to reducing conditions could be explained by mixing of oxidised magmatic-hydrothermal fluids with externally-derived reduced water during stage 4.

6.4.2 Oxygen and hydrogen isotopes

6.4.2.1 Introduction

The oxygen and deuterium isotopic compositions of hydrous minerals are used widely to constrain hydrothermal fluid sources (Taylor, 1997). The oxygen and deuterium isotopic systems have been used to determine fluid sources in porphyry, epithermal and geothermal environments (e.g., Browne, 1971; Sheppard et al., 1971; Taylor, 1974, 1997; Hayba et al., 1985; Hedenquist et al., 1998; Cooke and Simmons, 2000; Simmons, 2005). The origin of phyllic alteration has received particular attention as to whether the fluids that were responsible for its formation were magma-derived, a mixture of magmatic and meteoric waters or are dominantly meteoric in origin. Several studies of water-bearing hydrothermal minerals and fluid inclusions from North and South American copper porphyry systems indicate that phyllic alteration assemblages form in response to the predominantly meteoric waters (e.g., Sheppard et al., 1971; Gustafson and Hunt 1975; Taylor, 1997). However, other investigations into phyllic alteration assemblages from deposits such as El Salvador (Watanabe and Hedenquist, 2001), El Teniente and Rio Blanco (Kusakabe et al., 1990; Skewes et al., 2001; Frikken, 2004), Far Southeast (Hedenquist et al., 1998), Endeavour 48 (Wolfe, 1994), Endeavour 26 (Harris and Golding, 2002) and Cadia (Wilson, 2003) show evidence of δD and $\delta^{18}O$ isotopic compositions indicative of predominantly magmatic fluids.

TABLE 6.5 Measured $\delta^{18}O$ and δD compositions of composite illite-muscovite samples from E41. The $\delta^{18}O$ and δD isotopic compositions of waters in isotopic equilibrium with illite ± muscovite at 200°, 250°, 300° and 350°C have been calculated using the fractionation equations of Gilg and Sheppard (1996). $\delta^{18}O$ and δD results are reported relative to the Standard Mean Ocean Water (SMOW) standard.

					Waters compositions				
Sample	Mineral	Description	$\delta^{18}O$ (‰,VSMOW)	δD (‰,VSMOW)	$\delta^{18}O_{(fluid)}$ (200°C)	$\delta^{18}O_{(fluid)}$ (250°C)	$\delta^{18}O_{(fluid)}$ (300°C)	$\delta^{18}O_{(fluid)}$ (350°C)	δD
E41D2012, 335.7	Illite - muscovite	Quartz pyrite vein associated with strong illite – muscovite alteration halo	8.4	-61.0	1.4	3.4	4.8	6.0	-86.0
E41D2181, 140.9	Illite - muscovite	Pervasive illite – muscovite alteration	9.5	-58.3	2.6	4.5	6.0	7.1	-83.3
E41D2180, 104.2	Illite - muscovite	Illite – muscovite alteration halo associated with stage 4A	8.6	-54.4	1.7	3.6	5.1	6.2	-79.4
E41D2010, 197.0	Illite - muscovite	Illite – muscovite infill in stage 4 (multi stage vein)	5.0	-67.7	-2.0	0.0	1.4	2.6	-92.7

Fractionation factors:
Oxygen: $1000\ln\alpha_{illite/muscovite-water} = 2.39(10^6/T^2) - 3.76$ (Sheppard and Gilg, 1996)
Hydrogen: $1000\ln\alpha_{illite/muscovite-water} = 25 \pm 5$ (Sheppard and Gilg, 1996)

Based on the δD and $\delta^{18}O$ isotopic compositions, meteoric waters are inferred to be the dominant constituents of hydrothermal solutions in low-sulfidation epithermal environments (Cooke and Simmons, 2000). Magmatic water, however, may contribute up to 10 percent or more of the overall isotopic compositions of the mineralising solutions in some low-sulfidation epithermal systems (Simmons, 1995; Faure et al., 2002). This is particularly common for waters in equilibrium with low-temperature sericite-bearing assemblages in low-sulfidation epithermal systems associated with alkalic magmatism (Richards, 1995; Jensen and Barton 2000) and has been documented at Porgera (Richards and Kerrich, 1993), Emperor (Ahmad et al., 1987; Begg, 1996) and Gies (Zhang and Spry, 1994), where fluids inferred for hydrous alteration minerals, vein infills and breccia cements have δD and $\delta^{18}O$ signatures consistent with an involvement of magmatic fluids into low-temperature mineral assemblages.

6.4.2.2 Methodology

In this study four samples of illite – muscovite were analysed for their δD and $\delta^{18}O$ isotopic compositions in order to determine fluid sources for hydrothermal alteration associated with gold mineralisation (Table 6.5). The samples include an example of a highly mineralised stage 4C vein (E41D2010, 197.0 m), two samples collected from alteration haloes near mineralised stage 4A veins (E41D2012, 335.7 m; E41D2180, 104.4 m) and one sample of pervasive (pre- main-stage mineralisation) illite – muscovite alteration (E41D2180, 104.2 m) from west pod. Photographs of analysed samples are included in Appendix E.3. These samples allow an assessment as to whether there were significant differences in the hydrothermal fluids that produced vein-related and pervasive illite – muscovite alteration.

All four samples were sent to Dr. Kevin Faure at GNS Science, Rafter Stable Isotopes Laboratory in New Zealand. Rock samples were crushed, sieved and washed, and where possible 'sericite'/illite grains were hand-picked using a binocular microscope. In the case of sample DDH: E41D2181, 140.9 m, it was not possible to pick enough pure sample for hydrogen isotope analyses so illite-bearing material was concentrated and cleaned-up under the microscope to exclude any other hydrous silicates such as amphiboles. In all other cases, pure mineral separates were used for isotopic analyses. All results are reported relative to the Standard Mean Ocean Water (SMOW) standard.

Oxygen was extracted for isotopic analyses of illite – muscovite using a CO_2-laser and BrF_5, following the methodology of Sharp (1990). Samples were normalized to the international quartz standard (NBS-28). Values for four NBS-28 standards analysed with the samples had values that varied by less than 0.1‰. Samples and

standards were heated overnight to 150°C prior to loading into the vacuum extraction line to remove any adsorbed water. The samples were left overnight in a vapour of BrF_5. Blank BrF_5 runs were done until yield was less than 0.1 micro moles oxygen. Oxygen was passed through the fluorine-getter (in-line Hg diffusion pump), oxygen converted to CO_2 by a graphite furnace, yields recorded and CO_2 analysed on a Geo20-20 mass spectrometer.

For D-isotope analyses, illite – muscovite samples were analysed on a HEKAtech high temperature elemental analyser coupled with a GV Instruments IsoPrime mass spectrometer. Samples were pyrolysed at 1400ºC in silver capsules. All samples were analysed in triplicate. All results are reported with respect to VSMOW, normalized to the international standard IAEA-CH-7 (-100.33‰), NBS-22 (-120.0‰) and NBS-30 (-65 to 100.33‰). The standard deviation for samples measurements are reported, with standard deviations for standards usually better than 1.0.

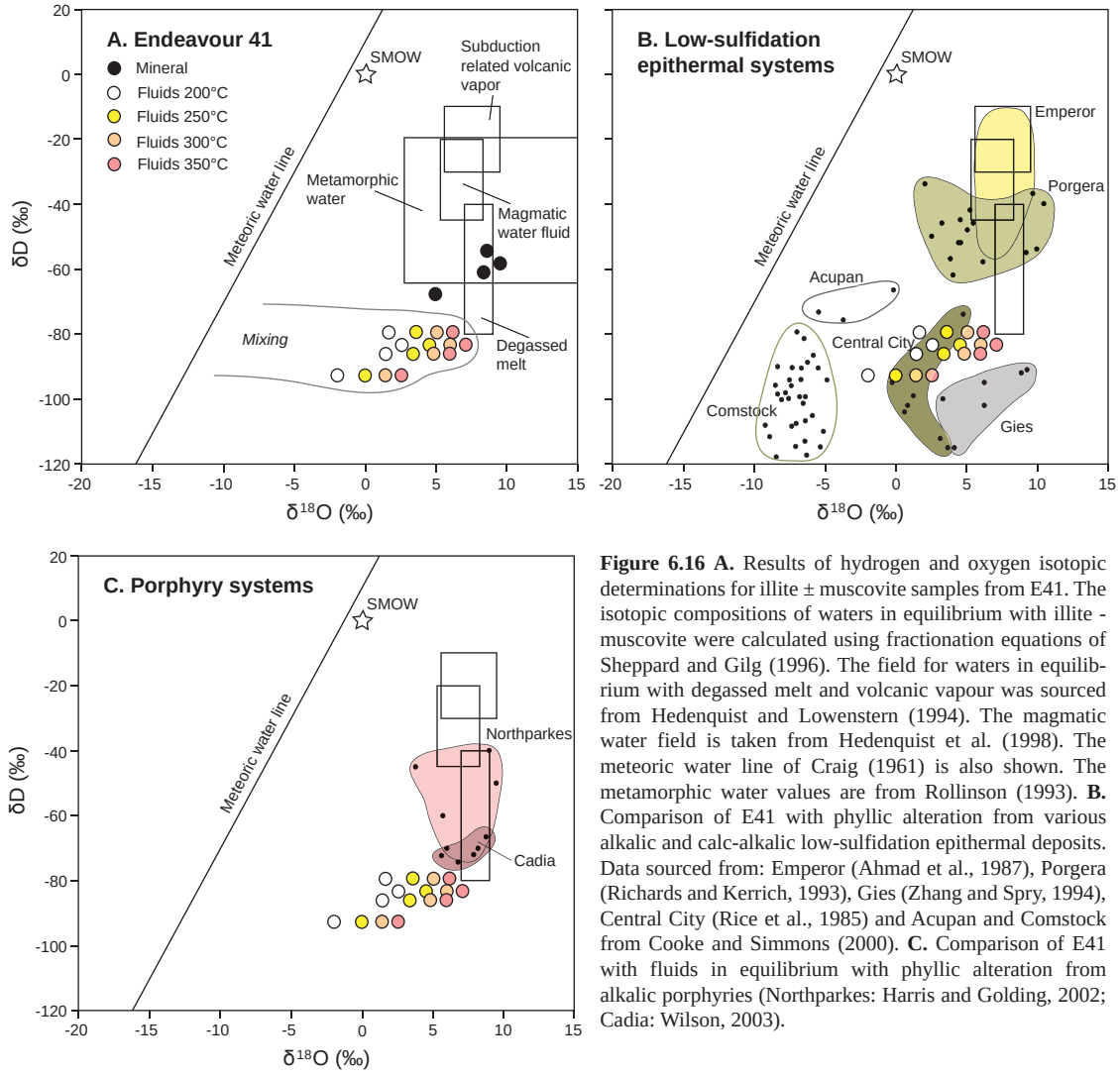

Figure 6.16 A. Results of hydrogen and oxygen isotopic determinations for illite ± muscovite samples from E41. The isotopic compositions of waters in equilibrium with illite - muscovite were calculated using fractionation equations of Sheppard and Gilg (1996). The field for waters in equilibrium with degassed melt and volcanic vapour was sourced from Hedenquist and Lowenstern (1994). The magmatic water field is taken from Hedenquist et al. (1998). The meteoric water line of Craig (1961) is also shown. The metamorphic water values are from Rollinson (1993). **B.** Comparison of E41 with phyllic alteration from various alkalic and calc-alkalic low-sulfidation epithermal deposits. Data sourced from: Emperor (Ahmad et al., 1987), Porgera (Richards and Kerrich, 1993), Gies (Zhang and Spry, 1994), Central City (Rice et al., 1985) and Acupan and Comstock from Cooke and Simmons (2000). **C.** Comparison of E41 with fluids in equilibrium with phyllic alteration from alkalic porphyries (Northparkes: Harris and Golding, 2002; Cadia: Wilson, 2003).

6.4.2.3 Results

The $\delta^{18}O$ and δD compositions of illite – muscovite at E41 range from +5 to +9.5‰ ($\delta^{18}O$) and -67.7 to -54.4‰ (δD; Table 6.5). The three samples of illite – muscovite alteration have a narrow range of values, whereas the sample of vein illite – muscovite has the most depleted δD value (Table 6.5 and Figure 6.16A).

In order to calculate the isotopic compositions of fluids in equilibrium with illite – muscovite, an estimate of the temperature of formation is required. This temperature remains poorly defined as workable fluid inclusions were not found in stage 4 gangue minerals. Illite is believed to form at temperature from 200 to 300ºC (e.g., Parry et al., 1984; Wilson et al, 1988; Reyes, 1990). In porphyry systems, crystallisation of muscovite has been documented to occur at temperatures as high as 350 to 400ºC (e.g., Cadia, Wilson, 2003; Bajo de la Alumbrera, Harris et al., 2005). Based on these constraints it is assumed that stage 4 was most likely deposited at temperature of 200º to 300ºC, given the abundance of illite relative to muscovite (section 5.3.3). The isotopic composition of water in isotopic equilibrium with illite – muscovite was therefore calculated at 200, 250, 300 and 350°C, using the fractionation equations of Sheppard and Gilg (1996; Table 6.5; 6.16A). Progressive cooling of these waters from 350º to 200ºC would drive their isotopic compositions towards lighter values of $\delta^{18}O$ while maintaining approximately constant δD (Fig. 6.16A).

6.4.2.4 Discussion

Fluids that precipitated illite – muscovite at E41 were characterised by low δD and depleted $\delta^{18}O$ values compared with magmatic fluids (Fig. 6.16A), consistent either with mixing of magmatic and meteoric waters, or isotopic exchange between meteoric waters and igneous wall rocks. Although O-D isotopic results do not preclude metamorphic waters, other factors such as the metal association (Au-Ag-Zn-Pb-Te) are more consistent with a magmatic fluid source (White and Hedenquist, 1990). As shown on Figure 6.16A, the O-D isotopic data rule out seawater involvement during stage 4 phyllic alteration. Calculated fluid values plot close to the box defined by degassed melt, which may indicate the involvement of residual fluids from a magma chamber that has already experienced significant degassing (Harris and Golding, 2002). The fluids responsible for phyllic alteration at the Cadia and Northparkes alkalic porphyry Cu-Au deposits have a clear magmatic signature (Fig. 6.16C) and provide indications of a likely magmatic fluid end-member for E41, if mixing between magmatic and meteoric water best explains the isotopic dataset.

Taylor (1997) showed that external waters typically have both depleted $\delta^{18}O$ and δD values ($\delta^{18}O<0$‰, $\delta D=0$ to -80‰). The limited ^{18}O-depletion at E41 may

indicate that meteoric fluids were subjected to extensive high-temperature ^{18}O isotope exchange with igneous wall rocks prior to mixing with magmatic waters (Rice et al., 1985). Alternatively, the degree of ^{18}O-enrichment in the fluids may be dependent on the extent and temperature of alteration, with feldspar-destructive sericitisation and carbonitisation at relatively low temperatures resulting in high $\delta^{18}O$ values (Richards and Kerrich, 1993). The E41 $\delta^{18}O$ fluid values are consistent with alkalic epithermal mineralising fluids as documented from Porgera (Richards and Kerrich, 1993), Emperor (Ahmad et al., 1987), Central City (Rice et al., 1985) and Gies (Zhang and Spry, 1994; 6.16B). The D-enrichment at Porgera and Emperor may relate to their tropical latitudes, as low latitude meteoric water are relatively enriched in D (Taylor, 1997). It appears likely that E41 formed at high latitudes, given the depletion in D. An alternative hypothesis is that E41 formed at high elevation (Rollinson, 1993) but this seems unlikely given the dominantly submarine island arc setting. It is important to note that the evidence of the involvement of meteoric waters at E41 implies the existence of emergent landforms at the time of stage 4 gold mineralisation.

Depletion of δD values can also result from boiling, as D preferentially partitions into the vapour phase (e.g., Harris and Golding, 2002). No evidence of boiling has been found in veins associated with stage 4 phyllic alteration but this process may also account for the D-depleted nature of fluids from E41.

6.4.3 Carbon-oxygen isotopes

6.4.3.1 Introduction

Several aqueous carbon species can occur in hydrothermal fluids (e.g., H_2CO_3, HCO_3^- $CO_{2(aq)}$, CO_3^{2-}, CH_4). Their presence and relative concentrations are sensitive to the temperature, pH, and fO_2 of the fluid (Ohmoto, 1972; Ohmoto and Goldhaber, 1997). Chemical reactions between these aqueous species can strongly affect carbon isotope fractionation (Ohmoto, 1986). Coupling carbon isotopic analyses with oxygen isotope analyses can allow for depositional processes to be inferred. In addition, carbon and oxygen isotopic variations, if analysed systematically, can also be used to provide a tracer for fluid flows (e.g., Halley, 2009).

6.4.3.2 Methodology

In this study the carbon-oxygen isotopic compositions of carbonates have been analysed in order to determine the nature and evolution of hydrothermal fluids at E41. Carbonates at E41 are present throughout the paragenesis (Fig. 5.1), providing a rare opportunity to investigate their compositional evolution from early-, through main-stage to post-mineralisation hydrothermal activity. Carbon and oxygen isotopic

TABLE 6.6 Carbon and oxygen isotope data for carbonates from E41.

Drill hole	Depth (m)	Paragenetic stage	Mineral	$\delta^{13}C_{PDB}$	$\delta^{18}O_{SMOW}$	Alteration halo	Alteration zone	Vein carbonate mineral association
E41D2011	97.7	2	calcite	-5.3	13.0	-	magnetite - epidote - calcite - chlorite	± epidote, ± garnet
E41D2012	221.7	3A-c	calcite	-4.6	11.7	weak illite - muscovite	weak epidote - illite - muscovite	± pyrite, ± quartz
E41D2014	225.5	3A-c	calcite	-4.8	12.1	-	epidote - illite - muscovite	± quartz
E41D2014	310.2	3B	calcite	-5.2	12.1	-	has cut epidote alteration facies	-
E41D2013	330.9	3B	calcite	-5.1	11.6	-	actinolite overprinted by K-feldspar - epidote	± quartz
E41D2180	103.9	4A	calcite+ankerite	-1.7	13.5	illite - muscovite	green illite - muscovite	-
E41D2180	100.4	4A	calcite+ankerite	-1.3	13.8	illite - muscovite	green illite - muscovite	-
E41D2180	109.9	4A	calcite+ankerite	-1.7	14.2	illite - muscovite	green illite - muscovite	-
E41D2012	335.8	4A	calcite	-0.6	11.7	illite - muscovite	illite - muscovite - calcite - ankerite	± pyrite
E41D2180	63.8	4A	calcite+ankerite	-4.4	14.1	illite - muscovite	illite - muscovite	± sulfides, ± ankerite
E41D2129	215.9	4A	calcite	-2.3	11.2	illite - muscovite	green illite - muscovite	± hematite, ± sulfides
E41D2013	114.9	4A	calcite+ankerite	-0.7	30.1	-	illite - muscovite - chlorite - calcite ± ankerite	-
E41D2012	247.5	4A	calcite	-3.7	11.3	illite - muscovite	epidote overprinted by illite - muscovite - calcite	± aptatite, ± hematite
E41D2011	195.5	4A	calcite	-0.6	11.6	illite - muscovite	illite - muscovite - chlorite - calcite ± ankerite	± hematite, ± sulfides, ± quartz
E41D2007	123.0	4A	calcite	-6.9	20.0	illite - muscovite	-	calcite-chlorite, ± clays
E41D2007	220.2	4A	calcite	-1.5	11.6	illite - muscovite	illite - muscovite- chlorite calcite ± ankerite	± clays, ± quartz
E41D2011	132.0	4A	calcite	-1.8	11.5	illite - muscovite	illite - muscovite	± quartz, ± clays
E41D2181	224.9	4C	calcite	-2.1	12.4	illite - muscovite	green illite - muscovite	± hematite
E41D2181	104.9	4C	calcite	-2.2	13.0	illite - muscovite	green illite - muscovite	± hematite, ± sulfides
E41D2181	159.1	4C	calcite	-3.0	14.2	illite - muscovite	green illite - muscovite	± pyrite
E41D2181	85.7	4C	calcite	-2.2	11.6	illite - muscovite	green illite - muscovite	± sulfides, ± quartz
E41D2010	247.7	4C	calcite	-1.7	12.1	illite - muscovite	illite - muscovite	± sulfides, ± quartz
E41D2010	197.0	4C	calcite	-1.9	11.4	illite - muscovite	illite - muscovite - calcite ± ankerite	-
E41D2008	151.8	4C	calcite	-2.1	10.9	illite - muscovite	shear zone - calcite - ankerite - chlorite - clays	-
E41D2180	135.8	6	ankerite+calcite	-2.6	13.6	-	pervasive illite - muscovite	-
E41D2181	171.7	6	ankerite+calcite	-2.5	13.4	-	cutting pervasive illite - muscovite alteration	± calcite
E41D2129	206.1	6	calcite	-2.1	11.2	-	-	± quartz, ± epidote
E41D2010	99.1	6	calcite	-3.2	11.3	-	epidote - illite - muscovite	± epidote
E41D2014	238.4	6	calcite	-3.8	11.9	-	has cut actinolite - magnetite - albite alteration	± chlorite
E41D2012	173.2	6	calcite	-2.6	11.2	-	-	-

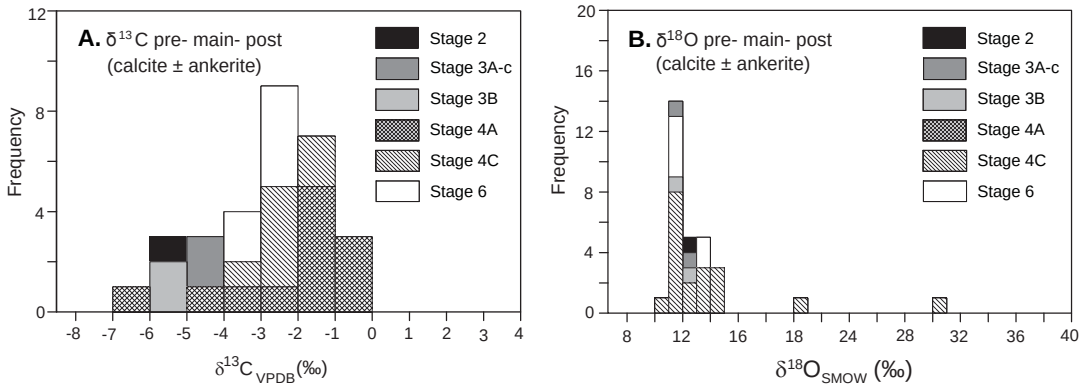

Figure 6.17 Cumulative frequency plots of C-O isotope values for carbonates from E41. Complete dataset is listed in Table 6.6.

analyses were undertaken at the Central Science Laboratory, University of Tasmania. The samples were prepared using the method of McCrea (1950), and the isotopic compositions of the extracted CO_2 were analysed using a Micromass 602D stable isotope mass spectrometer. Results are expressed in the standard δ (‰) notation relative to standard mean ocean water (SMOW) for oxygen, and Pee Dee belemnite (PDB) for carbon. The data were corrected for machine and experimental fractionation using internal standards, resulting in an isotopic error of ± 0.1‰ for $\delta^{13}C$ and ± 0.2‰ for $\delta^{18}O$.

6.4.3.3 Results

A total of thirty samples of pure calcite (n=23), and mixture of calcite ± ankerite (n=7) were analysed for their carbon and oxygen isotopic compositions (Table 6.6; Figure 6.17). Oxygen and carbon isotope analyses of calcite from main stage 3A-c and 3B are characterised by high $\delta^{18}O_{(SMOW)}$ values (stage 3A-c: +11.7 to +12.1‰; stage 3B: +11.6 to +12.1 ‰) and low $\delta^{13}C_{(PDB)}$ (stage 3A-c: -4.8 to -4.6‰; stage 3B: -5.2 to -5.1‰). One sample of stage 2 calcite yielded a $\delta^{18}O_{(SMOW)}$ value of +13.0‰ and a $\delta^{13}C_{(PDB)}$ value of -5.3‰. 4A carbonates are typified by $\delta^{18}O_{(SMOW)}$ from +11.2 to +30.1‰ and $\delta^{13}C_{(PDB)}$ of -6.9 to -0.6‰. Stage 4C veins have isotopic compositions between +10.9 to +14.2‰ ($\delta^{18}O_{(SMOW)}$) and -3.0 to -1.7‰ ($\delta^{13}C_{(PDB)}$). The isotopic composition of stage 6 carbonates varies from +11.2 to +13.6‰ ($\delta^{18}O_{(SMOW)}$) and -3.8 to -2.1‰ ($\delta^{13}C_{(PDB)}$).

6.4.3.4 Discussion

Carbon-oxygen isotopic zonation

Although the number of analysed samples is limited, there appears to be an isotopic zonation pattern recorded at E41. The $\delta^{13}C$ isotopic compositions have been contoured

TABLE 6.7 Carbon and oxygen isotopes data and calculated fluid values at specific temperature (see text for explanation).

Drill hole	Depth (m)	Paragenetic stage	Mineral	Mineral values (‰)		Calculated $\delta^{13}C_{(fluid)}$ values (‰)				Calculated $\delta^{18}O_{(fluid)}$ values (‰)			
				$\delta^{13}C_{PDB}$	$\delta^{18}O_{SMOW}$	200°C	250°C	300°C	350°C	200°C	250°C	300°C	350°C
E41D2011	97.7	2	calcite	-5.3	13.0	-	-	-3.2	-2.8	-	-	8.7	8.7
E41D2012	221.7	3A-c	calcite	-4.6	11.7	-	-	-2.6	-2.2	-	-	7.4	7.4
E41D2014	225.5	3A-c	calcite	-4.8	12.1	-	-	-2.8	-2.4	-	-	7.8	7.8
E41D2014	310.2	3B	calcite	-5.2	12.1	-	-	-3.2	-2.7	-	-	7.8	7.8
E41D2013	330.9	3B	calcite	-5.1	11.6	-	-	-3.1	-2.7	-	-	7.4	7.4
E41D2180	103.9	4A	calcite+ankerite	-1.7	13.5	-1.5	-0.4	0.3	0.8	3.9	6.2	9.2	9.2
E41D2180	100.4	4A	calcite+ankerite	-1.3	13.8	-1.1	0.0	0.7	1.2	4.3	6.5	9.5	9.5
E41D2180	109.9	4A	calcite+ankerite	-1.7	14.2	-1.5	-0.4	0.3	0.8	4.7	6.9	9.9	9.9
E41D2012	335.8	4A	calcite	-0.6	11.7	-0.4	0.7	1.4	1.9	2.2	4.4	7.4	7.4
E41D2180	63.8	4A	clacite+ankerite	-4.4	14.1	-4.2	-3.1	-2.4	-1.9	4.5	6.8	9.8	9.8
E41D2129	215.9	4A	calcite	-2.3	11.2	-2.1	-1.0	-0.2	0.2	1.7	3.9	6.9	6.9
E41D2013	114.9	4A	calcite+ankerite	-0.7	30.1	-0.5	0.6	1.3	1.7	20.6	22.9	25.9	25.9
E41D2012	247.5	4A	calcite	-3.7	11.3	-3.5	-2.4	-1.7	-1.2	1.8	4.0	7.0	7.0
E41D2011	195.5	4A	calcite	-0.6	11.6	-0.4	0.7	1.5	1.9	2.1	4.3	7.3	7.3
E41D2007	123.0	4A	calcite	-6.9	20.0	-6.7	-5.6	-4.9	-4.5	10.5	12.7	15.7	15.7
E41D2007	220.2	4A	calcite	-1.5	11.6	-1.3	-0.2	0.5	0.9	2.1	4.4	7.4	7.4
E41D2011	132.0	4A	calcite	-1.8	11.5	-1.6	-0.5	0.2	0.6	2.0	4.2	7.2	7.2
E41D2181	224.9	4C	calcite	-2.1	12.4	-1.9	-0.8	-0.0	0.4	2.9	5.2	8.2	8.2
E41D2181	104.9	4C	calcite	-2.2	13.0	-2.0	-0.9	-0.2	0.3	3.5	5.7	8.7	8.7
E41D2181	159.1	4C	calcite	-3.0	14.2	-2.8	-1.7	-1.0	-0.6	4.7	7.0	10.0	10.0
E41D2181	85.7	4C	calcite	-2.2	11.6	-2.0	-0.9	-0.2	0.2	2.0	4.3	7.3	7.3
E41D2010	247.7	4C	calcite	-1.7	12.1	-1.5	-0.4	0.4	0.8	2.6	4.9	7.9	7.9
E41D2010	197.0	4C	calcite	-1.9	11.4	-1.7	-0.6	0.1	0.5	1.9	4.1	7.1	7.1
E41D2008	151.8	4C	calcite	-2.1	10.9	-1.9	-0.8	-0.1	0.3	1.3	3.6	6.6	6.6
E41D2180	135.8	6	ankerite+calcite	-2.6	13.6	-2.4	-1.3	-	-	4.1	6.3	-	-
E41D2181	171.7	6	ankerite+calcite	-2.5	13.4	-2.3	-1.2	-	-	3.9	6.2	-	-
E41D2129	206.1	6	calcite	-2.1	11.2	-1.9	-0.8	-	-	1.7	3.9	-	-
E41D2010	99.1	6	calcite	-3.2	11.3	-3.0	-1.9	-	-	1.7	4.0	-	-
E41D2014	238.4	6	calcite	-3.8	11.9	-3.6	-2.5	-	-	2.4	4.6	-	-
E41D2012	173.2	6	calcite	-2.6	11.2	-2.4	-1.3	-	-	1.6	3.9	-	-

Fluids calculated using the calcite H_2O equilibrium equation from O'Neil et al. (1969) for $\delta^{18}O$ and calcite-CO_2 from Ohmoto and Rye (1976).

$^{13}C\ \Delta(200°C)=-0.19$; $^{13}C\ \Delta(250°C)=-1.3$; $^{13}C\ \Delta(300°C)=-2.01$; $^{13}C\ \Delta(300°C)=-2.44$

$^{18}O\ \Delta(200°C)=9.53$; $^{18}O\ \Delta(250°C)=7.27$; $^{18}O\ \Delta(300°C)=5.57$; $^{18}O\ \Delta(350°C)=4.27$

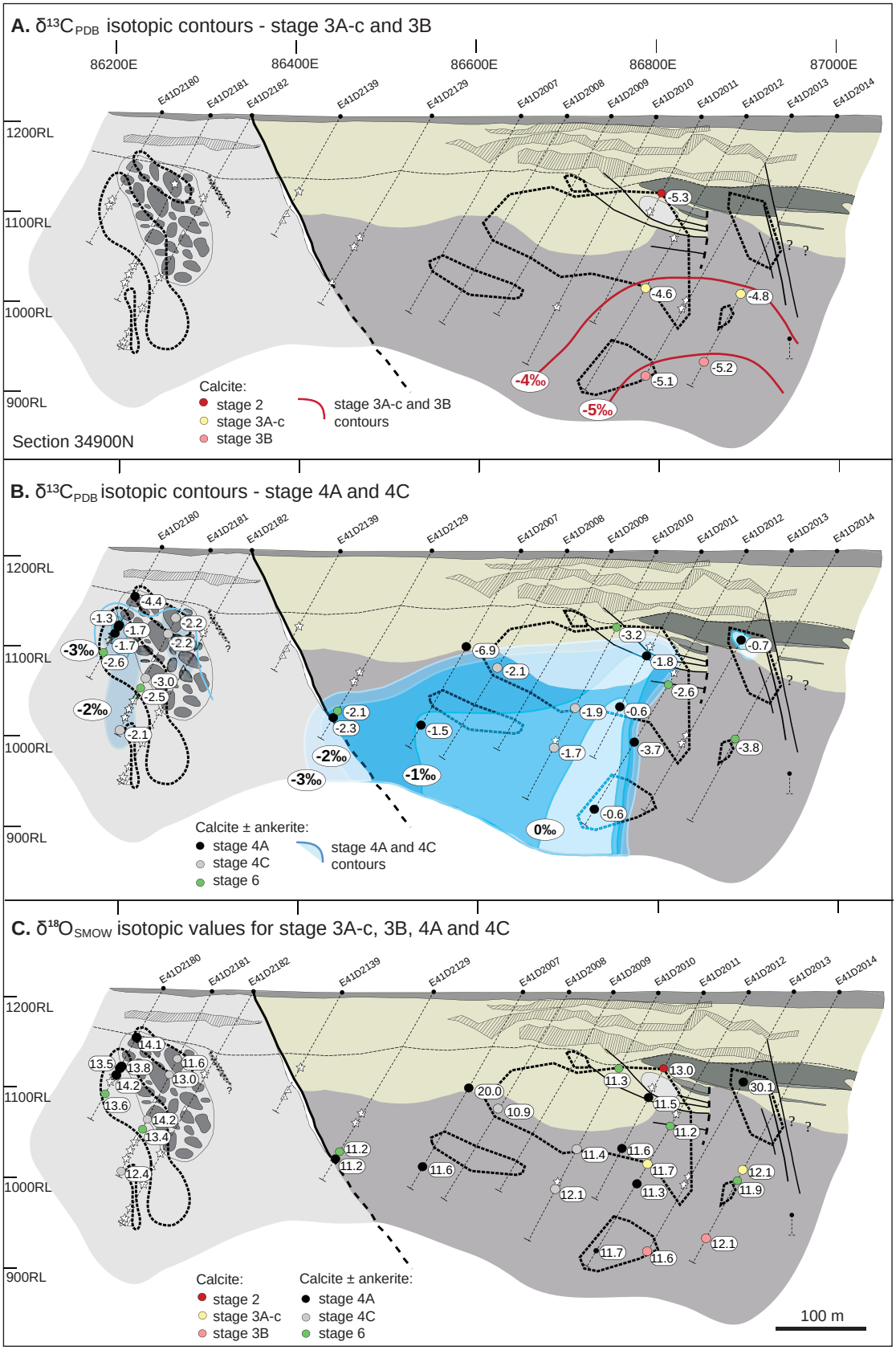

Figure 6.18 Spatial distribution of C-O isotopic compositions of carbonates. **A.** Distribution of $\delta^{13}C_{PDB}$ values for calcite from stage 2, 3A-c and 3B. Stage 3A-c and 3B calcite are represented by red contours. **B.** Contour diagram of $\delta^{13}C_{PDB}$ values of calcite ± ankerite from stage 4A and 4C. In general $\delta^{13}C_{PDB}$ values are lower away from the mineralised domains. Distribution of $\delta^{13}C$ values for stage 6 carbonates is also shown. Post-mineralisation stage 6 calcite values were not used for contouring. **C.** Spatial distribution of $\delta^{18}O_{SMOW}$ values for all analysed carbonates. Geology legend and grade contours same as in Figure 6.13.

for the quartz – pyrite (3A-c and 3B; Fig. 6.18A) and carbonate-base metal sulfide stage (4A and 4C; Fig. 6.18B). The highest $\delta^{13}C$ calcite values obtained from stage 3A-c and 3B characterise the eastern part of the east pod (Fig. 6.18A). This may define domains of magmatic-hydrothermal fluid upflow on the eastern edge of east pod.

The $\delta^{13}C$ isotopic values for stage 4 carbonates decrease away from the gold-mineralised domains at E41 deposit (Fig. 6.18B). Using fluid compositions calculated for 200ºC and 250ºC shifts the $\delta^{13}C$ signature to more ^{13}C-enriched values (Table 6.7). This shift towards heavier carbon isotopic values may indicate that: (a) boiling occurred during stage 4; because boiling is known to drive carbon isotopes towards heavier values (Zheng, 1990); and/or (b) that relatively more oxidised fluids were involved close to the mineralised domains. These domains characterised by $\delta^{13}C$ mineral values near 0‰ are comparable with ^{34}S-depleted zones of stage 4 sulfides (compare Fig. 6.14 and 6.18B), which is consistent with the involvement of oxidised fluids.

The $\delta^{18}O$ isotopic compositions of analysed carbonates are less variable and no obvious spatial relationships between $\delta^{18}O$ isotopic compositions and mineralised zones have been recognised at E41 (Fig. 6.18C). It is possible that the oxygen isotopic compositions of carbonates were more susceptible to resetting by later hydrothermal or ground water activity, as these waters are likely to contain significantly more oxygen than carbon.

Nature and source of fluids

Theoretical curves for the isotopic compositions of calcite precipitated from waters containing aqueous carbon as H_2CO_3 have been plotted on Figures 6.19 A, B and C. These curves were calculated using fractionation equations derived by O'Neil et al. (1967). Fluid inclusion data indicate that stage 3A-c formed at approximately 310º C (Table 6.3). A similar temperature of formation has been assumed for stages 2 and 3B. The curve on Figure 6.19A was modelled for the best fit to the temperatures obtained from fluid inclusion analyses. Stage 3A-c fluids are interpreted to have contained H_2CO_3 as the predominant carbon species because illite – muscovite and calcite occur together in stage 3A-c alteration halos. The $\delta^{18}O_{(fluid)}$ and $\delta^{13}C_{(fluid)}$ values during 3A-c and 3B vein formation are therefore estimated to have been around +6 and -3‰, respectively (Fig. 6.19A). A temperature interval of 200 to 250ºC was assumed for stages 4A and 4C, based on the abundance of illite in the stage 4 alteration halos. Isotopic compositions for stage 4A and 4C fluids (Fig. 6.19B) are estimated to have been +3‰ $\delta^{18}O_{(fluid)}$ and -1‰ $\delta^{13}C_{(fluid).}$ Calculated values for 6 fluid stage are -2 and -5‰ for $\delta^{18}O_{(fluid)}$ and $\delta^{13}C_{(fluid),}$ respectively, based on an assumed temperature of <200 ºC, consistent with the presence of prehnite (Hall et al., 1989; Gebre-Mariam et al., 1995).

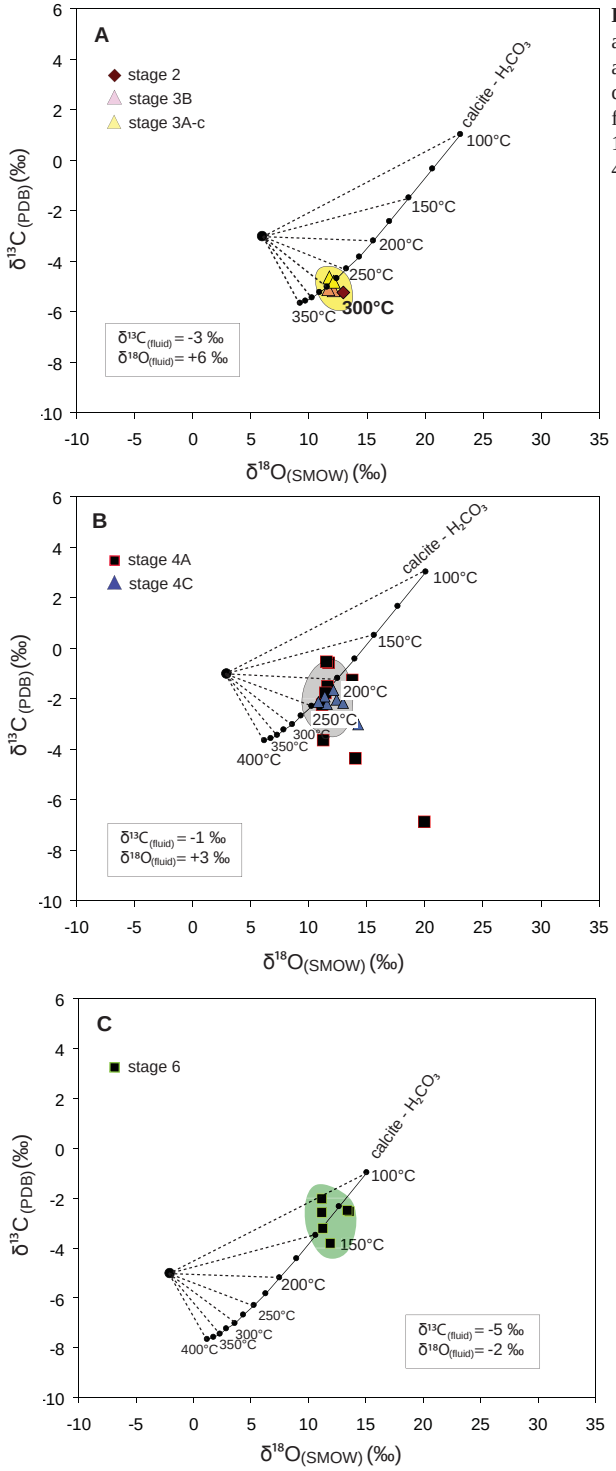

Figure 6.19 $\delta^{13}C$ vs. $\delta^{18}O$ plot for veins with calcite and ankerite. Also shown is calcite -H_2CO_3 fractionation curve calculated using fractionation equations derived by O'Neil et al. (1969). Estimated isotopic fluid compositions are plotted for (A) calcite of stage 1A, 3A-c and 3B, (B) calcite and ankerite from stage 4A and reopened veins and (C) calcite from stage 6.

It is commonly assumed that H_2CO_3 behaves like CO_2 isotopically (Ohmoto, 1986), and that magmatic CO_2 has $\delta^{13}C$ values between -5.5 and -3.0‰ (Taylor, 1987), whereas $\delta^{18}O$ values for magmatic waters range between +6 and +8‰ (Ohmoto, 1986; Fig. 6.20). The estimated $\delta^{13}C_{(fluid)}$ value of -3‰ and $\delta^{18}O$ value of +6‰ for calcite from stages 2, 3A-c and 3B at E41 are consistent with a magmatic origin for CO_2-bearing fluids (Fig. 6.19A) and calculated fluids for each samples are illustrated in Fig. 6.20.

These results are in accord with the magmatic-hydrothermal source inferred for stage 3 sulfides (section 6.4.1).

While $\delta^{18}O$ isotopic values determined for all carbonate samples from E41 are relatively constant, there are obvious shifts in $\delta^{13}C$ isotopic compositions for stages 4A and 4C (Fig. 6.19B). These carbonates are relatively enriched in $\delta^{13}C$ compared with stages 2, 3A-c and 3B (compare Fig. 6.19A and 6.19B), indicating that there may have been a different source of carbon for stages 4A and 4C. The estimated $\delta^{13}C_{(fluid)}$ value of -1‰ rules out a predominance of magmatically-derived CO_2 because such fluids are typically characterised by a range of $\delta^{13}C$ values from -5.5 to -3.0‰ (Taylor, 1987). Based on studies of different natural ^{13}C reservoirs (Kerridge, 1985; Field and Fifarek, 1986; Hoefs, 1987; Schidlowski, 1987), it appears that stage 4A and 4C carbon could have been derived from a sedimentary source. Marine carbonates have a narrow range of values between +2 and -1‰ whilst marine bicarbonate values are between +1 and -2 ‰ (Taylor, 1974; Ohmoto, 1986). The reported $\delta^{18}O$ values for meteoric waters have a wide range, from -40 to +5.7‰ (Rollinson, 1993; Fig. 6.20). The estimated $\delta^{18}O$ value of +3‰ for stage 4A and 4C carbonates (Fig. 6.19B and Fig. 6.20) is consistent with a meteoric source of fluids, possibly modified by interaction with igneous wallrocks. This interpretation is consistent with the conclusions made from the oxygen – deuterium isotope study (section 6.4.2). Limestones do not occur in the vicinity of E41. There are minor carbonaceous volcaniclastic facies, but these do not appear to have been involved in fluid-rock interaction, based on the measured $\delta^{13}C$ values from carbonates (organic C is > -20‰; Rollinson, 1993);

The $\delta^{13}C_{(fluid)}$ value of -5‰ and $\delta^{18}O$ value of -2‰ estimated for stage 6 carbonates are consistent with the involvement of evolved sea water (Rollinson, 1993) during water-rock interaction. Further study of the late stage veins is required to fully unravel the evolution of post-mineralisation fluids at E41.

Three important points can be drawn from the stable isotope analyses of E41 carbonates: (1) magmatic waters appear to have been an important source of carbon and oxygen for stage 2, 3A-c and 3B calcite; (2) the fluids that were responsible for the formation of stage 4A and 4C carbonates were possibly meteoric in origin and/or a mixture of meteoric and magmatic fluids that had re-equilibrated through water/rock interaction; and (3) stage 6 involved a modified seawater source of carbon and oxygen.

Comparison with epithermal calc-alkalic and alkalic epithermal deposits

Figure 6.20 compares the E41 carbonates to selected calc-alkalic and alkalic epithermal deposits. The alkalic epithermal systems are characterised by higher $\delta^{18}O$ values than

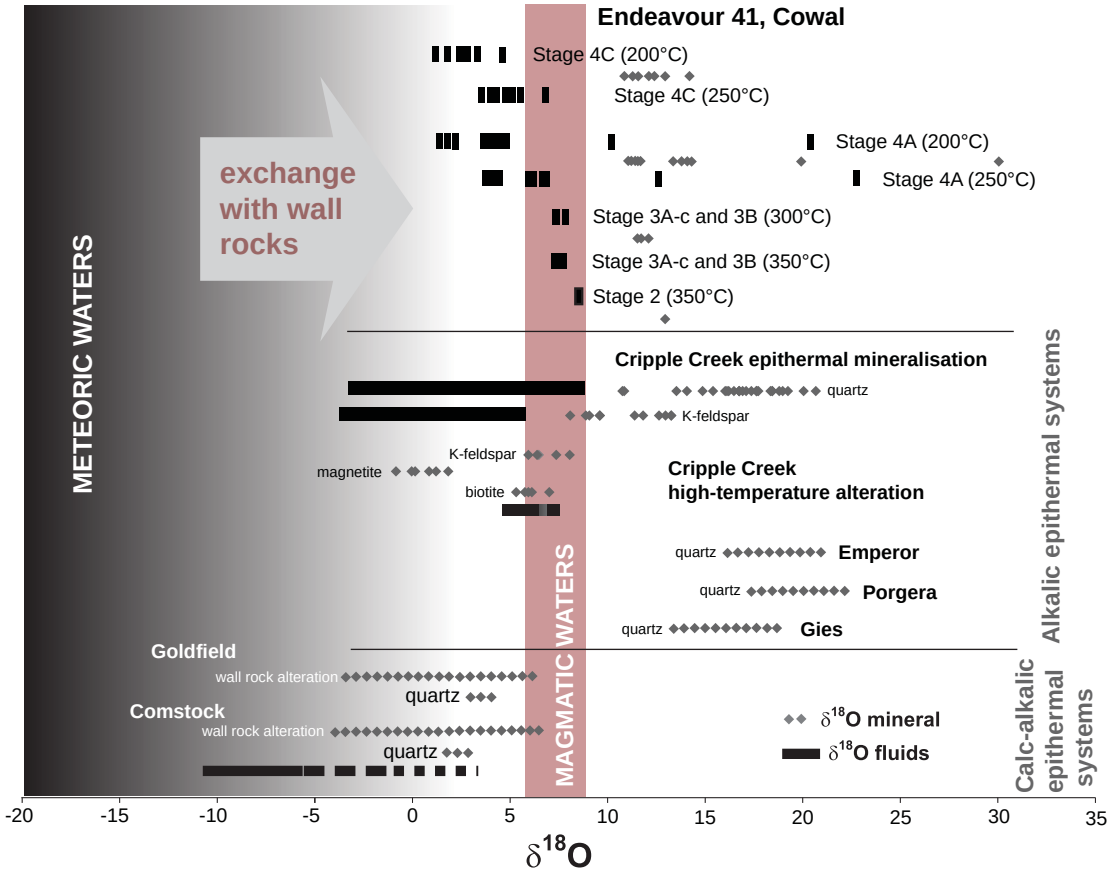

Figure 6.20 Mineral and fluid compositions from E41(data from Table 6.6 and Table 6.7; different symbols discriminate mineral and fluid values) compared with selected calc-alkalic and alkalic epithermal deposits. The isotopic compositions of E41 hydrothermal minerals and calculated fluids compositions are heavy relative to the calc-alkaline deposits. The E41 data are similar to those of Cripple Creek highlighting the greater contribution from magmatically-derived waters. Data for epithermal deposits were sourced from Jensen (2003) and Richards and Kerrich (1993). Magmatic waters values sourced from Ohmoto (1986). Meteoric waters values adapted from Rollinson (1993) .

their calc-alkalic counterparts (Fig. 6.20). Jensen (2003) argued that ^{18}O-enrichment is consistent with alkalic hydrothermal systems being dominated by magmatic fluids while Nesbitt and Muehlenbachs (1995) suggested that deep-convection of meteoric waters may result in ^{18}O-enrichment. In addition, Richards and Kerrich (1993) pointed out that pervasive carbonate and sericite alteration can also enriched minerals in ^{18}O. It appears that the presence of carbonate-dominated alteration and hence neutral pH of fluids in alkalic epithermals may be responsible for this distinctive ^{18}O signature in alkalic epithermal environments. E41 shares this ^{18}O-enriched signature with the alkalic family of epithermal deposits.

6.5 Lead isotopes

6.5.1 Introduction

The Pb radiogenic isotope system can provide important constraints on the timing of mineralisation and alteration, metal and magma sources and mixing processes

TABLE 6.8 Pb isotopic composition of galena (stage 4A and 4C) from E41.

Sample ID	Mineral	$^{207}Pb/^{206}Pb$	±2sd	$^{208}Pb/^{206}Pb$	±2sd	$^{206}Pb/^{204}Pb$	±2sd	$^{207}Pb/^{204}Pb$	±2sd	$^{208}Pb/^{204}Pb$	±2sd
E41D2011, 195.5	Galena	0.856	0.001	2.092	0.002	18.073	0.019	15.475	0.020	37.788	0.050
E41D2013, 114.9	Galena	0.856	0.001	2.092	0.002	18.094	0.017	15.495	0.016	37.824	0.035
E41D2129, 215.9	Galena	0.857	0.001	2.089	0.002	18.050	0.018	15.467	0.017	37.686	0.036
E41D2143, 288.9	Galena	0.858	0.001	2.093	0.002	18.055	0.018	15.491	0.017	37.768	0.037

(Richards and Noble, 1998; Tosdal et al., 1999). In this study, four galena samples from well-mineralised stage 4 veins were analysed for their Pb isotopic compositions in order to determine the timing of mineralisation at E41 and likely metal sources.

6.5.2 Methodology

Pb isotopes in galena crystals were analysed using the LA-ICPMS analytical method developed at CODES (Meffre et al., 2008). To determine the Pb isotopic composition of the galena, a small spot size (8 micron) and a low repetition rate (4 Hz) were used due to the typical high concentration of Pb in galena. Mass bias was determined using a sample of Broken Hill galena (UTAS; sample 154202) and checked with four different secondary standards previously analysed by solution LA-ICPMS using the method of Townsend et al. (1998). After analysis of the background gas composition, long lines and raster patterns (240 s at 1 micron/s) were ablated on the galena crystal while measuring the Pb isotopes, Hg ,U and Th. One primary standard and one secondary standard were analysed before and after analysed galena samples.

6.5.3 Results

Four spot analyses were completed for each galena grain. The dataset in presented in Appendix E.4. The $^{207}Pb/^{204}Pb$ ratios range from 15.49 to 15.47 while $^{206}Pb/^{204}Pb$ in galena grains have values of 18.05 to 18.09. The results are summarised in Table 6.8.

6.5.4 Discussion

Carr et al. (1995) developed a model based for the Pb isotopic evolution of Ordovician to Carboniferous mineralisation in the Lachlan Fold Belt. Mantle and crustal growth curves were constrained for the LFB using Pb isotopic signatures of a diverse range of ore deposits. The Pb systematics of individual ore deposits were explained in terms of mixing between crustal and mantle lead sources (Carr et al., 1995). The LFB's Ordovician epithermal- and porphyry-systems have Pb that is primarily mantle-derived

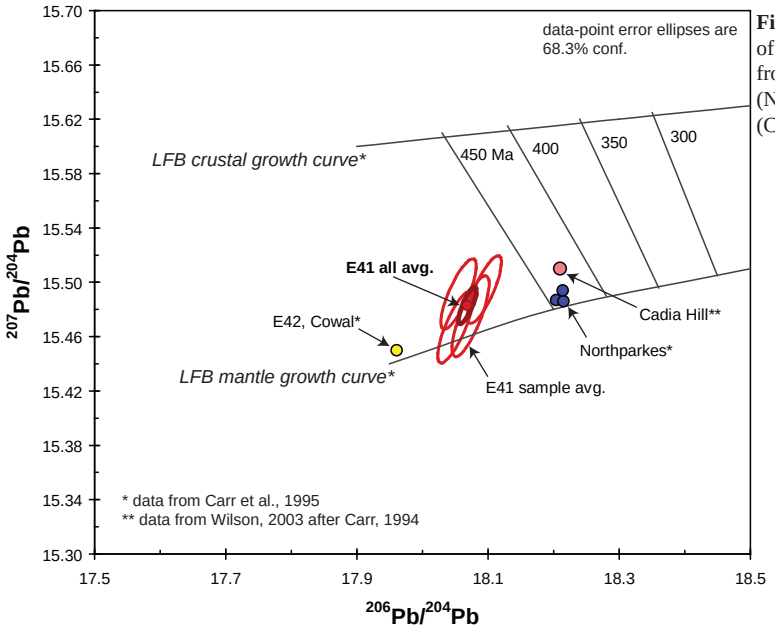

Figure 6.21 Pb isotopic composition of E41 compared with Pb isotope data from E42 (Cowal), E22, E26 and E27 (Northparkes), and Cadia Hill (Cadia).

(Carr et al., 1995), with little or no crustal Pb input. Carr et al. (1995) argued that mixing of enriched lithospheric mantle with a more primitive astenospheric mantle accounts for the wide range of $^{206}Pb/^{204}Pb$ ratios that characterise different styles of porphyry and epithermal mineralisation in the LFB. Carr et al.'s (1995) isochron conforms to independent age determinations of mineralisation constrained by other geochronological methods, particularly those at Northparkes and Cadia (Lickfold, 2002; Wilson, 2003; Wilson et al., 2007b) providing support for Carr et al.'s (1995) model of mixing of crustal and mantle components in the gold-copper mineralised centres of the LFB.

The Pb isotopic values obtained in this study are compared with the existing Pb isotopic data for the CIC and other mineralised centres in the Lachlan Fold Belt generated by Carr et al. (1995). Figure 6.21 plots galena samples from E41 onto Carr et al.'s (1995) growth curves for the LFB. Three samples from Northparkes (Carr et al., 1995), one galena sample from Cadia Hill (Wilson, 2003) and one galena sample from E42 (Carr et al., 1995) have been plotted for comparative purposes. The E41 galena samples all have similar $^{206}Pb/^{204}Pb$ and $^{207}Pb/^{204}Pb$ values (Fig.6.21; Table 6.8) suggesting that the fluids were derived from an isotopically homogeneous source and possibly have similar age. The E41 galena samples are interpreted to contain Pb mostly of mantle derivation (Fig. 6.21). The E42 galena sample analysed by Carr et al. (1995; Fig. 6.21) has a much lower $^{206}Pb/^{204}Pb$ ratio. It plots close to the LFB mantle growth curve (Fig. 6.21).

The uniform Pb isotopic compositions at E41, apart from indicating a homogeneous source, may also be explained by a large enough system such that

any isotopic heterogeneity was homogenised. The former is probably the case for an igneous related system at E41, but may not be the case for E42 where a magmatic connection may not be as evident. Additionally, since most of the rocks at Cowal contain ubiquitous older zircons, the lower $^{206}Pb/^{204}Pb$ compositions for E42 could simply reflect a greater input of older and less evolved Pb sources mixing with new juvenile Pb.

Samples from Northparkes and Cadia are ^{206}Pb-enriched compared to E41. They have isotopic compositions consistent with their formation ages (~440 Ma; Lickfold et al., 2007; Wilson et al., 2007b). In contrast, E41 and E42 plot at much older ages than their estimated age for formation (~455 Ma; Fig. 6.21). These discrepancies for E41 and E42 remain unexplained.

6.6 Summary

Geochemical investigations have provided several constraints on the formation of gold mineralisation at E41:

- Fluid inclusions from actinolite-bearing stage 1 and garnet-bearing stage 2 veins have low (~250ºC) homogenisation temperatures, suggesting either that these fluid inclusions have re-equilibrated, or that significant pressure corrections are required in order to constrain trapping temperature. The salinities of stages 1 and 2 were around 11.0 and 7.0 wt. % NaCl, respectively. Temperatures are likely to have been >350ºC based on mineralogical evidence.
- Stage 3A-c veins trapped vapour- and liquid-rich, moderate salinity (~ 9.0 wt. % NaCl) fluids under boiling conditions at temperatures around 310ºC.
- A paleodepth of ~1 km and hydrostatic pressure of around 100 bars has been estimated for gold mineralisation, based on coexisting liquid- and vapour-rich fluid inclusions in stage 3A-c veins.
- Gold is predominantly hosted by arsenian pyrite, with the highest gold concentrations detected in stage 4A pyrite and 4B arsenopyrite. Visible gold has been observed in stage 4A and 4C veins, but is subordinate to auriferous pyrite.
- Stable isotope analyses provide evidence for a magmatic-hydrothermal component prior to and during gold mineralisation. A ^{34}S-depleted isotopic signature of sulfides has been identified for several paragenetic stages, indicating the involvement SO_4^{2-}-dominated magmatic-hydrothermal fluids.
- Carbon-oxygen isotopes for carbonates from stage 2 and 3 veins are consistent with a predominantly magmatic source of C and O.
- Sulfur isotopic zonation patterns at E41 broadly correlate with domains of high-

gold grades and high-temperature, porphyry-like alteration facies, providing a potential vector to zones of upflow for the mineralising magmatic-hydrothermal fluids.

- Magmatic fluid pathways are also denoted by negative carbon isotopic compositions of stage 3 veins that partially overlap with ^{34}S-depleted domains. This isotopic patterns potentially point towards a magmatic centre located below the current level of epithermal gold mineralisation.
- Cooling and reduction of SO_4^{2-}-dominated fluid by Fe^{2+}-bearing altered-host rocks were important for sulfides deposition, and produced hematite alteration of feldspars in stage 3A-c and 3B.
- Hydrogen and oxygen stable isotopic compositions of fluids in equilibrium with phyllic alteration associated with stage 4 veins indicate an input of meteoric waters that partially re-equilibrated with igneous rocks through water/rock interaction. Carbon-oxygen isotopes of stage 4 carbonates support the involvement of meteoric waters during carbonate-base metal stage. Deep-convection of meteoric waters is suggested by $\delta^{18}O$-enrichment, and implies an emergent landforms at the time of mineralisation.
- Radiogenic Pb isotope compositions indicate a predominantly mantle-derived source of metals during stage 4 mineralisation with minor crustal components, consistent with the alkalic porphyry systems of Macquarie Arc.

Chapter 7
E41 Genetic Model

7.1 Introduction

This chapter provides a genetic model for the E41 gold deposit and discusses potential exploration implications of the research results. The principal objective of this dissertation was to unravel the characteristics and genesis of E41. The focus has been on the intrusive history, alteration assemblages and vein paragenesis. An extensive investigation into geochemistry of hydrothermal minerals further constrained the physicochemical conditions that prevailed prior- and during ore deposition at E41. Figure 7.1 is a series of cartoons that illustrate the magmatic-hydrothermal evolution of the E41 hydrothermal system.

7.2 Deposit model

7.2.1 Volcano – sedimentary succession, magmatism and tectonic setting

The E41 deposit is hosted by the early Middle Ordovician Cowal Volcanic Complex. The volcanic complex was deposited in a submarine oceanic island arc (the Early Ordovician to Early Silurian Macquarie Arc). The E41 volcano-sedimentary sequence is dominated by mudstone with intercalated lenses of polymictic volcaniclastic sandstone and breccia facies interpreted to have been deposited in a subaqueous environment. The mudstones were deposited in a deep water (below wave base) quiescent environment distal to a volcanic source (Fig. 3.21). Proximal volcanic deposits have been identified at E42 and E46 (Simpson and Cooke, 2006).

The host succession at E41 has been intruded by numerous sills, dykes and stocks, which define the E41 intrusive complex**.** Investigation into their whole rock geochemistry provides the following constraints on the origin of the intrusions and the tectonic setting(s) in which they were generated:

- Trace element geochemical features are typical of oxidised magmas produced in a subduction-related tectonic setting (enriched Rb, Sr, Ba, Pb and LREE and depleted Nb and Ti relative to N-MORB).
- The E41 intrusions were emplaced between 461 and ~447 Ma. They evolved from mafic to felsic and then back to mafic compositions. They have medium to high-K calc-alkaline to shoshonitic magmatic affinities ranging from basalt through to trachyte-trachydacite compositions.
- Major and trace element compositions of the diorites and monzonites show a positive variation of K_2O and antithetic variation of $TiO_{2,}$ MgO, CaO and Fe_2O_3

with respect to SiO_2, which is consistent with fractionation of clinopyroxene, followed by later fractionation of amphibole, plagioclase, Fe-Ti oxides and apatite.

- Both mafic and felsic magmatism were temporally and spatially related to main-stage gold mineralisation.
- Pyroxene-phyric dykes cross-cut K-feldspar – epidote alteration and provide evidence for the involvement of shoshonitic mafic melts during gold mineralisation.
- The shoshonitic monzonites and pyroxene-bearing dykes were generated via mid- to deep (40-50 km depth) 'wet' amphibole-bearing crystallisation of parental basalts derived from subduction-modified upper mantle.

Emplacement of alkalic melts into the shallow crustal levels was facilitated by deep-seated structures. North and north-east trending faults are spatially associated with the intrusions at E41, and in the broader Cowal district. There is a time gap at least of 15 m.y between the shoshonitic magmatic pulses throughout the Macquarie Arc (~455 Ma: Cowal epithermal system; and ~440 Ma: Cadia and Northparkes porphyries: Lickfold et al., 2007; Wilson et al., 2007b). There are, however, shoshonitic volcanics at Cadia that were deposited around 455 Ma (Wilson, 2007b; Fig. 3.22), which potentially implies temporal relationships of shoshonitic magmatism in the Cadia and Cowal districts.

It is inferred that deep seated (cross-arc) structures were reactivated during the evolution of the Macquarie Arc for the tapping of shoshonitic, subduction modified melts.

7.2.2 E41: A transitional porphyry-epithermal system

The E41 intrusive complex is associated with extensive zones of hydrothermal alteration that are interpreted to record a long-lived (3 m.y.?) hydrothermal system that evolved with respect to: temperature (>500º – 200ºC), fluid sources (magmatic to meteoric), acidity (near-neutral to moderately acidic), redox conditions (oxidised to reduced), and possibly confining pressures (lithostatic to hydrostatic; deep to shallow). There are close spatial and temporal relationships between intrusive activity and alteration as is typical for porphyry and epithermal deposits world-wide (e.g., Hedenquist et al., 1998; Cooke et al., 2005; Seedorff et al., 2005; Simmons et al., 2005).

This section integrates the intrusive and hydrothermal history of E41, starting with the early high-temperature hydrothermal events and followed by the epithermal stage of ore deposition.

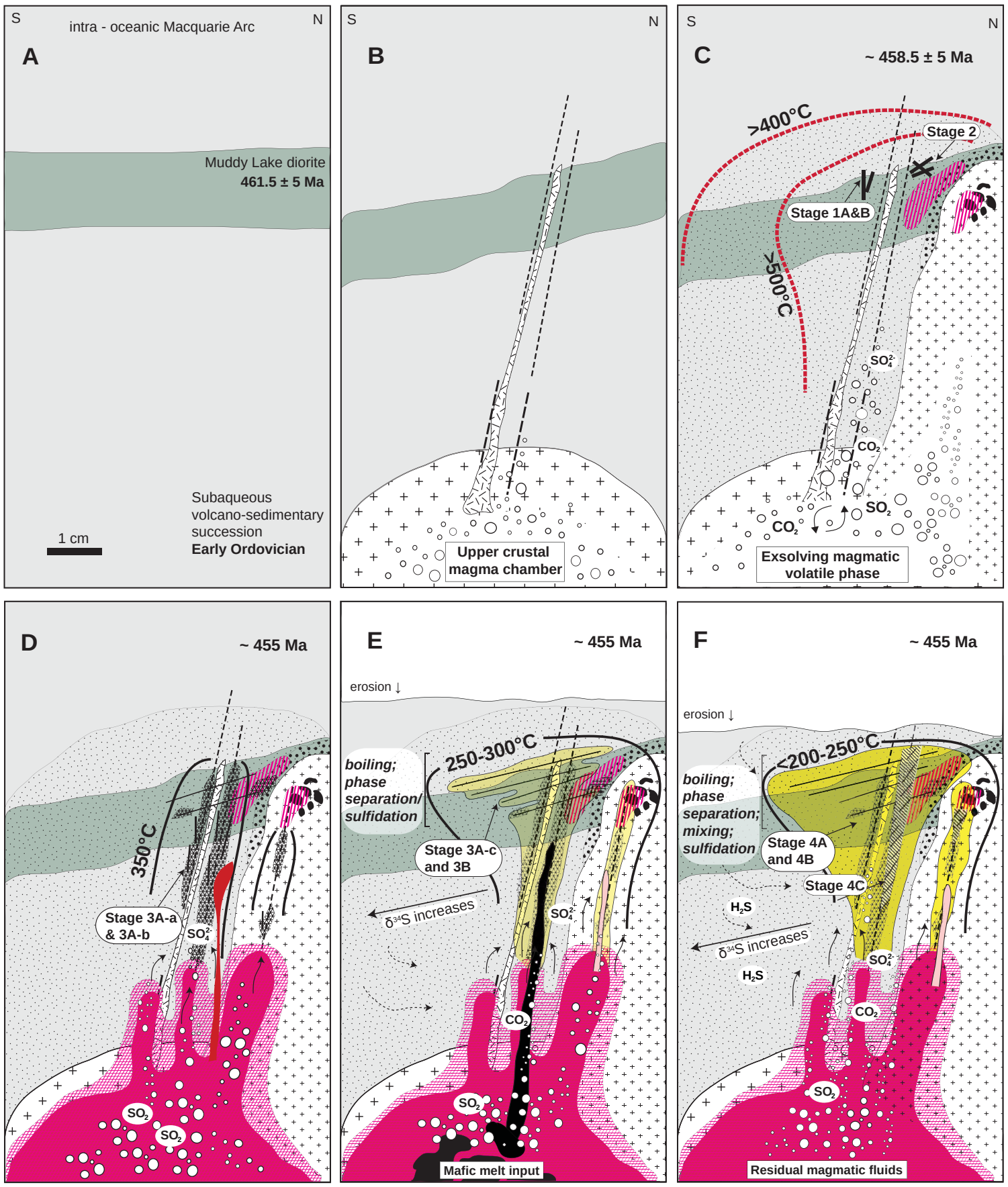

Figure 7.1 Conceptual genetic model for the E41 deposit from pre- to main-stage hydrothermal activity. **A.** Deposition of mudstone and polymictic volcaniclastic sandstone and breccias in a submarine oceanic island arc. Intrusion of the Muddy Lake diorite sill into the volcano-sedimentary succession at 461.5 ± 5 Ma. **B.** The stratigraphy was tilted during the early Late Ordovician, and dismembered by steeply dipping north- and northeast-trending faults. Following deformation, a series of dioritic dykes intruded the faults. **C.** Second boiling occurred within a mid-crustal high-K to shoshonitic magma chamber, producing mafic monzonite. The exsolved volatiles produced a high-temperature actinolite-, biotite- and magnetite-bearing alteration halo around the intrusive complex. Andradite and magnetite-bearing veins formed in the vicinity of steeply dipping structures at approximate depth of 3 km. Hematite alteration occurred within and around the mafic monzonite. Strong K-feldspar alteration was produced at the contact with the mafic monzonite. **D.** Continued intrusive and hydrothermal activity at depth resulted in the emplacement of monzonitic pipe-like intrusive bodies on the shoulders of the mafic monzonite. Quartz-monzonite dykelets are interpreted to have been derived from deeper-seated monzonitic bodies reflecting fractionation of the magma chamber. Weakly mineralised stage 3A-a and 3A-b quartz – pyrite veins formed along north- and northeast-trending steeply dipping fractures. A transitional propylitic-potassic alteration assemblage (epidote and K-feldspar – epidote) assemblage formed at this time. **E.** Emplacement of shoshonitic pyroxene-phyric dykes that cross cut the transitional propylitic-potassic alteration zones. The mafic melts are inferred to have fertilized fractionating felsic magma chamber through magma mixing and volatile input, causing exsolution of metal-rich fluids. The fluids were most likely rich in CO_2 and other alkali carbonate species that suppressed H^+ ions, preventing the production of widespread acidic-alteration. Stage 3A-c and 3B gold was deposited in response to boiling of moderately saline relatively oxidised fluids that produced weak illite – muscovite – carbonate alteration. The lower-temperature hydrothermal alteration assemblage is consistent with a shallower depth of formation (~1 km) than stages 3A-a and 3A-b, indicating progressive uplift and erosion of the surficial landforms. Some gold could have been precipitated by reduction of sulfate species by Fe^{2+} -bearing minerals in altered wall rocks. **F.** At this stage of hydrothermal evolution, the overlying landform was probably well emerged and eroded based on the evidence for meteoric water, but the system was still charged by fluids from the degassing alkalic magma chamber. Boiling is inferred to be a process for stage 4A gold precipitation. Mixing of meteoric with oxidised magmatic waters was also potentially important as an ore-forming mechanism. Sulfidation and reduction of ferric iron could also have assisted gold precipitation, particularly around faults. Gold was precipitated as auriferous pyrite, as gold inclusions in pyrite and sphalerite, and as gold tellurides. Intensely developed illite-dominated alteration haloes are associated with stage 4 veins. Stage 4A was cut by stage 4B gold-bearing arsenopyrite veins that recorded a shift to more reducing conditions, implying ingress of reduced fluids into the system. Stage 4C brecciated veins formed preferentially along steeply-dipping structures. It is interpreted that they reactivated some of the fractures pre-occupied by stage 3A-a and 3A-c. Brecciated 4C stage veins contains the highest gold grades. Late to post mineralisation events are not shown on this model. These include gypsum-, calcite-, epidote-, prehnite-, hematite-, and ankerite-bearing veins and dioritic dykes.

7.2.2.1 Early magmatic-hydrothermal activity (porphyry stage)

The earliest intrusive activity at E41 is marked by the emplacement of the Muddy Lake diorite (461 ± 5.2 Ma) into the volcano-sedimentary succession (Fig. 7.1A). After sill emplacement, the stratigraphy was tilted, probably during the early Late Ordovician. A series of dioritic dykes intruded steep-dipping structures that cut the tilted stratigraphy (Fig. 7.1B). A mafic monzonite intrusion, emplacement after tilting at 458.5 ± 5.2 Ma, provides the upper age constraint on deformation. The mafic monzonite is inferred to have initiated the E41 magmatic-hydrothermal system (Fig. 7.1C).

The earliest fluids that caused hydrothermal alteration at E41 were magmatic-hydrothermal. They produced potassic alteration (magnetite ± biotite facies) in clastic facies and high temperature propylitic alteration (actinolite – magnetite facies) in diorite (Fig. 7.1C). Minor disseminated chalcopyrite (pseudomorphing pyroxene and amphiboles) is associated with actinolite alteration. The development of the K-feldspar – albite ± hematite alteration halo ('patchy texture') was coeval with the mafic monzonite intrusion (Fig. 7.1C). The mineralogy and geochemical characteristics of the early alteration assemblages indicates that the fluids were relatively oxidised (hematite-stable), hot (~ >500º - 400ºC) (biotite- and actinolite-stable) and had near neutral to alkaline pH (feldspar-calcite stable). Weakly mineralised magnetite-bearing veins (stages 1A and 2; east pod), and actinolite- and orthoclase-bearing vein dykes (west pod) formed during this early phase of magmatic-hydrothermal activity. Negative sulfur isotopic compositions of chalcopyrite from stage 1B are consistent with an oxidised magmatic fluid source. Stage 2 garnet veins probably formed synchronous with early potassic and propylitic alteration from moderately saline fluids (7.5 eq. wt. % NaCl). The presence of andradite at E41 reflects oxidised fluids during the early stages of magmatic-hydrothermal evolution and/or implies low H_2S activity. Andradite also implies temperatures above 500ºC. Carbon-oxygen isotopic compositions of calcite are consistent with a predominantly magmatic source of these components during stage 2.

Burnham (1979; 1997) proposed a detailed model of the magmatic-hydrothermal evolution for porphyry environments. He argued that crystallisation of magma leads to accumulation of dissolved water and other volatile phases in the residual melt. Saturation of dissolved water leading to exsolution of a magmatic volatile phase can occur by increasing the water content of an undersaturated magma through progressive crystallisation (second boiling) and accumulation of volatiles in the residual melt. The volatiles build up near the top of the magma chamber during convective circulation and may increase the pressure within the magma chamber to exceed the combined lithostatic load and tensile strength of the overlying rocks (Burnham, 1979; Shinohara

and Hedenquist, 1997). This can cause catastrophic release of the accumulated volatiles or the intrusion into shallow crustal levels and may be associated with long period of degassing without a major explosive event (Burnham, 1985). Either the explosive activity or prolonged degassing can lead to the development of high-temperature alteration facies and associated Cu-Au porphyry mineralisation.

By analogy with this porphyry model, the E41 mafic monzonite is inferred to have been derived from a shallow crustal level magma chamber that may have experienced second boiling. Volatile built up in the underlying magma chamber, leading to the release of a batch of monzonitic magma accompanied by volatiles. The volatiles migrated into the surrounding country rocks and produced the high-temperature alteration assemblages and early veins around the mafic monzonite and the magma chamber at depth (Fig.7.1C). The presence of miarolitic cavities within the mafic monzonite intrusion provide evidence that this intrusion was volatile-rich, and provides a link between magmatic and hydrothermal activity.

Continued magmatic and hydrothermal activity resulted in the intrusion of monzonitic pipes on the shoulders of the mafic monzonite (Fig. 7.1D). Thin quartz-monzonite dykelets are interpreted to have been derived from monzonitic bodies at depth. Monzonitic and feldspar-phyric clasts in post-mineralisation hydrothermal breccia provide another line of evidence for the monzonitic intrusive bodies below the current level of exposure.

At this stage of hydrothermal activity, weakly mineralised stage 3A-a and 3A-b quartz – pyrite veins were formed along steeply dipping, north- and northeast-trending fractures. These veins are associated with transitional propylitic-potassic alteration (epidote, and K-feldspar – epidote). The presence of these minerals indicates that the mineralising fluid was oxidised, based on the negative sulfur isotopic signature combined with the presence of hematite, apatite and epidote. Although the lower temperature limit for epidote stability is inferred to be around 300ºC (Reyes, 1990), its association with K-feldspar may indicate higher temperature (~350ºC) for stage 3A-a and 3A-b veins formation. It may be that this transitional propylitic-potassic alteration facies grades downward to potassic alteration domains (Fig. 7.1D).

7.2.2.2 Main stage magmatic-hydrothermal activity (epithermal stage)

Main stage magmatic-hydrothermal events are associated with the formation of two gold-bearing vein stages. The key hydrothermal and magmatic events during this stage are:

- Intrusion of shoshonitic pyroxene-phyric dykes that have crosscut pre-existing transitional propylitic-potassic alteration (epidote and K-feldspar – epidote).

- Development of quartz – auriferous pyrite ± calcite ± adularia veins (stages 3A-c and 3B) on inclined, east-trending fractures that have cut steep 3A-a and 3A-b-bearing structures.
- Formation of stage 3A-c and 3B veins in association with discrete illite – muscovite – K-feldspar ± pyrite ± carbonate alteration halos.
- Intrusion of volumetrically minor aplite dykelets that have locally crosscut the 3A-c veins (west pod).
- Precipitation of high grade carbonate-base metal sulphide veins (stage 4). This vein stage consists of: calcite, ankerite, quartz, pyrite, sphalerite, galena, chalcopyrite, Ag-tellurides, tetrahedrite, hematite, apatite, illite ± muscovite and chlorite. Stage 4 has cut pre-existing stage 3 veins and associated alteration facies. It commonly constitutes a secondary infill in stage 3A-a, 3A-b, 3A-c and 3B veins. Gold was deposited as inclusions in pyrite and sphalerite, and in solid solution in auriferous pyrite.
- Formation of carbonate – illite – muscovite – chlorite ± pyrite ± sphalerite ± gold alteration halos around stage 4 veins.
- Deposition of ankerite and arsenopyrite-bearing stage 4B veins.
- Formation of strongly mineralised breccia veins due to reactivation of stage 3 structures.

7.2.2.3 Late and post-mineralisation magmatic-hydrothermal activity at E41

Late magmatic and hydrothermal activity produced minor dykes, and abundant barren carbonate veining together with other minor hydrothermal features. The most distinctive events are:

- The emplacement of a syenite dykelet and hornblende-phyric quartz rich dykes.
- Intrusion of plagioclase-phyric dyke, hornblende-phyric dyke and amygdaloidal dyke. These dykes recorded the cessation of magmatic activity in the Cowal district (456 – 445 Ma).
- Formation of polymictic matrix-supported hydrothermal breccia associated with strong illite – muscovite and ankerite alteration facies (west pod and one location between east and west pod).
- Precipitation of moderate albite – epidote and hematite – carbonate alteration associated with the intrusions of hornblende-phyric dykes and a amygdaloidal dyke.
- Formation of post mineralisation veins: gypsum veins and hematite – calcite ± specularite (stage 5); ubiquitous, chaotic epidote – calcite – prehnite veins

with hematite alteration halos (stage 6), and carbonate veins (stage 7).

- Development of fault-bounded phyllic alteration.

This late alteration and veining is interpreted to be related to post-mineralisation deformation. The C-O isotopic constraints from stage 6 calcite indicate the involvement of evolved seawater during precipitation. The presence of prehnite indicates that fluids had low temperatures (<200ºC). The presence of hematite and specularite in some of the late veins suggests oxidised fluid involvement. Resetting of the Ar-Ar geochronometers in stage 3 adularia occurred during the Kanimblan Orogeny (ca. 380 – 320 Ma), indicating that E41 was subjected to deformation and low temperature metamorphism at that time. Subsequent to Kanimblan Orogeny, the sequence was eroded and the Siluro-Devonian sedimentary and volcanic rocks of the Derriwong Group were deposited across the district.

7.3 Chemistry of ore forming solutions and gold deposition (epithermal stage)

Quartz – pyrite veins (Stage 3A-c and 3B)

Early hydrothermal features at E41 (stages 1 to 3A-b) are reminiscent of porphyry-style veining, whereas stage 3A-c quartz-pyrite veins marked a change in the nature of the hydrothermal system. The illite – muscovite – K-feldspar ± pyrite ± carbonate ± chlorite stable alteration assemblage associated with stage 3A-c veins was produced by lower-temperature (~310ºC), weakly acidic to neutral pH aqueous fluids with moderate salinities (average: 9.5 eq. wt. % NaCl). Isotopic compositions of pyrite from stage 3A-c and 3B are typically ^{34}S-depleted, implying the involvement of moderately oxidised fluids, near the H_2S-SO_4^{2-} buffer**.** Hematite alteration halos around stage 3B veins are evidence for oxidising conditions. Carbon-oxygen isotopic compositions of calcite (stage 3A-c and 3B) are consistent with a predominantly magmatic source of fluids.

Coexistence of vapour- and liquid-rich fluid inclusions in quartz growth zones provide evidence for boiling (Roedder, 1984; Bodnar et al., 1985a), which is inferred to be the principal mechanism of gold precipitation during stages 3A-c and 3B. Boiling of near neutral to alkaline pH solutions is also consistent with the presence of adularia in stage 3B veins (Simmons and Christenson, 1994; Simmons and Browne, 2000).

Boiling is considered to be the most important mechanism for ore precipitation in epithermal environments (e.g., Henley, 1985; Drummond and Ohmoto, 1985; Cooke and Simmons, 2000; Simmons, 2005), and it can chemically affect the aqueous fluids in several ways. For example, phase separation typically results in the loss of volatiles CO_2, HCl, SO_2, H_2S and H_2, causing an increase in pH and stabilising carbonate and

K-feldspar. Drummond and Ohmoto (1985) noted also that greater volatility of reduced gas species compared to oxidised gas species tends to cause an increase in the f_{O2} of the residual liquid. Thus, either pH increase or f_{O2} increase associated with boiling can cause a rapid drop in gold solubility, and subsequent gold deposition (e.g., Hedenquist and Henley, 1985).

It is inferred that at E41, boiling of the $Au(HS)_2^-$ - bearing fluids resulted in loss of H_2S to the vapour phase, destabilising $Au(HS)_2^-$ and resulting in gold deposition:

$$2Au(HS)^-_{2\,(aq)} + 2H^+_{(aq)} + H_2O = 2Au_{(s)} + 4H_2S_{(g)} + ½\ O_{2\,(aq)}$$

The illite – muscovite alteration that accompanied gold deposition during stage 3A-c and 3B formed halos of restricted extent (typically < 5 cm wide), in contrast to many low-sulfidation epithermal systems (e.g., White and Hedenquist, 1990; Simmons et al., 2005). This may reflect the high acid-buffering potential of the previously K-feldspar and carbonate-altered host rocks. Alternatively, high solubilities of potassium sulfate species and/or alkali carbonate ions in the mineralising fluids may have acted to suppress the activities of H^+ in solution (Jensen, 2003), limiting the opportunity for development of the moderately acidic conditions required to precipitate illite or muscovite.

Carbonate-base metal sulfide stage (Stage 4)

Gold, gold-silver tellurides and base metal sulfides were deposited during stage 4A, together with quartz, calcite and ankerite. Illite-bearing alteration halos associated with stage 4 veins are wider (up to 2 m) than those associated with stages 3A-c and 3B. Stage 4 sulfides are mostly characterised by negative $\delta^{34}S$ values, consistent with the involvement of oxidised magmatic fluids. Some stage 4A veins contain apatite, hematite and V-bearing illite, providing additional evidence for oxidising conditions. Minor occurrences of tellurides are intimately associated with high gold grades. The presence of tellurides may indicate a magmatic gas input (e.g., Cooke and McPhail, 2001). In contrast with previous vein stages, stage 4B veins were probably deposited from reduced fluids, based on the positive $\delta^{34}S$ values obtained from arsenopyrite.

Stage 4C formed preferentially along northeast-trending fractures that already contained stage 3A-a and 3A-b quartz - pyrite veins. Stage 4C may have been associated with vigorously boiling fluids, due to the presence of abundant hydrothermal breccia textures. Brecciation can cause sudden pressure and volume changes, which can be explained by phase separation in epithermal environments (e.g., Hedenquist and Henley, 1985). Precipitation of highly mineralised stage 4C carbonate-base metal

sulfide breccia cement is inferred to have occurred at temperatures of 200º to 250ºC based on the association with broad illite – muscovite – carbonate – chlorite alteration halos. As for stage 3A-c and 3B, gold during stage 4A was probably transported as $Au(HS)_2^-$ in near neutral to alkaline waters.

The D-O isotopic compositions of illite – muscovite associated with stage 4 indicate the involvement of meteoric waters, which implies emergent landforms at the time of stage 4 gold mineralisation. The contribution of external waters and the magmatic sulfur signature indicates that fluid mixing could have played a role during stage 4 mineralisation. The C-O isotopic compositions of stage 4 carbonates support this interpretation.

Sulfidation of wall rocks

The ^{34}S-depleted stage 3 pyrite and stage 4 sphalerite and pyrite that locally occur in alteration halos around mineralised fractures suggest that sulfides deposition could have been achieved through the reduction of oxidised sulfur species against Fe^{2+}-bearing minerals (i.e., chlorite, actinolite, magnetite, pyroxene) in the wall rock through the reactions:

$$ZnCl_{2(aq)} + H_2S \leftrightarrow ZnS + 2Cl^- + 2H^+$$

$$8\,[FeO]_{mineral} + SO_4^{2-}{}_{(aq)} + 2H^+_{(aq)} \leftrightarrow 4\,Fe_2O_3 + H_2S_{(aq)}$$

$$FeCl_2^- + 2\,H_2S + \tfrac{3}{4}\,O_2 \leftrightarrow FeS_2 + 2Cl^- + H^+ + \tfrac{3}{2}\,H_2O$$

Inorganic reduction of oxidized sulfur species can result in the precipitation of ^{34}S-depleted sulfides (Wilson et al., 2007a). Oxidising fluid conditions are consistent with the development of ferric (Fe^{3+}) iron-bearing minerals in the alteration halos associated with mineralised veins. This includes: epidote association with stage 3A-a, epidote and hematite related to 3A-b, hematite dusting of K-feldspar halos associated with some stage 3B veins, and local dissemination of hematite in highly mineralised stage 4A veins.

7.4 An alkalic porphyry-epithermal connection at E41?

Geological relationships combined with fluid inclusion and stable isotope studies have provided evidence for a close temporal relationship between porphyry-style alteration and epithermal gold mineralisation in alkalic epithermal systems (Ahmad et al., 1985; Richards, 1992; Richards and Kerrich, 1993; Richards, 1995; Begg, 1996; Carman,

1994; Jensen and Barton, 2000; Jensen, 2003; Carman, 2003; Simmons et al., 2005). At each of these deposits (Lihir, Emperor, Porgera and Cripple Creek), the magmatic-hydrothermal signature of the alkalic systems strongly reflects the nature of associated magmatism.

Alkalic magmas are typically mantle-derived, hydrous, and characterised by high oxidation states (e.g., high SO_2) and volatile contents (e.g., Sack et al., 1980; Richards, 1995; Jensen and Barton, 2000). The key feature of these magmas is the ability to retain chalcophile elements in the melt until or after the onset of volatile saturation. The oxidised nature of alkalic magmas has a significant influence on any associated magmatic-hydrothermal system.

Richards (1995) argued that the processes of magmatic-hydrothermal evolution including metal partitioning in alkalic epithermal system operate similarly as in typical porphyry type deposits, with Au segregating into a chloride-rich volatile phase, along with copper and other base metals. Gold behaves in an analogous manner to Cu (Candela, 1989). Copper deposition may occur after exsolution from a fractionating magma chamber. Gold may be precipitated during the early stages of hydrothermal activity (e.g., Emperor: Begg, 1996; Lihir: Carman, 2003) or may stay in solution and precipitate at some distance from the porphyry-style centre of hydrothermal activity. Richards (1995) speculated that whether the gold stays in solution or precipitate during the high-temperature stage may be dependent on the oxidation state and the H_2S content of the hydrothermal fluids. With decreasing temperature, magmatic SO_2 disproportionates (Rye et al., 1993), causing the activity of sulfide to increase, some Cu-bearing sulfides and base metals may precipitate at this stage. Gold may remain in solution by conversion from chloride to bisulfide complex (Hayashi and Ohmoto, 1991). Fluid evolution may then cause changes in pH, pressure, temperature and/or oxidation state, allowing gold to precipitate in distal portion of the magmatic-hydrothermal system. This means that there is potential for two stages of Au deposition in alkalic epithermal systems.

A two-stage model for alkalic-style mineralisation could explain elevated gold concentrations associated with late veins and faults in alkalic porphyry systems. At Mt. Milligan (Jago, 2008) and Ridgeway (Wilson, 2003), in addition to the Cu-Au ore zone proximal to the causative intrusions, gold has been precipitated in distal locations in association with phyllic-altered fault zones. These distal mineralising fluids had high salinities and deposited sulfides with ^{34}S-depleted signatures, together with tellurides (Wilson, 2003; Jago, 2008). It is concluded that the illite-bearing (phyllic) alteration associated with faults in alkalic porphyry systems are analogous to the gold-mineralised epithermal veins at E41 and other mineralised centres in the Cowal district,

and that these veins are transitional porphyry-epithermal features. Coupled with the recognition of transitional propylitic-potassic alteration facies, the steep structures that host gold-mineralised veins at E41 are therefore concluded to be feeders derived from a porphyry-style magmatic-hydrothermal system located below the current level of diamond drilling.

7.5 Exploration implications

The geologic and genetic model developed in this study highlights several points that should be considered when exploring for similar style of gold mineralisation:

- Together with the structurally-localized illite – muscovite alteration, and porphyry-style zoned hydrothermal alteration facies, the metal associations (Au-Ag-Zn-Pb-Te) indicate that the E41 and E42 deposits are likely to have formed in an epithermal environment, and are not an orogenic style of mineralization. This should be considered when planning future exploration activities in the Cowal district.
- E41 is the first documented occurrence of low-sulfidation alkalic epithermal mineralisation in the Macquarie Arc. There is potential for further discoveries of this style of deposit throughout the LFB, and possibly in other deeply eroded alkalic provinces such as British Columbia.
- The porphyry-style mineralisation at E43 (463.5 Ma) and gold mineralisation at E41 (~455 Ma) were related to Phase 2 magmatism in the Macquarie Arc, and as such are currently unique. It may be that other ore deposits formed during Phase 2 magmatism elsewhere.
- The syn-mineralisation intrusions of the CIC are characterised by high absolute REE concentrations with LREE enrichments, which discriminates them from the weakly or non-mineralised intrusions. This may be an indicator of magma fertility that could be applied in exploration.
- Gold mineralisation at E41 appears to be temporally related to the most fractionated intrusive rocks in the district which are coeval with pyroxene-phyric dykes, implying an interplay of mafic and felsic magmas during mineralisation. Evidence for coeval felsic and mafic magmatism is considered favorable sign for mineralisation.
- Northeast- and east-trending structures at the deposit and district scale, should be explored thoroughly as these appear to be the favorable hosts to mineralisation. In particular northeast-trending, structural fabrics appear to be important conduits for mineralising fluids.
- High-temperature actinolite – magnetite and magnetite – biotite alteration facies

as well as magnetite and garnet-bearing veins are indicative of a magmatic centre located in the vicinity of E41. The porphyry Cu-(Au?) potential of this magmatic centre needs to be tested through deep drilling.

- The garnet-bearing veins, although not related to mineralisation, were found proximal to the mineralised domains and this type of veining may be significant from an exploration perspective in terms of decreasing the target footprint.
- K-feldspar – epidote alteration (the transitional propylitic-potassic assemblage) and hematite reddening may be providing a vector towards a porphyry mineralisation centre, thus are inferred to have formed proximal to the mineralising fluid pathways and may be providing a vector towards a porphyry mineralisation centre, thus required deep-drill testing.
- The low-temperature alteration assemblages (phyllic alteration) in alkalic systems are relatively weakly developed, however, targeting faults, lithological contacts and dykes margins may increase the chance of discovery of mineralised fractures.
- Negative sulfur isotopic compositions are spatially related to mineralised domains. It appears that S isotopes can be used as a vector toward fluid pathways associated with mineralisation.
- There is a weak correlation between near 0‰ values of $\delta^{13}C$ and gold zones which could potentially be used as a vector toward mineralised domains.
- Zn, Te, As, Cu, Ag, Pb, Bi, P show strong to moderate positive correlation with gold and these elements can be used as an exploration tool for localizing mineralised areas.

7.6 Recommendations for further research

This study provides a starting point for future studies into the genesis of the Cowal district and of alkalic epithermal mineralisation in the Macquarie Arc. Recommendations for future research include:

- Geochronological analyses of pyroxene-phyric dykes should be undertaken in order to establish the timing of these shoshonitic intrusions and hence the timing of gold mineralisation.
- A district-scale geologic long section through E46, E42 and E41 should be constructed to help better understand the volcanic facies architecture, the intrusive history and spatial and temporal relationships between the three gold-mineralised centres.
- Mapping hydrothermal alteration facies on the long section (above) may identify high temperature alteration domains and potentially could help in the

discovery of porphyry mineralisation within the district.

- A systematic sampling and analyses of sulfur isotopic compositions throughout the district would supplement alteration facies and help with tracing magmatic fluid pathways.
- Additional analyses of ^{13}C isotopic compositions of carbonates should be considered in an attempt to determine whether there is a $\delta^{13}C$ zonation pattern recorded at E41, as this pilot studies indicate that $\delta^{13}C$ near 0‰ occur close to the mineralised domains and may be a vector to ore.
- Fluid inclusion studies of sphalerite from stage 4 (carbonate-base metal sulfide stage) could be used to determine homogenisation temperature and salinities.
- The geochemistry of pervasive epidote and epidote from propylitic-potassic alteration assemblage (K-feldspar – epidote alteration facies) may reflect compositional variations that could be used as a vector towards mineralised domains.
- The geochemistry of apatite associated with transitional propylitic-potassic alteration and REE-bearing apatite from highly mineralised epithermal veins could provide geochemical constraints on fluid variations in transitional-porphyry to epithermal environments, and would test whether apatite can be used as a vector towards alkalic epithermal deposits.
- Detailed structural analysis of vein arrays, dykes and faults at E41 to better understand structural controls on mineralization.

References

Ahmad, M., Solomon, M., and Walshe, J. L., 1987, Mineralogical and geochemical studies of the Emperor gold telluride deposit, Fiji: Economic Geology, v. 82, p. 345-370.

Allen, S. R., Hayward, B. W., and Mathews, E., 2007, A facies model for a submarine volcaniclastic apron: The Miocene Manukau Subgroup, New Zealand: GSA Bulletin, v. 119, p. 725 - 742.

Allen, S.R., 2004, The Parnell Grit beds revisited: are they all the products of sector collapse of western subaerial volcanoes of the Northland Volcanic Arc?: Bulletin of Volcanology, v. 67, p. 27-41.

Anderson, H., 2003, The geology of the dykes associated with the E42 deposit: Unpub. internal report, Barrick Gold of Australia Ltd.

Anderson, W.B., and Eaton, P.C., 1990, Gold mineralisation at the Emperor mine, Vatukoula, Fiji: Journal of Geochemical Exploration, v. 36, p. 267-296.

Ashley, P.M., 2003a, Petrographic report on twenty-six samples of drill core from the Cowal Gold Project, Central Western, New South Wales: Unpub. internal report, Barrick Gold of Australia Ltd., May, p. 105.

Ashley, P.M., 2003b, Petrographic report on thirty-two samples of drill core from the Cowal Gold Project, Central Western, New South Wales: Unpub. internal report, Barrick Gold of Australia Ltd., October, p. 122.

Ashley, P.M., 2004, Petrographic report on thirty samples of drill core from the E41 deposit and two surface samples, Lake Cowal Area, Central-Western, New South Wales: Unpub. internal report, Barrick Gold of Australia Ltd., p. 96.

Ashley, P.M., 2005, Petrographic report on twenty five samples of drill core from the E41 deposit, Cowal Gold Project, Central-Western, New South Wales: Unpub. internal report, Barrick Gold of Australia Ltd., p. 172.

Ayllon, F., Bakker, R.J., and Warr, L.N., 2003, Re-equilibration of fluid inclusions in diagenetic-anchizonal rocks of the Cinera-Matallana coal basin (NW Spain): Geofluids, v. 3, p. 49-68.

Baker, T., and Thompson, J.F.H., 1998, Fluid evolution at the Red Chris porphyry Cu-Au deposit, Northwest British Columbia: Geol. Soc Am, Abstracts with Programs 30: 367, p. 79-85.

Barrick Gold of Australia Ltd., 2007, Fourth quarter and year end report 2007: Barrick Gold Corporation Press Release February 21, 2008, p. 106.

Barron, L.M., 1999, Metamorphism, Dubbo 1:250 000 Geological Sheet SI/55-4, 2nd edition, Explanatory notes, Geological Survey of New South Wales, Sydney.

Bastrakov, E., 2000, Gold Metallogenesis at the Lake Cowal Prospect, NSW: Unpub. PhD thesis, Australian National University, Canberra, p. 114.

Bastrakov, E., Brooker, M., and Walshe, J.L., 1996, The origin of gold mineralisation at Lake Cowal, Endeavour 42 (NSW): Geological Society of Australia No. 41, p. 23.

Bates, R.L., and Jackson, J.A., 1980, Glossary of geology: American Geological Institute, Falls Church, VA, USA, p. 751.

Bath, A, 2009, Geology, geochronology and alteration of the Lowe Main Zone, Lorraine, alkalic porphyry Cu-Au-Ag±PGE deposit, north-central British Columbia: Unpub. PhD thesis, University of Tasmania, Hobart, p. 265.

Beane, R.E., 1974, Biotite Stability in the Porphyry Environment: Economic Geology, v. 69, p. 241-256.

Beane, R.E., and Titley, S.R., 1981, Porphyry copper deposits, Part II: Hydrothermal alteration and mineralisation, *in* Seventy-fifth anniversary volume, Skinner, B.J., ed., Society of Economic Geologists 75th Anniversary Volume, p. 235-269.

Begg, G., 1996, The structure and mineralisation history of the Emperor gold deposit, Fiji: Unpub. PhD thesis, Monash University, Melbourne, p. 466.

Begg, G., Loucks, R., Gray, D.R., Foster, D.A., Kent, A.J., and Cooke, D.R., 1997, Magmas, Fluids, and Tectonics: The Emperor Story, *in* New Developments in Research for Ore Deposit Exploration. SGEG Conference, Canberra, January 1997, Geological Society of Australia, Abstracts No 44, p. 7.

Bissig, T., 2007, Rocktypes at E43, Cowal district: PowerPoint presentation for Barrick Gold of Australia Ltd.

Bissig, T., Cooke, D.R., Simpson, K.A., and Tosdal, R.M., 2008, Shallow- and Deep-Level Alkalic Mineral Deposits: Developing an Integrated Exploration Model, Year 3 — Epithermal Module, Final update to sponsors, November 2008, Orange, NSW.

Blevin, P.L., 2002, The petrographic and compositional character of variably K-enriched magmatic suites associated with Ordovician porphyry Cu-Au mineralisation in the Lachlan Fold Belt, Australia: Mineralium Deposita, v. 37, p. 87-99.

Bodnar, R.J., 1993, Revised equation and table for determining the freezing point depression of H_2O-NaCl solutions: Geochemica et Cosmochimica Acta, v. 57, p. 683-684.

Bodnar, R.J., Reynolds, T.J., and Kuehn, C.A., 1985a, Fluid inclusions systematics in epithermal systems: Review in Economic Geology, v. 2, p. 73-97.

Bodnar, R.J., Burnham, C.W., and Sterner, S.M., 1985b, Synthetic fluid inclusion in natural quartz. III. Determination of phase equilibrium properties in the system H_2O-NaCl to 1000ºC and 1500 bars: Geochemica et Cosmochimica Acta, v. 49, p. 1861-1873.

Bonham, H.F., and Giles, D.L., 1983, Epithermal gold/silver deposits: the geothermal connection. Geothermal Resources Council, Special Report, v. 13, 257-262.

Borthwick, V.E.A., 2004, Characterisation of veining at the E42 gold deposit, Lake Cowal, NSW: Unpub. BSc (Hons) thesis, University of Sydney, p. 122.

Brathwaite, R.L., and Faure, K., 2002, The Waihi epithermal gold-silver base metal sulfide quartz vein system, New Zealand: Temperature and salinity controls on electrum and sulfide deposition: Economic Geology, v. 97, p. 269-290.

Brown, P.R.L., 1971, Mineralisation in the Broadlands geothermal field, Taupo volcanic zone New Zealand: Soc. Min. Geol. Jpn. Proc. IMA-IAGOD Mtg. Jpn, Special Issue, v. 12, p. 64-75.

Burnham, C.W., 1979, Magmas and hydrothermal fluids, *in* Barnes, H.L., ed., Geochemistry of Hydrothermal Ore Deposits, 2nd edition: New York, John Wiley, p. 71-136.

Burnham, C.W., 1997, Magmas and hydrothermal fluids, *in* Barnes, H.L., ed., Geochemistry of Hydrothermal Ore Deposits, 3rd edition: New York, John Wiley, p. 63-123.

Burnham, C. W., 1985, Energy Release in Subvolcanic Environments: Implications for Breccia Formation: Economic Geology, v. 80, p. 1515-1522.

Byrne, J., Tosdal, R., and Chamberlain, C., 2008, Magmatic-hydrothermal evolution and zonation of a breccia-centered Cu-Au alkalic porphyry: Southwest Zone, Galore Creek: Shallow- and Deep-Level Alkalic Mineral Deposits: Developing an Integrated Exploration Model, Year 3 — Porphyry Module, Final update to sponsors, September 2008, Williams Lake, Canada, p. 3.1 – 3.21.

Bywater, A., Williams, S., McInnes, P., and Dykmans, V., 2004, Development at the Cowal gold prospect, *in* Bierlien F.P. and Hough M.A., eds., Tectonics to Mineral Discovery – Deconstructing the Lachlan Fold Orogen, Geological Society of Australia Abstracts 74. p. 77-82.

Cameron, G.H., 1998, The hydrothermal evolution and genesis of the Porgera gold deposit: Unpub. PhD thesis, Australian National University, Canberra, p. 137.

Candela, G.H., 1989, Felsic magmas, volatiles, and metallogenesis: Reviews in Economic Geology, v. 4. p. 223-233.

Candela, P.A., and Blevin, P.L., 1995, Do some miarolitic granites preserve evidence of magmatic volatile phase permeability?: Economic Geology, v. 90, p. 2310-2316.

Cannell, J., 2003, Lithological units of the E42 deposit, description, classification and depositional setting: Unpub. internal report, Barrick Gold of Australia Ltd., p. 36.

Cannell, J., 2004, El Teniente porphyry Cu-Mo deposit: Unpub. PhD thesis, University of Tasmania, Hobart, p. 299.

Cannell, J., Cooke, D.R., Walshe, J.L., and Stein, H., 2005, Geology, mineralisation, alteration and structural evolution of the El Teniente porphyry Cu-Au deposit: Economic Geology, v. 100, p. 979-1003.

Carman, G.D., 1994, Genesis of the Ladolam gold deposit, Lihir Island, Papua New Guinea: Unpub. PhD thesis, Monash University, Melbourne, p. 279.

Carman, G.D., 2003, Geology, mineralisation and hydrothermal evolution of the Ladolam gold deposit, Lihir Island, Papua New Guinea: Society of Economic Geologists, Special Publication No.10, p. 247-284.

Chappell, B.W., and White, A.J.R., 1984, I- and S-type; granites in the Lachlan fold belt, southeastern Australia, *in* Xu, K., and Tu, G., eds., Geology of granites and their metallogenetic relations; proceedings of the international symposium, Beijing, China, Sci.Press, p. 87-101.

Carr, G.R., Dean, J.A., Suppel, D.W., and Heithersay, P.S., 1995, Precise lead isotope fingerprinting of hydrothermal activity associated with Ordovician to Carboniferous metallogenic events in the Lachlan fold belt of New South Wales: Economic Geology, v. 90, p. 1467-1505.

Cooke, D.R., and Bloom, M.S., 1990, Epithermal and subjacent porphyry mineralisation, Acupan, Baguio District, Philippines; a fluid-inclusion and paragenetic study: Journal of Geochemical Exploration, v. 35, p. 297-340.

Cooke, D.R., and McPhail, D.C., 1996, Telluride mineralisation in low sulfidation epithermal veins; contributions of magmatic volatiles: Abstracts - Geological Society of Australia, v. 41, p. 96.

Cooke, D.R., and Simmons, S.F., 2000, Characteristics and genesis of epithermal gold deposits: Economic Geology Reviews, v. 13, p. 221-244.

Cooke, D.R., and McPhail, D.C., 2001, Epithermal Au-Ag-Te mineralisation, Acupan, Baguio district, Philippines: Numerical simulations of mineral deposition: Economic Geology, v. 96, p. 109-131.

Cooke, D.R., Wilson, A.J., and Davies, A.G.S., 2004, Characteristics and genesis of porphyry copper-gold deposits, *in* Cooke, D. R., Deyell, C.L., Pongratz, J., eds., 24 Carat Gold Workshop Hobart: Hobart, CODES special publication No 5, University of Tasmania, p.17-34.

Cooke, D.R., Hollings, P., and Walsh, J.L., 2005, Giant porphyry deposits: Characteristics, distribution, and tectonic controls: Economic Geology, v. 100, p. 801-818.

Cooke, D.R., Chamberlain, C., and Tosdal, R., 2006, Porgera Au Mine, PNG: Shallow- and Deep Level Alkalic Mineral Deposits: Developing an Integrated Exploration Model. Sponsors meeting, Year 1-Epithermal Module Report, v. 1, p. 2.1-2.22.

Cooke, D.R., Wilson, A.J., House, M.J., Wolfe, R.C., Walshe, J.L., Lickfold, V., and Crawford,

A.J., 2007, Alkalic porphyry Au-Cu and associated mineral deposits of the Ordovician to Early Silurian Macquarie Arc, New South Wales: Australian Journal of Earth Sciences, v. 54, p. 445-463.

Corbett, G.J., and Leach, T.M., 1998, Southwest Pacific rim gold-copper systems: Structure, alteration and mineralisation: Society of Economic Geologists Special Publication No. 6, p. 236.

Craig, H., 1957, Isotopic standards of carbon and oxygen and corrective factors for mass spectrographic analysis of carbon dioxide: Geochemica et Cosmochimica Acta, v. 12. p. 133-149.

Crawford, A.J., and Keays, R.R., 1987, Petrogenesis of Victorian Cambrian tholeiites and implications for the origin of associated boninites: Journal of Petrology, v. 28, p. 1075-1109.

Crawford, A.J., Corbett, K.D., and Everard, J.L., 1992, Geochemistry of the Cambrian Volcanic-Hosted Massive Sulfide-Rich Mount Read Volcanics, Tasmania, and Some Tectonic Implications: Economic Geology, v. 87, p. 597-619.

Crawford, A.J., 1999, Lithogeochemistry and correlations of the Junee-Parkes-Narromine belt: an update: Hobart, Centre for Ore Deposit Research, p. 44.

Crawford, A.J., Meffre, S., Squire, R.J., Barron, L.M. and Falloon, T.J., 2007a, Middle and Late Ordovician magmatic evolution of the Macquarie Arc, Lachlan Orogen, New South Wales: Australian Journal of Earth Sciences, v. 54, p. 181-214.

Crawford, A.J., Cooke, D.R. and Fanning, C.M., 2007b, Geochemistry and age of magmatic rocks in the unexposed Narromine, Cowal and Fairholme Igneous Complexes in the Ordovician Macquarie Arc, central western New South Wales, Australian Journal of Earth Sciences, v. 54, p. 243-271.

Danyushevsky, L.V., Robinson, P., McGoldrick, P., Large, R., and Gilbert, S., 2003, LA-ICPMS of sulfides: Evaluation of an XRF glass disc standard for analysis of different sulfide matrixes: Goldschmidt Conference Abstracts, p. 73.

Danyushevsky, L.V., Robinson P., Gilbert, S., Norman, M., Large, R., Mc-Goldrick, P., and Shelley, J.M.G., A technique for routine quantitative multi-element analysis of sulphide minerals by laser ablation ICP-MS: Geochemistry: Exploration, Environment, Analysis (in press).

Davidson, J., Turner, S., Handley, H., Macpherson, C., and Dosseto, A., 2007, Amphibole “sponge” in arc crust?: Geology, v. 35, p. 787-970.

Davies, A.G.S., 2002, Geology and Genesis of the Kelian Gold Deposit, East Kalimantan, Indonesia: Unpub. PhD thesis, University of Tasmania, p. 404.

Davies, A.G.S., Cooke, D.R., Gemmell, J.B., van Leeuwen, T., Cesare, P., and Hartshorn, G., 2008, Hydrothermal Breccias and Veins at the Kelian Gold Mine, Kalimantan, Indonesia: Genesis of a Large Epithermal Gold Deposit: Economic Geology, v. 103, p. 717-757.

Deer, W.A., Howie, R.A., and Zussman, J., 1992, An Introduction to the Rock Forming Minerals: London, Longman, Green and Co. Ltd, p. 223-247.

Deyell, C.L., 2005, Sulfur isotope zonation at the Mt Polley alkalic porphyry Cu-Au deposit, British Columbia, Canada, *in* Mao, J., and Bierlein, F.P., eds., Mineral deposit research: meeting the global challenge (8th Biennial SGA meeting), p. 373-376.

Deyell, C.L., Tosdal, R., 2005, Sulfur isotopic zonation in alkalic porphyry Cu-Au systems II: application to mineral exploration in British Columbia, geological fieldwork: a summary of field activities and current research, 2005-1. p. 191- 208.

Dilles, J.H., Einaudi, M.T., Proffett, J.M., and Barton, M.D., 2000, Overview of the Yerington porphyry copper district: magmatic to nonmagmatic sources of hydrothermal fluids: their flow paths and alteration effects on rocks and Cu-Mo-Fe-Au ores: Society of Economic Geologists Guidebook Series, v. 32, p. 55-66.

Dilles, J.H., Farmer, G.L., and Field, C.W., 1995, Sodium-calcium alteration by non-magmatic saline fluids in porphyry copper deposits: results from Yerington, Nevada, *in* Thompson, J.F.H., ed., Magmas, Fluids and Ore Deposits Short Course Volume 23, Mineralogical Association of Canada, p. 309-338.

Drummond, S.E., and Ohmoto, H., 1985, Chemical evolution and mineral deposition in boiling hydrothermal systems: Economic Geology, v. 80, p. 126-147.

Dykmans, V.J., 2004a, Comparison of structures between E41 and E42: Unpub. internal report, Barrick Gold of Australia Ltd., p. 21.

Dykmans, V.J., 2004b, Cowal Gold Project – Geotech Report: Unpub. internal report, Barrick Gold of Australia Ltd., p. 124.

Einaudi, M.T., 1997, Mapping altered and mineralised rocks: an introduction to the 'Anaconda Method': Stanford University Guidebook, p. 10.

Einaudi, M.T., Meinert, L.D., and Newberry, R.J., 1981, Skarn Deposits: 75th Anniversary Volume, p. 317-391.

Einaudi, M.T., Hedenquist, J.W., and Inan, E., 2003, Sulfidation state of fluids in active and extinct hydrothermal systems: Transitions from porphyry to epithermal environments: Society of Economic Geologists Special Publication 10, p. 285-314.

Faure, K., Matsuhisa, Y., Metsugi, H., Mizota, C., and Hayashi, S., 2002, The Hishikari Au-Ag epithermal deposit, Japan: Oxygen and hydrogen isotope evidence in determining the source of paleohydrothermal fluids: Economic Geology, v. 97, p. 481-498.

Field, C.W., and Fifarek, R.H., 1986, Light stable isotope systematics in the epithermal environment, *in* Berger, B.R., and Bethke, P.M., eds., Geology and geochemistry of epithermal systems, Society of Economic Geologists, Review in Economic Geology, v. 2, p. 99-128.

Fleming, A.W., Handley, G.A., Williams, K.L., Hills, A.L., and Corbett, G.J., 1986, The Porgera gold deposit, Papua New Guinea: Economic Geology: v. 81, p. 660-680.

Floyd, P.A., and Winchester, J.A., 1975, Magma type and tectonic setting discrimination using immobile elements: Earth and Planetary Science Letters, v. 27, p. 103-131.

Fournier, R.O., 1987, Conceptual models of brine evolution in magmatic-hydrothermal systems: U.S. Geological Survey Professional Paper 1350, v. 2, p. 1487-1506.

Fournier, R.O., 1999, Hydrothermal Processes Related to Movement of Fluid from Plastic into Brittle Rock in the Magmatic-Epithermal Environment: Economic Geology, v. 94. p. 1193-1211.

Frikken, P., 2004, Breccia-hosted Cu-Mo mineralisation, Rio Blanco, Chile: Unpub. PhD thesis, University of Tasmania, Hobart, p. 248.

Garwin, S., 2002, The geological setting of intrusion-related hydrothermal systems near the Batu Hijau porphyry copper-gold deposit, Sumbawa, Indonesia: Society of Economic Geologists, Special Publication No. 9, p. 333 – 366.

Gebre-Mariam, M., Hagemann, S.G., and Groves, D.I., 1995, A classification scheme for epigenetic Archaean lode-gold deposits: Mineralium Deposita, v. 30, p. 408-410.

Gemmell, J.B., Sharpe, R., Jonasson, I.R., and Herzig, P.M., 2004, Sulfur isotope evidence for magmatic contributions to submarine and subaerial gold mineralisation: conical seamount and the Ladolam gold deposit, Papua New Guinea: Economic Geology, v. 99, p. 1711-1725.

Gemmell, J.B., 2007, Hydrothermal Alteration Associated with the Gosowong Epithermal Au-Ag Deposit, Halmahera, Indonesia: Mineralogy, Geochemistry, and Exploration Implications: Economic Geology, v. 102, p. 893-922.

Gill, J.B., 1981, Orogenic Andesites and Plate Tectonics, Heidelberg, Springer-Verlag, p. 390.

Girvan, S.W., 1992, Geology and mineralisation of the Copper Hill porphyry copper-gold deposit, near Molong, New South Wales: Unpub. BSc (Hons) thesis, Australian National University, Canberra.

Glen, R.A., Walshe, J.L., Barron, L.M. and Watkins, J.J., 1998, Ordovician convergent-margin volcanism and tectonism in the Lachlan sector of east Gondwana: Geology, v. 26, p. 751-754.

Glen, R.A. and Walshe, J.L., 1999, Cross-structures in the Lachlan Orogen: the Lachlan Transverse Zone example: Australian Journal of Earth Sciences, v. 46, p. 641-658.

Glen, R.A. and Fleming, G.D., 2000, Interpreted basement geology, central part of the Junee-Narromine Volcanic Belt, NSW (S/I, 55-3, 55-7, 55-11) 1:500 000 scale, Geological Survey of New South Wales, Sydney.

Glen, R.A., 2005, The Tasmanides of eastern Australia, *in* Vaughan, A.P.M., Leat, P.T. and Pankhurst, R.J., eds., Terrane Processes at the Margins of Gondwana: Geological Society of London, Special Publications, v. 246, p. 23-96.

Glen, D., 2006, The Lachlan Orogen: New boundaries, new data, new ideas, new deposits, *in* Lewis, P. C., ed., Mineral Exploration Geoscience in New South Wales, SMEDG Mines and Wines Conference, Cessnock NSW, Extended Abstract, p. 1-6.

Glen, R.A., Meffre, S. and Scott, R.J., 2007a, Benambran orogeny in the eastern Lachlan Orogen, Australia, Australian Journal of Earth Sciences, v. 54, p. 385-415.

Glen, R.A., Crawford, A.J., Percival, I.G., and Barron, L.M., 2007b, Early Ordovician development of the Macquarie Arc, Lachlan Orogen, New South Wales: Australian Journal of Earth Sciences, v. 54, 167-179.

Glen, R.A., Crawford, A.J. and Cooke, D.R., 2007c, Tectonic setting of porphyry Cu-Au mineralisation in the Ordovician – Early Silurian Macquarie Arc, eastern Lachlan Orogen, New South Wales: Australian Journal of Earth Sciences, v. 54, p. 465-479.

Glen, R.A., Spencer, R., Willmore, A., David, V. and Scott, R.J., 2007d, Junee-Narromine Volcanic Belt, Macquarie Arc, Lachlan Orogen, New South Wales: components and structure: Australian Journal of Earth Sciences, v. 54, p. 215-241.

Goldstein, R.H., and Reynolds, T.J., 1994, Systematics of fluid inclusions in diagenetic minerals: Society of Sedimentary Geology Short Course, v. 31, p.199.

Gray, D.R. and Foster, D.A., 2004, Tectonic evolution of the Lachlan Orogen, southeastern Australia: historical review, data synthesis and modern perspectives, Australian Journal of Earth Sciences, v. 51, p. 773-817.

Gray, N., Mandyczewsky, A., and Hine, R., 1995, Geology of the zoned gold skarn system at Junction Reefs, New South Wales: Economic Geology, v. 90, p. 1533-1552.

Green, T.H., 1980, Island arc and continent-building magmatism; a review of petrogenic models based on experimental petrology and geochemistry: Tectonophysics, v. 63, p. 367-385.

Groves, D.I., Goldfarb, R.J., Robert, F., and Hart, J.R., 2003, Gold Deposits in Metamorphic Belts: Overview of Current Understanding, Outstanding Problems, Future Research, and Exploration Significance: Economic Geology, v. 98, p.1-29.

Gustafson, W., 1974, The Stability of Andradite**,** Hedenbergite, and Related Minerals in the System Ca-Fe-Si-O-H: Journal of Petrology No 3, v. 15, p. 455-496.

Gustafson, L.B., and Hunt, J.P., 1975, The porphyry copper deposit at El Salvador, Chile: Economic Geology, v. 70, p. 857-912.

Haas, J.L., 1971, The Effect of Salinity on the Maximum Thermal Gradient of a Hydrothermal System at Hydrostatic Pressure: Economic Geology, v. 66, p. 940-946.

Hall, A.J., Banks, D., Fallick, A.E., and Hamilton, P.J., 1989, An hydrothermal origin for copper-impregnated prehnite and analcime from Boylestone Quarry, Barrhead, Scotland: Journal of the Geological Society No 4, v. 146, p. 701-713.

Halley, S., 2009, Mineral Mapping – Concepts of chemical Gradients: Ore Deposits Geochemistry, Hydrology and Geochronology Shortcourse, CODES, University of Tasmania.

Harper, B.L., 2000, Hydrothermal alteration at the Ridgeway porphyry gold-copper deposit, NSW: Unpub. BSc (Hons) thesis, University of Tasmania, Hobart, p. 130.

Harris, A.C., and Golding, S.D., 2002, New evidence of magmatic-fluid related phyllic alteration: Implications for the genesis of porphyry Cu deposits: Geology, v. 30, p. 335-338.

Harris, A., Kamenetsky, V.S., and White, N., 2004, The magmatic hydrothermal transition: Volatile separation in silicic rocks at Bajo de la Alumbrera porphyry Cu-Au deposit, NW Argentina: Resource Geology, v. 54, p. 341-356.

Harris, A.C., Golding, S.D., and White, N.C., 2005, Bajo de la Alumbrera Copper-Gold Deposit: Stable Isotope Evidence for a Porphyry-Related Hydrothermal System Dominated by Magmatic Aqueous Fluids: Economic Geology, v. 100, p. 863-886.

Harris, A.C., Cooke, D.R., Tosdal, R.M., and Golding, S.D., 2008, Porphyry-related ore deposits of the Lachlan Fold Belt, New South Wales, Australia: PACRIM Congress, The Pacific Rim: Mineral Endowment, Discoveries and Exploration Frontiers, Field Trip No.1., p. 36.

Hattori, K.H., and Keith, J.D., 2001, Contribution of mafic melts to porphyry copper mineralisation: evidence from Mount Pinatubo, Philippines, and Bingham Canyon, Utah, USA: Mineralium Deposita, v. 36, p. 799-806.

Hayashi, K.I., and Ohmoto, H., 1991, Solubility of gold in NaCl- and H_2S-bearing aqueous solutions at 250-350ºC: Geochemica et Cosmochimica Acta, v. 55, p. 2111-2126.

Hayba, D.O., Bethke, P.M., Heald, P., and Foley, N.K., 1985, Geologic, mineralogic and geochemical characteristics of volcanic-hosted epithermal precious metal deposits: Reviews in Economic Geology, v. 2, p. 129-167.

Hedenquist, J.W., and Henley, R.W., 1985, Hydrothermal eruptions in the Waiotapu geothermal system, New Zealand: Their origin, associated breccias, and relation to precious metal mineralisation: Economic Geology, v. 80, p. 1640–1668.

Hedenquist, J.W., and Lowenstern, J.B., 1994, The role of magmas in the formation of hydrothermal ore deposits: Nature, v. 370, p. 519-527.

Hedenquist, J.W., and Richards, J.P., 1998, The influence of geochemical techniques on the development of genetic models for porphyry copper deposits, *in* Richards J.P., and Larson, P.B., eds., Reviews in Economic Geology Volume 10. Techniques in Hydrothermal Ore

Deposits Geology, Littleton, Society of Economic Geologists, p. 235-256.

Hedenquist, J.W., Arribas, A., Jr., and Reynolds, T.J., 1998, Evolution of an intrusion-centered hydrothermal system: Far Southeast-Lepanto porphyry-epithermal Cu-Au deposits, Philippines: Economic Geology, v. 93, p. 373-405.

Heithersay, P.S., and Walsh, J.L., 1995, Endeavour 26 North: A porphyry copper-gold deposit in the Late Ordovician shoshonitic Goonumbla Volcanic Complex, New South Wales, Australia: Economic Geology, v. 90, p. 1506-1532.

Heithersay, P.S., O'Neill, W.J., Van der Helder, P., Moore, C.R. and Harbon, P.G., 1990, Goonumbla porphyry copper district – Endeavour 26 North, Endeavour 22 and Endeavour 27 copper-gold deposits, *in* Geology of the Mineral Deposits of Australia and Papua New Guinea, Hughes, F.E., eds., The Australian Institute of Mining and Metallurgy: Melbourne, p. 1385-1398.

Henley, R.W., 1985, The geothermal framework of epithermal deposits: Reviews in Economic Geology, v. 2, p. 1-24.

Henry, A.D., 2008, Endeavour 42 (New South Wales): Fracture Reactivation and Gold Mineralization in the Epithermal Environment Structural evolution of the Endeavour 42 gold deposit, NSW, Australia: Unpub. MSc thesis, Geological Sciences, University of British Columbia, Vancouver, p. 197.

Hoefs, J., 1987, Stable isotope geochemistry, 3rd edition, Springer-Verlag, Berlin.

Holliday, J.R., Wilson, A.J., Blevin, P.L., Tedder, I.J., Dunham, P.D. and Pfitzner, M., 2002, Porphyry gold-copper mineralisation in the Cadia district, eastern Lachlan Fold Belt, New South Wales, and its relationship to shoshonitic magmatism: Mineralium Deposita, v. 37, p. 100-116.

Huston, D. L., Power, M., Gemmell, J. B., and Large, R. R., 1995, Design, calibration and geological application of the first operational Australian laser ablation sulfur isotope microprobe: Australian Journal of Earth Science, v. 42, p. 549-555.

Ingpen, I.A., 1995, Geological, structural and tectonic history of the Temora, West Wyalong, Grenfell and Forbes area, New South Wales: implications for the structural controls on gold and copper mineralization: Unpub. MSc thesis, Monash University, Melbourne, p. 197.

Irvine, T.N., and Baragar, W.R.A., 1971, A guide to the chemical classification of the common volcanic rocks: Canadian Journal of Earth Sciences, v. 8, p. 523-548.

Izawa, E., Urashima, Y., Ibaraki, K., Suzuki, R., Yokoyama, T., Kawasaki, K., Koga, A., and Taguchi, S., 1990, The Hishikari deposit, high grade epithermal veins in Quaternary volcanics of southern Kyushu, Japan: Journal of Geochemical Exploration, v. 36, p. 1-56.

Jackson, M., 2008, Evolution of the northeast zone breccia body, Mount Polley mine, British Columbia: Unpub. MSc thesis, Geological Sciences, University of British Columbia, Vancouver, p. 245.

Jago, P., 2008, Metal- and alteration-zoning, and hydrothermal flow paths at the moderately-tilted, silica-saturated Mt. Milligan Cu-Au alkalic porphyry deposit: MSc thesis, Geological Sciences, University of British Columbia, Vancouver, p. 227.

Jensen, E.P., 2003, Magmatic and hydrothermal evolution of the Cripple Creek gold deposit, Colorado, and comparison with regional and global magmatic – hydrothermal systems associated with alkalic magmatism: Unpub. PhD thesis, University of Arizona, Tuscon, p. 801.

Jensen, E.P., and Barton, M.D., 2000, Gold deposits related to alkaline magmatism: Reviews in Economic Geology, v. 13, p. 279-314.

Johnson, H.D., and Baldwin, C.T., 1996, Shallow clastic seas, *in* Reading, H. G., ed., Sedimentary environments: processes, facies and stratigraphy. Blackwell Sciences, Cambridge, p. 232-280.

Jones, G.J., 1985, The Goonumbla porphyry copper deposits, New South Wales: Economic Geology and the Bulletin of the Society of Economic Geologists, v. 80, p. 591-613.

Joplin, G.A., 1968, The shoshonite association: a review: J. geol. Soc. Aust., v. 15(2), p. 275-294.

Kay, S.M., Mpodozis, C., and Coira, B., 1999, Neogene magmatism, tectonism, and mineral deposits of the Central Andes (22* to 33* latitude), *in* Skinner, B.J., ed., Geology and Ore Deposits of the Central Andes, Fort Collins, Society of Economic Geologists, p. 27-59.

Keith, J.D., Christiansen, E.H., Maughan, D.T., and Waite, K.A., 1998, The role of mafic alkaline magmas in felsic porphyry-Cu and Mo systems, *in* Lents, D.R., ed., Mineralised intrusion-related skarn systems. Shortcourse Handbook, v. 26, Ottawa, Mineralogical Association of Canada, p. 211-243.

Kerridge, J.F., 1985, Carbon, hydrogen, and nitrogen in carbonaceous chondrites: abundances and isotopic compositions in bulk samples: Geochemica et Cosmochimica Acta, v. 49, p. 1707-1714.

Kolkert, R., 1998, Carbonate-base metal veins peripheral to the Goonumbla Cu-Au deposits – vectors to mineralised centre?: Unpub. BSc (Hons) thesis, University of Tasmania, Hobart, p. 144.

Kusakabe, M., Hori, M., and Matsuhisa, Y., 1990, Primary mineralisation-alteration of the El Teniente and Rio Blanco porphyry copper deposits, Chile. Stable isotopes, fluid inclusions, and $Mg^{2+}/Fe^{2+}/Fe^{3+}$ ratios of hydrothermal biotite, *in* Herbert, H.K., and Ho, S.E., eds., Stable isotopes and fluid processes in mineralisation: Perth, University of Western Australia Press, p. 244-256.

Kwak, T.A.P., 1990, Geochemical and temperature controls on ore mineralisation at Emperor gold mine, Vatukoula, Fiji: Journal of Geochemical Exploration, v. 36, p. 297-337.

Lang, J.R., and Titley, S.R., 1998, Isotopic and geochemical characteristics of Laramide

magmatic systems in Arizona and implications for the genesis of porphyry copper deposits: Economic Geology, v. 93, p.138-170.

Lang, J.R., Stanley, C.R., and Thompson, J.F.H., 1995a, Porphyry copper-gold deposits related to alkalic igneous rocks in the Triassic-Jurassic arc terranes of British Columbia, *in* Schroeter, T. G., ed., Porphyry Deposits of the Northern Cordillera of North America 46, Vancouver, Canadian Institute of Mining, Metallurgy and Petroleum, p. 581-592.

Lang, J.R., Stanley, C.R., Thompson, J.F.H., and Dunne, K.P.E., 1995b, Na-K-Ca magmatic-hydrothermal alteration in alkalic porphyry Cu-Au deposits, British Columbia, *in* Thompson, J.F.H., ed., Magmas, Fluids, and Ore Deposits. Mineralogical Association of Canada Shortcourse, Victoria, v. 23, p. 339-366.

Large, R.R., Maslennikov, V., Robert, F., Danyushevsky, L.V., and Chang, Z., 2007, Multistage sedimentary and metamorphic origin of pyrite and gold in the giant Sukhoi Log deposit, Lena gold province, Russia: Economic Geology, v. 102, p. 1232–1267.

Large, R.R., Danyushevsky, L., Hollit, C., Maslennikov, V., Meffre, S., Gilbert, S., Bull, S., Scott, R., Emsbo, P., Thomas, H., Singh, B., and Foster J., 2009, Gold and Trace Element Zonation in Pyrite Using a Laser Imaging Technique: Implications for the Timing of Gold in Orogenic and Carlin-Style Sediment-Hosted Deposits: Economic Geology, v. 102, p. 1232–1267.

Le Maitre, R.W., 1989, A classification of igneous rocks and glossary of terms: recommendations of the International Union of Geological Sciences Subcommision on the Systematics of Igneous Rocks, Oxford, Blackwell Scientific Publications, p. 193.

Lickfold, V., 2002, Intrusive history and volatile evolution of the Endeavour Cu-Au porphyry deposits, Goonumbla district, NSW, Australia: Unpub. PhD thesis, University of Tasmania, Hobart, p. 245.

Lickfold, V., Cooke, D.R., Smith, S.G., and Ullrich, T., 2003, Endeavour Cu-Au porphyry deposits, Northparkes, NSW – Intrusive history and fluid evolution: Economic Geology, v. 98, p. 1607-1636.

Lickfold, V., Cooke, D.R., Crawford, A.J., and Fanning, C.M., 2007, Shoshonitic magmatism and the formation of the Northparkes porphyry Cu-Au deposits, New South Wales: Australian Journal of Earth Sciences, v. 54, p. 417-444.

Longerich, H.P., Jackson, S.E., and Gunther, D., 1996, Laser ablation inductively coupled plasma mass spectrometric transient signal data acquisition and analyte concentration calculation: Journal Analytical Atomic Spectrometry, v. 11, p. 899–904.

Love, M.C., 1992, Discovery and geology of the Lake Cowal NSW gold deposit: Geological Society of Australia Abstracts 32, p. 61-62.

Lowell, J.D., and Guilbert, J.M., 1970, Lateral and Vertical Alteration-Mineralisation Zoning in Porphyry Ore Deposits: Economic Geology, v. 65, p. 373-408.

Masterman, G.J., White, N.C., Wilson, C.J.L., and Pape, D., 2002, High-sulfidation gold

deposits in ancient volcanic terranes: insights from the mid-Paleozoic Peak Hill deposit, NSW: Society of Economic Geologists Newsletter, v. 51, p.1-16.

Masterman, G.J., Cooke, D.R., Berry, R.F., Clark, A.H., Archibald, D.A., Mathur, R., Walshe, J.L., and Duran, M., 2005, Magmatic, alteration and mineralisation history of copper-molybdenum porphyry deposits and related copper-silver high sulfidation epithermal mineralisation in the Collahuasi district, northern Chile: Economic Geology, v.100, p. 673-690.

Maughan, D.T., Keith, J.D., Christiansen, E.H., Pulsipher, T., Hattori, K., and Evans, N.J., 2002, Contribution from mafic alkaline magmas to the Bingham porphyry Cu-Au-Mo deposit, Utah, USA: Mineralium Deposita, v. 37, p. 14-37.

McCrea, J.M., 1950, On the isotopic chemistry of carbonates and palaeotemperature scale: J. Chem. Phys., v. 18, p, 849-857.

McEwan, C.J.A., Fallick, A.E., and Rice, C.M., 1996, The Rosita Hills epithermal Ag-base metal deposits, Colorado, USA: Mineralium Deposita, v. 31, p. 41–51.

McInnes, P., 1997, Final Report – Lake Cowal Gold Corridor Drilling: Unpub. internal report, Barrick Gold of Australia Ltd., p. 9.

McInnes, P., Miles, I.N., Radclyfee, D. and Brooker, M., 1998, Endeavour 42 (E42) gold deposit, Lake Cowal, Geology of Australian and Papua New Guinean Mineral Deposits, Monograph series – Australian Institute of Mining and Metallurgy, v. 22, p. 581-585.

McInnes, P., 2003, Hydrothermal alteration and associated gold mineralization at the E42 gold deposit: Unpub. internal report, Barrick Gold of Australia Ltd., p. 23.

McInnes, P., 2006, E41 deposit: Unpub. internal report, Barrick Gold of Australia Ltd.

McPhie, J., Doyle, M., and Allen, R., 1993, Volcanic textures: a guide to the interpretation of textures in volcanic rocks: Hobart, CODES Key Centre, University of Tasmania, p. 196.

Meffre, S., Large, R.R., Scott, R., Woodhead, J., Chang, Z., Gilbert, S.E., Danyushevsky, L.V., Maslennikov, V., and Hergt, J.M., 2008, Age and pyrite Pb-isotopic composition of the giant Sukhoi Log sediment-hosted gold deposit, Russia: Geochimica et Cosmochimica Acta, v. 72(9), p. 2377-2391.

Meffre, S., Scott, R.J., Glen, R.A. and Squire, R., 2007, Re-evaluation of contact relationships between Ordovician volcanic belts and the quartz-rich turbidites of the Lachlan Orogen, Australian Journal of Earth Sciences, v. 54, p. 363-383.

Meinert, L.D., Hedenquist, J.W., Satoh, H., and Matsuhisa, Y., 2003, Formation of Anhydrous and Hydrous Skarn in Cu-Au Ore Deposits by Magmatic Fluids: Economic Geology, v. 98, p. 147-156.

Meyer, C., and Hemley, J.J., 1967, Wall rock alteration, *in* Barnes, H.L., ed., Geochemistry of Hydrothermal Ore Deposits, First Edition: New York, Holt, Rinehart and Winston, p. 166-235.

Micko, J., Tosdal, R., Simpson, K., Chamberlain, C., and Schwab, D., 2008, Controls and hydrothermal zonation of central zone mineralisation at the Galore Creek alkalic Cu-Au porphyry deposit, northwestern British Columbia: Shallow- and Deep-Level Alkalic Mineral Deposits: Developing an Integrated Exploration Model, Year 3 — Porphyry Module, Final update to sponsors, September 2008, Williams Lake, Canada, p. 2.1 – 2.27.

Miles N., Brooker M.R., 1998, Endeavour 42 deposit, Lake Cowal, NSW: a structurally controlled gold deposit: Australian Journal of Earth Sciences, v. 45, p. 837-847.

Miles, I.N., 1993, The paleovolcanology of the Late Ordovician Lake Cowal Volcanics, central New South Wales: Unpub. BSc (Hons) thesis, Monash University, Melbourne.

Miller, J.M., Dugdaloe, L.J. and Wilson, C.J.L., 2001, Variable hanging wall palaeotransport during Silurian and Devonian thrusting in the western Lachlan Fold Belt: missing gold lodes, synchronous Melbourne Trough sedimentation and Grampians Group fold interference: Australian Journal of Earth Sciences, v. 48, p. 901-909.

Morrison, G.W., 1980, Characteristics and tectonic setting of the shoshonitic rock association: Lithos, v. 13, p. 97-108.

Moyle, A.L., Doyle, B.J., Hoogvliet, H., and Ware, A.R., 1990, Ladolam gold deposit, Lihir Island: *in* Hughes, F.E., ed., Geology of the mineral deposits of Australia and Papua New Guinea, Volume 2, Monograph Series - Australasian Institute of Mining and Metallurgy, v. 14, p. 1793-1805.

Muller, D., Kaminski, K., Uhlig, S., Graupner, T., Herzig, P. M., and Hunt, S., 2002, The transition from porphyry- to epithermal gold mineralisation at Ladolam, Lihir Island, Papua New Guinea: a reconnaissance study: Mineralium Deposita, v. 37, p. 61-74.

Munroe, S., Johnston, A., Simpson, R. and Hillsdon, P., 2005, Cowal Gold Project: Structural controls on mineralization and target identification, internal report for Barrick Australia Ltd., SRK Consulting Engineers and Scientists, SRK Project Number BKG003, p. 61.

Muntean, J.L., and Einaudi, M.T., 2001, Porphyry-epithermal transition: Maricunga belt, northern Chile: Economic Geology, v. 96, p. 743-772.

Nesbitt, B., and Muehlenbachs, K., 1995, Geochemical studies of the origins and effects of synorogenic crustal fluids in southern Omineca Belt of British Columbia, Canada: Geological Society of America Bulletin, v. 107, p. 1033-1050.

Nixon, G.T., and Peatfield, G.R., 2003, Geological setting of the Lorraine Cu-Au porphyry deposit, Duckling Creek Syenite Complex, North-central British Columbia: BC Ministry of Mines and Energy, Open File Report 2003-4, p. 24.

Norman, D.K., Parry, W.T., and Bowman, J.R., 1991, Petrology and geochemistry of propylitic alteration at Southwest Tintic, Utah: Economic Geology, v. 86, p. 13-28.

Norrish, K., and Chappell, B.W., 1977, X-ray fluorescence spectrometry, *in* Zussman, J., ed.,

Physical methods in determinative mineralogy: London, Academic Press, p. 201-272.

Ohmoto, H., 1972, Systematics of Sulfur and Carbon Isotopes in Hydrothermal Ore Deposits: Economic Geology, v. 67, p. 551-577.

Ohmoto, H., and Rye, R.O., 1979, Isotopes of sulfur and carbon, in H.L. Barnes, ed., Geochemistry of hydrothermal ore deposits, 2nd edition: New York, Wiley, p. 491-559.

Ohmoto, H., 1986, Stable isotope geochemistry of ore deposits: Reviews in Mineralogy, v. 16, p. 491-559.

Ohmoto, H., and Goldfaber, M.B., 1997, Sulfur and carbon Isotopes, *in* Barnes, H.L., ed., Geochemistry of Hydrothermal Ore Deposits, 3rd edition: New York, John Wiley and Sons, p. 517-600.

O'Neil, J.R., and Taylor, H.P., 1967, The oxygen isotope and cation exchange chemistry of feldspars: American Mineralogist, v. 52, p. 1414-1437.

O'Neil, J.R., Clayton, R.N., and Mayeda, T.K., 1969, Oxygen isotope fractionation in divalent metal carbonates: J. Chem. Phys., v. 51, p. 5547-5558.

Pals, D.W., Spry, P.G., and Chryssoulis, S., 2003, Invisible gold and tellurium in arsenic-rich pyrite from the Emperor gold deposit, Fiji: Implications for gold distribution and deposition: Bulletin of the Society of Economic Geologists, v. 98, p. 479-493.

Parry, W.T., Ballantyne, J.T., and Jacobs, D.C., 1984, Geochemistry of hydrothermal sericite from Roosevelt Hot Springs and the Tintic and Santa Rita porphyry copper systems, Economic Geology, v. 79, p.72-86.

Pass, H., 2008, Geochemistry, alteration and mineralisation of long section 17-34, NE Zone, Mt Polley Cu-Au Porphyry Deposit: Shallow- and Deep Level Alkalic Mineral Deposits: Developing an Integrated Exploration Model. Sponsors meeting, Year 3 — Porphyry Module, Final update to sponsors, September 2008, Williams Lake, Canada, v. 1, p. 5.1-5.34.

Pearce, J.A., 1982, Trace element characteristics of lavas from destructive plate boundaries, *in* Thorpe, R.S., ed., Andesites; orogenic andesites and related rocks: Chichester, United Kingdom, John Wiley & Sons. p. 219.

Pearce, J.A., and Peate, D.W., 1995, Tectonic implications of the composition of volcanic arc magmas: Annual Reviews of Earth and Planetary Sciences, v. 23, p. 251-285.

Pearce, J.A., 1996, A User's Guide to Basalts Discrimination Diagrams, *in* Wyman, D.A., ed., Trace Element Geochemistry of Volcanic Rocks: Application for Massive Sulfide Exploration: Geological Association of Canada, Shortcourse Note Volume 12, p. 79-113.

Peccerillo, A., and Taylor, S.R., 1976, Geochemistry of Eocene calc-alkaline volcanic rocks from the Kastamonu area, northern Turkey: Contributions to Mineralogy and Petrology, v. 58, p.63-81.

Percival, I.G., Glen, R.A., 2007, Ordovician to earliest Silurian history of the Macquarie Arc, Lachlan Orogen, New South Wales: Australian Journal of Earth Sciences, v. 54, p. 143-165.

Perkins, C., Walshe, J.L. and Morrison, G., 1995, Metallogenic episodes of the Tasman Fold Belt system, eastern Australia, Economic Geology, v. 90, p. 1443-1466.

Pittard, K., 2006, Cowal Aeromagnetic and Gravity Interpretation: Unpub. internal report, Barrick Gold of Australia Ltd.

Pollard, P.J., and Taylor, R.G., 2002, Paragenesis of the Grasberg Cu-Au deposit, Irian Jaya, Indonesia: results from logging section 13: Mineralium Deposita, v. 37, p. 117-136.

Pontual, S., Merry, N., and Gamson, P., 1997, Spectral interpretation field manual: Spectral analysis and guides for mineral exploration, Ausspec International, p. 169.

Potter, R.W., 1977, Pressure corrections for fluid inclusion homogenization temperatures based on the volumetric properties of the system NaCl-H_2O: USGS, Journal of Resources, v. 5, p. 603-607.

Powell, C.M., 1984, Uluru and Adelaidean regimes: Ordovician to Earliest Silurian; marginal sea and island arc, *in* Veevers, J.J., ed., Phanerozoic Earth history of Australia., Oxford Geological Sciences Series 2, Oxford, United Kingdom, Clarendon Press, p. 290-308.

Purvis, A.C., 2002, Mineralogical report No. 8209: Unpub. internal report, Barrick Gold of Australia Ltd., April, p.33.

Radclyffe, D., 1995, Regional scale propylitic alteration in the Northparkes mineral field: Unpub. BSc (Hons) thesis, University of Tasmania, Hobart, p. 118.

Rae, A. J., Cooke, D. R., Phillips, D., Yeats, C., Ryan, C., and Hermoso, D., 2004, Spatial and temporal relationships between hydrothermal alteration assemblages at the Palinpinon geothermal field, Philippines: implications for porphyry and epithermal ore deposits: Society of Economic Geologists Special Publication No 10, p. 223-246.

Reyes, A.G., 1990, Petrology of Philippines geothermal systems and the application of alteration mineralogy of their assessment: Journal of Volcanology and Geothermal Research, v. 43, p. 279-309.

Rice, C.M., Harmon, R.S., and Shepherd, T.J., 1985, Central City, Colorado: the upper part of an alkaline porphyry molybdenum system: Economic Geology, v. 80, p. 1769-1796.

Richards, J.P., 1995, Alkalic-type epithermal gold deposits, a review, *in* Thompson, J.F.H., ed., Magmas, Fluids, and Ore Deposits. Mineralogical Association of Canada Shortcourse, Victoria, v. 23, p. 367-400.

Richards, J.P., 2003, Tectono-magmatic precursors for porphyry Cu-(Mo-Au) deposit formation: Economic Geology, v. 98, p.1515-1533.

Richards, J.P., and Kerrich, R., 1993, The Porgera gold mine, Papua New Guinea - magmatic

hydrothermal to epithermal evolution of an alkalic-type precious-metal deposit: Economic Geology, v. 88, p. 1017-1052.

Richards, J.P., and Noble, S.R., 1998, Application of Radiogenic Isotope Systems to the Timing and Origin of Hydrothermal Processes, *in* Larson, J.P., ed., Techniques in hydrothermal ore deposits geology, 10: Boulder, Society of Economic Geologists, Inc., p. 195-233.

Richards, J.P., 1992, Magmatic-epithermal transition in alkalic systems: Porgera gold deposit, Papua New Guinea: Geology, v. 20, p.547-550.

Richards, J.R., and Kerrich, R., 2007, Special Paper: Adakite-Like Rocks: Their Diverse Origins and Questionable Role in Metallogenesis: Economic Geology, v. 102, p. 537-576.

Rickwood, P.C., 1989, Boundary line within petrologic diagrams which use oxides of major and minor elements: Lithos, v. 22, p. 247-263.

Robinson B.W., Kusakabe M. 1975, Quantitative preparation of sulfur dioxide, for $^{34}S/^{32}S$ analyses, from sulfides by combustion with cuprous oxide: Anal Chem., v. 47, p. 1179-1181.

Robinson, P., 2003, XRF analysis of flux-fused discs: Geoanalysis 2003, The 5th International Conference on the Analysis of Geological and Environmental Materials, Abstracts, p. 90.

Roedder, E., 1984, Fluid inclusions: Mineralogical Society of America, Reviews in Mineralogy, v. 12, p. 644.

Roedder, E., and Bodnar, R.J., 1980, Geologic pressure determination from fluid inclusion studies: Annual Reviews of Earth and Planetary Sciences, v. 8, p. 263-301.

Rogers, N.W., and Setterfield, T.N., 1994, Potassium and incompatible-element enrichment in shoshonitic lavas from the Tavua volcano, Fiji: Chemical Geology, v. 118, p. 43-62.

Rollinson, H., 1993, Using geochemical data: evaluation, presentation, interpretation: London, UK, Longman Group UK Limited, p. 352.

Ronacher, E., Richards, J.P., and Johnston, M.D., 2000, Evidence for fluid phase separation in high-grade ore zones at the Porgera gold deposit, Papua new Guinea: Mineralium Deposita, v. 35, p. 683-688.

Ronacher, E., Richards, J.P., Villeneuve, M. E., and Johnston, M. D., 2002, Short life-span of the ore-forming system at the Porgera gold deposit, Papua New Guinea: laser $^{40}Ar/^{39}Ar$ dates for roscoelite, biotite, and hornblende: Mineralium Deposita, v. 37, p. 75-86.

Ronacher, E., Richards, J.P., Reed, M.H., Bray, C.J., Spooner, E.T.C., and Adams, P.D., 2004, Characteristics and evolution of the hydrothermal fluid in the north zone high grade area, Porgera gold deposit, Papua New Guinea: Economic Geology, v. 99, p. 843-867.

Rye, R.O., 1993, The Evolution of Magmatic Fluids in the Epithermal Environment: The

Stable Isotope Perspective: Economic Geology, v. 88, p. 733-753.

Sack, R.O., Carmichael, I.S.E., Rivers, M., and Ghiorso, M.S., 1980, Ferric-ferrous equilibria in natural silicate liquids at 1 bar: Contributions to Mineralogy and Petrology, v. 75, p. 369-376.

Sanematsu, K., Watanabe, K., and Duncan, R.A., 2006, The history of vein formation determined by Ar-40/Ar-39 dating of adularia in the Hosen-1 vein at the Hishikari epithermal gold deposit, Japan: Economic Geology, v. 101, p. 685-698.

Scheibner, E., 1973, A plate tectonic model of the Palaeozoic tectonic history of New South Wales: Journal of the Geological Society of Australia, v. 20, p. 405-426.

Schidlowski, M., 1987, Application of stable isotopes to early biochemical evolution on earth: Annual Reviews of Earth and Planetary Sciences, v. 15, p. 47-72.

Seedorff, E., Dilles, J.H., Proffett, J.M., and Einaudi, M.T., 2005, Porphyry Deposits: Characteristics and Origin of Hypogene Features: Economic Geology 100th Anniversary Volume, p. 251-298.

Shannon, S.S. Jr., Finch, R.J., Ikramuddin, M., and Mutschler, F.E., 1983, Possible sedimentary sources of sulfur and copper in alkaline-suite porphyry copper system: The Geological Society of America, 96th Annual Meeting, Abstracts with programs, v. 15, p. 684.

Sharp, Z.D., 1990, Laser-based microanalytical method for the in situ determination of oxygen isotope ratios of silicates and oxides: Geochimica et Cosmochimica Acta, v. 54, p. 1353-1357.

Sheppard, S.M.F., and Gilg, H.A., 1996, Stable isotope geochemistry of clay minerals: Clay Minerals, v. 31, p. 1-24.

Sheppard, S.M.F., Nielsen, R.L., and Taylor, H.P.Jr., 1971, Hydrogen and oxygen isotope ratios in minerals from porphyry copper deposits: Economic Geology, v. 66, p. 515-542.

Shinohara, H., and Hedenquist, J.W., 1997, Constraints on magma degassing beneath the Far-Southeast porphyry Cu-Au deposit, Philippines: Journal of Petrology, v. 38(12), p. 1741-1752.

Sillitoe, R.H., 1973, The Tops and Bottoms of Porphyry Copper Deposits: Economic Geology, v. 68, p. 799-815.

Sillitoe, R.H., 1985, Ore-Related Breccias in Volcanoplutonic Arcs: Economic Geology, v. 80, p. 1467-1514.

Sillitoe, R.H., 1989, Gold deposits in western Pacific island arcs: the magmatic connection, in Keays, R.R., Ramsay, W. R. H., and Groves, D. I., ed., The geology of gold deposits: the perspective in 1988, Economic Geology Monograph 6, New Have, CT, The Economic Geology Publishing Company, p. 274-291.

Sillitoe, R.H., 1994, Erosion and Collapse of Volcanoes – Cause of Telescoping in Intrusion-

Centered Ore-Deposits: Geology, v. 22, p. 945-948.

Sillitoe, R.H., 2000, Gold-rich porphyry deposits; descriptive and genetic models and their role in exploration and discovery: Reviews in Economic Geology, v. 13, p. 315-345.

Sillitoe, R.H., 2002, Some metallogenic features of gold and copper deposits related to alkaline rocks and consequences for exploration: Mineralium Deposita, v. 37, p. 4-13.

Sillitoe, R.H., and Hedenquist, J.W., 2003, Linkages between volcanotectonic settings, ore-fluid compositions, and epithermal precious-metal deposits: Society of Economic Geologists Special Publication No. 10, p. 315-343.

Simmons, S.F., 1995, Magmatic contribution to low-sulfidation epithermal deposits: Magmas, fluids and ore deposits: Mineralogical Society of Canada Shortcourse, v. 23, p. 455-477.

Simmons, S.F., and Browne, P.R.L., 1997, Saline fluid inclusions in sphalerite from the Broadlands-Ohaaki geothermal system: A coincidental trapping of fluids boiled toward dryness: Economic Geology, v. 92, p. 485-489.

Simmons, S.F., Gemmell, J.B., and Sawkins, F.J., 1988, The St. Nino silver-lead-zinc vein, Fresnillo district, Zacateccas, Mexico: Part II. Physical and chemical nature of ore forming solutions: Economic Geology, v. 83, p. 1619-1642.

Simmons, S.F., and Browne, P.R.L., 2000, Hydrothermal minerals and precious metals in the Broadlands-Ohaaki geothermal system: Implication for understanding low-sulfidation epithermal environments: Economic Geology, v. 95, p. 971-999.

Simmons, S.F., White, N. C., and John, D. A., 2005, Geological characteristics of epithermal precious and base metal deposits, Economic Geology 100th Anniversary Volume, p. 485-522.

Simpson, K., 2008, Volcanic and sedimentary facie architecture of E46. Shallow- and deep level alkalic mineral deposits: developing an integrated exploration model. Sponsors meeting, Year 3-Epithermal Module Report, poster.

Simpson, K., and Cooke, D.R., 2006, Volcanic facies architecture of the E46 prospect, Lake Cowal, NSW. Shallow- and deep level alkalic mineral deposits: developing an integrated exploration model. Sponsors meeting, Year 1-Epithermal Module Report, v.1, p. 6.1-6.7.

Skewes, A., Arevalo, A., Holmgren, C., and Stern C.R., 2001, Stable isotope evidence for formation of the mineralised breccias in the Los Bronces and El Teniente copper deposits, central Chile. Extended abstracts: III Simposio Sudamercano de Geologica Isotopica., Pucon, Chile, 2001, p. 531-534.

Smith, S., Mowat, B., and Sharry, M., 2004, Macquarie Arc porphyry Au-Cu systems; a review of the critical exploration features: Abstracts – Geological Society of Australia, v. 74, p. 51-62.

Smolonogov, S., 2003, Cowal gold project E42 deposit geology report: Unpub. internal report, Barrick Gold of Australia Ltd., p. 162.

Spry, P.G., Paredes, M.M., Foster, F., TruckLe Jack, S., and Chadwick, T.H., 1996, Evidence for a genetic link between gold-silver telluride and porphyry molybdenum mineralization at the Golden Sunlight Deposit, Whitehall, Montana; fluid inclusion and stable isotope studies: Economic Geology and the Bulletin of the Society of Economic Geologists, v. 91, p. 507-526.

Spycher, N.F., and Reed, M.H., 1989, Evolution of a Broadlands-type epithermal ore fluid along alternative P-T paths: Implications for the transport and deposition of base, precious and volatile metals: Economic Geology, v. 84, p. 328-359.

Strickland, T., 2005, The geology of the E42 breccia complex, Cowal Au deposit, NSW: Unpub. BSc (Hons) thesis, University of Tasmania, Hobart, p. 130.

Sun, S., and McDonough, W.F., 1989, Chemical and isotopic systematics of oceanic basalts: implications for mantle composition and processes, in Saunders, A.D., and Norry, M.J., eds., Magmatism in the ocean basins: Geological Society of London, Special Publication, 42, p. 313-345.

Takenouchi, S., and Kennedy, G.C., 1965, The solubility of carbon dioxide in NaCl solutions at high temperatures and pressures: Am. J. Sci., v. 263, p. 445-454.

Taylor, B.E., and Liou, J.G., 1978, The low-temperature stability of andradite in C-O-H fluids: American Mineralogist, v. 63, p. 378-393.

Taylor, B.E., 1987, Stable Isotope Geochemistry of Low Temperature Fluids: Mineralogical Association of Canada, v. 13, p. 337-445.

Taylor, H.P., 1974, The Application of Oxygen and Hydrogen Isotope Studies to Problems in Hydrothermal Alteration and Ore Deposition: Economic Geology, v. 69, p. 843-883.

Taylor, H.P. Jr., 1997, Oxygen and Hydrogen Isotope Relationships in Hydrothermal Mineral Deposits, *in* Barnes, H.L., ed., Geochemistry of Hydrothermal Ore Deposits, 3rd edition: New York, John Wiley, p. 229-302.

Thompson, T.B., Trippel, A.D., and Dwelley, P.C., 1985, Mineralised veins and breccias of the Cripple Creek district, Colorado: Economic Geology, v. 80, p. 1669-1688.

Titley, S.R., 1982, The style and progress of mineralisation and alteration in porphyry copper systems: Tuscon, University of Arizona Press, p. 93-116.

Titley, S.R., and Beane, R.E., 1981, Porphyry copper deposits, Part I: Geologic settings, petrology, and tectonogenesis, *in* Seventy-fifth anniversary volume, Skinner, B.J., ed., Society of Economic Geologists 75th Anniversary Volume, p. 214-235.

Tosdal, R.M., Wooden, J.L., and Bouse, R.M., 1999, Pb Isotopes, Ore Deposits, and Metallogenic Terranes, in Lambert, D.D., and Ruiz, J., eds., Review in Economic Geology, 12: Boulder, Society of Economic Geologists, Inc., p. 1-28.

Tosdal, R.M., and Richards, J.P., 2001, Magmatic and structural controls on the development

of porphyry Cu ± Mo ± Au deposits: Reviews in Economic Geology, v. 14, p. 157-181.

Tosdal, R.M., 2007, U-Pb SHRIMP-RG ages of 5 rocks from the Cowal district, NSW, Australia: Unpub. Barrick Gold of Australia Ltd. internal report, p. 20.

Tosdal, R.M., 2008, New U-Pb Ages of intrusive rocks from the Cowal district, NSW, Australia: Unpub. Barrick Gold of Australia Ltd. internal report, p. 23.

Tosdal, R.M., Cooke, D.R., Simpson, K., Bissig, T., Bath, A., Byrne, K., Jackson, M., Jago, P., Micko, J., Pass, H. and Chamberlain, C., 2008, Executive Summary: Shallow- and Deep-Level Alkalic Mineral Deposits: Developing an Integrated Exploration Model, Year 3 — Porphyry Module, Final update to sponsors, September 2008, Williams Lake, Canada, p. 1.1 – 1.16.

Townsend, A.T., Yu Z., McGoldrick P., and Hutton J.A., 1998, Precise lead isotope ratios in Australian galena samples by high resolution inductively coupled plasma mass spectrometry: Journal of Analytical Atomic Spectrometry, v. 13(8), p. 809-813.

Ulrich, T., and Heinrich, C.A., 2002, Geology and alteration geochemistry of the porphyry Cu-Au deposit at Bajo de la Alumbrera, Argentina: Economic Geology, v. 97, p. 1865-1888.

Ulrich, T., Gunthur, D., and Heinrich, C.A., 2002, The evolution of a porphyry Cu-Au deposit, based on LA-ICPMS analysis of fluid inclusions: Bajo de la Alumbrera, Argentina: Economic Geology, v. 97, p. 1889-1920.

van Leeuwen, T.M., Leach, T.M., Hawke, A.A., Hawke, M.M., 1990, The Kelian disseminated gold deposit, East Kalimantan, Indonesia: Journal of Geochemical Exploration, v. 35, p. 1-61.

Verbeeten, A.C., 1996, Petrology, geochemistry and tectonic implications of magmatism along the northern Hunter Ridge and on Kadavu Island Group, Fiji: Unpub. PhD thesis, University of Tasmania, Hobart.

Vityk, M.O., and Bodnar, R.J., 1998, Statistical microthermometry of synthetic fluid inclusions in quartz during decompression re-equilibration: Contributions to Mineralogy and Petrology, v. 132, p. 149-162.

Walshe, J.L., Heithersay, P.S. and Morrison, G.W., 1995, Toward an understanding of the metallogeny of the Tasman Fold Belt system: Economic Geology, v. 90, p. 1382-1401.

Watanabe, Y., and Hedenquist, J.W., 2001, Mineralogic and stable isotope zonation in the surface over the El Salvador porphyry copper deposit, Chile: Economic Geology, v. 96, p. 1775-1798.

White, N.C., and Hedenquist, J.W., 1990, Epithermal environments and styles of mineralisation: variations and their causes, and guidelines for exploration, Journal of Geochemical Exploration, v. 36, p. 445-474.

Willman, C.E., Vandenberg, A.H.M., and Morand, V.J., 2002, Evolution of the southeastern

Lachlan Fold Belt in Victoria: Australian Journal of Earth Sciences, v. 49, p. 271–289.

Wilson, M.R, and Kurtis, K.T., 1988, Geochemistry of porphyry-hosted Au-Ag deposits in the Little Rocky Mountains, Montana, Economic Geology, v. 83, p. 1329-1346.

Wilson, A.J., 2003, The geology, genesis and exploration context of the Cadia gold-copper porphyry deposits, New South Wales, Australia.: Unpub. PhD thesis, University of Tasmania, Hobart, p. 335.

Wilson, A.J., Cooke, D.R., and Harper, B.L., 2003, The Ridgeway gold-copper deposit: A high-grade alkalic porphyry deposit in the Lachlan fold belt, New South Wales, Australia: Economic Geology and the Bulletin of the Society of Economic Geologists, v. 98, p. 1637-1666.

Wilson, A.J., Cooke, D.R., and Harper, B.L., 2005, The Ridgeway gold-copper deposit: A high-grade alkalic porphyry deposit in the Lachlan fold belt, New South Wales, Australia - A reply: Economic Geology, v. 100, p. 177-178.

Wilson, A.J., Cooke, D.R., Harper, B.J., and Deyell, C.L., 2007a, Sulfur isotopic zonation in the Cadia district, southeastern Australia: exploration significance and implication for the genesis of alkalic porphyry gold-copper deposits: Mineralium Deposita, v. 42, p. 465-487.

Wilson, A.J., Cooke, D.R., Stein, H.J., Fanning, C.M., Holliday, J.R., and Tedder, I.J., 2007b, U-Pb and Re-Os geochronologic evidence for two alkalic porphyry ore-forming events in the Cadia district: Economic Geology, v. 102, p. 3-26.

Wilson, M.J., 1989, Igneous Petrogenesis, London, Unwin Hyman, p. 466.

Winchester, J.A., and Floyd, P.A., 1977, Geochemical discrimination of different magma series and their differentiation products using immobile elements: Chemical Geology, v. 20, p. 325-343.

Winter, J.D., 2001, An introduction to igneous and metamorphic petrology, Prentice Hall Inc. p. 697.

Wolfe, R.C., 1994, The geology, paragenesis and alteration geochemistry of the E48 Cu-Au porphyry, Goonumbla, NSW: Unpub. BSc (Hons) thesis, University of Tasmania, Hobart, p.102.

Wolfe, R.C., Cooke, D.R., Hooper, B., and Heithersay, P.S., 1996, A magmatic origin for late-stage sericite-alunite alteration at the Endeavour 48 Cu-Au porphyry deposit, Goonumbla, NSW, in Kennard, J. M., ed., Geoscience for the community; 13th Australian geological convention., Abstracts – Geological Society of Australia 41, Sydney, NSW, Australia, Geological Society of Australia, p. 480.

Wolfe, R.C., 2001, Geology of the Didipio region and paragenesis of the Dinkidi Cu-Au porphyry deposit: Unpub. PhD thesis, University of Tasmania, Hobart, p. 183.

Wurst, A.T., 2004, Geology and genesis of the Permata-Batu Badinding – Hulubai and Kerikil

Au-Ag low sulfidation epithermal deposits, Mt Muro, Kalimantan, Indonesia: Unpub. PhD thesis, University of Tasmania, Hobart, p. 330.

Wyborn, D., 1992, The tectonic significance of Ordovician magmatism in the eastern Lachlan fold belt: Tectonophysics, v. 214, p. 177-192.

Yu, Z., Robinson, P., and McGoldrick, P., 2001, An Evaluation of Methods for the Chemical Decomposition of Geological Materials for Trace Element Determination using ICP-MS: The Journal of Geostandards and Geoanalysis, v. 25, p. 199-217.

Zhang, X., and Spry, P.G., 1994, Petrological, mineralogical, fluid inclusion, and stable isotope studies of the Gies gold-silver telluride deposit, Judith Mountains, Montana. Economic Geology, v. 89, 602-627.

Zheng, Y.F., 1990, Carbon-oxygen isotopic covariation in hydrothermal calcite during degassing of CO2: Mineralium Deposita, v. 25, p. 246-250.

Zukowski, W., 2009, Intrusive history, vein paragenesis, hydrothermal alteration and sulfur isotope signature of the E43 Cu-Au porphyry prospect located in the southern part of the Cowal District, NSW, Australia: Unpub. internal report, Barrick Gold of Australia Ltd., p. 31.

Zukowski, W., and Cooke, D.R., 2009, Sulfur Isotopic Zonation Patterns at Endeavour 41, an Alkalic Epithermal Gold Deposit in the Cowal District, NSW, Australia: Vectors Towards a Magmatic Centre: 10th Biennial SGA Meeting, Smart Science for Mineral Exploration and Mining Conference Volume, Townsville, Australia, v. 1. p. 551-553.

Zukowski, W., Cooke, D.R., Deyell, C.L., and McInnes, P., 2007a, The E41 gold prospect, Cowal district, NSW – transitional porphyry-epithermal mineralisation in an alkalic mineral province: Ores and Orogenesis, Circum Pacific Tectonics, Geology Evolution and Ore Deposits, Tuscon, Arizona, p. 190.

Zukowski, W., Cooke, D.R., Deyell, C.L. and McInnes, P., 2007b, Alkalic epithermal or porphyry? Hydrothermal alteration and vein paragenesis at the E41 gold prospect, Cowal district, NSW, Australia: 9th Biennial SGA meeting, Dublin, p. 403-406.